

Development of tools for probing order in single crystals using electron and photon spectroscopy

Thesis by
Tejas Deshpande

In Partial Fulfillment of the Requirements for the
Degree of
Doctor of Philosophy

The logo for the California Institute of Technology (Caltech), featuring the word "Caltech" in a bold, orange, sans-serif font.

California Institute of Technology
Pasadena, California

2020
(Defended September 19, 2019)

Acknowledgments

I would like to start off by acknowledging my PhD advisor, David Hsieh, for giving me the opportunity to work on a project as challenging as designing and building, from the ground up, a low-temperature high-resolution angle-resolved photoemission spectroscopy (ARPES) setup. Building this ARPES system was one of the most intellectually rewarding exercise I had encountered in my student lifetime. I appreciate David placing enough faith in me to lead a project of this magnitude.

I would also like to thank all the lab members, with whom I have had fun conversations about the technical and scientific aspects of research, and life in general. These include the following former and current lab members: Darius Torchinsky, Xiaoyue Ni, Hao Chu, Liuyan Zhao, John Harter, Lauren Niu, Sophie Ding, Carina Belvin, Alberto de la Torre, Alon Ron, Honglie Ning, Junyi Shan, Nick Laurita, Omar Mehio, Chen Li, and Kyle Seyler.

I would like to thank one of the most influential collaborators on the ARPES project: Alexei Fedorov. I learned a great deal about design of ultrahigh vacuum (UHV) systems from Alexei. I was overwhelmed with generating a complex SolidWorks model of the ARPES UHV system. But I always felt safe knowing that Alexei would keep an eye on the overall system functionality and catch any bugs that I missed.

I would also like to thank members of the Rosenbaum lab, without whom I would not have had the opportunity to learn about high-pressure techniques. They include Dan Silevitch, Xiang Li, and Yishu Wang.

I am also indebted to Caltech faculty members who were very friendly and, over the years, were willing to offer advice when I needed it. They include: Lesik Motrunich, Jason Alicea, Jim Eisenstein, Keith Schwab, Maria Spiropulu, Nick Hutzler, John Preskill, Jeff Kimble, Xie Chen, Stevan Nadj-Perge, Marco Bernardi, and Sandra Troian.

I would like to especially acknowledge another faculty member, from McGill University, who served as my undergraduate thesis advisor and mentor: Prof. Thomas Szkopek. Despite not being able to interact with him as much as some of my mentors in graduate school, I am forever indebted to him for setting me, in my opinion, on the “right” path in my journey towards academic excellence. I would not be able to say this had I never met him: my journey is far from over.

A special thanks to the IQIM committee members who contributed in organizing the IQIM seminars and finally took over after I left: Phillippe Faist, Alexandre Cooper-Roy, Ioana Craiciu, Tomas Jochym O’Connor, Andrea Coladangelo, Arian Jadbabaie, Jeannette Kemmer, Yuval Baum, and David Aasen.

I would also like to thank following non-technical staff who helped me with matters outside of research: Connie Rodriguez, Marcia Brown, Loly Ekmekjian, Cherie Capri, Bonnie Leung, Su Naing,

Jo Ann Hasbach, Louisa Fung, Scott Curtis, Jonathan Gross, Alan Rice, Sofie Leon, Mika Walton, Christy Jenstad, Jennifer Blankenship, Elsa Echegaray, RuthAnne Bevier, Chris Mach, Douglas Rees, Kate McAnulty, Daniel Yoder, Laura Flower Kim, Lee Coleman, Nilza Santana-Castillo, and Cecilia Gamboa.

I got to learn a lot from the following machinists: John van Deusen, Bruce Dominguez, Mike Roy, Joe Benson, and Ali Kiani.

I would like to thank the folks in facilities who helped me with some of the technical aspects of lab work on campus which are considered traditionally “boring” to a graduate student. These facilities members include: Jean-Michel Reynolds, Larry Martinez, Orlando Villegas, Mario Gonzalez, Gabrielle Ceja, Tony Allen, Marcos Carretino, Terry Scott, Raul Turcios, Delmy Emerson, Rick Germond, Raymond Merlin, Ed Rhoads, Raul Hernandez, Octavio Padilla, Mike Cronk, and Mike Anchondo. I would like to especially thank the following custodial staff who helped me keep the ARPES lab clean: Francisco Compean, Tony Ford, and Mauro Hernandez.

I would also like to thank engineers: Phillip Vaziri and Shawn Callahan.

I would also like to thank the following friends with whom I have had fun times in graduate school: Min-Feng Tu, Evan Miyazono, Scott Geraedts, Paraj Titum Bhattacharjee, Shu-Ping Lee, Victor Quito, David Aasen, Jacob Lin, Bassam Helou, Anandh Swaminathan, Karthik Seetharam, Kun Woo Kim, Sujeet Shukla, Joseph Redford, Elena Murchikova, Evgeny Mozgunov, Alexander Kubica, and Harish Ravi.

I would like to thank Jonah Glick for helping me proofread the thesis.

The following friends helped me get a life outside Caltech: Jeff Abend, LaVonne Madrigal, the Singh & Purandare families, Stephen Peters, Nirav and Karina Shah, Hetal & Yogin Patel, and Suzanne Verreault.

I would also like to thank a few canine buddies who made graduate school tolerable in the last couple of year. They are: Amigo, Bernie, Chappy, Elon, Hopper, Janu, Leo, Mia, Mishka, Mojo, Shadow, Toro, and Zenith. I will miss you the most after leaving California.

Finally, I would like to thank my parents, Makarand and Pratibha, and my brother, Rajas, for being supporting of my life ambitions and making sacrifices that allowed me to get this far.

Special thanks to Linnea Larson as well.

Abstract

Discovering novel quantum phases of matter—from emergent behavior of strongly-correlated electrons in solid-state systems to superfluidity in quantum degenerate liquids—has been a cornerstone of condensed matter physics for many decades. In the most recent decades, however, the discovery of topological phases has emphasized the importance of symmetry, in addition to the conventional paradigm of symmetry breaking, in the definition of the order parameter, Ψ , and hence the quantum phase it represents. Naturally, novel experimental tools, capable of coupling to said order parameter, directly or indirectly, are required to discover conventionally elusive quantum phases. In this thesis, I will discuss experimental techniques, using both photon and electron spectroscopy, to study exotic electronic phases in single crystals. The thesis will be divided into two unequal parts: (a) the development of a high-energy-resolution sub-Kelvin angle-resolved photoemission spectroscopy apparatus to study 3D time-reversal invariant topological superconductors, and (b) the experiments exploiting the non-linear and time-resolved aspects of femtosecond lasers to study a broad class of many-body systems.

Contents

| | | |
|----------|--|-----------|
| 1 | Quantum many-body order | 1 |
| 1.1 | Introduction | 1 |
| 1.2 | Studying order in the Ginzburg-Landau framework | 1 |
| 1.2.1 | Local order parameter | 2 |
| 1.2.2 | Group theory | 2 |
| 1.2.3 | Ginzburg-Landau theory of second-order phase transitions | 2 |
| 1.2.4 | Quantum order in the Ginzburg-Landau framework | 4 |
| 1.3 | Topological phases | 6 |
| 1.3.1 | The quantum Hall effect | 6 |
| 1.3.2 | Topological insulators | 9 |
| 1.4 | Empirical measurement of the order parameter | 10 |
| 1.4.1 | Conventional probes | 10 |
| 1.4.2 | Topological probes | 11 |
| 1.5 | Outlook | 11 |
| 1.5.1 | Generalizing local and topological order parameters | 11 |
| 1.5.2 | Systems out of equilibrium | 13 |
| 2 | Topological superconductivity | 14 |
| 2.1 | Introduction and motivation | 14 |
| 2.2 | Review of superconductivity | 15 |
| 2.2.1 | Phenomenology | 15 |

| | | |
|----------|--|-----------|
| 2.2.2 | BCS theory formalism | 15 |
| 2.3 | Topological superconductors | 18 |
| 2.3.1 | Properties of the superconducting gap | 18 |
| 2.3.2 | Minimal models of topological superconductors in 1D and 2D | 19 |
| 2.3.3 | 3D topological insulators | 23 |
| 2.3.4 | 3D topological superconductor | 27 |
| 2.4 | Experimental signatures of topological superconductors | 29 |
| 2.4.1 | Electrical transport | 29 |
| 2.4.2 | Scanning tunneling spectroscopy | 31 |
| 2.4.3 | Nuclear magnetic resonance | 32 |
| 2.4.4 | Angle-resolved photoelectron spectroscopy | 33 |
| 3 | Introduction to ARPES | 36 |
| 3.1 | Introduction | 36 |
| 3.2 | Scientific design goals | 36 |
| 3.3 | Measurement technique | 38 |
| 3.3.1 | ARPES model | 38 |
| 3.3.2 | Experimental degrees of freedom | 39 |
| 3.3.3 | Empirical figures of merit | 40 |
| 3.4 | Data interpretation | 42 |
| 3.4.1 | Studying many-body physics | 42 |
| 3.4.2 | Detection of Bogoliubov quasiparticles | 43 |
| 4 | Generation of photoelectrons | 45 |
| 4.1 | Laser-based ARPES photon sources | 45 |
| 4.1.1 | Non-resonant upconversion | 46 |
| 4.1.2 | Resonant upconversion | 47 |
| 4.2 | Space-charge effects | 48 |
| 4.3 | Introduction to continuous wave lasers | 49 |

| | |
|--|-----------|
| <i>CONTENTS</i> | vii |
| 4.3.1 Laser model | 49 |
| 4.3.2 Linewidth | 50 |
| 4.4 Fourth-harmonic-generation-based continuous wave laser | 50 |
| 4.4.1 Master oscillator and amplifier | 51 |
| 4.4.2 Efficient second harmonic generation | 53 |
| 4.4.3 Frequency-doubling cavity | 55 |
| 4.5 Potential future directions for ARPES laser sources | 58 |
| 5 Spectral analysis of photoelectrons | 59 |
| 5.1 Introduction to free-space electron spectrum analyzers | 59 |
| 5.1.1 Adaptation of optics terminology | 59 |
| 5.1.2 Hemispherical deflection analyzer | 60 |
| 5.1.3 Electrostatic lenses | 64 |
| 5.2 Technical challenges with charged particle optics | 65 |
| 5.2.1 Magnetic shielding | 65 |
| 5.2.2 Fringing fields | 66 |
| 5.2.3 Grounding and work function | 68 |
| 5.3 Properties of the R8000 electron analyzer | 69 |
| 5.3.1 Lens system | 69 |
| 5.3.2 Slits | 70 |
| 5.3.3 Analyzer | 71 |
| 5.3.4 Detector | 73 |
| 5.4 R8000 measurement performance | 73 |
| 5.4.1 Energy resolution | 73 |
| 5.4.2 Momentum resolution | 74 |

| | |
|--|-----------|
| 6 Vacuum system design | 76 |
| 6.1 Introduction to vacuum systems | 76 |
| 6.1.1 Need for vacuum | 76 |
| 6.1.2 Modeling a vacuum system | 77 |
| 6.1.3 Pressure measurement | 79 |
| 6.2 Ultrahigh vacuum design guidelines | 79 |
| 6.2.1 Outgassing management | 79 |
| 6.2.2 Surface properties | 80 |
| 6.2.3 Vacuum generation | 81 |
| 6.3 Components of the ARPES UHV system | 82 |
| 6.3.1 System overview | 82 |
| 6.3.2 Chambers | 83 |
| 6.3.3 Vacuum pumps | 85 |
| 6.3.4 Vacuum valves | 88 |
| 6.3.5 Vacuum seals | 89 |
| 6.3.6 Vacuum feedthroughs | 92 |
| 6.3.7 Sample handling system | 94 |
| 6.4 Procedure for achieving ultrahigh vacuum | 98 |
| 6.4.1 Roughing stage | 98 |
| 6.4.2 Switch to turbo pump | 98 |
| 6.4.3 Bake-out | 98 |
| 6.4.4 Ion pump and TSP | 100 |
| 6.5 Vacuum diagnostic equipment | 100 |
| 6.5.1 Residual gas analyzer | 100 |
| 6.5.2 Leak detector | 101 |

| | |
|--|------------|
| 7 Helium-3 cryostat | 102 |
| 7.1 Introduction | 102 |
| 7.1.1 Application of cryogenic technologies in ARPES | 102 |
| 7.1.2 Design requirements for sub-Kelvin ARPES | 103 |
| 7.1.3 Principle of operation of a Helium-3 cryostat | 104 |
| 7.2 Overview of subsystems | 105 |
| 7.3 Shielding structures | 107 |
| 7.3.1 Cryogen reservoirs | 107 |
| 7.3.2 Ultrahigh vacuum | 108 |
| 7.3.3 Radiation shields | 110 |
| 7.4 Helium-3 insert | 110 |
| 7.4.1 Helium-3 insert overview | 111 |
| 7.4.2 1 K system | 113 |
| 7.4.3 Helium-3 system | 116 |
| 7.5 Sample manipulation | 119 |
| 7.5.1 Motion transfer media | 120 |
| 7.5.2 Five-axis sample manipulation | 122 |
| 7.5.3 Sample loading | 127 |
| 7.5.4 Performance of the sample manipulation system | 128 |
| 7.5.5 Differential pumping | 130 |
| 7.6 Electrical network | 131 |
| 7.6.1 Temperature sensors | 131 |
| 7.6.2 Sensor-heater unit | 133 |
| 7.6.3 Wiring architecture | 134 |
| 7.7 Operation and performance | 137 |
| 7.7.1 Preventive measures | 137 |
| 7.7.2 Cryostat cool down steps | 138 |
| 7.7.3 Cooling power | 139 |
| 7.8 Customization | 140 |
| 7.8.1 Bellows replacement on liquid Helium-4 reservoir | 140 |
| 7.8.2 Sample probe welding | 143 |
| 7.8.3 Coarse x - y manipulator upgrade | 143 |
| 7.8.4 Redesign of the electrical system | 146 |

| | |
|---|------------|
| 8 ARPES assembly and optimization | 148 |
| 8.1 ARPES system assembly | 148 |
| 8.1.1 Lab infrastructure | 148 |
| 8.1.2 Mechanical support frame | 149 |
| 8.1.3 Support frame modularity | 150 |
| 8.1.4 Ultrahigh vacuum system setup | 151 |
| 8.1.5 Sample alignment | 153 |
| 8.2 Initial system performance | 153 |
| 8.2.1 First ARPES measurements | 154 |
| 8.2.2 Radiation shield configuration changes | 154 |
| 8.3 Electrical charging in vacuum | 155 |
| 8.4 Modifications to radiation shields | 157 |
| 8.4.1 Variable slot design | 157 |
| 8.4.2 Results | 158 |
| 8.5 Investigation of energy resolution and sample temperature | 160 |
| 8.5.1 Measurement of superconductor spectral gap | 160 |
| 8.5.2 Thermal conductance of the sample holder | 161 |
| 8.5.3 Investigation of noise sources | 162 |
| 8.6 Work in progress | 162 |
| 9 Optical probes of many-body order | 163 |
| 9.1 Novel probes of order | 163 |
| 9.1.1 Introduction | 163 |
| 9.1.2 Dimensionality of the order parameter | 164 |
| 9.1.3 Multipolar or hidden order | 164 |
| 9.2 Optical probes of the order parameter | 164 |
| 9.2.1 Nonlinear optics | 164 |
| 9.2.2 Ultrafast optics | 166 |
| 9.3 Probing order in single crystals using SHG | 166 |

| | |
|---|------------|
| <i>CONTENTS</i> | xi |
| 9.3.1 Phenomenological theory of second harmonic generation | 166 |
| 9.3.2 Rotationally anisotropic second harmonic generation | 168 |
| 9.3.3 Example of RA-SHG | 169 |
| 9.4 Optical spectroscopy under high pressure | 170 |
| 9.4.1 Scientific objective | 170 |
| 9.4.2 Diamond anvil cell | 171 |
| 9.4.3 Microscopy cryostat customization | 173 |
| 9.4.4 Work in progress | 175 |
| 9.5 Order in systems with time-periodic drive | 176 |
| 9.5.1 Introduction to time-periodic driven systems | 176 |
| 9.5.2 Photon Floquet systems | 177 |
| 9.5.3 Studying phonon-Floquet systems with ARPES | 177 |
| 10 Conclusions and future directions | 180 |
| A Superconductivity | 190 |
| A.1 BCS formalism | 190 |
| A.1.1 Solution to the interacting metal | 190 |
| A.1.2 Bogoliubov quasiparticles | 195 |
| A.2 Data on superconducting gap and critical temperature | 196 |
| B Vacuum system | 197 |
| B.1 Vacuum pumps | 197 |
| B.1.1 Turbomolecular pumps | 197 |
| B.1.2 Ion pump | 198 |
| B.1.3 Titanium sublimation pump | 199 |
| B.2 Vacuum valves | 200 |
| B.2.1 Gate valves | 200 |
| B.2.2 Pneumatic right-angle valve | 200 |
| B.2.3 Compressed air supply | 201 |

| | | |
|----------|---|------------|
| B.3 | Mechanical feedthroughs | 201 |
| B.3.1 | Transfer arms | 202 |
| B.3.2 | Port aligners | 202 |
| B.3.3 | Wobble stick | 202 |
| B.3.4 | Coarse x - y stage upgrade | 203 |
| B.4 | Optical windows | 203 |
| B.4.1 | Viewing windows | 203 |
| B.4.2 | Laser windows | 204 |
| B.5 | Vacuum hardware | 204 |
| B.5.1 | Sealants | 204 |
| B.5.2 | Fasteners | 204 |
| B.5.3 | Special gaskets | 204 |
| B.6 | Load-lock | 205 |
| B.7 | Diagnostics | 205 |
| B.7.1 | Pressure gauges | 205 |
| B.7.2 | Residual gas analyzer | 206 |
| B.8 | Bake-out | 206 |
| B.8.1 | Bake-out preparation | 206 |
| B.8.2 | Heat generation and distribution | 207 |
| B.8.3 | Insulation | 207 |
| B.8.4 | Temperature and pressure monitoring | 208 |
| C | Cryogenics | 209 |
| C.1 | Helium-3 plumbing circuit | 209 |
| C.1.1 | Gas handling system | 209 |
| C.1.2 | Pumping station | 211 |
| C.1.3 | Liquid Nitrogen cold trap | 211 |
| C.2 | Helium-3 cryostat cool down | 212 |
| C.2.1 | Cryogen stock | 212 |

| | | |
|----------|---|------------|
| C.2.2 | Leak tests | 213 |
| C.2.3 | Pre-cool Helium-3 circulation and impedance tests | 215 |
| C.2.4 | Liquid Nitrogen cool down | 217 |
| C.2.5 | Liquid Helium-4 cool down | 220 |
| C.2.6 | Helium-3 cool down | 223 |
| C.3 | Helium-3 cryostat's electrical system | 224 |
| C.3.1 | Sleeveless wiring | 225 |
| C.3.2 | Modular network with PEEK sleeves | 226 |
| C.3.3 | Wire heat sinking | 227 |
| C.3.4 | Fabrication | 228 |
| C.3.5 | Wiring labels | 229 |
| D | Optics | 231 |
| D.1 | Non-zero $\chi^{(2)}$ tensor elements | 231 |
| D.2 | RA-SHG analysis for of $\text{CH}_3\text{NH}_3\text{PbI}_3$ | 232 |
| D.3 | Phase matching | 232 |

List of Figures

| | | |
|-------|--|----|
| 1.2.1 | Surface plot of the Ginzburg-Landau free energy, $\mathcal{F}(\{\Psi\})$ (along z -axis), over a complex plane with the x -axis (y -axis) corresponding to $\text{Re}(\Psi)$ ($\text{Im}(\Psi)$). The free energy landscape is a monotonically increasing function of $ \Psi $ above the phase transition ($\alpha < \alpha_c$); but has a (blue dashed) line minima, with radius Δ (order parameter amplitude), below the phase transition ($\alpha < \alpha_c$). The blue (red) ball represents the state of the system in (out) of the ordered phase. | 3 |
| 1.3.1 | Cartoons of the experimental configuration of two different phases of the quantum Hall effect. The blue circles and curved black arrows represent electrons and their cyclotron motion respectively. The red arrows represent flux quanta ($\Phi_0 = h/e$) of an external magnetic field (B), or flux density, applied perpendicular to the green rectangle. The Hall voltage (V_H) is measured for a fixed excitation current (I). . . . | 7 |
| 1.3.2 | Evolution of the density of states as a function of magnetic field, B , perpendicular to a degenerate 2D electron system. The number of filled Landau levels determines the number of chiral edge channels. | 8 |
| 1.3.3 | Edge state transport is compared between the IQHE (left) and QSHE (right). For the IQHE, the magnetic field is pointing out of the page. | 9 |
| 1.3.4 | The bulk and boundary spectrum for two topological insulators, with five (left) and one (right) gapless Dirac states, plotted along a direction in the boundary Brillouin zone. The red and blue boundary states symmetric about the E axis are Kramers partners. | 10 |
| 1.5.1 | A conceptual phase diagram illustrating how adding a topological dimension to conventionally symmetry breaking phase and symmetry to conventionally topological phases makes a richer phase diagram. α_c , β_c , and γ_c represent critical points. . . . | 12 |
| 2.2.1 | The spectrum of a 3D metal (left) and the spectrum of the corresponding BCS superconductor (right). For $\tilde{t}(\mathbf{k}) \approx \hbar^2 \mathbf{k}^2 / 2m_{\text{band}} \equiv \hbar^2 (k_x^2 + k_y^2 + k_z^2) / 2m_{\text{band}}$, I can schematically plot the full $\tilde{t}(\mathbf{k})$ by limiting to just the k_x and k_y axes and plotting a family of parabolas with different k_z . These parabolas are displaced along the energy axis by $\Delta E(k_z) = (\hbar^2 k_z / m_{\text{band}}) \Delta k_z$ where $\Delta k_z \sim 2\pi / L_z$ with L_z being the system size along the z direction. In the thermodynamic limit, these parabolas would just look like a blob. | 17 |
| 2.3.1 | Pairing amplitudes of electrons on nearest neighbor sites in s , $p + ip$, and d wave superconductors on a 2D square lattice. | 18 |
| 2.3.2 | Unpaired (top) and paired (bottom) phases of the Kitaev chain. | 21 |

| | | |
|-------|--|----|
| 2.3.3 | Both 2D regions represent a superconductors with $p + ip$ pairing. Only the right one hosts two Majorana zero modes, one in the interior (γ_2) and exterior (γ_1) each. In this case, the most important ingredient for topological superconductivity is the half quantum of flux ($h/2e$) passing through the superconductor. | 23 |
| 2.3.4 | The crystal of Bi_2Se_3 . Left: the hexagonal unit cell consists of three quintuple layers. This non-primitive unit cell illustrates the layered nature of Bi_2Se_3 . Right: the rhombohedral unit cell is the primitive cell used to determine the first Brillouin in Fig. 2.3.5. [40]. | 24 |
| 2.3.5 | Left: the bulk Brillouin zone of Bi_2Se_3 with the symmetry points labeled. The surface Brillouin zone is a projection of its bulk counterpart along the z -axis or (111) direction in the primitive unit cell basis ($\mathbf{T}_1, \mathbf{T}_2, \mathbf{T}_3$) defined in Fig. 2.3.4. Right: ab initio calculation of the band structure of a Bi_2Se_3 slab of 6 quintuple layers. Reprinted figure with permission from Sobota <i>et al. Phys. Rev. Lett.</i> 113 , 157401. Copyright (2014) by the American Physical Society. [43]. The surface states are highlighted in red and blue. | 26 |
| 2.3.6 | Bogoliubov quasiparticle spectrum of a 3D topological superconductor in the surface Brillouin zone parallel to the x - y axis. The green paraboloids represent the bulk spectrum. The blue cone corresponding to the dispersion of Majorana quasiparticles on a surface parallel to the x - y axis. | 28 |
| 2.4.1 | Left: cartoon of the experimental layout. Middle: bulk nanowire bands at $B = 0$. Right: bulk nanowire bands at $B \neq 0$. From Mourik <i>et al. Science</i> 336 , 1003-1007. Reprinted with permission from AAAS. [49]. | 29 |
| 2.4.2 | Left: The zero bias conductance peak in transport measurements on InSb nanowires. From Mourik <i>et al. Science</i> 336 , 1003-1007. Reprinted with permission from AAAS. Right: energy level diagram of the interface between the electrical lead (left) connected to the superconducting nanowire (right). [49]. | 30 |
| 2.4.3 | Point contact spectroscopy measurement on $\text{Cu}_x\text{Bi}_2\text{Se}_3$ revealing the existence of a zero-bias conductance peak below $T_c \approx 3$ K. Reprinted figure with permission from Sasaki <i>et al. Phys. Rev. Lett.</i> 107 , 217001. Copyright (2010) by the American Physical Society. [42]. | 31 |
| 2.4.4 | Left: Scanning tunneling spectroscopy measurement on $\text{Cu}_x\text{Bi}_2\text{Se}_3$ revealing an s -wave-like superconducting gap with no zero-bias conductance peak. Reprinted figure with permission from Levy <i>et al. Phys. Rev. Lett.</i> 110 , 117001. Copyright (2013) by the American Physical Society. Middle: calculation of density of states of $\text{Cu}_x\text{Bi}_2\text{Se}_3$ assuming a bulk s -wave pairing and surface Dirac-fermion-induced parity mixing. Reprinted figure with permission from Mizushima <i>et al. Phys. Rev. B</i> 90 , 184516. Copyright (2014) by the American Physical Society. Right: Fermi surfaces at different electron doping densities in Bi_2Se_3 . [50, 51]. | 32 |
| 2.4.5 | Left: top view of the hexagonal unit cell from Fig. 2.3.4 illustrating the offset in the x - y plane of the A, B, and C stacking orientations. The pink arrow external DC magnetic field direction parallel to the x - y plane. Right: normalized Knight shift of ^{77}Se in $\text{Cu}_x\text{Bi}_2\text{Se}_3$ in the superconducting phase. Reprinted by permission from Springer Nature Customer Service Centre GmbH: <i>Nature Physics</i> 12 , 852-854, Matano <i>et al.</i> , Copyright 2016. [53]. | 33 |

| | | |
|-------|---|----|
| 2.4.6 | The plots inside the black outline box share the same abscissa and ordinate axis units. The left and right plots inside said box represent a schematic and ARPES data showing both bulk and surface electron states in $\text{FeTe}_{0.55}\text{Se}_{0.45}$ ($T_c \approx 14.5$ K) close to zero energy (i.e. Fermi level) respectively. The red and blue lines represent topological surface states with opposite spin projection. Top-right: evolution of the superconducting gap of the surface states below T_c . Bottom-right: STS data from $\text{FeTe}_{0.55}\text{Se}_{0.45}$. The red and black curves represent the normalized differential conductance, dI/dV , for STM tip location at and away from a vortex core respectively. From Zhang <i>et al.</i> <i>Science</i> 360 , 182-186 and Wang <i>et al.</i> <i>Science</i> 362 , 333-335. Reprinted with permission from AAAS. [12, 37]. | 34 |
| 3.2.1 | Three families of superconductors are depicted on a log-scale scatter plot of <i>maximum</i> superconducting (Δ_{max}) gap vs. T_c over two orders of magnitude. Δ_{max} has been defined as the energy difference between the highest occupied state at zero temperature and the chemical potential. References for gap measurements of the above low- T_c , high- T_c iron-based, and optimally doped high- T_c cuprate superconductors can be found in Sec. A.2. | 37 |
| 3.3.1 | A momentum- and real-space illustration of the photoemission process in a 2D metal toy model. | 39 |
| 3.3.2 | The semi-transparent blue region represents the fraction of the 2D Brillouin zone accessible with $h\nu = 6$ eV and $\phi_{\text{max}} = 20^\circ$ | 41 |
| 3.4.1 | Plot of $ u_{\mathbf{k}} ^2$ and $ v_{\mathbf{k}} ^2$ as a function of energy. The region between the vertical dashed lines has zero density of states in the bulk of a conventional superconductor. | 44 |
| 4.1.1 | Three schematic representation of abstract photon upconversion processes. The lengths of the upward- and downward-pointing arrows are proportional to the energy absorbed and emitted by the frequency conversion medium respectively. The pink arrows represent emission of photons of the desired energy. | 46 |
| 4.2.1 | ARPES data from Shockley states on the (111) surface of Copper using repetition rates of 80 MHz and 1 kHz. Reprinted from Passlack <i>et al.</i> <i>J. Appl. Phys.</i> 100 , 024912, with the permission of AIP Publishing. [68]. | 48 |
| 4.3.1 | Spatial representation of a basic Fabry-Pérot laser and spectrum of the light output by the laser. | 50 |
| 4.4.1 | Photograph of the 6 eV photon ($\lambda = 205.5$ nm) source laser. The red, blue, and purple lines represent 822 nm, 411 nm, and 205.5 nm light respectively. The three stages of the laser are annotated using white dashed line borders. | 51 |
| 4.4.2 | Left: optical layout of the external cavity diode laser (ECDL) in the Littrow configuration. Right: spectral properties of the ECDL components which determine the mode selection. | 52 |
| 4.4.3 | Optical layout for the fundamental light at 822 nm. | 53 |
| 4.4.4 | Left: cartoon illustration of the propagation of the fundamental (red) and second harmonic (blue) waves for the cases of phase mismatch (top) and matching (bottom). The two waves' phase fronts align only for the $\Delta k = 0$ case. Right: power of second harmonic as a function of propagation distance, z , inside the non-linear crystal for phase mismatched (green) and matched (purple) cases. The top of the plot shows a graphical definition of $\Delta k \equiv k_{\text{SHG}} - 2k_{\text{f}}$ | 54 |

| | | |
|-------|---|----|
| 4.4.5 | Curve showing phase matching angle as a function of fundamental wavelength in BBO at 20 °C. | 55 |
| 4.4.6 | Schematic representation of the bow-tie cavity used for second harmonic generation. | 56 |
| 4.4.7 | Comparison between a Pound-Drever-Hall system and proportional-integral-derivative controller | 57 |
| 5.1.1 | (a) Interface between media with different refractive indices, (b) interface between regions with and without an electric field, (c) electron trajectories deep inside the region with an electric field. | 60 |
| 5.1.2 | Illustration of the dispersion and imaging properties of an electrostatic hemispherical deflection analyzer. | 61 |
| 5.1.3 | Two electron beams with a difference in kinetic energy ΔE hitting the detector. . . | 63 |
| 5.1.4 | Schematic illustration of the functional behavior of the lens. | 64 |
| 5.2.1 | Magnetic shielding inside a μ -metal cylinder produced by concentration of the flux lines inside the red region with larger μ_r (10^3 - 10^5). The uncolored region has $\mu_r = 1$ | 66 |
| 5.2.2 | Section view of the double-layer μ -metal shielding inside the analysis chamber. . . . | 67 |
| 5.2.3 | The fringing fields at the edge of the HDA and electron trajectories in the presence of a Herzog plate. Reprinted from <i>Nucl. Instrum. Meth. A</i> 601 , 182-194, Wannberg, Copyright (2009), with permission from Elsevier. [80]. | 68 |
| 5.2.4 | Electric potential difference between metals with dissimilar work functions after their Fermi levels align. | 69 |
| 5.3.1 | Top view of the analyzer with the most important internal components. | 70 |
| 5.3.2 | Electron trajectories inside the lens operating in the angular mode. Reprinted from <i>Nucl. Instrum. Meth. A</i> 601 , 182-194, Wannberg, Copyright (2009), with permission from Elsevier. [80]. | 71 |
| 5.3.3 | Left: analyzer viewed along lens axis. Right: shape and dimensions of the slits in the R8000. | 71 |
| 5.3.4 | Fixed mode scan of a Bi ₂ Se ₃ single crystal taken at a 5 eV pass energy. | 72 |
| 5.4.1 | The energy distribution curve measured from Xe 5p _{3/2} state at 293 K. | 74 |
| 5.4.2 | Left: the geometry and orientation, with respect to the analyzer slit, of the wire-and-slit device. Right: energy-integrated angle-resolved spectrum measured from wire-and-slit device. | 75 |
| 6.3.1 | Photograph of the UHV system | 82 |
| 6.3.2 | (a) top and (b) side view of the outlines of the analysis, preparation, pump chambers, and the load lock. | 83 |

| | | |
|--------|--|-----|
| 6.3.3 | Left: photograph of the analysis chamber connected to the cryostat. Right: CAD model showing penetration of the μ -metal neck into the cryostat just short of hitting the radiation shield. | 84 |
| 6.3.4 | Photograph of the analysis chamber and electron analyzer during installation and testing of the latter. | 85 |
| 6.3.5 | CAD model of the pump chamber labeling various pumps, gauges, and valves. . . . | 86 |
| 6.3.6 | Left: a block diagram of the pumping circuit established by the turbomolecular pumps. Right: photograph of the HiPace turbomolecular pumps attached to the UHV system and the HiCube turbomolecular pump backing them. | 87 |
| 6.3.7 | Left: photograph of the 400 liter/second ion pump. Right: pumping speed of the ion pump as a function of pressure. | 88 |
| 6.3.8 | Section views of the Titanium sublimation pump. The fins on the Aluminum can provide additional surface area for sputtering Titanium. The can has three stainless-Steel-to-Aluminum bi-metal tubes to allow welding standard (i.e. stainless Steel) ConFlat flanges. | 89 |
| 6.3.9 | Photograph and CAD model of liquid Nitrogen feedthrough to its reservoir. The inset shows the inner and outer tubes tack welded prior to making an atmosphere-to-UHV seam welded seal. | 94 |
| 6.3.10 | Top: 2D sketch of the preparation chamber and the load lock. The sample garage and its grabber are shown in their retracted positions (blue) and when they meet inside the preparation chamber (red), using the transfer arms, when the manual gate valve is opened. Bottom: Photograph providing 3D perspective of the load-lock and preparation chamber orientations. | 95 |
| 6.3.11 | Top left: CAD models of the sample garage holding 6 sample holders. Top right: CAD model of an individual sample holder with a sample attached. Bottom: Photograph of a sample holder retrieved from the garage using a grabber. | 96 |
| 6.3.12 | Left: photograph of sample loaded into the cold finger using a transfer arm from the prep chamber as viewed from a side viewport. Right: photograph of sample close to being loaded into the cold finger viewed from the bottom of the analysis chamber . | 97 |
| 6.4.1 | Pressure drop during a typical bake-out. The red region shows portion of the pump down when the external walls of the vacuum chambers are heated to ≈ 150 °C. The green region shows the pressure drop as the system cools down to room temperature. | 99 |
| 7.1.1 | Vapor pressure as a function of temperature for common cryogenics [85]. The blue circles correspond to the cooling limit due to practical pumping limitations. Note that H_2 and N_2 solidify at lower temperatures. | 104 |
| 7.2.1 | The full height partial section view of the cryostat with the insets zooming into the lower parts. The inset inside the larger blue dashed box shows the coordinate system definition close to the zoomed in view of the CAD model of the sample. The manipulators of the five degrees of freedom (x, y, z, θ, ϕ) have been highlighted at the top and middle of the cryostat. Only the y coarse actuator is visible in this view. | 106 |
| 7.3.1 | CAD model (left) and photograph (right) of the liquid Nitrogen and liquid Helium-4 reservoirs. | 107 |

| | | |
|-------|---|-----|
| 7.3.2 | CAD model (left) and photo (right) of the reservoir insert. The bellows on the liquid Helium-4 reservoir is not shown for visual clarity. | 108 |
| 7.3.3 | CAD model and photograph of the main shroud | 109 |
| 7.3.4 | CAD model and photograph of the bottom shroud | 110 |
| 7.3.5 | CAD models and photograph of the 4 K and 77 K shields. The Helium-3 insert is not shown in the CAD model. | 111 |
| 7.4.1 | Left: CAD model of the full Helium-3 insert with a section view of the 4 K reservoir. Right: Photograph of Helium-3 insert being raised for attachment to the 4 K reservoir. The insets show details of the Indium seal. | 112 |
| 7.4.2 | Photograph of the region of Helium-3 insert containing the 1 K pot, 1 K plate, and related components. | 114 |
| 7.4.3 | The CAD model shows the 1 K pot plumbing (open) circuit with the 4 K reservoir made transparent. The photograph shows the needle valve whose conductance can be tuned using the fine threads. The copper mesh covers the inlet of the needle valve to avoid clogging from contaminants. | 114 |
| 7.4.4 | Photograph of the region of Helium-3 insert containing the 1 K pot, 1 K plate, and related components. | 115 |
| 7.4.5 | Photograph of the Helium-3 pot from two different viewing angles. | 116 |
| 7.4.6 | Left: color-coded sketch of the 1 K pot and condensing impedance. Right: photographs of the condensing impedance attached to the cryostat and in isolation. | 117 |
| 7.4.7 | Gas conduction paths during Helium-3 condensation | 118 |
| 7.4.8 | Gas conduction paths during Helium-3 circulation | 119 |
| 7.5.1 | CAD model of sample probe detailing the top and bottom ends. Photographs showing braided connections between the sample probe and the 4 K and 1.5 K thermal anchors. | 120 |
| 7.5.2 | The CAD model of the cold finger in isolation. The photographs show the braided connection of the cold finger to the Helium-3 pot and the tensioning nut. | 121 |
| 7.5.3 | Left: CAD model of z -axis linear stage in the measurement and sample loading positions. Right: photo of the z -axis linear stage. | 122 |
| 7.5.4 | CAD model and photograph of the θ -axis rotary stage at the top of the cryostat. | 123 |
| 7.5.5 | CAD model and photograph of the fine x - y stage at the top of the cryostat. | 124 |
| 7.5.6 | CAD models and photograph of the coarse x - y stage and its manipulators. The CAD model in the inset shows an exploded view of the x - y stage with only the PEEK braces visible. The vertical separation between the PEEK braces has been exaggerated. | 125 |

| | | |
|-------|---|-----|
| 7.5.7 | Left: CAD model of the rotator in its cradle. Cartoons of the strings, controlling the ϕ motion of the rotator, are depicted by red and blue lines. Middle: photograph of the rotator with a cleaved sample attached. Right: CAD model of the top section view of the rotator and full view of the mating sample holder. A graphite-coated epoxied sample is shown with its surface intersecting the ϕ rotation axis. | 126 |
| 7.5.8 | Left: CAD model of the cold finger and bottom shields used for sample loading. The 77 K bottom shield is made semi-transparent to show the 4 K bottom shield. Right: Photograph of the cold finger and 77 K bottom shield. | 129 |
| 7.5.9 | Pressure spikes in the analysis chamber due to a leak in the rotary seal | 130 |
| 7.6.1 | Calibration curves of the standard silicon diode (red) and the resistance temperature detectors (blue). The latter are individually calibrated for the sample and Helium-3 pot by the manufacturer. The diode voltage is measured with an excitation current of $10\ \mu\text{A}$ | 132 |
| 7.6.2 | CAD models and photographs of the components of the sensor packaging. | 133 |
| 7.6.3 | Left: CAD model of the heater block illustrating mounting locations of the firerod heater and silicon diode bobbin. Right: photograph of the heater block connected to the bottom of the 4 K reservoir via a heat sink. | 134 |
| 7.6.4 | 20-pin electrical feedthrough for the voltage and current transmission wires of the sensors and heaters | 135 |
| 7.6.5 | Photograph of a coiled 160 inch long cable for a single sensor-heater unit. | 136 |
| 7.6.6 | Heat sink or bobbin for thermally anchoring wires at the bottom of the 4 K reservoir | 137 |
| 7.7.1 | Measured cooling power of the cryostat measured up to $\approx 0.36\ \text{K}$ above the base temperature ($0.84\ \text{K}$) | 140 |
| 7.8.1 | Left: a zoomed-out view of the bellows with the leak. Middle top: a zoomed in view of the location to which the leak was narrowed down. Middle bottom: magnified view of the red box region showing a tear the $0.008''$ thick walls of the bellows. Right: a zoomed out view of the rigid $0.050''$ thick wall tube replacing the bellows. | 142 |
| 7.8.2 | Photograph of the bolted sample probe interface after welding. | 143 |
| 7.8.3 | Top left: illustration of errors in the motion of a linear translation stage. Top right: view of the x - y stage from the x -axis linear feedthrough port on the main shroud. Bottom: decoupling of the y -axis feedthrough shaft from the x - y stage due to slipped set screw. | 144 |
| 7.8.4 | CAD model of the upgraded x - y manipulation system with the sample probe. | 145 |
| 8.1.1 | Left: pocket due to raised ceiling and the chain hoist in said pocket. Right: empty space between optical tables for constructing the ARPES system. | 149 |
| 8.1.2 | Right: CAD model of Aluminum support frame. Left: results of an ANSYS simulation illustrating <i>exaggerated</i> deflection (see color bar) due to the weight of a 2000 lbs cryostat. A maximum deflection of $0.052''$ is predicted at the location of the support bracket on the cryostat's main shroud (c.f. Fig. 7.3.3) | 150 |

| | | |
|-------|--|-----|
| 8.1.3 | CAD model and photograph of the electron analyzer mounted on a mobile cart which attaches to the support frame. | 151 |
| 8.1.4 | Left: photograph of the cryostat after it has been removed from the support frame using the chain hoist. Right: photograph of the partially disassembled support frame. The stairway and a section of top deck are removed to allow horizontal motion of the cryostat when the latter is suspended from the chain hoist. | 152 |
| 8.3.1 | Four radiation shield configurations used to measure the spectrum of Bi_2Se_3 without baking out the vacuum system ($\approx 5 \times 10^{-9}$ torr pressure at 77 K). Cartoons of four measurement configurations, and the resulting spectra, are shown (left to right and top to bottom) for the following radiation shield tail assemblies: no shields, 1 K, 1 K + 4 K, and 1 K + 4 K + 77 K. The latter three have their slots coated with graphite. | 156 |
| 8.4.1 | Photographs of the modified radiation shield tails and cover plates. The 4 K (a) and 77 K (b) shield tails' slots were replaced with large rectangular cut outs. (c) Back side of the curved plate covering the rectangular cut out in the 4 K shield tail. (d) Front side of the cover plates with different slit widths. The black regions are graphite coated. | 157 |
| 8.4.2 | Four radiation shield configurations used to measure the spectrum of Bi_2Se_3 after a full bake-out of the vacuum system (6×10^{-10} torr pressure at room temperature). Cartoons of four measurement configurations, and the resulting spectra, are shown (left to right and top to bottom) for the following radiation shield tail assemblies: 1 K + uncovered 4 K, 1 K + covered 4 K, 1 K + covered 4 K + uncovered 77 K, and 1 K + covered 4 K + covered 77 K. The covered radiation shield tails have the slotted cover plates (c.f. Fig. 8.4.1) installed. | 159 |
| 9.3.1 | The experimental layout of the RA-SHG setup. From Harter <i>et al. Science</i> 356 , 295-299. Reprinted with permission from AAAS. [92]. | 169 |
| 9.3.2 | An example of RA-SHG measurements on single crystals of $\text{CH}_3\text{NH}_3\text{PbI}_3$ [98]. | 170 |
| 9.4.1 | Cross-section of a diamond anvil cell. The metal gasket seals the pressure-transmitting medium. | 171 |
| 9.4.2 | Left: photograph of the diamond anvil cell. Right: CAD section view of the diamond anvil cell illustrating the compression mechanism. | 173 |
| 9.4.3 | Left: stainless Steel gas membrane inside the cryostat-mounting cap. Right: Diamond cutlet and its seat fastened to the top anvil mount. | 174 |
| 9.4.4 | Left: photograph of the region of the cryostat where the diamond anvil cell is mounted. Right: custom Aluminum dome-shaped vacuum barrier to accommodate the diamond anvil cell. | 174 |
| 9.4.5 | Photographs showing the customization to the components of the microscopy cryostat to accommodate the space constraints and in situ pressure tuning requirements of the diamond anvil cell design from Sec. 9.4.2.3. | 175 |
| 9.5.1 | A cartoon illustration of the layout for a proposed phonon Floquet experiment. The inset conceptually illustrates temporal and spectral characteristics of the experiment. | 178 |
| A.1.1 | Schematic representation of a four-fermion scattering process | 192 |

| | | |
|-------|--|-----|
| C.1.1 | Block diagram representation of the plumbing circuit in the gas handling system. The circles with an arrow inside them are compound (i.e. dial) pressure gauges. The circles with the cross inside them denote valves. The blue circles are KF flanged ports for outgoing/incoming gas lines. The double-arrow denotes a relief valve. . . . | 210 |
| C.1.2 | Photograph of the Pfeiffer CombiLine™ pumping station. | 211 |
| C.1.3 | Left: section view of the CAD model of the liquid-Nitrogen-cooled charcoal cold trap assembly. Right: photograph of the cold trap head without the liquid Nitrogen dewar. | 212 |
| C.2.1 | Configuration of the gas handling system when leak testing the Helium-3 insert. The open (closed) valves and on (off) pumps are color-coded red (green). Pink lines with arrows represent the pumping path. | 214 |
| C.2.2 | Configuration of the gas handling system when circulating Helium-3 during the cool down. The open (closed) valves and on (off) pumps are color-coded red (green). Pink lines with arrows represent flow path of the Helium-3 gas. | 215 |
| C.2.3 | Configuration of the gas handling system when performing an impedance test. The open (closed) valves and on (off) pumps are color-coded red (green). Pink lines with arrows represent the flow of Helium-3 gas. The partially red and green valve indicates the valve used to regulate the amount of Helium-3 in the system. | 216 |
| C.2.4 | Rise in the tail pressure of the impedance capillary, as measured by G1, at 77 K and room temperature. The initial head pressures, as measured by P , are approximately 400 and 600 mbar respectively. | 217 |
| C.2.5 | Configuration of the gas handling system during Helium-3 condensation. The open (closed) valves and on (off) pumps are color-coded red (green). Pink lines with arrows represent the flow of Helium-3 gas. | 223 |
| C.2.6 | Configuration of the gas handling system during normal Helium-3 circulation. The open (closed) valves and on (off) pumps are color-coded red (green). Pink lines with arrows represent the flow of Helium-3 gas. | 224 |
| C.3.1 | Photograph of the sleeveless wiring network near the radiation shielding plate at the top of the 77 K reservoir | 225 |
| C.3.2 | CAD model of photograph of a bundle of two and one pair of insulated Manganin and Copper wires respectively. The photograph shows the protective braided PEEK sleeve. This entity is defined as a <i>wire module</i> | 226 |
| C.3.3 | The upper two photographs show Kapton-insulated Copper wires epoxied to the heat sinks to be connected to the 1 K plate (Silver epoxy) and the top of the 77 K reservoir (Torr seal). The lower photograph shows the heat sinks thermally anchored to the 1 K plate. | 227 |
| C.3.4 | An example of an apparatus for soldering Manganin wires on 4-pin connector. . . . | 228 |
| C.3.5 | Examples of metal-stamped labels for the feedthrough pins and wire bundles. . . . | 230 |
| D.1.1 | The non-zero elements of the $\chi^{(2)}$ tensor for classes mm2, 4mm, 6mm, 6, 4, and $\bar{4}$. . . | 231 |
| D.3.1 | Propagation of an electromagnetic wave through a birefringent material. | 233 |

Chapter 1

Order in a many-body quantum system

1.1 Introduction

The abstract notion of “order” in a system is associated with a set of rules by which the constituents of said system organize themselves. These rules are succinctly encapsulated in a physical quantity known as the “order parameter.” An order parameter, denoted by (say) Ψ , is defined as a quantity which is non-zero inside the ordered phase it represents and zero otherwise. In general, Ψ can be mathematically represented by a complex tensor which is an *explicit* function of position ($\mathbf{x} \equiv (x, y, z)$) and time (t)¹

$$\Psi(\mathbf{x}, t). \tag{1.1.1}$$

The rank of the Ψ tensor is an indicator of the system complexity² (c.f. Sec. 1.2.4 and 9.1).

Except for parts of Chap. 9, this thesis will mainly focus on systems in equilibrium. In other words, the explicit t dependence in Eq. (1.1.1) will be ignored. In this chapter, I will discuss two types of (equilibrium) theoretical schemes used to define Ψ : (a) Ginzburg-Landau and (b) topological.

1.2 Studying order in the Ginzburg-Landau framework

So far in my discussion of the order parameter, I made no assumptions about how one determines Ψ theoretically.³ The notion of an order parameter is sound regardless of the method one uses to compute it. This computation could involve either a bottom-up (e.g. statistical mechanics) or top-down (e.g. thermodynamics) approach. In this section, I will discuss the latter in an elegant mathematical framework put forth by Lev Landau, and later extended to inhomogeneous systems by Vitaly Ginzburg.

¹Depending on the details of the system, it might be more convenient to express the order parameter in terms of the spacetime conjugate variables energy/frequency (E/ω) or momentum (\mathbf{p}); here I'll only focus on the former.

²In this sentence, complexity is used as the antonym of simplicity. It is **not** referring to the fact that Ψ is a complex number.

³I argue that theory will inform how empirical measurements are mapped from a many-body system to the order parameter.

1.2.1 Local order parameter

The Ginzburg-Landau theory proved successful in explaining many-body systems which can be described by a “local” order parameter. This theory postulates that the nature of the local order parameter depends on the symmetries present in a system before and after undergoing a phase transition. In other words, a local order parameter is uniquely associated with a set of “broken symmetries.”

For example, consider the formation of (say) an elementally pure⁴ crystalline solid from its liquid state (or phase). The atoms in the liquid phase possess continuous translational symmetry in all three spatial dimension. After the crystal formation, however, the symmetry of the system is reduced to discrete translational symmetry. Besides the atom specie, the resultant crystal can be uniquely defined by a so-called “crystallographic space group.”

Group theory has provided an exhaustive list of 230 crystallographic space groups, all of which have examples in the real world. Similarly, a group-theoretic approach can be used to classify more sophisticated phases using the Ginzburg-Landau theory.

1.2.2 Group theory

Group theory offers an elegant framework to help one understand the mathematical structure (e.g. scalar, vector, tensor, etc.) of the order parameter [1]. Moreover, this approach highlights important properties (e.g. nematicity) of the phase corresponding to said order parameter.

Consider a system which is about to undergo a phase transition. The group G denotes the set of symmetries possessed by the parent system. After the phase transition, the system enters a phase with an order parameter Ψ , and the (reduced) symmetries of the corresponding phase are denoted by H . Then the symmetries of the order parameter, R , can be defined by the coset space⁵

$$R = \frac{G}{H}. \quad (1.2.1)$$

By analyzing the symmetries of these groups or cosets, one can place constraints on a (generally) complex tensorial order parameter. The effect of symmetry operations, belonging to R , on Ψ allows one to establish relationships between its tensor elements, thus making Ψ more analytically tractable.

1.2.3 Ginzburg-Landau theory of second-order phase transitions

The symmetries of Ψ correspond to the set of transformations, R , which map distinct states within the ground state “manifold” with the same free energy.⁶ Therefore, R is also referred to as the degeneracy space. For example, in the famous “Mexican hat” potential, $R = U(1)$. The degeneracy space is represented by the dashed red circle in Fig. 1.2.1. In the context of a many-body system, the Mexican hat potential serves as a useful tool in visualizing the variational analysis of the free energy in explaining a continuous phase transition.

Considering the simple case of a scalar complex inhomogeneous order parameter,

$$\Psi(\mathbf{x}) \equiv \Delta(\mathbf{x})e^{i\theta(\mathbf{x})}, \quad (1.2.2)$$

⁴I am limiting this example to a single specie atom for simplicity without loss of generality.

⁵ R is a group only if H is a normal subgroup of G .

⁶This so-called “Ginzburg-Landau free energy,” denoted $\mathcal{F}_{GL}(\{\Psi\})$, will be defined shortly.

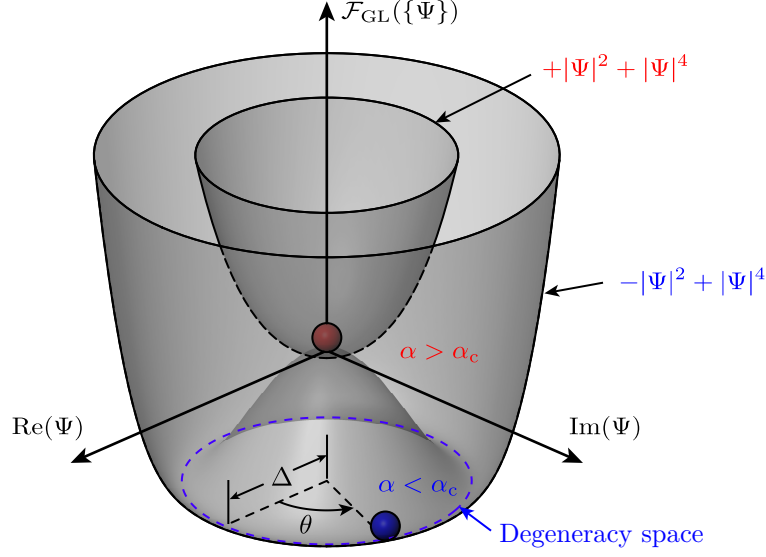


Figure 1.2.1: Surface plot of the Ginzburg-Landau free energy, $\mathcal{F}(\{\Psi\})$ (along z -axis), over a complex plane with the x -axis (y -axis) corresponding to $\text{Re}(\Psi)$ ($\text{Im}(\Psi)$). The free energy landscape is a monotonically increasing function of $|\Psi|$ above the phase transition ($\alpha < \alpha_c$); but has a (blue dashed) line minima, with radius Δ (order parameter amplitude), below the phase transition ($\alpha < \alpha_c$). The blue (red) ball represents the state of the system in (out) of the ordered phase.

the Ginzburg-Landau free energy, $\mathcal{F}_{\text{GL}}(\{\Psi\})$, can be written to lowest order as an explicit *functional* in Ψ as

$$\mathcal{F}_{\text{GL}}(\{\Psi\}) = c_0 + c_1|\nabla\Psi|^2 + c_2|\Psi|^2 + c_3|\Psi|^4 + \dots, \quad (1.2.3)$$

where in general the *real* coefficients c_n can be expressed as

$$c_n \equiv f_n(\{\alpha, \beta, \gamma, \dots\}), \quad (1.2.4)$$

where f_n is a function which depends on a set of parameters, $\{\alpha, \beta, \gamma, \dots\}$,⁷ which, in most cases, can be externally tuned to drive phase transitions in the many-body system. Some examples of such parameters include: temperature, pressure, external electromagnetic field(s), and atomic doping. The set of critical parameters $\{\alpha_c, \beta_c, \gamma_c, \dots\}$ determine the boundaries of the many-body phases described by Eq. (1.2.2).

Eq. (1.2.3) can be generalized to higher dimensionality (i.e. vector, tensor, etc.) order parameters. A careful analysis of symmetries from Sec. 1.2.2 offers the following prescription for writing down the right-hand side (RHS) of Eq. (1.2.3)

$$\mathcal{F}_{\text{GL}}(\{\Psi\}) = \mathcal{F}_{\text{GL}}(\{R\Psi\}). \quad (1.2.5)$$

Since the RHS of Eq. (1.2.3) involves only terms which are powers of $\Psi^*\Psi$ and $|\nabla\Psi|$, a $U(1)$ transformation, $\theta \rightarrow \theta + \theta_0$, in the ground state manifold leaves $\mathcal{F}_{\text{GL}}(\{\Psi\})$ invariant. Therefore, Eq. (1.2.3) is consistent with $R = U(1)$.

Consider a simple example of a homogeneous phase where the external parameter driving the phase transition is temperature (T). Then, by making the T -dependence explicit, I can write the order parameter as

$$\Psi(T) = \Delta(T)e^{i\theta_0}, \quad (1.2.6)$$

⁷ f_0 is continuous across phase boundaries characterized by the set of critical parameters $\{\alpha_c, \beta_c, \gamma_c, \dots\}$

where θ_0 is a constant. Plugging (1.2.6) into (1.2.3) I get

$$\mathcal{F}_{\text{GL}}(\{\Psi\}) = c_0(T) + c_2(T)\Delta^2(T) + c_3(T)\Delta^4(T) + \dots, \quad (1.2.7)$$

where $c_0(T)$ is continuous across the critical (i.e. phase transition) temperature T_c , $c_3(T) > 0$, and

$$c_2(T) \equiv \begin{cases} 0 & T > T_c \\ -\left|a\left(1 - \frac{T}{T_c}\right)\right|^b & T < T_c \end{cases}, \quad (1.2.8)$$

where a and b are real scalars. For $T > T_c$, the minima of Eq. (1.2.7) occurs at $\Delta(T) = 0$. Upon performing a variational analysis for $T < T_c$ I get⁸

$$\begin{aligned} \frac{\delta\mathcal{F}_{\text{GL}}(\{\Psi\})}{\delta\Delta(T)} &= -2|a|^b \left|1 - \frac{T}{T_c}\right|^b \Delta(T) + 4c_3(T)\Delta^3(T) + \dots, \\ &= 0, \\ \Delta(T) &= \sqrt{\frac{|a|^b}{2c_3(T)}} \left|1 - \frac{T}{T_c}\right|^{b/2}. \end{aligned} \quad (1.2.9)$$

1.2.4 Quantum order in the Ginzburg-Landau framework

One of the major successes of the group-theoretic Ginzburg-Landau theory is its description of phase transitions in both classical and quantum models of many-body systems. In this section, I will focus on the latter. The examples presented in Sec. 1.2.4.1-1.2.4.3⁹ follow the group-theoretic analysis discussed in Sec. 1.2.2. In the following examples, despite making a few remarks on the microscopic mechanisms (or formalisms) driving the quantum phases, a detailed discussion of microscopic theories is outside the scope of this section. The main purpose of this section is to phenomenologically emphasize the impact of broken symmetries on the structure of the order parameter.

1.2.4.1 Superfluid Helium-4

The order parameter of superfluid Helium-4 can be written as

$$\Psi = \Delta e^{i\theta}, \quad (1.2.10)$$

where Δ and θ represent the amplitude and phase stiffness of the Bose-Einstein condensate. Under ambient pressure, liquid Helium-4 undergoes a phase transition into the superfluid state at $T_c = 2.17$ K. In its lowest energy state, the superfluid phase stiffness, θ , acquires a fixed value. This phenomenon is referred to as the breaking of “U(1) gauge symmetry.” With the notations defined in Eq. (1.2.1), in this example, $G = \text{U}(1)$, $H = 1$, and $R = \text{U}(1)$. The following examples will involve progressively greater mathematical complexity.

1.2.4.2 Heisenberg ferromagnet in 3D

The Hamiltonian of a 3D Heisenberg ferromagnet on an arbitrary 3D lattice can be written as¹⁰

$$\hat{\mathcal{H}} = \sum_{ij} J_{ij} \hat{\mathbf{S}}_i \cdot \hat{\mathbf{S}}_j, \quad (1.2.11)$$

⁸The negative square root is accounted for by $\theta_0 \rightarrow \theta_0 \pm \pi$.

⁹These examples are borrowed from [2].

¹⁰Throughout the entire thesis, I will put a hat symbol on all quantum operators to distinguish them from c-numbers.

where $\hat{\mathbf{S}}_i \equiv (\hat{S}_i^x, \hat{S}_i^y, \hat{S}_i^z)$ is the three-component spin-1/2 operator on lattice site i , and $J_{ij} < 0$ is the *ferromagnetic* coupling between lattice sites i and j . Below the Curie temperature, T_c , the spins will order along a specific axis with a net magnetization vector $\mathbf{M} \propto \langle \sum_i \hat{\mathbf{S}}_i \rangle$.¹¹ In this case, the order parameter can be mathematically expressed as

$$\mathbf{M} = M \mathbf{n}(\theta, \phi), \quad (1.2.12)$$

where M is the magnitude of the magnetization and the vector $\mathbf{n}(\theta, \phi)$ points along the direction of magnetization; θ and ϕ are the polar and azimuthal angles, respectively, in spherical coordinates. Unlike the case of superfluid Helium-4, however, this system does possess U(1) symmetry corresponding to rotation of the system about the axis collinear to $\mathbf{n}(\theta, \phi)$. Then from Eq. (1.2.1); then $G = \text{SO}(3)$, $H = \text{U}(1)$, and

$$\begin{aligned} R &= \frac{\text{SO}(3)}{\text{U}(1)}, \\ &= \text{S}^2, \end{aligned} \quad (1.2.13)$$

which is a coset space (not group) represented by points, with a position vector (say) $\Theta \mathbf{n}(\theta, \phi)$, lying inside a sphere of radius π . The magnitude of the position vector, Θ , corresponds to the angle by which the ferromagnet is rotated about the axis collinear to $\mathbf{n}(\theta, \phi)$.

1.2.4.3 B phase of superfluid Helium-3

The prototypical Fermi liquid Helium-3 enters the Balian-Werthamer phase (or B phase) of the superfluid state from the normal state at $T_c \approx 0.9 \text{ mK}$ at ambient pressure. In this charge-neutral analog of superconductors, two fermionic Helium-3 atoms pair up to form Cooper pairs. In the B phase, the Cooper pair's total angular momentum (\mathbf{L}) and spin (\mathbf{S}) vectors order such that the relative angle between said vectors is fixed. Moreover, similar to superfluid Helium-4, U(1) gauge symmetry is also broken.

On a mathematical level, this case is simply one copy of the example from Sec. 1.2.4.1 and two copies from the example in Sec. 1.2.4.2. Then from Eq. (1.2.1) G , H , and R take on the following values. In the normal Helium-3 liquid, \mathbf{L} and \mathbf{S} are free to rotate and gauge symmetry is present. Therefore, $G = \text{SO}(3)_{\mathbf{L}} \times \text{SO}(3)_{\mathbf{S}} \times \text{U}(1)$ where the $\text{SO}(3)_{\mathbf{L}}$ ($\text{SO}(3)_{\mathbf{S}}$) group corresponds to the rotational symmetry of \mathbf{L} (\mathbf{S}). Since \mathbf{L} and \mathbf{S} are locked relative to one another in the superfluid B phase, and the gauge symmetry is broken, $H = \text{SO}(3)_{\mathbf{L}+\mathbf{S}}$, and

$$\begin{aligned} R &= \frac{\text{SO}(3)_{\mathbf{L}} \times \text{SO}(3)_{\mathbf{S}} \times \text{U}(1)}{\text{SO}(3)_{\mathbf{L}+\mathbf{S}}}, \\ &= \text{SO}(3)_{\mathbf{L}-\mathbf{S}} \times \text{U}(1), \end{aligned} \quad (1.2.14)$$

The order parameter corresponding to this phase is

$$\Psi = e^{i\theta} R_{\mu j}, \quad (1.2.15)$$

This example offers a perfect segue into a discussion of topological phases in the next section. It is the most complex example of the Ginzburg-Landau theory presented in this section; yet it simultaneously serves as an example of a topological phase.

¹¹ $\langle \sum_i \hat{\mathbf{S}}_i \rangle \equiv \langle \psi_{\text{GS}} | \sum_i \hat{\mathbf{S}}_i | \psi_{\text{GS}} \rangle$ where $|\psi_{\text{GS}}\rangle$ represents the *many-body* quantum ground state in the Fock space.

1.3 Topological phases

Topology has been a recurring theme in condensed matter physics for many years prior to its first unequivocal experimental evidence, in 1980, from the discovery of the so-called quantum Hall effect (QHE) [3]. In the 1970s, studies of topological phenomena like (say) defects in Helium-3 [4] and the Kosterlitz-Thouless transition [5] existed on the fringe. It was not until the discovery of the QHE, however, that the application of topological theories went mainstream. Such a paradigm shift can be attributed to the irrefutable inability of the Ginzburg-Landau theory in describing phase transitions in the QHE. In the following four decades, as the research community’s understanding of topology increased, several examples of topological phases were experimentally realized; some examples are 2D and 3D topological insulators (TIs) [6, 7], quantum anomalous Hall effect (QAHE) [8], Haldane model [9], Weyl semimetals (WSMs) [10], and topological superfluids/superconductors [11, 12].

The primary goal of the work presented in this thesis is the study of topological superconductors (TSCs). TSCs will be subject of Chap. 2. As a prerequisite, I will discuss the first two, and arguably most impactful, examples of topological phases, namely the QHE and TI. In Sec. 1.3.1, I will briefly review the phenomenology and topological properties of the QHE. In Sec. 1.3.2, I will highlight the key similarities and differences between the integer QHE (IQHE) and TIs, while emphasizing the protection aspect of topological phases.

1.3.1 The quantum Hall effect

On a purely phenomenological level, the QHE is an extension of the classical Hall effect; the latter was discovered in 1879 by Edwin Hall. In the classical Hall effect, the application of an external magnetic field to an electrical-current-carrying conductor results in a (transverse) voltage in a direction perpendicular to both the current flow and the magnetic field. This transverse Hall voltage (V_H) is the result of deflection of the charged-particle current due to the Lorentz force from the magnetic field (B). A classical analysis of such an effect in (say) a metal reveals that V_H scales linearly and *continuously* with B .

As the name suggests, the QHE differs from its classical counterpart due to the appearance of quantized steps in the plot of V_H versus B . The other difference is that the electron system exhibiting the QHE is confined to a 2D plane perpendicular to the external magnetic field. Furthermore, the steps in the V_H - B curve correspond to values of V_H that are related to fundamental constants h (Planck’s constant) and e (electron charge). Fig. 1.3.1 shows a cartoon of the QHE for two different (discrete) values of V_H . In both cases, it is noteworthy that $(h/e^2) I/V_H$ is a rational number. This fact hints at the possibility of novel underlying physics compared to the classical Hall effect.

Shortly after the discovery of the QHE, work by theorists such as Thouless, Kohmoto, Nightingale, and den Nijs (TKNN) [13], as well as Laughlin [14], elucidated the importance of topology in this novel phenomenon.¹² Moreover, a seemingly unrelated theoretical breakthrough, in 1984 [15], which introduced the notion of a “geometric phase” in a quantum system, made a significant impact on theoretical efforts aimed at explaining the QHE.

Further investigation revealed that the steps in the V_H - B curve represent distinct topological phases. These phases are labeled by a quantity known as the filling fraction, ν , which is given by

$$\nu \equiv \left(\frac{h}{e^2} \right) \frac{I}{V_H}, \quad (1.3.1)$$

¹²These theorists are the prominent ones. An all-inclusive list is much longer.

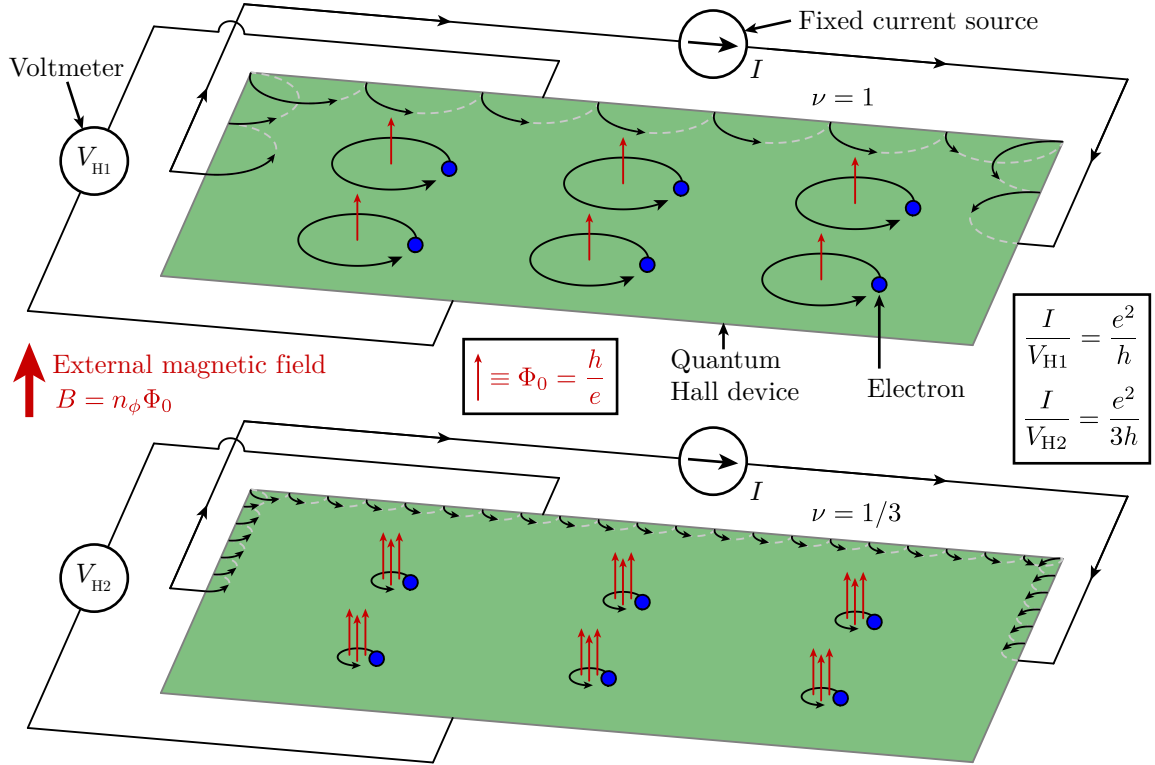


Figure 1.3.1: Cartoons of the experimental configuration of two different phases of the quantum Hall effect. The blue circles and curved black arrows represent electrons and their cyclotron motion respectively. The red arrows represent flux quanta ($\Phi_0 = h/e$) of an external magnetic field (B), or flux density, applied perpendicular to the green rectangle. The Hall voltage (V_H) is measured for a fixed excitation current (I).

As I alluded to earlier, transitions between states with different ν did not involve any symmetry breaking.¹³ As a result, the importance of topology was firmly established in the field of condensed matter physics.

Phenomenologically, the QHE phases can be sorted into two classes, based on whether ν is an integer or a fraction; the QHE in these two cases is dubbed the integer QHE (IQHE) and fractional QHE (FQHE) respectively. For the rest of this section, I will discuss the spectral characteristics of the QHE with the goal of: (a) providing physical insight into the definition and classification (\mathbb{Z}) of the order parameter of the QHE, (b) highlighting the topological protection aspect of the QHE's chiral edge states, and (c) establishing an analogy with the quantum spin Hall effect (c.f. Sec. 1.3.2). For brevity and convenience, I will limit the discussion to the IQHE. For the level of detail in the analysis presented here, the FQHE can be mapped to an effective IQHE using the composite fermion model [16].¹⁴ For such a mapping, it is often convenient to express (1.3.1) as

$$\nu \equiv \frac{n_e}{n_\phi}, \quad (1.3.2)$$

where n_e and n_ϕ are the areal density of electrons and external flux quanta ($\Phi_0 \equiv h/e$) respectively (c.f. Fig. 1.3.1).

¹³Of course, creation of the QHE requires time-reversal symmetry breaking. But the latter remains a constant across phase transitions between different ν .

¹⁴A rigorous analysis of the distinctions between the IQHE and FQHE is outside the scope of this discussion. The interested reader can refer to (say) [17].

The cartoon in Fig. 1.3.1 crudely illustrates the fact that the IQHE is an insulator in its (2D) bulk and a metal at the (1D) edges. These transport properties can be derived by modeling the IQHE at the semi-classical level. The spectrum of a quantum mechanical particle confined to a 2D plane, with a magnetic field perpendicular to said plane, was computed (ironically) by Lev Landau prior to the discovery of the IQHE [18]. Due to the mathematical similarity between the IQHE and the simple harmonic oscillator, the spectrum of the former consists of highly-degenerate states known as “Landau levels.” As a magnetic field (B) is turned on, the evolution of the density of states from an ordinary 2D electron system ($B = 0$) to that of the IQHE ($B \neq 0$) is illustrated in Fig. 1.3.2.

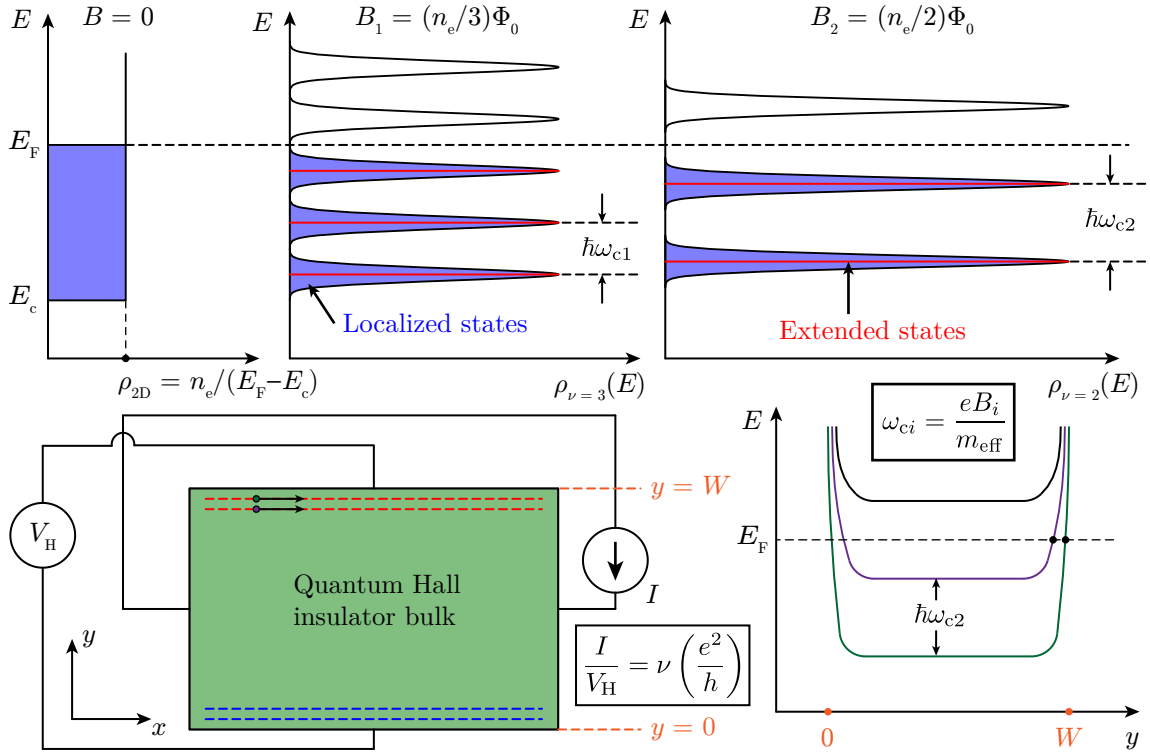


Figure 1.3.2: Evolution of the density of states as a function of magnetic field, B , perpendicular to a degenerate 2D electron system. The number of filled Landau levels determines the number of chiral edge channels.

One could crudely view the Landau levels as “flat bands,” and use an analogy to band theory to infer the transport properties of electrons in the IQHE. In this analogy, since the Fermi level is inside the spectral gap between consecutive bulk Landau levels, the bulk is an electrical insulator. On the other hand, since the Landau levels curve up at the edges (c.f. Fig. 1.3.2), the edge “bands” are partially filled; therefore, the IQHE edges are electrical conductors. It must be borne in mind, however, that unlike a band insulator, the spectral gap between Landau levels is a *mobility* gap.

Further insight can be gained into the transport properties of the IQHE by noting the fact that both: (a) number of fully occupied Landau levels in the bulk, and (b) the number of conducting edge channels, are equal to ν . This implies that, as long as the bulk spectrum is preserved, the conduction of the edge channels is robust. In other words, electrical transport at the edges is robust to local perturbations (e.g. impurities). As I will explain in Sec. 1.3.2, this robustness is the result of “chiral protection.” In fact, it is the protection aspect of the IQHE edge states which helps define the order parameter as

$$\begin{aligned} \Phi_{\text{IQHE}} &\equiv \nu, \\ &\in \mathbb{Z}. \end{aligned} \tag{1.3.3}$$

1.3.2 Topological insulators

The quantum spin Hall effect (QSHE) is the spin analog of the IQHE where spin-orbit coupling (SOC) plays the role of *spin-dependent* magnetic field. Since most non-magnetic materials¹⁵ have an equal number of spins of opposite projection, however, the net magnetic field in the QSHE is zero. The QSHE was predicted by Kane and Mele in 2005 in graphene [19]. But this proposal was experimentally infeasible, at that time, due to the low *intrinsic* spin-orbit coupling in graphene.¹⁶ The QSHE was first experimentally realized in HgTe/CdTe quantum wells [6] based on a proposal by Bernevig, Hughes, and Zhang [21].

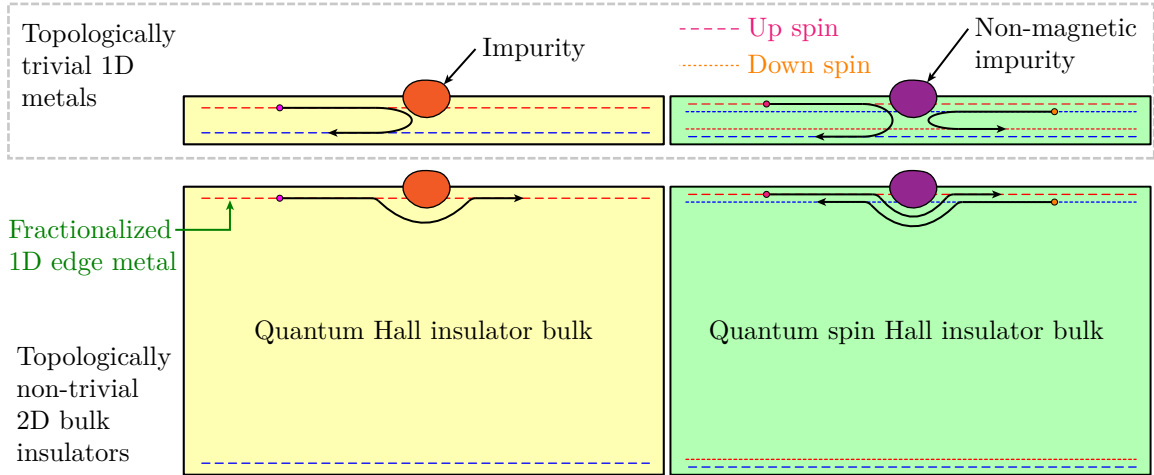


Figure 1.3.3: Edge state transport is compared between the IQHE (left) and QSHE (right). For the IQHE, the magnetic field is pointing out of the page.

Fig. 1.3.3 compares transport properties of the $\nu = 1$ IQHE with that of the QSHE. In fact, this comparison provides a unique insight into the edge transport protection mechanism of the IQHE. The magnetic field (out of the page) in the IQHE ensure that electrons only travel clockwise. This is referred to the chirality of the electron. Moreover, the spin degree of freedom has been frozen out due to the magnetic field. In that case, Fig. 1.3.3 illustrates that 1D transport is only robust to impurities when a 2D insulating bulk separates chiral 1D conduction channels. This can be crudely viewed as the electron skipping around the impurity (c.f. 1.3.1). In the QSHE, the spin degree of freedom is restored by making two copies of the IQHE with *opposite* chiralities. Moreover, it turns out that the QSHE edge states retain their robustness properties like the IQHE. But for QSHE, Landau levels do not exist. Therefore, a different spectral analysis is required to describe the QSHE.

The electronic spectrum of the QSHE (c.f. Fig. 1.3.4) is similar to that of the IQHE in the sense that there exists an excitation gap in the bulk and conductive gapless edge states. The bulk gap in the QSHE, however, corresponds to the energy threshold for creation of bulk fermionic quasiparticles, rather than a mobility gap as in the case of the IQHE. Another difference between IQHE and QSHE is the fact that the latter can be observed in 3D. The 3D analog of the QSHE, also referred to as the *topological insulator*, was soon discovered in the $\text{Bi}_x\text{Sb}_{1-x}$ alloy [7]. From here on out, any reference to topological insulators (TIs) will mean both 2D and 3D cases unless otherwise noted.

The topological order parameter, Φ_{TI} , in the case of topological insulators is very similar to that of the IQHE (c.f. Eq. (1.3.3)) with one caveat: ν is only allowed to be either 0 or 1. This can be better understood by looking at the protection of edge states in Fig. 1.3.4. For example, consider a

¹⁵Topological phenomena in magnetic materials form their own class of phases not discussed here (e.g. quantum anomalous Hall effect).

¹⁶Future proposals involved artificially increasing the *effective* SOC in graphene using 5d adatoms [20].

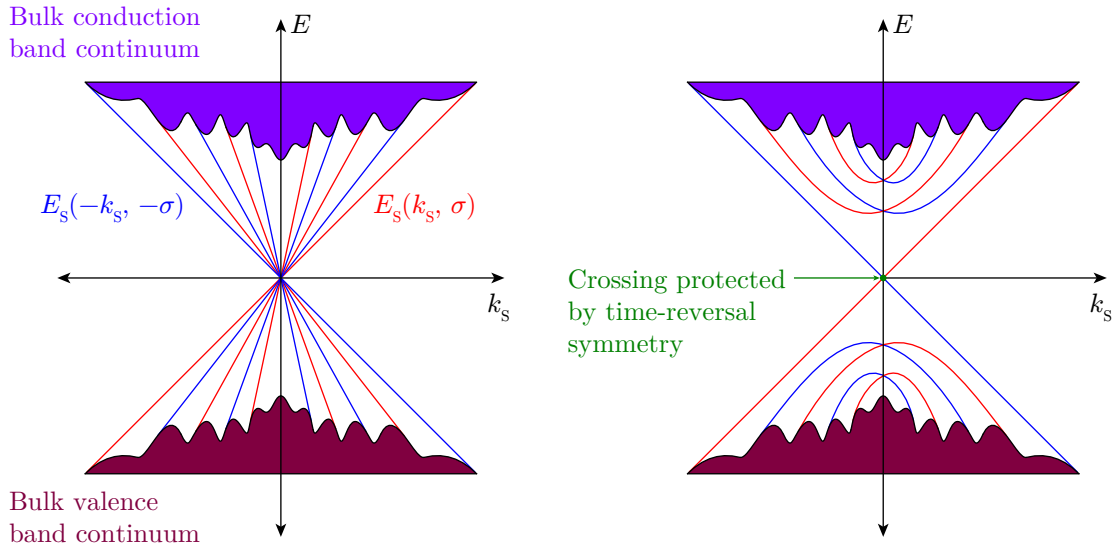


Figure 1.3.4: The bulk and boundary spectrum for two topological insulators, with five (left) and one (right) gapless Dirac states, plotted along a direction in the boundary Brillouin zone. The red and blue boundary states symmetric about the E axis are Kramers partners.

(2D or 3D) topological insulator with five Dirac cones.¹⁷ In topological insulators, the protection of edge states comes from time-reversal symmetry preservation, rather than its explicit breaking like in the IQHE. This means the system is robust to any *local* perturbations which obey time-reversal symmetry. In the example from Fig. 1.3.4, if a time-reversal symmetric perturbation were allowed to open a gap in the edge states, it can only do so for *pairs* of Dirac cones. As a result, this perturbation can *at most* open a gap in four (out of five) of the Dirac cones, thus leaving one cone gapless. Both cases shown in Fig. 1.3.4 represent the same topological phase as time-reversal symmetry was never broken. Whereas those two cases would be distinct in the IQHE. Therefore, one can define ν as

$$\nu = \text{number of edge states} \pmod{2}. \quad (1.3.4)$$

1.4 Empirical measurement of the order parameter

1.4.1 Conventional probes

Most microscopic probes of condensed matter systems, such as tunneling spectroscopy, x-ray diffraction, and neutron scattering, to name a few, are sensitive to the *local* region of the sample to which they have been tuned. In this discussion, I will refer to such probes as *conventional*. The biggest challenge in studying many-body order using conventional probes is primarily technical. One has to deal with challenges such as:

- growing single crystals of high quality,¹⁸

¹⁷From here on out, Dirac “cones” will mean both the (geometrically accurate) cones on the surface of 3D topological insulator and the (Kramers) pair of 1D bands at the edge of a 2D topological insulator.

¹⁸Here I define sample quality as the scarcity of lattice defects and impurities. Quality requirements/definitions may differ for different probes.

- creating a probe-accessible environment stable enough to sustain an ordered phase under extreme conditions of (say) temperature, magnetic field, and hydrostatic pressure,
- building detectors with sensitivity high enough to measure weak signals that carry information about the order parameter, and
- optimizing the *entire* measurement instrument (not just the detector) to measure system observables with high enough resolution.¹⁹

1.4.2 Topological probes

Using conventional probes to look for topological phases is much more subtle than overcoming technical barriers. One could argue that as one of the reasons behind topological phases only receiving mainstream attention since the 1980s. To date, the only unanimously accepted topological phases experimentally realized in *crystalline solids* are: IQHE, FQHE, TIs, QAHE, WSMs, and TSCs. For the moment, if I ignore technical limitations, and I imagine building novel probes *directly* sensitive to topological order parameters, then *some* of the challenges are:²⁰

- defining the probe-induced excitation and corresponding observable, and
- interpretation of the observable such that global order is evident.

Albeit the technical challenges will undoubtedly follow! An example which illustrates the above challenges using two *relatively* well-understood phases is as follows:

If one only focuses on the bulk of a 2D TI and the FQHE, with (hypothetically) no access to global information like (say) electrical transport, a local probe will see an ordinary-looking excitation gap in both cases. But if a *local* quasiparticle excitation is created in both cases, and its charge is measured using (say) a scanning single-electron transistor [22], it will be obvious that the system with a fractional quasiparticle charge is the FQHE. This was a contrived example²¹ used to make the point: it is conceivable that there might be a large number of topological phases which cannot be distinguished from one another using conventional probes.

For example, a category of topological phases which appears experimentally viable [23], and is theoretically intriguing [24], is that of quantum spin liquids (QSLs). One of the biggest challenges with studying QSLs is that they are, by definition, featureless. In other words, a system can only be a QSL if it is disordered according to the Ginzburg-Landau theory! There are currently theoretical and experimental efforts underway to address the challenge of theoretically and experimentally discovering QSLs [25].

1.5 Outlook

1.5.1 Generalizing local and topological order parameters

It is worth noting that the experimentally realized examples of topological phases, in crystalline solids, are hosted in systems (i.e. lattices) that can still be described by the Ginzburg-Landau theory.

¹⁹I'm limiting this discussion to (classical) technical resolution limitations. In other words, I won't discuss resolution limited by Heisenberg's uncertainty principle.

²⁰This is not an exhaustive list as topological phases are still being investigated.

²¹This example is contrived because electrical transport is possible on these systems.

So it's fair to say that the discovery of topological phases adds a new dimension to existing Ginzburg-Landau framework, rather than forming a mutually exclusive set. Recall that I briefly discussed the protection of edge states of topological insulators due to time-reversal symmetry (TRS) in Sec. 1.3.2. As evident from the example in Fig. 1.3.4, an argument could be made that topological insulators can, in fact, be uniquely described (or defined) in terms the protection aspect. Moreover, that protection was a direct result of time-reversal symmetry. It's conceivable that if a protection-offering symmetry (not necessarily TRS) is added to an existing ordered phase defined by the Ginzburg-Landau symmetry paradigm, then a new topological phase might be obtained. In other words, the protection-offering symmetry, along with the set of broken symmetries, can form a superset which uniquely labels the phase under discussion.

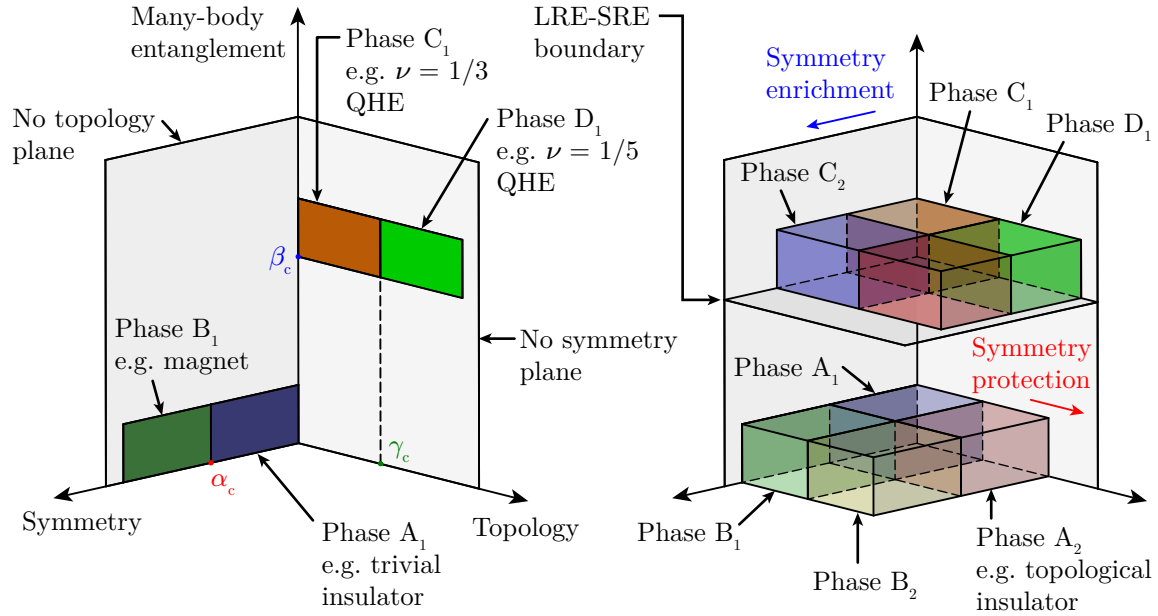


Figure 1.5.1: A conceptual phase diagram illustrating how adding a topological dimension to conventionally symmetry breaking phase and symmetry to conventionally topological phases makes a richer phase diagram. α_c , β_c , and γ_c represent critical points.

It turns out that it is indeed possible to divide a system exhibiting an ordered phase, according to Ginzburg-Landau theory, into a subset of phases based on the type of symmetry introduced; such systems are called “symmetry protected topological” phases (SPTs) [26]. Analogous to the use of group theory in the Ginzburg-Landau theory, SPTs can be classified using group cohomology. A conceptual phase diagram illustrating this idea is shown in Fig. 1.5.1 where I have introduced the notion of many-body entanglement.²²

Fig. 1.5.1 illustrates another important point: prior to the discovery of topological insulators, phases defined by symmetry breaking were limited to so-called short-range entangled (SRE) systems. Alternatively, phases described by a topological order parameter (e.g. FQHE) were limited to so-called long-range entangled (LRE) systems [27]. Therefore, the term long-range entanglement became synonymous with topological order. After the discovery of topological insulators, however, and the subsequent *mainstream*²³ recognition of SPTs, it became obvious that topological order is not limited to LRE systems. Interestingly, an awareness of SPTs led to the development of the notion of “symmetry-enriched topological” phases (SETs). The latter is achieved by adding a symmetry breaking dimension to an LRE phase.

²²The interested reader can refer to [27] for definition of long-range entangled states.

²³It is fascinating that Haldane theoretically discovered an SPT phase, in 1983, only three years after the discovery of the integer quantum Hall effect [28]!

The phase diagram in Fig. 1.5.1 is still being mapped out. It may serve as fruitful ground, for both experimentalists and theorists, in the discovery of novel forms of order. Perhaps this phase-mapping exercise can even provide new revelations about already-discovered exotic many-body orders.²⁴

1.5.2 Systems out of equilibrium

I will conclude this chapter by briefly listing areas of research which, in my opinion, have the *potential* of discovering unorthodox forms of order not yet conceivable. Such systems are *currently* outside the scope of both Ginzburg-Landau and topological classification schemes. One implicit property of all the phases I discussed so far was: equilibrium. Existence of equilibrium in a ordered state, in a condensed matter system, is usually taken for granted, probably due to the perceived intractability of the alternative. Some examples of such alternative phenomena include: (a) non-equilibrium dynamics of quasiparticle excitations, (b) time-varying systems in steady-state (e.g. Floquet), and (c) systems which do not thermalize (e.g. many-body localization). It remains to be seen if it is possible to combine these *seemingly* disparate many-body systems into unified theoretical framework.

²⁴Theorists currently disagree on where the integer quantum Hall effect qualifies as an LRE or SRE system!

Chapter 2

Topological superconductivity

2.1 Introduction and motivation

By the end of the 2000s decade, quantum Hall and topological insulators were arguably the only real-world examples of topological phases. However, the disparity between theoretical predictions and experimental realizations of topological phases started growing rapidly. The discussion in Sec. 1.5.1 represents a small sample of this disparity. Nevertheless, one topic which continued to fascinate both theorists and experimentalists was that of topological superconductivity.

On a conceptual level, the spectral similarities between insulators and superconductors made the extension of topology to the latter straightforward.¹ For experimentalists, the century-long experience with superconductors made realization of topological superconductors a realistic goal. For theorists, topological superconductivity provided a new avenue for exploring exotic topological field theories and quantum information.

Arguably one of the most appealing attributes of topological superconductors is their ability to host quasiparticles which mimic the Majorana fermions first predicted in the context of high-energy physics [29]. The behavior of these quasiparticles at the Fermi level is of great interest because they exhibit *anyonic* exchange statistics.² This property makes Majorana quasiparticles a promising tool for building low-decoherence qubits [31]. Therefore, a major collaborative effort developed in the early 2010s, between theorists and experimentalists, in the search for Majorana quasiparticles, or equivalently topological superconductors.

In 2012, I started researching topological materials. The primary objective of my thesis projects was the experimental discovery of 3D topological superconductors. I worked on developing electron and photon spectroscopic techniques to both directly and indirectly identify 3D topological superconductors. In this context, “direct” means detection of the Majorana quasiparticle. There exist, however, subtle indirect methods of inferring the existence of Majorana quasiparticles by studying properties of the superconducting state. I will briefly discuss a project involving the latter in Sec. 9.4.1.

In this chapter, I will review the properties of superconductors, and analyze the properties which make them topological. This analysis should serve as a prerequisite for the strategies experimentalists

¹Straightforward but not necessarily trivial.

²In a degenerate N -particle system of bosons (fermions), the exchange of *any* two bosons (fermions) results in the many-body wave function acquiring a factor of $+1$ (-1). In the case of anyons, a factor of $e^{i\theta}$ is acquired by the wave function. In general, θ can be a matrix [30].

have used to directly and indirectly identify topological superconductors. I will provide a few examples of these strategies based on a combination of their: (a) impact on the research community, and (b) direct relevance to my thesis projects (c.f. Sec. 2.4).³

2.2 Review of superconductivity

In this section, I will *briefly* review a handful of concepts and formalism required to study superconductivity. I will only cover formal and phenomenological aspects which aide in the analysis of properties of topological superconductors. A detailed discussion on this topic can be found in various textbooks (e.g. [2, 32]).

2.2.1 Phenomenology

Superconductivity is one of the first examples of experimentally observed macroscopic quantum phenomena. A superconductor is obtained by cooling a metal below its critical temperature, T_c . According to the Nobel-prize-winning Bardeen-Cooper-Schieffer (BCS) theory [33], superconductivity in metals results from the pairing of electrons (fermions), close to the Fermi surface, into bosonic entities called Cooper pairs, followed by a condensation of these Cooper pairs into a single macroscopic quantum state. This condensation phenomenon is similar to the Bose-Einstein condensation (BEC) observed in superfluid Helium-4.

In the simplest case, the order parameter, Ψ , of a superconductor is similar to that of superfluid Helium-4

$$\Psi = \Delta e^{i\theta}, \quad (2.2.1)$$

where Δ ($\in \mathbb{R}$) is proportional to the amount of energy required to break a Cooper pair into two electrons, and θ corresponds to the phase corresponding to macroscopic coherence of the condensate; the latter results from the breaking of U(1) gauge symmetry.

2.2.2 BCS theory formalism

2.2.2.1 Solution to the interacting metal problem

A simple second-quantized Hamiltonian of a metal, on a lattice, with electronic interactions can be written as

$$\hat{\mathcal{H}} = \sum_{i,j,\sigma} t_{ij} \hat{c}_{i,\sigma}^\dagger \hat{c}_{j,\sigma} + \sum_{i,j,k,l} \sum_{\alpha,\beta,\gamma,\delta} U_{ijkl,\alpha\beta\gamma\delta} \hat{c}_{i,\alpha}^\dagger \hat{c}_{j,\beta}^\dagger \hat{c}_{k,\gamma} \hat{c}_{l,\delta}, \quad (2.2.2)$$

where t_{ij} is the spin-independent hopping amplitude of the electron from site j to i ,⁴ $\hat{c}_{i,\sigma}^\dagger$ ($\hat{c}_{i,\sigma}$) is the creation (annihilation) operator for an electron on lattice site i with pseudo-spin σ ,⁵ and $U_{ijkl,\alpha\beta\gamma\delta}$ is a four-fermion scattering amplitude for two electrons at sites k and l , with spins γ and δ respectively, scattering into states at sites i and j , with spins α and β respectively.

In order to solve (2.2.2), in the context of superconductivity, I will make the following approximations:

³Of course, I will discuss (b) in greater detail.

⁴The assumption that t_{ij} is spin-independent holds in most materials. There exist exceptions like the edges of quantum spin Hall insulators. But I will ignore these esoteric cases for simplicity.

⁵I will keep the analysis general by using the pseudo-spin degree of freedom as real spin is may not always be a good quantum number. One example of the latter is systems with non-negligible spin-orbit coupling.

1. Zero-momentum pairing
2. Mean-field approximation
3. Momentum (\mathbf{k}) close to the Fermi wave vector (\mathbf{k}_F)
4. Energy (E) close to the Fermi energy (μ)⁶

In the mean-field approximation, (2.2.2) can be expressed in a convenient form as

$$\hat{\mathcal{H}}_{\text{MF}} = \sum_{\mathbf{k},\sigma} [\tilde{t}(\mathbf{k}) - \mu] \hat{c}_{\mathbf{k},\sigma}^\dagger \hat{c}_{\mathbf{k},\sigma} + \frac{1}{2} \sum_{\mathbf{k},\gamma,\delta} \Delta_{\mathbf{k},\gamma\delta}^* \hat{c}_{\mathbf{k},\gamma} \hat{c}_{-\mathbf{k},\delta} + \frac{1}{2} \sum_{\mathbf{k},\alpha,\beta} \Delta_{\mathbf{k},\alpha\beta} \hat{c}_{\mathbf{k},\alpha}^\dagger \hat{c}_{-\mathbf{k},\beta}^\dagger, \quad (2.2.3)$$

where Δ^* is a function of $U_{ijkl,\alpha\beta\gamma\delta}$, $\tilde{t}(\mathbf{k})$ is a function of t_{ij} , and μ is the chemical potential. For conventional (s -wave) superconductors, the pairing would be spin-singlet. So (2.2.3) can be further simplified to

$$\hat{\mathcal{H}}_{\text{MF}} = \sum_{\mathbf{k},\sigma} [\tilde{t}(\mathbf{k}) - \mu] \hat{c}_{\mathbf{k},\sigma}^\dagger \hat{c}_{\mathbf{k},\sigma} + \frac{1}{2} \sum_{\mathbf{k}} \left\{ \Delta_{\mathbf{k}}^* \hat{c}_{\mathbf{k},\uparrow} \hat{c}_{-\mathbf{k},\downarrow} + \Delta_{\mathbf{k}} \hat{c}_{\mathbf{k},\uparrow}^\dagger \hat{c}_{-\mathbf{k},\downarrow}^\dagger + \text{h.c.} \right\}, \quad (2.2.4)$$

where h.c. stands for Hermitian conjugate. After some formal manipulation (c.f. Sec. A.1.1), (2.2.4) can be written in a convenient matrix form as

$$\hat{\mathcal{H}}_{\text{MF}} = \sum_{\mathbf{k}} \hat{C}_{\mathbf{k}}^\dagger h_{\text{MF}}(\mathbf{k}) \hat{C}_{\mathbf{k}}, \quad (2.2.5)$$

where

$$\hat{C}_{\mathbf{k}} \equiv \begin{bmatrix} \hat{c}_{\mathbf{k},\uparrow} \\ \hat{c}_{-\mathbf{k},\downarrow}^\dagger \\ \hat{c}_{-\mathbf{k},\downarrow} \\ \hat{c}_{\mathbf{k},\uparrow}^\dagger \end{bmatrix}, \quad (2.2.6)$$

and

$$h_{\text{MF}}(\mathbf{k}) \equiv \begin{bmatrix} (\tilde{t}(\mathbf{k}) - \mu) & \Delta_{\mathbf{k}} & 0 & 0 \\ \Delta_{\mathbf{k}}^* & -(\tilde{t}(\mathbf{k}) - \mu) & 0 & 0 \\ 0 & 0 & (\tilde{t}(\mathbf{k}) - \mu) & \Delta_{\mathbf{k}} \\ 0 & 0 & \Delta_{\mathbf{k}}^* & -(\tilde{t}(\mathbf{k}) - \mu) \end{bmatrix}, \quad (2.2.7)$$

Upon diagonalizing the 4×4 matrix $h_{\text{MF}}(\mathbf{k})$ (see Sec. A.1.1) I get the following eigenvalues

$$\xi_{\pm}(\mathbf{k}) = \pm \sqrt{(\tilde{t}(\mathbf{k}) - \mu)^2 + |\Delta_{\mathbf{k}}|^2}, \quad (2.2.8)$$

where $\xi_{\pm}(\mathbf{k})$ represents the quasiparticle excitation energy relative to the Fermi level (μ). Then the effective “band structure” of the system is

$$E(\mathbf{k}) = \begin{cases} \mu + \xi_+(\mathbf{k}) & E > \mu \\ \mu + \xi_-(\mathbf{k}) & E < \mu \end{cases}, \quad (2.2.9)$$

It's worth noting that for $|\tilde{t}(\mathbf{k}) - \mu| \gg |\Delta_{\mathbf{k}}|$ the band structure of the normal metal is recovered ($E(\mathbf{k}) \approx \tilde{t}(\mathbf{k})$).⁷

Furthermore, based on the mathematical form of Eq. (2.2.8), it can be observed that $\hat{\mathcal{H}}_{\text{MF}}$ has been transformed into an approximate tight-binding model for a many-body system that *effectively* looks like an insulator with a single-particle gap $2|\Delta|$; the center of the gap is at the energy level μ . This spectrum can be conceptually represented in the surface plot to the right of Fig. 2.2.1.

⁶This is *crudely* reflected in the $|\tilde{t}(\mathbf{k}) - \mu| \gg |\Delta_{\mathbf{k}}|$ limit of Eq. (2.2.9). I slightly more detailed argument is presented at the end of Sec. A.1.1.

⁷In order to see this, a mathematical technicality in Eq. (2.2.8) has to be “swept under the rug.” The $|\tilde{t}(\mathbf{k}) - \mu| \gg |\Delta_{\mathbf{k}}|$ limit will strictly yield $\xi_{\pm}(\mathbf{k}) = \pm|\tilde{t}(\mathbf{k}) - \mu|$. One has to use physical intuition to argue that the μ in $\xi_{\pm}(\mathbf{k})$ will cancel the one in (2.2.9).

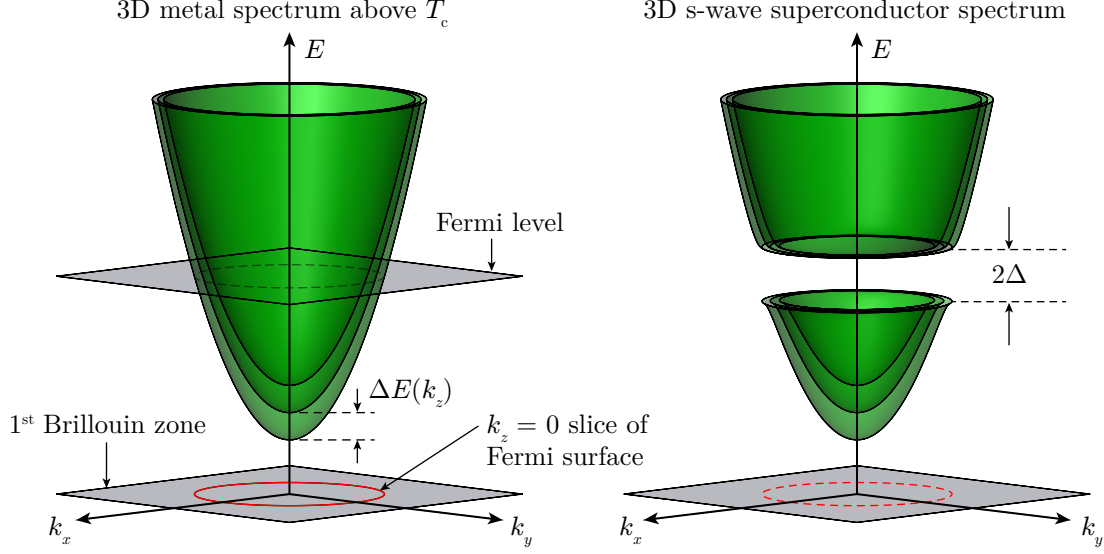


Figure 2.2.1: The spectrum of a 3D metal (left) and the spectrum of the corresponding BCS superconductor (right). For $\tilde{t}(\mathbf{k}) \approx \hbar^2 \mathbf{k}^2 / 2m_{\text{band}} \equiv \hbar^2 (k_x^2 + k_y^2 + k_z^2) / 2m_{\text{band}}$, I can schematically plot the full $\tilde{t}(\mathbf{k})$ by limiting to just the k_x and k_y axes and plotting a family of parabolas with different k_z . These parabolas are displaced along the energy axis by $\Delta E(k_z) = (\hbar^2 k_z / m_{\text{band}}) \Delta k_z$ where $\Delta k_z \sim 2\pi / L_z$ with L_z being the system size along the z direction. In the thermodynamic limit, these parabolas would just look like a blob.

2.2.2.2 Identity of the quasiparticles in the BCS spectrum

It is worth noting that after diagonalizing $\hat{\mathcal{H}}_{\text{MF}}$ in (2.2.5), the electronic basis $\hat{C}_{\mathbf{k}}$ (c.f. Eq. (2.2.6)) I started out in Eq. (2.2.2), is no longer a proper basis for the excitations described by Eq. (2.2.8). Upon computing the eigenvectors of the 4×4 matrix $h_{\text{MF}}(\mathbf{k})$ one can find a unitary transformation, $U_{4 \times 4}$, from $\hat{C}_{\mathbf{k}}$ to the diagonal basis of $\hat{\mathcal{H}}_{\text{MF}}$ denoted by (say) $\hat{B}_{\mathbf{k}}$

$$\hat{B}_{\mathbf{k}} = U_{4 \times 4} \hat{C}_{\mathbf{k}}, \quad (2.2.10)$$

Then one can define a new annihilation (creation) operator $\hat{b}_{\mathbf{k},\sigma}$ ($\hat{b}_{\mathbf{k},\sigma}^\dagger$) and

$$\hat{B}_{\mathbf{k}} \equiv \begin{bmatrix} \hat{b}_{\mathbf{k},\uparrow} \\ \hat{b}_{-\mathbf{k},\downarrow}^\dagger \\ \hat{b}_{-\mathbf{k},\downarrow} \\ \hat{b}_{\mathbf{k},\uparrow}^\dagger \end{bmatrix}, \quad (2.2.11)$$

in terms of the creation (annihilation) operator of the electron $\hat{c}_{\mathbf{k},\sigma}$ ($\hat{c}_{\mathbf{k},\sigma}^\dagger$) as

$$\begin{bmatrix} \hat{b}_{\mathbf{k},\uparrow} \\ \hat{b}_{-\mathbf{k},\downarrow}^\dagger \\ \hat{b}_{-\mathbf{k},\downarrow} \\ \hat{b}_{\mathbf{k},\uparrow}^\dagger \end{bmatrix} = \begin{bmatrix} u_{\mathbf{k}} & v_{\mathbf{k}}^* & 0 & 0 \\ v_{\mathbf{k}} & u_{\mathbf{k}}^* & 0 & 0 \\ 0 & 0 & v_{\mathbf{k}} & u_{\mathbf{k}}^* \\ 0 & 0 & u_{\mathbf{k}} & v_{\mathbf{k}}^* \end{bmatrix} \begin{bmatrix} \hat{c}_{\mathbf{k},\uparrow} \\ \hat{c}_{-\mathbf{k},\downarrow}^\dagger \\ \hat{c}_{-\mathbf{k},\downarrow} \\ \hat{c}_{\mathbf{k},\uparrow}^\dagger \end{bmatrix}, \quad (2.2.12)$$

where

$$|u_{\mathbf{k}}| = \frac{1}{\sqrt{2}} \left(1 + \frac{\tilde{t}(\mathbf{k}) - \mu}{\sqrt{(\tilde{t}(\mathbf{k}) - \mu)^2 + |\Delta_{\mathbf{k}}|^2}} \right)^{1/2}, \quad (2.2.13)$$

$$|v_{\mathbf{k}}| = \frac{1}{\sqrt{2}} \left(1 - \frac{\tilde{t}(\mathbf{k}) - \mu}{\sqrt{(\tilde{t}(\mathbf{k}) - \mu)^2 + |\Delta_{\mathbf{k}}|^2}} \right)^{1/2}. \quad (2.2.14)$$

The $\hat{b}_{\mathbf{k},\sigma}/\hat{b}_{\mathbf{k},\sigma}^\dagger$ operators correspond to what are known as the Bogoliubov quasiparticles.

In Sec. 2.3.2, I will introduce a special class of Bogoliubov quasiparticles known as *Majorana fermions* (or quasiparticles).⁸

2.3 Topological superconductors

2.3.1 Properties of the superconducting gap

2.3.1.1 Spatial symmetries

The properties of the gap(s) in the Bogoliubov quasiparticle spectrum of *any* class of superconductor convey a considerable amount of information about the nature of superconductivity in that system. Before looking at the gaps of unconventional superconductors, however, consider the BCS example from Sec. 2.2.2.1. For an *s*-wave superconductor, the gap function Δ has no \mathbf{k} dependence. This can be achieved using on-site or isotropic pairing.

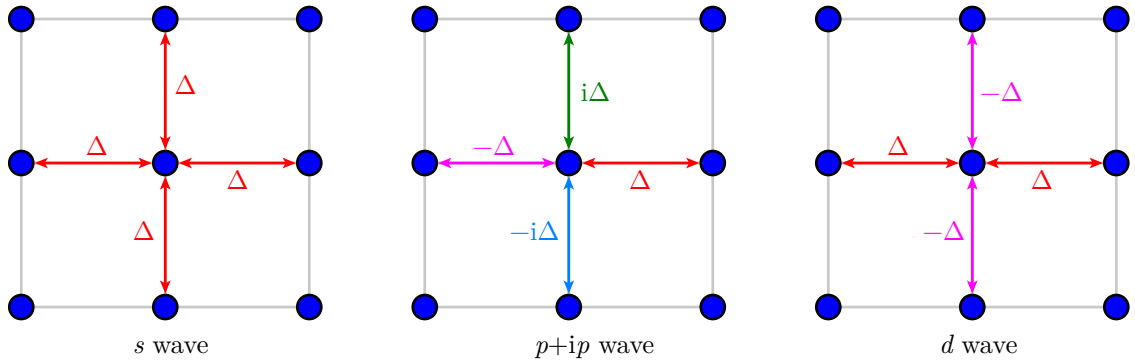


Figure 2.3.1: Pairing amplitudes of electrons on nearest neighbor sites in *s*, *p + ip*, and *d* wave superconductors on a 2D square lattice.

For non-*s*-wave superconductors, an on-site interaction cannot be used because there is no way of encoding pairing anisotropy. For (say) *p*- and *d*-wave superconductors, one needs to expand the sum (Eq. (2.2.2)) over all the j lattice sites nearest to a site i and use the appropriate pairing amplitude in each direction as shown in Fig. 2.3.1. For ease of visualization, I have discretized angular variation of Δ on a 2D square lattice. In general, gap functions of an ℓ -wave superconductor can be expressed as

⁸Majorana “fermions” is not technically accurate as they can exhibit anyonic statistics. Therefore, I will keep referring to them as Majorana quasiparticles.

a linear combination of spherical harmonic $Y_{\ell,m}$. For example, for p -wave superconductors ($\ell = 1$), the pairing amplitude between electrons at positions \mathbf{r} and \mathbf{r}' can be written as

$$\Delta(\mathbf{r}, \mathbf{r}') = \sum_{m=-1}^{+1} c_m(r) Y_{1,m}(\theta, \phi), \quad (2.3.1)$$

where $c_m(r)$ is the (complex) weight of the $Y_{1,m}(\theta, \phi)$ spherical harmonic and (r, θ, ϕ) are the spherical coordinates of vector $\mathbf{r} - \mathbf{r}'$.

2.3.1.2 Spin symmetries

Complementary information about the superconducting gap can be obtained by looking at the spin of Cooper pairs. Therefore, considering the spin degree of freedom explicitly, the superconducting gap function can be written, more generally, as

$$\Delta_{\alpha\beta}(\mathbf{r}, \mathbf{r}') = f(\mathbf{r}, \mathbf{r}') g_{\alpha\beta}, \quad (2.3.2)$$

where α and β represent the spin indices of the electrons, located at \mathbf{r} and \mathbf{r}' respectively, forming the Cooper pair. Now, according to fermionic exchange statistics, one expects

$$\Delta_{\alpha\beta}(\mathbf{r}, \mathbf{r}') = -\Delta_{\beta\alpha}(\mathbf{r}', \mathbf{r}). \quad (2.3.3)$$

This implies that either

$$\begin{aligned} f(\mathbf{r}, \mathbf{r}') &= f(\mathbf{r}', \mathbf{r}), \\ g_{\alpha\beta} &= -g_{\beta\alpha}, \end{aligned} \quad (2.3.4)$$

or

$$\begin{aligned} f(\mathbf{r}, \mathbf{r}') &= -f(\mathbf{r}', \mathbf{r}), \\ g_{\alpha\beta} &= g_{\beta\alpha}, \end{aligned} \quad (2.3.5)$$

holds. The cases (2.3.4) and (2.3.5) are referred to as spin-singlet and spin-triplet respectively. According to (2.3.1), spin-singlet and spin-triplet is associated with even and odd values of ℓ .

Since there is a direct correlation between spin and orbital components of the Cooper pair, it often suffices to consider one or the other. This distinction could, however, prove useful in (say) experimental probes which are sensitive to one versus the other. For example, probes like μ SR, which are sensitive to spin of the Cooper pairs, can indirectly infer the topological (e.g. p -wave) nature of a superconductor.

2.3.2 Minimal models of topological superconductors in 1D and 2D

In this section, I will cover topological superconductor (TSC) models in 1D and 2D. I'll cover the 3D case (Sec. 2.3.4) after a detour into topological insulators. That is because the intuition gained from 1D and 2D topological superconductors, combined with a review of 3D topological insulators, will help better understand the case of the 3D time-reversal invariant topological superconductor that I am interested in detecting using ARPES.

In Sec. 2.3.2.1, I will solve the Kitaev chain [34] and show how two so-called Majorana zero modes (MZMs) can be localized at the ends of a 1D wire. In Sec. 2.3.2.2, I will discuss the conditions for making a 2D $p + ip$ superconductor topological. But I would be remiss if I did not mention the

prediction, by Read and Green [35], of Majorana quasiparticles in the ($\nu = 5/2$) Moore-Read state, resulting from a superconductor-like state of paired *composite fermions*⁹ in the fractional quantum Hall effect. This prediction actually predated Kitaev's prediction of Majorana quasiparticles in 1D. My reason for choosing the examples in Sec. 2.3.2.1-2.3.2 is their conceptual similarity and simplicity.

2.3.2.1 1D

In the year 2000, Alexei Kitaev formulated an elegant and simple model of topological superconductivity on a 1D lattice [34]. The Hamiltonian for the so-called “Kitaev chain” on a 1D lattice with N sites can be written as

$$\hat{H} = - \sum_{i=1}^{N-1} \left(t_{\text{hop}} \hat{c}_i^\dagger \hat{c}_{i+1} + \Delta \hat{c}_i \hat{c}_{i+1} + \text{h.c.} \right) - \mu \sum_{i=1}^N \hat{c}_i^\dagger \hat{c}_i, \quad (2.3.6)$$

where \hat{c}_i^\dagger (\hat{c}_i) creates (annihilates) a spinless electron¹⁰ on lattice site i . The lattice constant is denoted a . The variable t_{hop} is the electron's hopping amplitude between nearest neighbor sites (i and $i \pm 1$). Moreover, based on the convention chosen in Fig. 2.3.1, the system is placed along the horizontal (i.e. x) axis. Hence, Δ is the pairing amplitude between electrons on nearest neighbor sites (i and $i \pm 1$). The quantity μ is the chemical potential. Finally, h.c. stands for Hermitian conjugate. Note that the mean-field approximation has already been incorporated into (2.3.6).

It is also worth noting, from Fig. 2.3.1, that (2.3.6) exhibits p -wave pairing. Swapping \hat{c}_i and \hat{c}_{i+1} in the second (pairing) term of (2.3.6) gives $-\Delta \hat{c}_{i+1} \hat{c}_i$, where the negative sign is the result fermionic anti-commutation relationship $\{\hat{c}_i, \hat{c}_{i+1}\} = 0$. A direct comparison with Fig. 2.3.1 would suggest the chain in (2.3.6) is parallel to the horizontal axis. So I do not need to consider the $i\Delta$ amplitude. That will matter in 2D.

Using the procedure I presented in Sec. 2.2.2, (2.3.6) can be diagonalized in momentum space. I will denote the crystal momentum as k_x . Upon performing a unitary Wannier-to-Bloch basis transformation (A.1.4), (2.3.6) can be written in the form given by (2.2.3), with the sum over spins dropped, and

$$\tilde{t}(k_x) - \mu = -2t_{\text{hop}} \cos(k_x a) - \mu, \quad (2.3.7)$$

$$\begin{aligned} \Delta_{k_x, \alpha\alpha} &\equiv \Delta_{k_x}, \\ &= 2\Delta \sin(k_x a). \end{aligned} \quad (2.3.8)$$

Note that (2.3.8) is consistent with the odd parity of a p -wave gap function. Moreover, the repeated spin index α , in (2.3.8), indicates spin-triplet pairing, which is obvious for pairing between spinless electrons.

Finally, using (2.2.8), the Bogoliubov dispersion relative to the chemical potential can be written as

$$\xi_{\pm}(k_x) = \pm \sqrt{(2t_{\text{hop}} \cos(k_x a) + \mu)^2 + 4\Delta^2 \sin^2(k_x a)}. \quad (2.3.9)$$

For appropriately chosen parameters t_{hop} , μ , and Δ , the Kitaev chain has a fully-gapped *bulk* Bogoliubov quasiparticle spectrum. For example, consider the following choice of parameters

$$\begin{aligned} t_{\text{hop}} &= \Delta, \\ \mu &= 0. \end{aligned} \quad (2.3.10)$$

⁹For the $\nu = 5/2$ case, the composite fermion is formed by “attaching” two flux quanta (i.e. h/e each) to a spin-polarized electron confined to a 2D sheet. The resulting system of composite fermions behaves like a Fermi liquid experiencing no magnetic field. The interested reader can find more information on composite fermions in [16].

¹⁰In this context, spinless means the spin degree of freedom has been suppressed. The operator \hat{c}_i should **not** be confused with a scalar quantum field; the latter is a boson. In practice, an example of a spinless fermion would be a spin-polarized electron due to (say) an external magnetic field.

Then, (2.3.9) reduces to

$$\xi_{\pm}(k_x) = \pm 2t_{\text{hop}}. \quad (2.3.11)$$

Based on the spectral analysis, in momentum space, there is naively no reason to suspect any qualitatively different physics from a conventional (s -wave) superconductor. It was Kitaev's unique approach of diagonalizing (2.3.6) in real space, however, that led to one of the first predictions of Majorana quasiparticles in a condensed matter system.¹¹ The real-space diagonalization procedure is as follows.

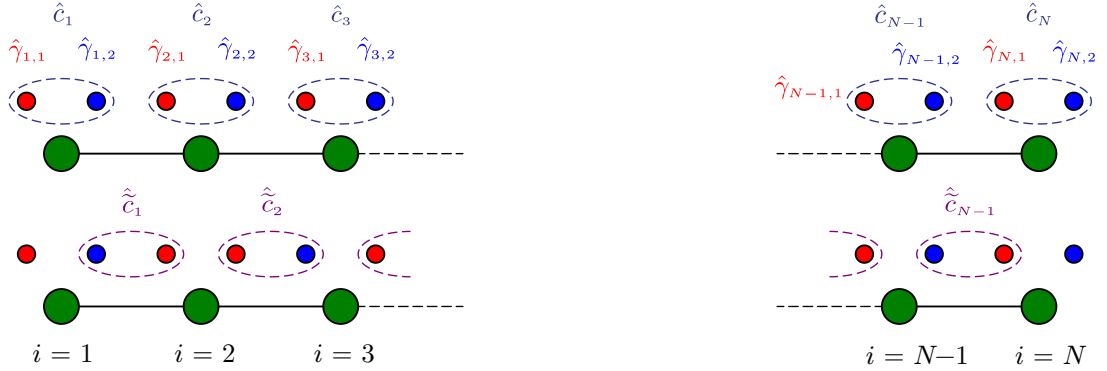


Figure 2.3.2: Unpaired (top) and paired (bottom) phases of the Kitaev chain.

I will express the electron operator, \hat{c}_i , as a coherent superposition of two new operators $\hat{\gamma}_{i,1}$ and $\hat{\gamma}_{i,2}$ as

$$\hat{c}_i = \frac{1}{2}(i\hat{\gamma}_{i,1} + \hat{\gamma}_{i,2}), \quad (2.3.12)$$

then $\hat{\gamma}_{i,1}$ and $\hat{\gamma}_{i,2}$ will each carry half the degrees of freedom of \hat{c}_i . These new operators can be crudely seen as the real and imaginary parts of the “standard” electron. Moreover, it is assumed that

$$\hat{\gamma}_{i,k} = \hat{\gamma}_{i,k}^\dagger, \quad (2.3.13)$$

where $i \in [1, N]$ and $k = 1, 2$. A straightforward manipulation of Eq. (2.3.12) gives

$$\begin{aligned} \hat{\gamma}_{i,1} &= i(\hat{c}_i^\dagger - \hat{c}_i), \\ \hat{\gamma}_{i,2} &= \hat{c}_i^\dagger + \hat{c}_i, \end{aligned} \quad (2.3.14)$$

This type of mathematical manipulation was first made in the context of high-energy physics, for the Dirac equation, by Ettore Majorana in 1937 [29]. Therefore, from here on out, I will refer to $\hat{\gamma}_{i,1}$ and $\hat{\gamma}_{i,2}$ as *Majorana operators*. The fact that the Majorana operators are fermions can be seen by plugging (2.3.12) into the standard fermion anti-commutation relation, $\{\hat{c}_i^\dagger, \hat{c}_j\} = \delta_{ij}$, to give

$$\{\hat{\gamma}_{i,k}, \hat{\gamma}_{j,\ell}\} = 2\delta_{ij}\delta_{k\ell}. \quad (2.3.15)$$

I will now show that Eq. (2.3.6) can be expressed purely in terms of Majorana operators. Plugging (2.3.12) into (2.3.6), assuming the parameters as Eq. (2.3.10) for mathematical simplicity,¹² and

¹¹I would once again like to emphasize that the first prediction of Majorana quasiparticles in a condensed matter system was made by Read and Green [35]. The Kitaev model was explored experimentally, a decade later, to greater extent due to its simplicity.

¹²Solving for the $t_{\text{top}} \neq \Delta$ case does not change the primary conclusions of this analysis.

using the anti-commutation relation (2.3.15), gives

$$\hat{\mathcal{H}} = -it_{\text{hop}} \sum_{i=1}^{N-1} \hat{\gamma}_{i,2} \hat{\gamma}_{i+1,1}. \quad (2.3.16)$$

Looking simply at (2.3.16), with no knowledge of (2.3.6), one can conclude that the system is entirely composed of Majorana quasiparticles. It's also worth noting that $\hat{\gamma}_{1,1}$ and $\hat{\gamma}_{N,2}$ are missing from (2.3.16). Since these operators don't contribute to the Hamiltonian (2.3.16), the Majorana quasiparticles at the ends of the Kitaev chain don't require any energy to create. In other words, the end Majorana quasiparticles occupy zero-energy states not accounted for by the bulk dispersion (2.3.11). Such a state corresponds to the case illustrated at the bottom of Fig. 2.3.2. This visual representation aides the real-space diagonalization of the Kitaev chain.

In order to finish the real-space diagonalization procedure, it is instructive to contrast the top and bottom cases of Fig. 2.3.2. The top case corresponds to the choice of the electron basis (2.3.12). In this case, there are no free or "unpaired" Majorana quasiparticles at the ends of the Kitaev chain. If, however, pairing between Majorana quasiparticles on nearest-neighbor sites occurred, then the appropriate electron basis would be

$$\hat{c}_i = \frac{1}{2}(\hat{\gamma}_{i+1,1} + i\hat{\gamma}_{i,2}). \quad (2.3.17)$$

It turns out that the Kitaev chain, with the parameters in (2.3.10), is diagonal in the basis given by (2.3.17)! This can be verified by plugging (2.3.17) and (2.3.10) back in (2.3.6). After some algebraic manipulation I get

$$\hat{\mathcal{H}} = -2t_{\text{hop}} \sum_{i=1}^{N-1} \left(\hat{c}_i^\dagger \hat{c}_{i+1} - \frac{1}{2} \right), \quad (2.3.18)$$

which is in agreement with the bulk dispersion (2.3.11) obtained using momentum-space diagonalization. In retrospect, it makes sense that the momentum-space diagonalization missed the unpaired Majorana quasiparticle since the latter has no k_x dependence.

It is relatively straightforward to perform this diagonalization exercise in higher dimensions. In 2D, for example, the only difference is that real-space diagonalization is performed along the x axis, while performing momentum-space diagonalization, as usual, along the y axis. In that case, the Majorana quasiparticles will have a k_y dispersion. I will discuss the 2D case in Sec. 2.3.2.2. Similarly, in 3D, if real-space diagonalization is done along the z -axis, the Majorana quasiparticles will disperse along the k_x and k_y axes. In Sec. 2.3.4, I will explain why ARPES is well-suited to investigate Majorana quasiparticles in the *spinful* analog of the 3D Kitaev model.

Back in 2000, the Kitaev chain did not receive much experimental attention. However, this model was revisited by the condensed matter theory community after the seminal prediction, by Fu and Kane [36], for observing Majorana quasiparticles by inducing superconductivity on the surface of topological insulators. While the Fu-Kane proposal was not experimentally realized until 2018 [12, 37] (c.f. Sec. 2.4.4), it did inspire investigations into how spin-orbit coupling could be exploited¹³ to circumvent the "fermion doubling theorem," and engineer nanowires capable of hosting the Majorana quasiparticles.¹⁴ One of *many* attempts to experimentally realize the Kitaev chain are discussed in Sec. 2.4.1.1.

¹³Ironically, Kitaev dismissed spin-orbit coupling, in his original paper [34], since it did not break time-reversal symmetry!

¹⁴Fermion doubling theorem [38] can be violated on individual surfaces of TIs considered as isolated systems. The fermion doubling theorem is restored, however, when all surfaces are considered as one system. Fu and Kane [36] proposed a clever workaround by inducing superconductivity only on one surface via the proximity effect.

2.3.2.2 2D

As I mentioned briefly in Sec. 2.3.2.1, it is relatively straightforward to extend (2.3.6) to (say) a 2D square lattice with the pairing amplitudes along the two crystal axis directions shown in Fig. 2.3.1. A mathematical mapping between electron and Majorana bases can be performed in a very similar way to the one from Sec. 2.3.2.1. So in the interest of space, I will skip the longer calculations of 2D which, in the end, lead to the same qualitative results: Majorana quasiparticles on the boundaries. There is, however, one caveat: p -wave (or $p + ip$) pairing in a 2D bulk, on its own, does *not* produce Majorana zero modes, unless an externally sourced half quantum of flux ($h/2e$) penetrates the 2D sheet. This point is illustrated using an annular region with $p + ip$ pairing in Fig. 2.3.3.

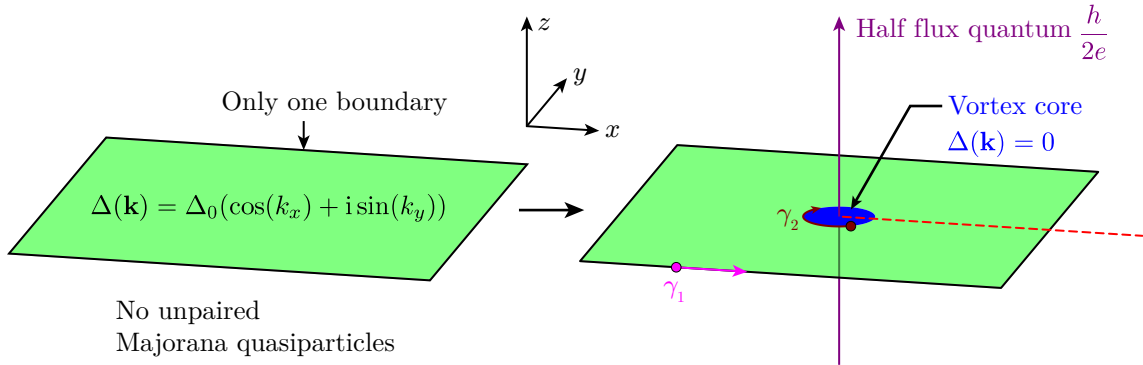


Figure 2.3.3: Both 2D regions represent a superconductors with $p + ip$ pairing. Only the right one hosts two Majorana zero modes, one in the interior (γ_2) and exterior (γ_1) each. In this case, the most important ingredient for topological superconductivity is the half quantum of flux ($h/2e$) passing through the superconductor.

I will try to explain the reason behind the necessity of the flux using physical arguments rather than rigorous calculations.¹⁵ If I consider a homogeneous simply-connected region with $p + ip$ pairing which, unlike the annular example in Fig. 2.3.3, has only one boundary, then it is impossible to have a Majorana quasiparticle on that one boundary as Majorana quasiparticles come in pairs. Therefore, if a $h/2e$ vortex is created in the simply-connected 2D sheet, then one Majorana quasiparticle will be localized to the vortex core and its partner will be on the outer edge. The vortex can be crudely viewed as the second boundary of the 2D sheet.

There is a long list of experimental proposals involving engineered 2D systems to realize the $p + ip$ superconductor. I will not discuss examples of such systems as they prove challenging to study using ARPES. The interested reader can find more details in this review article: [31]. Nonetheless, it is worth pointing out that the spinful analog of the 2D topological (or $p \pm ip$) superconductor was detected recently using ARPES [12, 37]; this example will be discussed in Sec. 2.4.4.

2.3.3 3D topological insulators

2.3.3.1 Introduction

As I briefly mentioned at the beginning of Sec. 2.3.2, I will now take a detour into topological insulators. The discussion of topological insulators from Sec. 1.3.2 was primarily aimed at establishing an

¹⁵To see how the half quantum of flux affects the edge spectrum, the interested reader can refer to [31].

analogy with the integer quantum Hall effect and demonstrating the non-locality of the order parameter of both systems. In this section, however, my goal is to construct an analogy between topological insulators and superconductors. In particular, I will demonstrate how the low-energy electronic spectrum of (arguably) the most famous 3D topological insulator, Bismuth Selenide (Bi_2Se_3), bears a resemblance to the spinful analog of the 3D Kitaev chain.

Throughout the rest of this thesis, it will be clear to the reader that Bi_2Se_3 is a versatile tool, not only in the study of topological insulators and superconductors, but also for benchmarking laser-based ARPES systems (c.f. Chap. 8). Moreover, doping Bi_2Se_3 , with metals like Copper, Niobium, Strontium, offers a route to unconventional superconductivity that can form a field in its own right [39]. Therefore, an in-depth analysis of the material properties of Bi_2Se_3 will be beneficial in a wide range of topics discussed in this thesis.

2.3.3.2 Properties of Bi_2Se_3

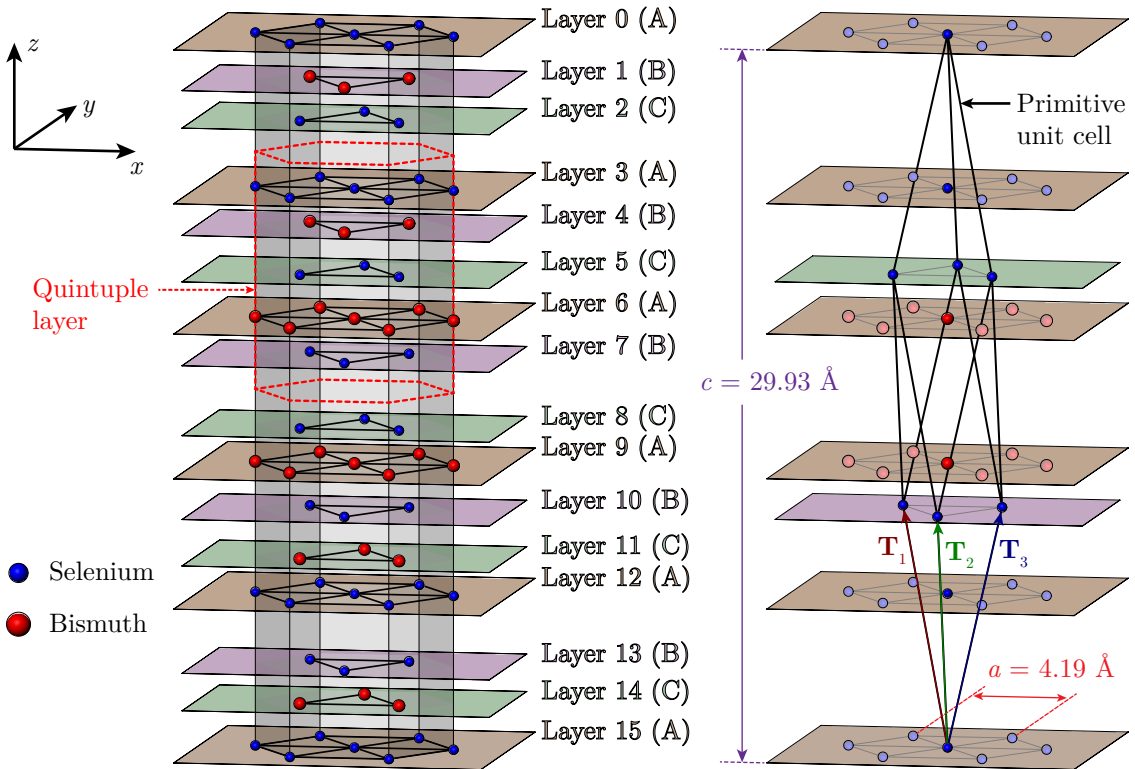


Figure 2.3.4: The crystal of Bi_2Se_3 . Left: the hexagonal unit cell consists of three quintuple layers. This non-primitive unit cell illustrates the layered nature of Bi_2Se_3 . Right: the rhombohedral unit cell is the primitive cell used to determine the first Brillouin in Fig. 2.3.5. [40].

In order to understand the electronic spectrum of Bi_2Se_3 , I'll first start with a discussion of its crystal structure. Fig. 2.3.4 shows two types of unit cells of Bi_2Se_3 : hexagonal (left) and rhombohedral (right) [40]. The hexagonal cell consists of 15 layers¹⁶ of 2D triangular lattices of Bismuth and Selenium. When viewed along the z -axis, the triangular lattices are shifted, in the x - y plane, relative to one another (c.f. Fig. 2.4.5), such that they can be divided into three classes of stacking orientation: A, B, and C. The sub-unit of physical significance, known as the ‘‘quintuple layer,’’ is

¹⁶The half of the 0th and 15th layers are included in the unit cell; hence only one of them contributes to the total number of layers in the unit cell. Both layers are illustrated in Fig. 2.3.4 for ease of visualization.

highlighted by the dashed red line. Inside the quintuple layer (QL), the bonding between the atoms has a strong covalent character. Therefore, the electronic properties of the quintuple layer have a significant contribution to the overall low-energy electronic spectrum of Bi_2Se_3 . In fact, if one were to model Bi_2Se_3 as a spinful analog of the 3D Kitaev chain,¹⁷ a convenient choice for real-space diagonalization would be along the z -axis, with the QL serving as one “lattice site” of the Kitaev chain.

Another advantage of visualizing the QL is that it demonstrates the layered nature of Bi_2Se_3 . Consecutive QLs are held together by weak van der Waals forces. As a result, Bi_2Se_3 cleaves easily along the z -axis. This makes Bi_2Se_3 well-suited for in situ cleaving in measurements like ARPES. It’s worth noting, however, that the hexagonal cell is **not** the primitive unit cell. The rhombohedral cell shown in Fig. 2.3.4 is actually the primitive unit cell. The latter determines the first Brillouin zone. So before switching to momentum space, it’s worth reviewing some of the properties of the rhombohedral cell. The atoms inside the rhombohedral cell are only part of 7 (out of 15) layers and are highlighted in bold colors. The translation vectors are given by

$$\begin{aligned}\mathbf{T}_1 &= -\frac{a}{2}\mathbf{e}_x + \frac{a}{2\sqrt{3}}\mathbf{e}_y + \frac{c}{3}\mathbf{e}_z, \\ \mathbf{T}_2 &= -\frac{a}{\sqrt{3}}\mathbf{e}_y + \frac{c}{3}\mathbf{e}_z, \\ \mathbf{T}_3 &= \frac{a}{2}\mathbf{e}_x + \frac{a}{2\sqrt{3}}\mathbf{e}_y + \frac{c}{3}\mathbf{e}_z,\end{aligned}\tag{2.3.19}$$

where \mathbf{e}_i represent unit vectors along the three axes ($i = x, y, z$). Using the formula for the reciprocal lattice vector

$$\mathbf{G}_i = 2\pi\varepsilon_{ijk} \frac{\mathbf{T}_j \times \mathbf{T}_k}{\mathbf{T}_1 \cdot (\mathbf{T}_2 \times \mathbf{T}_3)},\tag{2.3.20}$$

I get

$$\begin{aligned}\mathbf{G}_1 &= -\frac{2\pi}{a}\mathbf{e}_x + \frac{2\pi}{\sqrt{3}a}\mathbf{e}_y + \frac{2\pi}{c}\mathbf{e}_z, \\ \mathbf{G}_2 &= -\frac{4\pi}{\sqrt{3}a}\mathbf{e}_y + \frac{2\pi}{c}\mathbf{e}_z, \\ \mathbf{G}_3 &= \frac{2\pi}{a}\mathbf{e}_x + \frac{2\pi}{\sqrt{3}a}\mathbf{e}_y + \frac{2\pi}{c}\mathbf{e}_z.\end{aligned}\tag{2.3.21}$$

The Wigner-Seitz cell computed using (2.3.21) gives the first *bulk* Brillouin zone shown in Fig. 2.3.5. Moreover, the surface Brillouin zone, corresponding to the top surface of the QL, is also shown in Fig. 2.3.5 by taking the $k_z = 0$ slice of the bulk Brillouin zone.

The right of Fig. 2.3.5 shows an ab initio calculation of the low-energy electronic spectrum of a Bi_2Se_3 slab of 6 quintuple layers plotted along the high symmetry directions of the surface Brillouin zone [43]. The Dirac-like surface states are highlighted in red and blue. The light blue dashed box shows the range of the spectrum, of electron-doped Bi_2Se_3 , that can be measured using ARPES with 6 eV photons. It is common for Bi_2Se_3 to be electron doped, due to the existence of Selenium vacancies, giving rise to a Fermi level higher than the ab initio calculation shown in Fig. 2.3.5. As a result, ARPES can measure states $\approx 0.2\text{-}0.3\text{ eV}$ above the point of intersection of the surface states (i.e. the Dirac point). Examples of measured spectra are shown in Fig. 8.4.2.

Note the spectral resemblance of the Bi_2Se_3 spectrum to the right side of the cartoon spectrum in Fig. 1.3.4. Owing to the physical mechanism I discussed in Sec. 1.3.2, various experimental probes have verified the topological protection of surface states of Bi_2Se_3 [44].

¹⁷It is now known that metal-doped Bi_2Se_3 forms a 2D p -wave superconductor [39]. In the initial stages of the discovery of superconductivity in metal-doped Bi_2Se_3 , however, the latter was a promising candidate for a 3D p -wave superconductor [41, 42].

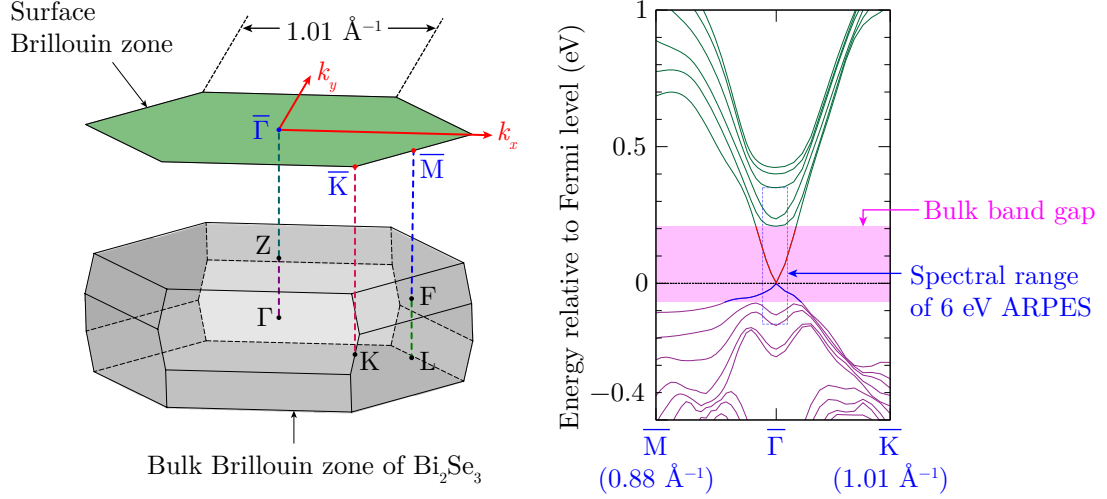


Figure 2.3.5: Left: the bulk Brillouin zone of Bi_2Se_3 with the symmetry points labeled. The surface Brillouin zone is a projection of its bulk counterpart along the z -axis or (111) direction in the primitive unit cell basis ($\mathbf{T}_1, \mathbf{T}_2, \mathbf{T}_3$) defined in Fig. 2.3.4. Right: ab initio calculation of the band structure of a Bi_2Se_3 slab of 6 quintuple layers. Reprinted figure with permission from Sobota *et al. Phys. Rev. Lett.* **113**, 157401. Copyright (2014) by the American Physical Society. [43]. The surface states are highlighted in red and blue.

2.3.3.3 Tight-binding model of Bi_2Se_3

In order to gain insight into the low-energy electron dynamics in Bi_2Se_3 , for (say) modeling its response to experimental probes, it is often convenient to construct an *approximate* tight-binding Hamiltonian. Upon fitting the tight-binding parameters to the results of ab initio calculations [45], a Dirac-like 4×4 Hamiltonian, valid close to the Γ point (c.f. Fig. 2.3.5), can be written as

$$\mathcal{H}(\mathbf{k}) = \varepsilon(\mathbf{k}) + \begin{bmatrix} \mathcal{M}(\mathbf{k}) & 0 & A_1 k_z & A_2(k_x - ik_y) \\ 0 & \mathcal{M}(\mathbf{k}) & A_2(k_x + ik_y) & -A_1 k_z \\ A_1 k_z & A_2(k_x - ik_y) & -\mathcal{M}(\mathbf{k}) & 0 \\ A_2(k_x + ik_y) & -A_1 k_z & 0 & -\mathcal{M}(\mathbf{k}) \end{bmatrix}, \quad (2.3.22)$$

$$\varepsilon(\mathbf{k}) \equiv C + D_1 k_z^2 + D_2(k_x^2 + k_y^2),$$

$$\mathcal{M}(\mathbf{k}) \equiv M - B_1 k_z^2 - B_2(k_x^2 + k_y^2),$$

which is represented in a basis formed by hybridization of p_z orbitals of Bismuth and Selenium. For notational simplicity, I will denote electron operators in this basis as

$$\hat{C}_{\mathbf{k}} \equiv \begin{bmatrix} \hat{e}_{\mathbf{k},+} \\ \hat{e}_{\mathbf{k},-} \\ \hat{h}_{\mathbf{k},+}^\dagger \\ \hat{h}_{\mathbf{k},-}^\dagger \end{bmatrix}, \quad (2.3.23)$$

where the labels e and h correspond to bands above and below the Fermi level respectively. Moreover, \pm labels the two pseudospin¹⁸ states corresponding to each band.

The values of the parameters in the tight-binding Hamiltonian in Eq. (2.3.22) are listed in Table 2.1. In Sec. 2.3.4, I will show that the Hamiltonian for the 3D time-reversal invariant superconductor or superfluid (e.g. B phase of Helium-3) is similar to that of Bi_2Se_3 . Therefore, topologically protected Bogoliubov quasiparticles are expected on the surfaces of these types of superconductors.

¹⁸I am using the pseudospin basis here because, due the large spin-orbit coupling in Bi_2Se_3 , real spin is not a good quantum number.

| Tight-binding parameter | Value for Bi ₂ Se ₃ |
|-------------------------|---|
| M | 0.28 eV |
| A_1 | 2.2 eV · Å |
| A_2 | 4.1 eV · Å |
| B_1 | 10 eV · Å ² |
| B_2 | 56.6 eV · Å ² |
| C | -6.8 meV |
| D_1 | 1.3 eV · Å ² |
| D_2 | 19.6 eV · Å ² |

Table 2.1: Values of the parameters in the tight-binding Hamiltonian for Bi₂Se₃ given by Eq. (2.3.22)

2.3.3.4 Superconductivity in Bi₂Se₃

Shortly after the discovery of 3D topological insulator materials, such as Bi₂Se₃, researchers started investigating ways of inducing superconductivity in them. This was either done by (a) depositing a conventional superconductor (e.g. Niobium) on the surface of Bi₂Se₃ and realize superconductivity in the helical surface states via the proximity effect, or (b) doping Bi₂Se₃ with (typically) metals to induce superconductivity in the 3D bulk. In this thesis I will only focus on the latter.

It turned out that by intercalating Copper (Cu) atoms between the quintuple layers of Bi₂Se₃, a superconductor of $T_c = 3.8$ K was obtained. This material, denoted Cu _{x} Bi₂Se₃ ($x = 0.1-0.3$), was a subject of intense experimental and theoretical scrutiny after its discovery. I will talk about some of the early experimental efforts in detecting Majorana quasiparticles in Cu _{x} Bi₂Se₃ using transport (Sec. 2.4.1) and STM (2.4.2). This discussion will serve as a prerequisite for the type of experiments I am interested in: ARPES and optical spectroscopy in Niobium-doped Bi₂Se₃ ($T_c = 3.2$ K).

2.3.4 3D topological superconductor

Soon after the discovery of topological insulators, a connection was made between the low-energy tight-binding Hamiltonian of Bi₂Se₃ (c.f. Eq. (2.3.22)) and the Bogoliubov-de Gennes Hamiltonian of the B phase of superfluid Helium-3 [46]. At the time, the latter was discovered almost four decades ago [11]. In [46], the authors showed that the consequences of this seemingly superficial mathematical similarity were significant. In this section, I will resume the discussion of topological superconductors, from Sec. 2.3.2, and build on my discussion of Bi₂Se₃, from Sec. 2.3.3, to *qualitatively* describe the properties of the hitherto undiscovered¹⁹ 3D time-reversal invariant topological superconductor.

Starting with a Hamiltonian similar to Eq. (2.2.7), and encoding a p -wave pairing symmetry in 3D, I can write the bulk Hamiltonian as

$$h_{\text{MF}}^{\text{bulk}}(\mathbf{k}) = \begin{bmatrix} (\tilde{t}(\mathbf{k}) - \mu) & 0 & \Delta k_z & \Delta(k_x - ik_y) \\ 0 & (\tilde{t}(\mathbf{k}) - \mu) & \Delta(k_x + ik_y) & -\Delta k_z \\ \Delta k_z & \Delta(k_x + ik_y) & -(\tilde{t}(\mathbf{k}) - \mu) & 0 \\ \Delta(k_x - ik_y) & -\Delta k_z & 0 & -(\tilde{t}(\mathbf{k}) - \mu) \end{bmatrix}, \quad (2.3.24)$$

in a basis defined by

$$\hat{C}_{\mathbf{k}} \equiv \begin{bmatrix} \hat{c}_{\mathbf{k},+} \\ \hat{c}_{-\mathbf{k},-} \\ \hat{c}_{-\mathbf{k},+}^\dagger \\ \hat{c}_{\mathbf{k},-}^\dagger \end{bmatrix}, \quad (2.3.25)$$

¹⁹In this discussion, am setting the standard for “discovery” as a smoking gun signature of a 2D Majorana cone.

where I am once again using a pseudospin basis to allow for the possibility of strong spin-orbit coupling. In order to encode the 3D p -wave pairing symmetry, I have rearranged the 4×4 matrix in (2.3.24) compared to Eq. (2.2.7).

Mathematically, (2.3.22) and (2.3.24) are similar. Physically, the orbital hybridization coefficients (A_1 and A_2) have been replaced by the superconducting gap amplitude (Δ). From a theoretical point of view, if one were to diagonalize (2.3.24) in real space along the z -axis, then similar to the Bi_2Se_3 case, one would expect gapless topologically protected surface states. One major difference, however, would be that these surface states would be occupied by Majorana quasiparticles.

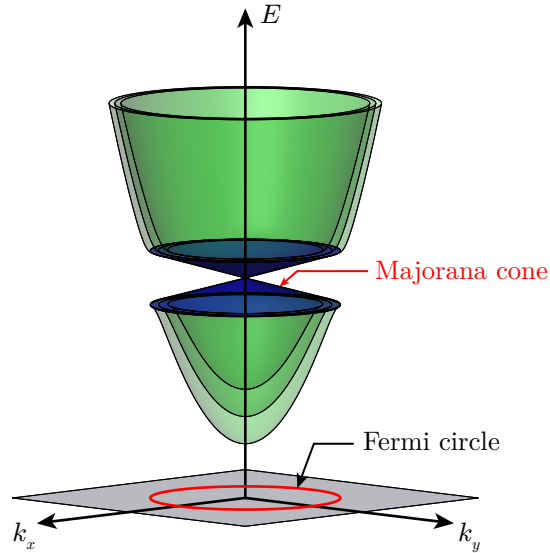


Figure 2.3.6: Bogoliubov quasiparticle spectrum of a 3D topological superconductor in the surface Brillouin zone parallel to the x - y axis. The green paraboloids represent the bulk spectrum. The blue cone corresponding to the dispersion of Majorana quasiparticles on a surface parallel to the x - y axis.

Following an illustration scheme introduced in Fig. 2.2.1, an example of the *qualitative* spectrum of a 3D topological superconductor is shown in Fig. 2.3.6. Another difference between the 3D topological insulators and their superconducting counterparts is that the topological order parameter does not have \mathbb{Z}_2 classification. In other words, the two cases shown in the cartoon in Fig. 1.3.4 would correspond to *different* topological phases in a superconductor.

In principle, mapping the dispersion of Majorana surface states can be performed, using ARPES, similar to the mapping of Dirac electrons in Bi_2Se_3 [47]. In practice, however, one has to consider instrument limitations and availability of materials. I'll start with the former first.

Note that the bulk spectral gap in Bi_2Se_3 (c.f. Fig. 2.3.5) is almost a factor of 300 larger than the average superconducting gap of low- T_c ²⁰ superconductors (≈ 1 meV). This makes resolving the Majorana states very challenging with *typical* state-of-the-art ARPES energy resolutions ($\lesssim 1$ meV). Moreover, sample cooling limitations of these ARPES systems do not allow accessing the superconducting phase of the most promising topological superconductor candidates. Overcoming these technical barriers is the primary goal of the ARPES system discussed in this thesis.

The other challenge in detecting 3D topological superconductors is availability of materials. In the case of 1D and 2D topological superconductors, the ingredients necessary make a superconductor

²⁰I am limiting this discussion to low- T_c superconductors because their high- T_c counterparts have nodes in their bulk gap. In that case, the analogy to Bi_2Se_3 breaks down.

can often be engineered using (say) micro/nano-fabrication and external fields (e.g. electric and magnetic). Unfortunately, most of these tools cannot be *easily* applied to bulk 3D materials. To my knowledge, the only evidence of a 3D topological superconductor has been reported in transport experiments on Potassium-doped β -PdBi₂ [48].

2.4 Experimental signatures of topological superconductors

In the following sections, I will discuss a handful of prominent experimental efforts which saw signatures of topological superconductivity.²¹ Moreover, the results from many of these experiments have yet to be accepted unanimously as “smoking gun” signatures of Majorana quasiparticles.

2.4.1 Electrical transport

2.4.1.1 Nanowires

Here I will revisit the Kitaev chain from Sec. 2.3.2.1. In particular, I will discuss the physical ingredients that will give rise to the “unpairing” of Majorana quasiparticles at the ends of the 1D lattice. The experimental setup involves an Indium Antimonide (InSb) nanowire with high spin-orbit coupling placed on an *s*-wave superconductor in the presence of an external magnetic field, B , along the length of the nanowire (c.f. Fig. 2.4.2). Moreover, the chemical potential of the nanowire is controlled by electrostatic gating (not shown in Fig. 2.4.1).

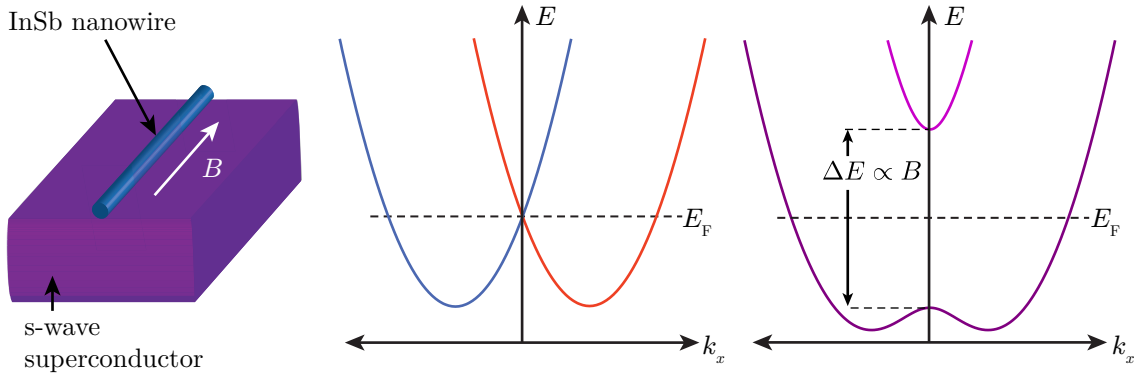


Figure 2.4.1: Left: cartoon of the experimental layout. Middle: bulk nanowire bands at $B = 0$. Right: bulk nanowire bands at $B \neq 0$. From Mourik *et al. Science* **336**, 1003-1007. Reprinted with permission from AAAS. [49].

The Hamiltonian of the system shown in Fig. 2.4.1 can be written in real space as

$$\hat{\mathcal{H}}(k_x) = \frac{k_x^2}{2m_{\text{eff}}} - E_F + \tilde{\alpha}k_x\hat{\sigma}_y + \frac{1}{2}\tilde{B}\hat{\sigma}_z, \quad (2.4.1)$$

where k_x is the quasiparticle momentum along the length of the nanowire, m_{eff} is the effective mass of the electron, μ is the chemical potential, $\tilde{\alpha}$ is a material parameter of the InSb nanowire representing the strength of the Rashba spin-orbit coupling, \tilde{B} is an *energy scale* associated with the Zeeman splitting from the external magnetic field (B), and finally $\hat{\sigma}_y$ and $\hat{\sigma}_z$ are the Pauli matrices

²¹This is not an exhaustive survey. That requires *several* review articles of its own.

associated with the spin degree of freedom. The the energy dispersion, $\varepsilon_{\pm}(k_x)$, can be computed by diagonalizing the Hamiltonian in (2.4.1) as

$$\varepsilon_{\pm}(k_x) = \frac{k_x^2}{2m_{\text{eff}}} - E_F \pm \sqrt{(\tilde{\alpha}k_x)^2 + \tilde{B}^2}. \quad (2.4.2)$$

The (parabolic) line plot of $\varepsilon_{-}(k_x)$ (red) and $\varepsilon_{+}(k_x)$ (blue) is shown in Fig. 2.4.1 in the limit $\tilde{B} = 0$. A non-zero B (and hence \tilde{B}) causes a gap to open at $k_x = 0$ resulting in an upper and lower band. The dashed line shows the chemical potential, E_F , near which the s -wave superconductor will cause pairing of electrons in the lower band due to the proximity effect. E_F has to be large enough to intersect the lower band but not so large that it intersects the upper band as well. In this intermediate regime, the system will exhibit topological superconductivity.

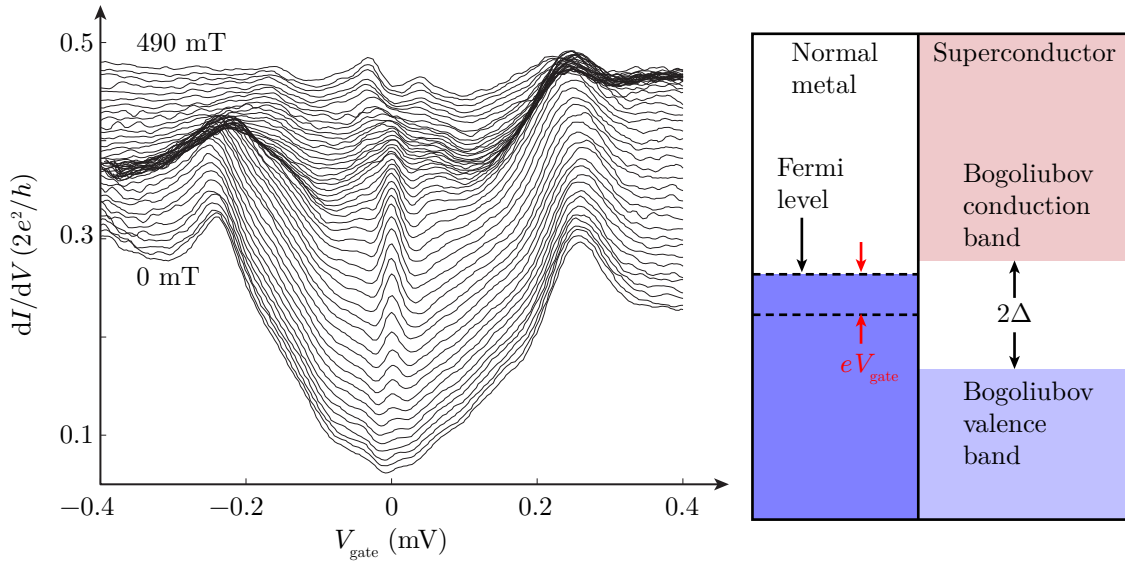


Figure 2.4.2: Left: The zero bias conductance peak in transport measurements on InSb nanowires. From Mourik *et al.* *Science* **336**, 1003-1007. Reprinted with permission from AAAS. Right: energy level diagram of the interface between the electrical lead (left) connected to the superconducting nanowire (right). [49].

The right of Fig. 2.4.2 shows an energy level diagram of the interface between the electrical lead (left) connected to the superconducting nanowire (right). The gate voltage used to control the Fermi level of the electrical lead, V_{gate} , has been defined relative to the center of the superconducting gap. If the superconducting nanowire is indeed the 1D Kitaev chain, then a mid-gap quantum state, occupied by a Majorana quasiparticle, will exist at the interface between nanowire and the electrical lead. As a result, this discrete quantum state would cause a spike in the longitudinal differential conductance dI/dV . The plot on the left of Fig. 2.4.2 shows multiple dI/dV vs. V_{gate} curves for different values of the magnetic field, B (c.f. Fig. 2.4.1). For intermediate values of B , corresponding to the opening of a topological energy gap, a spike in dI/dV was indeed observed. This spike is commonly known as the zero-bias conductance peak (ZBCP).

There has been considerable amount of debate in the community on whether the zero-bias conductance peak is truly coming from the Majorana rather than a parasitic effect. To my knowledge, a consensus has not been reached on this matter.

2.4.1.2 3D superconductor

Another contentious experiment associated with the ambiguity of the zero-bias conductance peak origin is that of a soft-point contact spectroscopy measurement performed on $\text{Cu}_x\text{Bi}_2\text{Se}_3$ [42]. As discussed in Sec. 2.3.3, at the time of its discovery, $\text{Cu}_x\text{Bi}_2\text{Se}_3$ was considered a promising candidate for 3D topological superconductors [41]. As shown in Fig. 2.4.3, a zero-bias conductance peak was indeed seen below T_c , this seemingly confirming the prediction in [41]. However, as I will show in Sec. 2.4.2, conflicting reports were observed by scanning tunneling spectroscopy measurements performed by Levy *et al.* [50].

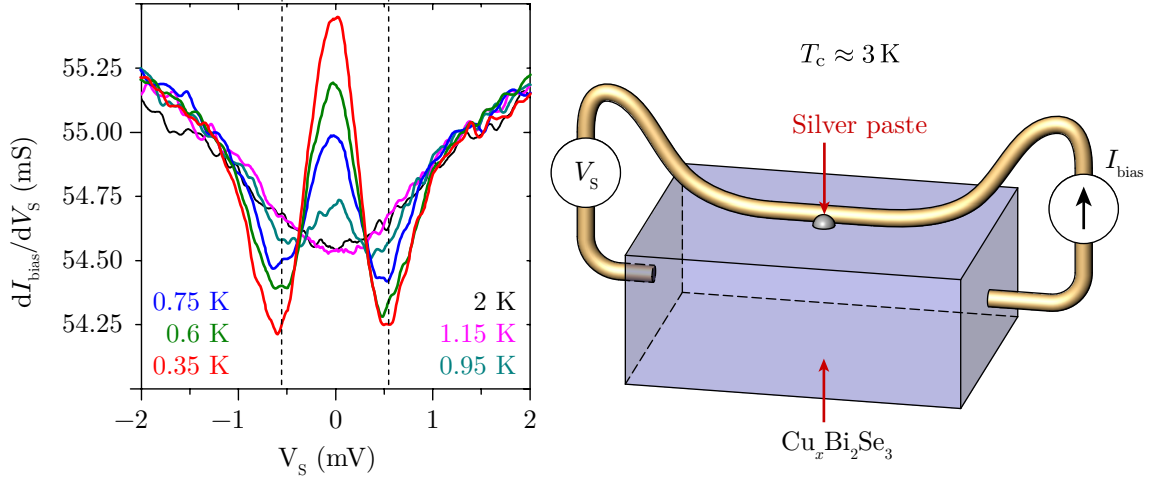


Figure 2.4.3: Point contact spectroscopy measurement on $\text{Cu}_x\text{Bi}_2\text{Se}_3$ revealing the existence of a zero-bias conductance peak below $T_c \approx 3\text{ K}$. Reprinted figure with permission from Sasaki *et al. Phys. Rev. Lett.* **107**, 217001. Copyright (2010) by the American Physical Society. [42].

2.4.2 Scanning tunneling spectroscopy

The top left side of Fig. 2.4.4 shows the scanning tunneling spectrum²² measured from the (111) surface²³ of $\text{Cu}_x\text{Bi}_2\text{Se}_3$. A good fit to the s -wave pairing gap was obtained and no ZBCP was seen. Some time after this scanning tunneling spectroscopy (STS) result, there was a theoretical study by Mizushima *et al.* [51], which attempted to explain the discrepancy between [42] and [50], without assuming experimental error in either one. Mizushima *et al.* suggested a reconciliation based on the evolution of the Fermi surface upon doping.

Moreover, a combined quantum oscillations (Shubnikov-de Haas) and ARPES study, which followed the STS experiment [50], analyzed the evolution of the Fermi surface of $\text{Cu}_x\text{Bi}_2\text{Se}_3$ as a function of doping level [52]. They reported a Lifshitz transition (c.f. bottom of Fig. 2.4.4) involving two different Fermi surface topologies: cylindrical (blue) and ellipsoid (red). Mizushima *et al.* [51] claimed that the STS measurement saw the former, in which case, there would be no Majorana quasiparticle present on the (111) surface. In contrast to the scanning tunneling microscopy (STM) tip, the soft-point contact spectroscopy apparatus, shown in Fig. 2.4.3, involved a large silver contact made to

²²A scanning tunneling spectroscopy (STS) measurement can be crudely thought of as point contact spectroscopy (PCS) without the contact. In other words, in the former, the measured differential conductance (dI/dV) is the result of tunneling of electrons, through ultrahigh vacuum, between a sharp electrically conductive tip and the sample under test. Moreover, because said tip is atomically sharp, STS has much greater spatial resolution compared to PCS.

²³The Miller indices of the (111) plane correspond to the primitive basis defined in Eq. (2.3.19). In Fig. 2.3.4, this corresponds to the top of a quintuple layer (i.e. parallel to the x - y plane).

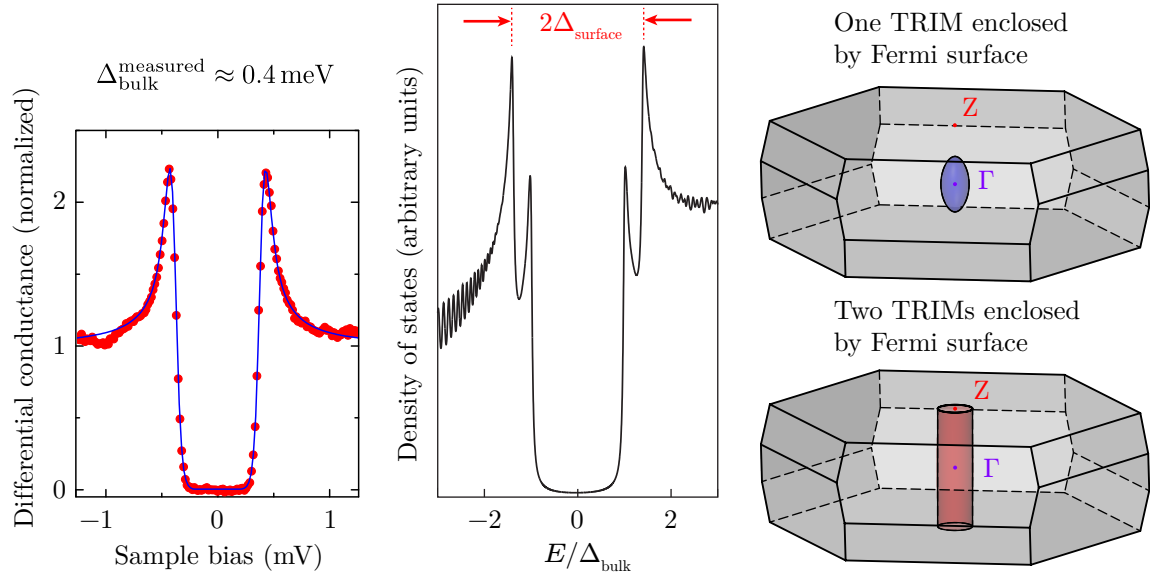


Figure 2.4.4: Left: Scanning tunneling spectroscopy measurement on $\text{Cu}_x\text{Bi}_2\text{Se}_3$ revealing an s -wave-like superconducting gap with no zero-bias conductance peak. Reprinted figure with permission from Levy *et al. Phys. Rev. Lett.* **110**, 117001. Copyright (2013) by the American Physical Society. Middle: calculation of density of states of $\text{Cu}_x\text{Bi}_2\text{Se}_3$ assuming a bulk s -wave pairing and surface Dirac-fermion-induced parity mixing. Reprinted figure with permission from Mizushima *et al. Phys. Rev. B* **90**, 184516. Copyright (2014) by the American Physical Society. Right: Fermi surfaces at different electron doping densities in Bi_2Se_3 . [50, 51].

the sample on the (111) surface. This means that the silver contact would spread over surface pits, and get access to crystal facets other than (111), and thus be sensitive to the Majorana quasiparticle.

Mizushima *et al.* [51] went one step further by showing that if the bulk did indeed exhibit s -wave pairing, as the STM experiment [50] claimed, a double-peak structure should have appeared (c.f. top right of Fig. 2.4.4). According to the calculations of Mizushima *et al.* [51], the second coherence peak arises due to an anomalous enhancement of the pairing potential due to parity mixing induced by the surface the Dirac fermions. In other words, the STM measurement actually confirmed that the bulk was not s -wave by *not* seeing the second coherence peak! Unfortunately, unlike preliminary estimates [41], this explanation also meant that $\text{Cu}_x\text{Bi}_2\text{Se}_3$ was *not* a 3D topological superconductor; it was instead a quasi-2D topological superconductor.

2.4.3 Nuclear magnetic resonance

The discrepancy between tunneling and point contact spectroscopy was eventually resolved by an experiment which performed nuclear magnetic resonance (NMR) measurements on ^{77}Se as a function of temperature in $\text{Cu}_x\text{Bi}_2\text{Se}_3$ [53]. In this experiment, the objective was to measure the electronic spin susceptibility of $\text{Cu}_x\text{Bi}_2\text{Se}_3$ as a function of temperature and angle of the DC magnetic field, θ , defined relative to the crystal axes shown in Fig. 2.4.5. Changes in the spin susceptibility, as a function of an experimental parameter (e.g. temperature), can be measured by monitoring the changes in the NMR frequency of ^{77}Se . This frequency shift is the result of hyperfine coupling between the nuclear spin of ^{77}Se and the spin of conduction electrons or Cooper pairs in $\text{Cu}_x\text{Bi}_2\text{Se}_3$. In practice, this frequency shift is reported in terms of a quantity known as the *Knight shift*.²⁴

²⁴The Knight shift is the offset of the measured NMR resonance frequency from a reference frequency. The Knight shift is directly proportional to the spin susceptibility rather than the absolute value of the NMR resonance frequency.

One of the hallmarks of conventional (s -wave) superconductors is the vanishing of spin susceptibility below the superconducting transition temperature, T_c . The reason for this is that spin-singlet pairing in s -wave superconductors (c.f. Sec. 2.3.1.2) leads to Cooper pairs with zero spin. In a p -wave superconductor, however, spin-triplet pairing of the Cooper pairs would result in a finite spin susceptibility of the Cooper pairs. In other words, there is no abrupt transition in the Knight shift as the temperature is swept across T_c for a p -wave superconductor. In [53], such a transition in the Knight shift was observed only with the DC magnetic field *perpendicular* to the x - y plane (c.f. Fig. 2.4.5). This hinted that $\text{Cu}_x\text{Bi}_2\text{Se}_3$ was a quasi-2D p -wave superconductor in the x - y plane.

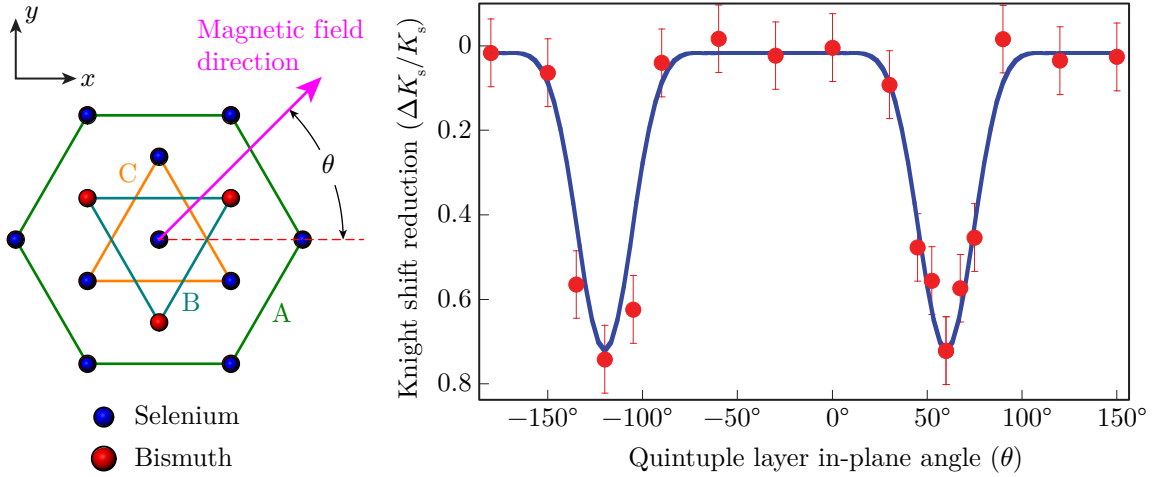


Figure 2.4.5: Left: top view of the hexagonal unit cell from Fig. 2.3.4 illustrating the offset in the x - y plane of the A, B, and C stacking orientations. The pink arrow external DC magnetic field direction parallel to the x - y plane. Right: normalized Knight shift of ^{77}Se in $\text{Cu}_x\text{Bi}_2\text{Se}_3$ in the superconducting phase. Reprinted by permission from Springer Nature Customer Service Centre GmbH: *Nature Physics* **12**, 852-854, Matano *et al.*, Copyright 2016. [53].

Furthermore, for $T < T_c$, as the angle of the DC magnetic field, θ , in x - y plane was swept, a two-fold symmetry in the Knight shift, K , was observed. This two-fold symmetry is most easily visualized with a plot of

$$\frac{\Delta K_s}{K_s} = \frac{K(3\text{K}) - K(1.4\text{K})}{K(3\text{K}) - K_0}, \quad (2.4.3)$$

as a function of θ . K_0 is the Knight shift of undoped Bi_2Se_3 . This plot is shown to the right of Fig. 2.4.5. This two-fold symmetry is consistent with the symmetry of a p -wave superconducting order parameter (c.f. Fig. 2.3.1)

Subsequent experimental and theoretical work on Strontium-doped Bi_2Se_3 ($\text{Sr}_x\text{Bi}_2\text{Se}_3$) and Niobium-doped Bi_2Se_3 ($\text{Nb}_x\text{Bi}_2\text{Se}_3$) has confirmed that $\text{Cu}_x\text{Bi}_2\text{Se}_3$ belongs to a class of superconductors exhibiting nematicity [39].

2.4.4 Angle-resolved photoelectron spectroscopy

The theoretical and experimental efforts to realize a topologically superconducting system, that I have discussed so far, involve starting with or engineering a topological system, and then trying to induce pairing in that system. The experiment I will discuss in this section takes the opposite approach: finding topology in a system primarily investigated for its superconducting properties.

Studies of Copper- and Iron-based high- T_c superconductors is commonplace in an experimental field like ARPES. For these superconductor classes, experimental studies mostly focus on “solving the high- T_c problem,” which has indeed been one of the biggest challenges in modern physics. The iron-based superconductor $\text{FeTe}_{0.55}\text{Se}_{0.45}$ fits this category. The electronic structure is very similar to most iron-based superconductor materials: hole-like (electron-like) bands around the center (corner) of the Brillouin zone. However, after a careful band structure analysis, one finds that the odd parity p_z band from Selenium (Se) and the even parity d_{xz} band from Iron (Fe) hybridize to open a topologically non-trivial gap of 10 meV near the Fermi level. It turns out that the spin-orbit coupling arising from Tellurium (Te) doping pushes the p_z band below the Fermi level, thus causing it to hybridize with the d_{xz} band.

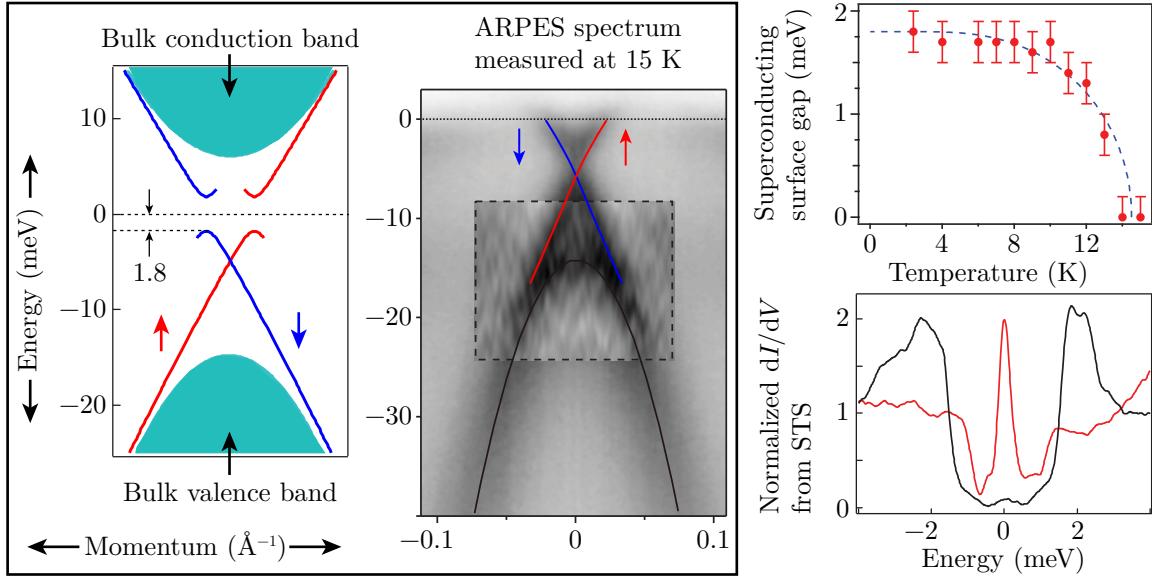


Figure 2.4.6: The plots inside the black outline box share the same abscissa and ordinate axis units. The left and right plots inside said box represent a schematic and ARPES data showing both bulk and surface electron states in $\text{FeTe}_{0.55}\text{Se}_{0.45}$ ($T_c \approx 14.5$ K) close to zero energy (i.e. Fermi level) respectively. The red and blue lines represent topological surface states with opposite spin projection. Top-right: evolution of the superconducting gap of the surface states below T_c . Bottom-right: STS data from $\text{FeTe}_{0.55}\text{Se}_{0.45}$. The red and black curves represent the normalized differential conductance, dI/dV , for STM tip location at and away from a vortex core respectively. From Zhang *et al. Science* **360**, 182-186 and Wang *et al. Science* **362**, 333-335. Reprinted with permission from AAAS. [12, 37].

Since the hybridization gap is generated due to an inversion between bands of opposite parity, it is naturally accompanied by topological surface states. The left of Fig. 2.4.6 shows an ARPES spectrum taken from the (001) crystal surface revealing the existence of the predicted topological surface states [12]. The ARPES data was collected using a high-energy-resolution setup ($\Delta E \approx 1.5$ meV) which made it possible to resolve a superconducting gap ≈ 1.8 meV in the topological surface states. The evolution of the surface state gap as a function of temperature (below $T_c \approx 14.5$ K) is shown to the top-right of Fig. 2.4.6.

Furthermore, the spin-momentum locking in the surface states was verified using high-resolution spin-resolved ARPES ($\Delta E \approx 5.5$ meV), thus proving their topological nature. This spin-resolved data, combined with the evidence of surface superconductivity, proved that the superconductivity on the (001) surface of $\text{FeTe}_{0.55}\text{Se}_{0.45}$ is indeed topological. Further evidence of topological superconductivity was provided by scanning tunneling spectroscopy (STS) measurements which revealed a zero-bias conductance peak at the vortex cores of $\text{FeTe}_{0.55}\text{Se}_{0.45}$ on the (001) surface in the presence

of an external magnetic field of 0.5 T [37]. This is the first experimental observation of the model proposed by Fu and Kane [36].

Chapter 3

Introduction to angle-resolved photoelectron spectroscopy

3.1 Introduction

The dependence of ARPES on the photon energy was famously revealed by the discovery of the *photoelectric effect* by Heinrich Hertz in 1887 [54]. The Nobel-prize-winning theory, which invoked the quantum nature of light, by Albert Einstein in 1905 [55], was able to explain the photoelectric effect. According to this theory, only photons with energy larger than the work function, Φ , for a given material, result in photoelectrons with a flux proportional to the intensity of the photon source.

Since its discovery, the photoelectric effect has been exploited to infer properties of matter with increasingly greater accuracy [56]. Arguably, one of the fields most significantly benefiting from the photoelectric effect is condensed matter physics. The reason for this is that the quintessential physical quantity of interest in crystalline solids, namely the electronic band structure, can in principle be fully determined using a photon-in-electron-out experimental probe based on the photoelectric effect called angle-resolved photoemission spectroscopy (ARPES).

3.2 Scientific design goals

My goal is to study 3D topological (or *p*-wave) superconductors by mapping out their superconducting energy gap(s), $\{\Delta_1(\mathbf{k}), \Delta_2(\mathbf{k}), \Delta_3(\mathbf{k}), \dots\}$, using ARPES.¹ The two minimum, but not sufficient, requirements for reliably studying said superconductors with this method are high energy resolution and low temperatures. In this section, I will focus exclusively on these two requirements from a *phenomenological* perspective. In chapters 4-6, I will discuss the technical details such as: (a) properties of the photon source, (b) electron detection, and (c) magnetic shielding, that are specific to the apparatus I designed. A discussion of low-temperature techniques requires a chapter of its own (Chap. 7).

¹ARPES is especially well-suited to characterize superconductors with more than one gap because, in most cases, the location of different gaps in momentum space is different. Momentum-averaged techniques, like STS, does show signs of (say) a double-gap superconductor like (say) MgB₂ with more than one coherence peaks; but it is unable to determine the gaps as a function of *absolute* momentum without theoretical support.

Fig. 3.2.1 illustrates a phenomenological correlation between energy resolution and temperature in the study of superconductors. A log-scale scatter plot of *maximum* superconducting (Δ_{\max}) gap vs. critical temperature (T_c), at ambient pressure, is shown for a small selection of *unconventional* superconductors. A comparison to BCS superconductors is offered by a dashed line, $\Delta_{\max} = 1.76 k_B T_c$,² where k_B is the Boltzmann constant; this mathematical relationship corresponds to one of the most important analytical results of the BCS theory. The scatter plot shows three families of unconventional superconductors: (a) copper-based, (b) iron-based, and (c) low- T_c (< 10 K) superconductors over two orders of magnitude in both axes. Here Δ_{\max} is defined as:

$$\Delta_{\max} \equiv \lim_{T \rightarrow 0} [\max [\Delta(\mathbf{k}, \{x, P, \dots\})]], \quad (3.2.1)$$

where \mathbf{k} is the crystal momentum, T is the temperature, and $\{x, P, \dots\}$ represents a set of parameters unique to the material and test conditions (except temperature). For example, the size of the gap is influenced by factors such as doping level (x) and hydrostatic pressure (P). For example, in the case of (say) optimally hole-doped ($x \approx 0.15$) $\text{La}_{2-x}\text{Sr}_x\text{CuO}_4$, with a $T_c = 39$ K, in the $T \rightarrow 0$ limit, at *ambient pressure*,³ gives $\Delta \approx 10$ meV when measured along the anti-nodal direction in momentum space.

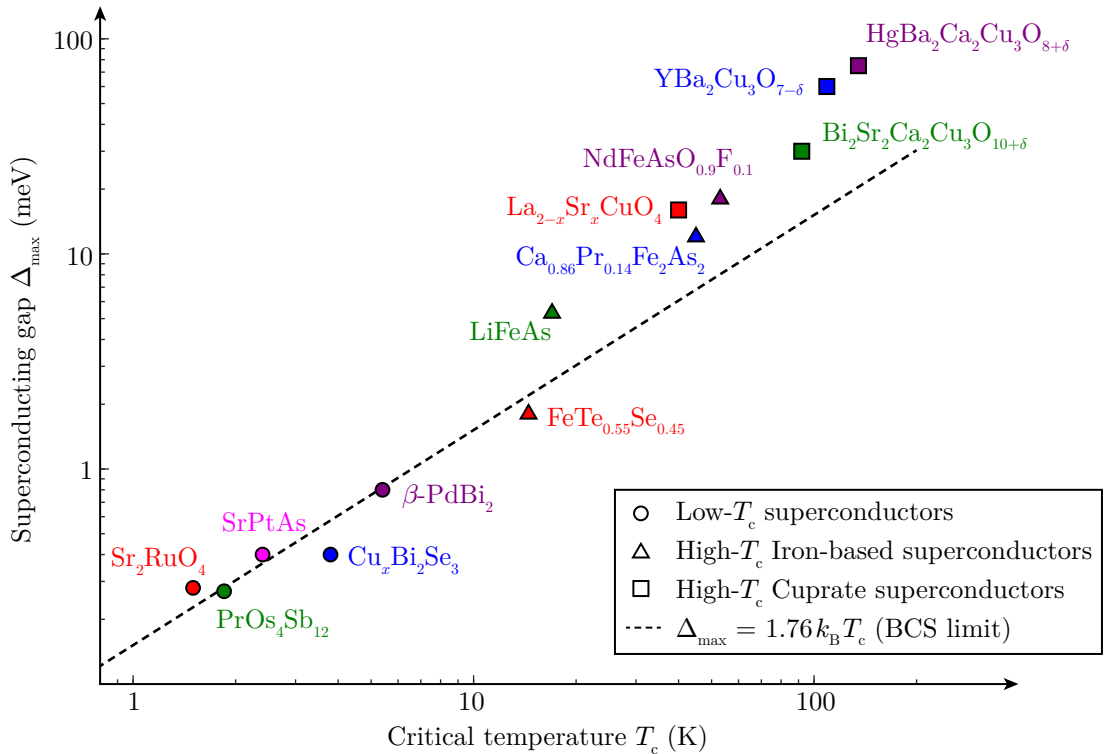


Figure 3.2.1: Three families of superconductors are depicted on a log-scale scatter plot of *maximum* superconducting (Δ_{\max}) gap vs. T_c over two orders of magnitude. Δ_{\max} has been defined as the energy difference between the highest occupied state at zero temperature and the chemical potential. References for gap measurements of the above low- T_c , high- T_c iron-based, and optimally doped high- T_c cuprate superconductors can be found in Sec. A.2.

The main takeaway from this plot is: despite deviations from the BCS limit, the maximum attainable

²The subscript “max” is less relevant in the case of BCS superconductors; but is included here for the sake of notational consistency.

³It was difficult to find pressure-dependent empirical studies of the gap for *all* the examples listed in Fig. 3.2.1. Therefore, in order to compare the superconductors on an equal footing, Eq. (3.2.1) was evaluated at the same (ambient) pressure.

gap size, Δ_{\max} , scales with the T_c . Therefore, energy resolution and temperature go hand-in-hand in spectroscopic studies of superconductors. Chap. 7 discusses details of how traditional cryogenic tools (^3He) were adapted to achieve a base temperature of 0.84 K in the ARPES setup discussed in this thesis. This means the best *total* energy resolution, ΔE_{total} , needs to be of the order of ≈ 0.13 meV ($= 1.76 k_B \times 0.84$ K). I will conclude this section with a brief discussion of factors affecting the energy resolution. This crude analysis guided my efforts in the design of the aforementioned ARPES system. In Sec. 3.3.3.2, I will give a broad overview of the factors influencing ΔE_{total} .

3.3 Measurement technique

3.3.1 ARPES model

In this section, I will present a simple model illustrating the working principle of ARPES. This model should be sufficient in both: (a) the interpretation of the data presented in Chap. 8, and (b) understanding the requirements on the experimental tools used to perform ARPES (Chap. 4-7). I will limit this discussion to the following experimental parameters:

I will assume the photon energy $E_{\text{photon}} = h\nu$ is fixed to 6 eV (c.f. Chap. 4). I will not assume any details about the electron detection process with the exception of a “slit,” whose properties are briefly described in Sec. 3.3.2.⁴ Moreover, I will not impose any performance constraints on the detector. For simplicity, I will also assume zero temperature ($T = 0$). The latter constraint will be trivially relaxed⁵ in future discussions analyzing data.

Consider a toy model of a non-interacting metal on a 2D lattice.⁶ The energy dispersion of the highest occupied (electron-like) band, $E(k_x, k_y)$, will be given by

$$E(\mathbf{k}) = \frac{\hbar^2}{2m_{\text{band}}(\mathbf{k})}(k_x^2 + k_y^2) + E_c, \quad (3.3.1)$$

where \hbar is the reduced Planck’s constant, $m_{\text{band}}(\mathbf{k})$ is the effective mass⁷ of an electron with crystal momentum $\mathbf{k} \equiv (k_x, k_y)$, and E_c is the band minimum. The work function, Φ , which is defined as the energy difference between the Fermi level and vacuum,⁸ is assumed to be approximately 4 eV. The dispersion relation in Eq. (3.3.1) is schematically plotted as a surface plot on the left of Fig. 3.3.1.

In this example, Eq. (3.3.1) is only valid in the first Brillouin zone as highlighted by the square green region in Fig. 3.3.1. The red (blue) region of the top-open paraboloid-shaped surface, which intersects the E_F plane, corresponds to the occupied (unoccupied) electronic states. Assuming that the lowest state in the semi-transparent red region (at $\mathbf{k} = 0$) is less than 2 eV below E_F , then the absorption of 6 eV photons by the electrons in the semi-transparent red region, by a sufficiently luminous light source will result in the photoemission process. This process is schematically represented as an upward translation of the semi-transparent red region along the E axis by 4 eV ($= h\nu - \Phi$). This translated version of the band is plotted, at the top of Fig. 3.3.1, as a function of *real* momenta $\mathbf{p} = (p_x, p_y)$ since the electrons are no longer bound to the lattice.⁹ Moreover, the vertical axis now represents the photoelectrons’ kinetic energy (E_{kin}).

⁴Detailed discussion of the slit can be found in Chap. 5.

⁵I will later use the Fermi-Dirac function for $T \neq 0$. Here I am assuming $T = 0$ only for mathematical simplicity.

⁶The choice of 2D is dictated by the fact that energy-momentum dispersion along k_z requires changing photon energy. This discussion assumes a fixed photon energy of 6 eV (c.f. Chap. 4).

⁷The \mathbf{k} -dependence of the effective mass is a way of extending the model to non-parabolic band structures. For simplicity, I’m assuming isotropic (i.e. scalar) effective mass.

⁸“Vacuum” is defined as a continuum state of an electron that is no longer bound to the 2D metal.

⁹There *will* be a finite p_z . Its value will not matter in this analysis.

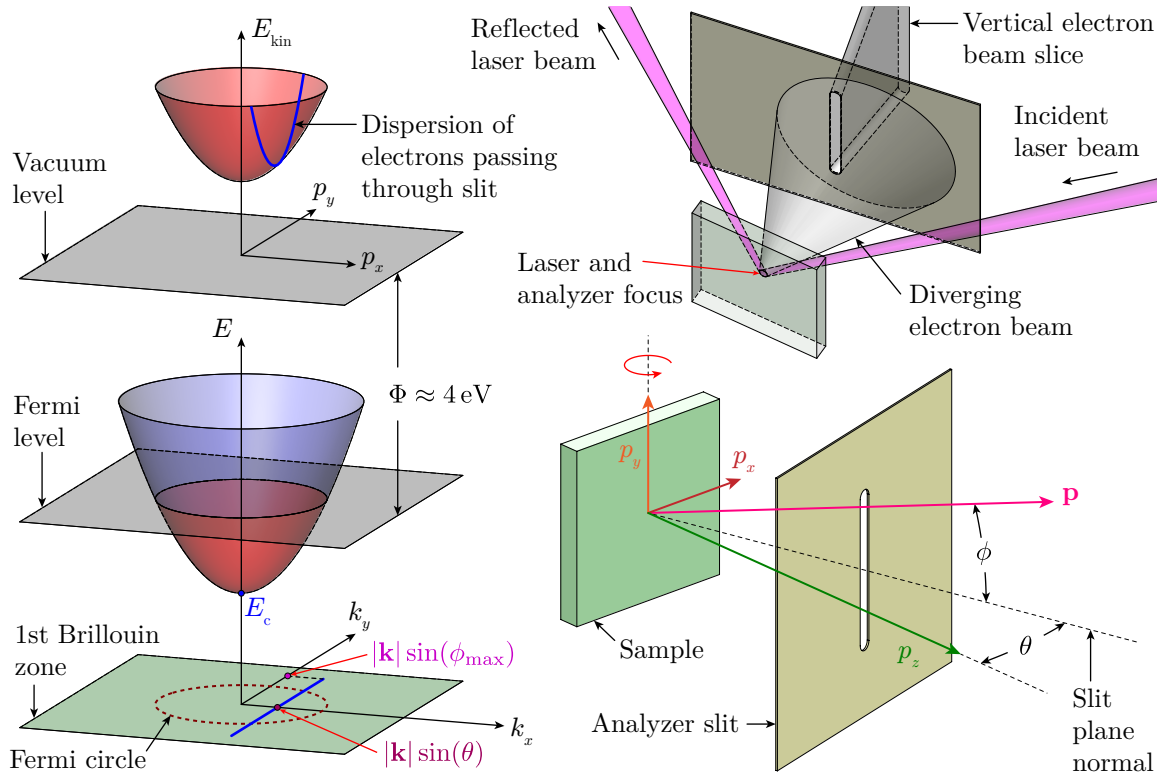


Figure 3.3.1: A momentum- and real-space illustration of the photoemission process in a 2D metal toy model.

In a well-calibrated ARPES system, by sweeping the voltages inside the detector,¹⁰ combined with a series of sample manipulations, the entire red surface in the top plot of Fig. 3.3.1 can be mapped out numerically. These external degrees of freedom, as well as the photon energy, determine the extent to which the region of the parameter space, shown in Fig. 3.3.1, is accessible by a given ARPES apparatus. The effect of each degree of freedom on the measurement is discussed in detail in the next section.

3.3.2 Experimental degrees of freedom

I will now switch from momentum space to real space where most of the experimental degrees of freedom exist. An explicit list of said degrees of freedom is as follows:

- energy of photons, $h\nu$, used to generate photoelectrons,
- the orientation of the sample, (θ, ϕ) , with respect to the analyzer (c.f. Fig. 3.3.1),
- width of the slit, w , through which the electrons enter the detector, and finally
- the pass energy, E_{pass} ,¹¹ of the detector

¹⁰Details of internal detector voltages will be discussed in Chapter 5

¹¹I will ignore this degree of freedom in this section. It will be discussed in Chapter 5

The ultimate goal is to use these degrees of freedom to obtain the function $E(k_x, k_y)$ in Fig. 3.3.1. By simple energy conservation, I get

$$\begin{aligned} E_{\text{kin}}(k_x, k_y) &= h\nu - \Phi - [E_{\text{F}} - E(k_x, k_y)], \\ &\equiv h\nu - \Phi - E_{\text{B}}(k_x, k_y), \end{aligned} \quad (3.3.2)$$

where in the second line I have defined a new function, $E_{\text{B}}(k_x, k_y)$, known as the *binding energy*.¹² Unfortunately, momentum is *not* conserved when the electron makes a transition from the lattice potential to the vacuum. But it turns out that momentum parallel to the crystal surface is conserved modulo the reciprocal lattice vector. In this discussion, I will ignore cases where in-plane momenta are displaced by the reciprocal lattice vector. Then I can write the components of the real momentum \mathbf{p} as

$$\begin{aligned} p_x &= \hbar k_x, \\ &= |\mathbf{p}| \cos(\phi) \sin(\theta), \end{aligned} \quad (3.3.3)$$

$$\begin{aligned} p_y &= \hbar k_y, \\ &= |\mathbf{p}| \sin(\phi), \end{aligned} \quad (3.3.4)$$

where $|\mathbf{p}|$ is the magnitude of the momentum in vacuum. By comparing (3.3.2), (3.3.3), and (3.3.4), it is evident that k_x and k_y can be completely controlled by the set of external degrees of freedom, $(h\nu, \theta, \phi)$, assuming the sample is known (i.e. fixed $E_{\text{B}}(k_x, k_y)$ and Φ). Since

$$E_{\text{kin}} = \frac{|\mathbf{p}|^2}{2m_0},$$

where m_0 is the free electron mass, I can re-write (3.3.3), and (3.3.4) in an even more convenient form given by

$$\begin{aligned} k_x &= \frac{\sqrt{2m_0 E_{\text{kin}}}}{\hbar} \cos(\phi) \sin(\theta), \\ &= \frac{1}{\hbar} [2m_0 (h\nu - \Phi - E_{\text{B}}(k_x, k_y))]^{1/2} \cos(\phi) \sin(\theta), \end{aligned} \quad (3.3.5)$$

$$k_y = \frac{1}{\hbar} [2m_0 (h\nu - \Phi - E_{\text{B}}(k_x, k_y))]^{1/2} \sin(\phi). \quad (3.3.6)$$

With (3.3.5) and (3.3.6) the functional map $(k_x, k_y) \rightarrow E_{\text{B}}$ is fully defined.

The technique with which the set of three quantities, $(E_{\text{kin}}, p_x, p_y)$, are measured in practice works as follows. The electron detector is calibrated to simultaneously measure the set (E_{kin}, ϕ) in the form of a 2D image on a CCD. This means that the detector will image the red curve “sliced” from the upward translated semi-transparent red region, from Fig. 3.3.1, for a fixed value of k_y and parallel to the k_x axis. This is what I alluded to earlier as a “single shot” measurement. Once a single shot measurement is complete, the angle the sample surface makes relative to the slit plate, θ , is stepped in small increments to raster scan the entire paraboloid.

3.3.3 Empirical figures of merit

The types of materials that can be studied using ARPES depends on the range of binding energies and crystal momenta accessible to said ARPES system. Moreover, for spectral measurements within the range of an ARPES system, resolution limits the different type of phenomena that can be probed in a given material (e.g. superconductivity). For the types of ARPES measurements discussed in this thesis, range and resolution will be the most important instrument figures of merit. In this section, I will discuss the relationship between the experimental degrees of freedom (c.f. Sec. 3.3.2) and range/resolution.

¹²It is a standard convention to report ARPES data in terms of the binding energy.

3.3.3.1 Spectral range

It is evident from Eq. (3.3.2) that probing larger binding energies require larger photon energies. For the types of phenomena I am interested in studying using ARPES, however, the most relevant spectral measurements need to be performed close to the Fermi level. Nonetheless, photon energy plays an important role in determining the momentum range.

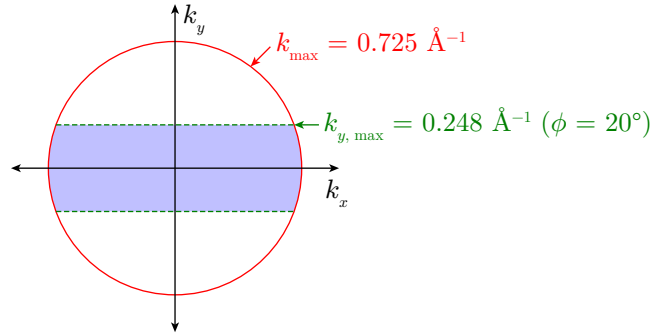


Figure 3.3.2: The semi-transparent blue region represents the fraction of the 2D Brillouin zone accessible with $h\nu = 6$ eV and $\phi_{\max} = 20^\circ$.

It can be noted in Eq. (3.3.5) and (3.3.6) that, in the parameter regime where the trigonometric factors approach 1, the crystal momentum scales with the square root of the electron's kinetic energy. In other words, for a given photon energy, $h\nu$, the upper limit on the measurable momenta is

$$k_{\max} = \frac{\sqrt{2m_0(h\nu - \Phi)}}{\hbar}. \quad (3.3.7)$$

In case of a 6 eV photon source, this limit is graphically illustrated in Fig. 3.3.2 as the region inside the circle with radius k_{\max} . Various technical factors further limit the range of accessible momenta. For example, the electrostatic lens of the R8000 electron analyzer can measure ϕ up to $\approx 20^\circ$ (c.f. Fig. 5.3.2). The semi-transparent blue region in Fig. 3.3.2 shows the region of the 2D Brillouin zone which can be accessed with $\phi_{\max} = 20^\circ$.

ϕ is limited by the electron analyzer in the configuration in Fig. 3.3.1. It is, however, possible to access larger ϕ values by tilting the sample about its x -axis (c.f. Fig. 7.2.1 and 7.5.2.5).

3.3.3.2 Spectral resolution

Controlling the energy and momentum resolution is more challenging compared to their range. As I discussed in Sec. 3.2, the *total* energy resolution, ΔE_{total} , is of great importance for studying superconductors; hence I will focus on energy resolution.

In the simplest model, ΔE_{total} can be written as

$$\Delta E_{\text{total}} = \sqrt{(h\Delta\nu)^2 + \Delta E_{\text{analyzer}}^2 + \Delta E_{\text{noise}}^2}, \quad (3.3.8)$$

where h is the Planck's constant and $\Delta\nu$ is the frequency uncertainty of the light source. $\Delta E_{\text{analyzer}}$ is intrinsic resolution of the electron analyzer (c.f. Eq. (5.1.13)). Finally, ΔE_{noise} is defined as the uncertainty in the energy of a photoelectron induced by uncontrollable factors in the environment of the sample under test (e.g. stray electric/magnetic fields).

The ΔE_{total} from Eq. (3.3.8) can be measured directly from the photoemission data. This is done by looking at the (normalized) angle-integrated spectrum from a *polycrystalline* gold sample near the Fermi level, E_F , and fitting it to the Fermi-Dirac distribution function

$$f_{\text{FD}}(E, T) \equiv \frac{1}{1 + \exp\left(\frac{E - E_F}{k_B T}\right)}, \quad (3.3.9)$$

convoluted with a Gaussian with full-width at half maximum (FWHM) ΔE_{total}

$$g(E, \Delta E_{\text{total}}) \propto \exp\left(-4 \ln(2) \frac{E^2}{\Delta E_{\text{total}}^2}\right). \quad (3.3.10)$$

The variation in the density of the states very close to the Fermi level of polycrystalline gold can be ignored. Using the temperature (T) as an input parameter, ΔE_{total} can be extracted from the fit. Alternatively, in principle, if ΔE_{total} is known accurately, T can be inferred from the fit.

3.4 Data interpretation

For the toy model discussed in Sec. 3.3.1, interpretation of the photoelectron signal seen by the detector is straightforward: said photoelectron once existed in an electronic quantum state labeled by (E_B, \mathbf{k}) inside the crystal. The most important assumption that made this interpretation possible is that the electronic system under investigation was non-interacting.¹³

In real materials, however, electron-electron interactions cannot be ignored. Moreover, in the case of superconductors, even the species of particle being studied is ambiguous. In this section, I will both describe a more realistic interpretation of ARPES data, and explain why the simplified model discussed in Sec. 3.3.1 still serves as a valuable analytical tool.

3.4.1 Studying many-body physics

As I stated above, electron-electron interactions in real materials *apparently* makes the toy model discussed in Sec. 3.3.1 invalid. But it's worth pointing out that, since the formulation of band theory of solids in 1928 [57], ignoring electron-electron interactions was routine in the interpretation of data from various experimental probes (e.g. electrical transport). Therefore, the reason behind the success of band theory remained a puzzle.

In 1956, Lev Landau constructed a theoretical framework, known as the Fermi liquid theory, which could explain the aforementioned puzzle [58]. This framework introduced the notion of a quasiparticle (or ‘‘Landau quasiparticle’’). According to the Fermi liquid theory, given the typical electron densities in solids, the Coulomb force emanating from an electron (hole) is, on average, screened by a ‘‘cloud’’ of electron-hole pair excitations. The electron (hole) and the cloud form a composite entity called the quasi-electron (quasi-hole); the latter mimics a non-interacting electron (hole). The quasi-electron retains its charge and spin while acquiring an effective mass differing from that of a free electron. This phenomenon is analogous to the electron acquiring an effective mass in the presence of a lattice.

However, the mapping between a particle and its quasiparticle is not perfect. The imperfection of said mapping manifests itself in the quasiparticle having a finite lifetime. For example, for a 3D

¹³In this discussion, the term non-interacting will mean no electron-electron interactions other than exchange interaction.

Fermi liquid, the quasiparticle lifetime scales inversely with the square its energy relative to the Fermi level. In other words, the quasiparticle is well-defined at the Fermi level. Since experimental probes of Fermi liquids (e.g. electrical transport) are only sensitive to electron dynamics close to the Fermi level, the existence of long-lived quasiparticles allowed one to ignore electron-electron interactions.

In an ARPES measurement, the quantity being measured is the spectral function, $A(\mathbf{k}, E)$. In an interacting many-electron system, the spectral function is used, in the quantum field theoretic framework, to quantifying the probability of finding an electron with energy E and a momentum \mathbf{k} . The spectral function can be expressed as

$$A(\mathbf{k}, E) = \frac{1}{\pi} |\text{Im} [G(\mathbf{k}, E)]| , \quad (3.4.1)$$

where $G(\mathbf{k}, E)$ is the electron's Green's function, the latter of which encodes properties of the quasi-electron. As a result, the properties of the quasi-electron can be inferred from an ARPES spectrum. The finite quasiparticle lifetime manifests itself in the broadening of the photoelectron spectrum in the energy axis. As a result, many of the predictions of the Fermi liquid theory have been *directly* verified using ARPES.¹⁴

Furthermore, the ability to *directly* measure $A(\mathbf{k}, E)$ makes ARPES one of the most valuable tools in microscopic investigations of non-Fermi liquids. In other words, ARPES can provide valuable information about the dynamics of excitations in an electronic system even when the quasiparticle is ill-defined. The interested reader can find details of studies of many-body physics using ARPES in [56].

For studies of electronic phases within the scope this thesis, however, I will use ARPES merely as a probe of energy-momentum dispersion in Fermi liquids. In particular, I am interested in studying “non-interacting” superconductors. A non-interacting superconductor can be spectrally treated as a Fermionic insulator where the Bogoliubov quasiparticles form a Fermi liquid. In fact, most of the theoretical proposals for realizing Majorana quasiparticles assume a non-interacting superconductor. By extension, the Majorana quasiparticles are also expected to form a Fermi liquid. However, it is conceivable that non-Fermi liquid materials might be capable of hosting Majorana quasiparticles as well.¹⁵ Hence the possibility of studying many-body physics aspects of topological superconductors might be relevant.

3.4.2 Detection of Bogoliubov quasiparticles

I showed in Sec. 2.2.2.2 that the mean-field Hamiltonian I obtained in (2.2.5) was not diagonal in the electron basis $\hat{C}_{\mathbf{k}}$ (c.f. Eq. (2.2.6)). Instead it was diagonal in a basis defined by Bogoliubov operators (c.f. Eq. (2.2.11)). Back then, the definition of Bogoliubov operators was merely a mathematical manipulation. It turns out that spectral techniques like ARPES measure the spectral functions corresponding to these Bogoliubov operators.

The Bogoliubov operators are defined as a linear combination electron-like and hole-like operators with the respective probability amplitudes given by $u_{\mathbf{k}}$ and $v_{\mathbf{k}}$ (c.f. Eq. (2.2.12)). Fig. 3.4.1 shows a plot of the respective probabilities using Eq. (2.2.13) and (2.2.14). It can be noted that, for energies much higher and lower than the Fermi level (μ), the Bogoliubov state is almost completely electron-like and hole-like respectively.

¹⁴Even though ARPES is not the only probe to do so.

¹⁵In Sec. 2.4.4, topological superconductivity in a iron-based superconductor, $\text{FeTe}_{0.55}\text{Se}_{0.45}$, was investigated in the Fermi liquid regime. In general, iron-based superconductor exhibit non-Fermi liquid behavior.

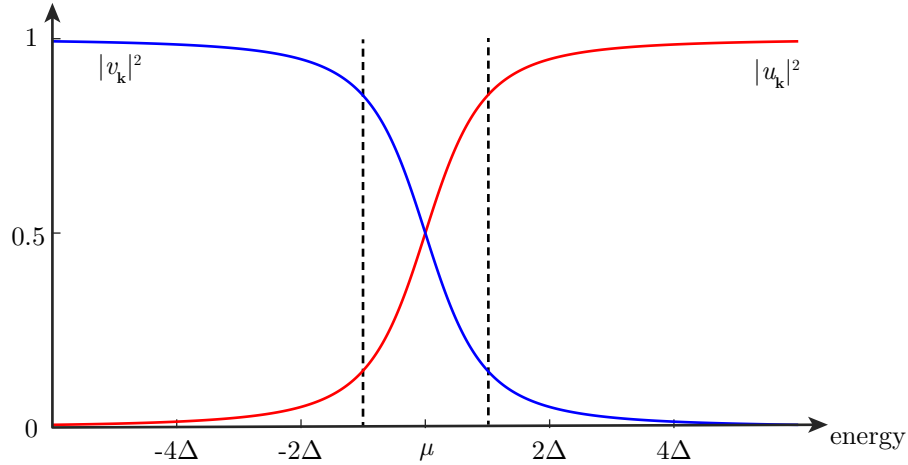


Figure 3.4.1: Plot of $|u_{\mathbf{k}}|^2$ and $|v_{\mathbf{k}}|^2$ as a function of energy. The region between the vertical dashed lines has zero density of states in the bulk of a conventional superconductor.

Since ARPES measures occupied states, only the dispersion of the Bogoliubov states at energies lower than binding energy of $\mu - \Delta$ will be measured. After absorbing energy from a photon, the Bogoliubov quasiparticle in the lower Bogoliubov band (c.f. Fig. 2.2.1) will move up the energy axis, with its electron-like nature ($u_{\mathbf{k}}$) monotonically increasing with energy (c.f. Fig. 3.4.1). By the time it overcomes the work function, the Bogoliubov particle would have completely transformed into an electron. As discussed in Sec. 3.3.2, the resulting photoelectron's in-plane momentum will be preserved, and the corresponding intensity will be proportional to the density of states at the energy level from which it originated. Moreover, the binding energy of the Bogoliubov particle can be inferred from the photoelectron kinetic energy (c.f. Eq. (3.3.2)). In other words, the energy-momentum dispersion of a Bogoliubov state inside a superconductor can be mapped as if it were the band structure of a normal metal.

As I discussed in Sec. 2.3, p -wave superconductors are predicted to have gapless Majorana states in the energy range $(-\Delta, \Delta)$ on the boundaries of said superconductors. For the case of 3D p -wave superconductors, the dispersion of the lower Majorana cone (c.f. Fig. 2.3.6) can be mapped using ARPES via the quasiparticle excitation process I discussed in the previous paragraph.

Chapter 4

Generation of photoelectrons

In this chapter, I will discuss the details of photoelectron generation from a solid-state medium using electromagnetic excitation. In particular, I will only focus on laser-based photon sources. I will start with an overview of different laser systems used for performing ARPES, discuss their pros and cons (Sec. 4.1), and eventually discuss the design and performance of the continuous wave 6 eV laser used to perform the ARPES experiments presented in this thesis.

4.1 Laser-based ARPES photon sources

The use of lasers for producing photoelectrons in an ARPES experiments grew at a significant rate towards the end of the 2000s decade. Reports of the first measurement of photoelectron energy-momentum dispersion¹ using a laser photon source were made in 2006 [60]. This paradigm shift opened up the possibility of achieving unprecedented levels of energy resolution in ARPES experiments. One of the technical limitations of these photon sources, however, was their pulse nature, which introduced so-called space-charge effects.² The ARPES system described in this thesis is one of the few systems which employ a continuous wave laser photon source.

What is common, however, to both continuous and pulsed ARPES laser sources is the process of *photon upconversion*, where the absorption of two or more photons is followed by the emission of a photon with energy higher than any of the absorbed photons. Fig. 4.1.1 illustrates some abstract examples of the upconversion process. Laser-based ARPES sources require photon upconversion because the technology to achieve lasing at the desired ARPES wavelengths does not currently exist. In this section, I will first go over the different laser-based photon upconversion methods that have been implemented to date, and conclude with a discussion of the impact of the space-charge effect on pulsed laser ARPES systems.

Photon upconversion is, by definition, a nonlinear optical process, which is typically very weak. It can be observed in nature with sufficiently sensitive photodetectors. Building a stable light source, which exploits nonlinear optics as the primary driver, however, requires some engineering. In other words, the nonlinear processes driven by conventional light sources (e.g. the fundamental laser) need to be artificially amplified. A straightforward amplification scheme is increasing the photon count from the fundamental laser. This can be achieved in two ways: non-resonant and resonant upconversion.

¹In the 1990s, lased-based photoemission experiments were limited to momentum-integrated measurements [59].

²These will be discussed further in Sec. 4.2.

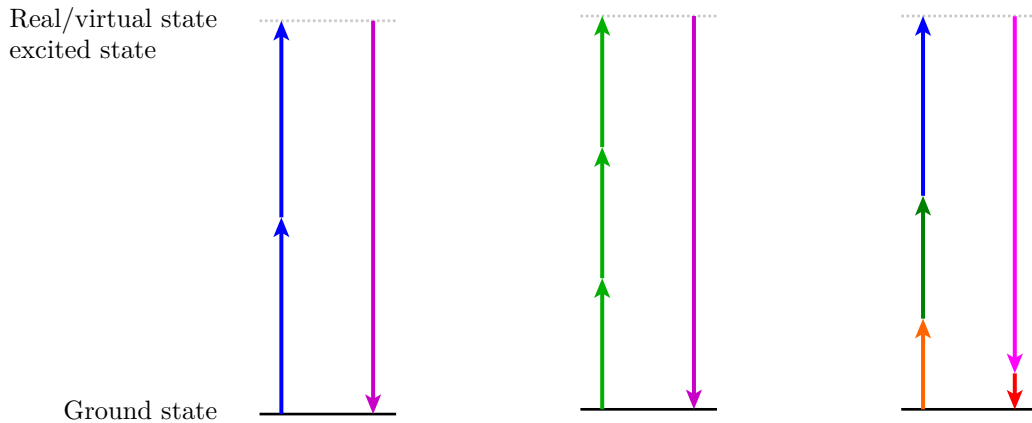


Figure 4.1.1: Three schematic representation of abstract photon upconversion processes. The lengths of the upward- and downward-pointing arrows are proportional to the energy absorbed and emitted by the frequency conversion medium respectively. The pink arrows represent emission of photons of the desired energy.

I will discuss both non-resonant and resonant upconversion methods in Sec. 4.1.1 and Sec. 4.1.2 respectively. In theory, both of these methods could be implemented using either pulsed or continuous wave lasers. In practice, however, the use of pulsed and continuous wave lasers are common for non-resonant and resonant upconversion methods respectively.

4.1.1 Non-resonant upconversion

Non-resonant upconversion methods amplify a weak nonlinear process by increasing the power of the fundamental laser. Pulsed lasers are ideal for this method as they can achieve peak powers several orders of magnitude higher than their continuous counterparts.

4.1.1.1 Solid-state non-resonant upconversion

Certain transparent³ crystalline solids have a non-zero second-order nonlinear optical susceptibility ($\chi^{(2)}$) due to the lack of inversion symmetry in their bulk. If (say) monochromatic light, with wavelength λ , and a sufficiently large electric field amplitude, passes through a crystal with nonzero $\chi^{(2)}$, light with wavelength $\lambda/2$ will be generated via a perturbative nonlinear upconversion process known as second harmonic generation (SHG). In terms of electronic transitions inside the crystal, SHG can be viewed as the leftmost process shown in Fig. 4.1.1, where the excited state is a virtual state, and the difference in energy levels is less than the electronic band gap.

A common upconversion scheme used in pulsed laser ARPES experiments is passing infrared light through a $\chi^{(2)}$ crystal twice. For example, in [60], light from a Titanium:Sapphire mode-locked laser, with a center wavelength of 840 nm, was frequency doubled twice, using two β -BaB₂O₄ (BBO) crystals, to produce the fourth harmonic at a center wavelength of 210 nm (6 eV). The lower limit for wavelength of the fourth harmonic generated by BBO is 189 nm which is close to its bulk band gap. However, other $\chi^{(2)}$ crystals like KBe₂BO₃F₂ (KBBF), due to their higher band gap (8.1 eV), allow ARPES experiments to be performed at (say) 7 eV photon energies [61, 62].

³Transparent at the wavelengths corresponding to the fundamental and second harmonic.

4.1.1.2 Gas-based non-resonant upconversion

Unfortunately, finding $\chi^{(2)}$ crystals with increasingly higher band gap materials is not sustainable. Therefore, in order to reach photon energies in (say) the 10s of eV range, one has to go beyond upconversion methods using perturbative nonlinear mechanisms. Such techniques, which typically involve generating the n^{th} harmonic, with n being as high as a few 10s, are referred to as high-harmonic generation (HHG). This non-perturbative upconversion process is a result of *tunnel ionization* of the atoms. Tunnel ionization occurs when the peak electric field of the fundamental light pulse approaches the magnitude of the electric field experienced by electrons from the nucleus. The tunnel ionization process is followed by the electron-ion recombination which results in HHG.

This form of HHG has been observed in both solid-state [63] and dilute gas media [64, 65]. The former, however, is a new field which requires considerable research and development before its application to ARPES. The latter, which was discovered over two decades prior to the former, has matured to a level where commercial gas-based HHG systems are available. In fact, gas-based HHG was employed to achieve photoemission using lasers for the first time [59].⁴ HHG in gases has the advantage of achieving higher photon energies compared to their solid-state counterparts because the high-harmonic “cut off” in gases scales quadratically as a function of the peak electric field in the fundamental pulse; for solids this scaling is linear.⁵

4.1.2 Resonant upconversion

As I showed in Sec. 4.1.1, non-resonant methods involved exploiting high peak powers of pulsed lasers to increase photon number, which in turn amplified weak nonlinear processes. A resonant upconversion method amplifies a nonlinear process by “trapping” photons inside a resonator. Therefore peak power requirements are relaxed compared to non-resonant upconversion methods. This allows the use of either pulsed lasers with longer (hundreds of picoseconds) pulses or continuous wave lasers. As a result, space-charge effects and linewidths can be minimized to improve energy resolution. The resonator used in these methods can take the form of an optical cavity or an atomic transition.

4.1.2.1 Solid-state resonant upconversion

Similar to the fourth-harmonic generation approach taken in Sec. 4.1.1.1, light from a *single mode continuous wave* (fundamental) laser is successively passed through two frequency doubling stages, each with a nonlinear crystal. However, in this case both nonlinear crystals are placed inside their own resonant cavities. The resonance condition is achieved and maintained by stabilizing the cavity length to an integer multiple of the fundamental laser wavelength. Under this condition, the electromagnetic energy of the fundamental laser is built up inside the cavity, and a second harmonic conversion efficiency comparable to the pulsed case is obtained.

This is the basic operating principle of the laser used to perform the ARPES presented in this thesis. The technical details about this laser’s operation are discussed in Sec. 4.4. The only other ARPES system, to the best of my knowledge, which uses this type of laser belongs the Baumberger group [66]. The most important benefit of this method is its applicability to continuous wave (CW) lasers. CW lasers routinely achieve MHz-level linewidths corresponding to energy uncertainties in the neV range thus making high energy resolution ARPES possible.

⁴These photoemission measurements were, however, performed in the angle-integrated mode, thus making [60] (as I said in Sec. 4.1) the first true laser-based ARPES measurement.

⁵Analogously, the band gap of $\chi^{(2)}$ crystals can be thought of as a cut off for perturbative upconversion.

4.1.2.2 Gas-based resonant upconversion

In a gas-based resonant upconversion method, an appropriate internal electronic transition of an atom is used to resonantly absorb two or more photons. The wavelength and polarization of the absorbed photons are experimentally tuned to satisfy the selection rules of the atomic transition in going to the excited state. Then, depending on the decay channels available to the excited state, a photon with energy less than or equal to the sum of energies of the absorbed photons will be emitted.⁶ For example, in [67], the $5p^6\ ^1S_0 \rightarrow 5p^5\ 6p$ transition in Xenon was exploited to resonantly produce the second harmonic of 256 nm light. The linewidth of this source, similar to the solid-state resonant upconversion method, was narrow (few GHz) primarily due its dependence on a resonant atomic transition.

4.2 Space-charge effects

One of the most important factors in the success of pulsed lasers in achieving high-harmonic generation is their ability to pack a large amount of electromagnetic energy density (few mJ/cm²), and hence a large number of photons, in a pulse of short duration (100s of femtoseconds). Naturally, a high photon density would produce a proportional photoelectrons density per pulse. Unlike photons, however, electrons repel one another through the Coulomb force, eventually resulting in two effects on the measured electron spectrum:

1. broadening in the energy distribution,⁷ and
2. shift in the kinetic energy distribution.

An example of these broadening effects is shown in Fig. 4.2.1.

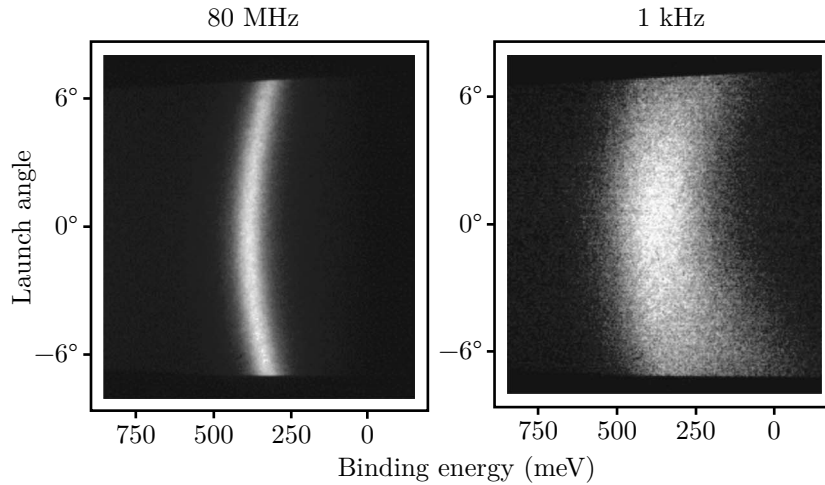


Figure 4.2.1: ARPES data from Shockley states on the (111) surface of Copper using repetition rates of 80 MHz and 1 kHz. Reprinted from Passlack *et al. J. Appl. Phys.* **100**, 024912, with the permission of AIP Publishing. [68].

The magnitude of these two effects depends on the following parameters of the incident laser beam:

⁶The photon energy will be less than the sum of energies of the absorbed photons if the photon does not immediately return to the same state in which it started.

⁷It's worth noting that this energy broadening is in addition to the broadening coming from the energy-time uncertainty of a pulse.

1. photon energy,
2. pulse duration,
3. pulse repetition rate (c.f. Fig. 4.2.1),
4. energy per pulse, and
5. beam waist at the sample.

A systematic theoretical and experimental quantification of the above factors can be found in [69, 70].

4.3 Introduction to continuous wave lasers

In Sec. 4.1 I provided a bird’s-eye view of the application of lasers in ARPES. In this section, I will cover details of continuous wave lasers which I briefly mentioned in Sec. 4.1.2.1. Before getting into technical details, however, it is instructive to review some basic principles of continuous wave laser operation. Moreover, I will provide physical intuition for commonplace technical parameters, like (say) linewidth and free spectral range, which constitute the “laser vocabulary,” and will be frequently referenced in the detailed description of the Toptica TA-FHGTM system in Sec. 4.4.

4.3.1 Laser model

In this section, I will discuss a basic model of a laser at the phenomenological level. In other words, I will forgo a quantum mechanical description of light-matter interaction inside the gain medium for the sake of brevity. I will treat the gain medium as a lumped optical circuit element characterized by a gain function $A(\nu)$. Furthermore, this model incorporates feedback using a so-called Fabry-Pérot cavity.

Fig. 4.3.1 (a) shows the structure of the laser model under discussion. Assuming a Gaussian (TEM₀₀) transverse mode,⁸ the light inside the Fabry-Pérot cavity forms a standing wave between the high reflector and output coupler under steady-state operation. As a result, lasing can only occur for a set of discrete *axial* modes. These axial modes are schematically represented, in the frequency domain, by a train of Lorentzians in Fig. 4.3.1. The spacing between consecutive axial modes in the frequency domain is defined as the *free spectral range*, $\Delta\nu_{\text{FSR}}$, given by

$$\Delta\nu_{\text{FSR}} = \frac{c}{2L}, \quad (4.3.1)$$

where c is the speed of light and L is the mirror-to-mirror⁹ *optical* path length¹⁰ of the cavity.

⁸The Gaussian mode is most common in practice.

⁹Mirror-to-mirror means one-way (or half the round-trip) cavity length.

¹⁰Say the optical phase change in the electromagnetic wave (i.e. laser beam) traveling from point A to B is ϕ . Then the optical path length, L , between A and B is the physical distance, L' , the laser beam would have traveled in vacuum after a phase change of ϕ . For example, if points A and B are within a medium of refractive index n , then $L = nL'$.

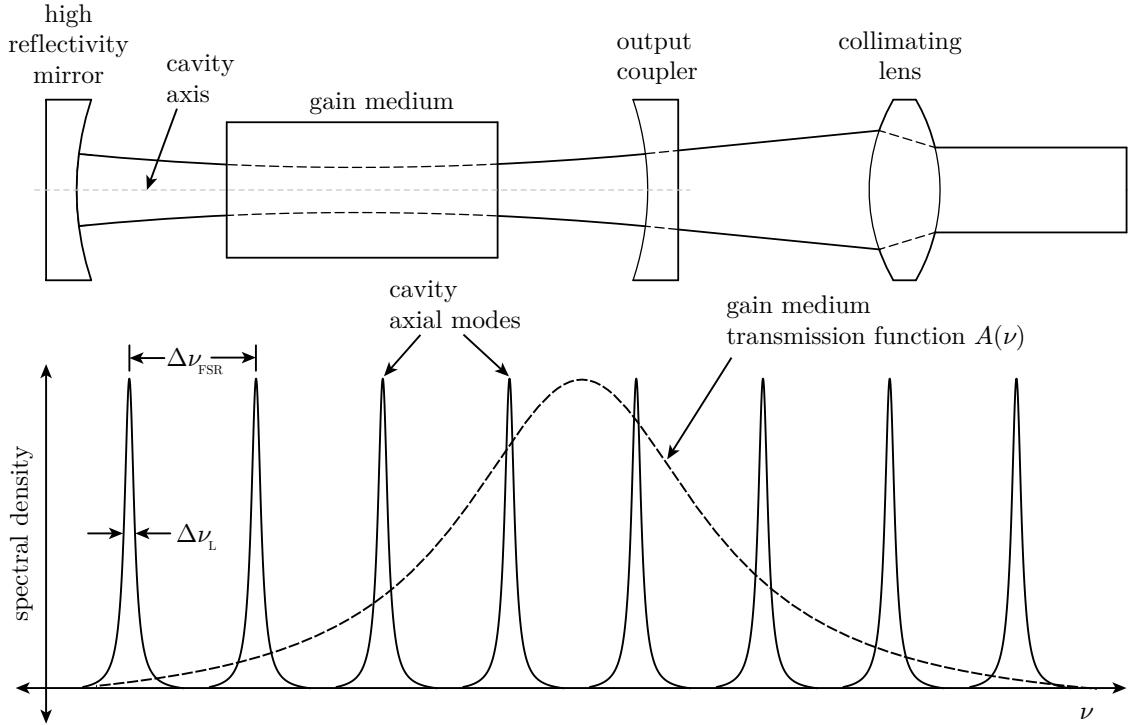


Figure 4.3.1: Spatial representation of a basic Fabry-Pérot laser and spectrum of the light output by the laser.

4.3.2 Linewidth

On a phenomenological level, linewidth is defined as the width of a spectral density function, typically expressed in the frequency or spatial domain, about a center frequency (ν_0) or wavelength ($\lambda_0 = c/\nu_0$). This quantity has several interpretations. In this section, I will mainly discuss linewidth in the context of a laser's frequency spectrum. A single-mode continuous wave laser operates at a fixed frequency, say ν_0 , which can, in theory, be defined to arbitrary precision. In practice, however, there is always some window of uncertainty, say $\Delta\nu_L$ around ν_0 , in which the actual laser frequency lies with a probability higher than a threshold.

For example, if the power spectral density of a laser beam fits a Lorentzian, then one can define $\Delta\nu_L$ as the full width at half maximum (FWHM) of said function (c.f. Fig. 4.3.1). A non-zero $\Delta\nu_L$ is the result of phase noise, in the laser electromagnetic wave, resulting from sources like spontaneous emission, fluctuations in the resonator cavity length, pump power fluctuations, etc. Moreover, the timescale of these noise sources affects the definition of linewidth. For example, while fluctuations in the cavity length due to acoustic vibrations, greater than (say) a few kHz, would contribute to broadening of linewidth $\Delta\nu_L$, temperature fluctuations over the span of (say) hours are referred to as frequency drifts in ν_0 .

4.4 Fourth-harmonic-generation-based continuous wave laser

The ARPES experiments presented in this thesis used the Toptica TA-FHGTM laser system shown in Fig. 4.4.1.¹¹ As I discussed in Sec. 4.1, this system falls into the resonant solid-state upconversion

¹¹TA: tapered amplifier. FHG: fourth harmonic generation

category. The fundamental light, with 822 nm wavelength, is quadrupled using two BBO crystals to produce a 1 mW power laser beam, with 205.5 nm wavelength, for direct use as an ARPES photon source [71].

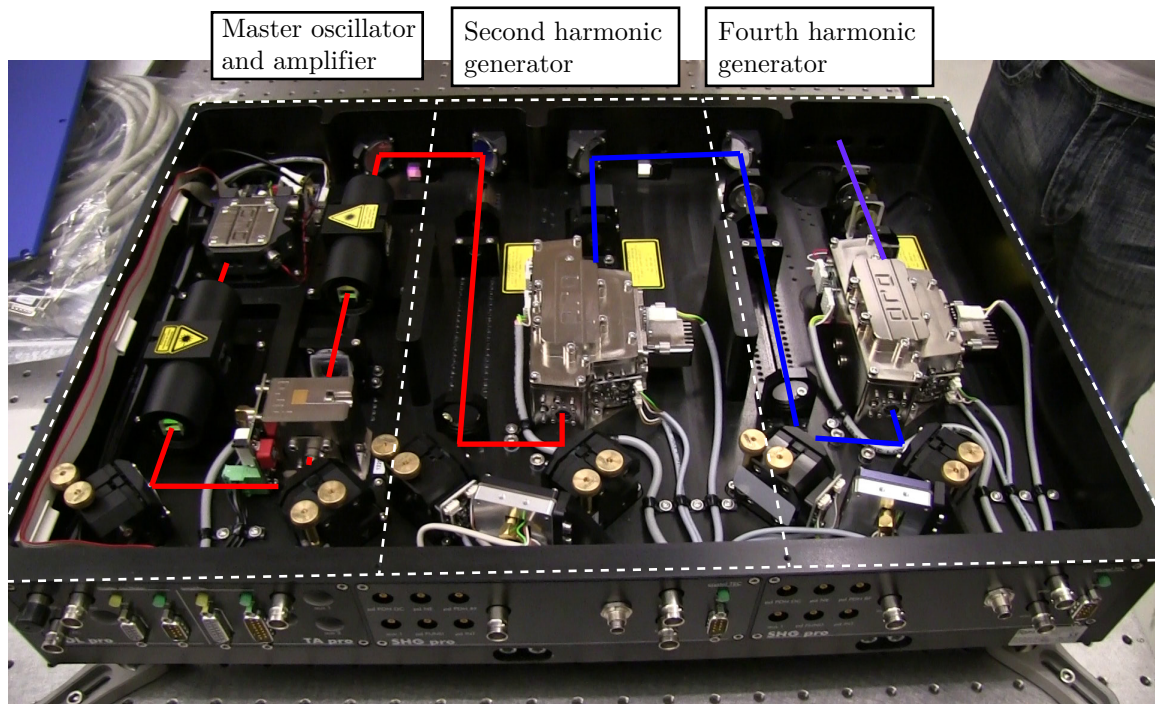


Figure 4.4.1: Photograph of the 6 eV photon ($\lambda = 205.5$ nm) source laser. The red, blue, and purple lines represent 822 nm, 411 nm, and 205.5 nm light respectively. The three stages of the laser are annotated using white dashed line borders.

In Sec. 4.4.1-4.4.3, I will elaborate on the role of the three stages of the Toptica TA-FHG shown in Fig. 4.4.1. Furthermore, I will discuss the working principles and technical specifications of the various components constituting each stage.

4.4.1 Master oscillator and amplifier

The first stage of the Toptica TA-FHGTM is responsible for delivering a narrow-linewidth (1 MHz) high-power ($\gtrsim 2.5$ W) laser beam, at the fundamental wavelength (822 nm), to the second harmonic (411 nm) generator. This stage consists of two main components: (a) master oscillator, and (b) amplifier. The master oscillator consists of the so-called *external cavity diode laser* (ECDL). One of the advantages of semiconductor-based master oscillators, such as the ECDL, is their ability to tune and stabilize the frequency/wavelength of laser cavity mostly electronically.¹² This feature is also beneficial in locking the frequency-doubling cavities (c.f. Sec. 4.4.3). One drawback of ECDLs is their power being typically limited to few 10s of mW. But this shortcoming can be remedied using a *relatively* inexpensive tapered amplifier.¹³

Fig. 4.4.2 shows a cartoon of the ECDL structure. The two main components of the ECDL are: (a) laser diode, and (b) reflective diffraction grating. Both components and related accessories are installed in a monolithic enclosure. The temperature of said enclosure is stabilized to 20 °C using

¹²Tuning can also be done mechanically using manual set screw and/or piezo actuation of the ECDL grating.

¹³For example, in (say) Titanium:Sapphire lasers, expensive optical pumps are required for high power outputs.

a thermo-electric cooler (TEC) element; the latter is heat sunk to the (black) monolithic Topptica TA-FHGTM enclosure shown in Fig. 4.4.1. The measured power output of the ECDL is ≈ 40 mW.

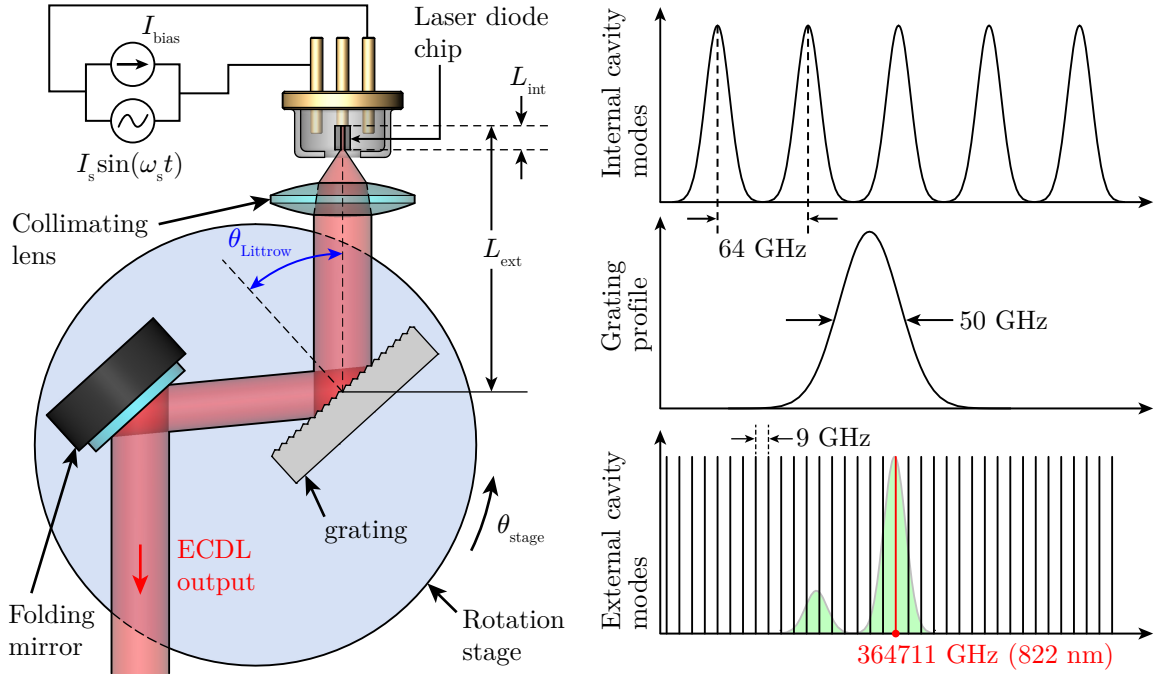


Figure 4.4.2: Left: optical layout of the external cavity diode laser (ECDL) in the Littrow configuration. Right: spectral properties of the ECDL components which determine the mode selection.

The AlGaAs laser diode has a maximum power output of 50 mW with the gain function centered at 820 nm. The end and output facets ($\approx 1 \mu\text{m} \times 3 \mu\text{m}$) of the diode chip are high- and anti-reflection (AR) coated, respectively, thus forming the *internal* Fabry-Pérot cavity of *optical* path length $L_{\text{int}} \approx 2.3$ mm. The refractive index of the optical waveguide is $n_{\text{WG}} \approx 3.5$. The wavelength of the laser diode can be tuned by changing the bias current and chip temperature. With the chip in thermal equilibrium with the TEC-regulated ECDL enclosure,¹⁴ the laser diode is supplied a bias current (I_{bias}) of 94 mA. Both I_{bias} and the factory-set grating position tune the ECDL to the desired wavelength (822 nm).

The light emitted by the output facet of the laser diode is collimated with a short-focal-length diffracted-limited lens onto a reflective diffraction grating (1800 lines/mm). The first-order diffracted beam is retro-reflected, and fed back into the internal Fabry-Pérot cavity, after refocusing the beam into the AR-coated output facet of the laser diode. Consequently, the grating and the end facet of the laser diode form an *external* Fabry-Pérot cavity of optical path length $L_{\text{ext}} \approx 17$ mm. Moreover, the zeroth-order diffracted beam is guided, using a folding mirror, to the ECDL enclosure's exit aperture. This ECDL structure is known as the ‘‘Littrow configuration.’’

In the Littrow configuration, the first-order diffraction angle, θ_{Littrow} , is given by

$$\theta_{\text{Littrow}} = \sin^{-1} \left(\frac{\lambda_{\text{ECDL}}}{2d_{\text{grating}}} \right), \quad (4.4.1)$$

where λ_{ECDL} is the wavelength of light and d_{grating} (556 nm) is the spacing between consecutive lines of the grating. In practice, θ_{Littrow} is mechanically controlled to tune λ_{ECDL} . As shown in Fig. 4.4.2, grating and folding mirror are mounted on a rotation stage. The angular position (θ_{stage}) of the

¹⁴A thermistor cemented to the laser diode package assembly provides temperature feedback.

latter can be coarse- or fine-tuned using a set screw or a piezo actuator respectively. An advantage of this design is that changing θ_{stage} allows wavelength tuning, by simultaneously changing θ_{Littrow} and L_{ext} , with negligible change in the beam pointing. As I stated earlier, θ_{Littrow} and L_{ext} is usually factory-set. For $\lambda_{\text{ECDL}} = 822 \text{ nm}$, Eq. (4.4.1) gives $\theta_{\text{Littrow}} = 47.7^\circ$.

The right side of Fig. 4.4.2 illustrates the factors which control the selection of the longitudinal mode (i.e. f_{ECDL} or $\lambda_{\text{ECDL}} = c/f_{\text{ECDL}}$). The top plot shows the mode structure of the internal cavity with a nominal free spectral range $\Delta\nu_{\text{FSR}}^{\text{internal}} = 64 \text{ GHz}$. The middle plot shows the feedback profile of the grating given by

$$\Delta\nu_{\text{grating}} = \frac{c}{m\lambda_{\text{ECDL}}N_{\text{grating}}}, \quad (4.4.2)$$

where m is the diffraction order and N_{grating} is the number of lines of the grating illuminated by the laser beam. In this case, $m = 1$ and $\Delta\nu_{\text{grating}} = 50 \text{ GHz}$. Finally, the bottom plot shows the mode structure of the external cavity with a nominal free spectral range $\Delta\nu_{\text{FSR}}^{\text{external}} = 9 \text{ GHz}$. The semi-transparent green curve represents the combined gain of the internal cavity (top curve) and grating feedback profile (middle curve). Based on this gain curve, the red line corresponds to the selected mode (822 nm).

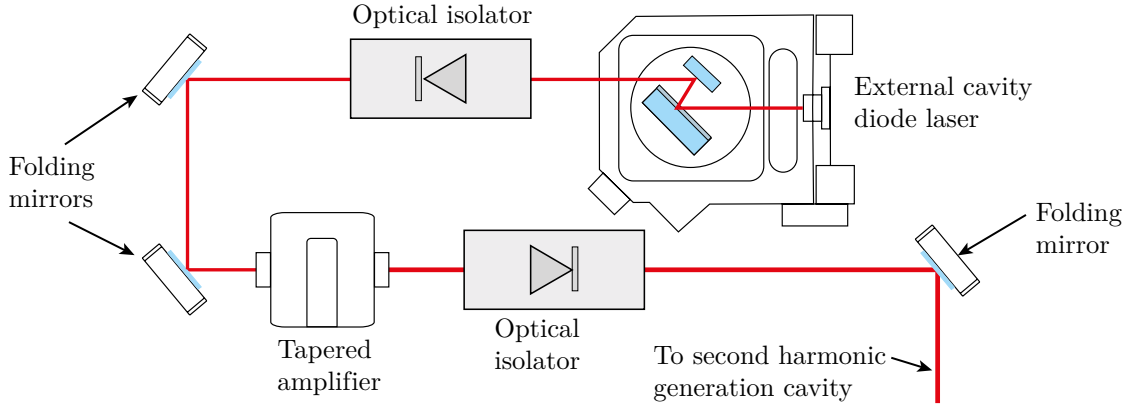


Figure 4.4.3: Optical layout for the fundamental light at 822 nm.

Fig. 4.4.3 shows the path of the fundamental (822 nm) beam after leaving the ECDL. The optical isolator allows light to travel in only one direction. This is done to avoid the light reflected from downstream optics from entering the ECDL and affecting its mode structure. The model used in this laser provides a 60 dB isolation.

After the isolator, the power of the fundamental (822 nm) is increased by almost a factor of 60 using a tapered amplifier. The conversion efficiencies for SHG (411 nm) and FHG (205.5 nm) production are $\approx 40\%$ and $\approx 0.1\%$ respectively. In order to have sufficient power for locking the FHG cavity, a large amount ($\approx 1 \text{ W}$) of SHG is required. Therefore the 40 mW output of the ECDL needs to be amplified to 2.5 W. The temperature of the tapered amplifier enclosure is stabilized using a TEC.

4.4.2 Efficient second harmonic generation

In this section, I will discuss the technical details of the SHG process I glossed over in Sec. 4.1.1.1 and Sec. 4.1.2.1. In particular, I will elaborate on the challenges associated with resonant upconversion and the corresponding solutions implemented in the TA-FHG system.

According to conventional laser wisdom, the magnitude of an atomic-level optical process scales with system size. Therefore, it is natural to assume the same for the SHG process in $\chi^{(2)}$ crystals. However, this assumption only holds under the condition of *phase matching* [72]. In the context of SHG, phase matching corresponds to a condition where the fundamental and second harmonic, with frequencies ω and 2ω respectively, co-propagate in phase. This requires the refractive indices at both the fundamental, $n(\omega)$, and second harmonic, $n(2\omega)$, frequencies to be equal.

The degree of phase matching is typically quantified in terms of the wave vector mismatch

$$\Delta k \equiv k_f - 2k_{\text{SHG}}, \quad (4.4.3)$$

where k_{SHG} and k_f correspond to the wave vectors of the second harmonic and fundamental respectively and can be expressed in terms of refractive index as

$$k_{\text{SHG}} = \frac{2\omega n(2\omega)}{c}, \quad (4.4.4)$$

$$k_f = \frac{\omega n(\omega)}{c}. \quad (4.4.5)$$

Plugging (4.4.4) and (4.4.5) in (4.4.3) I get

$$\Delta k = \frac{2\omega}{c} [n(\omega) - n(2\omega)].$$

Obviously, the phase matching condition corresponds to $\Delta k = 0$. In Fig. 4.4.4, it is obvious that if $\Delta k \neq 0$, the second harmonic power does not scale with system size, because the SHG in different parts of the crystal won't add up constructively. Moreover, since refractive index is a function of temperature, Δk will no longer vanish if the crystal temperature deviates from its nominal value by a few °C (or Kelvin).

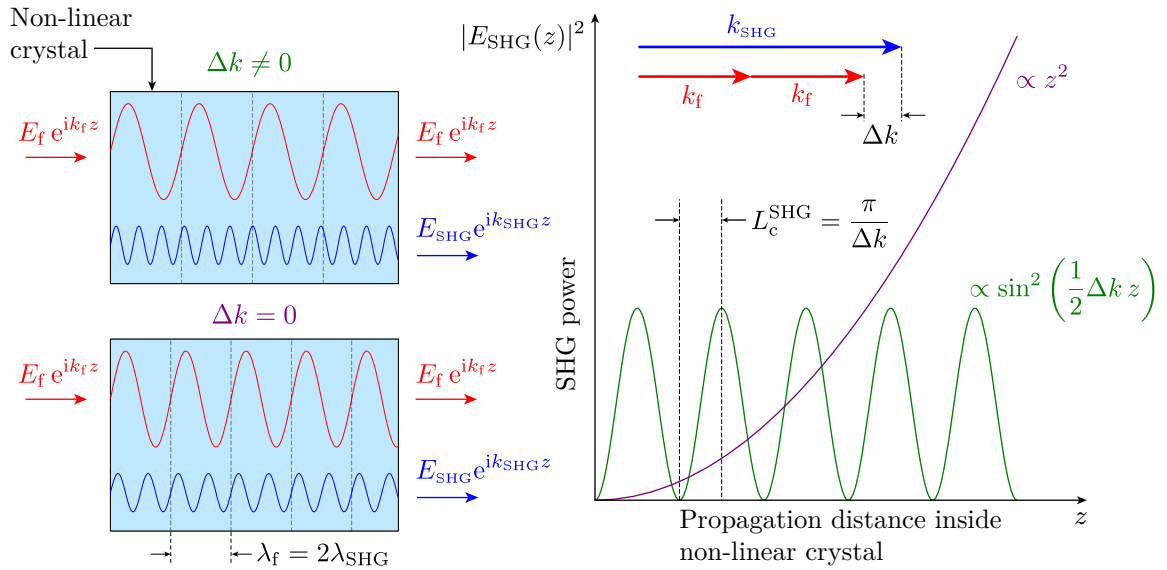


Figure 4.4.4: Left: cartoon illustration of the propagation of the fundamental (red) and second harmonic (blue) waves for the cases of phase mismatch (top) and matching (bottom). The two waves' phase fronts align only for the $\Delta k = 0$ case. Right: power of second harmonic as a function of propagation distance, z , inside the non-linear crystal for phase mismatched (green) and matched (purple) cases. The top of the plot shows a graphical definition of $\Delta k \equiv k_{\text{SHG}} - 2k_f$.

Typically, the refractive index is a monotonic function of ω away from a resonant absorption line.¹⁵ So phase matching is not possible in an isotropic medium. In an anisotropic (or birefringent) $\chi^{(2)}$

¹⁵Being away from resonance is essential for transparency for both fundamental and second harmonic wavelengths.

crystal like BBO, however, one can obtain two refractive index functions, say $n_1(\omega)$ and $n_2(\omega)$, for orthogonal light polarizations. Then the condition $n_1(\omega) = n_2(2\omega)$ can be satisfied if a specific propagation direction is chosen. The direction of propagation is typically specified in terms of an angle, known as the phase-matching angle, with respect to the optical axis. The optical axis in a birefringent material is defined as the direction along which all polarizations at a given wavelength experience the same refractive index.

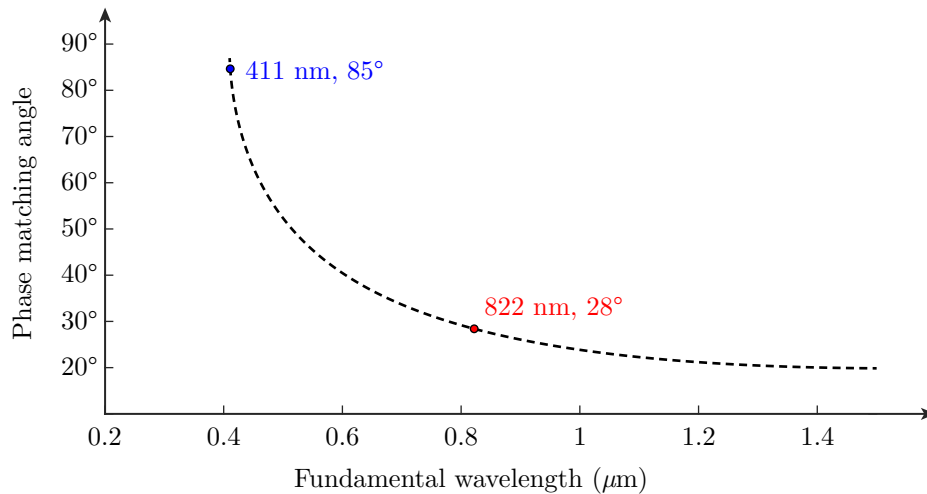


Figure 4.4.5: Curve showing phase matching angle as a function of fundamental wavelength in BBO at 20 °C.

As an example, Fig. 4.4.5 shows the variation of the phase-matching angle of the BBO crystal, at 20 °C, as a function of the fundamental wavelength. Moreover, the phase-matching angles of 28° (822 nm \rightarrow 411 nm) and 85° (411 nm \rightarrow 205.5 nm) are highlighted for the two types of conversions of interest in the Toptica TA-FHG.¹⁶ The details of computing the phase matching condition can be found in Sec. D.3.

4.4.3 Frequency-doubling cavity

The most important component of the final two stages of the Toptica TA-FHG (c.f. Fig. 4.4.1) is the frequency-doubling cavity. The first and second cavity generate the second (411 nm) and fourth harmonic (205.5 nm) of the fundamental (822 nm) respectively. In this section, I will discuss some of the technical aspects of the frequency-doubling cavity which allow said cavity to produce an efficient and stable second harmonic laser beam.

4.4.3.1 Optical layout of the bow-tie cavity

Fig. 4.4.6 shows the optical layout of the frequency-doubling cavity. Due to the shape of this configuration, this cavity is commonly referred to as the “bow-tie cavity.” The bow-tie cavity is a type of twisted ring resonator with four mirrors:

1. Input coupler (M_1) for the fundamental light (822 nm or 411 nm) from the previous stage,
2. Piezo actuated folding mirror (M_2),

¹⁶Note that the two BBO crystals are actually **not** maintained at 20 °C (c.f. Sec. 4.4.3.1).

3. Beam guiding mirror into the nonlinear crystal (M_3), and
4. Output coupling mirror for the second harmonic (M_4).

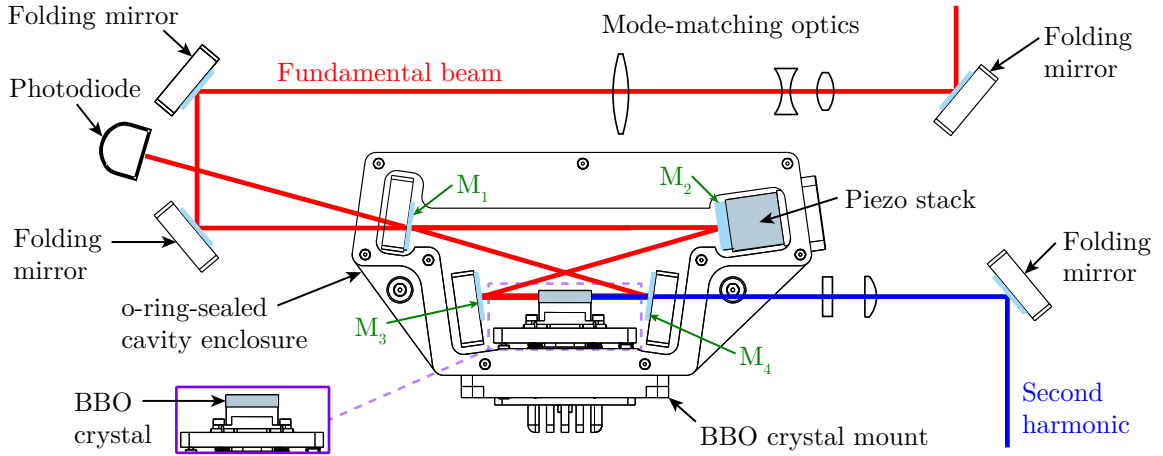


Figure 4.4.6: Schematic representation of the bow-tie cavity used for second harmonic generation.

M_3 and M_4 are curved mirrors to focus the fundamental into the nonlinear crystal. The conversion efficiency is controlled by the cavity length determined by M_2 . When the cavity length is equal to an integer multiple of the fundamental wavelength, a resonance condition, corresponding to the maximum power density of the fundamental in the cavity, is achieved. The second harmonic conversion efficiency is highly sensitive to the resonance condition.

Furthermore, the temperature of the BBO crystal in the second (411 nm) and fourth (205.5 nm) harmonic generation cavities is maintained at 30 °C and 40 °C using a thermo-electric cooler (TEC) respectively.

4.4.3.2 Locking of the bow-tie cavity

In addition to phase-matching, optimal conversion efficiency from the bow-tie doubling cavity requires the cavity to always be on resonance. The resonance condition occurs when the cavity length is an integer multiple of fundamental wavelength. In practical implementations of these cavities, however, the cavity length continually fluctuates due to noise sources such as temperature fluctuations and acoustic vibrations. Such fluctuations would result in large power swings in the second harmonic signal which cannot be tolerated for most experimental applications. The aforementioned environmental disturbances can, however, be mitigated using an *active* cavity stabilization technique known as the Pound-Drever-Hall (PDH) method [73].

A laser stabilized using PDH is an example of a feedback loop utilizing the proportional-integral-derivative (PID) controller. In the Toptica TA-FHG,TM a conceptual layout of the PDH stabilization scheme is shown in Fig. 4.4.7.

I will now present a mathematical model for the PDH scheme with references to specific components in the Toptica laser system. A local sinusoidal oscillator with frequency, $\omega_s = 2\pi \times 5$ MHz, is superposed on to the drive current of the ECDL; the drive current then has the form

$$I_{\text{drive}}(t) = I_{\text{bias}} + I_s \sin(\omega_s t). \quad (4.4.6)$$

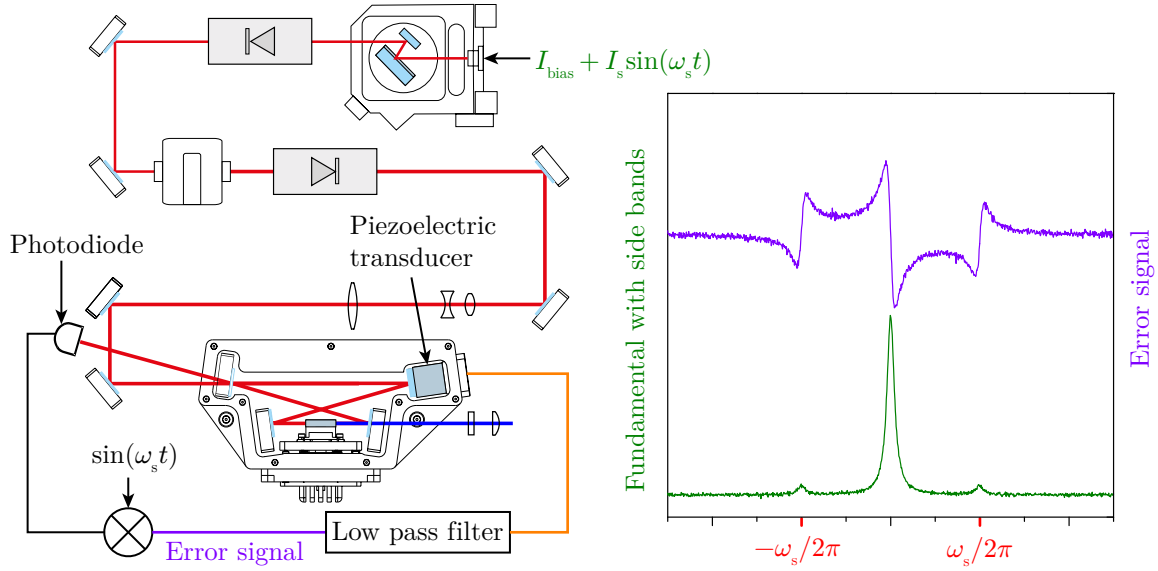


Figure 4.4.7: Comparison between a Pound-Drever-Hall system and proportional-integral-derivative controller

This results in a modulation of the electron-hole pair density inside the diode laser, away from its equilibrium value (set by I_{bias}), at the same frequency ω_s ; which in turn causes an oscillation in the optical path length, due to change in refractive index, at frequency ω_s as well. Then the modulation of the phase of the electric field incident on the cavity, $E_{\text{incident}}(t)$, can be written as:

$$\begin{aligned}
 E_{\text{incident}}(t) &= \frac{E_0}{2} \exp(i(\omega_c t + A_s \sin(\omega_s t))) + \text{c.c.}, \\
 &= \frac{E_0}{2} \sum_{n=-\infty}^{\infty} J_n(A_s) e^{i(\omega_c + n\omega_s)t} + \text{c.c.}, \\
 &\approx \frac{E_0}{2} \left[J_0(A_s) e^{i\omega_c t} + J_{+1}(A_s) e^{i(\omega_c + \omega_s)t} + J_{-1}(A_s) e^{i(\omega_c - \omega_s)t} \right] + \text{c.c.}, \quad (4.4.7)
 \end{aligned}$$

where $J_n(A_s)$ is the n^{th} order Bessel function with optical phase modulation amplitude, A_s , as its argument. Only keeping the ± 1 orders of the Bessel function suffices for the PDH scheme to work reliably. The power spectral density of the incident beam is shown in Fig. 4.4.7. It can be noted that two side bands, at an offset of ± 5 MHz to carrier frequency, have appeared; their height can be controlled by the modulation amplitude A_s (or I_s). The power in the carrier (P_c) and side bands (P_s) are

$$\begin{aligned}
 P_c &= J_0^2(A_m) P_{\text{incident}}, \\
 P_s &= J_1^2(A_m) P_{\text{incident}}, \\
 P_{\text{incident}} &\gtrsim P_c + 2P_s,
 \end{aligned}$$

where P_{incident} is the total power of the incident beam.

The photodiode measures the power of the reflected light. The electric field of the reflected light in the frequency domain, $\tilde{E}_{\text{reflected}}$, is given by

$$\tilde{E}_{\text{reflected}}(\omega, L) = R(\omega, L) \tilde{E}_{\text{incident}}(\omega),$$

where $R(\omega, L)$ is the electric field reflectivity expressed as an explicit function of cavity length L .

For a lossless symmetric cavity, $R(\omega, L)$ takes the

$$\begin{aligned} R(\omega, L) &= \frac{r(\omega)(e^{i\phi(\omega, L)} - 1)}{1 - r^2(\omega)e^{i\phi(\omega, L)}}, \\ \phi(\omega, L) &= \frac{2L\omega}{c}, \\ &= \frac{\omega}{\Delta\nu_{\text{FSR}}(L)}, \end{aligned}$$

where $r(\omega)$ is the reflectivity of the mirrors and $\phi(\omega, L)$ is the phase acquired by the fundamental in one round trip. Then the reflected field in the time domain ($E_{\text{reflected}}(t)$) is

$$\begin{aligned} E_{\text{reflected}}(t, L) &= \frac{E_0}{2} \left[R(\omega_c, L)J_0(A_s)e^{i\omega_0 t} + R(\omega_c + \omega_s, L)J_{+1}(A_s)e^{i(\omega_c + \omega_s)t} \right. \\ &\quad \left. + R(\omega_c - \omega_s, L)J_{-1}(A_s)e^{i(\omega_c - \omega_s)t} \right] + \text{c.c.}, \end{aligned} \quad (4.4.8)$$

The expression for power spectral density of the reflected beam, measured by the photodiode, is obtained by squaring Eq. (4.4.8) to give

$$\begin{aligned} P_{\text{reflected}}(\omega, L) &= P_c |R(\omega_c, L)|^2 + P_s \{ |R(\omega_c + \omega_s, L)|^2 + |R(\omega_c - \omega_s, L)|^2 \} \\ &\quad + 2\sqrt{P_c P_s} \Re [R(\omega_c, L)R^*(\omega_c + \omega_s, L) - R^*(\omega_c, L)R(\omega_c - \omega_s, L)] \cos(\omega_s t) \\ &\quad + 2\sqrt{P_c P_s} \Im [R(\omega_c, L)R^*(\omega_c + \omega_s, L) - R^*(\omega_c, L)R(\omega_c - \omega_s, L)] \sin(\omega_s t) \\ &\quad + (\text{terms oscillating at } 2\omega_s), \end{aligned} \quad (4.4.9)$$

After demodulating (or mixing down) $P_{\text{reflected}}(\omega, L)$, using the same local oscillator used to modulate the diode laser current in Eq. (4.4.6), I recover the term

$$e(t) \equiv 2\sqrt{P_c P_s} \Im [R(\omega_c, L(t))R^*(\omega_c + \omega_s, L(t)) - R^*(\omega_c, L(t))R(\omega_c - \omega_s, L(t))] , \quad (4.4.10)$$

which is defined as the error signal, $e(t)$. The frequency domain plot of the incident power and error signal is shown in Fig. 4.4.7.

4.5 Potential future directions for ARPES laser sources

Close of the turn of the millennium, up to 20 nW of 121.56 nm wavelength (10.2 eV photon energy) coherent continuous wave photons were produced [74, 75], using *resonant* four-wave mixing of three fundamental lasers at 257 nm (570 mW), 399 nm (500 mW), and 545 nm (1.2 W), inside a Mercury vapor cell. The laser linewidth was reported to be well below 10 MHz (≈ 40 neV). The motivation of these efforts were performing laser cooling and spectroscopy on the Lyman- α transition (1s-2p) of antihydrogen (or hydrogen) which had a natural linewidth of ≈ 100 MHz. Efforts are currently underway to increase the power of the three fundamental lasers, 254 nm (0.5 W),¹⁷ 408 nm (5 W), and 545 nm (1.2 W), by almost an order of magnitude each, which will in principle increase the 10.2 eV output power by three orders of magnitude. The projected minimum and maximum power outputs are 4.4 μ W (2.7×10^{12} photons/second) and 175 μ W (10^{14} photons/second) respectively [76].

¹⁷The 254 nm laser is the Toptica TA-FHG discussed in this chapter with the ECDL operating at 1016 nm.

Chapter 5

Angle-resolved spectral analysis of photoelectrons

The previous chapter focused on the generation of photoelectrons using electromagnetic fields. I will assume the photoelectron generation process confines said electrons to a small region around the “focal point” of the electron spectrum analyzer (abbreviated as *analyzer*) without altering the energy and momentum information they carry. In this chapter, I will only analyze the trajectories of these electrons from the focal point (source) to the appropriate detector (destination). The analyzer effectively acts like an intermediate “free space circuit,” between the source (input) and destination (output), and tunably controls the electron trajectories. I will start with a brief discussion of the building blocks of the aforementioned circuit and later discuss specific details of VG Scienta’s R8000 analyzer used to perform all ARPES experiments presented in this thesis.

5.1 Introduction to free-space electron spectrum analyzers

5.1.1 Adaptation of optics terminology

It turns out that analyzing and controlling free space electron trajectories has more in common with a free space “optical circuit” compared to a circuit consisting of electron waveguides (e.g. resistors, capacitors, etc.). Therefore, I will use the language of optics in discussing properties of the components of the analyzer. Moreover, I will soon illustrate that optical components, such as lenses and prisms/gratings, have analogs in free space “electron optics.” For example, Fig. 5.1.1 shows the analogy between photons and electrons as they cross an interface between vacuum and an energy dispersive medium.

One thing worth noting in Fig. 5.1.1 (a) is that the optical axis is a straight line. While this is simple and intuitive in the case of optics, it is not a good choice for electron optics due to the fact that electrons are charged. Note that, while the refracted rays in Fig. 5.1.1 (a) will keep moving in a straight line, the refracted electrons in Fig. 5.1.1 (b) will eventually hit the lower electrode as shown in Fig. 5.1.1 (c). In order to determine an appropriate optical axis for electrons, it is convenient to view the dispersed trajectories as part of a divergent beam. In the case of a hemispherical deflection analyzer, which I will discuss next, the optical axis can be defined as the average trajectory of this diverging beam.

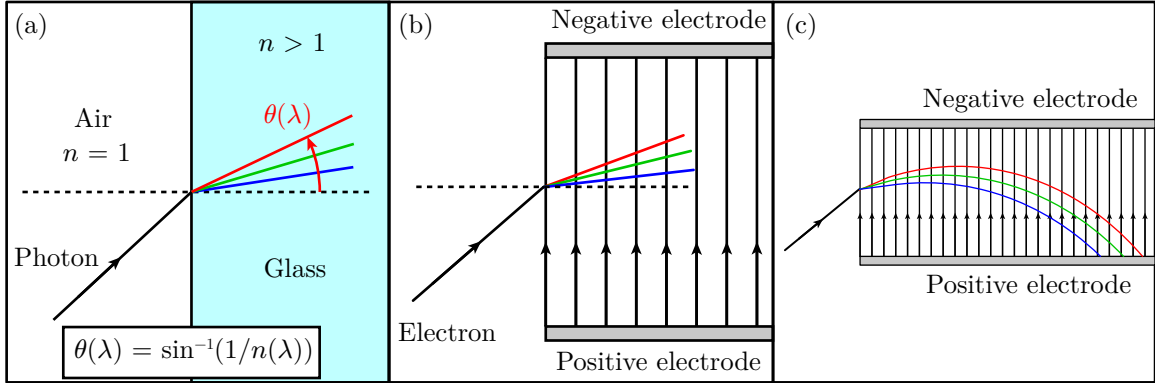


Figure 5.1.1: (a) Interface between media with different refractive indices, (b) interface between regions with and without an electric field, (c) electron trajectories deep inside the region with an electric field.

5.1.2 Hemispherical deflection analyzer

One of the most widely used electron spectrum analyzers in ARPES is the electrostatic hemispherical deflection analyzer (HDA). Some of the major advantages offered by this deflector-style class of electrostatic analyzers is its high energy resolution and superior energy- and angle-resolved imaging properties compared to its cylindrical and parallel plate counterparts. In this section, I will discuss the operating principle and theoretical performance of the HDA.

5.1.2.1 Geometry and imaging properties of the HDA

The geometry of the hemispherical deflection analyzer is illustrated in a simplified sketch in Fig. 5.1.2. It consists of two concentric hemispheres of radii R_1 and R_2 maintained at voltages V_1 and V_2 respectively. Moreover, I have defined a reference hemisphere of radius

$$R_0 = \frac{R_1 + R_2}{2}. \quad (5.1.1)$$

Due to spherical symmetry, away from the equator,¹ the electric field only has a radial component given by

$$E_r(r) = -\frac{V_2 - V_1}{R_2 - R_1} \frac{R_1 R_2}{r^2}, \quad (5.1.2)$$

where r is defined as the distance from the origin in a spherical coordinate system.

Electrons enter the analyzer through a curved slit² whose center intersects the reference sphere. Electrons which enter the HDA on and tangential to the reference sphere, with a specific kinetic energy known as the pass energy (E_{pass}), have trajectories that lie on said sphere and maintain their kinetic energy. These electrons are often referred to, in the electron optics language, as reference particles. When performing a ray-tracing analysis in an arbitrary plane, passing through the center of the hemisphere, the trajectories of the reference particles (dark green curves in Fig. 5.1.2) are convenient choices as the optical axes in their respective planes. In that way, dispersion properties of non-reference electrons can be studied as deviations from the optical axis, thus making the analysis and design of electron optical components closer to their optical counterparts (c.f. Fig. 5.1.1). It is also worth noting that all the reference electron trajectories re-focus after a 180° angular displacement, thus making them ideal for electron imaging applications.

¹The electric field near the equator will be dealt with in Sec. 5.2.2

²The reason for using curved slits will be explained in Sec. 5.3.2

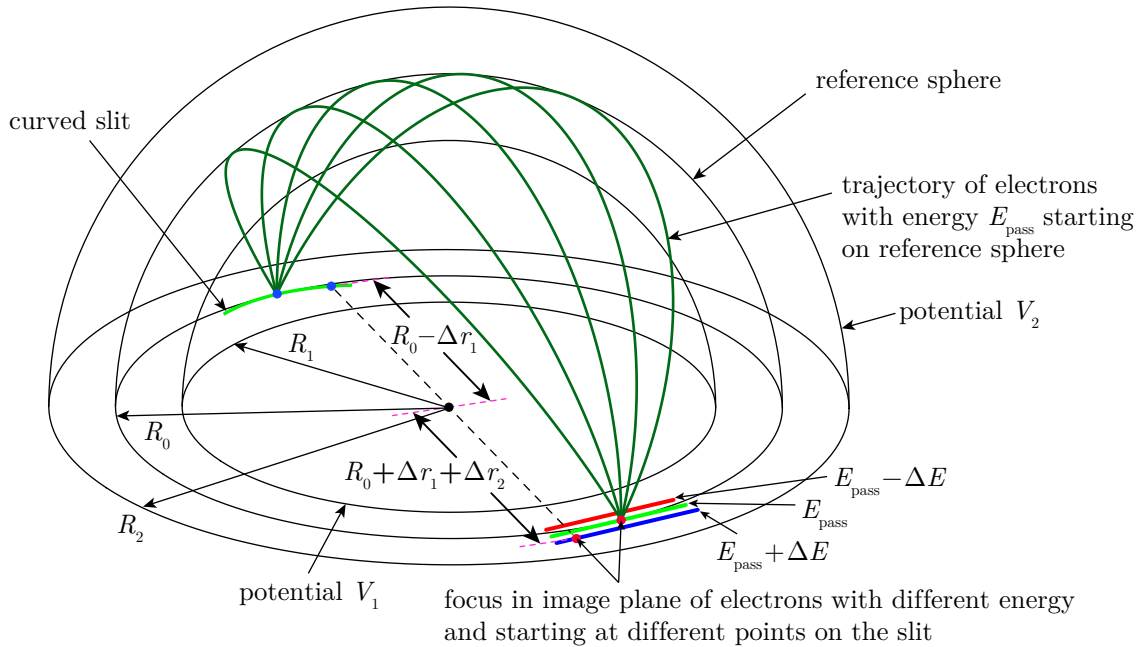


Figure 5.1.2: Illustration of the dispersion and imaging properties of an electrostatic hemispherical deflection analyzer.

5.1.2.2 Analytical dispersion analysis

I'll start with a discussion of some properties of reference electrons and then present a model for imaging non-reference electrons. As I stated in the previous section, the reference electrons' motion is confined to the reference sphere. This is only possible if the outward centrifugal force is balanced by the inward force from the electric field. The velocity of the reference electron in terms of its kinetic energy, E_{pass} , can be written as

$$v_{\text{reference}} = \left(\frac{2E_{\text{pass}}}{m} \right)^{1/2}, \quad (5.1.3)$$

where m is the mass of the electron. Then the centrifugal force experienced by the reference electron in the reference sphere (radius R_0) can be computed as

$$F_{\text{centrifugal}} = \frac{mv_{\text{reference}}^2}{R_0}, \quad (5.1.4)$$

$$= \frac{2E_{\text{pass}}}{R_0}, \quad (5.1.5)$$

where I obtained (5.1.5) simply by substituting (5.1.3) in (5.1.4). Now, equating (5.1.5) to $E_r(R_0)$ (c.f. Eq. (5.1.2)), and doing some algebra, I get

$$\begin{aligned} \Delta V &\equiv V_1 - V_2, \\ &= E_{\text{pass}} \left(\frac{R_2}{R_1} - \frac{R_1}{R_2} \right). \end{aligned} \quad (5.1.6)$$

Therefore, E_{pass} can simply be controlled by tuning the voltage across the hemispherical capacitor shown in Fig. 5.1.2. I will show in Sec. 5.3.3.2 that E_{pass} , defined as the “pass energy,” is typically swept across an energy range of interest to obtain high resolution angle-resolved spectral images.

Now, I will discuss the properties of the non-reference electrons. I will start with a few simple cases:

1. electrons with energy $E_{\text{kinetic}} = E_{\text{pass}} + \Delta E$ entering the analyzer on and tangential to the reference sphere (radius R_0)
2. electrons with energy E_{pass} entering the analyzer on and tangential to a sphere of radius $R_0 + \Delta R_{\text{entrance}}$

For the first case, the electrons follow elliptical trajectories, and after undergoing 180° of angular displacement, focus a point with a E_{kinetic} -dependent radial distance, $R(E_{\text{kinetic}})$, from the center of the hemisphere given by

$$\begin{aligned} R(E_{\text{kinetic}}) &\equiv R(E_{\text{pass}} + \Delta E), \\ &= R_0 \left\{ 1 + 2 \left(\frac{\Delta E}{E_{\text{pass}}} \right) + 4 \left(\frac{\Delta E}{E_{\text{pass}}} \right)^2 + \dots \right\}. \end{aligned} \quad (5.1.7)$$

For the second case, the electrons once again follow elliptical trajectories, and focus at a radial distance of $R_0 - \Delta R_{\text{entrance}}$ from the center of the hemisphere, such that the point of entrance, point of exit, and the origin (c.f. Fig. 5.1.2) lie in the same plane.

In cases 1 and 2, the directions of the two types of displacement of the electrons' focus correspond to two independent (non-orthogonal) unit vectors spanning a 2D subspace in which imaging plane lies. In other words, the vector sum of these displacements would provide the focal point for the trajectories of electrons with energy $E_{\text{kinetic}} = E_{\text{pass}} + \Delta E$ entering the analyzer on and tangential to a sphere of radius $R_0 + \Delta R_{\text{entrance}}$. An example of this third case is illustrated in Fig. 5.1.2 without ray tracing.

Finally, there is a fourth case, where electrons enter at a non-zero angle α relative to the tangent to a hemisphere with (in general) a radius $R_0 + \Delta R_{\text{entrance}}$. To first order, these electrons re-focus in the imaging plane at a distance $R_0 - \Delta R_{\text{entrance}}$ from the origin. Second order de-focusing effects are discussed in Sec. 5.1.2.3.

5.1.2.3 Energy resolution

As evident from Eq. (3.3.8), the analyzer plays an important role in determining the overall energy resolution of an ARPES system. Therefore, in this section I will present a simplified analysis of the factors affecting energy resolution *inside* the hemispherical deflection analyzer.

Consider two monochromatic “pencil” beams³ of electrons, with energies separated by ΔE_a and beam waist w each, entering the analyzer through a slit centered on and tangential to the reference sphere. After entering the analyzer, these two beams are dispersed by the radial electric field region, and form two radially separated spots on the imaging plane. As I discussed in 5.1.2.2, since the focal plane coincides with the imaging plane, the diameter of these spots is w . This scenario is illustrated in Fig. 5.1.3

It is convenient to express the kinetic energies of electrons in beams (say) E_1 and E_2 as

$$E_1 = E_{\text{pass}} + \Delta E_1, \quad (5.1.8)$$

$$\begin{aligned} E_2 &= E_{\text{pass}} + \Delta E_2, \\ &= E_{\text{pass}} + \Delta E_1 + \Delta E_a, \end{aligned} \quad (5.1.9)$$

³The electronic density in a pencil beam is assumed step function going to zero at a finite radius.

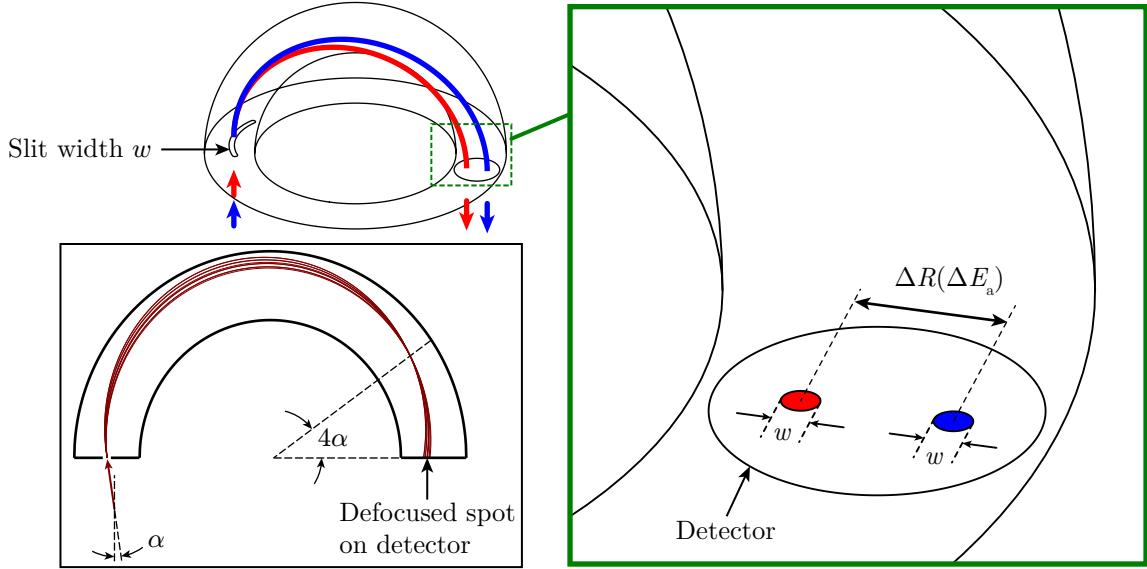


Figure 5.1.3: Two electron beams with a difference in kinetic energy ΔE hitting the detector.

where in the last line I've made explicit the assumption that E_1 and E_2 differ by ΔE . I can now use (5.1.8), (5.1.9), and (5.1.7) to compute the separation between the centers of the two spots, $\Delta R(\Delta E_a)$, given by

$$\begin{aligned} \Delta R(\Delta E_a) &= 2R_0 \left\{ \frac{\Delta E_a}{E_{\text{pass}}} + 2 \left(\frac{E_{\text{pass}} + \Delta E_1 + \Delta E_a}{E_{\text{pass}}} \right)^2 - 2 \left(\frac{E_{\text{pass}} + \Delta E_1}{E_{\text{pass}}} \right)^2 + \dots \right\}, \\ &\approx 2R_0 \frac{\Delta E_a}{E_{\text{pass}}}. \end{aligned} \quad (5.1.10)$$

I will discuss the reason for ignoring the quadratic terms in Sec. 5.2.2. From Fig. 5.1.3 it is clear that in order for the detector to tell the two spots apart, $\Delta R(\Delta E_a)$ cannot be less than w . The value of ΔE_a at which $\Delta R(\Delta E_a) = w$ is satisfied corresponds to the analyzer's maximum energy resolution, $\Delta E_{\text{analyzer}}$, which is given by

$$\Delta E_{\text{analyzer}} = E_{\text{pass}} \left(\frac{w}{2R_0} \right). \quad (5.1.11)$$

A technical figure of merit for this type of analyzers is the resolving power, \mathcal{R} , defined as

$$\mathcal{R} \equiv \frac{E_{\text{pass}}}{\Delta E_{\text{analyzer}}}. \quad (5.1.12)$$

In the case of the VG Scienta's R8000, $R_0 = 200$ mm and $w_{\text{min}} = 0.05$ mm. Therefore, according to Eq. (5.1.11), the theoretical resolving power $\mathcal{R}_{\text{R8000}}$, is given by

$$\begin{aligned} \mathcal{R}_{\text{R8000}} &= \frac{2R_0}{w_{\text{min}}}, \\ &= 8000, \end{aligned}$$

and hence the name.

As I mentioned towards the end of in Sec. 5.1.2.2, there exists a case where electrons enter at a non-zero angle α relative to the tangent to a hemisphere; these electrons get focused on a plane which is rotated by 4α relative to the imaging plane (c.f. Fig. 5.1.3). This is a second-order de-focusing

effect, which results in a beam spot broadening characterized by an energy-independent shift of $2R_0\alpha^2$ towards the analyzer center. Incorporating this additional factor into the right hand side of Eq. (5.1.10), (5.1.11) can be rewritten as

$$\Delta E_{\text{analyzer}} = E_{\text{pass}} \left(\frac{w}{2R_0} + \alpha^2 \right). \quad (5.1.13)$$

The electron optics inside analyzers are typically designed such that $\alpha < 1^\circ$.⁴ For the extreme case of $\alpha = 1^\circ$ (17.5 mrad), this term can be ignored for resolving powers much less than $1/\alpha^2$ (≈ 3300). For example, for the last three rows of Table 5.1 ($\mathcal{R} \approx 1800$), Eq. (5.1.11) is a valid approximation.

5.1.3 Electrostatic lenses

All of the analyses in Sec. 5.1.2 considered electrons with energies close to the pass energy (E_{pass}) entering the analyzer region at a well-defined angle and location (e.g. slit). In a generic spectroscopic measurement, however, the beam of electrons being analyzed, from an unknown source, may not possess a kinetic energy distribution anywhere near E_{pass} . Moreover, the directionality of the electron source is unknown. For example, when analyzing photoemission from a solid, the generated photoelectrons form a diverging beam from an effective focal point on said solid's surface. Such a beam would have to be re-focused at the position of the analyzer's entrance. The electron-optical element which can achieve this task is an electromagnetic lens.

In electron optics, a wide variety of electrostatic and magnetic lens systems exist. In this section, I will limit the discussion to electrostatic lenses with a cylindrical symmetry. For example, the four-cylinder electrostatic lens in the R8000 analyzer is shown in Fig. 5.3.1. Based on the voltages applied to these cylinders, the lens can perform the following functions: (a) focus a non-directional electron beam onto the analyzer's entrance slit, and (b) change the average kinetic energy of beam's spectral distribution to the pass energy.

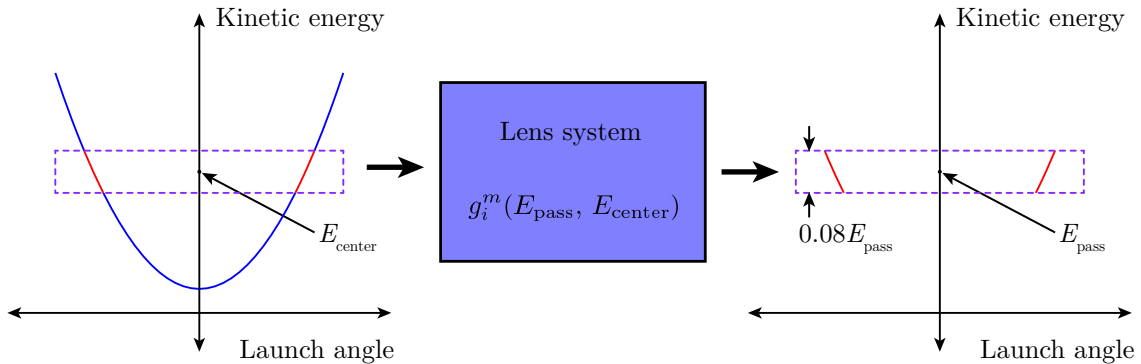


Figure 5.1.4: Schematic illustration of the functional behavior of the lens.

These two requirements can be better explained in terms of the example shown in Fig. 5.1.4. Consider the case where photoelectrons are generated from a parabolic band on the surface of a crystalline sample. In order to image a part of this band, which is highlighted in the dashed box, the center kinetic energy of said box, E_{center} , needs to be accelerated or decelerated to E_{pass} . The details of the lens inside the black box sets the height (i.e. energy width) of that box. For example, the lens system in the R8000 (c.f. Sec. 5.3.1) sets the box height to be 8% of E_{pass} . This percentage is in

⁴The manufacturer VG Scienta does not provide any estimates of α for the R8000. In fact, their manual uses the expression (5.1.11), and ignores α .

turn determined by the size of the detector; for the R8000 the detector has a 40 mm diameter (c.f. Sec. 5.3.4). The lens system can be characterized by a function $f(E_{\text{pass}}, E_{\text{center}})$ which is a discrete and continuous function of E_{pass} and E_{center} respectively. At a fixed pass energy, and hence a fixed energy resolution (c.f. Eq. (5.1.11)), the value of E_{center} can be swept electronically to recover the entire parabolic band. This is referred to as the swept mode of data collection (c.f. Sec. 5.3.3.2).

5.2 Technical challenges with charged particle optics

The electron optical aspects of the HDA discussed in Sec. 5.1 ignored some technical details that affect real analyzers. While an exhaustive survey of technical design details is outside the scope of this thesis, in this section I will discuss a small selection of topics which are relevant to high resolution ARPES. An understanding of these topics will be useful in appreciating some choices made in the design of both the R8000 HDA (c.f. Sec. 5.3) and its mating analysis chamber (c.f. Sec. 5.2.1 and Sec. 6.3.2.1).

5.2.1 Magnetic shielding

The electron optical devices I have discussed so far have been electrostatic. The reason for that is technical: generating and precisely controlling the voltages, which in turn generate the electric fields, is easier than magnetic fields. In real systems, however, the magnetic fields in the region of purely electrostatic electron detection are not zero. The major contribution to the magnetic background is from the earth's magnetic field (40-60 μT). Moreover, sources like magnetic materials (e.g. ferrous fasteners) in the vicinity of the experiment can increase the magnetic field background.

In an ARPES experiment, the photoelectrons experience a *practically* inestimable amount of Lorentz force from the magnetic field background. Inside the hemispherical analyzer, these unknown magnetic fields will deflect electrons from their original trajectories, resulting in an error in energy and momentum measurement. Fortunately, the effects of such parasitic Lorentz forces can be mitigated by adequate magnetic shielding.

Achieving shielding using the Meissner effect in a superconductor is prohibitive in terms of cost and complexity for an application like ARPES. Alternatively, the shielding provided by a high-magnetic-permeability material typically meets the requirements of an ARPES experiment. In this section, I will discuss the details of the latter.

The left of Fig. 5.2.1 shows an example of an infinite cylinder with an external magnetic field, B_{external} , perpendicular to said cylinder's axis. The cylinder is made out of a Nickel alloy, known as μ -metal, with a *relative* magnetic permeability, μ_r , in the range 10^3 - 10^5 . As a result, when the external magnetic field penetrates the cylinder, a large fraction of the total flux is confined to cylinder walls, with a very small leakage into the inner region. The reduced magnetic flux inside the cylinder corresponds to a field, B_{in} , much smaller than B_{external} . A figure of merit for a particular magnetic shield is defined as the shielding factor, S , given by

$$S \equiv \frac{B_{\text{external}}}{B_{\text{in}}}. \quad (5.2.1)$$

For this analysis, I will ignore the geometric details of the shield except its thickness. A more rigorous analysis can be found in [77]. On a qualitative level the shielding factor, S_{single} , is given by

$$S_{\text{single}} \propto \mu_r t, \quad (5.2.2)$$

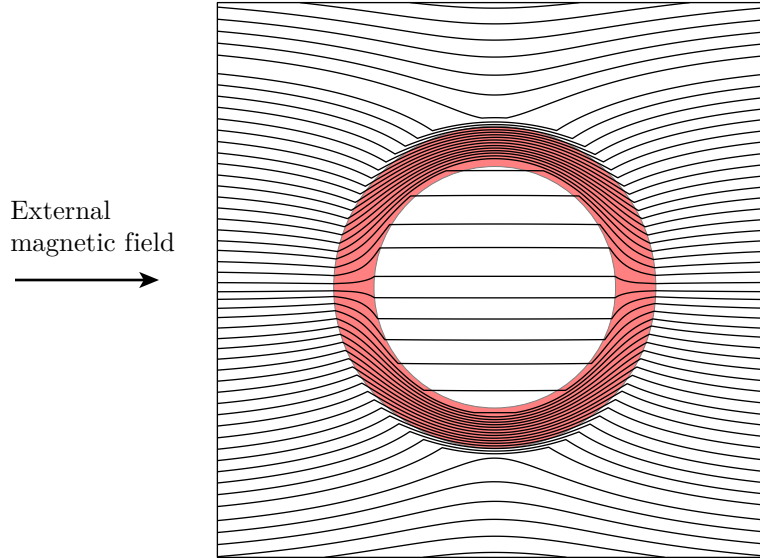


Figure 5.2.1: Magnetic shielding inside a μ -metal cylinder produced by concentration of the flux lines inside the red region with larger μ_r (10^3 - 10^5). The uncolored region has $\mu_r = 1$

where t is the thickness of the cylinder wall.

Now, if I consider two concentric cylinders, with thicknesses t_1 and t_2 , and permeabilities μ_1 and μ_2 , the overall shielding factor, S_{double} , is

$$S_{\text{double}} \propto \mu_{r1} t_1 \mu_{r2} t_2. \quad (5.2.3)$$

The advantage of this double-layer shielding configuration can be appreciated by estimating the shielding factor of a single cylinder with thickness $t_1 + t_2$. Using Eq. (5.2.2), the shielding factor would be proportional to $\mu_r(t_1 + t_2)$. For $\mu_{r1} \approx \mu_{r2}$ in Eq. (5.2.3), it is obvious that the shielding offered by two thin cylinders is greater than a single thick cylinder. Moreover, the former is more cost-effective.

The ARPES system discussed in this thesis uses the double-layer shielding approach. The R8000 analyzer and the custom analysis chamber have two 3 mm thick μ -metal layers. The design of the μ -metal shielding inside the analyzer is not provided by the manufacturer. Approximate geometries of the μ -metal shield inside the analysis chamber are shown in Fig. 5.2.2. Based on the co-ordinate system defined in the figure, the values for external and internal magnetic field at the origin (i.e. sample position) were (0.733, 7.992, -43.620) μT and (2, 7, -33) nT respectively.

5.2.2 Fringing fields

In Fig. 5.1.1, I assumed an abrupt transition in the electric field at the edge of the capacitor. All of the discussions of the HDA in Sec. 5.1.2 implicitly made this assumption as well. Unfortunately, this assumption is not valid in real systems. In a practical capacitor-style electrostatic device, the electric field lines curve at the edges, thus giving rise to “fringing fields.” In this section, I will discuss how fringing field effects can be mitigated such that the analysis presented in Sec. 5.1.2 is still valid.

One of the techniques which minimizes the effects of fringing fields uses the so-called Herzog plates [78]. The Herzog plates in the R8000 can be seen in Fig. 5.3.1. These plates are maintained at a

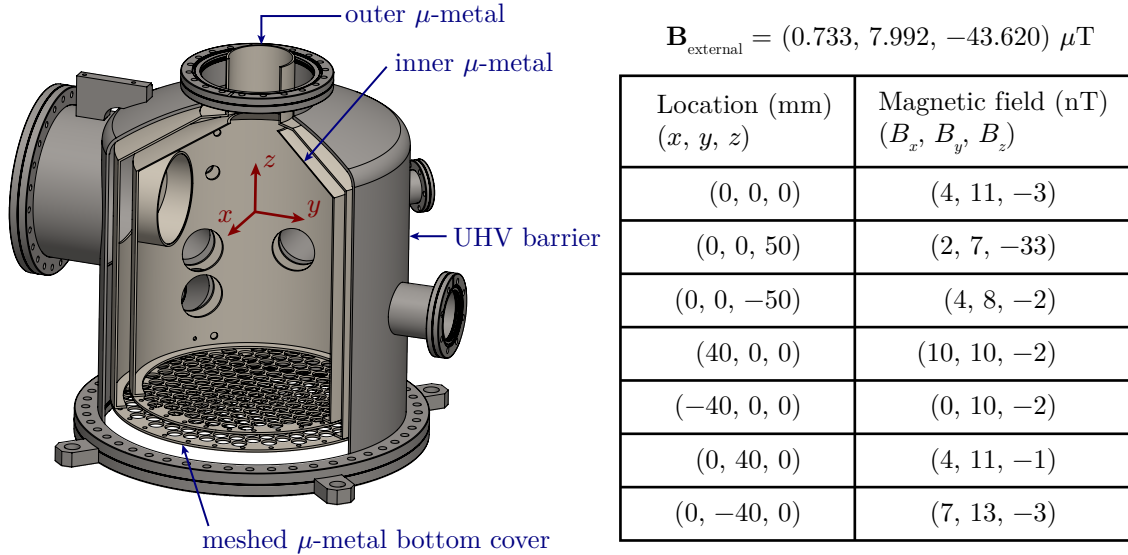


Figure 5.2.2: Section view of the double-layer μ -metal shielding inside the analysis chamber.

fixed potential, V_H , with a distance, d_H , from the HDA equator, and act as shunts for the HDA's fringing field. Moreover, an aperture of size w_H allows for electrons to enter the HDA with minimal distortion from the fringing fields. For a given R_1 and R_2 , the parameters w_H , d_H , and V_H can be tuned to reduce the fringing fields, depending on the specific requirements of a device. The most widely used values are $w_H = 0.5(R_2 - R_1)$ and $d_H \approx 0.2(R_2 - R_1)$ [79]; the optimal V_H depends on pass energy, E_{pass} .

The electrons entering the HDA, in the presence of a Herzog plate, are radially concentrated to a small region defined by the analyzer's slit of width w (c.f. 5.3.2). It is evident from the table in Fig. 5.3.3 that typically $w \ll R_2 - R_1$.⁵ Therefore, any residual fields, after field shunting from the Herzog plate, will deflect the electrons uniformly. Such deviations can be corrected using fringe field corrector electrodes (c.f. Fig. 5.3.1).

On the detector end, the microchannel plate (MCP) acts as the Herzog plate itself.⁶ Due to space constraints, additional fringe field corrector electrodes are not possible. Moreover, unlike the HDA entrance, the dispersion of electron trajectories in terms of angle and energy, on the detector end, does not allow simple fringe field corrector electrodes to correct the trajectories of electrons in *each* energy- and angle-resolved channel. But for the reasons I will explain below, no corrections on the detector end are necessary.

Consider 11 monochromatic beams with equally spaced kinetic energies, by ΔE_h , with the energies ranging from $E_{\text{pass}} - 5\Delta E_h$ to $E_{\text{pass}} + 5\Delta E_h$. Due to fringing fields, the deviation of these beams from the ideal trajectory, say ΔR_{fringe} , would be energy dependent

$$\Delta R_{\text{fringe}} \propto (|n| - 5) \Delta E_h^2, \quad (5.2.4)$$

where, in this example, $n = -5, -4, \dots, 5$. Fig. 5.2.3 shows this deviation by plotting the realistic trajectories (solid lines) next to ones with no fringing fields (dashed lines). As evident from Eq. (5.2.4), dependence of ΔR_{fringe} on the kinetic energy turns out to be quadratic. Serendipitously, the quadratic term in Eq. (5.1.7) cancels the fringe-field-induced quadratic shift.

⁵For the R8000, $R_2 - R_1 = 80$ mm

⁶Note that potential of this Herzog plate, in general, would be different from the primary Herzog plate shown in Fig. 5.3.1. However, in cases like the R8000 discussed here, a field termination mesh is used in front of the MCP.

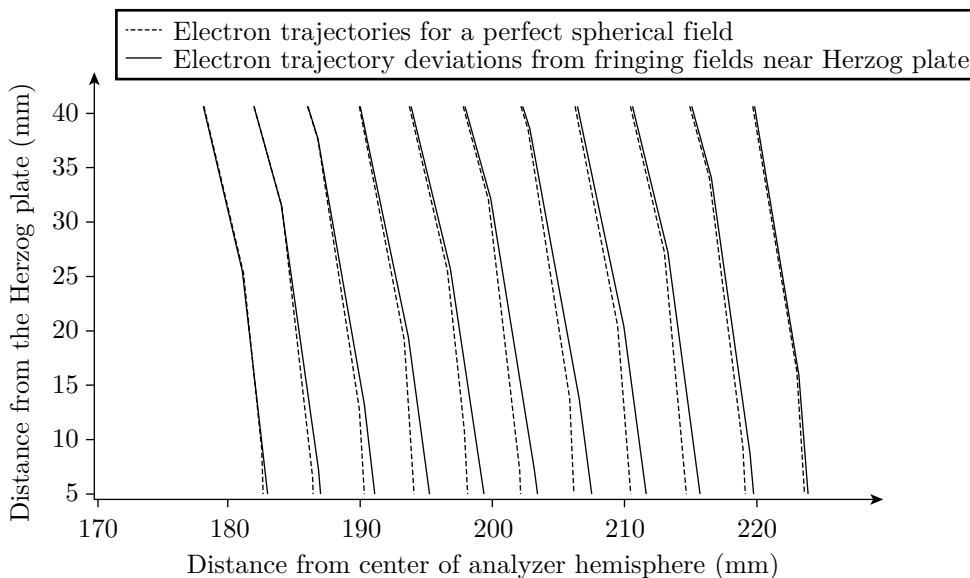


Figure 5.2.3: The fringing fields at the edge of the HDA and electron trajectories in the presence of a Herzog plate. Reprinted from *Nucl. Instrum. Meth. A* **601**, 182-194, Wannberg, Copyright (2009), with permission from Elsevier. [80].

5.2.3 Grounding and work function

An ARPES experiment can be viewed as an electrical circuit where charge current flows from the analyzer to the sample.⁷ In order to avoid a build up of charge on either, a third circuit component is required: an (ideally) infinite charge reservoir or ground. Improper grounding can result in ground loops which, for example, can induce effectively random time-dependent Fermi level oscillations in the analyzer and sample. This acts as another noise source in the measurement. Naturally, the demands on grounding quality increase with the experiments demanding higher energy resolution.

Achieving proper grounding in an ARPES system typically involves heuristically connecting different external metallic surfaces of the vacuum system with a good conductor (e.g. copper braid) to short out any potential ground loops. For the ARPES system discussed in this thesis, the grounding provided by the aluminum support frame appeared to suffice. In other words, making additional connections between different components via copper braids did not improve the energy resolution.

The work function of the surfaces in proximity of the electron trajectories has a significant impact on said trajectories. Work function mismatch between two dissimilar surfaces can lead to an electric field between said surfaces. I'll illustrate this phenomenon with an example.

Consider a model where two perfect metals⁸ placed in perfect vacuum are separated from each other by a small distance. The sketch in Fig. 5.2.4 is a representation of this scenario. The “vacuum” level corresponds to a continuum of states where the electron is not bound to the metal.

When the two metals are completely isolated from one another the vacuum levels will be aligned. Now, consider the two metals by a zero resistance wire. In this case, the Fermi levels of two metals will align after some charge transfer across the wire. As a result, the vacuum levels are no longer aligned. A slightly more rigorous analysis will show that the difference in the vacuum levels creates

⁷I'm using a conventional definition of current whose direction is opposite to that of the flow of electrons.

⁸For ARPES, insulators are kept away from the measurement area.

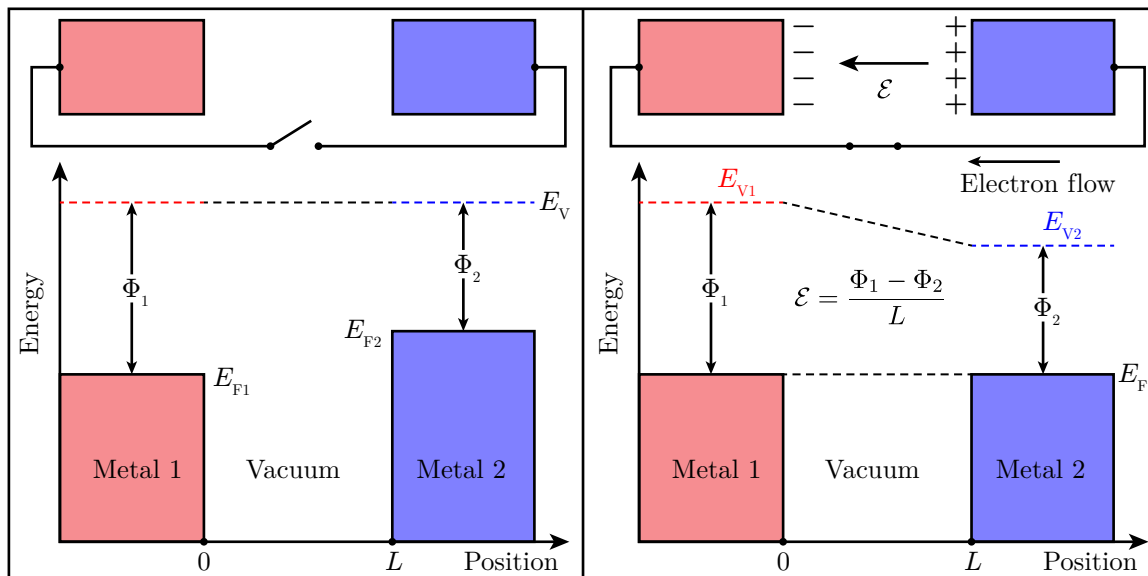


Figure 5.2.4: Electric potential difference between metals with dissimilar work functions after their Fermi levels align.

a potential gradient corresponding to an electric field. The only situation in which the potential gradient is zero is when the work function of the two metals is identical.

In an ARPES system, well-grounded dissimilar metals will have an electric field between their surfaces. Imperfections on the metal surfaces (e.g. machining tracks, scratches, etc.) will give rise to an effectively random electric field. Photoelectrons which experience this random field will experience scattering events that will lead to a loss in the energy-momentum information they are carrying.

These issues can be mitigated by *proper*⁹ coating metallic surfaces with colloidal graphite prepared with a proprietary recipe [81].

5.3 Properties of the R8000 electron analyzer

After a brief overview of the principles of electron optics in Sec. 5.1, I will now discuss the specific details of the R8000 electron analyzer from VG Scienta. The model label “R8000” indicates a maximum resolving power of 8000.

5.3.1 Lens system

In Sec. 5.1.3 I introduced the cylindrical electrostatic lens and discussed its operating principle. Moreover, in Fig. 5.1.4, I treated the lens as a black box and defined it only in terms of its inputs and outputs. In this section, I will provide a specific example of lens system in the R8000.

As shown in Fig. 5.3.2, the R8000’s lens system consists of 4 concentric cylinders. Following the nomenclature defined by the R8000 manual, each cylinder is referred to as a lens, with the following

⁹Preferably in a clean room.

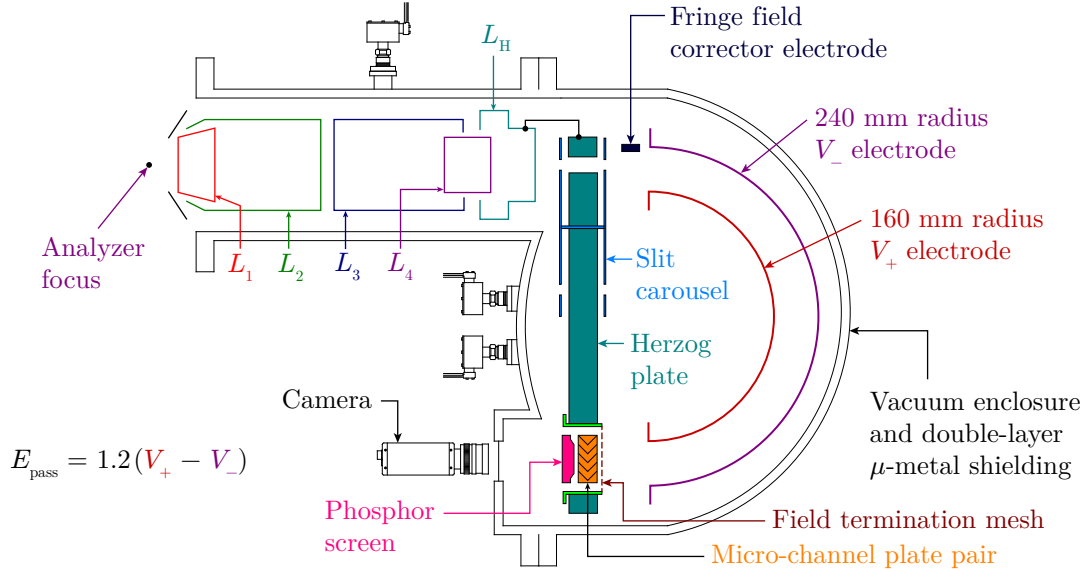


Figure 5.3.1: Top view of the analyzer with the most important internal components.

labels: L_1 , L_2 , L_3 , and L_4 . These four cylinders are applied a voltage given by the functions $g_i^m(E_{\text{pass}}, E_{\text{center}})$ with the index i ($i = 1, 2, 3, 4$) corresponding to the cylinders. These functions are similar to the function $f(E_{\text{pass}}, E_{\text{center}})$ I defined in Sec. 5.1.3. The index “ m ” corresponds to the mode of operation. The functions $g_i^m(E_{\text{pass}}, E_{\text{center}})$ are encoded in so-called *lens tables* provided by the manufacturer after factory calibration.

The R8000 lens system can operate in many different modes, all of which can be categorized into two types: transmission and angular. The former acts like an energy-resolved microscope. In other words, using the transmission mode, one can image the sample in real space. Since the transmission mode *typically* gives higher electron counts, it is often used to fine tune the sample position, such that the sample surface coincides with the focus of the lens system. For the ARPES system discussed in this thesis, however, the transmission mode was not used for sample alignment. Due to the hysteresis in the cryostat’s manipulators (c.f. Sec. 7.5.4), the angular mode was more useful, practically, in aligning the sample with respect to the lens.

The angular mode is most commonly used for ARPES data collection. In this mode, the lens re-focuses photoelectrons emitted by the sample surface, with a specific launch angle, onto a specific point along the slit length. This is illustrated in Fig. 5.3.2 where the different colors correspond to different launch angles. The lens tables are calibrated such that the position of the re-focused photoelectrons along the slit length varies linearly with its launch angle. The calibration can be done, for example, by using a wire-slit device (c.f. Sec. 5.4.2).

5.3.2 Slits

Based on the imaging properties of the HDA discussed in Sec. 5.1.2.2 the slit is *effectively* imaged onto the detector with a negative magnification. Moreover, recall that because the electrons entering the analyzer on and tangential to a sphere of radius $R_0 + \Delta R_{\text{entrance}}$ get imaged on the detector at a distance of $R_0 - \Delta R_{\text{entrance}}$ from the center of the HDA, a straight object forms a curved image with radius $R_0/2$ and vice-versa. Both these imaging properties are illustrated in Fig. 5.3.3. The three arcs correspond to angle-resolved slices of the spectrum taken at three different kinetic energies.

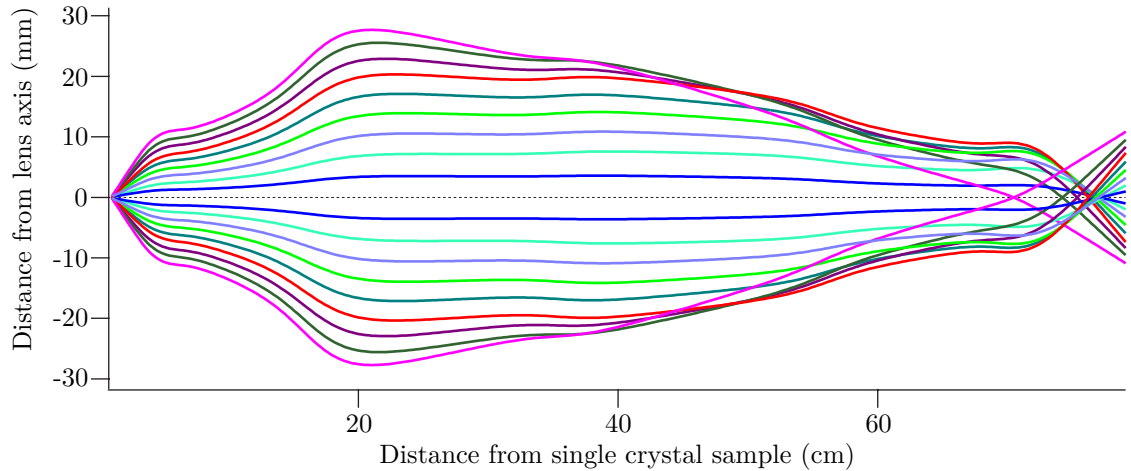


Figure 5.3.2: Electron trajectories inside the lens operating in the angular mode. Reprinted from *Nucl. Instrum. Meth. A* **601**, 182-194, Wannberg, Copyright (2009), with permission from Elsevier. [80].

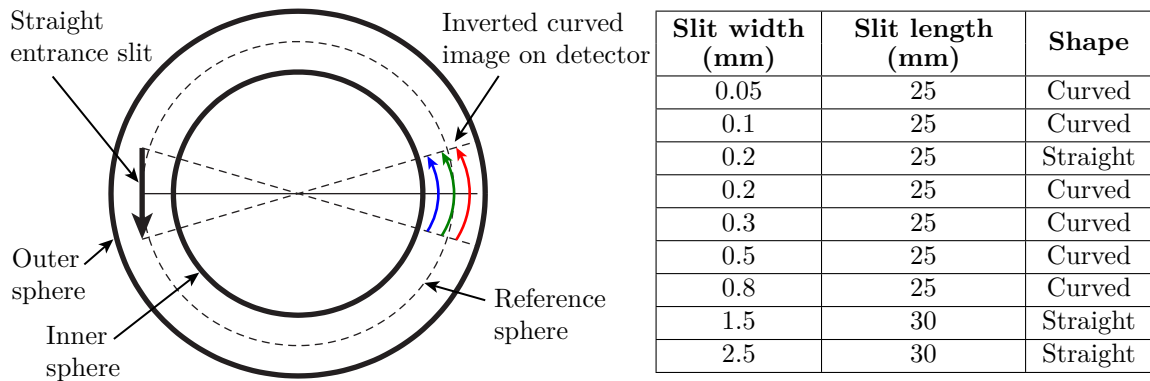


Figure 5.3.3: Left: analyzer viewed along lens axis. Right: shape and dimensions of the slits in the R8000.

In order to avoid the inconvenience of image post-processing, most HDAs make the slits curved. In the R8000, slits of different shape and dimensions are shown in a table in Fig. 5.3.3. The plates with these slits are mounted on a carousel which can be rotated using a mechanical feedthrough. This feature allows in situ switching of the slits in the R8000. Typically a larger slit is used for sample alignment due to the larger number of electron counts. Once the sample is satisfactorily aligned, the instrument operator can switch to a narrower slit for better energy resolution (c.f. Eq. (5.1.10)), and average for longer to compensate for lower electrons counts.

5.3.3 Analyzer

A top view of the analyzer region of the R8000 is shown in Fig. 5.3.1. The radii of the inner (R_{inner}) and outer (R_{outer}) electrodes are 160 mm and 240 mm respectively and the radius of the reference hemisphere (R_0) is 200 mm. As discussed in Sec. 5.2.2, a Herzog plate is used to minimize fringing fields. The electrode just outside the analyzer entrance, labeled “FO,” is used to correct for residual effects of the fringing fields on the electrons’ trajectories.

The selected pass energy determines the potentials on the inner and outer spheres (c.f. Eq. (5.1.6)). The potentials of the Herzog plates and FO are changed accordingly. For example, for a pass energy of 1 eV, the potentials on the inner sphere, outer sphere, Herzog plate, and FO relative to the analyzer ground are -1.0143 V, -1.813 V, -0.6813 V, and -0.7643 V respectively.

The analyzer can be used for data collection in two modes: fixed and swept. I will discuss the features of each mode in the next two sections.

5.3.3.1 Fixed mode

In the fixed mode, the spectrum is recorded in a single shot for a pre-defined kinetic energy window. Fig. 5.3.4 shows the spectrum of a Bi_2Se_3 single crystal measured in the fixed mode with pass energy 5 eV. As I mentioned earlier, the hysteresis in the cryostat's manipulators (c.f. Sec. 7.5.4.1) make it more convenient to align the sample in the fixed mode. One of the drawbacks of the fixed mode, however, is its limited energy range. As schematically shown in Fig. 5.1.4, the lens only allows transmission of electrons, with kinetic energies in a fixed window, from the sample to the analyzer. The height of said window is typically a fraction of the pass energy.

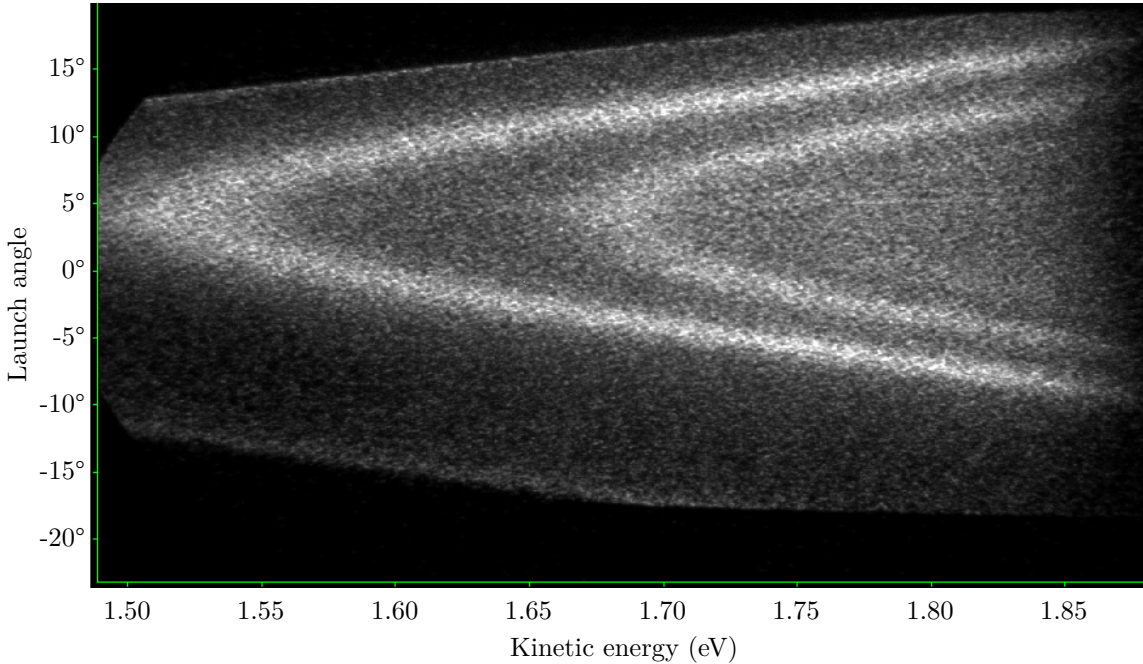


Figure 5.3.4: Fixed mode scan of a Bi_2Se_3 single crystal taken at a 5 eV pass energy.

In the case of the R8000, the diameter, d_{active} , of the active area of the detector is 32 mm (c.f. Sec. 5.3.4). Using Eq. (5.1.7) to first order, the energy range, E_{range} , covered by the detector in a single shot can be computed as

$$\begin{aligned} d_{\text{active}} &= 2R_0 \left(\frac{E_{\text{range}}}{E_{\text{pass}}} \right), \\ E_{\text{range}} &= 0.08E_{\text{pass}}. \end{aligned} \quad (5.3.1)$$

For example, the fixed mode scan shown in Fig. 5.3.4 covers kinetic energies in the range 1.50-1.90 eV¹⁰ which is 8% of the pass energy of 5 eV. Fortunately for Bi_2Se_3 , sufficient band structure

¹⁰The 1.90 eV clipped due to space constraints of the plot.

information exists in this range to align the sample. For other samples, the energy window can be extended by increasing the pass energy (c.f. Eq. (5.3.1)).

5.3.3.2 Swept mode

As I discussed in the previous section, sample alignment is easier when using the fixed mode with a large pass energy. However, fast and high resolution data collection requires extending E_{range} while keeping the E_{pass} small (c.f. Eq. (5.3.1)). These two conflicting requirements can be met with a swept mode scan.

In the swept mode, the lens sweeps the window shown in Fig. 5.3.4 along the energy axis for a given pass energy. The swept mode counterpart of the scan shown in Fig. 5.3.4 can be found in Fig. 8.4.2.

5.3.4 Detector

As I illustrated in Sec. 5.1.2, the electrons exiting the analyzer form a 2D image. Images like the one shown in Fig. 5.3.4 need to be discretized into a 2D numeric array for further analysis. The R8000 converts the 2D image, formed by a dispersed free-space electron beam, into an optical image which can be recorded (i.e. pixelated) using a CCD camera. Fig. 5.3.1 shows the layout of the detector assembly used in the R8000. It consists of a stack of the following elements:

1. **Phosphor screen:** this is a cathodoluminescent material which converts electrons to photons; the latter can be imaged by the CCD camera. However, the quantum efficiency of the phosphor screen is too low to perform this electron-to-photon conversion using the electrons directly exiting the analyzer. Therefore an intermediate amplification step is provided by the MCP.
2. **Microchannel plate (MCP):** the R8000 detector assembly consists of a pair of MCPs arranged in the chevron configuration. One electron exiting the analyzer generates an avalanche effect in the MCP pair resulting in the production of 10^6 electrons.
3. **Field termination mesh:** the field termination mesh allows a homogeneous termination of the analyzer field. It is at the same potential as the Herzog plate used for minimizing fringing fields.

5.4 R8000 measurement performance

5.4.1 Energy resolution

In Sec. 5.1.2.3, I showed the theoretical energy resolution to be

$$\Delta E_{\text{theory}} \approx E_{\text{pass}} \frac{w}{2R_0}. \quad (5.4.1)$$

Factory tests were performed on the R8000 ($R_0 = 200$ mm) at VG Scienta to benchmark the energy resolution at different pass energies (E_{pass}). A light source with photon energy corresponding to Helium I α line ($\hbar\omega = 21.218$ eV) was used to generate photoelectrons in a dilute gas of Xenon atoms (>90% purity) confined to a 0.8 mm diameter capillary placed in a test chamber with adequate vacuum and magnetic shielding. The R8000 was used to measure the linewidth (FWHM) of the

energy distribution curve (EDC) of the $5p_{3/2}$ state with a binding energy, E_B , of 12.130 eV. The average kinetic energy of the electron spectrum is

$$\begin{aligned} E_{\text{kinetic}} &= \hbar\omega - E_B, \\ &= 9.088 \text{ eV}. \end{aligned} \quad (5.4.2)$$

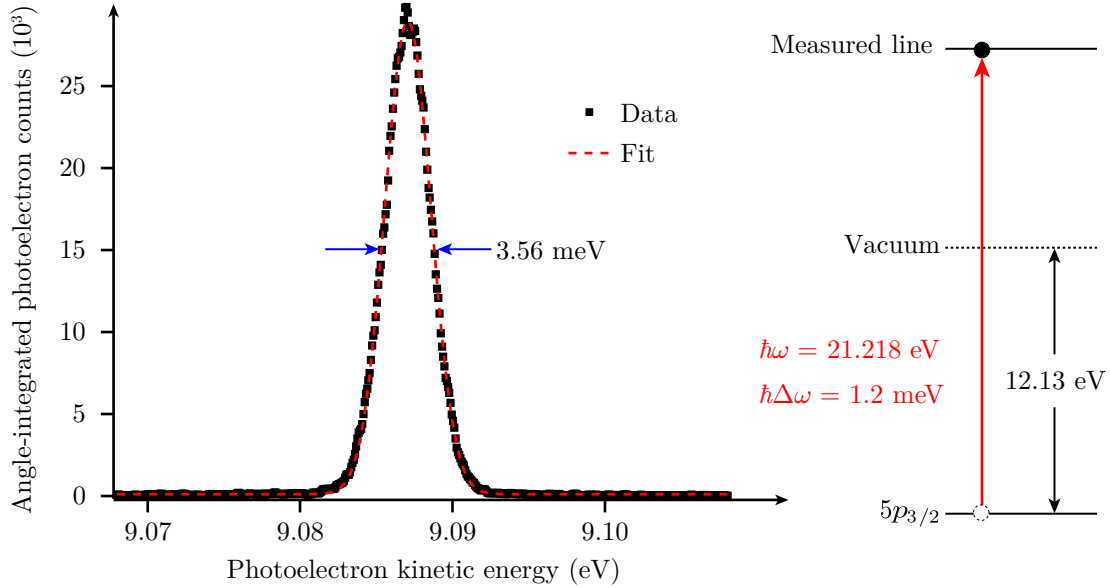


Figure 5.4.1: The energy distribution curve measured from Xe $5p_{3/2}$ state at 293 K.

In Fig. 5.4.1, the EDC measured at $E_{\text{pass}} = 1 \text{ eV}$ was fitted to a sech^2 curve with FWHM of 3.56 meV. Then the intrinsic energy resolution of the analyzer $\Delta E_{\text{intrinsic}}$, as a function of E_{pass} , can be computed using the formula

$$\Delta E_{\text{intrinsic}}(E_{\text{pass}}) = \sqrt{\Delta E_{\text{measured}}^2(E_{\text{pass}}) - \Delta E_{\text{Doppler}}^2 - \Delta E_{\text{photon}}^2}, \quad (5.4.3)$$

where ΔE_{photon} ($\hbar\Delta\omega = 1.2 \text{ meV}$) is the linewidth of the Helium discharge lamp and $\Delta E_{\text{Doppler}}$ (meV) is the Doppler broadening of the electron transition from the $5p_{3/2}$ state of Xenon in the gas phase, given by [82]

$$\Delta E_{\text{Doppler}} = 0.722 \left(\frac{E_{\text{kinetic}} T}{M_{\text{Xe}}} \right)^{1/2}, \quad (5.4.4)$$

where E_{kinetic} is the average kinetic energy (eV) of the photoelectrons (c.f. Eq. (5.4.2)), T is the temperature (Kelvin), and M_{Xe} is the mass of the Xenon atom (atomic mass units). At room temperature $\Delta E_{\text{Doppler}} = 3.25 \text{ meV}$.

The measurement shown in Fig. 5.4.1 was repeated for pass energies between 1-10 eV. Using a curved slit ($w = 0.2 \text{ mm}$), Eq. (5.4.1) and (5.4.3) the theoretical and measured intrinsic energy resolutions are compared in Table 5.1.

5.4.2 Momentum resolution

The apparatus used to measure the momentum resolution of the R8000 is schematically shown in Fig. 5.4.2. A “wire-and-slit device” is placed in front of the analyzer. The 0.05 mm diameter and

| Pass energy (E_{pass}) | Measured resolution ($\Delta E_{\text{intrinsic}}$) | Theoretical resolution (ΔE_{theory}) |
|-----------------------------------|---|---|
| 1 eV | 0.8 meV | 0.5 meV |
| 2 eV | 1.1 meV | 1 meV |
| 5 eV | 2.4 meV | 2.5 meV |
| 10 eV | 5.4 meV | 5 meV |

Table 5.1: Table comparing the measured intrinsic ($E_{\text{intrinsic}}$) and theoretical (ΔE_{theory}) energy resolution as a function of pass energy (E_{pass}).

25 mm long wire is perpendicular to the analyzer slit and intersects the analyzer focus. The plate in front of the wire has a periodic array of slits. Two consecutive slits subtend an angle 2.5° on the wire.

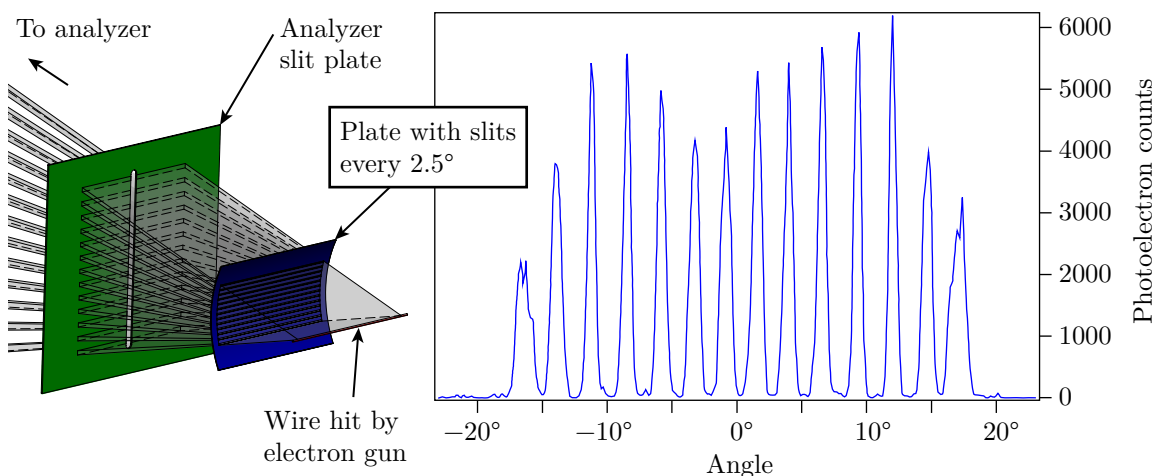


Figure 5.4.2: Left: the geometry and orientation, with respect to the analyzer slit, of the wire-and-slit device. Right: energy-integrated angle-resolved spectrum measured from wire-and-slit device.

An electron gun is used to excite the wire such that it produces secondary electrons. Once these secondary electrons pass through the equally-spaced slits, they have a well-defined angular separation between them, before they enter the analyzer slit. Operating the R8000 in all of the available angular lens mode, an energy-integrated angle-resolved spectrum measurement was recorded (c.f. Fig. 5.4.2). The kinetic energies that were integrated over ranged from 5-35 eV. The FWHM for all lines was less than 1° ; this met the factory test standards.

Chapter 6

Vacuum system design

6.1 Introduction to vacuum systems

6.1.1 Need for vacuum

Like most experimental methods, vacuum is an essential component of angle-resolved photoelectron spectroscopy. In particular, said spectroscopy needs to be performed under vacuum for two main reasons: (a) maintaining a pristine sample surface, and (b) ballistic photoelectron propagation. These two factors are discussed in detail in the following sections (Sec. 6.1.1.1 and 6.1.1.2).

6.1.1.1 Maintaining a pristine sample surface

The surface of the sample being measured using angle-resolved photoelectron spectroscopy must be free of contaminants. In order to ensure the measured photoelectron spectrum corresponds to the sample being studied, adsorption of foreign atoms and molecules must be kept to a minimum. Two examples of sources of foreign atoms are: (a) physical contact from sample handling, and (b) gaseous atoms and molecules in the atmosphere. While the former depends on sample preparation techniques,¹ the latter can be mitigated by placing the sample under ultrahigh vacuum.

The importance of low pressure, P ,² is evident from the degree of sample surface contamination, $n_{\text{contaminant}}(t)$, measured in number of adsorbed atoms per cm^2 , from ambient gas molecules in the vacuum chamber [83]

$$n_{\text{contaminant}}(t) = 2.63 \times 10^{22} \sum_{i=1}^{N_{\text{species}}} s_i \cdot t \cdot \frac{P_i}{\sqrt{M_i T}}, \quad (6.1.1)$$

where the index $i \in [1, N_{\text{species}}]$ labels the gas specie, $s_i \in [0, 1]$ is the sticking coefficient, t is the exposure time (seconds), P_i is the partial pressure (millibar), M_i is the molecular mass (grams/mole), and T is the temperature (Kelvin). The probability with which an atom or molecule impinging on a surface of interest sticks to said surface is obviously defined as the sticking coefficient for the respective atomic molecular specie. Moreover, $t = 0$ can be defined at the moment the sample is cleaved.

¹Two examples of sample preparation are in situ: (a) growth, (b) cleaving (c.f. Sec. 6.3.7).

²Total pressure $P = \sum_{i=1}^{N_{\text{species}}} P_i$.

The most important implication of Eq. (6.1.1) is that for large enough (say) $t = t_{\max}$, the sample surface will be covered by such a large density of residual gas molecules that the ARPES data will be overwhelmed by the properties of the gas molecules adsorbed onto the sample, and not the sample itself. Some empirical estimates from realistic ARPES system³ suggest at a low 10^{-10} torr level total pressure t_{\max} can be of the order of a few hours.

6.1.1.2 Ballistic photoelectron propagation

Photoelectrons typically travel a distance of a few meters from the sample to the detector. During this time, if the electrons undergo a sufficient number of collisions with residual gas atoms/molecules, they might not reach the detector at all. The statistically average distance an electron travels before it collides with the first atom/molecule is defined as the *mean free path*. The mean free path is inversely proportional to the pressure in the chamber. Therefore, it is important to have the pressure in the chamber be low enough such that the mean free path is larger than their total travel distance; this is referred to as ballistic propagation. Ballistic propagation in typical ARPES apparatuses occurs at pressures better than 10^{-5} - 10^{-6} torr.

6.1.2 Modeling a vacuum system

Theoretical modeling of vacuum systems often informs decisions in designing said system. The simplified analytical model presented here is intended to capture the essence of advanced techniques like Monte-Carlo simulations.

6.1.2.1 Base pressure

As evident from Sec. 6.1.1, the quantity of most interest in any vacuum system is the base pressure P_{base} (torr). The base pressure in a vacuum system is reached when the rate of pumping gas, Q_{pump} , is equal to the *intrinsic*⁴ gas load, Q_{gas} (both in torr×liters/second). At any time during the pump down, Q_{pump} is defined in terms of the instantaneous pressure, P (torr), and the pumping speed, S_{pump} (liters/second), as

$$Q_{\text{pump}}(t) = P(t) \cdot S_{\text{pump}}(P(t)), \quad (6.1.2)$$

where all three quantities are expressed as explicit functions of time (t). It is obvious from Eq. (6.1.2) that $Q_{\text{pump}}(t)$ will monotonically decrease as a function of t due to the fact that $P(t)$ exhibits the same behavior. However, the behavior of $S_{\text{pump}}(P(t))$ is non-trivial; for most practical pumps $S_{\text{pump}}(P(t))$ is, in general, a non-monotonically decreasing explicit function of $P(t)$. For large enough t , when $Q_{\text{pump}}(t) = Q_{\text{gas}}$, the following holds

$$P_{\text{base}} = \frac{Q_{\text{gas}}}{S_{\text{base}}}, \quad (6.1.3)$$

where $S_{\text{base}} \equiv S_{\text{pump}}(P_{\text{base}})$. It is worth noting that P_{base} does not depend on the volume of the vacuum chamber. The reason for this will become clear in Sec. 6.1.2.2.

³For (say) Bi₂Se₃, which was the most measured material in this thesis work, $s_i \approx 10^{-2}$ according to [83].

⁴In this case, intrinsic gas load is defined as coming from outgassing, leaks, and intentional introduction of atoms/molecules are part of a UHV process (e.g. MBE).

6.1.2.2 Molecular conductance

In Sec. 6.1.2.1, I implicitly assumed the quantities, Q_{gas} , $Q_{\text{pump}}(t)$, $P(t)$, and $S_{\text{pump}}(t)$,⁵ are homogeneous. While modeling inhomogeneities are typically limited to Monte-Carlo-based analyses, some insight can be gained at the analytical level by introducing the notion of conductance in a “plumbing circuit.” In this analogy, $P(t)$ and $Q_{\text{pump}}(t)$ would *loosely* correspond to voltage and current respectively. To illustrate this analogy, consider a cylindrical tube with length L and diameter D . Assuming the system is at steady state, none of the quantities will have time dependence. The pressure at the two ends of the tube is P_1 and P_2 ($P_1 > P_2$); they will correspond to the pressure in a vacuum chamber and at the pump respectively. Then, using a lumped circuit model, I have

$$Q_{\text{pump}} \equiv C(P_1 - P_2), \quad (6.1.4)$$

$$C = \frac{1}{6} \left(\frac{2\pi k_{\text{B}} T}{M} \right)^{1/2} \frac{D^3}{L}, \quad (6.1.5)$$

where C is defined as the conductance of the tube, M is the average molecular mass, T is the temperature, and k_{B} is Boltzmann’s constant. Quite often, it is more important to analyze pressure dynamics inside the vacuum chamber, and tube is of little interest. In that case, the effect of the pressure gradient across the tube can be ignored by introducing an effective pumping speed

$$S_{\text{eff}} = \left(\frac{1}{C} + \frac{1}{S_{\text{pump}}} \right)^{-1}. \quad (6.1.6)$$

For any finite C (i.e. non-infinite), S_{eff} will be less than S_{pump} . Moreover, S_{eff} will get smaller as C reduces. According to Eq. (6.1.3), the base pressure will suffer if the conductance is poorly chosen.

6.1.2.3 Pump down

Using the model discussed above, and assuming $S_{\text{eff}} \approx \text{constant}$, the drop in the pressure inside a vacuum chamber, $P(t)$, is given by

$$P(t) = \frac{Q_{\text{gas}}}{S_{\text{eff}}} - \left(\frac{Q_{\text{gas}}}{S_{\text{eff}}} - P(0) \right) \exp\left(-\frac{S_{\text{eff}}}{V}t\right), \quad (6.1.7)$$

where V is the volume of the chamber. For $t \rightarrow \infty$, the exponential term vanishes, and the base is reached

$$\begin{aligned} \lim_{t \rightarrow \infty} P(t) &\equiv P_{\text{base}}, \\ &= \frac{Q_{\text{gas}}}{S_{\text{eff}}}, \end{aligned} \quad (6.1.8)$$

which is consistent with Eq. (6.1.3). It is worth noting that P_{base} does not depend on the volume of the container.⁶ The volume only affects the rate at which the pressure drops. Achieving lower pressures requires minimizing Q_{gas} (c.f. Sec. 6.2.1) and increasing S_{eff} (c.f. 6.2.3).

In a typical pump down from atmosphere to UHV, most of the assumptions made in Eq. (6.1.7) are invalid, since pumping mechanisms and speed change (c.f. Sec. 6.2.3.1) as the system goes through different pressure regimes (atmosphere \rightarrow rough \rightarrow high \rightarrow ultrahigh). Nonetheless, Eq. (6.1.7) highlights the importance of S_{eff} in recovery time.

⁵I will refrain from using the full expression $S_{\text{pump}}(P(t))$ as far as the circuit analogy is concerned.

⁶In practice, larger chamber volume means larger surface area. So P_{base} *indirectly* depends on volume since Q_{gas} will increase with the surface area.

In modern UHV systems, in-vacuum motion is commonplace. For example, when a transfer arm (c.f. Sec. 6.3.6.1) moves, there is a spike in the pressure due to friction between the shaft and the bushing. Moreover, when moving samples from a lower (e.g. load lock) to higher (e.g. preparation chamber) vacuum region, the pressure in the latter can be up to an order of magnitude higher than its base pressure, even when the two are isolated following the sample transfer. Typically, one has to wait for the original base pressure to recover before resuming normal operations. This recovery time can be greatly reduced with a large S_{eff} .

6.1.3 Pressure measurement

6.1.3.1 Total pressure

Total pressure measurement is the most common type in any vacuum system. The range of pressure measurement determines the type of pressure gauge required. The ARPES system discussed in this thesis has two types of gauges on the analysis (c.f. Sec. 6.3.2.1) and preparation (c.f. Sec. 6.3.2.3) chamber each: (a) Pirani and (b) ion gauge.

The use of a Pirani gauge is commonplace for measuring pressures from atmosphere (760 torr) to 10^{-4} torr. The Pirani gauge infers pressure based on the heat lost by a heated filament to the gas left in the vacuum chamber. Since the heat transferred to gases at pressures below 10^{-4} torr is too low to measure with commercial electronics, a different technology is needed for lower pressures.

The Bayard-Alpert gauge starts working close to where the Pirani stops and goes all the way down to 10^{-11} torr. The Bayard-Alpert gauge infers pressure by measuring the conductance of ionized gas molecules it generates from collisions with the electrons emitted by the gauge's hot filament. At lower pressures, the ionization probability reduces due to the reduced gas density. Close to 10^{-11} , the ionic current becomes too low for the ion gauge controller's electronics to measure accurately. The Bayard-Alpert gauge is also commonly known as the ionization or ion gauge.

6.1.3.2 Partial pressure

Partial pressure measurement is common to vacuum systems designed for processes involving intentional introduction of gas loads (e.g. molecular beam epitaxy). Nevertheless, in other vacuum systems, it also serves as a valuable diagnostic tool for (say) detecting leaks (c.f. Sec. 6.5.1) or contamination. A partial pressure measurement can, in principle, be used for total pressure measurement by adding up the former of the dominant gas species in the vacuum system.

6.2 Ultrahigh vacuum design guidelines

6.2.1 Outgassing management

Once a vacuum system reaches its base pressure, the primary contributions to Q_{gas} is the “outgassing” of materials inside vacuum. Outgassing is the phenomenon of solids releasing gases which were once dissolved in said solids or adsorbed onto their surfaces. Outgassing also includes sublimation of the solid itself. On relatively short time scales (\approx months), outgassing dominates over gas loads from diffusion through the atmosphere-UHV barriers such as the walls of the vacuum chamber, glass windows, and copper gaskets. Therefore, the choices of materials in a UHV system are limited. It's worth noting that discussion of UHV in the document will preclude discussions of intentional gas loads from sources like (say) gold evaporators or molecular beam epitaxy.

6.2.1.1 Metals

On average, metals have lower outgassing rates than non-metals. Therefore in-vacuum components should be metallic whenever possible to achieve low base pressures. For example, gate valves (c.f. Sec. 6.3.4.1) either have a viton or metal gate seal.⁷ Only the latter can work down to extreme high vacuum ($< 10^{-12}$ torr).

Furthermore, since metals can withstand higher temperature bake-outs (c.f. Sec. 6.4.3), achieving UHV is easier.

Some of the most commonly used in-vacuum metal components are made of oxygen-free high conductivity (OFHC) copper, Aluminum, Titanium, Tantalum, stainless Steel, Molybdenum, Indium, Tungsten, Gold, and Silver.

6.2.1.2 Non-metals

Most vacuum systems have at least one component which is required to be electrically insulating. For example, the cathode and anode in an ion pump (c.f. Sec. 6.3.3.2) are maintained at a potential difference of several thousand volts. Hence they need ceramic standoffs for electrical isolation. In such cases, the higher outgassing rates of non-metals can be mitigated by higher pumping speeds or special surface treatments.

While some non-metals are a necessity, others (like Kapton) are chosen for convenience or cost reasons. Moreover, non-metallic components are rated for lower temperatures than their metallic counterparts, thus requiring longer bake-outs. It is often up to the vacuum system designer to weigh the operational benefits of non-metallic components against its performance disadvantages.

Some of the most commonly used in-vacuum non-metal components are made of polyether ether ketone (PEEK), Viton, Kapton, TeflonTM, ceramics, resin-based epoxies, and silicone-backed adhesive tapes.

6.2.2 Surface properties

In addition to the choice of appropriate UHV-compatible materials, their fabrication and handling also has an impact on vacuum properties. In this section, I will discuss some of the most common surface treatment methods used for machined and/or welded vacuum components.

6.2.2.1 Machined components

For a machined part, it is preferable to remove material from all sides of the stock material to eliminate the ambiguity of the latter's surface quality. Sanding and mechanical polishing the part after machining should be avoided. For the latter, the polishing compound used to fill surface pits is usually not UHV compatible. Sanding can, however, be performed with the appropriate abrasive (e.g. Silicon Carbide).

After machining, the parts need to be cleaned using sonication. First, they have to be degreased (e.g. using Micro 90) to remove cutting fluids and oil from machining. Second, they should undergo the standard acetone sonication to remove any organic residue. The third, and final, step involves rinsing the part with isopropanol or methanol, immediately after the part's removal from the acetone bath, before the top film of acetone can dry off. Use of sonication with either alcohol, for thorough rinsing, is optional.

⁷The bonnet for both is assumed to be metal-sealed.

6.2.2.2 Welded joints

The most commonly welded vacuum components are made of stainless Steel and Aluminum. For the latter, the weld beads are relatively clean, and cleaning steps similar to the machined parts can be employed. For the former, the weld beads exist in a highly oxidized state; they are typically cleaned using acidic chemical passivation or electropolishing.

6.2.2.3 Electropolishing

Electropolishing is an electrochemical process which is the opposite of electroplating. During electropolishing, the highest points of a rough surface are removed. Vacuum chambers are electropolished to reduce the effective area of their surfaces exposed to vacuum. Unfortunately, a side effect of electropolishing is that it enriches the target surface with H_2 ; said surface subsequently becomes the dominant source of H_2 outgassing at low pressures (typically 10^{-11} torr). If this H_2 gas load is unacceptable, electropolished chambers need an additional H_2 degassing step inside a vacuum furnace.

All three custom chambers (c.f. Sec. 6.3.2), the analyzer (c.f. Fig. 8.1.3), and all stainless Steel components of the cryostat were electropolished. For the latter, the dominant electropolished surface area belongs to the so-called shielding structures (c.f. Sec. 7.3). None of the vacuum components were H_2 degassed for cost reasons.

6.2.3 Vacuum generation

6.2.3.1 Choice of pumps

It is obvious from Eq. (6.1.6) and (6.1.8) that, for a given gas load, using pumps with a higher speed will result in lower base pressures. In practice, the choice of pump speed is typically heuristic and conservative because estimating Q_{gas} is non-trivial. As I briefly mentioned in Sec. 6.1.2.1, one caveat with most practical pumps is that pumping speed is pressure-dependent. As the vacuum system transitions from atmosphere \rightarrow rough vacuum \rightarrow high vacuum \rightarrow ultrahigh vacuum, different pumping mechanisms have the highest speed. Therefore different types of pumps are used.

Typically, pumps which operate at or below high vacuum have moving parts. For such pumps, it is common to lubricate bearings to extend their lifetime. Lubricants like oils and greases are localized to the exhaust of these pumps to avoid outgassing into the vacuum chamber. Unfortunately, backstreaming of oil is inevitable once the pressure inside the chamber is low enough. While the use of mechanical pumps in vacuum generation can be temporary, the oil backstream can stick to the chamber walls for a long time, resulting in longer bake-outs and/or higher base pressures. Therefore, it is generally advisable to use oil-free alternatives.

The fraction of light gases (e.g. H_2) inside vacuum chambers increases once said chamber reaches the UHV range. This is due to the fact that (say) turbo pumps have a relatively lower compression ratio for gases like H_2 . In that case, pumping action is achieved using a getter like Titanium (c.f. 6.3.3.3). Since most stainless steel chambers have a considerable permeation of H_2 , a getter is critical in getting from 10^{-10} to 10^{-11} torr. Moreover, in the UHV range, ion pumps (c.f. 6.3.3.2) are preferred for vibration-sensitive applications.

6.2.3.2 Design of conduction paths

In addition to using high speed pumps, with the appropriate pumping mechanisms, the placement of said pumps, with respect to the vacuum region of interest, is also important. As evident from Eq. (6.1.6), the effective pumping speed will suffer considerably if conductance to the pump is smaller than said pump's intrinsic speed ($C < S_{\text{pump}}$). Therefore, the vacuum chamber design needs to take into account the pressure gradient it can tolerate between the pump and the region of interest.

In some cases, a small conductance is desired. For example, using Eq. (6.1.4), regions of high vacuum (P_1) and ultrahigh vacuum (P_2) can be connected if C is low enough⁸ that a gas load Q_{pump} from the high vacuum region can be handled by pump connected to the ultrahigh vacuum side. This configuration is often referred to as differential pumping. This could be used for (say) connecting a vacuum ultraviolet light source, using gas-based high-harmonic generation (c.f. Sec. 4.1.1.2 and 4.1.2.2), to an ARPES analysis chamber.

Another important design consideration, involving conductance, is elimination of virtual leaks. For example, if a bolt is tightly fastened into a blind hole when the vacuum system is at atmosphere, air gets trapped in the gaps between the screw and hole. The region where the head of the screw pushes down on a flat surface forms an air flow path with very poor conductance. When the chamber is under vacuum, the trapped gas will act as a source of gas load, and hence appear to be a “leak.” Such problems can be mitigated with either the use of vented screws or drilling a secondary hole to the side of the blind hole. The ARPES Helium-3 cryostat uses several custom vented screws.

6.3 Components of the ARPES UHV system

6.3.1 System overview

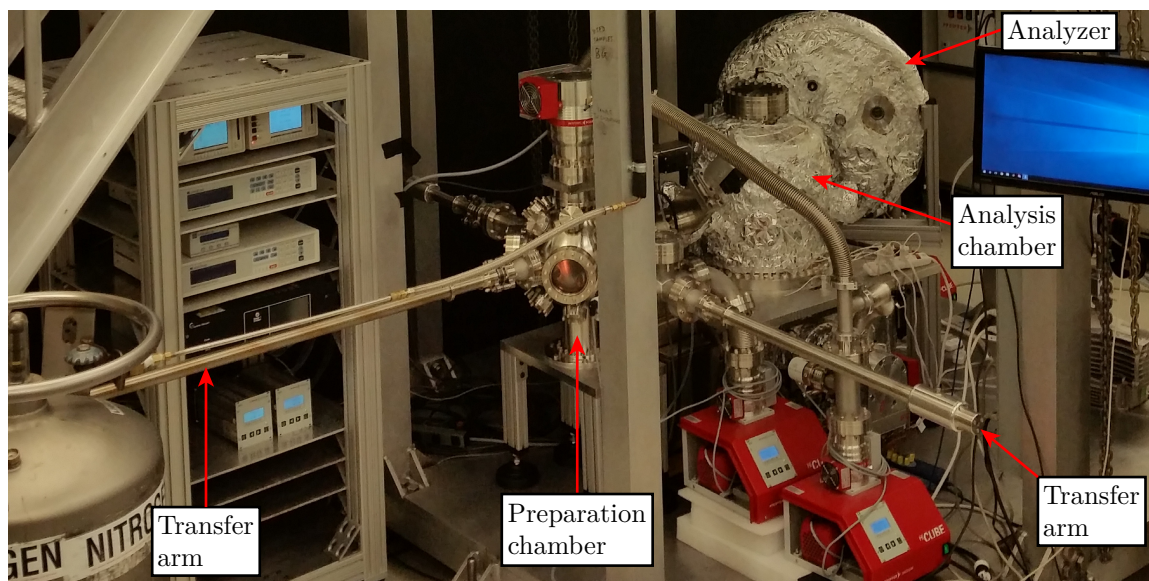


Figure 6.3.1: Photograph of the UHV system

⁸ C can be made small by a passive or active vacuum module. The former simply depends on the geometry of the conduction path. The latter could involve additional pump distributed along the pressure gradient.

An overview of the UHV system is shown in Fig. 6.3.1. The UHV system comprises of custom stainless steel chambers being pumped on by a combination of pumps with unique pumping mechanisms and serving different purposes. In other words, different types of pumps are *relatively* more or less effective in removing different gas species in different pressure ranges. The pumps and chambers are organized into three primary vacuum spaces across which samples are transported using magnetic “transfer arms.”

6.3.2 Chambers

This system consists of three custom chambers, not including the cryostat and analyzer, for the performing the functions of sample analysis, system pumping, and sample preparation. A fourth vacuum space, called the “load lock,” is built out of a standard 5-way cross. A top-down and sideways sketch of these vacuum spaces is shown in Fig. 6.3.2.

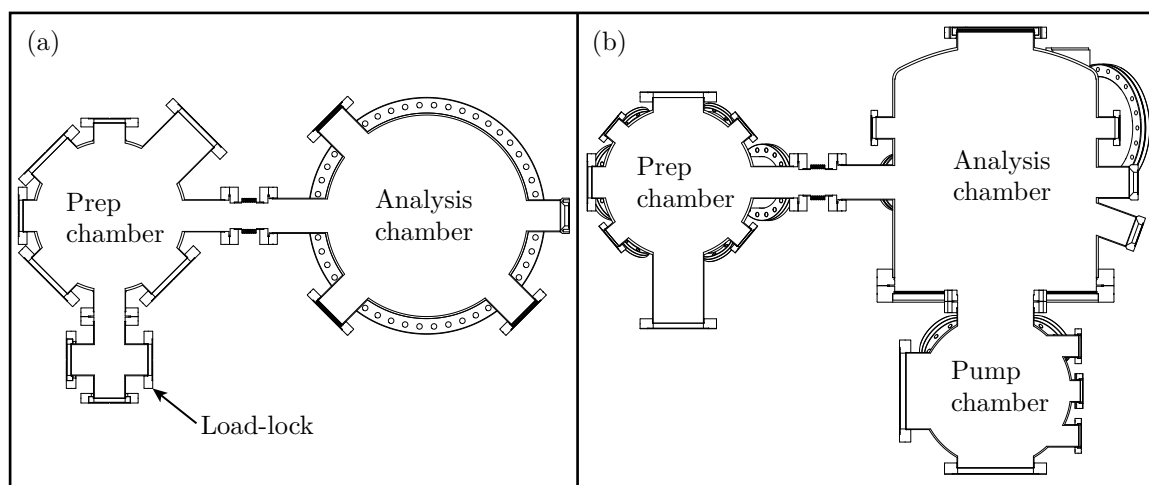


Figure 6.3.2: (a) top and (b) side view of the outlines of the analysis, preparation, pump chambers, and the load lock.

6.3.2.1 Analysis chamber

As the name suggests, the properties of the sample of interest are analyzed inside the analysis chamber. As a result, the light source, electron detector, and cryostat need to come together inside the analysis chamber. The design of the analysis chamber needs to accommodate these three critical elements to make ultralow temperature and high energy resolution ARPES possible.

The challenge in integrating the cryostat into the analysis chamber primarily involves overcoming space constraints. The performance of the cryostat improves, in terms of both cooling power and ease of sample manipulation, if the sample manipulator is made shorter and radiation shields are made larger respectively. Both of these spatial requirements by the cryostat are incompatible with adequate ($< 0.1 \mu\text{T}$) magnetic shielding by the μ -metal layers inside the analysis chamber.

The cylindrical μ -metal sleeve (c.f. Fig. 6.3.3), through which the manipulator and shields enter the analysis chamber, requires a longer length and smaller diameter for better magnetic shielding. I chose a μ -metal sleeve inner diameter of 85 mm and a length that made the sleeve enter the cryostat just short of hitting the shoulder of the 77 K radiation shield tail. The target magnetic shielding

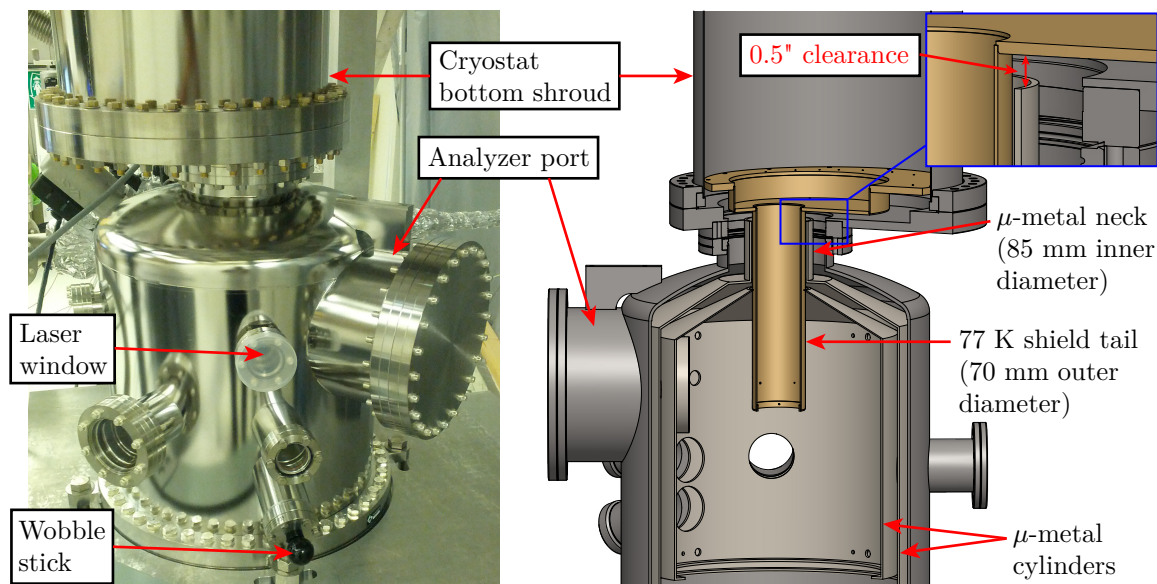


Figure 6.3.3: Left: photograph of the analysis chamber connected to the cryostat. Right: CAD model showing penetration of the μ -metal neck into the cryostat just short of hitting the radiation shield.

was eventually met during factory tests using this design. This solution, however, came at the price of significantly increased complexity in assembly.

Fig. 6.3.4 illustrates the assembly procedure for the analyzer. The cryostat was detached from the analysis chamber during the installation and testing of the analyzer. The most challenging aspect of the assembly was ensuring proper mating of the μ -metal cones. In the first attempt, improper mating resulted in damage to the screws which set the position of the two μ -metal layers inside the analysis chamber.

An internal photograph of the analysis chamber, after both the analyzer and cryostat were attached, can be found in Fig. 6.3.12.

6.3.2.2 Pump chamber

In the previous section, I discussed trade-offs between the design of the analysis chamber and the three elements critical to ultralow temperature and high-energy resolution ARPES: light source, electron detector, and cryostat. There is, however, a fourth element which I took for granted: generation of UHV. Since UHV is essential for maintaining a pristine sample surface, the dominant gas pumping sources need to be as close to said sample as possible. Ideally, I would like to attach the three primary pumps used in this ARPES system (c.f. Sec. 6.3.3) directly to the analysis chamber; that, however, is not practical for the following reasons.

Each of the three pumps have a circular conductance cross-section with a 6" diameter. Firstly, the analysis chamber walls don't have enough surface area to accommodate all three pumps without interfering with some of the other vacuum elements (e.g. laser windows, wobble stick, analyzer). Secondly, it would be impossible to meet the analysis chamber's magnetic shielding specifications with three 6" diameter holes in the μ -metal lining.

I reached a reasonable compromise to this dilemma by clustering all three pumps around an auxiliary spherical chamber dubbed the "pump chamber." The CAD model of the pump chamber along with

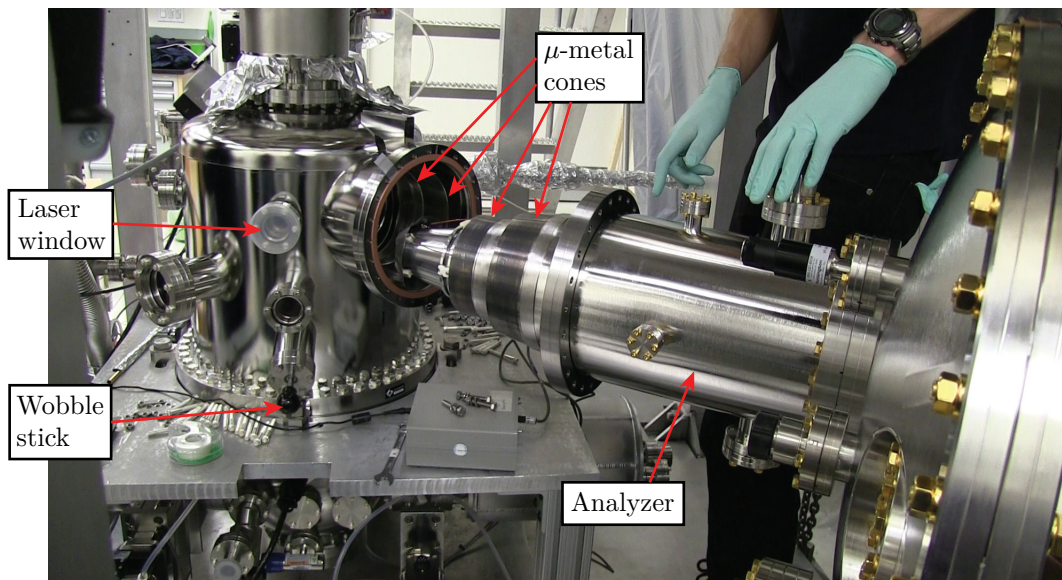


Figure 6.3.4: Photograph of the analysis chamber and electron analyzer during installation and testing of the latter.

the three pumps is shown in Fig. 6.3.5. As shown in the sketch in Fig. 6.3.2 (a), the pump chamber is connected directly underneath the analysis chamber. A pair of μ -metal sheets with a periodic array of holes is inserted in between the analysis and pump chambers to allow for both gas conductance to the pumps and magnetic shielding of the sample region.

6.3.2.3 Preparation chamber

The preparation chamber serves as an intermediate vacuum stage between the load-lock (c.f. Sec. 6.3.7.1) and the analysis chamber (c.f. Sec. 6.3.2.1). It is often abbreviated as the “prep chamber.” UHV is generated and maintained in the prep chamber using a 300 liters/second turbomolecular pump (c.f. Sec. 6.3.3.1). Isolation from the analysis chamber and load-lock is maintained, most of the time, using two manual gate valves. Photographs of the prep chamber and its connections to other vacuum spaces are shown in Fig. 6.3.10 and Fig. 6.3.6.

The primary role of the prep chamber is sample processing and analysis. Therefore, storing several samples in the prep chamber is necessary. This is achieved using an in-vacuum storage unit called the sample garage (c.f. Sec. 6.3.7.2). At the time of writing, the prep chamber was only used for the latter. The sample garage and sample holder are transported from the load-lock to prep chamber and prep chamber to analysis chamber, respectively, using transfer arms (c.f. Sec. 6.3.6.1). A photograph of the sample holder and garage actuation is shown in Fig. 6.3.11.

6.3.3 Vacuum pumps

6.3.3.1 Turbomolecular pump

The system consists of three turbo pumps *directly*⁹ responsible for achieving and maintaining UHV. The analysis and prep chambers have a HiPace 700 M and 300 M turbos connected directly to the

⁹There is a 4th turbo for pumping down the load lock.

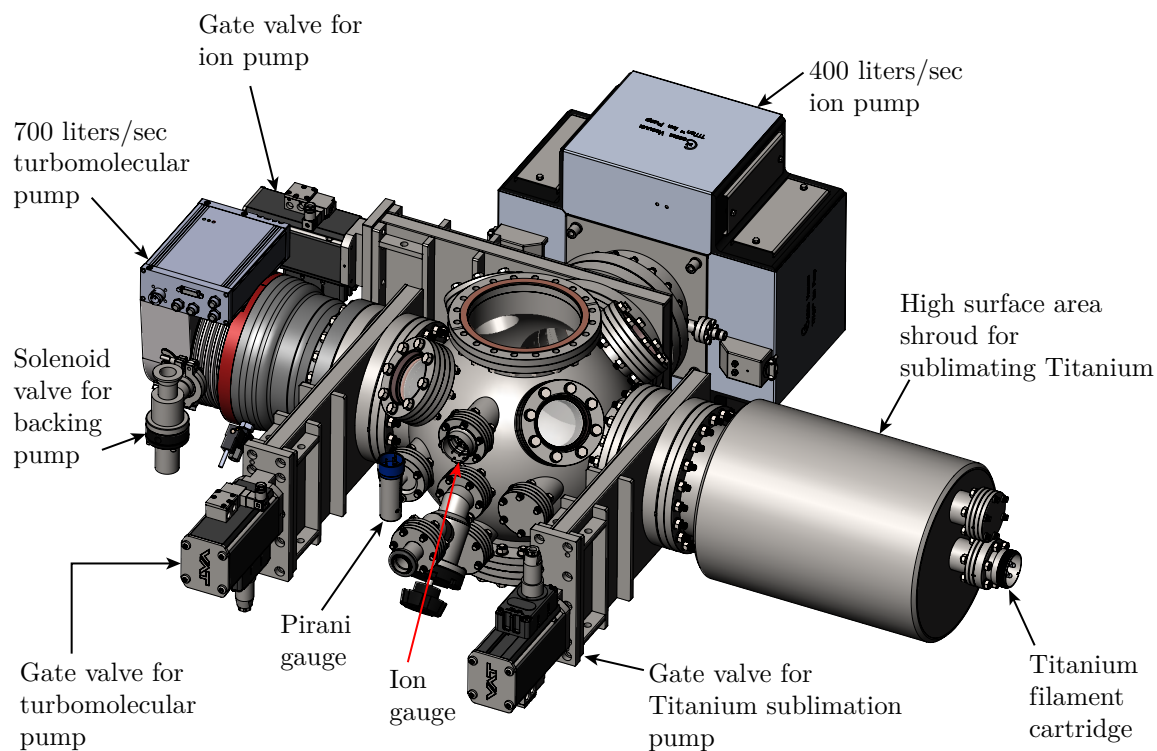


Figure 6.3.5: CAD model of the pump chamber labeling various pumps, gauges, and valves.

respective chambers. The number (300 or 700) corresponds to the approximate pumping speed and the “M” indicates that the rotor is levitated using electromagnets. The latter considerably extends the pump lifetime compared to pumps where the rotor is supported by mechanical bearings.

The two HiPace turbos are backed by a single HiCube turbo unit with an ≈ 70 liters/second pumping speed.¹⁰ The turbo-backing-turbo configuration allows the analysis and prep chambers to reach low 10^{-10} torr without the assistance of other pumping mechanism designed exclusively for UHV (e.g. ion pump, TSP, etc.). In other words, with a backing pressure of mid- 10^{-7} torr created by the HiCube, the two HiPaces comfortably achieve an average compression ratio of $\approx 10^3$ under UHV chamber conditions.

6.3.3.2 Ion pump

The ion pump generates pumping action in the molecular flow regime by ionizing and trapping gas molecules. The reason for this is that ionized particles are easier to control with a static electric field (typically 1000s of V/cm). Unlike the turbo pump, the ion pump does not have an exhaust for the molecules trapped (or pumped) by it; these molecules permanently remain inside the pump in an inert state. As a result, issues such as back-streaming from the exhaust port can be eliminated. Since the ion pump cannot operate at pressures above 10^{-4} torr, most UHV systems use a turbo to get to high vacuum (10^{-6} or better), turn on the ion pump, and finally valve of said turbo. Performing this switch in pumping mechanism at lower pressures extends the lifetime of the ion pump.

¹⁰The HiCube turbo is backed by a diaphragm pump.

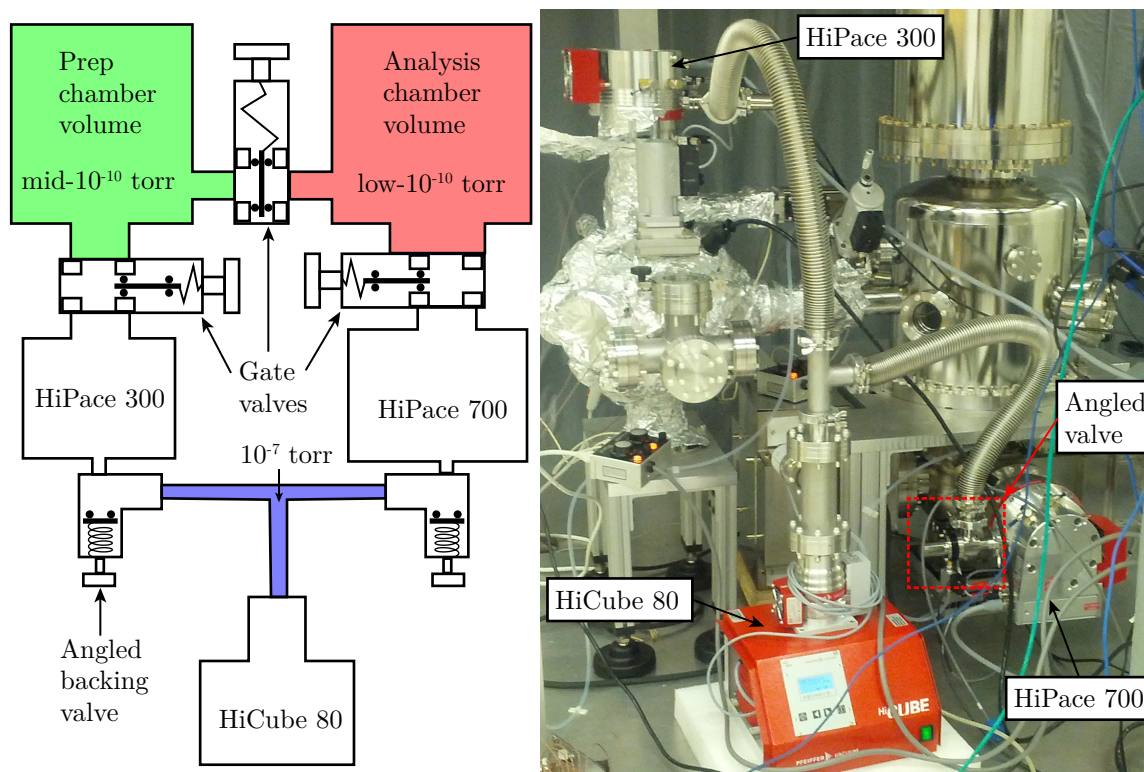


Figure 6.3.6: Left: a block diagram of the pumping circuit established by the turbomolecular pumps. Right: photograph of the HiPace turbomolecular pumps attached to the UHV system and the HiCube turbomolecular pump backing them.

For the UHV system discussed in this thesis, the Gamma Vacuum TiTan 400L ion pump (c.f. Fig. 6.3.7) was used to pump the analysis chamber. With the pumping speeds offered by the turbo (HiPace 700 M), it is sufficient to keep the ion pump off for most of the bake-out (average temperature 100 °C). The ion pump was turned on shortly prior to turning off the bake-out at a pressure of about 4×10^{-8} torr. After the bake-out is turned off, and the system returns to room temperature, the turbo and ion pump together achieve a base pressure of 2×10^{-10} torr. This configuration was empirically determined to provide the lowest base pressure and fastest pressure spike¹¹ recovery.

6.3.3.3 Titanium sublimation pump

Similar to the ion pump, the titanium sublimation pump (TSP) provides pumping action by trapping molecules. As a vacuum system approaches UHV, the fraction of the residual Hydrogen gas molecules (H_2) in the chamber increases; this is because the ion and turbo pumps are less effective in pumping lighter gases like H_2 . It turns out that the sticking coefficient of H_2 to Titanium is high enough to trap the former.

The H_2 hitting Titanium dissociates into H atoms thus reducing the partial pressure of H_2 in the vacuum chamber. The rate at which the H_2 partial pressure drops in this manner, in other words the H_2 pumping speed, depends on the surface area of Titanium. The easiest way of getting a large surface area of Titanium is by sublimating it onto the chamber walls. This is achieved by heating a Titanium filament by passing around 40 A of current through said filament.

¹¹For example, friction from sample holder handling generates pressure spikes.

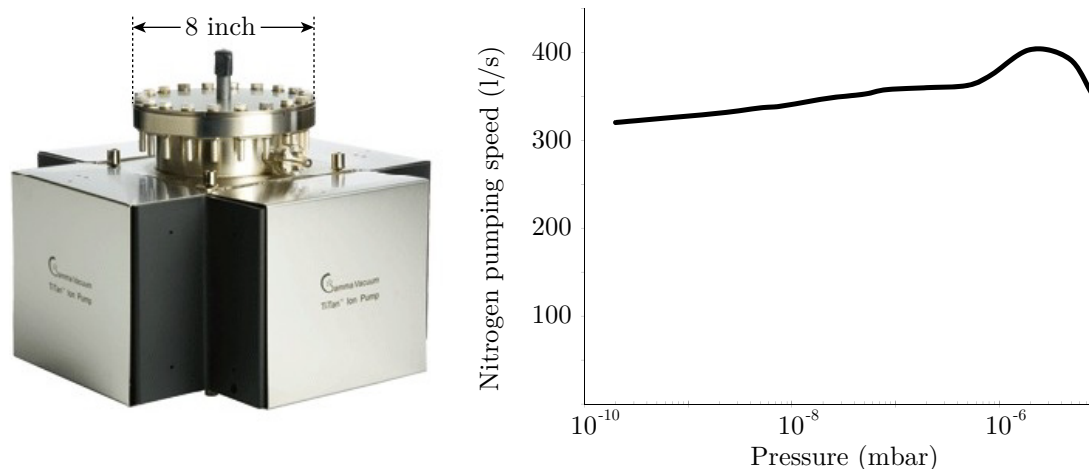


Figure 6.3.7: Left: photograph of the 400 liter/second ion pump. Right: pumping speed of the ion pump as a function of pressure.

| Gas specie | Pumping speed per unit area (liters/sec/cm ²) | |
|------------------|---|------|
| | room temperature | 77 K |
| H ₂ | 2.6 | 17 |
| CO | 8.2 | 11 |
| H ₂ O | 7.3 | 14.6 |

Table 6.1: Pumping speed of the Titanium sublimation pump for different gas species at room temperature and 77 K.

Fig. 6.3.8 shows a section of the TSP installed on the pump chamber. The Titanium filament is inserted in a vacuum shroud made of a cylindrical Aluminum can with internal “fins.” The fins increase the surface-to-volume ratio. The pumping speed per unit area of the TSP for different species is shown in Table 6.1. A crude estimate of the *physical*¹² surface area of the TSP can be $\approx 6000 \text{ cm}^2$. For H₂, that corresponds to a pumping speed of $> 15000 \text{ liters/second}$ at room temperature.

6.3.4 Vacuum valves

6.3.4.1 Gate valves

As the name suggests, the gate valve isolates two vacuum regions using a gate. The gate can be sealed using either an o-ring or a metal-on-metal seal. Since the latter is 5 times more expensive, the former was used in the entire ARPES UHV system. However, the o-ring sealed gate valve cannot be used for maintaining large pressure differences. Therefore, it was only used to isolate two vacuum regions.

One of the advantages of gate valves, over angled-valves, is their line of sight. This is ideal when (say) transporting samples from one chamber to another. Moreover, due to the relative abundance of large area ($\geq 6''$ diameter) gate valves,¹³ they can be used to isolate pumps with large pumping

¹²The effective surface area will be different based on Titanium coverage which is difficult to quantify precisely.

¹³Angled valves are less common for larger cross-sections.

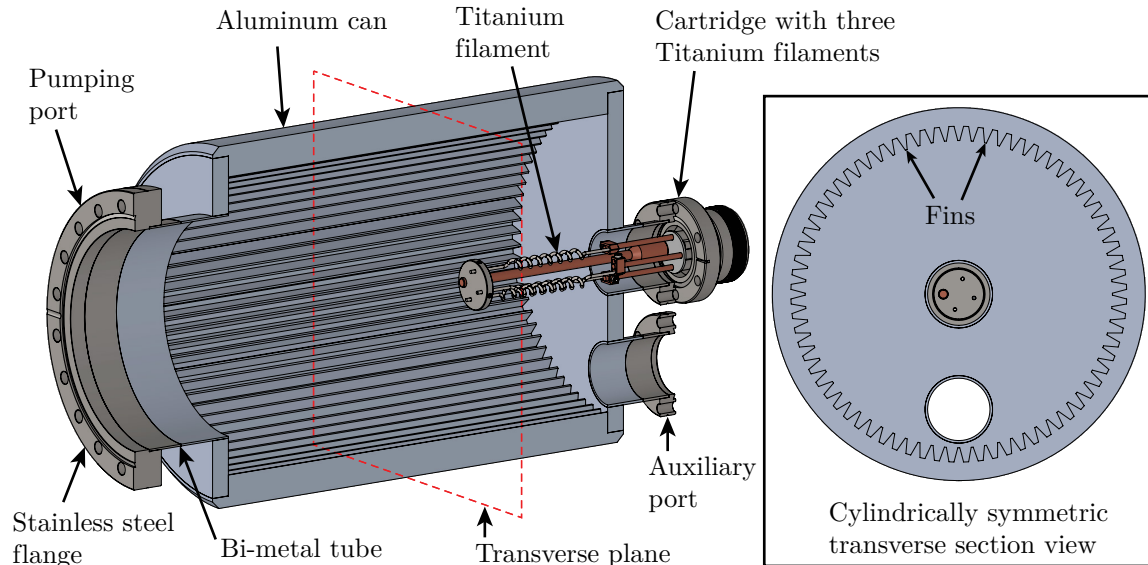


Figure 6.3.8: Section views of the Titanium sublimation pump. The fins on the Aluminum can provide additional surface area for sputtering Titanium. The can has three stainless-Steel-to-Aluminum bi-metal tubes to allow welding standard (i.e. stainless Steel) ConFlat flanges.

speeds (c.f. Fig. 6.3.5). Based on the gate actuation method, two types of gate valves are used in the ARPES UHV system: (a) manual and (b) pneumatic.

Pneumatic gate valves have the advantage of automatic isolation using an interlock system. For example, an interlock system can automatically valve off a pump which experiences unexpected failure. However, manual gate valves are highly advisable when mechanical transport is performed across said valves. Accidental triggering of the interlock can cause the gate to crash into (say) a transfer arm.

6.3.4.2 Angled valve

Angled valves are typically cheaper alternatives to gate valves. They are used in less critical systems like the isolation of the exhaust of the two large HiPace turbomolecular pumps (c.f. Fig. 6.3.6).

6.3.5 Vacuum seals

In this section, the term “sealing” will mean connecting two prefabricated vacuum systems, say A and B, such that after the seal is made, A + B effectively act as a single vacuum system. For example, vacuum seals need to be made between the three types of UHV components I discussed so far: chambers, pumps, and valves. As briefly mentioned in Sec. 6.3.2.1, two other important components which require a UHV seal, with the analysis chamber, are the electron analyzer and cryostat. The latter is the most complex component in the system with the added hassle of ensuring vacuum seals function down to sub-Kelvin range.

Until now, however, I have excluded *explicit* discussion of UHV components which are part of the cryostat. Starting with this section, and for the rest of this chapter, I will discuss UHV components

used in both cryogenic and non-cryogenic applications. This will hopefully provide a smooth transition to the next chapter about the cryostat. Moreover, given the complexity of an ARPES Helium-3 cryostat, discussing vacuum details in the next chapter will become inconvenient diversions. To that end, I will start with an exhaustive survey of the different types of vacuum sealing mechanisms employed in this UHV system and discuss their respective pros and cons.

6.3.5.1 Welding

Welding is one of the most reliable vacuum sealing methods. The most commonly used welding technique is known as Tungsten inert gas (TIG) welding. Welded joints can withstand consider amounts of mechanical and thermal stresses. This makes welding the ideal choice for fabrication of vacuum shrouds (e.g. c.f. Sec. 7.3.2.2). Moreover, in a cryogenic system, components like (say) cryogen reservoirs, which have an atmosphere-to-UHV interface (c.f. 7.3.1), and bear the weight of up to a few hundred liters of cryogen, are sealed by welding.

In order to reap the benefits of welded seals, however, certain guidelines need to be followed for both UHV and cryogenics. For example, in UHV applications, seam¹⁴ welding needs to be performed on the vacuum side. If the vacuum side is inaccessible, a penetration weld¹⁵ can be performed from the atmosphere side. These precautions avoid air being trapped in the joint (i.e. virtual leaks).

Another important precaution to observe is welding stresses. Welding is, by design, a *local* fusion process. Therefore, thermally-induced stresses build up close to the weld joints. These stresses can be relieved using an annealing step. Alternatively, the impact of these stresses can be minimized by ensuring proper heat sinking. In the case of a cryogenic joint, it is preferable if heat sinking is provided by the host material itself, which is only possible if the parts being joined have the same thickness.¹⁶ For example, joining 0.008" thick bellows to 0.030" thick tube can lead to the former tearing after repeated thermal cycles (c.f. 7.8.1).

6.3.5.2 Brazing and soldering

TIG welding can only be used to join electrically conductive materials. However, most modern vacuum systems cannot function without an insulator-to-metal seal. The most prominent examples of the latter are metal-to-glass seals for vacuum windows and metal-to-ceramic seals for insulation of electrical feedthroughs. For these cases, vacuum seals are achieved using a technique known as brazing, where an intermediate (or “filler”) metal is melted and flown between the items to be joined. The filler metal is chosen such that: (a) it has good adhesion to, and (b) its melting point is lower than the items being joined. Moreover, the filler metal has to be UHV compatible.

Soldering is a form of brazing where the melting point of the filler metal is lower than 840 °F. This typically makes soldering a little easier than brazing. For the ARPES Helium-3 cryostat, soldering was used to make UHV seals between dissimilar metals like copper and stainless steel using a (Silver-based) proprietary filler metal with a melting point of 640 °F.¹⁷

As evident from the above example, an advantage of brazing/soldering over welding (c.f. Sec. 6.3.5.1) is their ability to join dissimilar metals. However, brazed/soldered joints have a lower thermal and mechanical stress tolerance compared to their welded counterparts. Therefore, welding is preferred when relieving such stresses on a vacuum seal is impractical.

¹⁴Continuous string of weld beads along the length of the joint.

¹⁵The weld beads extend from the atmosphere to the UHV side.

¹⁶In some cases, difference in thickness can be bypassed using weld reliefs.

¹⁷Note that the 50 Ω heater on the condensing impedance (c.f. Sec. 7.4.3.2) has enough power to melt the solder between the thinner stainless Steel impedance and the thicker Copper tube. This solder melting once led to an atmosphere-to-UHV leak in the cryostat.

6.3.5.3 Explosion bonding

Explosion bonding or welding combines the advantages of both welding and brazing/soldering. Explosion bonding is the process of joining two dissimilar metals by melting them. For example, in the case of the TSP can (c.f. Sec. 6.3.3.3), it is possible to TIG weld stainless Steel flanges on to a shroud with an Aluminum body by using bi-metal tubes generated using explosion bonding. The stainless Steel flanges are necessary because Aluminum is not hard enough to bite into the Copper gasket sealing the TSP to the pump chamber.¹⁸ One of the major advantages of using Aluminum walls in UHV systems is their low H₂ permeation. This is, of course, important for TSPs whose main role is H₂ pumping.

6.3.5.4 ConFlat

The need for modularity in a UHV system increases with its size and complexity. Therefore, the use of detachable vacuum seals is inevitable. A “hard on soft” sealing standard called ConFlat is most common in UHV systems. For most stainless Steel chambers, this sealing technology involves pressing together two flanges, made of stainless Steel, with a Copper gasket sandwiched between them. A cold flow of the softer gasket material results in a seal which can withstand bake-out temperatures of up to 450 °C.

The ARPES UHV system has ConFlat flange sizes with outer diameters ranging from 1.33" (heat switch) to 16.5" (bottom shroud). A great amount of care must be taken to avoid scratches on the knife edge of a ConFlat flange. Such scratches can generate discontinuities in the gasket cold flow thus resulting in a leakage path. In most cases, the part or the flange has to be replaced. In few cases, when the scratches are minor, the flange *might* be salvaged using a rubber abrasive (Cratex) to smooth out rough edges.

6.3.5.5 Wire seal

The wire seal is similar to ConFlat in terms of sealing mechanism. Both types of seals rely on cold flow of a soft metal (e.g. Copper) to fill the gaps between two hard metals (e.g. stainless Steel). The difference is between the methods of generating the cold flow. Geometrically, the wire seal is similar to an o-ring, except made of Copper. The Copper ring is squashed between a gap in the vertical walls of male and female flanges.

Flanges with outer diameter (OD) greater than 16.5" require wire seals.¹⁹ The following UHV seals in the ARPES Helium-3 cryostat require wire seals: (a) reservoir insert to main shroud (c.f. Sec. 7.3.2.2) and (b) main to bottom shroud (c.f. Sec. 7.3.2.3). Both of these seals involve a 27.125" OD flange.

6.3.5.6 Indium

Indium seals have a similar mechanism as that of Copper gaskets and wire seals: cold flow. The difference is that Indium is significantly softer than Copper. Therefore the cold flow occurs at much lower flange pressure. But the two biggest advantages Indium seals have over their Copper counterparts are:

¹⁸Special Aluminum flanges with Chromium Nitride knife edge coatings are available. But they limit the bake-out temperature and require special (i.e. more expensive) gaskets.

¹⁹Some wire seal flanges with ODs less than 16.5" are available. But no ConFlat flanges above 16.5" OD exist.

- **Cold welding:** this property is the result of the clay-like nature of Indium. In other words, two pieces can fuse with a little pressure with no heat at all.
- **Cryogenic operation:** Indium seals are more reliable than their Copper counterparts at cryogenic temperatures because the former retains its softness.

In fact, the original seal between the Helium-3 insert and the 4 K reservoir was designed to be ConFlat. However, due to uncertainty in the relative thermal contraction between Copper and stainless Steel at 4 K, said ConFlat flange was re-machined to accommodate an Indium-sealed flange (c.f. Fig. 7.4.1).

6.3.5.7 Rubber

The most common rubber seals in the ARPES UHV systems exist in the form of Viton o-rings. O-rings are less common than ConFlat gaskets in UHV systems because have a higher outgassing rate and lower bake-out temperature rating compared to the latter (c.f. Sec. 6.2.1.2). Moreover, even in cases where o-rings are used in UHV (e.g. gate valves), they are not used as atmosphere-to-UHV seals. This is because, over long time scales (more than days), o-rings will transmit gas molecules from atmosphere to UHV via permeation.

O-rings can, however, be used to maintain UHV over long periods when isolating two vacuum regions. Some examples are the gate valves separating: (a) the analysis and prep chambers, (b), prep chamber and load-lock, and (c) vacuum pumps and pump chamber. Furthermore, o-rings are used in downstream vacuum components, like angled valves and pumps, located at the exhaust of the turbomolecular pumps directly pumping on UHV.

6.3.5.8 Dynamic seals

So far I have only discussed static seals. In other words, if the seal is mechanically displaced, a leak can open up. Some seals, however, need to accommodate relative motion between two vacuum surfaces. An example of a vacuum component requiring such a seal is the θ manipulator on the cryostat (c.f. Sec. 7.5.2.2). Such components use a dynamic seal.

One of the challenges in the design of dynamic seals is finding a compromise between: (a) application of a sealing force, and (b) reducing friction, between components moving relative to one another. One solution to achieving this goal is the use of a spring-loaded Teflon gasket.

The design of the θ manipulator on the cryostat involves two concentric Teflon gaskets, with the region between said gaskets pumped to rough or high vacuum. Sec. 7.5.5 discusses the impact pumping this region has on the quality of vacuum.

A discussion of dynamic seals serves as a perfect segue into the next section where I discuss mechanical feedthroughs (c.f. Sec. 6.3.6.1). In a crude way, mechanical feedthroughs can be thought of as dynamic seals.

6.3.6 Vacuum feedthroughs

So far in this chapter, I have explicitly discussed elements of a UHV system which serve as a barrier between UHV and the outside world. They could be passive barriers like chamber walls and seals or active ones like pumps. Unfortunately, these barriers do not allow any control of in-vacuum components from the atmosphere. A feedthrough is a device which uses special materials and/or sealing mechanisms which allows the exchange of mechanical, electrical, optical, and thermal power across the vacuum-atmosphere barrier.

6.3.6.1 Mechanical

As a rule of thumb, the need for relative motion between two or more in-vacuum components increases with the size of the vacuum system. Motion inside vacuum can be achieved in two ways: (a) direct transmission of mechanical power from atmosphere to vacuum, or (b) in-vacuum power conversion (e.g. electrical to mechanical). The UHV system discussed in this thesis only uses the former.

For ARPES, the mechanical feedthroughs are the most important type. The five sample degrees of freedom in the ARPES Helium-3 cryostat are implemented using different types of mechanical feedthroughs. Deformation of edge-welded bellows makes linear translation feedthroughs (c.f. Sec. 7.5.2.1) and angular motion of the wobble stick (c.f. Sec. 6.3.7.3) and port aligners possible. Whereas relative rotation of two flanges using an o-ring seal accomplish rotary motion (c.f. Sec. 7.5.2.2). Moreover, two mechanical feedthroughs essential for tasks related to cooling the cryostat are the: (a) heat switch, and (b) needle valve. Only the former is an atmosphere-to-UHV feedthrough (c.f. Fig. 7.4.1).

Furthermore, in-vacuum sample handling is achieved using magnetically-actuated transporters called “transfer arms.” Transfer arms are used to move individual sample holders (c.f. Sec. 6.3.7.1), as well as a unit (i.e. sample garage) holding a collection of sample holders (c.f. Sec. 6.3.7.2), between the preparation chamber, analysis chamber, and load-lock. The transfer arm works as follows:

The transfer arm consists of a rigid shaft concentric with a larger hollow tube. The latter serves as the atmosphere-to-UHV barrier. The shaft is held in place by a linear bushing which allows translation and rotation of the shaft about its cylindrical axis. Transmission of mechanical power from atmosphere to the in-vacuum shaft is achieved in a contactless manner using permanent magnets.

6.3.6.2 Electrical

Most electrical feedthroughs involve a metal-to-insulator vacuum seal in order to transmit electrical power from atmosphere to vacuum through the metal. Electrical power is often transmitted to a UHV system for operation of essential vacuum generation equipment like ion pumps (c.f. Sec. 6.3.3.2) and TSPs (c.f. Sec. 6.3.3.3). An electrical interface which can withstand (say) 7000 V and 40 A is required for the former and latter respectively. Moreover, diagnostic equipment like total (c.f. Sec. 6.1.3.1) and partial (c.f. Sec. 6.1.3.2) pressure gauges also require electrical signals to function. For the ARPES Helium-3 cryostat, a hundred electrical feedthroughs are required for temperature sensors (c.f. Sec. 7.6.1) and heaters (c.f. Sec. 7.6.2).

6.3.6.3 Fluid

In complex cryogenic systems like a Helium-3 cryostat, various liquids and gases (i.e. fluids) are supplied to components (e.g. cryogen reservoirs) that are maintained under vacuum. While these fluids are not directly exposed to vacuum, they perform critical heat exchange tasks in subsystems (e.g. the Helium-3 loop) responsible for the operation of the cryostat. The fill tube of (say) the liquid Nitrogen reservoir is an example of such a feedthrough.

Fig. 6.3.9 illustrates the structure of the liquid Nitrogen feedthrough. This fill tube is double-walled like a dewar for thermal isolation. The region between the walls of the two concentric tubes is maintained at UHV. An atmosphere-to-UHV seal is made between these tubes by weld seams between the two tubes to an intermediate tube adapter. All other fluid feedthroughs in this system use this sealing method.

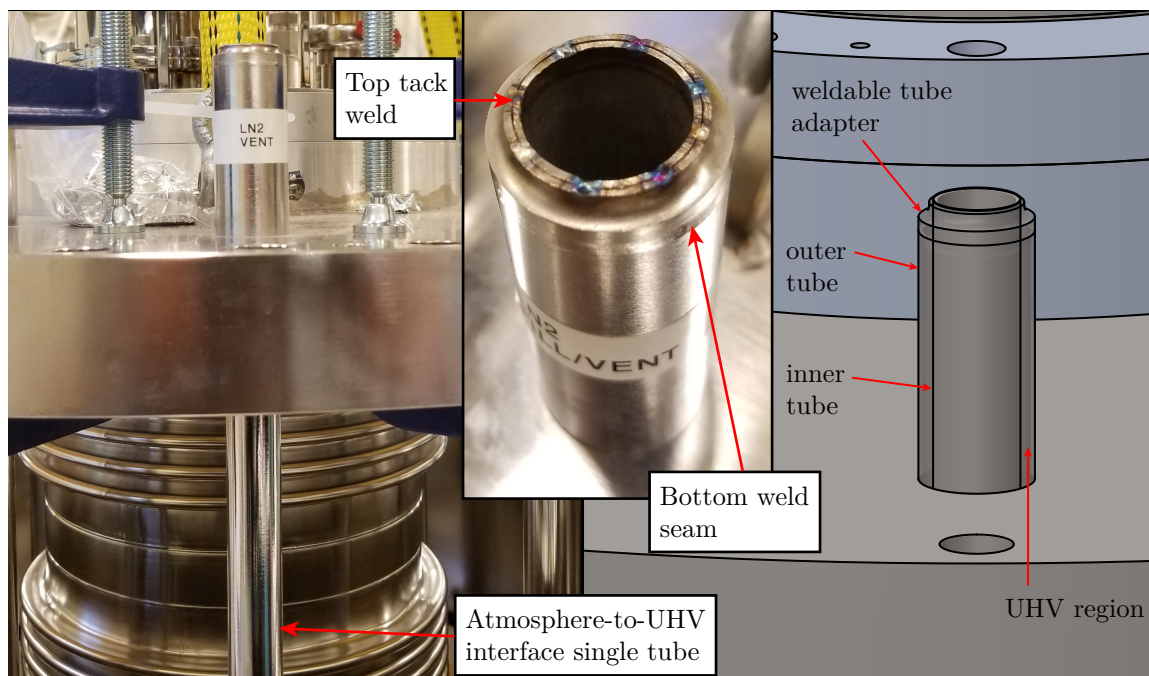


Figure 6.3.9: Photograph and CAD model of liquid Nitrogen feedthrough to its reservoir. The inset shows the inner and outer tubes tack welded prior to making an atmosphere-to-UHV seam welded seal.

6.3.7 Sample handling system

The previous sections described the basic building blocks of the UHV system. A subset of these building blocks can be combined to implement complex in situ processes. One such process is the sample handling system; it consists of three stages: load-lock, sample storage, and sample loading.

In Sec. 6.1.1.1, I explained the necessity of a pristine sample surface in an ARPES experiment. This requires either: (a) having an in situ sample growth apparatus, or (b) cleaving the sample in UHV. The sample handling system discussed here has been designed with sufficient modularity to achieve the latter in the short term, while still permitting potential future upgrades to accommodate the former; but from here on out, option (b) will be implied.

6.3.7.1 Load-lock

It is common for a *well-optimized*²⁰ ARPES system to perform a large number of measurement runs, with a wide variety of samples, without venting the analysis chamber. It is often impractical to store enough samples in the analysis chamber to perform every conceivable ARPES measurement while the system is operational. A load lock solves this problem. The sample handling system under discussion, in particular, permits the transfer of cleavable samples from atmosphere to the analysis chamber without venting the analysis or prep chambers.

The most important components of the load-lock system are shown in Fig. 6.3.10. A batch of up to 12 sample holders, initially in atmosphere, can be simultaneously loaded into the prep chamber (base

²⁰In Chap. 8, the system optimization process involved venting the system more than 10 times over a period of 3 years.

pressure 2×10^{-10} torr) using a *sample garage*. Once the load lock is pumped down to $\approx 10^{-7}$ torr using a HiCube 80 turbo pump, the *manual*²¹ gate valve between the prep chamber and load lock is opened, and the sample garage is exchanged inside the prep chamber, between two transfer arms using custom “grabbers.” The pressure in the prep chamber during the transfer is typically in the low 10^{-8} torr range. Once the sample garage is properly supported by the left transfer arm, the right transfer arm retracts into the load lock, and the gate valve is closed. After closing the gate valve, the pressure in the prep chamber is typically in the high 10^{-10} torr or low 10^{-9} torr pressure range. Depending on the number of sample holders in the garage per load, it takes between several hours to a day for the pressure inside the prep chamber to return to its original base pressure (2×10^{-10} torr).

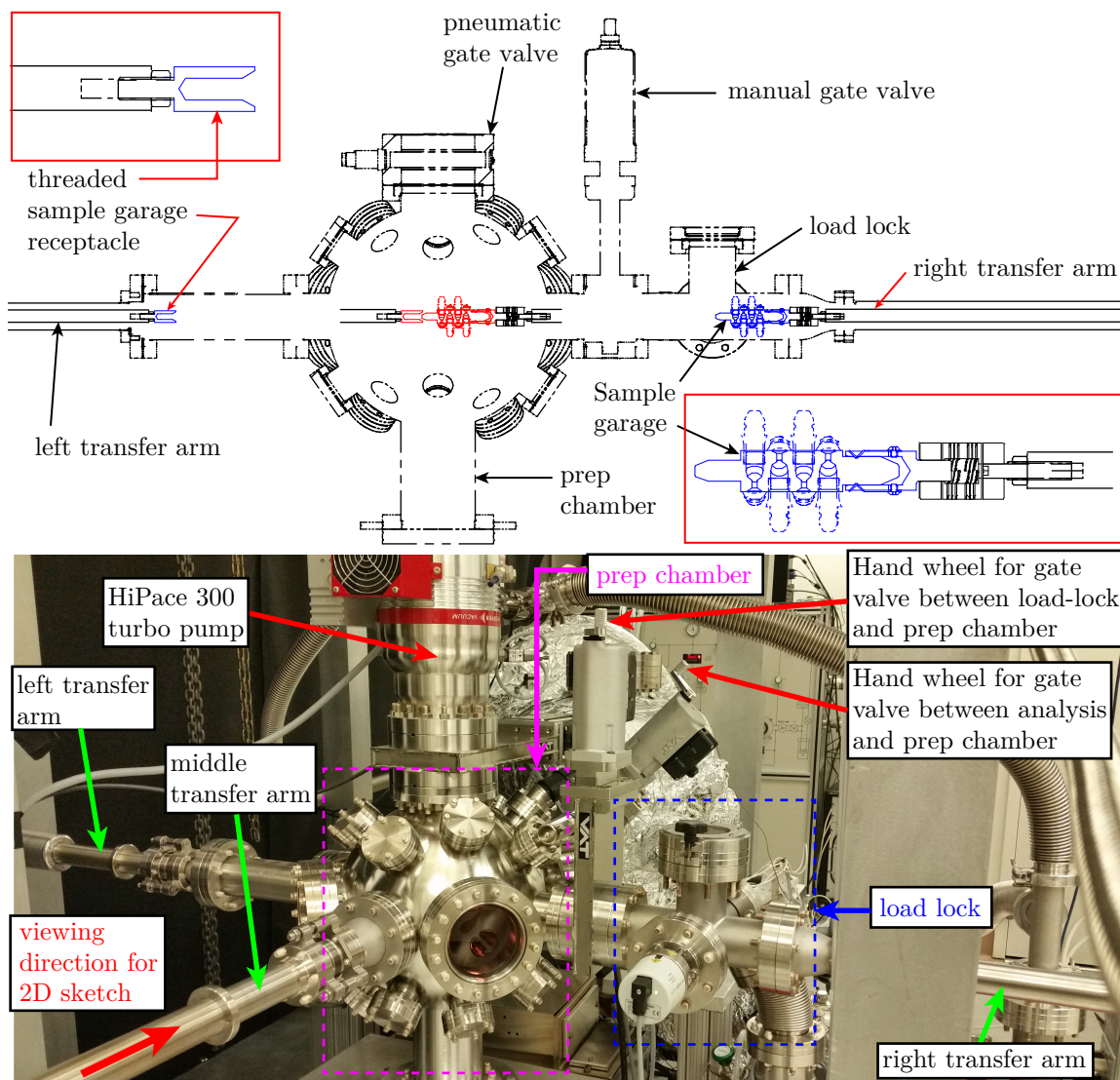


Figure 6.3.10: Top: 2D sketch of the preparation chamber and the load lock. The sample garage and its grabber are shown in their retracted positions (blue) and when they meet inside the preparation chamber (red), using the transfer arms, when the manual gate valve is opened. Bottom: Photograph providing 3D perspective of the load-lock and preparation chamber orientations.

²¹A pneumatic gate valve is inadvisable to prevent accidental collision between the gate and the transfer arm.

6.3.7.2 Sample garage

In this section, I will discuss the design of the sample garage/holder and the respective grabbers, and the mechanisms built into them for in situ manipulation. Fig. 6.3.11 shows the CAD models of the sample garage and sample holder in isolation. The former is machined, from a single stainless Steel stock, into a hexagon with two 3/8"-16 holes on each face (total 12). The pair of holes on adjacent faces have an offset, along the axis of symmetry of the hexagon, to accommodate the size of the sample holder. This configuration allows for each 3/8"-16 hole to have a vent hole²² on the opposite face of the hexagon.

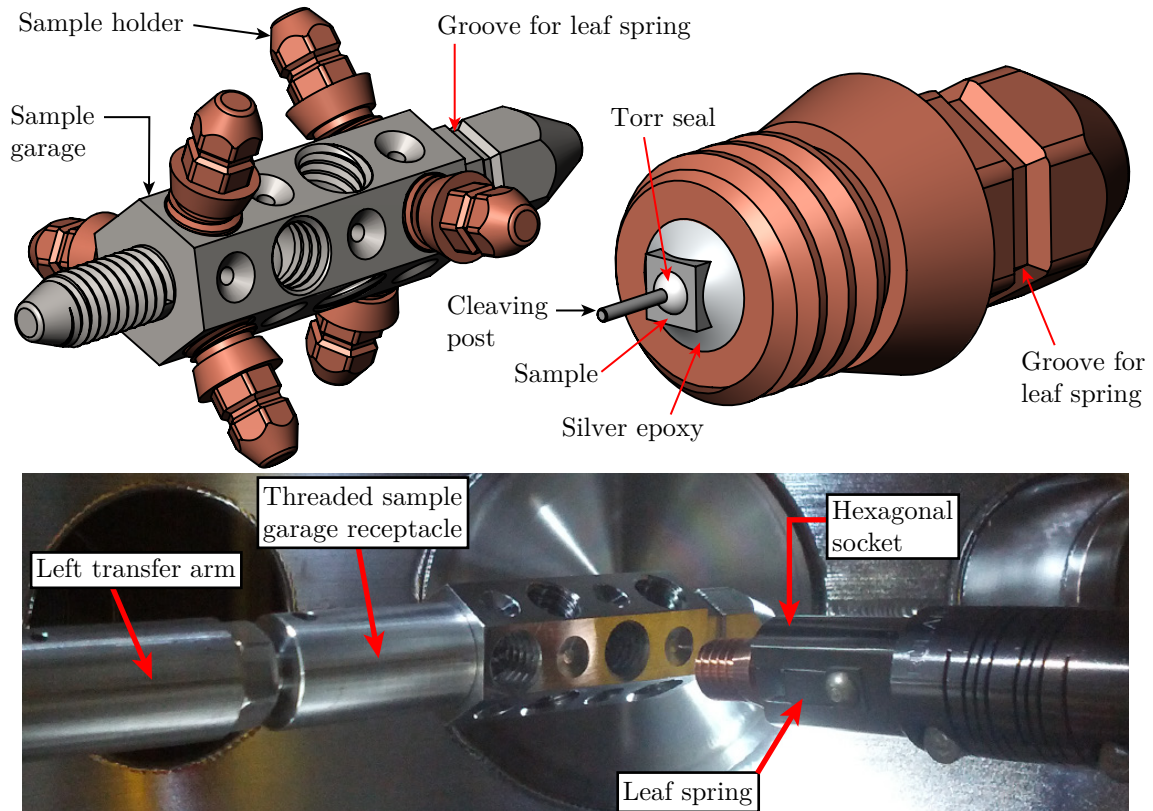


Figure 6.3.11: Top left: CAD models of the sample garage holding 6 sample holders. Top right: CAD model of an individual sample holder with a sample attached. Bottom: Photograph of a sample holder retrieved from the garage using a grabber.

Furthermore, at the two ends of the hexagon, there exist: (a) 3/8"-16 threaded rod, and (b) smaller hexagonal rod. Both these features have tapers on their ends to aide in the garage's coupling with its grabbers from either side. The threaded rod screws into the receptacle (or grabber) shown in Fig. 6.3.10 on the left transfer arm. The torque required for screwing the garage into the receptacle is applied using the tapered hexagonal rod on the other end of the garage. The grabber on the right transfer arm in Fig. 6.3.10 consists of a hexagonal socket which mates with the hexagonal rod on the garage. As a result, screwing action of the garage into the receptacle can be produced by the rotational degree of freedom of the transfer arm. The same screwing mechanism is implemented for "parking" the sample holder in the sample garage.

²²This is done to avoid virtual leaks (c.f. Sec. 6.2.3.2). In practice, however, the sample holders were never tightened fully to avoid the cleaving posts, from different sample holders, from touching each other. Therefore, the vent holes might be overkill.

Another important feature of the grabber with the hexagonal socket is the leaf spring. While the hexagonal socket secures the angular position of the sample holder/garage with respect to their respective grabbers, (unintended) linear motion (or slipping) of the former, along the axis of the hexagonal socket, needs to be avoided during translational motion of the transfer arm. This form of linear motion is constrained by a V-shaped spring-loaded metal plate which engages with grooves in the hexagonal rods on the sample holder/garage. The magnitude of *net* axial forces experienced by the sample holder/grabber depends on factors like their weight, peak acceleration/deceleration of the transfer arms, friction with their grabbers, etc. The lack of accurate models for these effects can be mitigated by a heuristically tuning the spring constant of the V-shaped metal plate using a screw (c.f. Fig. 6.3.11). This design is also referred to as the leaf-spring design.

6.3.7.3 Sample loading and cleaving

The photograph in Fig. 6.3.11 shows a sample holder extracted from the garage using the middle transfer arm (c.f. Fig. 6.3.10). Once the left transfer arm retracts, the manual gate valve between the analysis and prep chambers (c.f. Fig. 6.3.10) is opened, and the middle transfer arm extends into the analysis chamber.

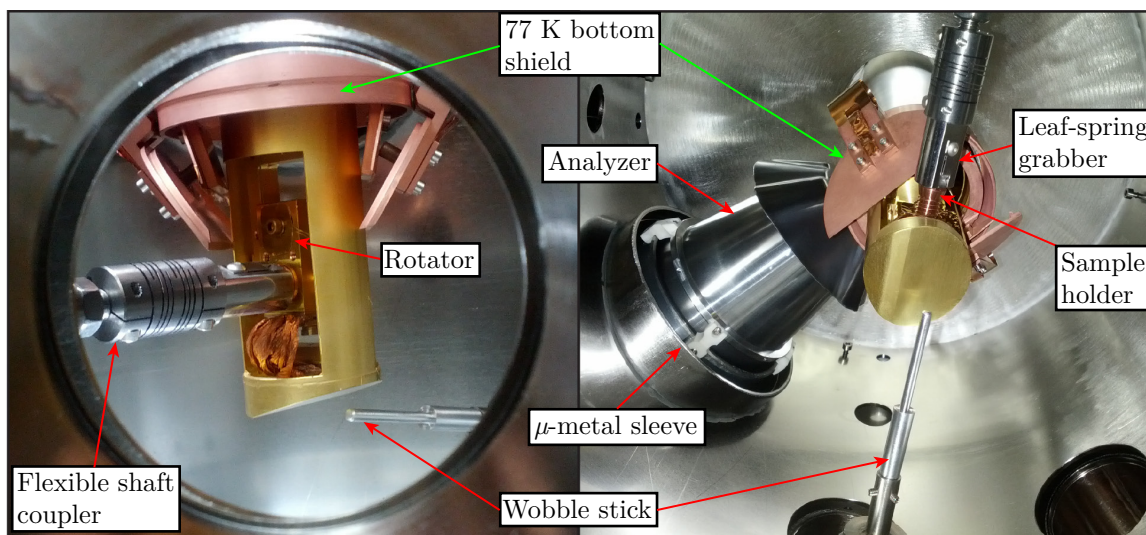


Figure 6.3.12: Left: photograph of sample loaded into the cold finger using a transfer arm from the prep chamber as viewed from a side viewport. Right: photograph of sample close to being loaded into the cold finger viewed from the bottom of the analysis chamber

Fig. 6.3.12 shows the sample holder being loaded into the cold finger. The cold finger is lowered into this loading position using the z - and θ -axis manipulators (c.f. Sec. 7.5.2.1 and Sec. 7.5.2.2) of the cryostat. The cold finger moves 4.25" down²³ and approximately 45° counterclockwise (from top), relative to its average position during measurement, to reach the loading position. Moreover, the ϕ angle of the rotator is coarse-aligned (c.f. Sec. 7.5.2.5), with visual feedback, for optimal mating with the sample holder. Minor misalignments in these three variables (z , θ , and ϕ)²⁴ can be compensated by the flexible shaft coupler. Once the sample holder is screwed into the cold finger, the middle transfer arm retracts back into the prep chamber, and the gate valve to the latter is closed. After the

²³Prior to lowering the cold finger, its x and y coordinates have to be tuned such that the cold finger is approximately concentric to the radiation shield tails. Due to the hysteresis of the coarse x - y manipulator (c.f. Sec. 7.5.4), this process has resulted in damage to the cold finger on *several* occasions.

²⁴It was empirically determined that the radiation shields do not allow any practical x - y motion of cold finger in its lowered position.

pressure in the analysis chamber reaches its original base value, a bellows-sealed wobble stick is used to knock off the cleaving post from the sample (c.f. Fig. 6.3.11), thus exposing an atomically clean surface. Using the various manipulators discussed above, the cold finger is returned to its original position, and the sample is aligned with respect to the analyzer and laser beam for measurement.

6.4 Procedure for achieving ultrahigh vacuum

6.4.1 Roughing stage

The process of lowering the pressure in the vacuum chamber from atmosphere (760 torr) to $\approx 10^{-3}$ torr is referred to as the roughing stage. The two HiPaces (c.f. Fig. 6.3.6) can only be turned on when the pressure at their exhaust is $< 10^{-2}$ torr. On the other hand, the HiCube backing turbo can be turned on at atmospheric pressures due to its own roughing diaphragm pump. But the diaphragm pump is inadequate to “rough out” the entire system (≈ 1500 liters) in a reasonable amount of time (< 1 hour) due to its low speed of 3-10 liters/min above 1 torr.²⁵

Alternatively, a scroll pump (Edwards nXDS10i), with a high enough pumping speed (≈ 3 liters/sec above 1 torr), is a cost-effective method of pumping down a vacuum system of this size in roughly 20-30 min. The scroll pump is attached to the angled valve on the pump chamber (c.f. Fig. 6.3.5). The transition between the scroll pump to the turbo pumps is discussed in the next section.

6.4.2 Switch to turbo pump

For the initial²⁶ roughing out stage, the gate valve between the analysis and preparation chamber volumes (c.f. Fig. 6.3.6) was kept open. At the same time, the HiCube backing the two HiPaces was turned on, with the gate valves in front of the latter in the closed position. When the scroll pump brought down the pressure inside both volumes to $\approx 10^{-3}$ torr, the angled valve was closed, and the gate valves in front of the two HiPaces were opened. Both HiPaces were turned on, and allowed to pump down until the pressure was in the 10^{-7} torr range.

6.4.3 Bake-out

The transition from 10^{-7} to 10^{-10} torr mainly involves removal of water molecules adsorbed onto the vacuum surfaces, from the water vapor in the atmosphere, during the vacuum system fabrication and assembly. One of the easiest ways of expediting the desorption of water molecules from a surface is application of heat. Therefore, the vacuum chamber walls are typically heated up to ≈ 150 °C²⁷ in a process referred to as the “bake-out.” In addition to water, the bake-out also removes contaminants²⁸ that might have been introduced during handling of vacuum surfaces under ambient conditions. The length of the bake-out can change depending on the level of contamination.

For the ARPES Helium-3 cryostat, there is a significant impediment to the bake-out: the integrity of the Indium seal (c.f. Sec. 6.3.5.6) can be compromised above ≈ 90 °C. One option is to limit

²⁵Typically, the speed of roughing pumps drops precipitously below 1 torr.

²⁶This condition corresponds to when the system was assembled for the first time and all volumes were at atmosphere. This situation was never encountered again since the system was only partially vented using gate valves.

²⁷Usually the bake-out temperature is set by the vacuum component with the lowest temperature rating.

²⁸The definition of a contaminant depends on the context. For a vacuum system, a contaminant is something that would act as a significant gas load at base pressure. Bake-outs can practically deal with such contaminants if their volume is small. Such contaminants would be evaporated and pumped out during the bake-out process.

the bake-out temperature to under 90 °C. It was empirically found that low-temperature bake-outs typically take a month. Since this time frame was unacceptable for future ARPES optimization steps (c.f. Sec. 8.4.2), an alternative bake-out strategy was devised; the corresponding bake-out procedure is described below.

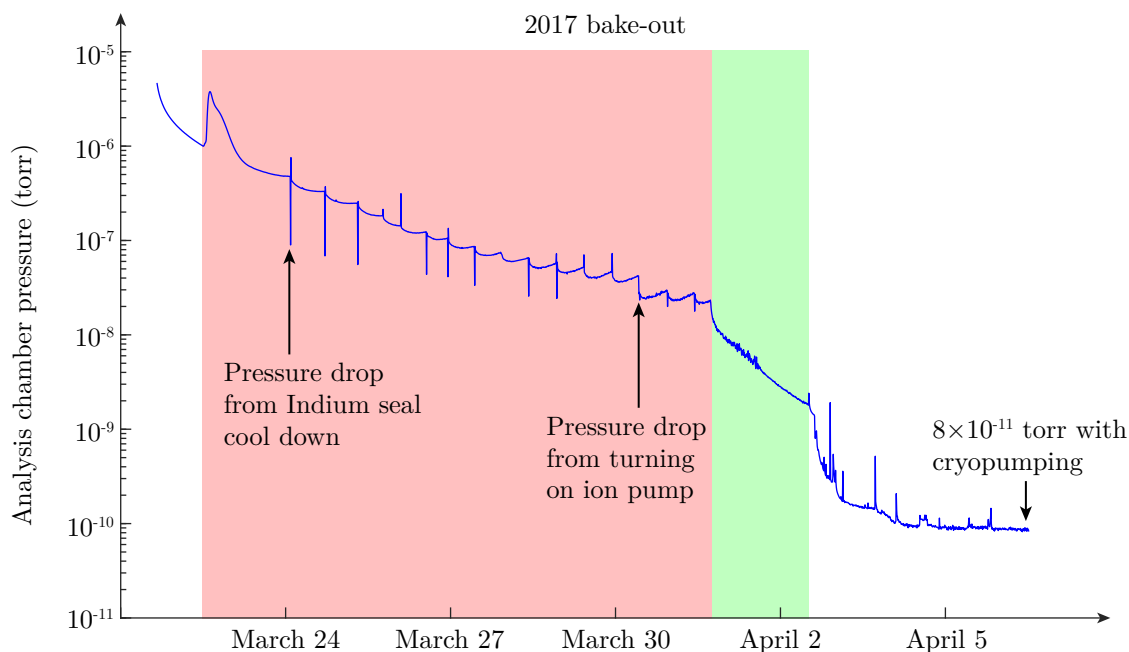


Figure 6.4.1: Pressure drop during a typical bake-out. The red region shows portion of the pump down when the external walls of the vacuum chambers are heated to ≈ 150 °C. The green region shows the pressure drop as the system cools down to room temperature.

Every accessible (or external) surface, serving as a barrier to UHV, is heated to ≈ 150 °C. Inaccessible surfaces, like the inner walls of the 4 K reservoir, are radiatively heated from the external surfaces. The bottom of the 4 K reservoir is periodically cooled down using small amounts of liquid Nitrogen to prevent the temperature of the Indium seal from exceeding 90 °C. Each cool down step typically lowers the temperature of the Indium seal by 10-20 °C, and recovers back to ≈ 90 °C after roughly half a day. This process is repeated for the entire duration of the bake-out. Fig. 6.4.1 shows a plot of the pressure over a typical pump down cycle after the roughing stage.

Just prior to turning off the bake-out, the ion gauge and TSP need to be *degassed*. The process of degassing is analogous to a local bake-out. The filaments of both ion gauge and TSP are electronically heated up to remove as many adsorbed gas molecules as possible. While the walls of the chambers are still hot, the desorbed gas molecules are more likely to get pumped out by the turbo pump(s). Degassing is important because, when the TSP filament is eventually fired after the system returns to room temperature, the pumping speed of the sputtered Titanium is reduced due to the additional gas load from the molecules desorbed from the TSP filament.

In the case of the ion gauge, a larger current is passed through its filament to improve its pressure sensitivity at lower pressures. This current increase could lead to a large amount of gas load from desorption of gas molecules from the ion gauge filament. This gas load can be minimized if the gauge is degassed during the bake-out. Similar degassing should be performed for a residual gas analyzer (c.f. Sec. 6.5.1) if present.

6.4.4 Ion pump and TSP

As I discussed in Sec. 6.3.3, the difference between conventional pumps like a turbomolecular pump and molecule-trapping pumps, like the ion pump and TSP, is that the latter has no exhaust. In other words, the “pumped” gas molecules remain inside the vacuum system in an inert state.²⁹ A natural consequence of this unconventional form of pumping is finite pumping time. In other words, there is a finite number of gas molecules that the ion pump and TSP can trap. Therefore, these pumps are typically reserved for operation at very low pressures to extend their lifetime.

For example, as evident from Fig. 6.4.1, the ion pump is only turned on towards the end of the bake-out. The primary advantage of TSPs is their high pumping speed for H_2 (c.f. Sec. 6.3.3.3). Typically, H_2 pumping only becomes important in the low 10^{-10} torr range. The 8×10^{-11} torr pressure achieved at the end of the plot in Fig. 6.4.1 is due to a combination of the getting process from the TSP and cryopumping from the liquid Helium-4 in the 4 K reservoir. Moreover, the pumping speed of the TSP depends on the temperature on which the Titanium is being sputtered. Titanium acts as a better getter when sputtered onto a colder surface. Hence the TSP is not used until the system has cooled down from the bake-out.

6.5 Vacuum diagnostic equipment

While vacuum science has come a long way in the 20th and 21st centuries, it is still common for modern vacuum systems used in cutting-edge academic research to be one of a kind. Consequently, each new vacuum design comes with its unique set of “bugs.” Under these circumstances, debugging tools are vital to the smooth operation of a vacuum system. In this section, I will discuss two specific diagnostic tools used to detect and fix problems in this ARPES system: residual gas analyzer and the leak detector.

6.5.1 Residual gas analyzer

The residual gas analyzer (RGA) is an instrument commonly used in UHV systems to infer the distribution of the masses³⁰ of the residual gas atoms/molecules. Similar to the ion gauge (c.f. Sec. 6.1.3.1), the RGA measures a current of ionized gas molecules, generated by said RGA, using electrons emitted by a hot filament. The difference is that the RGA places a quadrupole band pass mass filter³¹ between the source and detector of the ion circuit. By sweeping the pass band of the filter, the RGA records the mass spectrum of the residual gas inside the vacuum system.

The RGA is often used for performing troubleshooting steps like leak detection and contamination analysis at UHV pressures. This is in contrast to a conventional leak detector (c.f. Sec. 6.5.2) which works only at rough vacuum. In the ARPES UHV system, there were two examples where the use of an RGA was beneficial; these involved detecting leaks in the: (a) rotary seal (c.f. Sec. 7.5.5), and (b) 4 K reservoir (c.f. Sec. 7.8.1). In both cases, the leak was too small to suspect above UHV pressures. Therefore, the RGA helped in confirming the leaks prior to venting the system. Some details of the leak detection process are discussed in Sec. 6.5.2.

²⁹I will ignore rare cases where the inert gas molecules are released back into the vacuum chamber.

³⁰Actually the RGA measures the mass-to-charge ratio of an ionized molecule or atom. For example, an RGA cannot distinguish between a singly-ionized water molecule ($^1H_2^{16}O^{+1}$) and a doubly-ionized isotope 36 of the Argon atom ($^{36}Ar^{2+}$).

³¹This filter consists of 4 parallel electrodes whose RF and DC voltages can be tuned.

6.5.2 Leak detector

The leak detector is an instrument which focuses on the *quantification* of the gas load (i.e. Q_{gas} defined in Sec. 6.1.2) from a compromised vacuum seal. The leak detector can be operated in two modes: (a) spray and (b) sniffer. In this section, I will focus on the former in order to compare the leak detector with an RGA.³²

The spray mode works as follows. The vacuum system to be tested is connected to the leak test instrument (RGA or leak detector). A test gas, like ^4He , is sprayed around all accessible seals of the test vacuum system. ^4He atoms would enter the vacuum system if and where a leak exists and get detected by the RGA or leak detector. The latter would provide a value of Q_{gas} for the ^4He atoms. The RGA would only confirm the existence of a leak above a certain threshold $Q_{\text{gas}}^{\text{min}}$.

For complex systems, with a large number and type of vacuum seals, it is easier to localize the leak with a leak detector compared to an RGA. The reason for this is as follows. When the test ^4He atoms leave the nozzle used for spraying, they will spread across the room, and a fraction of atoms would eventually find their way to the leak. These atoms would be detected by both the RGA and the leak detector. When the nozzle is brought close to the leak location, however, the leak detector would measure a sharp rise in Q_{gas} . Moreover, the value of Q_{gas} will fall equally sharply as the nozzle moves away from the leak. On other hand, the RGA signal will monotonically keep rising as long as the nozzle is spraying ^4He . Of course, the RGA signal will increase as the nozzle is brought close to leak; but the raised signal level will persist even when the nozzle is moved away from the leak.

For example, a leak detector was used in narrowing down the location of a tear in the bellows on the 4 K reservoir (c.f. Fig. 7.8.1). Moreover, a leak detector is also useful for finding leaks in the seals of vacuum systems *prior* to their regular operation. For example, the 27.125" Copper wire seal flange connection between the reservoir insert (c.f. Sec. 7.3.2.1) and the main shroud (c.f. Sec. 7.3.2.2) was tested using the leak detector prior to the tedious atmosphere-to-UHV pump down procedure (c.f. Fig. 6.4.1). Moreover, there would be considerable overhead, associated with the cryostat disassembly, if a leak in this flange connected discovered after the bake-out.

³²The RGA cannot be operated in sniffer mode.

Chapter 7

Helium-3 cryostat

7.1 Introduction

Cryogenics has been an integral part of experimental condensed matter physics research for almost a century. Discoveries like superconductivity in Mercury (1911) and superfluidity in Helium-3 (1972) [11] were made possible by technical innovations in cryogenics such as: (a) the ability to liquefy Helium (4.2 K) for the former, and (b) the ability to reach few milliKelvin (mK) by demagnetizing nuclear spins for the latter.¹ Since the development of the nuclear demagnetization refrigeration technique, however, the focus of traditional cryogenics² has been on increasing the versatility and user-friendliness of cryogenic systems, rather than lowering the base temperature. Some examples of such developments involve adding more degrees of freedom to measure a sample (e.g. scanning probe microscopy and vector magnets) and switching to closed-loop, a.k.a. dry, cryogenic systems (e.g. pulse tube), to name a few.

7.1.1 Application of cryogenic technologies in ARPES

7.1.1.1 Historical overview

Traditional ARPES systems use conductive heat transfer with liquid Helium-4 coolant, which has a boiling point of 4 K, to perform low temperature measurements. Depending on system details,³ the base temperatures of such systems ranges from few 10s of Kelvin to $\gtrsim 4$ K. In some cases, temperatures below 4 K were accomplished by evaporative cooling of liquid Helium-4 in conjunction with optimization of the sample environment. The former is achieved by reducing the vapor pressure of liquid Helium-4 with a high-mass-conductance Helium-4 gas pump (c.f. Fig. 7.1.1). Examples of the latter include improving thermal conductance to the sample and radiation shielding [62]. Crossing the 1 K barrier in an ARPES system, however, was not accomplished until the early 2010s [84]. The first ARPES system capable of achieving sub-Kelvin temperatures (0.7 K) employed a ³He system.

¹The original experiment [11] which discovered superfluidity in Helium-3 reached about 2 mK. The same nuclear demagnetization technology can, however, achieve temperatures lower than 1 mK.

²By “traditional” I mean techniques involving thermalization. This excludes (say) laser cooling and related methods.

³Typically the unique sample degrees of freedom of a specific ARPES system determines its cooling power requirements. The ability to meet said requirements, in turn, depends on factors such as the maximum attainable thermal conductance to the sample and liquid Helium-4 budget.

7.1.1.2 Cryogenics challenges for ARPES

One of the reasons why achieving low temperatures in ARPES systems has lagged behind other experimental techniques is the high cooling power requirement of ARPES. This requirement stems from a fundamental measurement constraint: the (current) lack of “electron windows,” allowing free-space propagation of said electrons, in a manner that would preserve the energy and momentum information carried by photoelectrons emitted by the (thermally shielded) sample. A hypothetical electron window, maintained at cryogenic temperatures, would allow photoelectrons to propagate from the sample to the detector (at room temperature), while blocking black body radiation from said detector.⁴ In contrast, free-space techniques such as neutron scattering and muon spin spectroscopy do not face this limitation, since the corresponding sub-atomic particles, i.e. neutrons and muons respectively, can pass through the radiation shields of (say) a dilution refrigerator without significant impacts on the measurement signal. Alternatively, experiments involving *primarily* guided electron propagation, like (say) electrical transport and scanning tunneling spectroscopy, have the advantage of isolation from ambient heat sources by thermally heat sinking the current-carrying wires to one or more low-temperature thermal reservoirs using (say) “bobbins” (c.f. Sec. 7.6.3.3).⁵

7.1.2 Design requirements for sub-Kelvin ARPES

The most important step in finding unorthodox applications for advanced cryogenic technologies is defining the requirements and limitations of the target application. For ARPES, the cryogenic system needs to meet the following requirements:

1. **High cooling power:** ARPES requires free-space electron propagation with state-of-the-art high-resolution analyzers constrained to room temperature operation. Therefore, there is no way around exposing the sample to a heat load on the order of 10s of milliWatts. This requirement precludes the use of current dilution refrigerator technology.
2. **Infinite hold time:** at a synchrotron beamline, the amount of time allotted per user is limited. Therefore, logistically these beamlines are kept operational 24×7 . This requirement precludes the possibility of a sorption-pump-based Helium-3 system.
3. **Cryogenic vacuum seals:** the choice of materials used in construction and handling of the cryostat is severely constrained by their ability to withstand temperature extremes: sub-K (sample) to 450 K (bake-out). While permanent seals, like welding and brazing, can withstand these extremes, temporary seals, like ConFlat-style Copper gaskets, are less reliable sealants at cryogenic temperatures.
4. **Load-lock capability:** the sample needs to be either (a) cleaved under UHV, or (b) transferred from the growth to the analysis chamber without leaving the UHV environment. Due to potentially month-long bake-out times, venting the system for each new sample is impractical. Moreover, due to space constraints inside the cryostat, as a result of radiation shielding requirements, loading more than one sample at once, followed by measurement in parallel, is also impractical. Therefore, the cryostat needs a *sequential* sample load-lock (c.f. Sec. 6.3.7).

⁴With current state-of-the-art technology, cooling the detector to cryogenic temperatures is significantly more technically challenging than increasing the cooling power of the cryostat.

⁵While free-space electron propagation is possible, like (say) from the tunneling tip to the sample, majority of the electrical current delivery is guided by cryogenically heat-sunk wires.

7.1.3 Principle of operation of a Helium-3 cryostat

Similar to the pumped Helium-4 systems, which I briefly discussed in Sec. 7.1.1.1, the Helium-3 cryostat can achieve temperatures below its boiling point by reducing the cryogen (i.e. Helium-3) vapor pressure. Therefore, the performance of the cryostat can be quantified by studying the relationship between vapor pressure, P_{vap} , above and temperature, T , of the cryogen. Fig. 7.1.1 shows the $P_{\text{vap}}-T$ curves for common cryogens.

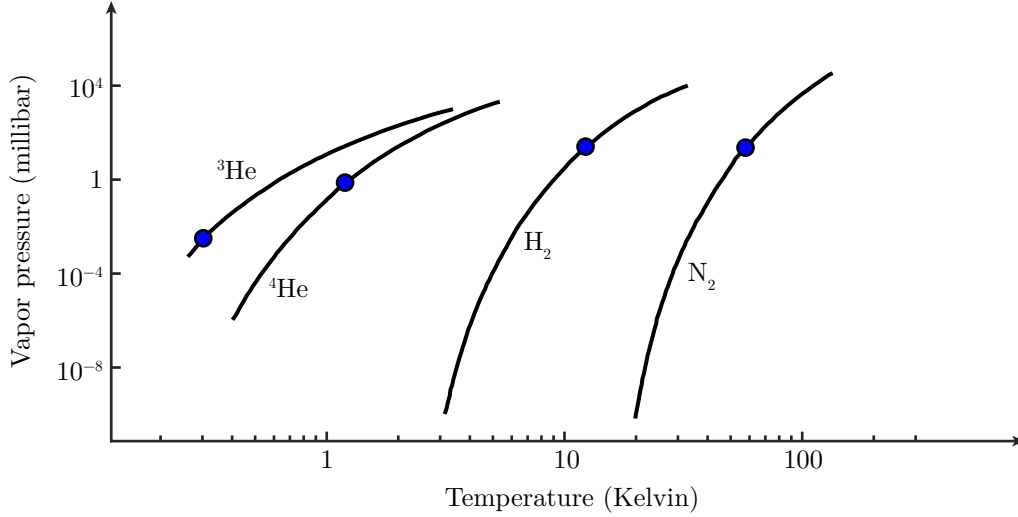


Figure 7.1.1: Vapor pressure as a function of temperature for common cryogens [85]. The blue circles correspond to the cooling limit due to practical pumping limitations. Note that H_2 and N_2 solidify at lower temperatures.

The first-order liquid-gas phase transition is modeled by the Clausius-Clapeyron relation

$$\frac{dP_{\text{vap}}}{dT} = \frac{L_{\text{vap}}}{T(V_{\text{gas}} - V_{\text{liq}})}, \quad (7.1.1)$$

where L_{vap} is the latent heat of vaporization and $V_{\text{gas}}/V_{\text{liq}}$ are the volumes of the cryogen in its gaseous/liquid state. By approximating L_{vap} to a constant and assuming $V_{\text{gas}} \gg V_{\text{liq}}$, and assuming the ideal gas law

$$P_{\text{vap}}V_{\text{gas}} = n_{\text{gas}}k_{\text{B}}T,$$

where n_{gas} is the number of gas atoms and k_{B} is the Boltzmann constant, Eq. (7.1.1) can be solved to give

$$P_{\text{vap}} \propto \exp\left[-\left(\frac{L_{\text{vap}}}{n_{\text{gas}}k_{\text{B}}}\right)\frac{1}{T}\right], \quad (7.1.2)$$

Eq. (7.1.2) approximately reproduces Fig. 7.1.1.⁶

An important figure of merit for a cryostat is its cooling power. Therefore, it is instructive to derive an approximate expression for the cooling power of a cryogen, whose temperature (T) is lowered, by lowering its vapor pressure (P_{vap}) using an external pump according to Eq. (7.1.2). When an atom evaporates from the liquid phase of the cryogen, it absorbs the latent heat of vaporization per

⁶In general, Eq. (7.1.2) will be invalid when L_{vap} depends strongly on T . For example, for the sake of simplicity, Fig. 7.1.1 ignores the superfluid or λ transition in Helium-4, where L_{vap} can no longer be treated as T independent.

atom (\bar{L}_{vap}) from said cryogen, and gets removed by the external pump. This process results in a *net* removal of heat from the cryogen.

If the number of atoms evaporating per unit time is denoted Γ_{vap} , then the rate of heat removal, W_{cool} , or cooling power, will be given by

$$W_{\text{cool}} = \bar{L}_{\text{vap}}\Gamma_{\text{vap}}. \quad (7.1.3)$$

Under equilibrium, the rate of atoms evaporating per unit time is equal to the rate of atom removal by the pump. Therefore, Γ_{vap} is equal to Q_{pump} defined in Sec. 6.1.2.1. Then using a time-independent version of Eq. (6.1.2), and plugging it in (7.1.3), I get

$$\begin{aligned} W_{\text{cool}} &= \bar{L}_{\text{vap}}P_{\text{vap}}S_{\text{pump}}, \\ &\propto \exp\left[-\left(\frac{L_{\text{vap}}}{n_{\text{gas,eq}}k_{\text{B}}}\right)\frac{1}{T}\right]S_{\text{pump}}, \end{aligned} \quad (7.1.4)$$

where in the second line of Eq. (7.1.4) I have simply plugged in Eq. (7.1.2). Moreover, $n_{\text{gas,eq}}$ is defined as the number of atoms in the gaseous phase under equilibrium between the pump and rate of evaporation.

The most striking observation from Eq. (7.1.4) is the disparity in the scaling of W_{cool} with T as opposed to S_{pump} . In other words, while cooling power is exponentially suppressed at lower temperatures, the former only increases linearly with the pump's speed. Therefore, practical limitations of pumps typically limit the base temperature achievable with most cryogens.

7.2 Overview of subsystems

In this section, I will give a broad overview of the various logical subsystems and their respective roles in the operation of the cryostat. The details of these subsystems will be discussed in Sections 7.3-7.6. For the following discussion, refer to Fig. 7.2.1.

The cryostat can be divided into the following subsystems:

- **Shielding structures:** the role of these types of components is isolation of performance-critical subsystems from the environment. This includes both vacuum barriers and cryogenic shielding.
- **Helium-3 insert:** this subsystem is directly responsible for generating the coldest point in the cryostat: the Helium-3 pot. Therefore, the shielding structures shield the Helium-3 insert. The Helium-3 insert is an important component of the closed-loop Helium-3 plumbing circuit. It is responsible for cooling room temperature Helium-3, in stages, until it condenses inside the Helium-3 pot. The condensation process is assisted by an external pump and an open-loop Helium-4 circuit called the “1 K system.” The Helium-3 pot conductively cools down the sample through the cold finger.
- **Sample manipulation system:** this subsystem consists primarily of mechanical feedthroughs which enable five-axis manipulation of the sample being measured using ARPES.
- **Electrical network:** temperature sensors, heaters, and their wiring architecture form the electrical network inside the cryostat.

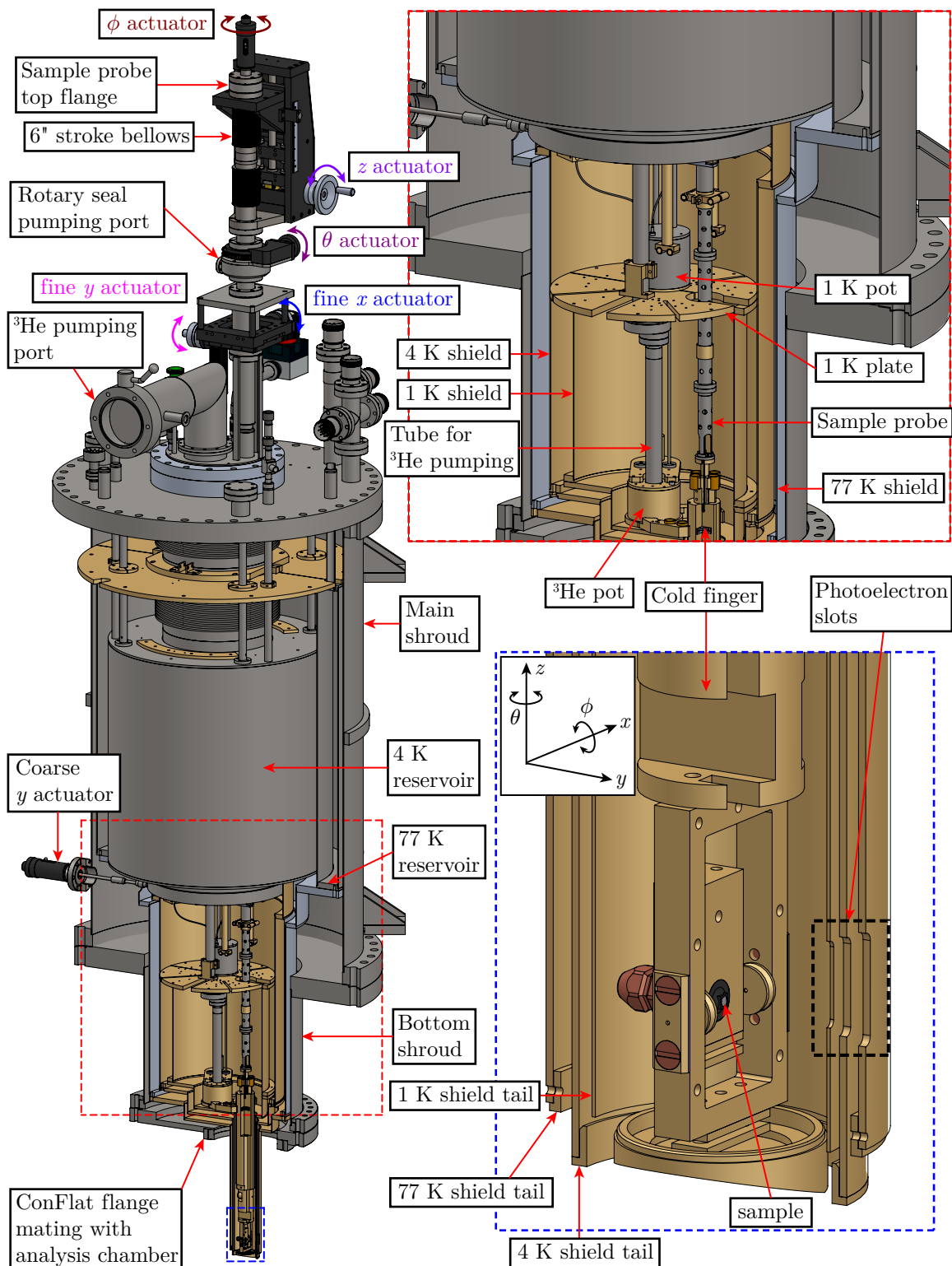


Figure 7.2.1: The full height partial section view of the cryostat with the insets zooming into the lower parts. The inset inside the larger blue dashed box shows the coordinate system definition close to the zoomed in view of the CAD model of the sample. The manipulators of the five degrees of freedom (x , y , z , θ , ϕ) have been highlighted at the top and middle of the cryostat. Only the y coarse actuator is visible in this view.

7.3 Shielding structures

7.3.1 Cryogen reservoirs

As I discussed in 7.1.2, the ARPES Helium-3 cryostat demands high cooling power and long hold times. In order to meet these two requirements, the cryostat has two built-in dewars, one containing liquid Nitrogen, and the other containing liquid Helium-4. The primary goal of the former is shielding the latter from black-body radiation. Moreover, due to the high latent heat of vaporization of liquid Nitrogen (≈ 6 kJ/mol), losses from boil off are much smaller than liquid Helium-4 (≈ 85 J/mol).

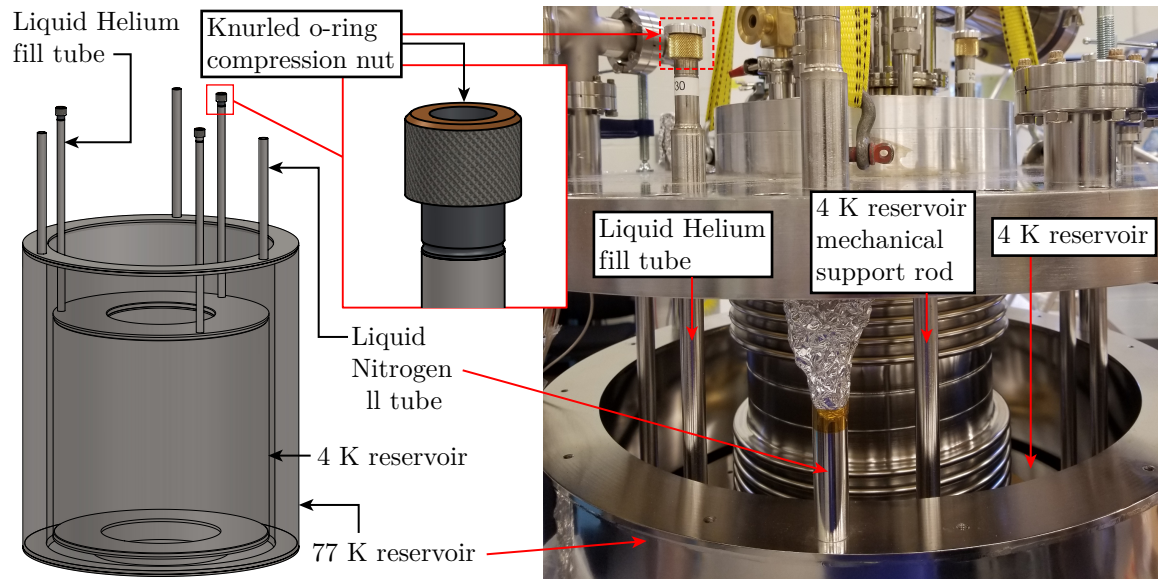


Figure 7.3.1: CAD model (left) and photograph (right) of the liquid Nitrogen and liquid Helium-4 reservoirs.

Fig. 7.3.1 shows simplified CAD models of the liquid Nitrogen and liquid Helium-4 reservoirs. The liquid Nitrogen reservoir (a.k.a. 77 K reservoir) forms a closed annular volume only accessible through three so-called “fill tubes.” These three tubes, in either reservoir, are used for filling liquid cryogen, venting boiled off gas, and inserting a cryogen level sensor.

The liquid Helium-4 reservoir (a.k.a. 4 K reservoir) has a hole in the middle such that an appropriately-sized object can be immersed in liquid Helium-4 for cooling. I will later show in Sec. 7.4 that this object is the Helium-3 insert. It’s worth noting that the top of the 4 K reservoir is not open in the way shown in Fig. 7.3.1. A bellows connects the top hole and to vacuum flange (c.f. Fig. 7.3.2), thus making the 4 K reservoir closed like the 77 K reservoir. The representation in Fig. 7.3.1 was chosen for ease of visualization.

An important difference between the 4 K and 77 K reservoirs is that the former needs to be sealed to avoid water vapor condensation. Therefore, the three fill tubes of the 4 K reservoir have threaded ends to accommodate an o-ring compression nut;⁷ this type of connection is commonly referred to as the “quick disconnect.” Connections to Helium-4 transfer lines or bayonets, bleed valves, and blanks can be made with the quick disconnect connectors. I will discuss the importance of avoiding moisture in the 4 K reservoir in Sec. 7.7.1.2.

⁷The o-rings won’t form a vacuum-tight seal during normal cryostat operation because of their loss of elasticity at lower temperatures. However, at room temperature, these quick disconnect connectors can be used to (say) pump on the 4 K reservoir for diagnostics. The leak in the 4 K reservoir was discovered using this method (c.f. Sec. 7.8.1.1).

7.3.2 Ultrahigh vacuum

7.3.2.1 Reservoir insert

The cryogen reservoirs I discussed in Sec. 7.3.1 are fixed relative to one another by a custom 27.125" outer diameter (OD) wire seal blank flange; I'll refer to it as the "top flange" (c.f. Fig. 7.3.2). Moreover, the weight of both reservoirs is supported by a welded connection to the top flange. In addition to being load-bearing, this welded connection also serves as a vacuum seal. The welded vacuum seal is made on the three fill tubes for both reservoirs. For the liquid Helium-4 reservoir, an additional welded vacuum seal is made with the top flange via a hydraulically formed bellows. I will refer to this entire assembly as the "reservoir insert."

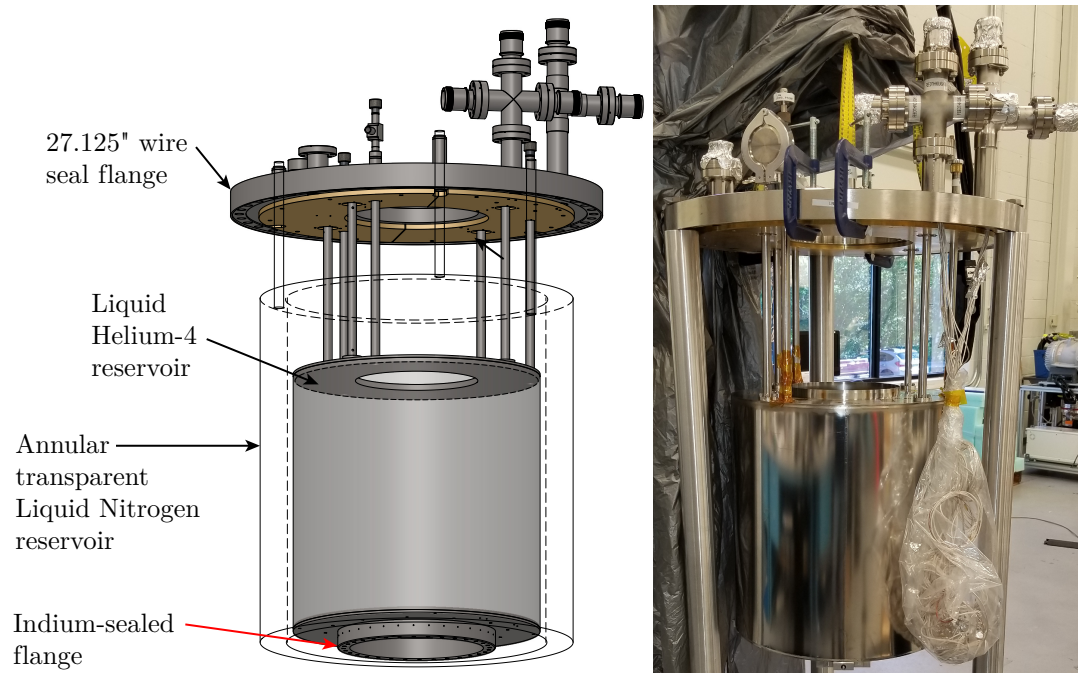


Figure 7.3.2: CAD model (left) and photo (right) of the reservoir insert. The bellows on the liquid Helium-4 reservoir is not shown for visual clarity.

Fig. 7.3.2 shows both a CAD model and a photo of the reservoir insert. In the former, I have shown a transparent liquid Nitrogen reservoir to illustrate their relative locations. As the name suggests, the reservoir insert is inserted into a long vertical vacuum can known as the "main shroud." Details of the main shroud are presented in Sec. 7.3.2.2. Fig. 7.3.2 illustrates another important feature of the reservoir insert: the liquid Helium-4 reservoir has an indium-sealed flange at the bottom. This flange mates with the Helium-3 insert discussed in Sec. 7.4.3.

7.3.2.2 Main shroud

The atmosphere-to-UHV barrier enclosing most of the liquid Nitrogen and Helium-4 reservoirs is referred to as the "main shroud." The CAD model and photo of the main shroud is shown in Fig. 7.3.3. The main shroud is a (vertical) custom stainless steel nipple with a 24" outer diameter (OD) tube and two 27.125" OD wire seal flanges at the top and bottom. The flange-to-flange distance is ≈ 40 ".

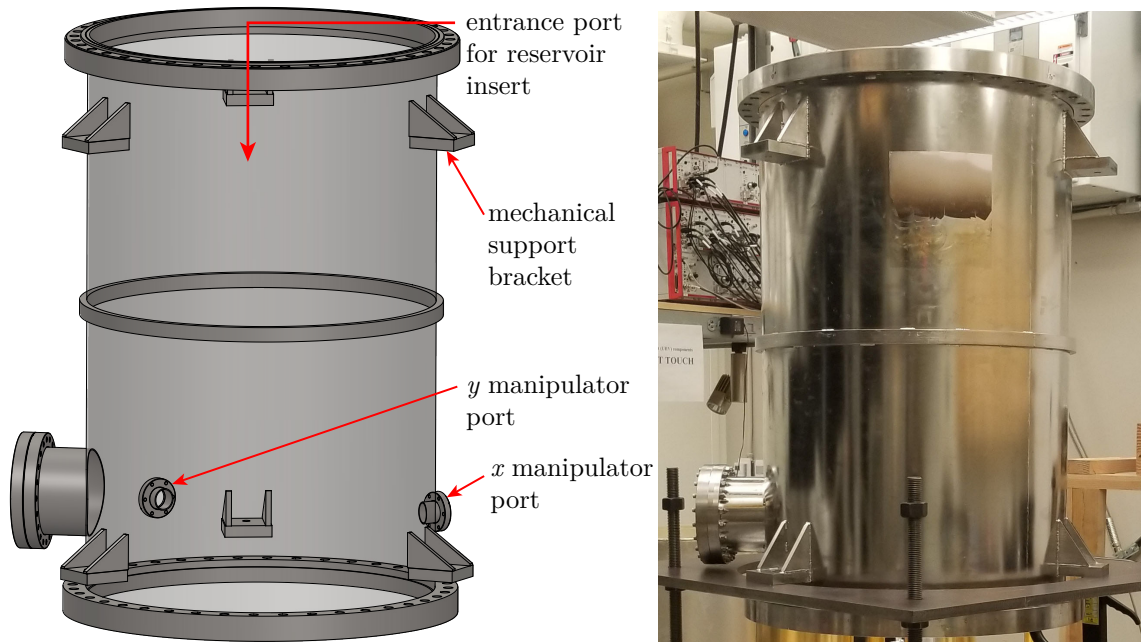


Figure 7.3.3: CAD model and photograph of the main shroud

The reservoir insert (c.f. Sec. 7.3.2.1) enters the main shroud through and mates with the top flange. The main shroud also has two horizontally inward-pointing 2.75" OD ConFlat flanges at 90° with respect to each other. These two ports are used for attaching mechanical feedthroughs for controlling the coarse x - y stage.

7.3.2.3 Bottom shroud

The bottom shroud attaches to the bottom 27.125" OD wire-seal flange of the main shroud (c.f. Fig. 7.3.3). The 8" ConFlat flange, at the bottom of the bottom shroud, attaches to the top flange of the analysis chamber (c.f. Fig. 6.3.3). The cylindrical tube in the middle encloses the bottom of the radiation shields⁸ and the Helium-3 pot. The reason for dividing the cryostat's atmosphere-to-UHV barrier into the main and bottom shroud is ease of assembly.

During assembly, a connection between the following components has to be made *after* the reservoir insert (c.f. Fig. 7.3.2) is mated with the main shroud (c.f. Fig. 7.3.3): (a) the coarse x - y stage (c.f. Fig. 7.3.5 and Sec. 7.5.2.4) located at the bottom of the 4 K reservoir, and (b) the x and y linear mechanical feedthroughs located on the main shroud (c.f. Fig. 7.3.3). This connection can only be made when the bottom shroud is detached from the main shroud. Moreover, the clearance offered by this configuration allows convenient attachment of the radiation shields (c.f. Fig. 7.3.5) to their respective reservoirs.⁹

⁸The shield tails start close to the the 16.5"-to-8" ConFlat reducer at the bottom of the bottom shroud (c.f. Fig. 7.3.4).

⁹In principle, the radiation shields can be attached to their respective reservoirs (c.f. Fig. 7.3.5) prior to mating the reservoir insert (7.3.2) and main shroud (c.f. Fig. 7.3.3). But it is not possible to do so inside the Caltech lab (B203 Downs) due to ceiling height limitations.

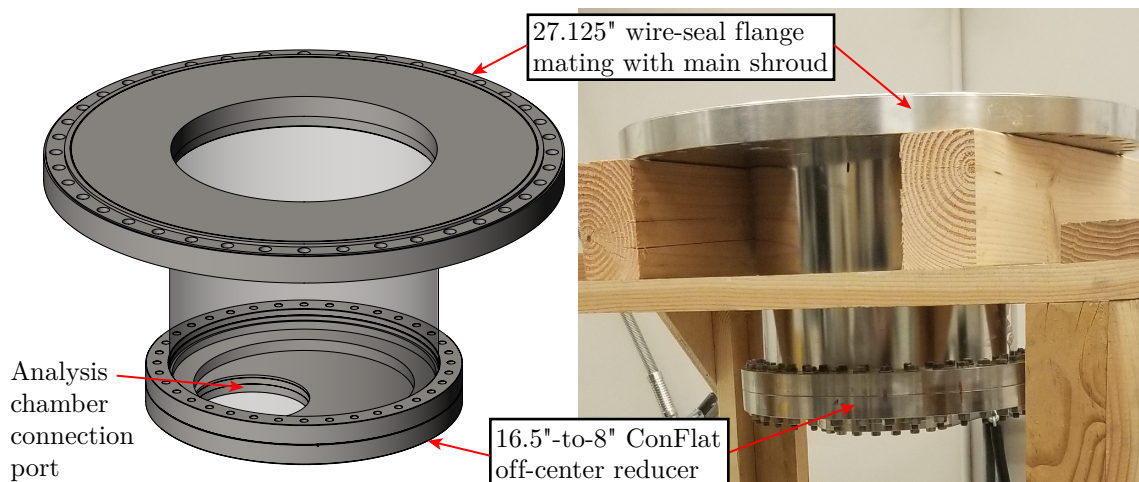


Figure 7.3.4: CAD model and photograph of the bottom shroud

7.3.3 Radiation shields

The radiation shields are extensions of their respective cryogen reservoirs (c.f. Sec. 7.3.1) and hence serve the same role: blocking heat loads from external black body radiation. The difference is that the former shield the UHV section of the Helium-3 insert, sample probe, and cold finger. The connection of the 4 K and 77 K radiation shields to their respective reservoirs is illustrated in the CAD model in Fig. 7.3.5.

The 4 K and 77 K radiation shields are made of oxygen-free high-conductivity (OFHC) Copper and Aluminum respectively. As shown in the photograph in Fig. 7.3.5, the 4 K and 77 K radiation shields are gold- and silver-plated, respectively, to achieve higher thermal conductivity across bolted connections. Moreover, gold/silver plating also mitigates the loss of emissivity from handling and exposure to atmosphere.¹⁰ The tail of the 77 K shield was later gold-plated during optimization of the ARPES spectrum (c.f. Chap. 8).

For ease of assembly, the shields are divided into two sections. The lower sections primarily shield the cold finger from black body radiation; they are called shield tails.¹¹ The shield tails contain slots and holes for transmission of electrons and photons, respectively, during an ARPES measurement. The hole at the bottom of the shield tails is covered by so-called bottom shields (c.f. Fig. 7.5.8) with spring-loaded doors, which are used for sample loading.

There is a third shield called the 1 K shield and its corresponding tail. From the point of view of cryostat construction, it makes sense to consider the 1 K shield as part of the Helium-3 insert. Therefore, details of the 1 K shield are discussed in Sec. 7.4.2.3.

7.4 Helium-3 insert

The Helium-3 insert is the most critical subsystem from a cooling perspective. The Helium-3 insert is directly responsible for achieving sub-Kelvin temperatures due to the pre-cooling and radiation shielding offered by the shielding structures (c.f. Sec. 7.3). The Helium-3 insert consists of two main subsystems: 1 K and Helium-3. These subsystems are discussed in detail in Sec. 7.4.2 and Sec. 7.4.3.

¹⁰Moreover, as can be noted in Fig. 7.3.5, gold plating is more durable since silver tarnishes over time.

¹¹The top section of the shields don't have a qualifier. They are simply referred to as shields.

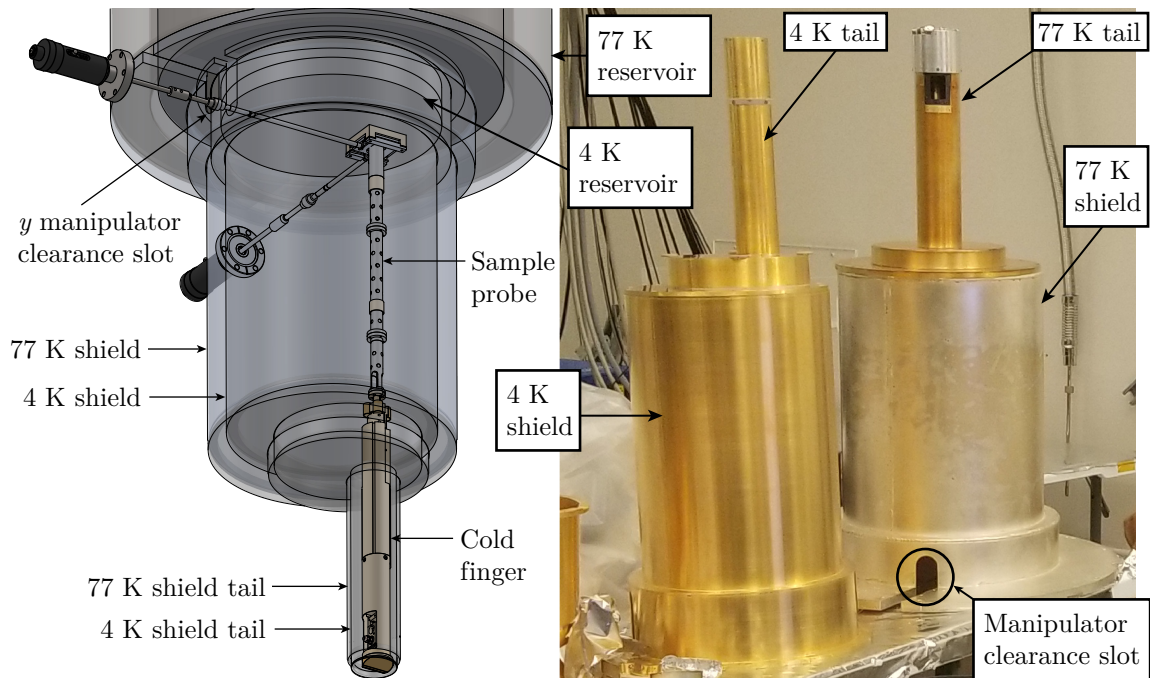


Figure 7.3.5: CAD models and photograph of the 4 K and 77 K shields. The Helium-3 insert is not shown in the CAD model.

7.4.1 Helium-3 insert overview

7.4.1.1 Construction

A full view of the Helium-3 insert is shown in the CAD model Fig. 7.4.1. As I briefly mentioned in Sec. 7.3.1, the hole in the middle of the 4 K reservoir is filled by the Helium-3 insert. The Helium-3 insert can be divided into two regions based on the vacuum environment: (a) atmosphere, and (b) UHV. The Indium-sealed flange above the 1 K pot separates these two volumes.

The attachment process of the Helium-3 insert to the 4 K reservoir is shown in the photographs in Fig. 7.4.1. The insets show the details of the flange making the atmosphere-to-UHV seal using Indium. As I briefly mentioned in Sec. 6.3.5.6, this flange was originally supposed to be ConFlat. However, the manufacturer (MDC Vacuum Products, LLC) could not guarantee a reliable seal at 4 K. Hence the ConFlat flange was re-machined, such that the ConFlat knife edge was removed, and a groove was added to accommodate a 0.040" Indium wire.

At the top of the insert, a pair of o-ring-sealed flanges make an “atmosphere-to-atmosphere” seal. The primary role of this seal is keeping water vapor out of the 4 K reservoir. In fact, recall that this moisture isolation scheme is implemented for all ports of the 4 K reservoir (c.f. Sec. 7.3.1). I will discuss the importance of this seal in Sec. 7.7.1.2.

7.4.1.2 Insert components at atmosphere

The components of the Helium-3 insert above the Indium-sealed flange mainly consist of fluid and mechanical feedthroughs (c.f. Sec. 6.3.6). These feedthroughs require cooling, thermal isolation, and heat exchange mechanisms because they interface with room temperature components. Therefore, a

significant fraction of their surface area is in direct contact with liquid Helium-4 in the 4 K reservoir. Heat exchange between the Helium-3 gas flowing in and out of the insert is achieved through direct contact of the tubes carrying said gas. The thermal contact is increased by coiling the tube returning Helium-3 around the tube pumping it out.

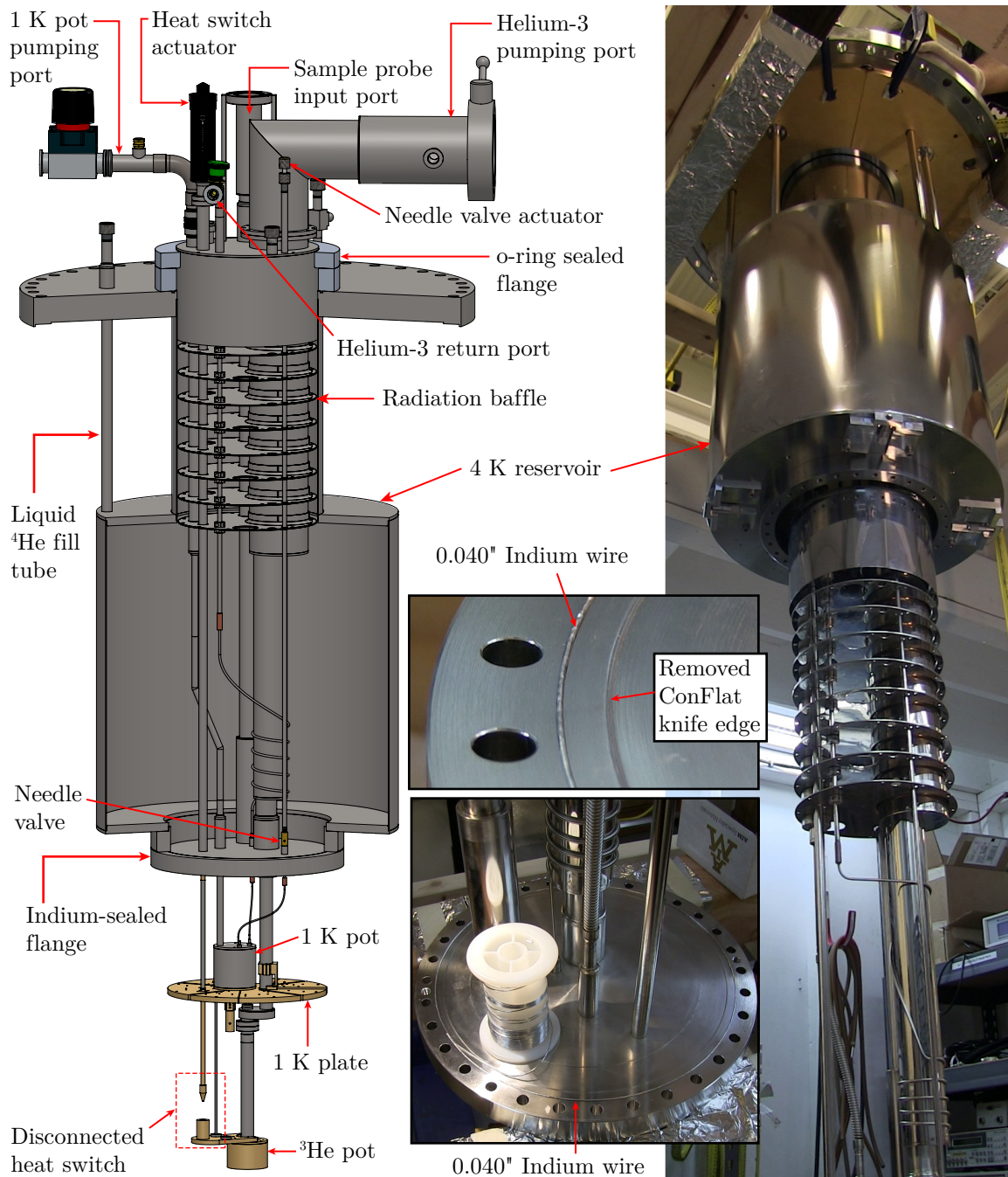


Figure 7.4.1: Left: CAD model of the full Helium-3 insert with a section view of the 4 K reservoir. Right: Photograph of Helium-3 insert being raised for attachment to the 4 K reservoir. The insets show details of the Indium seal.

Another element which assists heat exchange is the stack of the radiation baffles at the neck of the 4

K reservoir. The primary role of the baffles, however, is shielding the liquid Helium-4 inside the 4 K reservoir from 300 K black body radiation. This shielding reduces the liquid Helium-4 boil off rate.¹² Moreover, these baffles generate a large flow resistance for the boiled off Helium-4 gas escaping the 4 K reservoir. Consequently, the relatively cold Helium-4 vapor carries heat away from the baffles as the former escapes through a vent valve at the top of the Helium-3 insert.

An o-ring-sealed knurled knob at the top of the insert controls the angle of a shaft which controls the conductance of the needle valve (c.f. Sec. 7.4.2.2). This valve consists of a needle-shaped “plug.” The degree to which the plug blocks flow of fluids through an orifice is controlled by a fine-threaded shaft end screwing into the nut containing the orifice (c.f. Fig. 7.4.3).

7.4.1.3 Insert components at UHV

Below the Indium-sealed flange, the 1 K and Helium-3 pots are placed under UHV. As shown in the CAD model in Fig. 7.4.1, the mechanical heat switch maintains a temperature gradient, from 300 K at the top linear feedthrough, to 1.5 K at the bottom near the 1 K pot. Similar to the sample probe (c.f. Sec. 7.5.1.1), the shaft transmitting mechanical power to the heat switch is thermally anchored to the bottom of the 4 K reservoir and 1 K plate.¹³

7.4.2 1 K system

7.4.2.1 1 K pot

Similar to the liquid Nitrogen and liquid Helium-4 reservoirs, discussed in Sec. 7.3.1, the 1 K pot acts like a mini-reservoir. The 1 K pot is responsible for both pre-cooling and maintaining certain parts of the cryostat below 4 K. Moreover, like other reservoirs, the 1 K pot has a corresponding “1 K shield” (c.f. Sec. 7.4.2.3) which blocks the 4 K black body radiation heat load to components of the Helium-3 circulation system.

Fig. 7.4.2 shows a photograph of the region of the Helium-3 insert close to the 1 K pot. The 1 K pot is a cylindrical container with a capacity of 150 mL. The top and side walls of the 1 K pot are made of stainless steel, with the appropriate cryogen-carrying tube connections, such that all UHV seals are made via either welding or soldering. The bottom of the 1 K pot is made of (gold-plated) copper which is in thermal contact with a circular gold-plated copper plate known as the “1 K plate.” The bottom plate of the 1 K pot has one cryogen-carrying (detachable) VCR connector.

In addition to providing radiation shielding, the 1 K pot is responsible for the liquefaction of Helium-3 in its closed-loop plumbing circuit. Prior to the condensation of Helium-3 in its pot, the 1 K pot is the only component of the cryostat with a temperature (≈ 1.5 K) lower than the boiling point of Helium-3 (3.2 K); this makes the 1 K pot the only available coolant for Helium-3 liquefaction.¹⁴ Therefore, the capillary carrying Helium-3 gas towards its pot is passed through the 1 K pot (c.f. Fig. 7.4.6). The male VCR connector at the bottom of the 1 K pot connects to a condensing impedance (c.f. Sec. 7.4.3.2) which helps build sufficient Helium-3 gas pressure to achieve condensation.

¹²Liquid Helium-4 is a scarce and expensive resource in a wet system like this.

¹³The thermally anchoring braids are not shown in the CAD model in Fig. 7.4.1 for visual clarity. Photographs of these braids are shown in Fig. 7.4.5 (1.5 K), Fig. 7.5.1 (1.5 K), and Fig. 7.5.6 (4 K).

¹⁴Actually, the 1 K pot was specifically introduced for condensing Helium-3.

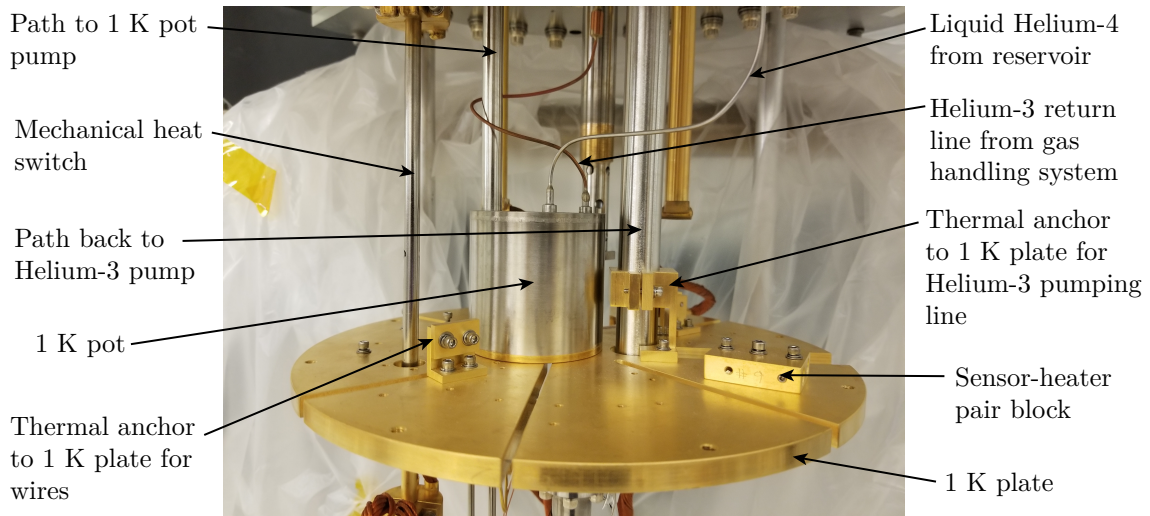


Figure 7.4.2: Photograph of the region of Helium-3 insert containing the 1 K pot, 1 K plate, and related components.

7.4.2.2 Helium-4 open circuit

The layout of components involved in generating the cooling action in the 1 K pot are shown in Fig. 7.4.3 (except the pump). A thin capillary carries liquid Helium-4 from the bottom of the 4 K reservoir to the 1 K pot. Liquid Helium-4 starts accumulating inside the 1 K pot after said pot reaches a temperature of 4 K. The largest stainless steel tube, connected at the top of the 1 K pot, leads to an external pump which provides a high mass conductance of gaseous Helium-4. Therefore, the lowering of the vapor pressure inside the 1 K pot, according to the Clausius-Clapeyron relation (c.f. Eq. (7.1.1)), results in the lowering of boiling point of the liquid Helium-4 inside the 1 K pot.

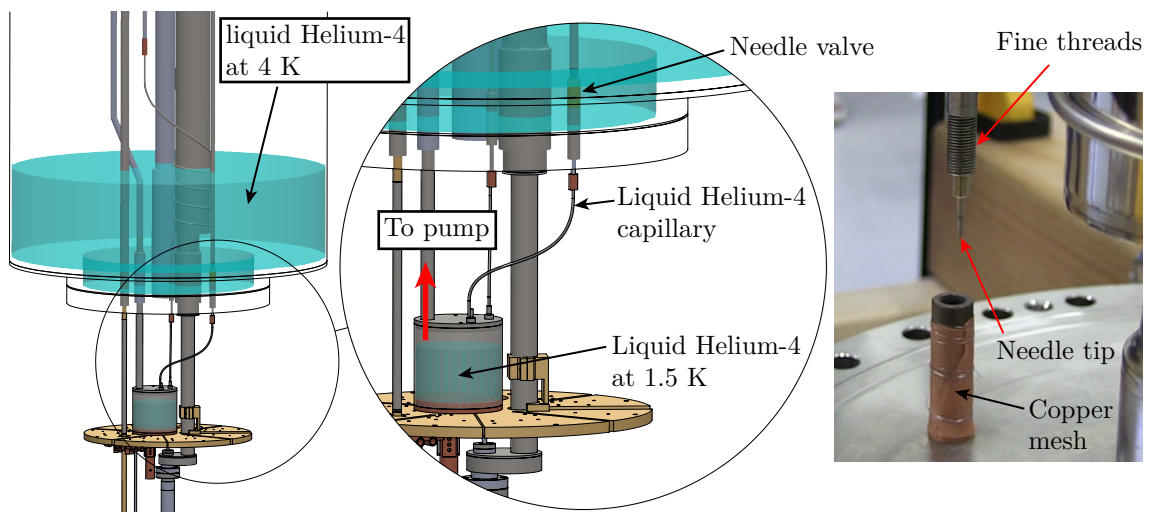


Figure 7.4.3: The CAD model shows the 1 K pot plumbing (open) circuit with the 4 K reservoir made transparent. The photograph shows the needle valve whose conductance can be tuned using the fine threads. The copper mesh covers the inlet of the needle valve to avoid clogging from contaminants.

This layout, referred to as a “plumbing circuit,” is considered open because the Helium gas removed

from the 1 K pot is not fed back into the 4 K reservoir.¹⁵ Nevertheless, a quasi steady-state condition is reached, in the 1 K pot, when the rate of inflow of liquid Helium-4 from the 4 K reservoir equals the rate outflow of gaseous Helium-4 to the external pump. The former can be controlled used a so-called “needle valve.” The quasi steady-state condition was empirically found to be stable over different values of liquid Helium-4 inflow rates (i.e. needle valve setting).

To first order, the rate of liquid Helium-4 inflow controls the amount of 4 K heat load on the 1 K pot.¹⁶ Hence reducing the inflow rate lowers the temperature of the 1 K pot. However, lowering the inflow rate too much can disturb the quasi steady-state condition. The balance between these competing factors determines the base temperature of the 1 K pot. In practice, the needle valve conductance needs to be fine-tuned during each cool down. The lowest 1 K pot temperature achieved to date is 1.56 K.

7.4.2.3 1 K plate and shield

The 1 K plate serves as an extension of the 1 K pot. The 1 K plate is machined out of a single circular copper plate of 9.5" diameter and 0.3125" thickness followed by gold-plating. Due to the high conduction path between the 1 K pot and plate (c.f. Fig. 7.4.2), the temperature difference between the two was never found to exceed a few 10s of mK under normal operation. The various holes and slots in the plate provide clearance for the sample probe (c.f. Sec. 7.5.1.1) and tubes carrying gases or liquids.

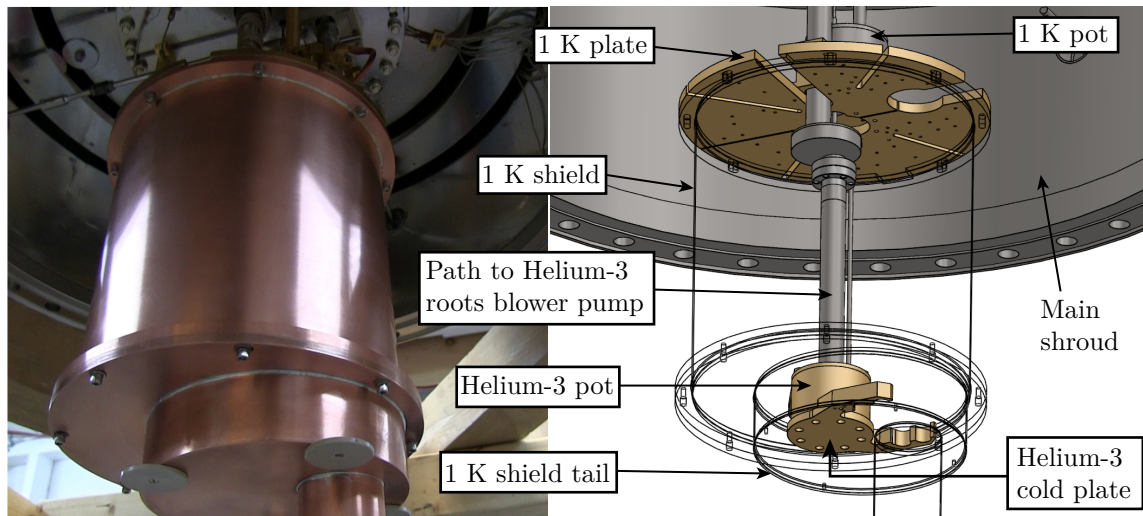


Figure 7.4.4: Photograph of the region of Helium-3 insert containing the 1 K pot, 1 K plate, and related components.

Fig. 7.4.4 shows how the 1 K shield and tail¹⁷ are attached to the 1 K plate. As illustrated in the CAD model, the 1 K shield encloses the Helium-3 pot. As a result, the blocking of the 4 K black body radiation allows the Helium-3 pot and related components to get to sub-Kelvin temperatures. For a 1 K shield temperature of ≈ 1.5 K, the Helium-3 pot can sustain a base temperature of ≈ 0.5 K with tens of mW of cooling power. Moreover, the extension of the 1 K shield, called the “1 K tail,” shields the sample and cold finger (c.f. Sec. 7.5.1.2).

¹⁵Turning this circuit into a closed one would require a Helium recovery system. At the time of writing this thesis, a Helium recovery system was not installed.

¹⁶To second order, the 1 K pot experiences heat load from the 4 K radiation shield.

¹⁷The photograph of the 1 K shield and tail was taken during the first cool down test prior to gold plating.

As evident from Fig. 7.4.2, the 1 K plate has a considerable amount of surface area. This available space is used for heat sinking. For example, the Helium-3 pumping line is heat sunk using a gold-plated anchor to the right of the 1 K plate (viewed from Fig. 7.4.2). Moreover, the 1 K plate is also used for attaching auxiliary sensors/heaters and heat sinking wires (c.f. Sec. 7.6.3.3).

7.4.3 Helium-3 system

7.4.3.1 Helium-3 pot

The Helium-3 pot is a mini-reservoir, analogous to the 1 K pot, maintained at a lower temperature (0.5 K). Unlike the 1 K pot, however, the Helium-3 pot is part of a closed loop, where the Helium-3 gas pumped out from its pot is fed back into said pot in liquid form. Photographs of the Helium-3 pot are shown in Fig. 7.4.5.

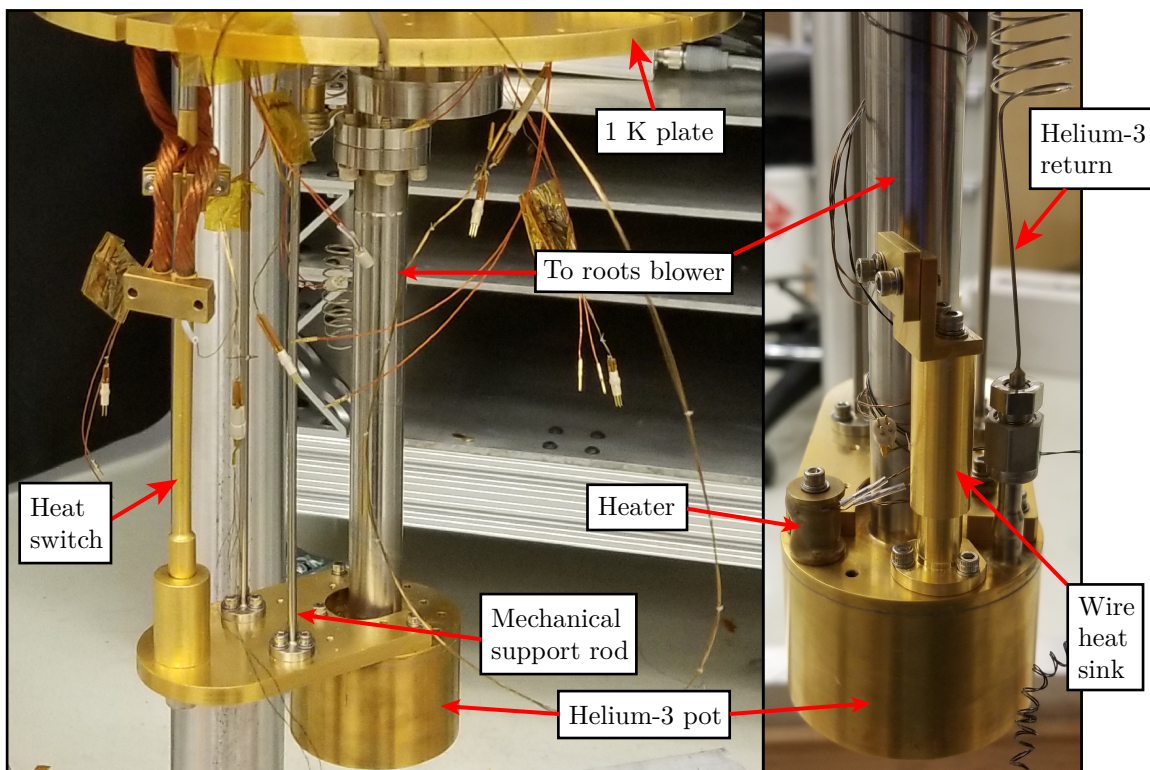


Figure 7.4.5: Photograph of the Helium-3 pot from two different viewing angles.

The Helium-3 pot conductively cools the sample, located on the cold finger (c.f. Sec. 7.5.1.2), using Copper braids. The Helium-3 pot itself is conductively pre-cooled by the 1 K pot. However, the conduction channel between the two pots cannot be permanent. Otherwise, 1 K pot would act as a source of heat load when the Helium-3 pot brings down the boiling point of Helium-3 below 1.5 K. Therefore, the conduction channel between the two pots is established using a mechanical heat switch. Fig. 7.4.5 shows the heat switch in the closed (i.e. conductive) position.

The Helium-3 pot has a temperature sensor and a wire-wound heater to monitor and control its temperature. A thermal anchor on top of the Helium-3 pot allows heat sinking the temperature sensor and heater wires leading to the sample on the cold finger.

7.4.3.2 Condensing impedance

At the end of Sec. 7.4.2.1 I discussed the role of the 1 K pot in accumulating liquid Helium-3 in its pot. The former is the only cryostat component cold enough (≈ 1.5 K) to be maintained below the Helium-3 boiling point (3.2 K). A sketch of the capillary which carries Helium-3 gas towards its pot is shown in Fig. 7.4.6 and has been color-coded to *crudely* illustrate a temperature gradient.¹⁸ However, in order get sufficient amount of liquid in the Helium-3 pot for achieving optimal base temperature and cooling power, the pressure in the capillary needs to be raised to several 10s or few 100s of mbar [85]. This is achieved with a condensing impedance.

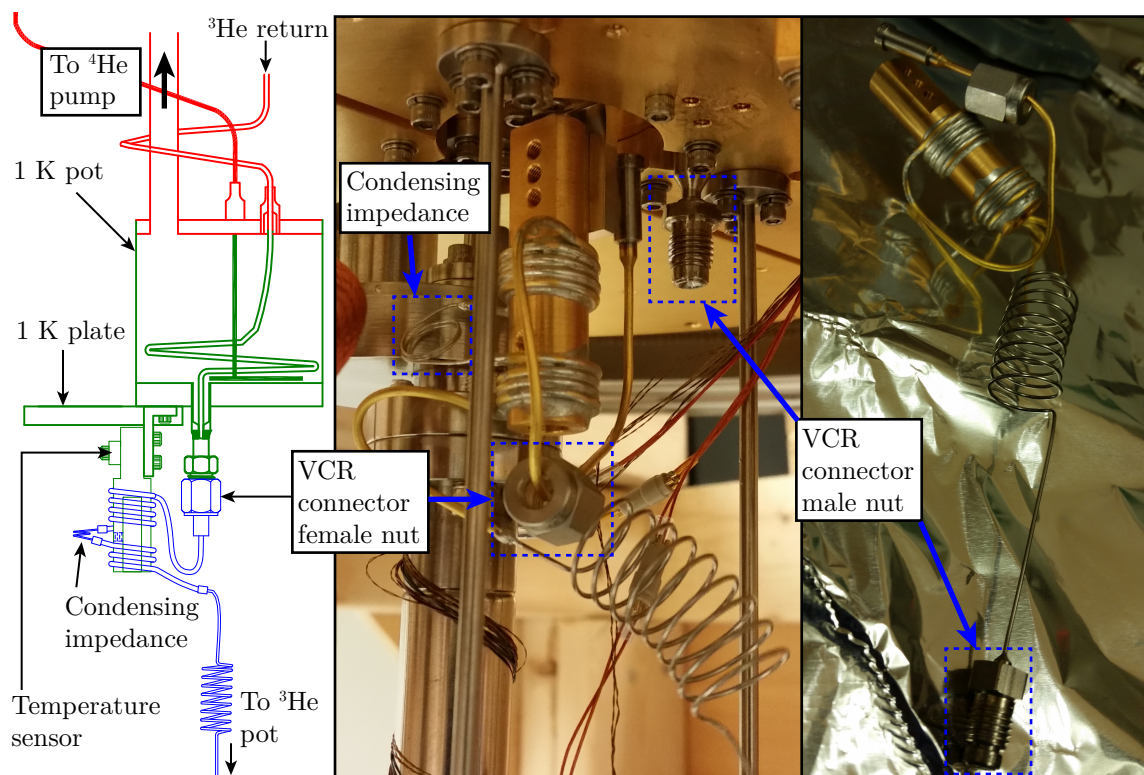


Figure 7.4.6: Left: color-coded sketch of the 1 K pot and condensing impedance. Right: photographs of the condensing impedance attached to the cryostat and in isolation.

The ARPES Helium-3 cryostat has a detachable *condensing impedance unit* whose photograph is shown in Fig. 7.4.6. The unit has two VCR connectors to form UHV seals with the 1 K and Helium-3 pots on each side. The actual impedance (in the unit) is a narrow coiled stainless steel tube connected to two heat sunk gold-plated copper tubes on either side. The gold-plated copper block, to which the copper tubes are heat sunk, is in thermal contact with the 1 K plate, and has a temperature sensor and a 50Ω firerod heater attached. The sensor/heater pair is used for diagnostics and troubleshooting.

7.4.3.3 Conduction paths

As I mentioned earlier, the cooling action performed by Helium-3 is due to a continuous closed-loop cycle. Two of the most important components of the cycle are the Helium-3 pot (c.f. Sec. 7.4.3.1) and

¹⁸Change in Helium-3 temperature is not as abrupt as the transition indicated by the colors in the sketch in Fig. 7.4.6. The three colors simply represent three conceptual stages of the cooling process.

condensing impedance (c.f. Sec. 7.4.3.2) discussed in the previous sections. Both of these components are inside the cryostat. The component which (conceptually) completes the loop is an external one: the pumping station. The manner in which various elements of the loop are interconnected, and the direction of flow of Helium-3, define a specific “plumbing circuit.” Each unique circuit establishes a specific task in the operation of the Helium-3 cryostat. In this section, I will discuss the circuits associated with the following tasks: (a) condensation and (b) circulation.

The pumping station consists of two pumps: roots blower (OKTA 500) and backing pump (Duo 65). Most of the circuits can be implemented with just the latter. The former is only used during “normal circulation” when a large pumping speed ($> 1001/s$) is needed to lower the boiling point of Helium-3. The pumping speed of the backing pump is roughly an order of magnitude lower than the roots blower.

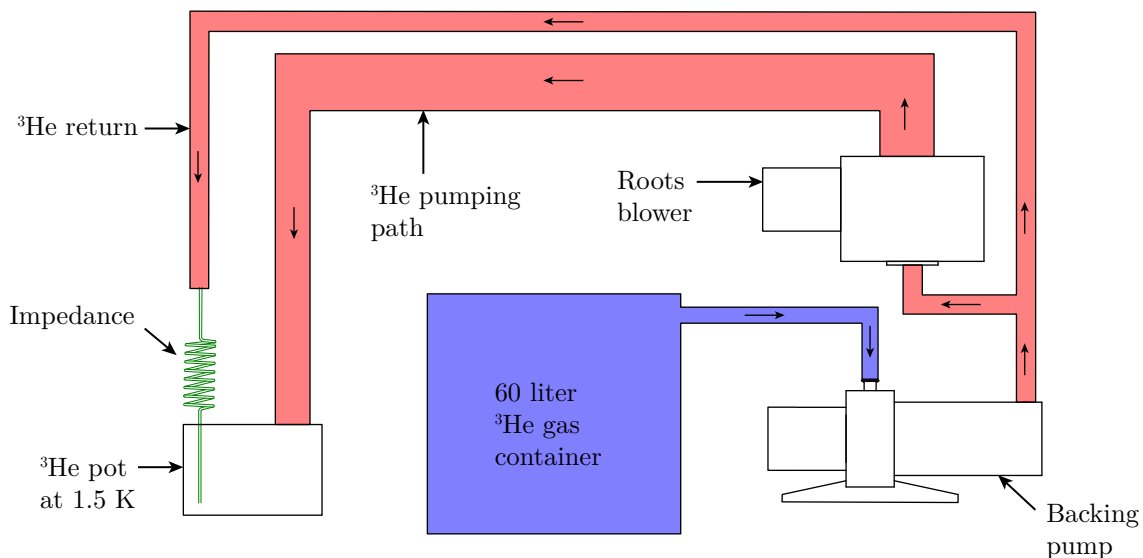


Figure 7.4.7: Gas conduction paths during Helium-3 condensation

I’ll start with the circuit which comes chronologically first in the cool down process: condensation. When the cryostat is not in operation, Helium-3 is stored in gas form in a 60 liter container shown in Fig. 7.4.7. The condensation circuit is only established after the Helium-3 pot has been pre-cooled to 1.5 K by the 1 K pot (c.f. Sec. 7.4.2.2) using the heat switch (c.f. Sec. 7.4.3.1).¹⁹ The boiling point of Helium-3 is 3.2 K.

As shown in Fig. 7.4.7,²⁰ the backing pump is used to transfer Helium-3 gas from its room temperature container to the bottom of the Helium-3 insert at 1.5 K. The exhaust of the backing pump maintains a pressure of a few hundred mbar on *both* sides of the impedance in order to initiate the condensation process. The reason both sides of the impedance are pumped with Helium-3 gas is that the former is designed to maintain a large pressure difference. Therefore, by effectively “shorting out” the impedance,²¹ the condensation process can be expedited with a larger surface at 1.5 K.

Once sufficient amount of Helium-3 has condensed in its pot, the “normal circulation” circuit is established as shown in Fig. 7.4.8. Analogous to the 1 K pot, a steady-state condition is established when the rate of Helium-3 condensation on the higher pressure end (red) matches the rate of evaporation on the lower pressure end (blue). Moreover, due to the reduction in the Helium-3 vapor

¹⁹The heat switch will be disconnected prior to establishing the condensation circuit.

²⁰Due to the complexity of the Helium-3 plumbing circuit, Fig. 7.4.7 and 7.4.8 are shown in block diagram form, in contrast to the *relatively* simple 1 K plumbing circuit (c.f. Fig. 7.4.3).

²¹Pressure difference is analogous to voltage.

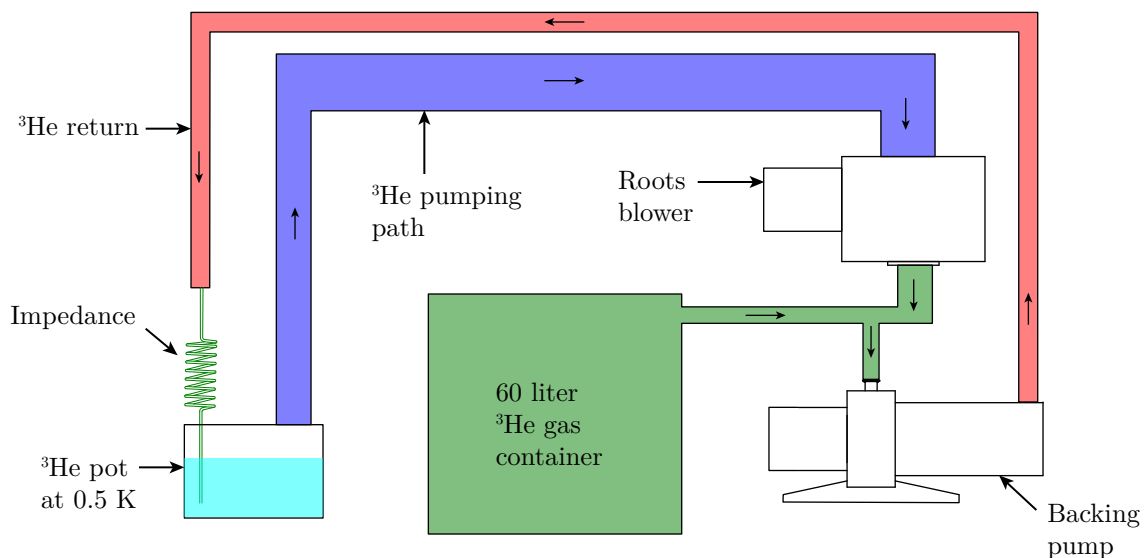


Figure 7.4.8: Gas conduction paths during Helium-3 circulation

pressure due to the high-speed roots blower, boiling point of the liquid Helium-3 accumulated in pot is reduced to 0.5 K.

7.4.3.4 Gas handling system

In Sec. 7.4.3.3, I discussed two of the most important Helium-3 plumbing circuits for the tasks of: (a) condensation and (b) circulation. As evident from Fig. 7.4.7 and Fig. 7.4.8, switching between these two configurations is not possible without valves. Moreover, different circuit configurations are required for maintenance and troubleshooting tasks like leak tests, impedance flow tests, and Helium-3 gas cleaning. In order to accommodate all these requirements, a network of conduction paths and valves is incorporated into a single modular unit known as the gas handling system. Moreover, the 60 liter ^3He gas container (a.k.a. “dump”) is located inside the gas handling system. Due to the technical nature of the design and operation of the gas handling system, its block diagram, and related subsystems, are discussed in Sec. C.2.6.

7.5 Sample manipulation

The components of the Helium-3 ARPES cryostat I discussed in Sec. 7.3 and 7.4 are not unique to ARPES. Of course, some of the requirements discussed in Sec. 7.1.2 influence the aforementioned components; but any changes to these components do not *qualitatively* modify the Helium-3 technology. Moreover, as I alluded at the beginning of Sec. 7.1, an important research and development direction in modern cryogenics is versatility. I will argue that, for the ARPES case, sample manipulation requirements, and consequently measurement constraints,²² was the major barrier in the adoption of Helium-3 technology. In this chapter, I will discuss the developments made in sample manipulation inside a Helium-3 cryostat, which made sub-Kelvin ARPES possible.

²²These two are inseparable.

7.5.1 Motion transfer media

It is obvious that the sample cannot be *directly* coupled to external motional degrees of freedom without heating up the sample. Therefore, there needs to exist a “temperature adapter,” defined such that one end of said adapter is at 300 K, and the other end is at sub-Kelvin temperatures. This adapter consists of a complex subsystem, consisting of several moving parts, which will transfer motion from the external motional degrees of freedom to the sample. The two most important motion transfer media in the ARPES Helium-3 cryostat are: the sample probe and cold finger.

7.5.1.1 Sample probe

The sample probe is a 7 feet long thin-walled stainless steel tube extending from the top of the cryostat to the cold finger (c.f. Sec. 7.5.1.2). It is assembled from shorter tubular sections attached to one another through rigid bolted connections. Assuming perfect rigidity, the sample would perfectly track the sample probe’s x , y , z , and θ coordinates. UHV manipulators at the top of the cryostat control these four degrees of freedom of the sample probe (c.f. Sec. 7.5.2.1, 7.5.2.3, and 7.5.2.2). In practice, however, due to the flexure of the sample probe, additional manipulators are installed closer to the sample (c.f. Sec. 7.5.2.4).

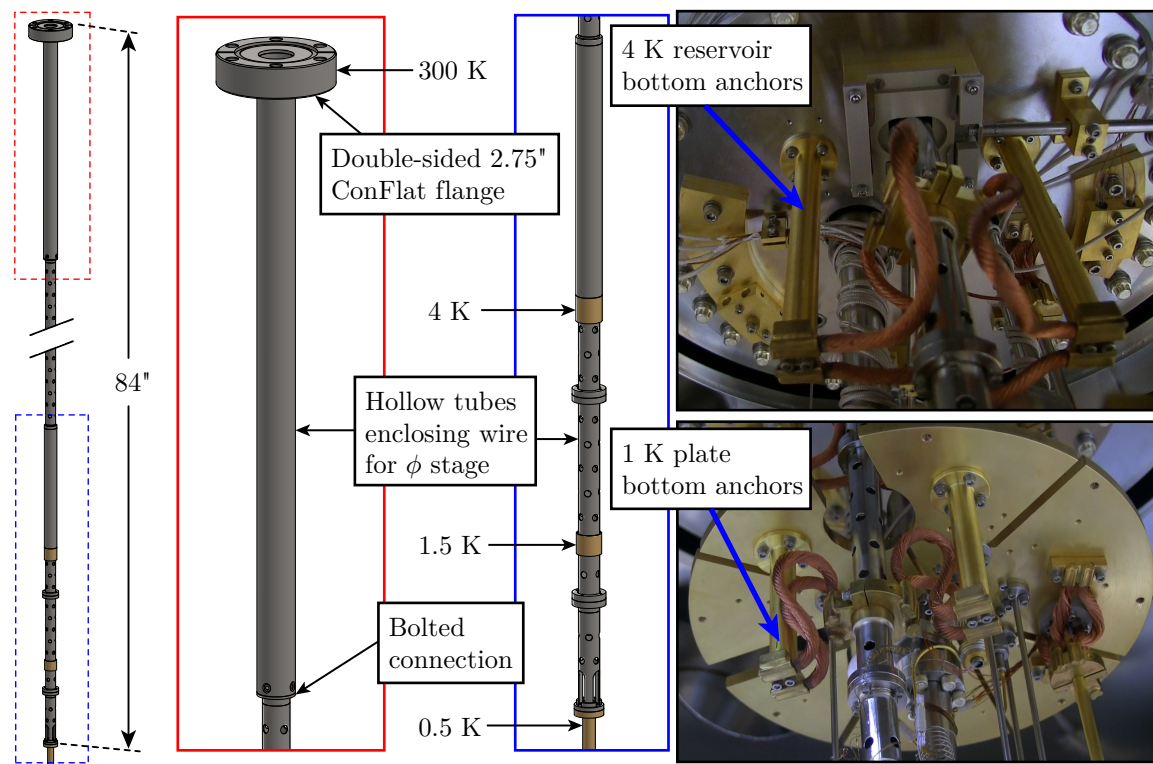


Figure 7.5.1: CAD model of sample probe detailing the top and bottom ends. Photographs showing braided connections between the sample probe and the 4 K and 1.5 K thermal anchors.

Fig. 7.5.1.1 shows CAD models of the sample probe in isolation. Note that the top and bottom of the sample probe are maintained at 300 K and ≈ 0.5 K respectively. As a result, the sample probe needs to be heat sunk, via thermal anchors, at multiple points along its length. At each point, gold-plated copper rings have been soldered to the stainless steel tube to improve thermal conductance to the thermal anchor. As shown in the photographs in Fig. 7.5.1, there are two thermal anchors at: (a)

the bottom of the Helium-4 reservoir, and (b) the 1 K plate. Copper braids are used to connect to the thermal anchors to the respective gold-plated copper rings on the sample probe. The walls of the sample probe tube are made thin (0.020") to reduce the thermal load on the two thermal anchors and the sample.

Finally, the space inside the tube is used for sending a thin stainless steel wire to actuate a spring-pulley system that controls the ϕ degree of freedom of the sample (c.f. 7.5.2.5).

7.5.1.2 Cold finger

The cold finger is a performance-critical component of the cryostat. In addition to sample manipulation, the cold finger provides a high-thermal-conductance path between the Helium-3 pot and sample; thus allowing the latter to reach sub-Kelvin temperatures. For the cryostat presented in this thesis, the cold finger was empirically found to maintain a temperature gradient of ≈ 0.3 K at base temperature. The cold finger is fabricated by gold-plating a cylinder machined from a single piece of oxygen-free high-conductivity (OFHC) Copper. Fig. 7.5.2 shows a CAD model of the cold finger in isolation. Moreover, the model clearly shows the cold finger's connection to the sample probe and rotator cradle at the top and bottom respectively. The sample is attached to the rotator.

The cold finger has grooves machined along its length to guide the strings controlling the ϕ degree of freedom of the rotator (c.f. Sec. 7.5.2.5). A cylindrical pocket, with a horizontal axis, is machined into the cold finger to accommodate a wire-wound heater which regulates the sample temperature. The cold finger also has open pockets at the top to accommodate a nut which controls the tension in the ϕ -motion actuating strings. The various features (pockets and grooves), that are machined into the cold finger, are designed such that the objects (e.g. tensioning nut) inside said features do not touch the 1 K shield, and consequently limit the motion of the cold finger.

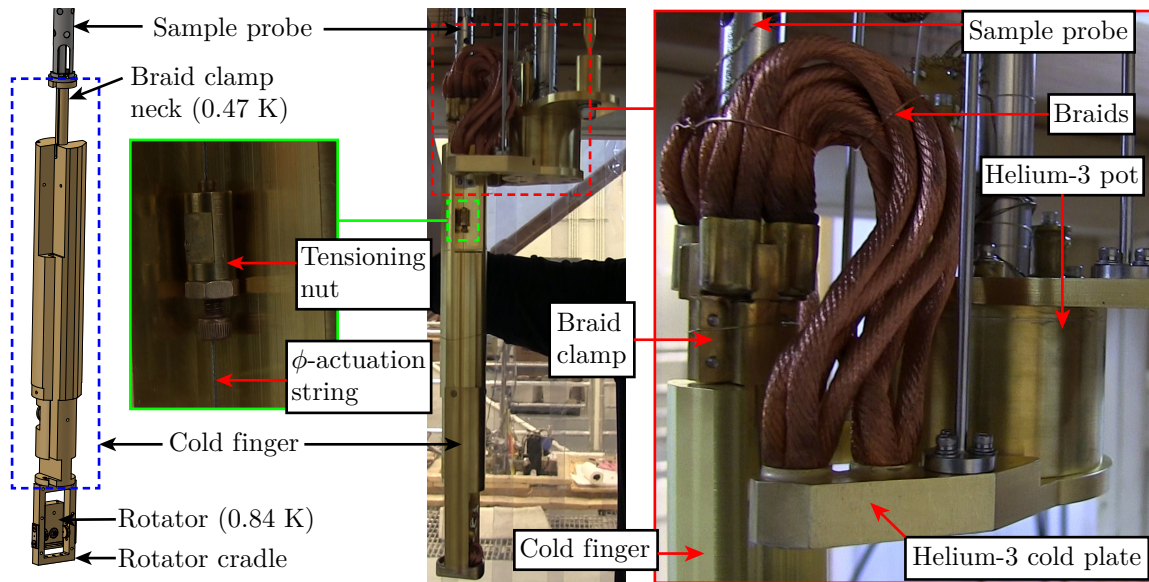


Figure 7.5.2: The CAD model of the cold finger in isolation. The photographs show the braided connection of the cold finger to the Helium-3 pot and the tensioning nut.

The photographs on the right of Fig. 7.5.2 show the OFHC Copper braids connecting the Helium-3 pot to the cold finger. The braids are Silver-soldered to circular clamp which attaches to the “neck” on the cold finger. The other end of the braids are Silver-soldered to a Helium-3 cold plate which is fastened to the bottom of the Helium-3 pot. The CAD model of the Helium-3 cold plate, without

the braids, can be clearly seen in Fig. 7.4.4.²³ The braids allow motion of the cold finger while maintaining a thermal link between the sample and the Helium-3 pot. The length of the braids is primarily determined by the sample's z -axis linear degree of freedom which has a range of 4.25" (c.f. Sec. 7.5.2.1).

7.5.2 Five-axis sample manipulation

7.5.2.1 z -axis manipulator

The z -axis manipulation of the sample is done from the top of the cryostat. CAD models and a photograph of the corresponding manipulation stage is shown in Fig. 7.5.3. In-vacuum actuation is made possible by edge-welded bellows terminated with 2.75" ConFlat flanges on both sides. The two flanges are attached to the fixed (bottom) and mobile (top) plates of the translation stage. The double-sided flange at the top of the sample probe attaches to the flange on the mobile plate. As a result, the sample probe can move up and down by the maximum stroke of the bellows (6").

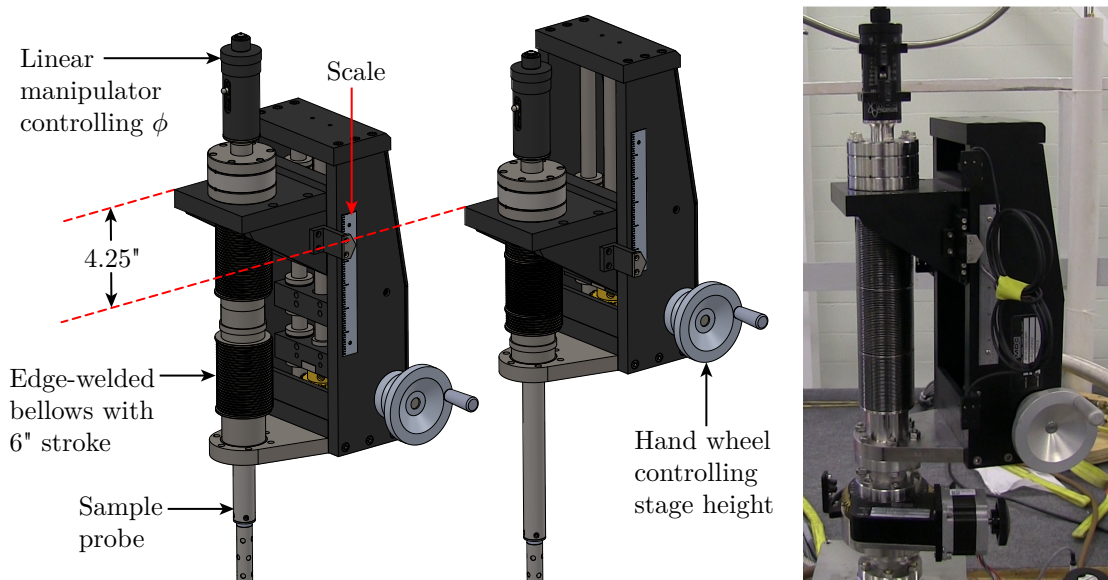


Figure 7.5.3: Left: CAD model of z -axis linear stage in the measurement and sample loading positions. Right: photo of the z -axis linear stage.

The ARPES system discussed in this thesis was designed such that sample loading and measurement planes are vertically separated by 4.25". This height difference was determined by the length of the copper braids connecting the sample probe and cold finger to various cooling stages. The top side of the sample probe flange is used to connect another bellows-actuated linear manipulator for controlling the ϕ sample degree of freedom (c.f. Sec. 7.5.2.5). The scale on the z -axis manipulator can only be used for bookkeeping at a *fixed* temperature because the sample probe and cold finger lengths change due to thermal contraction/expansion. The operator typically relies on visual feedback to judge sample height.

²³For the sake of contrast, Fig. 7.4.5 shows the Helium-3 pot without the Helium-3 cold plate.

7.5.2.2 θ -axis manipulator

The θ -axis rotary stage, shown in Fig. 7.5.4, is located at the top of the cryostat, directly underneath the z -axis linear stage (c.f. 7.5.2.1). This rotary stage consists of two concentric 2.75" ConFlat flanges, with the top flange attached to the z stage, and the bottom flange attached to the fine x - y stage (c.f. 7.5.2.3). The top flange can rotate about its cylindrical axis using a worm-gear mechanism. Thus the polar angle, θ , of the sample probe (c.f. Sec. 7.5.1.1), defined in the x - y plane, can be changed relative to the rest of the cryostat (c.f. Fig. 7.2.1). However, the entire z -axis translation stage rotates with the θ manipulator.

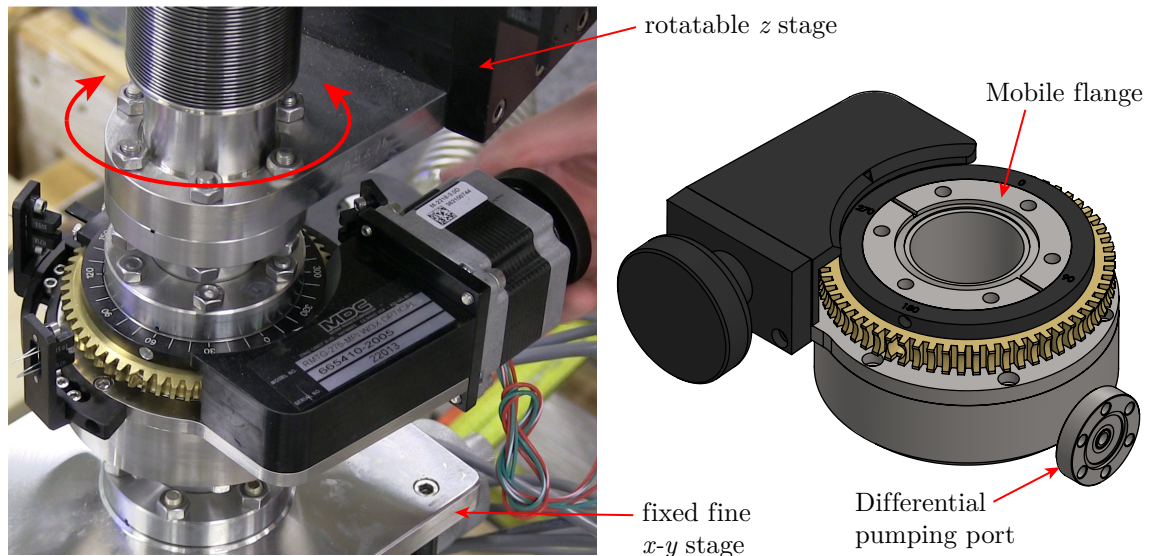


Figure 7.5.4: CAD model and photograph of the θ -axis rotary stage at the top of the cryostat.

The region between the rotating and fixed flanges is sealed using two concentric Teflon™ elastomer sliding seals of different diameter. The inner and outer seals make UHV-to-high-vacuum and high-vacuum-to-atmosphere seals respectively. High vacuum in the region between the two seals is generated by a HiCube 80 turbomolecular pump. This configuration is a type of differential pumping (c.f. Sec. 7.5.5).

7.5.2.3 Fine x - y manipulator

The x - y stage, shown in Fig. 7.5.5, is located at the top of the cryostat, directly underneath the θ -axis rotary stage. This stage consists of two 2.75" ConFlat flanges, with the top one attached to the θ -axis rotary stage, and the bottom one directly attached to the Helium-3 insert. The top and bottom flanges are connected by edge-welded bellows. Motion of the bottom flange, in the x - y plane, is driven by a professionally-manufactured two-axis linear translation stage, which generates a twist in the bellows. This design considerably reduces the demands on the x - y stage since said stage is at room temperature and in atmosphere. As a result, this x - y stage is considerably more reliable than its in-vacuum counterpart.

The stage has a 1" stroke in each of the orthogonal directions. The sample probe is fixed relative to the top flange. Therefore the x - y stage generates relative horizontal motion between the Helium-3 insert and the sample probe. In principle, the sample's x - y coordinates should match that of the sample probe. However, this not the case, in practice, due to the sample probe flexure I alluded

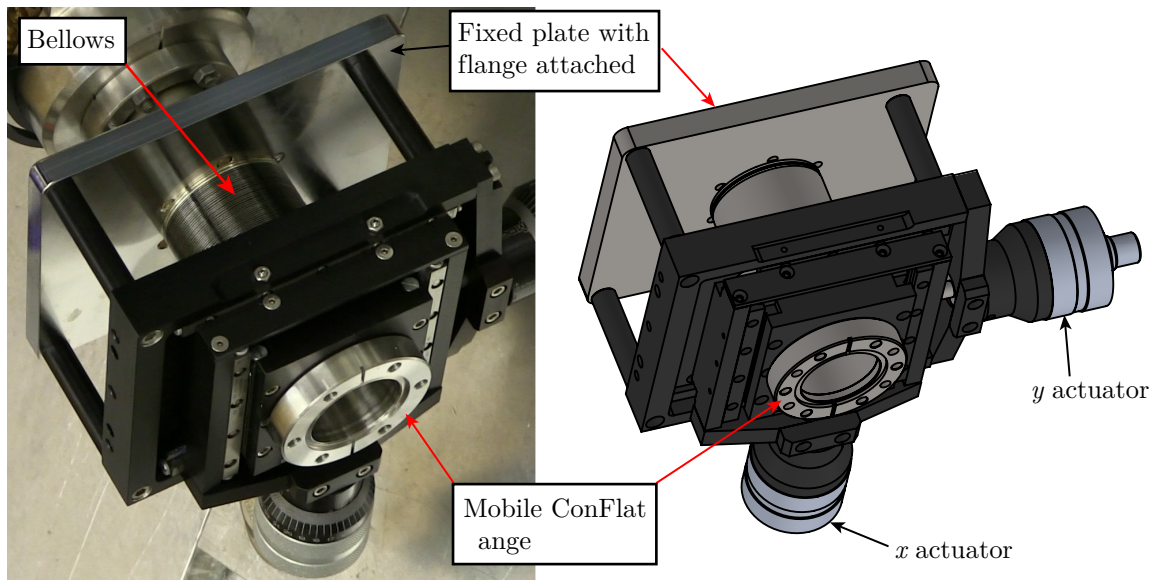


Figure 7.5.5: CAD model and photograph of the fine x - y stage at the top of the cryostat.

to in Sec. 7.5.1.1. Therefore, an additional coarse x - y stage (c.f. Sec. 7.5.2.4) is needed close to the sample.

The coarse x - y stage is at a vertical distance of $\approx 30''$ from the sample. By comparison, the stage shown Fig. 7.5.5 is at a vertical distance of $\approx 80''$ from the sample. Due to the existence of a bottom (coarse) x - y stage, the sample probe pivots about said stage when the top x - y stage moves. Due to the large lever arm, the top stage is capable of very fine adjustments during sample alignment. Therefore, the top stage is also referred to as the fine x - y stage.

7.5.2.4 Coarse x - y manipulator

In Sec. 7.5.1.1, I briefly mentioned that two pairs of x - y manipulators are required to move the sample probe due to non-negligible flexing in the latter. One pair of x - y manipulators is located at the top of the cryostat; it is called the “fine x - y manipulator” (c.f. Sec. 7.5.2.3). The second pair is located close to the bottom of the 4 K reservoir. The latter is referred to as the “coarse x - y manipulator” because, due to its proximity to the sample, its motion results in larger sample displacement compared to the former. Moreover, unlike the fine x - y manipulator, its coarse counterpart has the x - y translation stage located in vacuum at cryogenic temperatures.

Fig. 7.5.6 shows the CAD model of the coarse x - y stage, in isolation, installed on the sample probe. The coarse x - y stage is controlled by two shafts each coupled to a linear UHV feedthrough. Each shaft consists of an assembly of the following segments:

- three solid rods with $1/4''$ diameter,
- one rigid and one flexible shaft coupler, and
- a linear bushing.

The CAD model in the inset illustrates the motion transfer mechanism of the coarse x - y stage using the PEEK braces with orthogonal slots; this is referred to as the “crisscross design.” The photograph

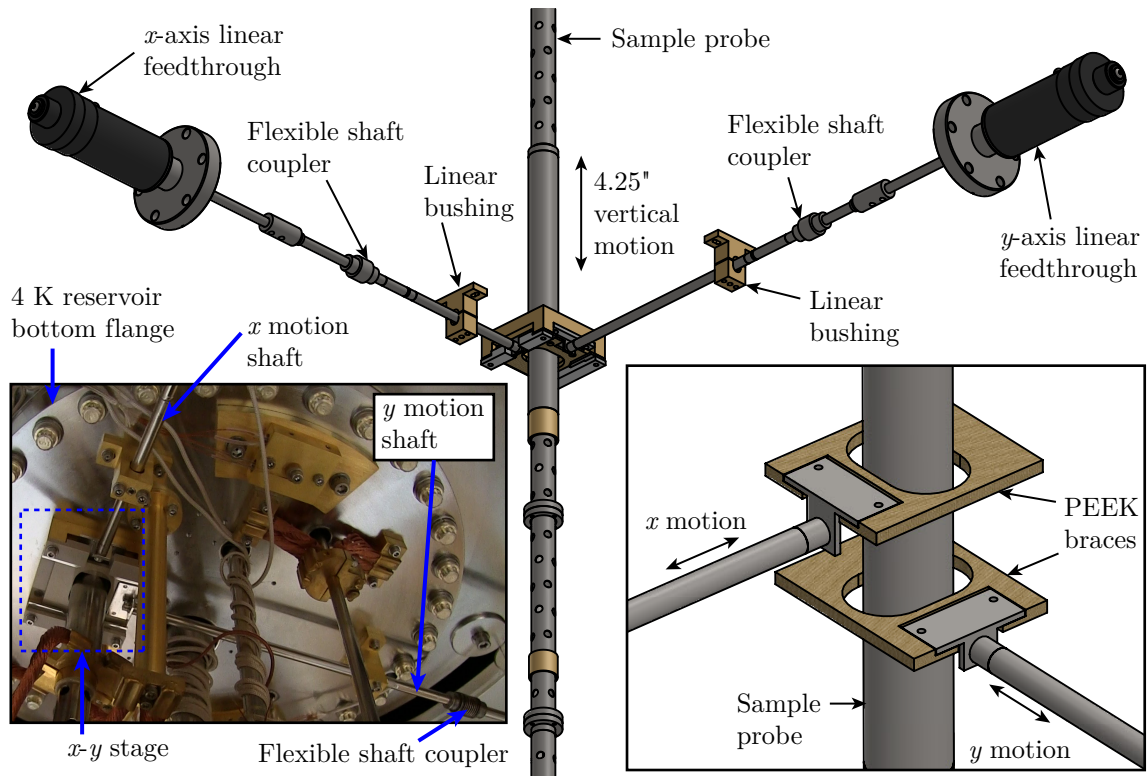


Figure 7.5.6: CAD models and photograph of the coarse x - y stage and its manipulators. The CAD model in the inset shows an exploded view of the x - y stage with only the PEEK braces visible. The vertical separation between the PEEK braces has been exaggerated.

shows the flexible shaft coupler on the y -axis shaft. This couplers primary role is to correct angular misalignment between the Helium-3 insert and main shroud. A secondary role of the flexible shaft couplers is providing compensation for thermal contraction of the shafts.

Finally, note that in addition to motion along the z -axis, the crisscross design also allows the sample probe to rotate about its cylindrical axis. Therefore, the coarse x - y stage is compatible with θ manipulation, which is discussed in the next section.

7.5.2.5 ϕ -axis manipulator

In Sec. 3.3.3.1, I discussed the importance of increasing the ϕ angle of the sample in order to record electron launch angles larger than 20° . The latter limit was set by the lens of the electron analyzer (c.f. Fig. 5.3.2). Overcoming this instrument limit allows larger access to the sample's Brillouin zone. For example, the sample's ϕ degree of freedom was critical in performing measurements of superconducting gap of $\text{Bi}_2\text{Sr}_2\text{CaCu}_2\text{O}_{8+x}$ (c.f. Sec. 8.5.2.3) close to the anti-nodal direction in the Brillouin zone. In this section, I will discuss some features associated with the ϕ motion mechanics and its impact on cooling performance.

The ϕ -axis manipulator allows rotation of the sample along an axis perpendicular to the sample probe cylindrical axis of symmetry (c.f. Fig. 7.2.1). Therefore, unlike the other other four degrees of freedom of the sample, ϕ -axis motion is not common with sample probe. As a result, implementation of ϕ -axis motion requires a new structural unit known as the *rotator*. The left of Fig. 7.5.7 shows the CAD model of the rotator in its "cradle." Both the rotator and cradle are machined out of a

single piece of oxygen-free high-conductivity (OFHC) Copper and subsequently gold-plated. The rotation of the “pulley” relative to the cradle is facilitated by a Sapphire bearing (not shown).

The two annealed stainless Steel strings attached to the pulleys apply opposing torque to the rotator. A cartoon of these strings, rendered over the CAD model to the left of Fig. 7.5.7, provide conceptual illustrations of the mechanical forces driving said strings. The front (red) string is connected to an extension spring placed inside the hollow region of the sample probe (c.f. Sec. 7.5.1.1). The fixed end of the spring is close to the bottom of the 1.5 K thermal anchoring point of the sample probe (c.f. Fig. 7.5.1). The back (blue) string is connected to the linear UHV feedthrough attached to the top of the z -axis stage (c.f. Fig. 7.5.3). Recall that the tension in the strings can be tuned using nuts close to the cold finger (c.f. Fig. 7.5.2).

A photograph of the entire rotator assembly can be seen at the middle of Fig. 7.5.7. A smaller version of the Copper braids, shown in Fig. 7.5.2, is used to establish a thermal link between the rotator and its cradle. As shown in Fig. 7.5.2, the latter is rigidly fastened to the cold finger. These two sets of braids are critical to achieving a low sample base temperature. The other factor affecting sample’s base temperature is the thermal contact between the rotator and the sample holder.

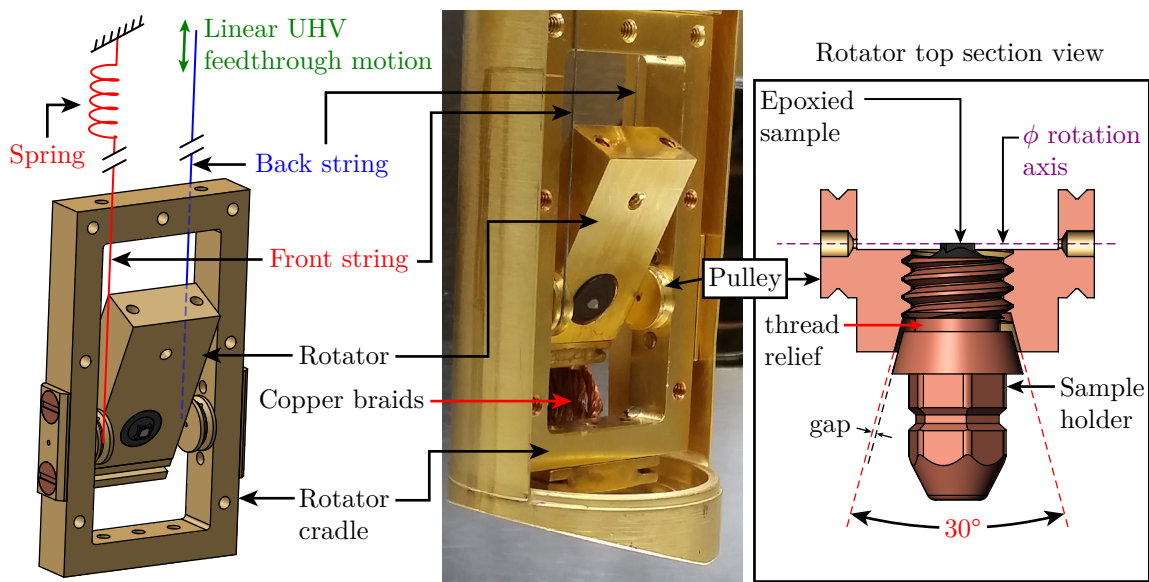


Figure 7.5.7: Left: CAD model of the rotator in its cradle. Cartoons of the strings, controlling the ϕ motion of the rotator, are depicted by red and blue lines. Middle: photograph of the rotator with a cleaved sample attached. Right: CAD model of the top section view of the rotator and full view of the mating sample holder. A graphite-coated epoxied sample is shown with its surface intersecting the ϕ rotation axis.

The CAD model on the right of Fig. 7.5.7 shows a top section view of the rotator with the sample holder attached. When the z -axis stage is lowered to the loading configuration, the sample holder is screwed into the rotator ($3/8$ "-16 threads) using the sample handling system (c.f. Sec. 6.3.7). Moreover, a graphite-covered cleaved sample is shown epoxied to the sample holder. By contrast, the CAD model of an uncleaved sample without graphite can be seen in Fig. 6.3.11. The 30° countersink on the rotator guides the sample holder until their threads engage. The flexible shaft coupler on the transfer arm takes up the slack as the sample holder is guided by the rotator’s countersink (c.f. Fig. 6.3.12).

As shown in the CAD model on the right of Fig. 7.5.7, it is ideal if the ϕ axis of rotation coincide with the sample surface. In that case, defocusing of the electron optics can be minimized when ϕ

is changed. In practice, this condition is rarely achieved due to sample-to-sample height variation. In cases where base temperature is not a priority (e.g. Sec. 8.4.2), the sample surface can *coarsely* be made coincident with the ϕ axis of rotation by tuning the extent to which the sample holder is screwed into the rotator. In such cases, there will be a small gap (see Fig. 7.5.7) between 30° tapered surfaces. Of course, for (say) sub-Kelvin measurements, such a gap is unacceptable because it will result in a significant reduction in the thermal conductance between the sample and the Helium-3 pot. Even if the sample holder is screwed in tightly, a small gap between the tapered surfaces can occur in the absence of a thread relief. The importance of the latter was noticed in Sec. 8.5.2.2.

The gap between the sample holder and rotator is especially important due to the fact the temperature sensor is attached to the rotator. The back of the rotator has a pocket (not shown in Fig. 7.5.7) which has a Cernox sensor mounted on a bobbin (c.f. Fig. 7.6.2). In the presence of the spatial gap, there would be a large discrepancy between the measured temperature and the actual sample temperature. After the thread relief was introduced into the sample holder, this temperature discrepancy was empirically confirmed to be negligible down to ≈ 2 K.

7.5.3 Sample loading

7.5.3.1 Introduction and motivation

The (room temperature) sample handling system is designed to load the sample holder onto the cold finger using the custom grabber on the transfer arm (c.f. 6.3.7). Therefore, the radiation shield tails (c.f. Sec. 7.3.3), surrounding the sample, need to allow mechanical access to said grabber. A straightforward solution is introducing a hole in the radiation shield tails. The hole would have to be large enough to either allow: (a) the grabber to pass through the shield tails when the cold finger is in the measurement position or (b) the cold finger to pass through the shields into a region accessible by the grabber.

As discussed in Sec. 6.3.7.3, given the system dimensions, only option (b) is compatible with sample cleaving using a wobble stick. Therefore, the cold finger is lowered by 4.25" (c.f. 7.5.2.1) through a hole at the bottom of the shield tails (c.f. Fig. 7.3.5) where the grabber can access it. This approach works for high temperature operation ($\gtrsim 80$ K). For lower temperatures, however, the cold finger would experience heat loads, through the bottom hole, which would result in liquid Helium-4 boil off rates larger than the acceptable cryogen budget. Moreover, reaching sub-Kelvin base temperatures would be impossible for both options (a) or (b).

One solution to achieving sample loading without compromising cryostat performance is the use of mobile radiation shields. For this approach, the radiation shield tails would have to be retrofitted with a mechanical device which blocks black body radiation (no higher than 77 K) when the cold finger is in the measurement position. In the ARPES Helium-3 cryostat design, two mechanical devices consisting pairs of spring-loaded doors are attached to the bottom of the 4 K and 77 K radiation shield tails (c.f. Fig. 7.5.8). The device is called the “bottom shield.” In the following sections, I will discuss the challenges associated with the design and implementation of the bottom shields.

7.5.3.2 Design constraints

The design of the bottom shields was constrained by their size and the properties of construction materials. All materials used in the construction have to be:

- UHV compatible,
- thermally conductive at low temperatures, and
- non-magnetic.

To determine the optimal bottom shield dimensions, a good balance has to be struck between the following competing requirements:

1. Larger inner diameter makes it easier to manipulate the cold finger. The lower limit on this parameter would be the diameter of the cold finger plus some minimum diametric clearance (≥ 0.1 ").
2. Smaller outer diameter makes ARPES system assembly easier. The upper limit on this parameter would be the inner diameter of the μ -metal sleeve (c.f. Sec. 6.3.2.1) minus some minimum diametric clearance (≥ 0.25 "²⁴).

7.5.3.3 Fabrication and installation

The CAD model in Fig. 7.5.8 illustrates the design of the 4 K and 77 K bottom shields. The former is simply a smaller version of the latter. The cylinder and two doors are machined out of a single piece of 6061-T6 aluminum. The doors pivot about 1/2" long #2-56 aluminum screws and remain in the open position under gravity. Wire-wound torsion springs provide the restoring force which closes the doors. The cylinder and doors each have copper plates to clamp down on aluminum foil responsible for improving thermal conductance.²⁵

The choice of aluminum²⁶ and oxygen-free high conductivity (OFHC) copper for all custom machined parts meets all three material requirements listed in Sec. 7.5.3.2. Most torsion springs available commercially are made of magnetic materials. As a result, the torsion springs were custom made from phosphor bronze wires, which met all three material requirements. The material of the countersink screws, used to clamp the aluminum foil on the doors, was chosen to be Molybdenum primary because it was the only material available in the desired size. Molybdenum also meets all three material requirements.

7.5.4 Performance of the sample manipulation system

The five-axis sample manipulation system introduced in Sec. 7.5.2 had its pros and cons. One of the major pros was the thermal design of the sample probe. As shown in Fig. 7.5.1, the sample probe managed to sustain a temperature gradient from 300 K to 0.5 K by heat sinking itself to multiple thermal anchors using high-conductivity flexible copper braids. This allowed for the control of the sample's fine x - y , z , and θ degrees of freedom using professionally manufactured linear and rotary stages. These four degrees of freedom were empirically found to be the most reliable during measurements.

On the other hand, the sample degrees of freedom located inside vacuum, namely the coarse x - y and ϕ stages, were the cons. The most severe problem in these stages was hysteresis. The following examples illustrate the impact of hysteresis on these three degrees of freedom:

²⁴In earlier version of the bottom shields (c.f. 6.3.12) required the cumbersome approach of removing the pump chamber (c.f. Sec. 6.3.2.2) because it would not fit through the μ -metal sleeve.

²⁵Contact between the cylinder and doors through the screw in the hinge is poor, by design, to minimize friction.

²⁶Prototypes of the cylinder and doors were machined from aluminum stock due to its lower cost compared to OFHC copper. Since the performance of the prototypes was empirically found to be satisfactory, they were used in the final version.

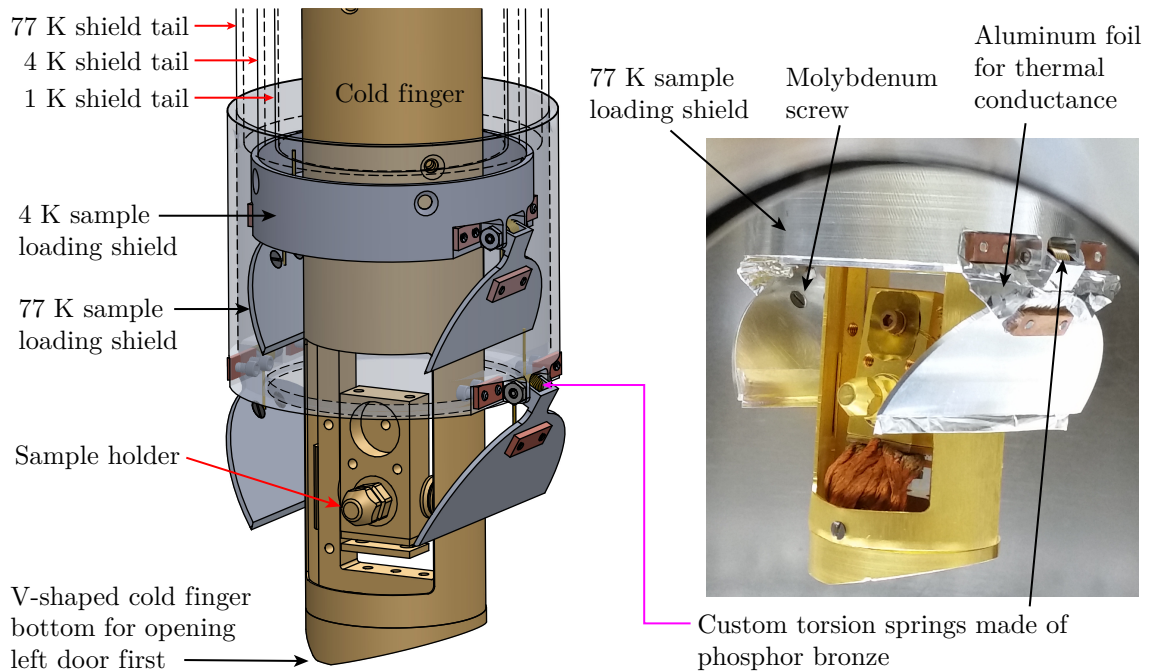


Figure 7.5.8: Left: CAD model of the cold finger and bottom shields used for sample loading. The 77 K bottom shield is made semi-transparent to show the 4 K bottom shield. Right: Photograph of the cold finger and 77 K bottom shield.

7.5.4.1 x - y manipulators

While focusing the spectral image of the Dirac surface states of Bi_2Se_3 , using the fixed mode of the R8000 (c.f. Sec. 5.3.3.1), small changes ($< 0.025''$) in the linear feedthrough would move the sample probe in a completely unpredictable way. Reversing this change to recover the original spectrum, using these hysteretic x - y manipulators, could take as long as 10-30 min. In some cases, faster recovery times could be achieved by changing the laser pointing. However, the latter was achieved at the cost of losing laser polarization control.

Furthermore, hysteresis in the x - y manipulators made it very difficult to achieve electron-optical focusing of the sample. As a result, a raster scan of the Brillouin zone was not feasible. Hysteresis in the x - y manipulators also led to damages to the cold finger components when lowering the latter to its sample loading/cleaving position (c.f. Sec. 6.3.7.3). Due to the inability to accurately center the cold finger with respect to the radiation shield tails, the former would crash into the bottom shields.

It was later identified that the primary factors causing hysteresis were the flexible shaft couplers in the coarse x - y manipulator (c.f. Sec. 7.8.3) and the looseness of the bolted connection in the sample probe (c.f. Sec. 7.8.2 and Fig. 7.5.1).

7.5.4.2 ϕ -stage

Once the coarse x - y manipulators managed to get a sample like Bi_2Se_3 into the analyzer's focus, ϕ motion was expected to cause a shift in the spectral image in the momentum direction, while keeping the sample *approximately* in focus. However, this shift was not always observed. The reason for this

is that only a limited range of the ϕ -controlling linear feedthrough, on top of the z -axis stage (c.f. Sec. 7.5.2.5), would make the sample's ϕ angle change. This was confirmed based on visual feedback of the ϕ stage motion during both sample loading and when the system was vented.

Unfortunately, the range of operation of the ϕ -feedthrough could not be encoded due to lack of reproducibility in the measurement configuration. In practice, approximate reproducibility was only achieved with visual feedback when the cold finger was in the sample loading position (c.f. Sec. 6.3.7.3). In other words, the ϕ axis was only useful for sample loading but not measurement.²⁷

7.5.5 Differential pumping

In this section, I will discuss an important factor that influences the performance of the θ -axis manipulator (c.f. Sec. 7.5.2.2): differential pumping. Unlike Sec. 7.5.4, however, this factor is not a design flaw. Moreover, the performance I'm referring to is associated with vacuum quality, and not the θ manipulation.

During initial operation of the ARPES UHV system, attaching the port shown Fig. 7.5.4 (a.k.a. differential pumping port) to the HiCube 80 turbomolecular pump did not *appear* to make a difference to the vacuum level inside the analysis chamber. Over time, however, the pressure reading by the ion gauge developed temporary fluctuations seemingly at random times. Therefore, these fluctuations were initially dismissed as gauge artifacts.

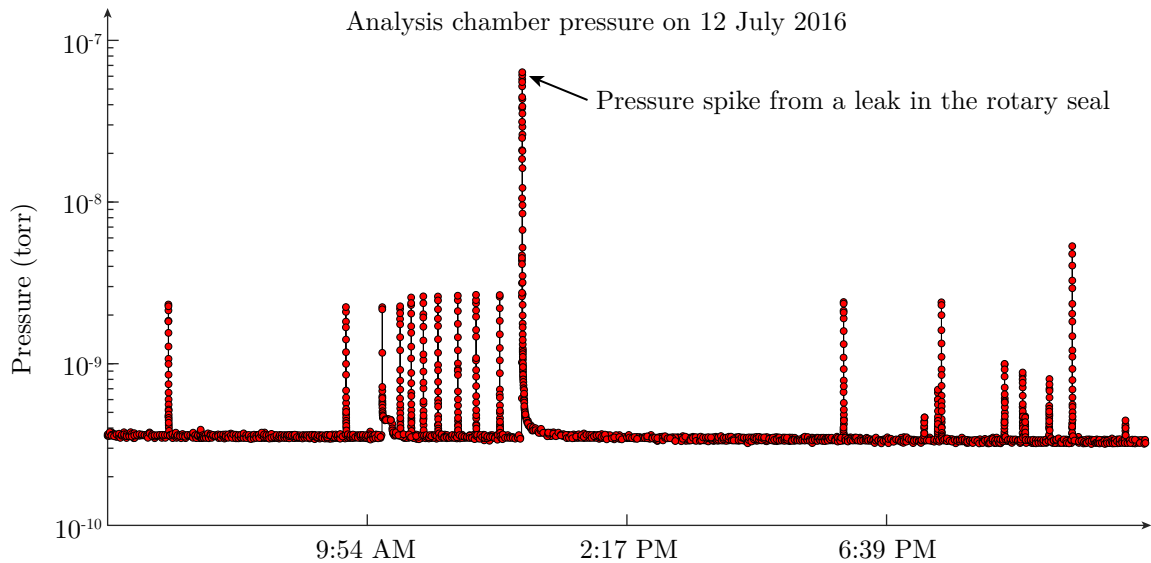


Figure 7.5.9: Pressure spikes in the analysis chamber due to a leak in the rotary seal

After a more meticulous analysis, the pressure fluctuations were confirmed as real. Fig. 7.5.9 shows plot of the analysis chamber pressure measured over a day. The pressure spikes lasted between few tens of seconds to a little over one minute. Moreover, the temporal frequency of appearance of these peaks did not fit any known systematic effects.

Using an RGA (c.f. Sec. 6.5.1), the most likely source of the leak was narrowed down to the θ -axis manipulator. Subsequent troubleshooting revealed that the pressure spikes disappeared after the

²⁷Actually, the ϕ degree of freedom was used to measure the superconducting gap of $\text{Bi}_2\text{Sr}_2\text{CaCu}_2\text{O}_{8+x}$ close to the anti-node (c.f. Sec. 8.5.2.3). But the value of ϕ was unknown. So this measurement was not quantitatively accurate in momentum space.

differential pumping port was connected to the HiCube 80 turbomolecular pump. Moreover, when the differential pumping port was not pumped, the frequency of the spikes would increase, still with no discernible pattern, as θ was changed.

7.6 Electrical network

The electrical network in a complex system, such as the ARPES Helium-3 cryostat, greatly improves the ease of operation of the latter. This network consists of four important components: sensors, heaters, wires, and electrical feedthroughs. In order to meet the cryostat's operational requirements, however, these components must be fabricated and assembled in a manner that satisfies stringent temperature and vacuum isolation constraints. This involves choosing the appropriate construction materials, sensing/heating mechanisms, and wiring architecture. In Sec. 7.6.1-7.6.3, I will discuss the details of implementation of the electrical network in the ARPES Helium-3 cryostat.

7.6.1 Temperature sensors

7.6.1.1 Importance of temperature sensors

Temperature sensors are an integral part of any cryogenic experiment. The most important temperature sensor, in cryogenic systems of any size or complexity, is the one closest to the sample being interrogated by the experiment. The reading from this *primary* sensor needs to be accurate, precise, and stable in order to reliably interpret the results of the experiment.

Quite often it is convenient, and critical in some cases, to have temperature feedback from secondary sensors to aide in the cryostat's operation. Typically, an increase in the cryostat's size and complexity introduces greater uncertainty in the functioning of different subsystems. For example, in the ARPES Helium-3 cryostat, issues like (say) blockages in the condensing impedance or the capillary carrying liquid Helium-4 from its reservoir to the 1 K pot, thermal shorts resulting from physical contact with mobile components (e.g. cold finger touching the 1 K shield), and residual liquid Nitrogen freezing in the 4 K reservoir or 1 K pot, to name a few, are common in day-to-day operations. Placing a dedicated sensor at each of these different locations greatly reduces operator error and simplifies troubleshooting steps.

As a rule of thumb, the number of sensors used in a cryostat scales with the size and complexity of the latter. Moreover, the specifications for sensors in different parts of the cryostat are different. Therefore, sensor properties like temperature range, sensitivity, robustness to environmental conditions (e.g. magnetism, radioactivity, etc.), accuracy, and stability need to be considered in the choice of sensors. For example, the demand for accuracy and stability of the sensor on the 77 K reservoir is significantly less than the one on (say) the Helium-3 pot. Moreover, in this example, the desired temperature range of operation is different. Therefore, a cheaper uncalibrated²⁸ silicon diode sensor is used for the former, while a calibrated resistance temperature detector is used for the latter.

The ARPES Helium-3 cryostat has a total of 16 temperature sensors. Their properties are listed in Table 7.1.

²⁸Here uncalibrated means the sensor follows a standard calibration curve. Sensor-to-sensor variations are not accounted for in this category of commercial sensors. The users can choose to later calibrate this sensor on their own.

| Type of temperature sensor | Range of operation (Kelvin) | Quantity |
|---------------------------------------|-----------------------------|----------|
| Silicon diode | 1.5 to 500 | 14 |
| Resistance temperature detector (RTD) | 0.3 to 420 | 2 |

Table 7.1: Properties of temperature sensors inside the ARPES Helium-3 cryostat

7.6.1.2 Sensor calibration

Both the silicon diode and RTD sensors infer temperature, T , based on voltage drops, V , measured across said sensors, when a fixed current is passed through them. Each type of sensor has a unique voltage function, $V_{\text{sensor}}(T)$, mapping temperature to voltage. An important figure of merit for either sensor is its sensitivity, S_{sensor} , which is defined as

$$S_{\text{sensor}}(T) \equiv \frac{d}{dT} V_{\text{sensor}}(T). \quad (7.6.1)$$

Typically, a high sensitivity is desired in the temperature range of interest.

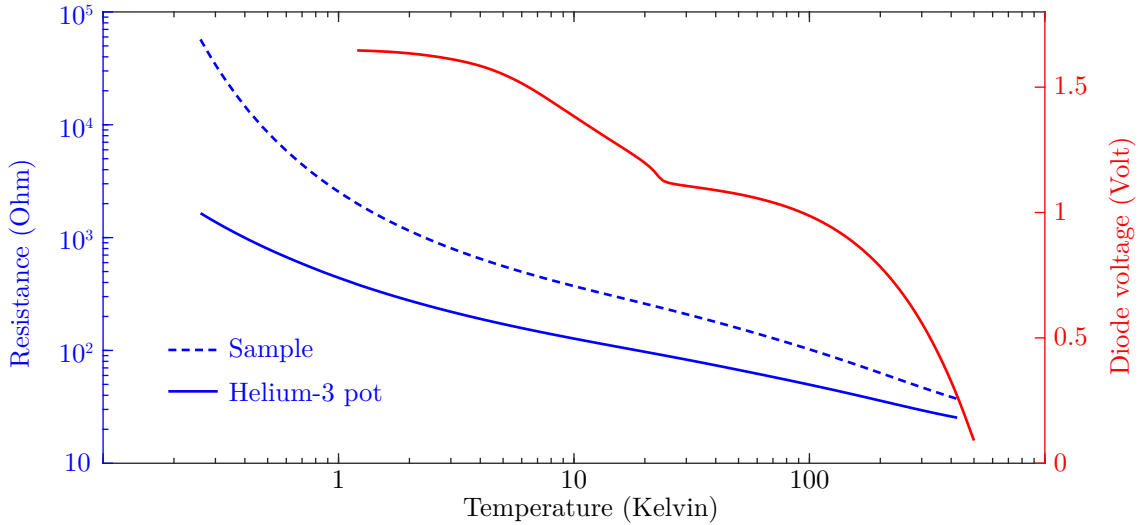


Figure 7.6.1: Calibration curves of the standard silicon diode (red) and the resistance temperature detectors (blue). The latter are individually calibrated for the sample and Helium-3 pot by the manufacturer. The diode voltage is measured with an excitation current of $10 \mu\text{A}$.

Under certain conditions, $V_{\text{sensor}}(T)$ and $S_{\text{sensor}}(T)$ can be modeled theoretically. In practice, however, commercial sensors are calibrated across their range of operation, where voltage and sensitivity functions are measured empirically, denoted $V_{\text{sensor}}^{\text{calibration}}(T)$ and $S_{\text{sensor}}^{\text{calibration}}(T)$ respectively. These are often referred to as the sensor's standard calibration curves. For higher accuracy, sensors can be individually calibrated to account for sensor-to-sensor variation. These types of sensors are referred to as *calibrated sensors*. Alternatively, if they follow the standard calibration curves, they are referred to as *uncalibrated sensors*. In the ARPES Helium-3 cryostat, all 14 silicon diode sensors are uncalibrated. The two RTDs located on the Helium-3 pot and sample rotator are calibrated. Fig. 7.6.1 shows the standard calibration curve of the silicon diode (Lakeshore DT-670) and the Cernox RTD sensor (Lakeshore CX-1010) mounted on the sample rotator and Helium-3 pot.

7.6.1.3 Packaging, wiring and measurement

For cryogenic temperature sensors, the measurement leads are typically wires with a large resistance (c.f. Sec. 7.6.3.2). Therefore electrical measurements on sensors are performed in the standard four-

point configuration which, in principle, is independent of the properties of the measurement leads. As an example, I will illustrate the measurement setup for the silicon diode sensor from Lakeshore (DT-670-SD).

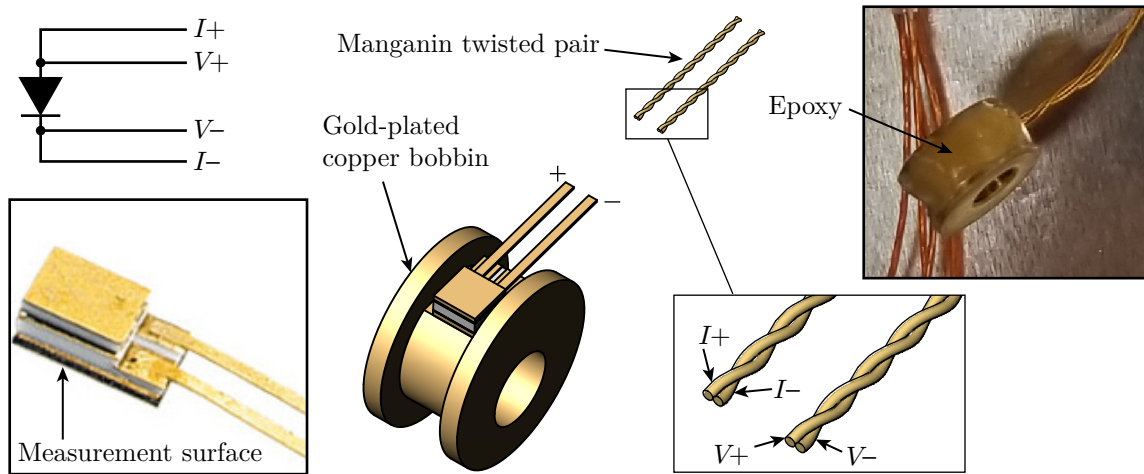


Figure 7.6.2: CAD models and photographs of the components of the sensor packaging.

Fig. 7.6.2 shows a photograph of a two-terminal package containing the silicon diode chip. Due to heat carried by the measurement leads, the temperature of the chip could be higher than the measurement surface on the packaging. As a result, the sensor could read a higher temperature than that of the surface of interest. Therefore, the Manganin wires connecting to the chip's leads are wrapped around a bobbin using a thermally conductive epoxy (EPO-TEK® H70E).²⁹ The bobbin keeps the wires, packaging, chip, and the surface of interest in thermal equilibrium.

7.6.2 Sensor-heater unit

In most cryostats, the temperature sensor has an accompanying heater to control the temperature of the sample on which the experiment is being performed. In large cryostats, like (say) the ARPES Helium-3 cryostat, secondary heaters accompany the corresponding sensors for assisting in cryostat operation. Moreover, these sensors can also be used to perform bake-outs of the surfaces of the cryostat exposed to UHV. The cryostat has a total of 15 heater assemblies. Their properties are listed in Table 7.2.

| Type of heater | Accompanying sensor | Quantity |
|----------------|---------------------------------|--------------------------------------|
| Firerod | Silicon diode | 25 $(2 \times 12 + 1)$ ³⁰ |
| Wire-wound | Resistance temperature detector | 2 |

Table 7.2: Properties of heaters inside the ARPES Helium-3 cryostat

Given the large number of silicon diodes and firerod heaters, it is convenient to group them together is a sensor-heater unit known as a “heater block.” An example of a heater block is shown in Fig. 7.6.3. A single firerod heater is a 50 Ω resistor packaged inside a stainless steel barrel with two terminals. The circumference of the cylinder dissipates the heat generated by an internal resistive element. The maximum power rating for this heater is 50 W.

²⁹This epoxy has to also be electrically insulating.

³⁰There are 12 heater blocks in the system Fig. 7.6.3. The heater on the condensing impedance (c.f. Sec. 7.4.3.2) uses only one 50 Ω firerod heater.

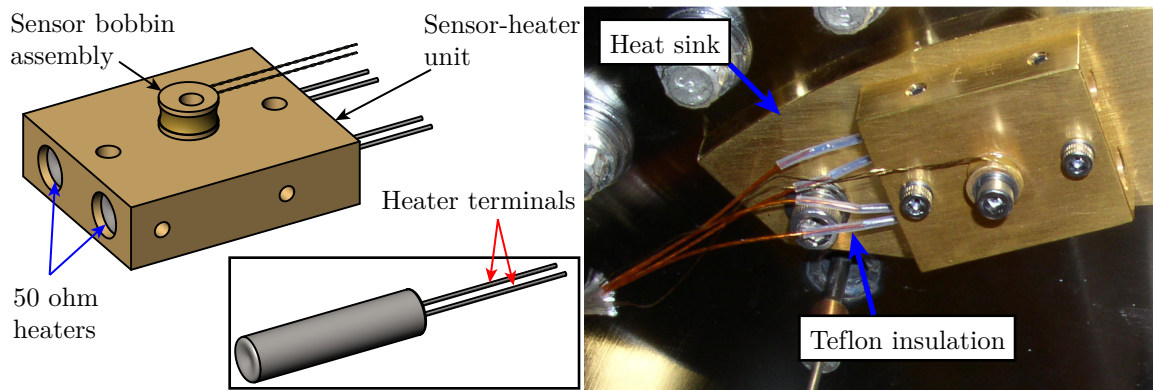


Figure 7.6.3: Left: CAD model of the heater block illustrating mounting locations of the fired rod heater and silicon diode bobbin. Right: photograph of the heater block connected to the bottom of the 4 K reservoir via a heat sink.

For a single heater block, two firerod heaters are inserted in a slightly oversized hole. Thermal contact between the heater and heater block is achieved using two set screws per heater. Moreover, the resistors in the two heaters are connected in parallel to double the heating power. The silicon diode bobbin is screwed on to the top of the heater block. The temperature of each heater block can be maintained at a desired temperature by establishing an electronic feedback loop between the silicon diode sensor and an effective 100 W heater.

Fig. 7.6.3 also shows a photograph of a sensor blocked installed at the bottom of the 4 K reservoir. The intermediate gold-plated copper plate plays the role of a heat sink which distributes the heat generated by the firerod heaters over a larger area. The heat sink is used whenever the heater block is installed on a surface with relatively poor thermal conductivity like stainless steel. In such cases, if no heat sink were installed, and if the heaters are operating at full capacity (100 W), a large amount of heat would be trapped inside the heater block. This could damage the sensor and heaters.

7.6.3 Wiring architecture

7.6.3.1 UHV feedthroughs

The wires transmitting voltage and current, to the sensors and heaters under UHV, are connected to their respective electronic controllers in atmosphere. Therefore, a 20-pin electrical feedthrough, with the appropriate current and voltage rating, serves as the first component of the sensor-heater wiring network. Photographs and a section view of the CAD model of the 20-pin feedthrough are shown in Fig. 7.6.4.

The Manganin (sensor) and Copper (heater) wires (c.f. Sec. 7.6.3.2) are soldered onto pin connectors compatible with the feedthrough's pin size (0.056" diameter). These connectors are spring loaded to allow a connection to the pins by simply sliding them onto the latter.³¹

As evident from right photograph in Fig. 7.6.4, the density of wires close to the feedthrough is the highest in the entire cryostat. Therefore, it is important to label the wires. The manufacturer used plastic rings for color-coding the various wire bundles.³²

³¹While rewiring the cryostat (c.f. Sec. 7.8.4), these pins were replaced because their UHV compatibility could not be verified.

³²These plastic rings were later replaced with UHV-compatible labels (c.f. Sec. C.3.5)

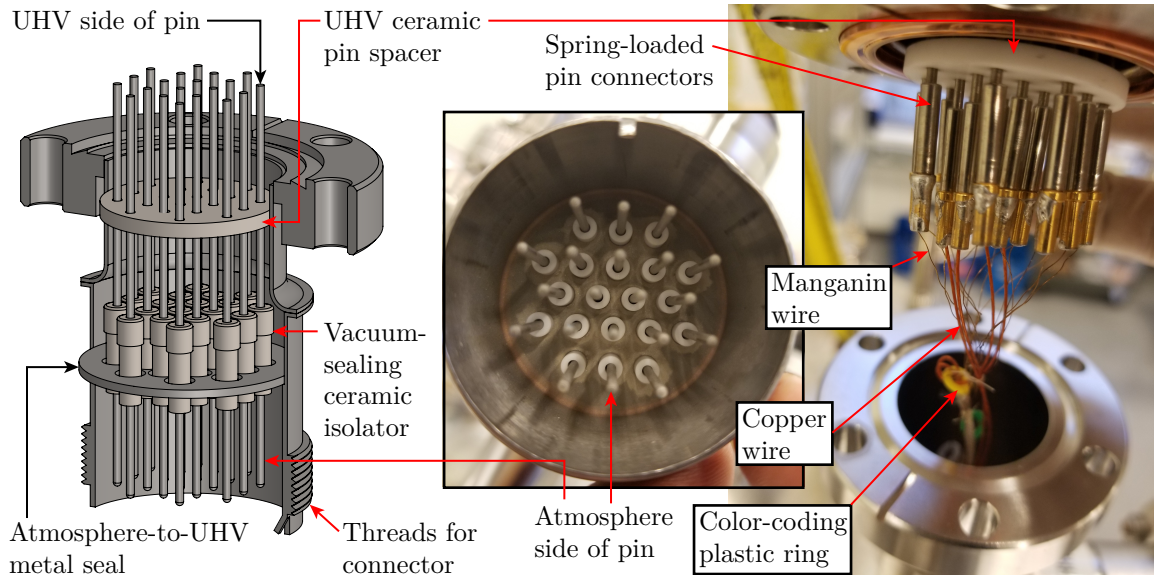


Figure 7.6.4: 20-pin electrical feedthrough for the voltage and current transmission wires of the sensors and heaters

7.6.3.2 Wire bundles

The connections between the UHV feedthrough pins and the respective sensor and heater terminals is made using solid core manganin and copper wires respectively. The electrical (σ) and thermal (κ) conductivities of the wire conductors are proportional. For the ideal metal, the σ - κ relationship is given by,

$$\frac{\kappa}{\sigma T} = \frac{\pi^2}{3} \left(\frac{k_B}{e} \right)^2, \quad (7.6.2)$$

which is known as the Wiedemann-Franz law. The quantities T , k_B , and e are the temperature, Boltzmann constant, and electron charge respectively.

For sensors, it is imperative to minimize heat load from the room-temperature feedthroughs in order to obtain accurate temperature readings (c.f. 7.6.1.3). Therefore, the diameter of the wires transmitting current and voltage to the sensor needs to be as small as practically possible. The properties of the two types of wires are listed in Table 7.3.

| Property | Sensor | Heater |
|----------------------|---------------|--------|
| Conductor material | Manganin | Copper |
| Solid core diameter | 0.005" | 0.010" |
| Insulation material | Polyimide | Kapton |
| Insulation thickness | microns range | 0.005" |

Table 7.3: Properties of the current and voltage transmission wires for the sensors and heaters.

In addition to small diameters, the length of wire typically also made very long (several feet). While long and thin wires improve the cryostat performance, they make the wiring process more difficult. This problem can be mitigated to some degree by bundling the wires into cables and using a protective sleeve. The latter, however, has its own set of challenges associated with it.

For example, consider the 160" long wire bundle, shown in Fig. 7.6.5, which carries all the wires required for a single sensor-heater unit (c.f. Sec. 7.6.2). It consists of a pair of Kapton-insulated

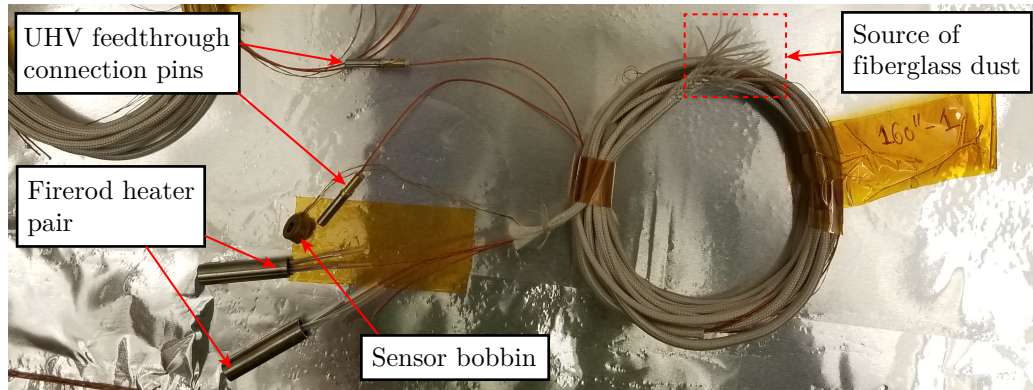


Figure 7.6.5: Photograph of a coiled 160 inch long cable for a single sensor-heater unit.

copper wires and two Magnanin twisted wire pairs. The former is mechanically stable due to the 0.005" thick Kapton insulation. However, the latter can easily break while handling. Therefore, the entire bundle is passed through a fiberglass sleeve.

7.6.3.3 Heat sinks

In addition to using wires with high thermal resistance (c.f. Sec. 7.6.3.2), heat loads to the sensors and heaters can be minimized by heat sinking. This is analogous to heat sinking of the heat switch (c.f. Sec. 7.4.1.3) and sample probe (c.f. Sec. 7.5.1.1). There exist four heat sinking stages:

1. Top of the 77 K reservoir,
2. Bottom of the 4 K reservoir,
3. 1 K plate, and
4. Helium-3 pot.

As a rule of thumb, the length of the wires between two consecutive heat sink stages, with temperatures (say) T_1 and T_2 ($< T_1$), should be made proportional to $\Delta T \equiv T_1 - T_2$.³³

Fig. 7.6.6 shows wires being heat sunk to the bottom of the 4 K reservoir. The fiberglass sleeving is stripped to improve thermal conductance to the wire's metallic core. After clamping the stripped wire bundles to bobbin, heat is exchanged through the Manganin and Copper wires' respective insulation (c.f. Table 7.3).

7.6.3.4 Electrical connectors

The six wires belonging to the sensor and heaters,³⁴ attached to (say) the bottom of the 4 K reservoir (c.f. Fig. 7.6.3), form continuous wire segments up to their connection to the 20-pin feedthrough (c.f. Fig. 7.6.4). However, it is more convenient to divide the wires into more than one segment for sensors/heaters of some of the lower cryostat components. Some of these components include the rotator, 77 K shield tails, and Helium-3 pot. Different wire segments are connected using 4-pin PEEK connectors (c.f. Sec. C.3.4).

³³A more detailed analysis would take into account the length of the wires as well as the cooling power and heat load budget of each heat sinking stage.

³⁴2 for the heater and 4 for the sensor.

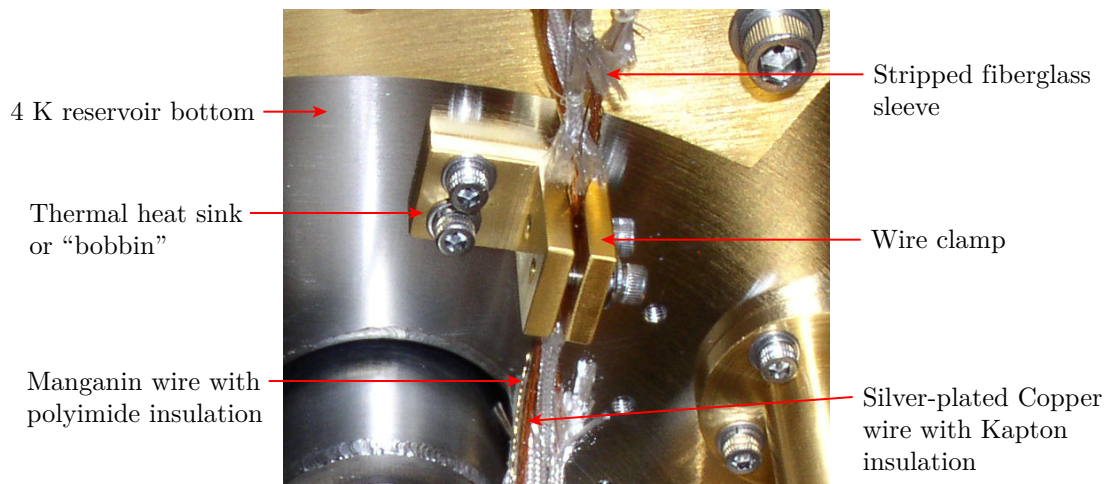


Figure 7.6.6: Heat sink or bobbin for thermally anchoring wires at the bottom of the 4 K reservoir

7.7 Operation and performance

7.7.1 Preventive measures

7.7.1.1 Leak tests

It is important to ensure that all the cryogen circulation paths³⁵ are leak-tight prior to cryostat operation (a.k.a. the cool down). Leak tests are performed on the seals between three types of interfaces: (a) rough vacuum and atmosphere, (b) rough vacuum and UHV, and (c) atmosphere and UHV. For typical lab operation schedules, while the cryostat is under UHV, it will undergo multiple thermal cycles due to cool downs and bake-outs. As a result, properties of the vacuum seals could change significantly over time (e.g. c.f. Sec. 7.8.1).

In some cases, a leak is easily noticeable (e.g. atmosphere to UHV), while in others (e.g. rough vacuum to atmosphere) a dedicated leak test is required. Depending the vacuum interface being tested, two types of instruments (c.f. Sec. 6.5) can be used for leak detection: (a) leak detector and (b) residual gas analyzer (RGA). The former is typically used for rough-vacuum-to-atmosphere seals. The latter is used for any type of seal to UHV. Some examples of cryostat subsystems requiring leak tests, when the cryostat is at UHV, are:

- Helium-3 insert (c.f. Sec. C.2.2.1)
- 1 K pot circuit (c.f. Sec. C.2.2.2)
- 4 K and 77 K reservoirs (c.f. Sec. C.2.2.3)

Details of these examples will be discussed in Sec. C.2.2

³⁵This includes both open- and closed-loop.

7.7.1.2 Sealing of Helium-4 reservoir

It is impractical to completely eliminate ice formation, from condensation of water vapor, inside the 4 K and 77 K reservoirs. With proper care, however, the effects of ice formation inside reservoirs on the cryostat's performance can be minimized. The 77 K reservoir is a relatively simple volume of sturdy construction.³⁶ Therefore, there is negligible impact on the cryostat operation from ice formation inside the 77 K reservoir. On the other hand, the 4 K reservoir is responsible for housing a complex and delicate component: the Helium-3 insert.

It is evident from Fig. 7.4.1 that several operation-critical components of the Helium-3 insert, above the Indium-sealed flange, are immersed in liquid Helium-4. In Sec. 7.4.1.2, I labeled these components as the ones “in atmosphere.” While this region (i.e. 4 K reservoir) is indeed maintained close to atmospheric pressure, it is not directly exposed to atmosphere. In other words, the 4 K reservoir is o-ring sealed³⁷ from atmosphere to prevent “contamination” of said reservoir from water vapor. On average, since the pressure inside the 4 K reservoir is no more than 4 psi higher than atmosphere, the sealing requirements on the o-rings is relaxed to some degree. In other words, the o-ring seals can be temporarily undone during cryogen fills.

7.7.1.3 Cryogen boil-off management

The 4 K and 77 K reservoirs produce a large amount of Helium-4 and Nitrogen gas, respectively, during the initial cool down³⁸ due to cryogen boil off. For almost two years following the installation (December 2014) and initial sub-Kelvin cool down test of the cryostat in the lab, and one year since the assembly of the ARPES system (Summer 2015), most of the (debugging) measurements (c.f. Sec. 8.2-8.4), were performed with just a liquid Nitrogen cool down for cost reasons.

During the first couple of liquid Helium cool downs, however, the importance of cryogen boil-off management became evident. The boiled off Helium-4 gas would get trapped in a 14' × 9' × 2' pocket in the ceiling (c.f. Fig. 8.1.1) and trigger the smoke detector.³⁹ This problem was solved by implementing the “Helium diversion system.” This system consists of ≈ 1" PVC tubes, valves, bellows, and gas-tight connectors guiding boiled off gas from the 4 K reservoir to the building exhaust.

7.7.2 Cryostat cool down steps

7.7.2.1 Liquid Nitrogen cool down

The first step in the cool down involves bringing all the subsystems of the cryostat from room temperature to as close to 77 K as possible. Therefore, both the 77 K and 4 K reservoirs are filled with liquid Nitrogen. The latter is only partially filled. The 1 K pot gets cooled to 77 K by the liquid Nitrogen carried to it from the 4 K reservoir through the capillary. The 1 K pot, in turn, cools down the Helium-3 pot and cold finger through the heat switch. The latter is manually engaged by the operator during this step. Once the system reaches its base temperature, for this step, the system is prepared for a liquid Helium-4 transfer.

³⁶The walls of 77 K reservoir are constructed by (TIG) welding together stainless Steel plates and tubes of appreciable thickness. The only thin-walled components are the fill tubes. But the latter are not immersed in liquid Nitrogen and experience less thermal stresses compared to the rest of the reservoir.

³⁷“Sealed” is a loose term. While o-rings don't form a adequate vacuum-tight seal at low temperatures, they nonetheless prevent a high conductance path for water vapor.

³⁸The boil off from refills of cold reservoirs is considerable less. This is because, during refills, cooling *usually* does not start all the way from 300 K.

³⁹This was first noticed in September 2016.

7.7.2.2 Liquid Helium-4 cool down

After evacuating the 4 K reservoir and 1 K pot of residual liquid Nitrogen,⁴⁰ liquid Helium-4 is transferred to the 4 K reservoir. The cool down to 4 K proceeds in qualitatively the same way as that from room temperature to 77 K. The 1 K pot gets cooled directly by the liquid Helium-4 it receives from the capillary and the Helium-3 pot and cold finger, in turn, get cooled by 1 K pot through the heat switch. The difference is that liquid Helium-4 inside the 1 K pot can reach 1.5 K because it is being pumped on by a high mass conductance pump. As discussed in Sec. 7.4.2.2, the exact base temperature of the 1 K pot depends on the optimization of the needle valve. At the nominal 1 K pot temperature of 1.5 K,⁴¹ the lowest sample temperature achieved was between 1.8-2 K.

7.7.2.3 Helium-3 cool down

Helium-3 gas can condense in its pot once the 1 K pot temperature falls below the former's boiling point (3.2 K). Recall that, at this point, the Helium-3 and 1 K pots are thermally shorted by the heat switch. Once the 1 K pot reaches its base temperature (≈ 1.5 K), however, the heat switch is disengaged to prevent heat leakage from the 1 K subsystem to the Helium-3 pot, as the latter continues to cool below 1.5 K during Helium-3 condensation.

The Helium-3 condensation step is initiated by: (a) turning on the backing pump (Pfeiffer DUO65) of the pumping station, and (b) setting up a gas conductance path which allows the backing pump to push Helium-3 gas from its storage container to the Helium-3 pot from *both* sides of the impedance (c.f. Fig. 7.4.7). In other words, the impedance is “shorted” in this plumbing circuit.⁴² The exhaust of the backing pump maintains the pumping and return paths of the Helium-3 insert at relatively high pressure to facilitate the condensation process.

After sufficient condensation is achieved, the flow of Helium-3 is changed (c.f. Fig. 7.4.8) such that a continuous flow loop is set up from the Helium-3 pot to the appropriate pump and back. Turning on the roots blower during circulation reduces the base temperature down to 0.84 K. At this temperature, the ambient heat load is balanced by the rate at which the roots blower removes heat from the evaporatively cooled liquid Helium-3 (c.f. Sec. 7.1.3).

7.7.3 Cooling power

Cooling power is the most important figure of merit in *any* cryostat. Achieving a low base temperature is important. However, it is even more important to maintain said base temperature. As I discussed in Sec. 7.7.2.3, the base temperature is reached when the heat load equals the cooling rate. The cooling power quantifies the stability of this balance by measuring the rise in the base temperature when a well-controlled heat load is introduced. Moreover, in some cases, cooling power measurements can provide crude estimates, by extrapolation, of the amount of heat load experienced by the cold finger at base temperature.

Fig. 7.7.1 shows the cooling power curve of the ARPES Helium-3 cryostat measured from the base temperature (0.84 K) to 1.2 K. The controlled heat load source was the wire-wound heater on the rotator. According to crude estimates, the ambient heat load on the sample is between 10-15 mW

⁴⁰The importance and details of this step are discussed in Sec. C.2.5.1.

⁴¹“1 K pot” is a pseudonym.

⁴²Recall that the impedance, by design, maintains a large pressure gradient. If Helium-3 was only pumped from one side of the impedance, very little gas would make it to the other side, thereby limiting the 1.5 K surface area available for condensation.

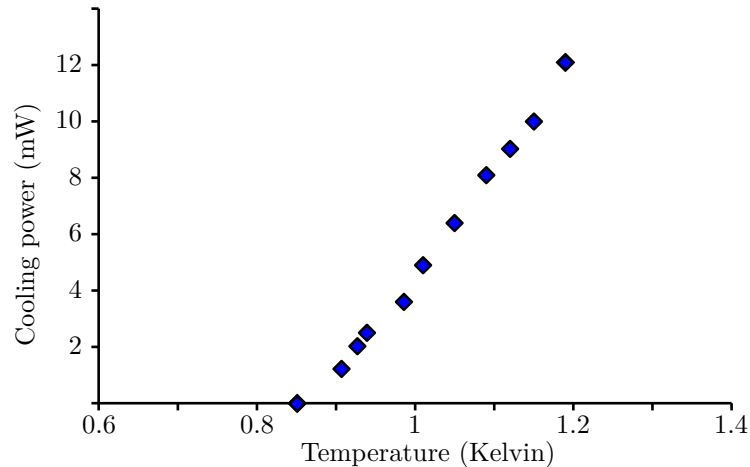


Figure 7.7.1: Measured cooling power of the cryostat measured up to ≈ 0.36 K above the base temperature (0.84 K)

at base temperature, a majority of which comes from the vertical slits in the radiation shield. For comparison, the heat loads experienced by a dilution refrigerator at base temperature (10s of mK) are the 10s of μ W range.

7.8 Customization

7.8.1 Bellows replacement on liquid Helium-4 reservoir

7.8.1.1 Introduction

After a bake-out following measurements on $\text{Bi}_2\text{Sr}_2\text{CaCu}_2\text{O}_{8+x}$ (c.f. Sec. 8.5.2.3), a base pressure of 10^{-9} torr was achieved at room temperature, which was a factor of 5 higher than usual. After eliminating the possibility of compromised flange seals and contamination, the raised base pressure was confirmed, using an RGA, to be the result of an atmosphere-to-UHV leak in the 4 K reservoir. Moreover, by inserting a nozzle spraying Helium-4 gas into the 4 K reservoir, the leak was confirmed to be at the top of said reservoir. This observation led to the conclusion that the leak was most likely a compromised weld joint.

The ensuing repair process proceeded as follows:

1. Leak tests without major disassembly
2. Removal of the liquid Nitrogen reservoir
3. Isolation of the leak to the 4 K reservoir bellows
4. Removal of the Helium-3 insert
5. Replacement of the bellows with a rigid tube
6. Reassembly of all mechanical components and leak tests

7. Rewiring of the electrical system

Steps 1-6 were performed at the cryostat manufacturer's facility⁴³ due to their access to the necessary repair tools. Step 7 was performed at Caltech. Moreover, the customization steps discussed in this section (i.e. Sec. 7.8) were performed in parallel with step 7.

7.8.1.2 Cryostat disassembly

In this section, I will focus on steps 1-4 listed in Sec. 7.8.1.1. As I will discuss below, the cryostat was disassembled to a greater degree as the location of the leak was narrowed down.

At first, leak tests on the accessible regions of the 4 K reservoir were performed with only the main shroud (c.f. Sec. 7.3.2.2) and sample probe (c.f. Sec. 7.5.1.1) removed. Access to the 4 K reservoir was partially blocked by the 77 K reservoir (c.f. Fig. 7.3.1). The goal of this leak test was to determine if the leak existed in a region of the 4 K reservoir which was accessible without removal of the 77 K reservoir. Unfortunately, that was not found to be the case.

The 77 K reservoir was detached from the reservoir insert (c.f. Sec. 7.3.2.1) by grinding off the weld seam between the two concentric tubes on each of the three liquid Nitrogen feedthroughs (c.f. Fig. 6.3.9). I designed and machined a jig to support the weight of the 77 K reservoir. Moreover, the jig included Mitutoyo micrometers, acting as spacers between the 4 K and 77 K reservoirs, in order to encode the original position of the 77 K reservoir.⁴⁴ This was done to minimize the dislocation of the 77 K reservoir when it was welded back to the reservoir insert.

Leak tests performed after the 77 K reservoir removal revealed that the leak was located in the 4 K reservoir bellows (c.f. Fig. 7.8.1). Silver soldering (c.f. Sec. 6.3.5.2) was used to patch the tear in the bellows. Unfortunately, the tear expanded when heat was applied during soldering, leading to a "tear chasing" condition. In other words, when applying Silver solder to the tear in one location of the bellows, the heat from the torch led to the tear propagating along the circumference of the bellows, and opening up a secondary tear in a different location. Ultimately, it was decided that the bellows had to be replaced with a rigid 0.050" thick tube. Removing the bellows involves grinding its weld seal with: (a) the 27.125" OD wire seal flange at the top, and (b) the 0.030" thick ring adapter at the bottom. The latter serves as an adapter to the top of the 4 K reservoir.

Prior to removing the bellows, however, it was important to protect the Helium-3 insert from dust generated in the grinding of the welded joints in the bellows. Besides, it was topologically not possible to install the rigid tube without removing the insert. Therefore, Helium-3 insert was removed by disconnecting the Indium-sealed flanges (c.f. Fig. 7.4.1) at the bottom of the 4 K reservoir.

7.8.1.3 Bellows replacement

After removing the Helium-3 insert, and employing appropriate protective measures to the UHV parts from dust,⁴⁵ the weld seals on the bellows with the wire seal flange and the 0.030" thick ring adapter were ground using an abrasive tool, and the bellows was removed and discarded. Subsequently, 0.050" thick sheet metal was rolled up and TIG welded (c.f. Sec. 6.3.5.1) along a seam

⁴³The manufacturer is Janis Research Company, LLC.

⁴⁴Note that these micrometers encoded the position of the 77 K reservoir relative to the 4 K reservoir. Back then, I had not anticipated replacing the bellows with a rigid tube. The process of replacing the bellows could have slightly shifted the position of the 4 K reservoir, and hence the 77 K reservoir.

⁴⁵For example, the blind holes on top the 4 K reservoir were covered with Kapton tape (c.f. Fig. 7.8.1) to avoid accumulation of dust in them.

into a 9" diameter tube. The length of the tube (≈ 1 foot) was fine tuned to fit the gap between the aforementioned flange and the ring. Moreover, the top end of the tube was flared, on a lathe, to eliminate the gap between the tube and the wire seal flange. After a satisfactory fitting of the tube was achieved, it was leak tested to 8×10^{-9} mbar \cdot l/s,⁴⁶ before the final electropolishing step.

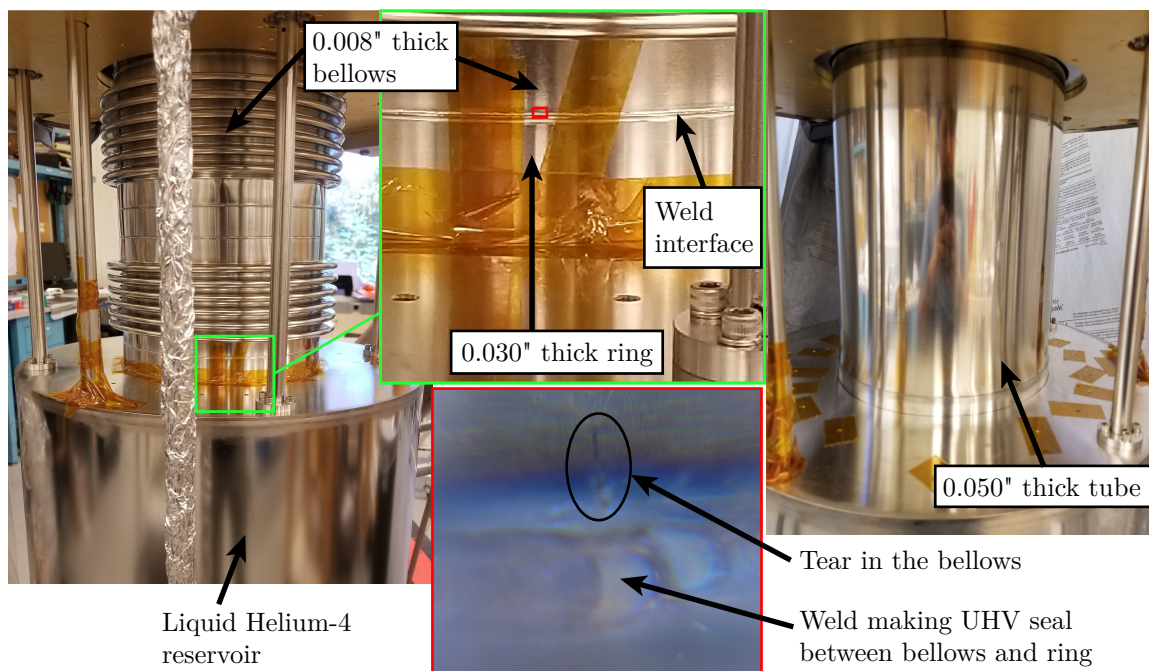


Figure 7.8.1: Left: a zoomed-out view of the bellows with the leak. Middle top: a zoomed in view of the location to which the leak was narrowed down. Middle bottom: magnified view of the red box region showing a tear the 0.008" thick walls of the bellows. Right: a zoomed out view of the rigid 0.050" thick wall tube replacing the bellows.

After electropolishing, the tube was fitted between the wire seal flange and the 0.030" thick ring adapter, and an atmosphere-to-UHV seal was formed by TIG welds on both sides. A custom round aluminum clamp was installed around the 0.030" thick ring adapter to act as a heat sink during welding. The heat sink would minimize warpage of the two thin walled tubes being joined, thus minimizing the thermal stresses which originally caused the bellows to tear. The top wire seal flange acted like its own heat sink.

7.8.1.4 Cryostat reassembly and testing

The Helium-3 insert was re-attached to the 4 K reservoir after the rigid tube installation (c.f. Fig. 7.4.1). A new Indium seal was made between the bottom flange of the 4 K reservoir and the insert. On the other hand, the insert's o-ring seal with the top wire-seal flange was reused after cleaning. Both seals passed a room temperature leak test.

An atmosphere-to-UHV seal was made between the wire-seal flange and the 77 K reservoir using TIG welding (c.f. Fig. 6.3.9). Final leak tests were performed at room temperature and 77 K after the main shroud (c.f. Fig. 7.3.3) was installed.⁴⁷ These leak tests simultaneously verified leak-free connections of the insert as well as the new rigid tube.

⁴⁶This was a preliminary leak test. A more thorough leak test was performed after installing the tube and the Helium-3 insert on the cryostat (c.f. Sec. 7.8.1.4).

⁴⁷The 77 K leak test could not be performed without vacuum isolation from the main shroud.

After the system passed the final leak tests, the only step left (i.e. step 7) was re-wiring the cryostat (c.f. Sec. 7.8.1.2). The removal of the 77 K reservoir and the Helium-3 insert also required complete disassembly of the wiring network for the cryostat's sensors and heaters. Unlike the leak repair process, re-wiring did not require specialized tools. Therefore, in order to reduce the cryostat's repair cost, it was decided to finish re-wiring the cryostat at Caltech.

7.8.2 Sample probe welding

As I stated in Sec. 7.8.1.1, most of the repair process took place at the cryostat manufacturer's (i.e. Janis) facility. The shipment of the cryostat to Janis required partial disassembly due to space constraints at Caltech.⁴⁸ One of the most important components removed was the sample probe (c.f. Sec. 7.5.1.1). During the sample probe's removal, it was noticed that the bolted connection at its top was wobbly (c.f. Fig. 7.5.1). One of the four countersink screws had fallen off and the rest were loose. It was very likely that this loose connection contributed to the hysteresis observed in the x - y manipulation (c.f. Sec. 7.5.4.1).



Figure 7.8.2: Photograph of the bolted sample probe interface after welding.

The cryostat was shipped back to Caltech after completion of repair steps 1-6 (c.f. Sec. 7.8.1.1). During the cryostat's reassembly, the bolted connection was closely inspected. It was decided that the only way to ensure rigidity at the bolted connection was by welding. Therefore, four weld seams were tacked at the interface of the connection. A photograph of the sample probe after welding is shown in Fig. 7.8.2.

7.8.3 Coarse x - y manipulator upgrade

7.8.3.1 Introduction and motivation

In Sec. 7.5.4, I discussed some of the problems with the x - y manipulator from the user's point of view. In this section, I will present a diagnosis for these problems, and elaborate on some other issues encountered in day-to-day operation of the coarse x - y manipulator. In the following two sections (Sec. 7.8.3.2 and 7.8.3.3), I will discuss the design, fabrication and installation of a new x - y manipulation systems which solves the problems described below.

A range of technical problems, beyond x - y manipulators, required venting and disassembly of the cryostat on multiple occasions. During these servicing periods, I visually observed and confirmed that the flexible shaft coupler was a major source of manipulator hysteresis. For example, a certain

⁴⁸These space constraints are related to sizes of doors, elevators, and hallways leading to and out of the lab.

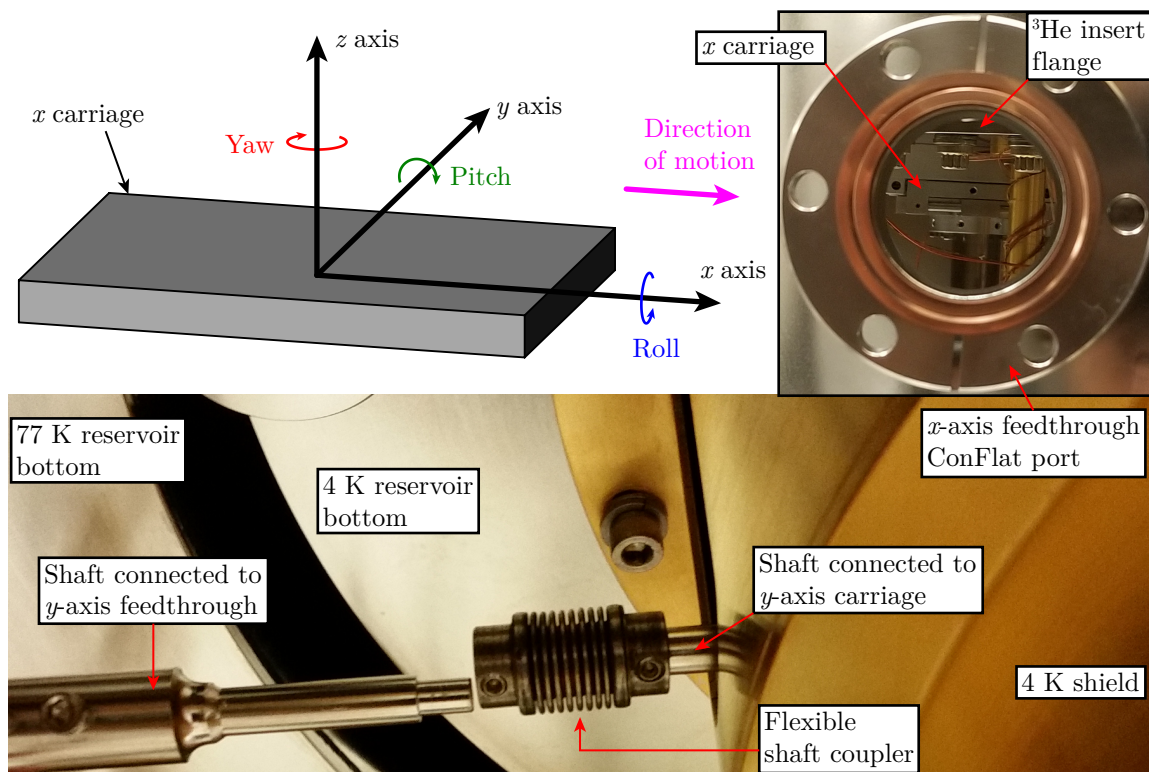


Figure 7.8.3: Top left: illustration of errors in the motion of a linear translation stage. Top right: view of the *x*-*y* stage from the *x*-axis linear feedthrough port on the main shroud. Bottom: decoupling of the *y*-axis feedthrough shaft from the *x*-*y* stage due to slipped set screw.

amount of displacement of (say) the *x*-axis linear feedthrough did not produce an equal shift in the *x*-axis stage's position due to expansion or contraction of the flexible shaft coupler. Hysteresis resulted in this actuation mechanism due to the unpredictability of said coupler's state of expansion or contraction. The cryostat manufacturer installed the flexible shaft couplers for two reasons:

1. correction of misalignment between the linear feedthrough ports on the main shroud (c.f. Fig. 7.3.3) and the Helium-3 insert (c.f. Fig. 7.4.1),⁴⁹ and
2. compensation for thermal expansion and contraction of the shafts due to temperature cycling.

The two slotted PEEK braces (c.f. Fig. 7.5.6) in the crisscross design were also problematic. While the contact between these braces and the stainless steel section of the sample probe had low friction, the former was too soft to effectively actuate the latter without deformation. This deformation introduced hysteresis to a lesser degree than the flexible shaft coupler.

The linear bushing (c.f. Fig. 7.5.6) only centered the shafts in the horizontal plane. In other words, the *x* and *y*-axis carriages had too much pitch angular error. Moreover, upon disassembling of the *x*-*y* stage,⁵⁰ I noticed a significant yaw angular error as well (c.f. Fig. 7.8.3).

Some other mundane problems had to do with the shafts and the linear UHV feedthroughs. On one occasion, the set screw holding the flexible shaft coupler and the shaft slipped during sample

⁴⁹Recall that the *x*-*y* stage is installed at the bottom of the Indium-sealed flange of the insert

⁵⁰This was prior to shipping the cryostat to Janis for the leak repair.

manipulation, leading to a decoupling of the feedthrough from the x - y stage (c.f. Fig. 7.8.3). On multiple occasions, the feedthrough's internal mechanism would fail due to slipping of the retaining ring from its groove. Fortunately, the latter was located in atmosphere; hence no venting was necessary. But it was a nuisance nonetheless.

7.8.3.2 Design improvements

The design of the new coarse x - y manipulator is shown in Fig. 7.8.4. The motion of the two carriages is constrained along the respective axes using 1/8" diameter solid guide rods. The machining tolerances of the carriages were chosen such that the close fit between the latter and its guide rods significantly improved yaw angular error (c.f. Sec. 7.8.3.3) compared to the crisscross design using PEEK braces (c.f. Fig. 7.5.6). Moreover, the new linear bushings constrained the shaft motion in all directions transverse to its axis. As a result, pitch angular error was considerably minimized.

In the crisscross design, the slot in each carriage, or PEEK brace, pushed sample probe independently. However, the finite thickness of the PEEK brace was not ideal for the pivoting motion of the sample probe, about the coarse x - y stage, when the fine x - y stage was actuated (c.f. Sec. 7.5.2.3). In the new design, the interaction between the sample probe and the coarse x - y stage is reduced to a point by the introduction of ball bearings; the latter offers several advantages.

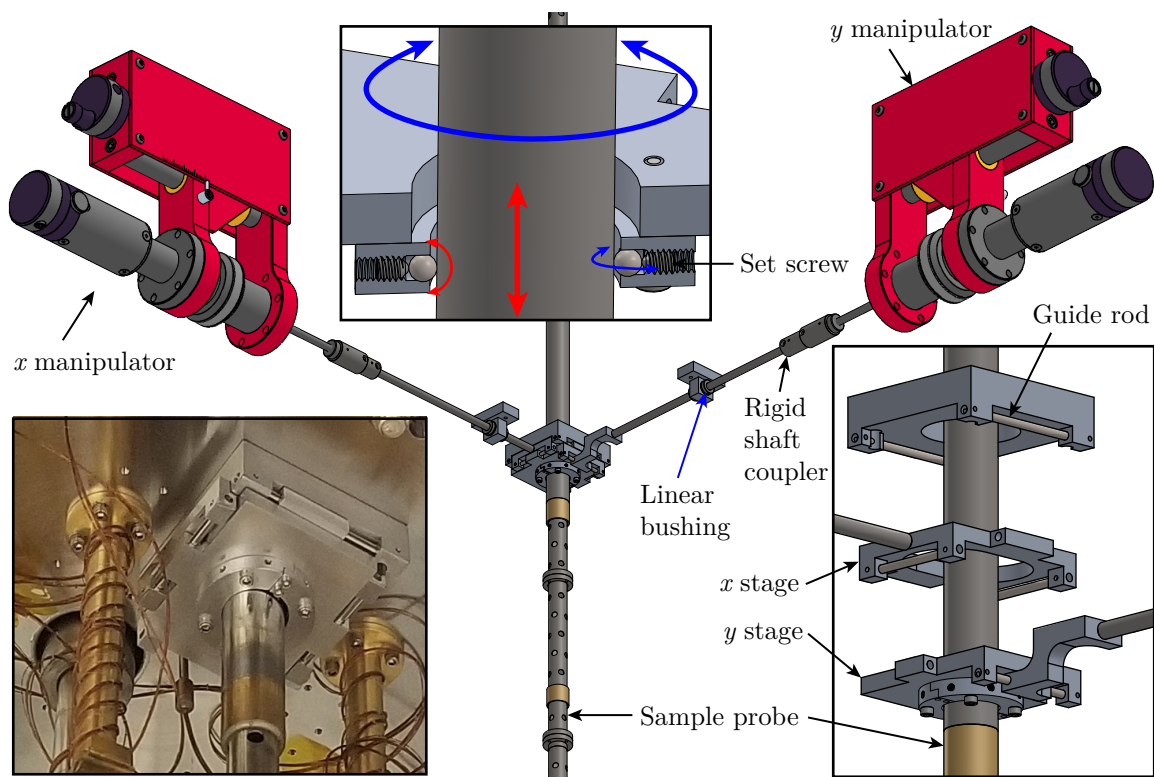


Figure 7.8.4: CAD model of the upgraded x - y manipulation system with the sample probe.

Since the stage uses precision-ground stainless Steel ball bearings, they do not suffer from the PEEK deformation problem of the old design. Moreover, the increased Steel-to-Steel friction is mitigated by the rolling motion of the ball bearings. Fig. 7.8.4 shows the rotation of the ball bearings as the sample probe moves linearly along the z -axis and rotates along the θ -axis. In fact, the force exerted by the ball bearings on the sample probe can be tuned using set screws.

In addition to the x - y stage, the linear feedthroughs were also upgraded (c.f. 7.8.4). In order to eliminate the primary source of hysteresis, the flexible shaft couplers were replaced by rigid ones. Thermal expansion and contraction of the shafts was mitigated by making the shaft detachable in situ. This was implemented with an additional rotary manipulator which screwed the feedthrough shaft into the shaft connected to the x - y stage.

7.8.3.3 Fabrication and installation

One of the most critical step of x - y stage fabrication was the fit between the guide rods and the carriages. The guide rods were made of precision ground 1/8" diameter (tolerance 0.0002") 316 stainless Steel dowel pins. The carriages were made of Aluminum for reasons of cost and ease of machining. The holes in the carriages, for the guide rods, were sized by precision reaming. Successively larger diameter reamers were used until a good balance between closeness of fit and friction was obtained.⁵¹ A UHV-compatible graphite lubricant was used.

Misalignment between the linear feedthrough ports on the main shroud (c.f. Fig. 7.3.3) and the Helium-3 insert (c.f. Fig. 7.4.1) was compensated by retrofitting the linear bushing mount heights and locations of tapped holes used to attach the shaft connecting to the linear feedthrough. A view of the tapped hole in the x carriage from its linear feedthrough port is shown in Fig. 7.8.3.

7.8.4 Redesign of the electrical system

7.8.4.1 Introduction and motivation

Re-installation of the electrical network (c.f. Sec. 7.6) was the last step of the leak repair process (c.f. 7.8.1.1). Prior to fixing the leak, when the wiring system was being uninstalled, I noticed several problems which impeded proper operation of the ARPES system. Firstly, the spring-loaded pins used to connect wires to the 20-pin feedthroughs, as well as the plastic rings used for color-coding the wires, were not UHV compatible (c.f. Fig. 7.6.4). Secondly, some of wires were found to be cut on the sharp edges of the 1 K plate from shear stresses exerted on the former by the motion of the sample probe.

Moreover, a serious issue which was observed early on, during normal cryostat operation, was that of the dust generated by the fiberglass sleeves (c.f. Fig. 7.6.5). During the sample loading process (c.f. Fig. 7.5.8), pieces of the fiberglass were seen falling into the analysis chamber. This presented a fatal risk to the analyzer operation. If sufficient amount of an insulating material, like fiberglass dust, accumulated close to the analyzer, the former could charge up during an ARPES measurement, and result in damage to expensive components of the latter.

All of above problems made it clear that a complete redesign of the electrical network was necessary.

7.8.4.2 Design, fabrication and installation

The re-wiring process went through two designs: (a) sleeveless (c.f. Sec. C.3.1), (b) and sleeved. Here I will only discuss the latter since it is the one that is implemented in the cryostat at the time of writing. The details of design, fabrication, and installation are discussed in Sec. C.3.2-C.3.5. A summary of the advantages this design offered over the original one (i.e. before the leak repair) are as follows:

⁵¹The following reamer sizes were experimented with until the appropriate fit was obtained: 0.1253", 0.1255", 0.1256", 0.1257", and 0.1260".

1. **Routing:** attention was paid to keep wires away from moving parts like the sample probe and braids.
2. **Modular design:** instead of a continuous wire bundle from the feedthrough to the respective sensors and heaters, a composite wire bundle was created out of shorter wire bundle segments called *wire modules* (c.f. Fig. C.3.2). For example, a 15 feet long wire bundle was divided into three 5 feet long wire modules. In this design, if one of the modules was damaged, the repair effort for manageable in a considerably shorter time.
3. **Elimination of fiberglass:** protective sleeves around each wire module were made of braided PEEK sleeves (c.f. Fig. C.3.2). PEEK is considerably more immune to disintegration compared to its fiberglass counterpart. Therefore, the risk posed by fiberglass dust to the analyzer was eliminated.
4. **UHV compatibility:** the UHV-incompatible feedthrough pins (c.f. Fig. 7.6.4), from the original wiring system, were replaced by mechanically similar ones made of gold-plated Beryllium Copper. Moreover, the UHV-incompatible plastic rings (c.f. Fig. 7.6.4) used at the feedthroughs for color-coding the wires were replaced by stamped aluminum blanks (c.f. Sec. C.3.5).
5. **Heat sinking:** heat sinking of the wires was done by epoxying them to bobbins (c.f. Sec. C.3.3). This improved thermal conductance to the bobbin, increased modularity, and most importantly, reduced the risk of wire-cutting due to thermal contraction during cool downs.⁵²

⁵²During the initial installation of the cryostat at Caltech, the first liquid Nitrogen cool down resulted in some of the sensor and heater wires being cut due to thermal contraction.

Chapter 8

Assembly and optimization of the ARPES system

In chapters 4-7, I discussed the design, construction, and installation of the *individual* tools necessary for low-temperature and high-resolution ARPES. In this chapter, I will discuss the process involved in the integration of these tools to form a functioning ARPES system. I will start by describing the system assembly, followed by efforts to acquire and optimize data, and conclude with system specifications achieved at the time of writing of this thesis.

8.1 ARPES system assembly

8.1.1 Lab infrastructure

It is instructive to survey the available lab infrastructure in order to appreciate some of the choices made in designing and implementing the ARPES system configuration. The ARPES system was supposed to be constructed in the space between the two optical tables shown in Fig. 8.1.1. This would allow convenient access to laser light sources, both continuous wave and pulsed, for not only ARPES, but also (potentially) low-temperature optics.

It is convenient to set the height of the sample, under ARPES or optics measurement, close to the *average* height of the laser beams. With the optical table heights roughly 3 feet above the ground, and the height of most optics mounted on said tables being less than a foot, the sample height could not be any higher than 4 feet. Fig. 7.2.1 shows that the sample is located at the bottom of the Helium-3 cryostat. The total height of the cryostat is a little less than 9 feet. The standard ceiling height in the lab is 13 feet. To account for overhead, associated with operations like cryostat cool downs and setting up bake-outs, a fractional footprint (14 feet \times 9 feet) of the total lab ceiling was raised by 3 feet. The resultant “inverted ditch,” referred to as the *ARPES pocket*, is shown to the left of Fig. 8.1.1.

A chain hoist is installed on the ARPES pocket ceiling. This hoist can travel along the long direction (\lesssim 14 feet) of the ARPES pocket on an I-beam. In addition to the initial assembly, the hoist was used frequently to raise and retract the cryostat from the analysis chamber (c.f. Fig. 6.3.3). For example, the eight spectra, shown in Fig. 8.3.1 and Fig. 8.4.2, each required raising the cryostat with the hoist.

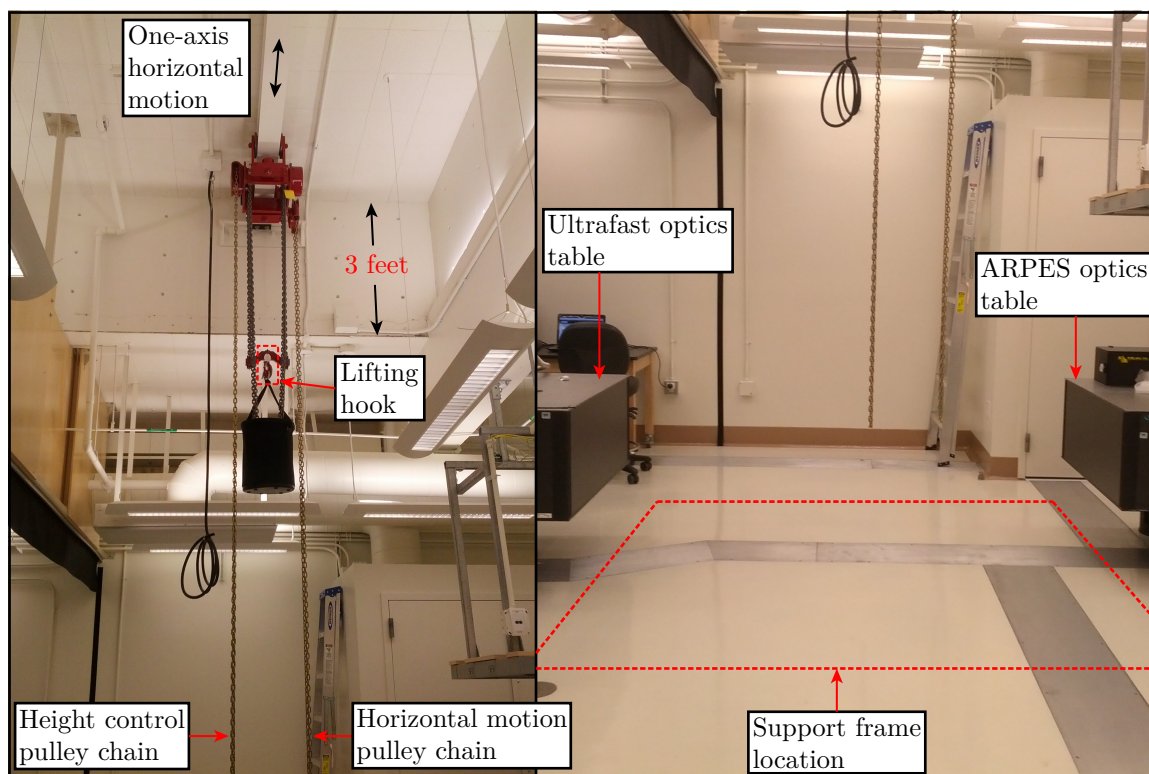


Figure 8.1.1: Left: pocket due to raised ceiling and the chain hoist in said pocket. Right: empty space between optical tables for constructing the ARPES system.

8.1.2 Mechanical support frame

In order to conveniently gain access to the system’s operation-critical controls, which are distributed across a vacuum system of almost 50 cubic feet in volume, and weighing close to 4000 lbs, it was essential to build a mechanical support structure around it. Due to the sensitivity of ARPES to magnetic fields, I decided to build this support frame by welding together stock aluminum parts.¹ The frame was assembled by bolting together smaller welded pieces, rather than welding all of it together, due to transportation limitations² and the infeasibility of welding inside the lab. The footprint of the support frame is roughly 8 feet \times 8 feet; its top tightly fits inside the ARPES pocket closer to the optical tables (c.f. Fig. 8.1.1).

The CAD model and results of a structural simulation of the support frame are shown in Fig. 8.1.2. The support frame has two decks. The top deck supports the weight of the cryostat (\approx 2000 lbs) and the personnel operating it. The lower deck houses the rest of the UHV system: three vacuum chambers, pumps, and related accessories. The entire support frame rests on more than a dozen leveling feet which can be used for height adjustment. Moreover, the frame can be partially disassembled such that it is possible to remove operation-critical components like the cryostat and analyzer for (say) servicing without disturbing any of the other equipment (e.g. chambers and pumps). The latter requires significant time and personnel resources to disassemble and re-assemble.

During the support frame design, there was uncertainty in the optimal “out-of-the-box” operation

¹Extruded square and rectangular tubes (most of them with 0.5" wall thickness) and 1" thick plates were machined, and subsequently welded, to form a composite aluminum part. These parts were eventually re-machined, after welding, to meet assembly tolerances. Fabrication of standard items like guard rails and stairways was relatively straightforward.

²The bottleneck was the size of the doors and elevator shafts in the lab building.

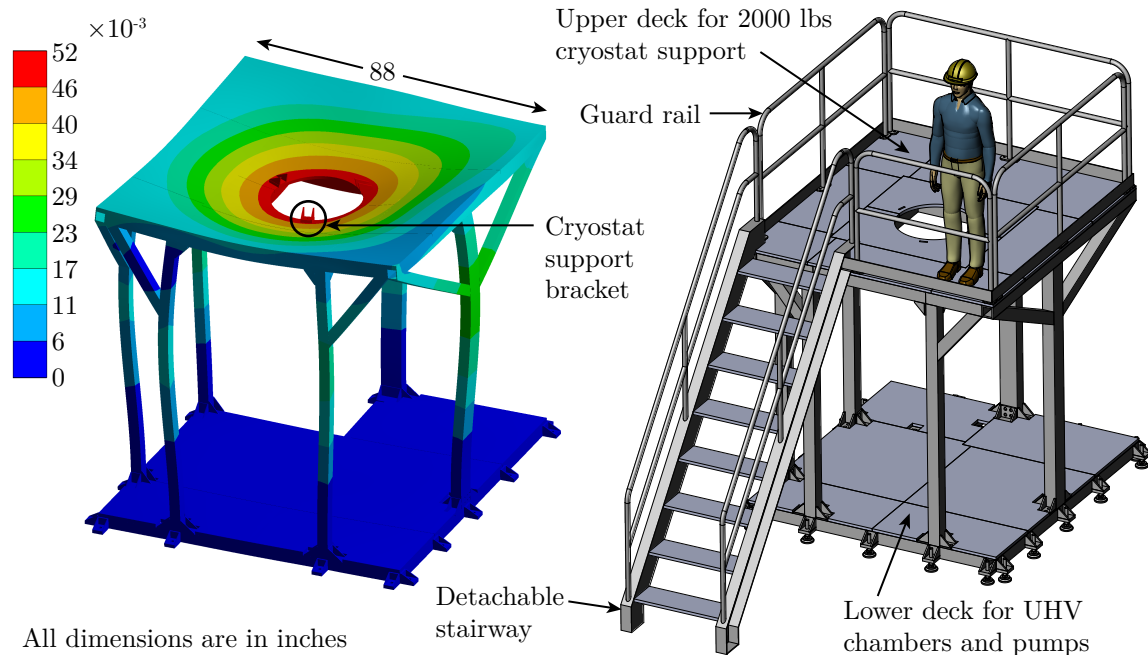


Figure 8.1.2: Right: CAD model of Aluminum support frame. Left: results of an ANSYS simulation illustrating *exaggerated* deflection (see color bar) due to the weight of a 2000 lbs cryostat. A maximum deflection of 0.052" is predicted at the location of the support bracket on the cryostat's main shroud (c.f. Fig. 7.3.3)

of state-of-the-art components like the sub-meV energy resolution R8000 analyzer and sub-Kelvin cryostat. Since these components were the workhorses of the ARPES system, building in the ability service or replace them seemed like a wise decision. This design choice paid off for the cryostat (for e.g., c.f. Sec. 7.8.1). The analyzer did not experience any major problems during the measurements presented in this thesis.

8.1.3 Support frame modularity

8.1.3.1 Analyzer cart

In Fig. 8.1.2, the support frame model from the simulation shows a rectangular segment missing at the back-left corner of the lower deck.³ That segment is reserved for a so-called *analyzer cart* shown in Fig. 8.1.3. The analyzer cart is designed such that it mechanically supports the analyzer both: (a) during transportation, and (b) when the analyzer is connected to the analysis chamber (c.f. Sec. 6.3.2.1). In the latter configuration, the cart is raised, using leveling feet, such that the cart's top plate is flush with its counterpart on the support frame's lower deck. Moreover, the heights of the four casters are chosen such that they are not in contact with the lab floor in configuration (b).

The analyzer rests on the cart using a U-shaped cradle. The cradle has four motional degrees of freedom: three translations and one rotation. Translation along the two horizontal axes (say x and y) is achieved using slide carriages with Teflon™ bushings. The turn table on the top carriage allows rotation at arbitrary (x, y) coordinates. On top of the turn table, is the height adjustment plate.

³This rectangular segment was excluded from the simulation for tractability of the latter. Moreover, this segment is not designed to be critical to the support frame's structural integrity.

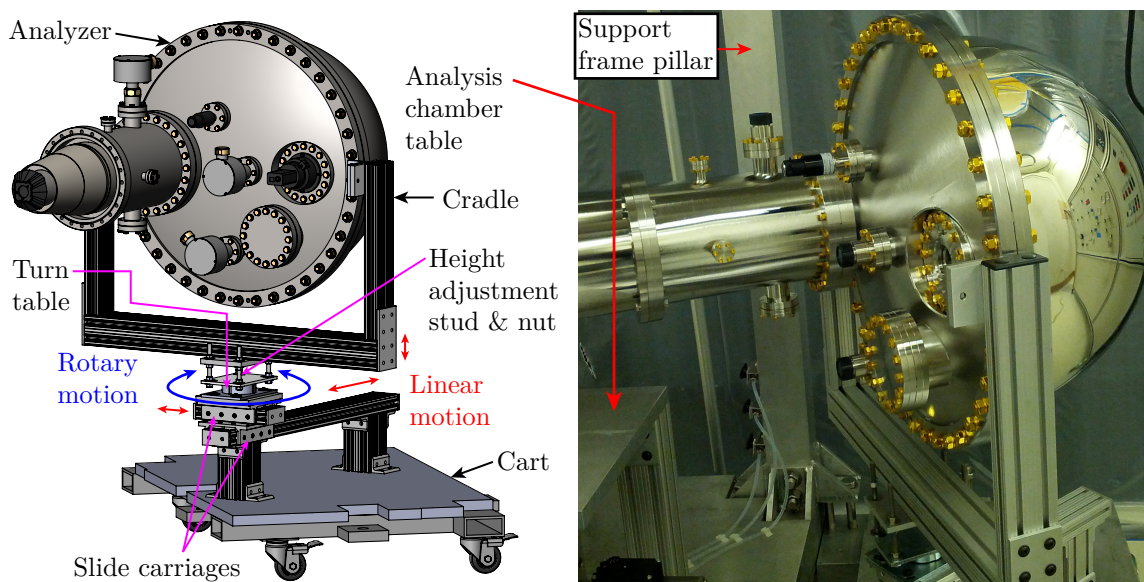


Figure 8.1.3: CAD model and photograph of the electron analyzer mounted on a mobile cart which attaches to the support frame.

The vertical translation of this plate is achieved using four stud-nut pairs. Finally, the cradle rigidly connects the height adjustment plate to the analyzer. Mating the analyzer with the analysis chamber required all four motional degrees of freedom of the cradle during the former's initial installation.⁴

8.1.3.2 Cryostat mobility

It is obvious from Fig. 8.1.2 that the cryostat passes through hole in the middle of the top deck. Moreover, the top three support brackets on the main shroud (c.f. Fig. 7.3.3) rest on two 1" thick rectangular Aluminum plates, each with a semicircle cut out at its edge. The support frame is designed such that, by removing these two plates, the stairway, and a small section of the top deck, the cryostat can be translated along the long direction of the ARPES pocket using the chain hoist (c.f. Fig. 8.1.1).

Fig. 8.1.4 shows photographs of the cryostat and the support frame when the former has been removed from the latter for servicing. Note that the *entire* vacuum system on the lower deck was left intact. This feature proved very beneficial when: (a) performing on-site repairs on the cryostat (i.e. the situation in Fig. 8.1.4), (b) making hardware changes to the cryostat during the ARPES system optimization (c.f. Sec. 8.2-8.5), and (c) shipping the cryostat to its vendor (c.f. 7.8.1).

8.1.4 Ultrahigh vacuum system setup

In this section, I will primarily focus on the aspects of the UHV system involving its mechanical assembly, rather than its standard operation. For details about the design and standard operation of the UHV system, the reader is referred to Chap. 6.

⁴At the time of writing, the analyzer has never been disconnected from the analysis chamber.

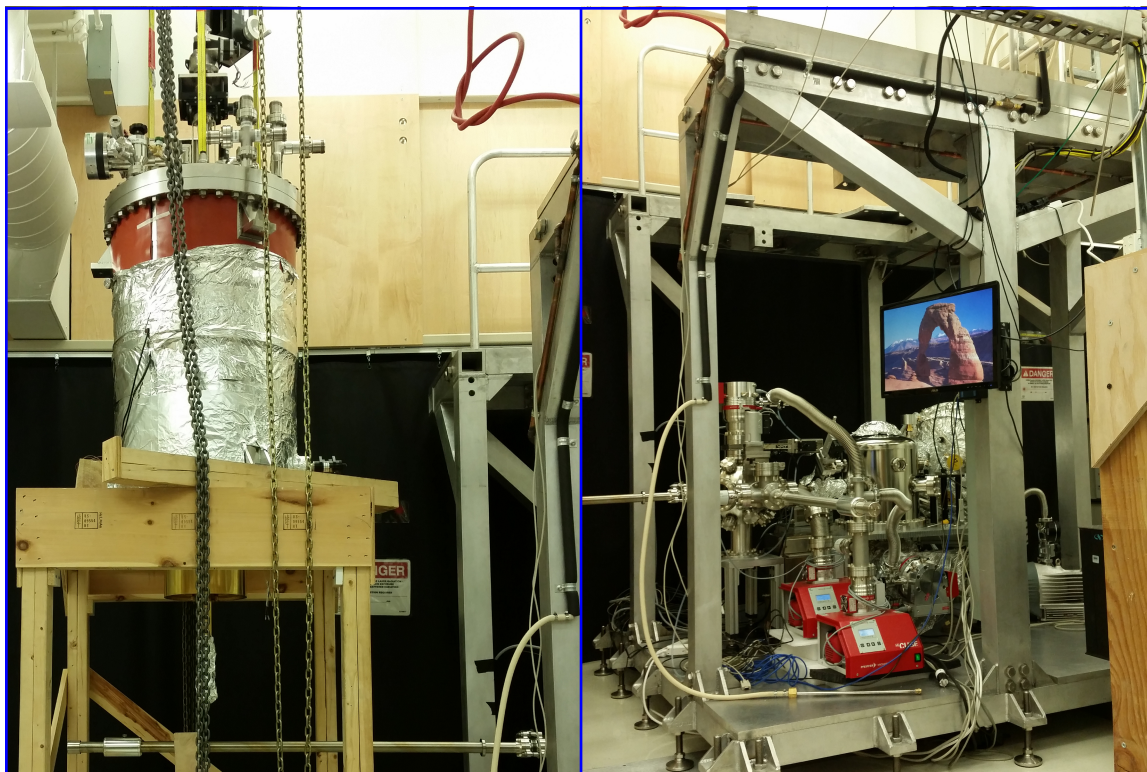


Figure 8.1.4: Left: photograph of the cryostat after it has been removed from the support frame using the chain hoist. Right: photograph of the partially disassembled support frame. The stairway and a section of top deck are removed to allow horizontal motion of the cryostat when the latter is suspended from the chain hoist.

8.1.4.1 Mechanical assembly

The analysis and preparation chambers are fastened to two custom Aluminum tables. These tables have their tops made of rectangular/square 1" thick Aluminum plates; their 80/20 feet rest on the lower deck of the support frame (c.f. Fig. 8.1.4). The table on which the analysis chamber rests also supports the weight of the pump chamber (c.f. Fig. 6.3.2). In order to ensure optimal mating between the cryostat and the analysis chamber, the cryostat was first placed on the top deck of the support frame, and the analysis chamber was raised, using the analysis chamber table's leveling feet, until the gap between the mating ConFlat was closed. Once the ConFlat flange was tightened, and verified to be leak tight, the leveling feet of the analysis chamber table were adjusted, by hand, to minimize the mechanical stress between the analysis chamber and the cryostat.

In the future, whenever the cryostat and analysis chamber needed to be separated, the cryostat was lifted using the chain hoist, without disturbing the vertical position of the analysis chamber. Disassembly was done in this way because, after the analyzer was attached to the analysis chamber, it was not possible to move the analysis chamber. Moreover, moving the analyzer could not be practically⁵ done without in-person technical assistance from the manufacturer (VG Scienta).

⁵It would be costly to fix *potential* degradation of the analyzer performance, compared to the installation specifications, if the analyzer was moved without a trained technician.

8.1.4.2 Bake-out setup

In this section, I will describe the tools and procedures involved in initiating the bake-out. Details of the bake-out process, once it has been setup, can be found in Sec. 6.4.3. In order to distinguish these two bake-out steps, I will refer to the former as the “bake-out jig.” In the design and implementation of a bake-out jig, it is important to consider heat: (a) generation, (b) distribution, and (c) insulation. The details of the tools used in achieving (a)-(c) changed over time. Here I will only discuss the version of the bake-out jig in use at the time of writing. Readers interested in learning about pros and cons of the different jig versions are referred to Sec. B.8.

Fiberglass-insulated resistive cords (3/16" diameter) were used for heat generation. These cords were designed such that directly plugging them into the mains outlet (120 VAC) resulted in 1.8 W/in² of heat dissipation from Joule heating. The cords were wrapped around all accessible surfaces, serving as atmosphere-to-UHV barriers, such that consecutive loops of the cord were approximately equally spaced. The cords were held in place by high-temperature tie-downs or tapes.

One of the most important figures of merit of a bake-out jig is its temperature uniformity. In the case of large temperature inhomogeneity, gas desorbed from hot surfaces will stick to “cold spots,” instead of getting pumped out of the system. Therefore, ensuring uniform distribution from the heating element (cords) to the surface exposed to vacuum is vital. However, since stainless Steel is a poor conductor of heat, the space between the cord loops was filled with Aluminum foil. Moreover, optimal thermal conductivity between the cords and the foil was established.

Finally, the Aluminum foil covered surfaces were insulated with 1/4" thick ceramic fiber sheets. An outermost layer of Aluminum foil was applied to the insulation sheet to avoid the spread of dust from the latter. The insulation helped raise the temperature of the stainless Steel chamber walls to 150 °C. The temperature at different points in the system was monitored using thermocouples for the entire duration of the bake-out.

8.1.5 Sample alignment

In order to excite the sample inside the analysis chamber, a laser beam of ≈ 1 mm waist needs to be guided from an optical table to the support frame, and through the analysis chamber optical window. The beam originates from the Toptica TA-FHG laser (c.f. Fig. 4.4.1) firmly fastened to said optical table. The beam path can be traced, up to the analysis chamber, by looking at its fluorescence from (say) an ordinary white piece of paper. Unfortunately, the beam does not fluoresce from any surface inside vacuum chamber. This posed a major challenge for sample alignment.

Even if one manages to load a UHV-compatible fluorescent material close to the sample, alignment is still challenging as the beam can be blocked by other surfaces, such as (say) the μ -metal and/or radiation shields, on its way to the sample. A more elegant solution is to use a bright tracer beam which is visible even in the toughest lighting and fluorescence conditions. A few mW Helium-Neon (HeNe) laser met these criteria.

8.2 Initial system performance

This section discusses the performance of the system immediately after the system was assembled and the problems that were encountered. The rest of the chapter discusses how the original assembly needed to be modified in order to mitigate said problems.

8.2.1 First ARPES measurements

At the end of the bake-out, it was decided to test the system with an electron-doped Bi_2Se_3 ⁶ sample following a liquid Nitrogen cool down.⁷ Bi_2Se_3 was chosen for the following reasons:

- Bi_2Se_3 cleaved easily due to its layered nature.
- Empirically verified Bi_2Se_3 bands had a measurable cross-section with 6 eV photon excitation
- The Fermi momentum (0.1 \AA^{-1}) of the electrons occupying the surface states above the Dirac point should be accessible with minimal sample alignment

Unfortunately, any statistically significant photoelectrons were not observed in the first attempts at data acquisition from Bi_2Se_3 . Eventually, photoelectrons were measured from the sample by tweaking some *test* voltages in the analyzer. While these test voltages deflected electrons away from their optimal trajectories, this step served as a debugging step in ensuring that photoemission was indeed occurring from the sample. This led to the conclusion that the information carried by the photoelectrons was lost before said photoelectrons reached the analyzer. In other words, some unknown parasitic electromagnetic forces around the sample randomly scattered the photoelectrons.

8.2.2 Radiation shield configuration changes

Having exhausted all other options, the (baked out) system was vented for further troubleshooting. Subsequently, a series of modifications to the radiation shield tail configurations were attempted, since said shield tails were the most obvious system components with which the photoelectrons could interact before reaching the analyzer. Alternatively, if no change in the photoelectron spectrum was observed as a function of shield tail configuration, then the possibility of shields as being the source of the problem could be ruled out. In that case, other factors (laser, analyzer, etc.) would have to be investigated.

By comparing the four panels in Fig. 8.3.1, it was evident that the shield tail configuration did indeed have a major impact on the spectrum. The top left panel in Fig. 8.3.1 shows the best Bi_2Se_3 spectrum recorded to date; in this case, no radiation shield tails were used whatsoever. With no radiation shielding, the lowest sample temperature achieved was $\approx 100 \text{ K}$. Furthermore, the spectrum obtained from the no-shield configuration served as a reference for future measurements with shields. In other words, the no-shield case set an “upper bound” on the spectrum quality.

Following the no-shield configuration, the three shield tails were added, one at a time, while continuing to measure Bi_2Se_3 . Eventually, a trick was discovered in obtaining a discernible spectrum from Bi_2Se_3 : graphite-coating the region of the radiation shields closest to the photoelectron trajectories (i.e. around the slot). Graphite-coating minimizes electrostatic interaction between the shields and photoelectrons. Electrostatic forces most likely originated from a work function mismatch between different metal surfaces close to the photoelectron trajectories. The effects of work function mismatch are discussed in Sec. 5.2.3.

⁶The actual formula of a majority of the samples used was $\text{Fe}_x\text{Bi}_2\text{Se}_3$ where $x = 0.1-0.3$. The iron atoms present in between the quintuple layers, which only consist of covalently bonded Bismuth and Selenium atoms, made cleaving of the quintuple layers from each other easier. The iron dopants had no measurable difference compared to undoped Bi_2Se_3 .

⁷Cool down to liquid Nitrogen temperatures was necessary because the vertical slots on the three radiation shields were positioned such that they aligned with respect to each other after thermal contraction.

8.3 Electrical charging in vacuum

One way to minimize work function mismatch between two dissimilar metals is to coat both their surface with the same material. Since the electron-optical components of the analyzer are coated with graphite, the same material was chosen for coating the shield tails. Fig. 8.3.1 shows the radiation shield tails with black graphite coating. The coating is achieved by spraying the shields with a mixture of graphite dissolved in a liquid propellant; this commercial product is called Aerodag-G.

While performing the tests shown in Fig. 8.3.1, a puzzling phenomenon was encountered, involving disappearance of photoelectrons over time, with all other variables the same. Most of the experiments were performed close to 77 K. When the sample was heated to above 100 K, the photoelectrons reappeared. After further investigation, a semi-reproducible cause-effect relationship between temperature and photoelectron counts was established. The appearance and disappearance of photoelectrons was attributed to in-vacuum charging effects.

At the time, despite a lack of knowledge about the exact mechanism behind the relationship between temperature and charging, this correlation was exploited in order to avoid long bake-out times. In other words, measurements were only performed at temperatures $\gtrsim 100$ K. The leading hypothesis for explaining this phenomenon was that, when the system is not baked out, a very small amount of water vapor in the chamber condenses on the cryogenically cooled radiation shields. The 6 eV laser beam reflecting off the atomically flat mirror-like surface of the sample eventually, after multiple reflections, ends up ionizing the top layer of the condensed water vapor. Normally, due to the high electrical conductivity of the radiation shield tails, this unbalanced charge would get neutralized. But because the layer of water vapor is thicker when the system is not baked out, there exists an insulating layer between the radiation shields and the topmost ionized layer. It is likely that warming up the system causes the ionized layer to evaporate, thus alleviating the charging problem to some degree.

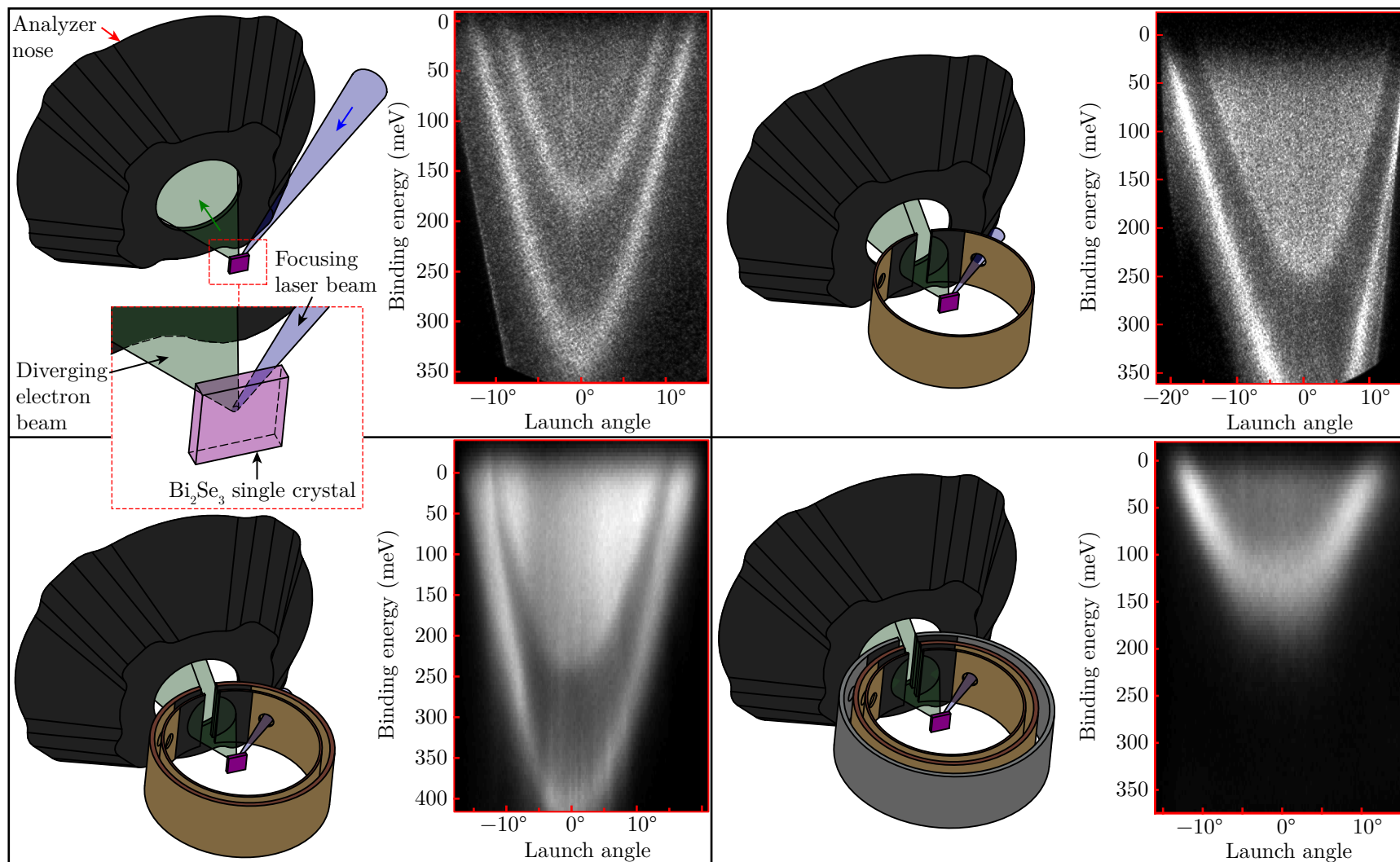


Figure 8.3.1: Four radiation shield configurations used to measure the spectrum of Bi_2Se_3 without baking out the vacuum system ($\approx 5 \times 10^{-9}$ torr pressure at 77 K). Cartoons of four measurement configurations, and the resulting spectra, are shown (left to right and top to bottom) for the following radiation shield tail assemblies: no shields, 1 K, 1 K + 4 K, and 1 K + 4 K + 77 K. The latter three have their slots coated with graphite.

8.4 Modifications to radiation shields

As evident from Fig. 8.3.1, the quality of the Bi_2Se_3 spectrum without any shields was never recovered in any of the multiple measurement configurations with shields. Therefore, the most plausible explanation for the cause of spectral distortion was fringing electric fields in the path of the electrons' trajectory (from sample to analyzer) due to mechanical imperfections (e.g. machining burs and scratches) in the slots.

Therefore, it was decided to widen the width of the slots in the shield tails, in order to reduce the magnitude of the fringing fields near the center of the slot, thus minimizing spectral distortion. Widening the slots, however, would increase the heat load on the sample, and thus compromise the base temperature. Hence it was important to get the perfect balance between improvement in the spectrum and raising of base temperature. Unfortunately, the only tractable method to quantify the amount of spectral distortion as a function of slot width was trial-and-error. In other words, theoretically modeling the impact of the fringing fields from the radiation shield tails, together with the proprietary R8000 analyzer's electron-optics design, was practically infeasible.

8.4.1 Variable slot design

Evaluation of the spectral distortion as a function of slot width, using trial-and-error, requires multiple shield configurations. However, it was too expensive and time-consuming to re-machine the shield tails to change the slot size after each measurement. Moreover, switching to a smaller slot size was not possible without re-machining the entire shield. Therefore, I came up with an elegant solution that involved the use of detachable plates. Examples of these so-called cover plates is shown in Fig. 8.4.1. For the 4 K (Fig. 8.4.1 (a)) and 77 K shield tails (Fig. 8.4.1 (b)), half a dozen plates per shield, with varying slot widths, were fabricated. All cover plates were graphite-coated for minimizing work function mismatch.

However, the cover plate design was not implemented for the 1 K shield because: (a) it would affect the base temperature, and (b) the quality of the spectrum, from Fig. 8.3.1, for the original 1 K shield tail designs was acceptable. Widening the slots in the 4 K and 77 K shields would simply increase the rate at which the system would boil off liquid Helium-4 and liquid Nitrogen respectively. Larger boil off was considered a reasonable compromise.

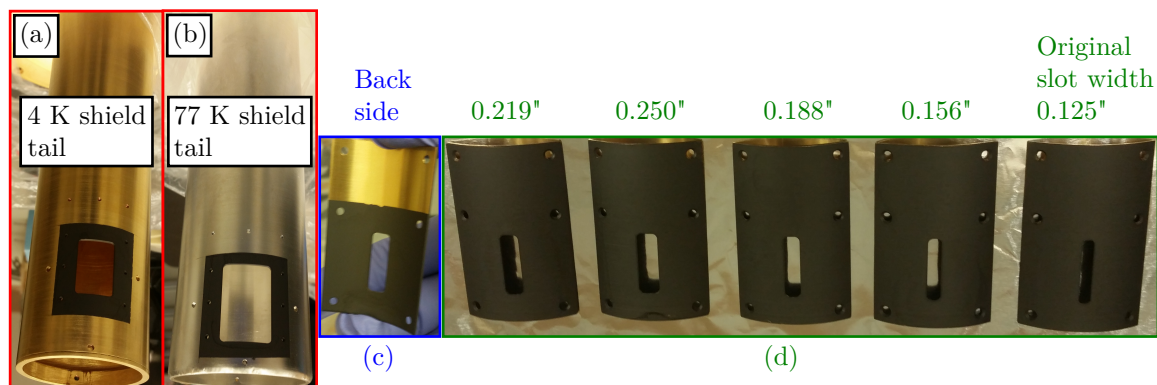


Figure 8.4.1: Photographs of the modified radiation shield tails and cover plates. The 4 K (a) and 77 K (b) shield tails' slots were replaced with large rectangular cut outs. (c) Back side of the curved plate covering the rectangular cut out in the 4 K shield tail. (d) Front side of the cover plates with different slit widths. The black regions are graphite coated.

8.4.2 Results

Upon completion of re-machining of the 4 K and 77 K shield tails and the fabrication of the slotted cover plates, initial measurements were performed with just the 4 K shield without a cover; the spectrum obtained from this configuration would serve as a reference for measurements performed with the cover plates. Unfortunately, electrical charging was observed again, and no data collection was possible. Moreover, no amount of temperature increase was able to eliminate or even reduce charging. This observation proved that the correlation between temperature and charging could no longer be exploited. Therefore, after that point, it was decided to bake the system every single time the system was vented. After another month-long bake-out, a decent quality Bi_2Se_3 spectrum was obtained. The result is shown in top left panel of Fig. 8.4.2.

Subsequently, multiple different shield tail + cover plate configurations were used. The different panels in Fig. 8.4.2 summarize the results of these configurations. Fortunately, after the first month-long bake-out, subsequent bake-outs lasted only 2-3 weeks. Surprisingly, the spectrum quality did not degrade as more shield tails and cover plates were added. As a result, the degradation observed across the four panels in Fig. 8.3.1 was attributed solely to lack of bake-outs. Note that the bottom right panel of Fig. 8.4.2 corresponds to the original slot covers. Therefore, contrary to initial expectation, sacrificing the base temperature was not required.

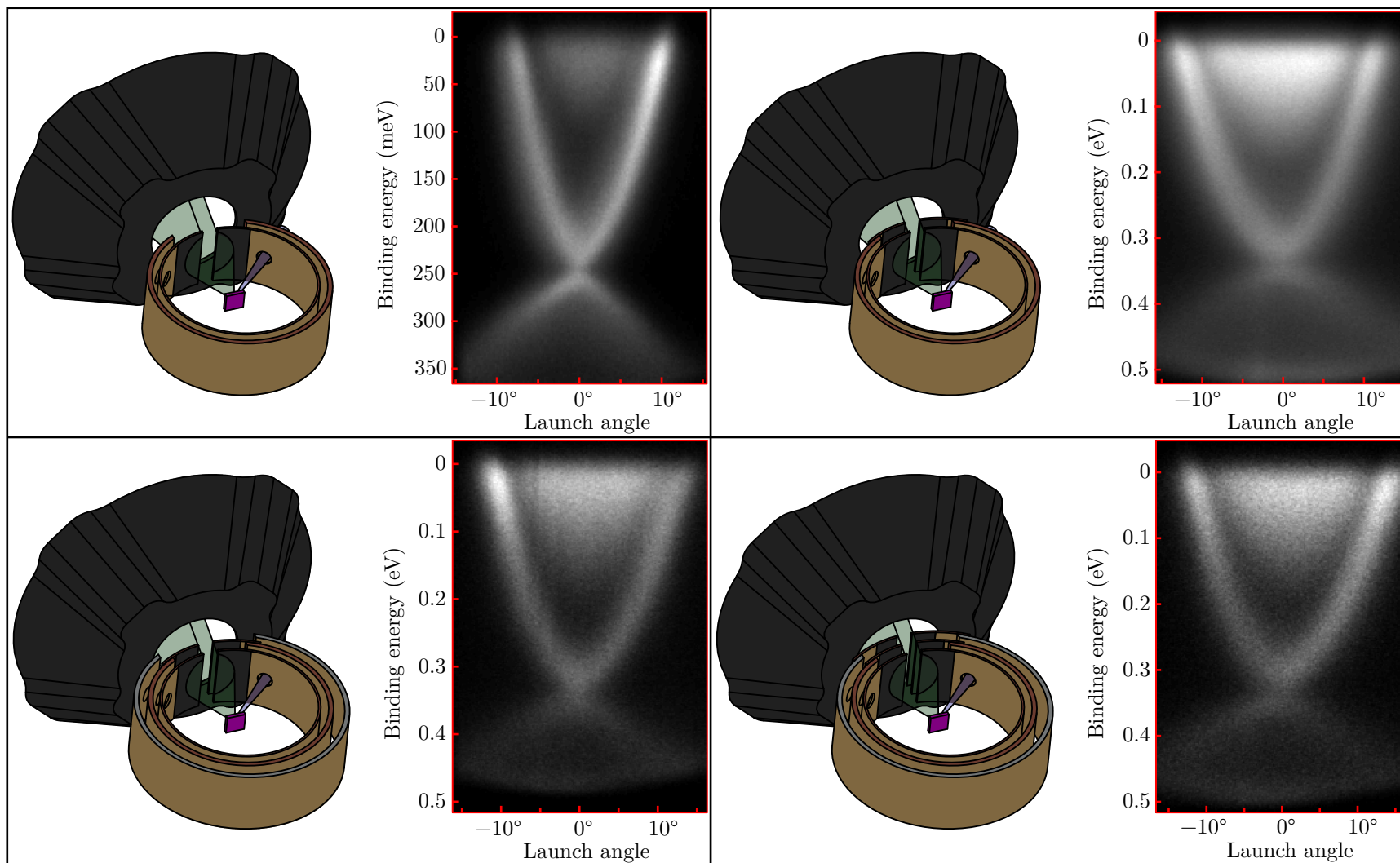


Figure 8.4.2: Four radiation shield configurations used to measure the spectrum of Bi_2Se_3 after a full bake-out of the vacuum system (6×10^{-10} torr pressure at room temperature). Cartoons of four measurement configurations, and the resulting spectra, are shown (left to right and top to bottom) for the following radiation shield tail assemblies: 1 K + uncovered 4 K, 1 K + covered 4 K, 1 K + covered 4 K + uncovered 77 K, and 1 K + covered 4 K + covered 77 K. The covered radiation shield tails have the slotted cover plates (c.f. Fig. 8.4.1) installed.

8.5 Investigation of energy resolution and sample temperature

The conclusion of the spectral enhancement procedure, discussed in Sec. 8.2-8.4, marked the beginning of a systematic effort towards characterization and optimization of the most important figure of merit of the ARPES system: energy resolution. In Sec. 3.3.3.2, I showed how energy resolution can be empirically determined by measuring the angle-integrated spectrum of polycrystalline gold. At that time, however, the ARPES system did not have the capability of in situ gold thin film growth. Moreover, since this was the first time low-temperature ($k_B T < 1$ meV) data was being collected, it was unclear how well the *actual* sample temperature agreed with the reading from the Cernox sensor (c.f. Fig. 7.6.1).

8.5.1 Measurement of superconductor spectral gap

One advantage of testing energy resolution with superconductors is the ability to simultaneously fit the data with two free parameters: sample temperature, T , and energy resolution, ΔE_{total} (c.f. (8.5.1) and (3.3.10)). In other words, more information can be extracted by fitting the predicted density of states from BCS theory compared to the fit using the Fermi-Dirac distribution function. In a typical ARPES energy distribution curve (EDC) of a superconductor below T_c , loss of spectral weight due to the gap opening at E_F can be seen by a ‘‘Fermi edge shift.’’ Even if the T_c of the sample deviates from optimum value quoted in the literature, due to (say) sample quality issues, another fit of gap vs. temperature can be performed by sweeping the latter to find the temperature at which where the former goes to zero.

Therefore, the system was cooled down to ≈ 2 K,⁸ and the energy distribution curves (EDCs) from well-understood BCS superconductors like Lead ($T_c = 7.2$ K) and Niobium ($T_c = 9.3$ K) was measured. Unfortunately, none of the measured EDCs qualitatively agreed with the form of the BCS density of states

$$\rho_{\text{BCS}}(E, T) \propto \frac{E - E_F}{\sqrt{(E - E_F)^2 - \Delta^2(T)}}, \quad (8.5.1)$$

convolved with the Gaussian in Eq. (3.3.10). Moreover, no statistically significant Fermi edge shift was observed whatsoever. In order to rule out sample issues, measurements were also performed on single crystal samples of PbTaSe₂ whose T_c ($= 3.8$ K) was verified by a collaborator (i.e. sample grower). It was hoped that, if a Fermi edge shift was observed with PbTaSe₂, the energy resolution test could simultaneously serve as a scientifically promising measurement on a topological superconductor candidate [86]. Unfortunately, the measured EDCs still did not show a Fermi edge shift.

Upon further analysis, it was concluded that there were two possible (or a combination of the two) explanations for not seeing a Fermi edge shift:

- the energy uncertainty, ΔE_{total} (c.f. Eq. (3.3.8)), was significantly larger than the superconducting gap sizes, and/or
- the *local* temperature of the sample region, whose spectrum is measured by the analyzer, was higher than T_c .

The latter was tested first.

⁸A cool down to 0.84 K was not done because of a technical reason: the He-3 circulation system was offline.

8.5.2 Thermal conductance of the sample holder

Recall that the Cernox temperature sensor is located on the rotator (c.f. Sec. 7.5.2.5). Moreover, the sample being measured is Silver-epoxied to a sample holder; and the latter is screwed into the rotator (c.f. Fig. 7.5.7). It is conceivable that, for poor thermal contact between the rotator and sample holder, the temperature difference between the two objects can be large enough that the former and latter are above and below T_c respectively. In order to check if this was the case, the following two steps were taken to improve thermal contact between the rotator and sample holder: (a) gold-plating the sample holder, and (b) introducing a thread relief in the sample holder.

8.5.2.1 Gold-plating sample holder

Gold-plating the sample holder was attempted first because venting the vacuum system was not required. In other words, the sample handling system (c.f. Sec. 6.3.7) was used to attach a newly gold-plated sample holder to the rotator. Moreover, a higher critical temperature superconductor CaFeAs_2 ($T_c = 17\text{ K}$) was used. Unfortunately, no Fermi edge shift was observed.

8.5.2.2 Modifying sample holder

Shortly after the gold-plating step, when the vacuum system was vented to fix damages to the cold finger, a spatial gap between the sample holder and the rotator was noticed. I briefly mentioned the observation of this gap in Sec. 7.5.2.5. All the ARPES measurements I have discussed, so far in this chapter, were performed using sample holders which lacked a “thread relief.” An example of a thread relief is shown in Fig. 7.5.7. In the absence of that thread relief, the 30° countersink surfaces of the sample holder and the rotator would not touch.

Therefore, one of the spare sample holders was re-machined such that it had: (a) a thread relief, and (b) a flat surface to *directly* mount the Cernox sensor. The latter would eliminate ambiguity in the temperature of the sample holder. Moreover, since the vacuum system was vented, the sample holder was screwed into the rotator using much greater torque than what would have been possible with the long transfer arm part of the sample handling system (c.f. Fig. 6.3.12). The ARPES system was then pumped down and cooled to 1.85 K. Note that this was the temperature measured directly on the sample holder.

Unfortunately, measurements of the EDC of Niobium still did not detect a superconducting gap. This evidence strongly favored the explanation that poor energy resolution was the reason for the lack of a spectral gap in the EDC measurements performed thus far.

8.5.2.3 Switch to high- T_c superconductor

After failing to see superconducting gaps in *relatively* low- T_c superconductors, namely PbTaSe_2 ($T_c = 3.8\text{ K}$), Lead ($T_c = 7.2\text{ K}$), Niobium ($T_c = 9.3\text{ K}$), and doped CaFeAs_2 ($T_c = 17\text{ K}$), it was decided to measure superconductors with a much larger gap and T_c . Optimally doped $\text{Bi}_2\text{Sr}_2\text{CaCu}_2\text{O}_{8+x}$ (Bi-2212) samples, with a $T_c = 91\text{ K}$, were mounted on a new sample holder which could accommodate ≈ 6 samples. Once again, the Cernox sensor was directly mounted on the sample holder.

EDC measurements from $\text{Bi}_2\text{Sr}_2\text{CaCu}_2\text{O}_{8+x}$ samples finally revealed a superconducting gap. Moreover, by fitting the EDC to Eq. (8.5.1) convolved with a Gaussian, the energy resolution, ΔE_{total} , was found to be $\approx 5\text{ meV}$. Moreover, by fitting the gap size as a function of temperature near

T_c , no significant discrepancy was found between the Cernox temperature sensor reading and the temperature inferred from the spectrum.

In summary, poor energy resolution was found to be the most significant factor contributing to the lack of a Fermi edge shift in initial EDC measurements.

8.5.3 Investigation of noise sources

During measurements of $\text{Bi}_2\text{Sr}_2\text{CaCu}_2\text{O}_{8+x}$, I unsuccessfully tried grounding and/or eliminating electrical and mechanical noise sources that could potentially degrade the energy resolution. The next logical step was to investigate the impact of the radiation shield tails on the energy resolution. All of the existing shield tails were removed, and replaced with only a “truncated” 77 K shield tail.

The truncated shield tail was similar to the original one in every way except having the bottom cylinder “chopped off” to expose the entire cold finger near the sample. The upper portion of the truncated 77 K shield tail would shield the 1 K and Helium-3 subsystems from 300 K black body radiation and minimize liquid Helium-4 boil off. Obviously, getting to very low temperatures was not a priority of this test; it was merely a debugging step to locate the source of the noise source degrading the energy resolution.

Unfortunately, measurements with the truncated 77 K shield tail could not be performed because of a leak in the cryostat (c.f. Sec. 7.8.1). The cryostat was under repair till summer 2019.

8.6 Work in progress

At the time of writing, the cryostat is awaiting a bake-out with the truncated 77 K shield tail installed. This is the first bake out since the leak was repaired. When the cryostat was offline, due to the leak repair process, some peers informed me that the exact grade of graphite used to coat the radiation shields has a significant effect on the energy resolution [81]. Therefore, a new grade of graphite from VG Scienta was recently acquired for coating the radiation shield tails. This graphite will be applied the next time the vacuum system is vented.

Chapter 9

Optical probes of many-body order

9.1 Novel probes of order

In Sec. 1.4, I discussed some of the challenges associated with empirical measurement of topological order parameters. The fundamental reason behind these challenges was that the non-local nature of topological order parameters made the latter invisible to local probes. In this section, I will give examples of how even some sophisticated types of local orders can be invisible to local probes.

9.1.1 Introduction

Based on the discussion in Chap. 1, the importance of symmetries in the classification of many-body phases cannot be understated. I discussed how symmetry breaking (protection) plays a very important role in the definition of a local (topological) order parameter, Ψ . In Chap. 3-8, I focused on measuring Ψ solely using the photon-in-electron-out technique I developed for my primary thesis project: low-temperature high-resolution ARPES.

However, experimental condensed matter physics is deluged with probes of Ψ which employ a diverse set of techniques, classified based on input and output particles/fields. Some examples of alternatives to photon-in-electron-out probes are:

- photon-in-photon-out (e.g. Raman spectroscopy, resonant inelastic x-ray scattering (RIXS), etc.),
- electron-in-electron-out (e.g. transport, scanning tunneling microscopy (STM), etc.),
- neutron-in-neutron-out (e.g. neutron scattering), and
- muon-in-positron-out (e.g. muon spin rotation/resonance/relaxation (μ SR)).

Depending on the complexity of Ψ , a subset of the aforementioned probes are used in conjunction to extract the maximum possible information on Ψ . Nonetheless, in some cases like say “hidden order” (c.f. Sec. 9.1.3), even identifying the Ginzburg-Landau order parameter can prove challenging with the aforementioned probes at one’s disposal.

In Sec. 1.4, I discussed the necessity of developing novel probes for measuring topological order parameters. In this chapter, I will argue the same for local order parameters. I will show that novel probes with “higher dimensionality” are essential in identifying unconventional local orders.

9.1.2 Dimensionality of the order parameter

Thus far the highest dimensionality Ψ I have presented is the complex rank-2 tensor, $\Psi = e^{i\theta} R_{\mu j}$, in the case of the B phase of superfluid Helium-3 (c.f. Sec. 1.2.4.3). But it is conceivable that a many-body system with a sufficiently large number of degrees of freedom can have a Ψ with rank higher than two. In this context, one could define the “dimensionality of the probe” as the ease with which the Ψ of a given dimension is measured. Here is an example:

The data set produced by (say) ARPES corresponds to the energy- (E) and momentum-resolved ($\mathbf{k} = (k_x, k_y, k_z)$) electronic density of states (DOS), denoted by (say) $\rho_{\text{ARPES}}(E, \mathbf{k})$, in a solid state system. By comparison, using a technique known as quasiparticle interference [87], STM also measures the electronic DOS, denoted by (say) $\rho_{\text{STM}}(E, \mathbf{q})$, where \mathbf{q} is the wave vector associated with the interference of two quasiparticles with absolute momenta (say) \mathbf{k}_1 and \mathbf{k}_2 ($\mathbf{q} \equiv \mathbf{k}_1 - \mathbf{k}_2$). Although $\rho_{\text{ARPES}}(E, \mathbf{k})$ and $\rho_{\text{STM}}(E, \mathbf{q})$ are very similar-looking, the caveat in the latter is the lack knowledge of *absolute* momentum (\mathbf{k}). This knowledge gap can be filled by theoretically modeling the electronic spectrum; albeit with fewer free parameters than (say) transport. In this sense, I argue that ARPES is a higher-dimensional probe compared to STM.¹

9.1.3 Multipolar or hidden order

There are indeed examples of order parameters which were not initially discovered because their higher dimensionality. These types of order parameters are often referred to in the literature as multipolar order parameters [88]. Since the order parameters of some of these complex systems remained elusive for a long time, reports in the literature sometimes refer to these phases as “hidden” order. Arguably the most famous example of hidden order is the case of the heavy-fermion superconductor URu₂Si₂ [89]. The hidden order in URu₂Si₂ was a mystery since its first report in 1984 [90]. It took 29 years to theoretically define the order parameter as a spinor which broke “double time-reversal symmetry” [91].

9.2 Optical probes of the order parameter

In this section, I will provide a broad overview of the different types of physics that can be studied using the optical techniques I will discuss in Sec. 9.3-9.5. In particular, I will focus on how these optics-based techniques can provide complementary information to ARPES in the investigation of both Ginzburg-Landau and topological order parameters.

9.2.1 Nonlinear optics

9.2.1.1 Theoretical modeling and terminology

The non-linear optical properties of a given medium can be modeled, at the phenomenological level, by solving Maxwell’s equation with a source term, $\mathbf{S}(\mathbf{x}, t)$, which encodes nature of the light-matter interactions. Maxwell’s equation can be written as

$$\left(\nabla^2 - \frac{1}{c^2} \frac{\partial^2}{\partial t^2} \right) \mathbf{E}(\mathbf{x}, t) = \mathbf{S}(\mathbf{x}, t), \quad (9.2.1)$$

¹I am making an information-theoretic argument: a lower-dimensional probe simply requires more data acquisition and/or theoretical support, compared to its higher-dimensional counterpart, in extracting the same amount of information from a many-body system.

where $\mathbf{E}(\mathbf{x}, t)$ is the electric field associated with the light interacting with the medium, c is the speed of light, and $\mathbf{x} \equiv (x, y, z)$. The i^{th} component of the source term can be expanded in terms of a power series as

$$S_i(\mathbf{x}, t) = \mu_0 \frac{\partial^2 P_i(\mathbf{x}, t)}{\partial t^2} + \mu_0 \left(\varepsilon_{ijk} \nabla_j \frac{\partial^2 M_k(\mathbf{x}, t)}{\partial t^2} \right) - \mu_0 \left(\nabla_j \frac{\partial^2 Q_{ij}(\mathbf{x}, t)}{\partial t^2} \right) + \dots, \quad (9.2.2)$$

where $P_i(\mathbf{x}, t)$, $M_k(\mathbf{x}, t)$, and $Q_{ij}(\mathbf{x}, t)$ represent the components of the electric dipole (vector), magnetic dipole (vector), and electric quadrupole (matrix) terms respectively. μ_0 is the vacuum permeability, ε_{ijk} is the rank-3 Levi-Civita tensor, and the indices i, j, k can take values of (say) the Cartesian coordinates x, y , and z .

For the examples discussed in this chapter, I will limit the discussion only to electric dipole transitions. Then $P_i(\mathbf{x}, t)$ can be conveniently expressed, in the frequency domain, as a series expansion in the amplitude of the electric field of light as

$$P_i = \chi_{ij}^{(1)} E_j + \chi_{ijk}^{(2)} E_j E_k + \chi_{ijkl}^{(3)} E_j E_k E_l + \dots, \quad (9.2.3)$$

where the tensor $\chi^{(n)}$ represents the n^{th} order optical susceptibility, which is an intrinsic property of the system being probed. Moreover, the right-hand side of (9.2.3) has been represented in the Einstein notation. For convenience, I have also ignored spatial dependence of P_i in (9.2.3). This approximation will suffice for the purposes of this discussion.

In Sec. 9.3.1, I will demonstrate that $\chi^{(n)}$ encodes symmetry information of the system being interrogated, with (say) a laser, where the light-matter interaction can be modeled by (9.2.3). While the example I will focus on involves only the $\chi^{(2)}$ tensor, in principle one can measure higher orders of optical susceptibility, depending the level of detail at which one seeks to probe the system under test. In other words, it is conceivable that higher order $\chi^{(n)}$ tensors are capable of measuring higher dimensional order parameters. In Sec. 9.2.1.2, I will discuss an example of a $\chi^{(2)}$ measurement which revealed the nature of a rank-2 order parameter; it could be argued that the latter was more challenging to measure for lower dimensional probes (e.g. electrical transport).

9.2.1.2 Application of non-linear optics to study hidden order

$\text{Cd}_2\text{Re}_2\text{O}_7$ is a strongly-correlated spin-orbit-coupled metal which undergoes a nematic phase transition at 200 K with the rank-2 order parameter Q_{ij} . A phenomenological Hamiltonian for the relevant electronic degrees of freedom can be written as

$$\hat{\mathcal{H}} = \sum_{ij} Q_{ij} \hat{\sigma}_i k_j, \quad (9.2.4)$$

where $\hat{\sigma}$ is the Pauli spin associated with the real spin and \mathbf{k} is the crystal momentum. This type of order was discovered by studying the point-group symmetry breaking inferred from the second-order optical susceptibility ($\chi^{(2)}$) as a function of temperature [92]. This is another example of a higher dimensional order parameter which required a higher dimensional probe capable of *directly* measuring $\chi^{(2)}$. I will revisit this particular system in Sec. 9.4.1 and discuss the prospects of probing Q_{ij} as a function of temperature and hydrostatic pressure.

9.2.2 Ultrafast optics

In my discussion, so far, of the order parameter, Ψ , the time (t) degree of freedom from Eq. (1.1.1) has been unused. That is because I have limited the discussion to systems in thermal equilibrium. The Ginzburg-Landau and topological classifications were *traditionally* developed to describe systems in equilibrium. These approaches can be extended to non-equilibrium (or time-dependent) phenomena, or substituted with new methods, at the cost of computationally expensive methods such as (say) Keldysh [93]. That is why I argue that a plethora of non-equilibrium phenomena currently under investigation have their roots in experiment.

In some cases, non-equilibrium phenomena serve as a means to infer the properties of an equilibrium system. For example, the temporal relaxation profile of photon-induced excitations (e.g. electron-hole, holon-doublon, etc.) can reveal whether the optical excitation spectrum of the host material is gapped or gapless. This technique is ideal studying, for example, metal-insulator transitions in correlated systems and the nodal structure of the superconducting gap in unconventional superconductors [94].

In other cases, many-body systems out of equilibrium exhibit properties that are either: (a) superior to their equilibrium counterparts (e.g. higher T_c in superconductors), or (b) not at all observable under equilibrium (e.g. Floquet systems). One of the leading examples of the former are the pursuit of room-temperature superconductivity in the high- T_c cuprates using a phenomenon called: *Josephson plasma resonance* [95]. Moreover, the observation of a Higgs mode of a superconductor in condensed matter systems² was recently observed using ultrafast techniques.³

Furthermore, study of Floquet systems⁴ has made its way into contemporary condensed matter physics since the topological insulator discovery. The appeal of Floquet systems lies in the fact that non-trivial band topology can be engineering in ordinary insulators using light. This offers a continuous tunability of topological phase transitions which are relatively challenging in materials under equilibrium. Such Floquet-assisted phase transitions represent a class of, the more general, photo-induced phase transitions which are relatively unexplored, and are part of a currently thriving area of research.

9.3 Probing order in single crystals using second harmonic generation

9.3.1 Phenomenological theory of second harmonic generation

In this section, I will discuss a phenomenological theory of second harmonic generation. A quantum mechanical interpretation of the second harmonic process is outside the scope of this section. For the most part, I will employ concepts and tools from classical electromagnetism. In other words, the probe is classical, but the ordered system may be quantum.

9.3.1.1 Second-order optical susceptibility

The second-order optical susceptibility can be phenomenologically defined, in the frequency (ω) domain, by the SHG process described by

$$P_i(2\omega) = \chi_{ijk}^{(2)} E_j(\omega) E_k(\omega), \quad (9.3.1)$$

²This was first observed in a cold atom many-body system.

³In this chapter, I will often use “ultrafast” and “non-equilibrium” interchangeably because I will only consider non-equilibrium systems that directly result from ultrafast methods.

⁴This was actually studied theoretically long ago by Gaston Floquet in 1883!

where $E_j(\omega)$ and $E_k(\omega)$ are components of a 3D vector, in Cartesian space, corresponding to the electric field of the incident laser beam. $P_i(2\omega)$ is the component of another 3D vector corresponding to the second-order polarization field induced by the incident field. $\chi_{ijk}^{(2)}$ is a rank-3 tensor relating the sets of fields in (9.3.1). In general, the mathematical object $\chi_{ijk}^{(2)}$ can be faithfully represented by a maximum of 27 independent complex scalars. In the context of Eq. (9.3.1), however, an inherent redundancy becomes apparent: the equation is invariant under the index swap $j \leftrightarrow k$. This redundancy is often referred to as the *permutation symmetry*. Therefore, the number of independent elements is reduced to 18 ($= 27 - 3 \times 3$).

Due to the permutation symmetry, the full $\chi_{ijk}^{(2)}$ tensor can be reduced to a convenient 3×6 matrix representation

$$\chi_{ijk}^{(2)} \equiv \begin{bmatrix} \chi_{xxx} & \chi_{xyy} & \chi_{xzz} & \chi_{xyz} & \chi_{xxz} & \chi_{xxy} \\ \chi_{xxy} & \chi_{yyy} & \chi_{yzz} & \chi_{yyz} & \chi_{xyz} & \chi_{xyy} \\ \chi_{xxz} & \chi_{yyz} & \chi_{zzz} & \chi_{yzz} & \chi_{xzz} & \chi_{xyz} \end{bmatrix}. \quad (9.3.2)$$

In the reduced representation, Eq. (9.3.1) can be re-written explicitly in terms of the tensor components as

$$\begin{bmatrix} P_x(2\omega) \\ P_y(2\omega) \\ P_z(2\omega) \end{bmatrix} = \begin{bmatrix} \chi_{xxx} & \chi_{xyy} & \chi_{xzz} & \chi_{xyz} & \chi_{xxz} & \chi_{xxy} \\ \chi_{xxy} & \chi_{yyy} & \chi_{yzz} & \chi_{yyz} & \chi_{xyz} & \chi_{xyy} \\ \chi_{xxz} & \chi_{yyz} & \chi_{zzz} & \chi_{yzz} & \chi_{xzz} & \chi_{xyz} \end{bmatrix} \begin{bmatrix} E_x^2(\omega) \\ E_y^2(\omega) \\ E_z^2(\omega) \\ 2E_y(\omega)E_z(\omega) \\ 2E_z(\omega)E_x(\omega) \\ 2E_x(\omega)E_y(\omega) \end{bmatrix}. \quad (9.3.3)$$

If the non-linear medium possesses certain symmetries, however, Eq. (9.3.3) can be further simplified. In other words, I will show in Sec. 9.3.1.2 how point group symmetries of a lattice can reduce the number of independent components of $\chi_{ijk}^{(2)}$ to fewer than 18.

9.3.1.2 Applications of the Neumann's principle to single crystals

The Neumann's principle states:

A tensor describing any physical property of a crystal must be invariant under all symmetry operations of the crystal.

In mathematical language, Neumann's principle can be described as follows: if a coordinate transformation

$$\chi_{ijk}^{(2)'} = \sum_{\alpha, \beta, \gamma = x, y, z} R_{i\alpha} R_{j\beta} R_{k\gamma} \chi_{\alpha\beta\gamma}^{(2)}, \quad (9.3.4)$$

is performed on $\chi_{ijk}^{(2)}$, and R corresponds to a symmetry of the crystal, then

$$\chi_{ijk}^{(2)'} = \chi_{ijk}^{(2)}. \quad (9.3.5)$$

This means that the $\chi_{ijk}^{(2)}$ of a crystalline system encodes the information about the point group symmetries of said system. The point group is a set of symmetries operations defined about a fixed point (e.g. inversion, rotation, mirroring) that leave the crystal system invariant. There exist 32

crystallographic point groups. They can be divided into (say) the following two classes: inversion symmetric and inversion breaking.

For example, consider a crystal system with inversion symmetry. This means that $R_{i\alpha}$ will be given by

$$\begin{pmatrix} x' \\ y' \\ z' \end{pmatrix} = \underbrace{\begin{pmatrix} -1 & 0 & 0 \\ 0 & -1 & 0 \\ 0 & 0 & -1 \end{pmatrix}}_{R_{i\alpha} = -\delta_{i\alpha}} \begin{pmatrix} x \\ y \\ z \end{pmatrix}, \quad (9.3.6)$$

Then using (9.3.4) and (9.3.6) in (9.3.5) I get

$$\begin{aligned} \chi_{ijk}^{(2)} &= \sum_{\alpha\beta\gamma} (-\delta_{i\alpha})(-\delta_{j\beta})(-\delta_{k\gamma})\chi_{\alpha\beta\gamma}^{(2)}, \\ &= -\chi_{ijk}^{(2)}, \\ &= 0. \end{aligned} \quad (9.3.7)$$

This seemingly trivial result has a non-trivial implication for experiment: crystalline systems which are inversion symmetric do **not** support second harmonic generation. The importance of the ability to make this distinction is illustrated with an example in Sec. 9.3.3.

For crystalline system which do not possess inversion symmetry, when the Neumann principle is applied using the remaining set of symmetries $\{R_{i\alpha}\}$, the $\chi_{ijk}^{(2)}$ tensor reduces in one or both of the following ways:

1. Certain components can vanish
2. Two or more components can become dependent

Some examples of the reduced form of the $\chi_{ijk}^{(2)}$, for inversion-breaking point groups, are listed Sec. D.1.

In this chapter, I will limit the discussion to studying second harmonic processes generated in 3D crystals. In that case, measuring $\chi_{ijk}^{(2)}$ can provide the following information about the 3D crystal:

- identification the point group of an inversion asymmetric 3D bulk,
- identification of the surface point group for bulk inversion symmetric 3D crystals,
- any form (electronic and/or crystalline) of phase transition (as a function of (say) temperature, pressure, etc.) which breaks inversion symmetry on the surface and/or the bulk.

9.3.2 Rotationally anisotropic second harmonic generation

A mere presence of second harmonic generation (SHG) does not prove inversion symmetry breaking. The second harmonic signal could be generated from parasitic sources such as lattice defects which break inversion symmetry and sample surface imperfections like pits and scratches. The SHG process needs to be measured as a function of one or more parameters. In particular, a technique known as rotationally anisotropic second harmonic generation (RA-SHG) measures the intensity of the second harmonic light reflected from the surface of a crystalline sample, and monitors the second harmonic

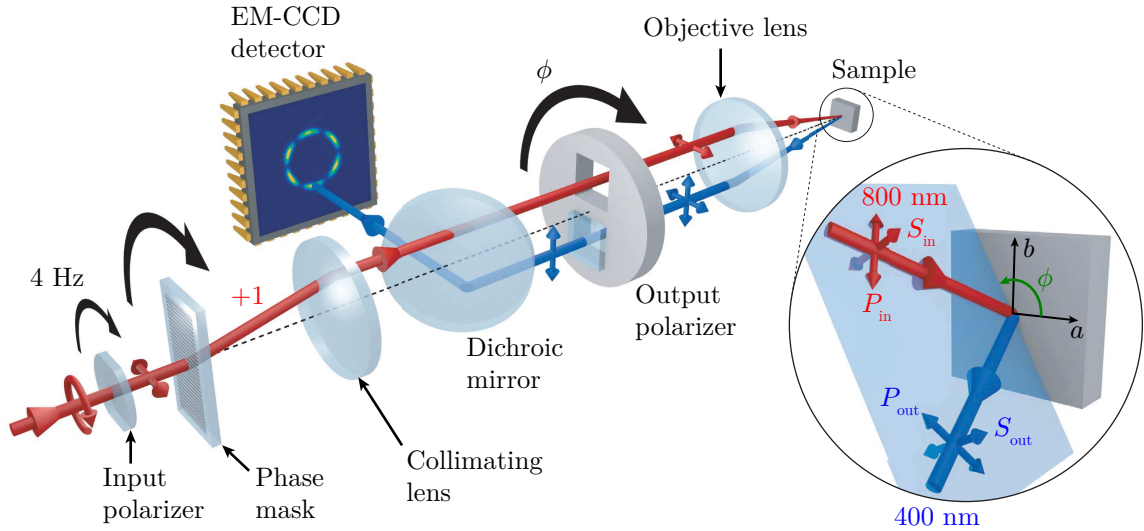


Figure 9.3.1: The experimental layout of the RA-SHG setup. From Harter *et al. Science* **356**, 295-299. Reprinted with permission from AAAS. [92].

signal as a function of scattering plane angle (ϕ) and the polarizations of the input (S_{in}/P_{in}) and output (S_{out}/P_{out}) beams [96]. The weakness of the second harmonic signal limits this measurement scheme to femtosecond lasers due to their high peak electric fields. Fig. 9.3.1 provides a cartoon illustration of one implementation of the RA-SHG setup [92, 97].

First consider a horizontal scattering plane. An incoming 100 fs pulse with 800 nm center wavelength is linearly polarized along the vertical direction. The polarized pulse subsequently undergoes diffraction through a phase mask. Only one of the first order diffracted beams is allowed to propagate and is focused onto the sample. The purpose of the phase mask is to introduce a non-zero angle of incidence (θ) on the sample. The dashed black line, collinear with the path of the laser beam before going through the phase mask, will be later referred to as the system axis. The predominately 800 nm beam (not shown in Fig. 9.3.1) and a very weak 400 nm beam, which are reflected from the sample, are first made parallel to the system axis, and then polarized along the horizontal direction. These two beams then encounter a dichroic mirror which transmits the 800 nm beam (which is blocked) and reflects the 400 nm beam onto a CCD camera.

9.3.3 Example of RA-SHG

In this section, I will discuss an example of an SHG measurement from an organometallic single crystal methylammonium lead iodide ($\text{CH}_3\text{NH}_3\text{PbI}_3$). This material is one of the leading candidates of perovskite solar cells. One of the major debates in this research field is centered around the inversion symmetry or lack thereof in the room-temperature crystal structure of $\text{CH}_3\text{NH}_3\text{PbI}_3$. The results of RA-SHG from the aforementioned setup (c.f. Sec. 9.3.2) are shown in Fig. 9.3.2.

In the literature, two different space groups have been reported for this material: $I4/mmm$ (centrosymmetric) and $I4cm$ (non-centrosymmetric). In Fig. 9.3.2, the bulk point group corresponding to the latter is plotted as a black solid line. For the $I4/mmm$ case, the point group of the (100) surface is $mm2$. As noted in Fig. 9.3.2, the data fits well to the $mm2$ space group. This result can be interpreted as follows: the bulk point group of $I4/mmm$ is $4/mmm$, which is centrosymmetric. Therefore, if the bulk space group was $I4/mmm$, no SHG signal can originate from the bulk of the

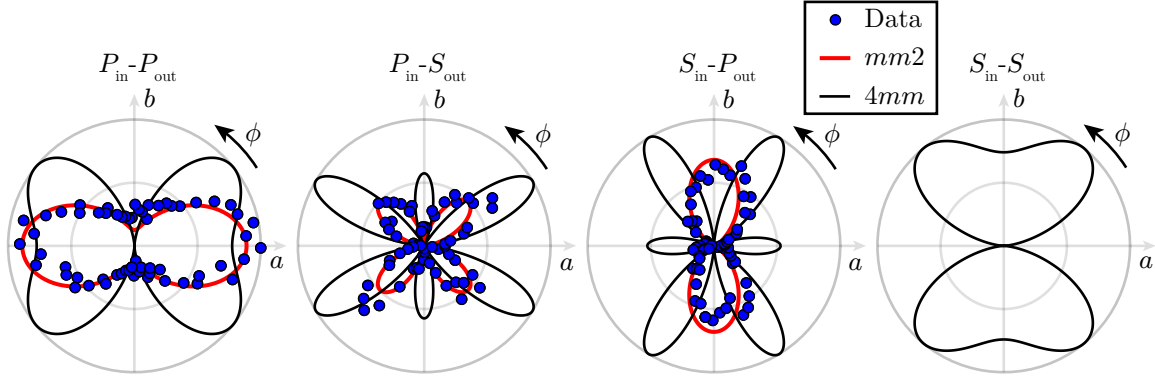


Figure 9.3.2: An example of RA-SHG measurements on single crystals of $\text{CH}_3\text{NH}_3\text{PbI}_3$ [98].

crystal. In this case, the only SHG signal will come from the surface with $mm2$ point group as the surface always breaks inversion symmetry normal to the surface. If the bulk of this crystal had been $I4cm$, the SHG generated in the bulk would have overwhelmed any surface contribution and showed up as the black curves in Fig. 9.3.2.

In this case, RA-SHG was able to settle an ambiguity in the x-ray diffraction measurements, by indirectly distinguishing between space groups $I4/mmm$ and $I4cm$, by looking at their respective point groups.

9.4 Optical spectroscopy under high pressure

Pressure adds an important dimension in the phase diagram of a many-body system. It can selectively enhance or suppress different phases present in a system under ambient pressure. Exploring the pressure dimension, in a given material's phase diagram, offers a deeper insight into the microscopic mechanisms responsible for (say) competing phases⁵ hosted by said material under ambient pressure. In this section, I will limit the discussion to studies of hydrostatic pressure. With the current technology, the pressure-transmitting medium, in which the sample under test is immersed, can transmit light but not *free-space* electrons. Therefore, this experimental degree of freedom is, unfortunately, not available in ARPES. But optical probes such as RA-SHG and pump-probe are possible.

9.4.1 Scientific objective

In section 9.2.1.2, I discussed the role SHG played in revealing the nature of the hidden order parameter Q_{ij} in $\text{Cd}_2\text{Re}_2\text{O}_7$ (c.f. Eq. (9.2.4)). The reason SHG was able to detect said order parameter is that the latter is odd under inversion. The odd-parity phase, characterized by Q_{ij} occurs below 200 K. Moreover, $\text{Cd}_2\text{Re}_2\text{O}_7$ becomes a superconductor below 1 K. This raises the possibility that the superconducting order parameter might inherit odd parity from its parent nematic phase. Since odd-parity is a precursor to topological superconductivity (c.f. Sec. 2.3.1), an SHG investigation might complement my ARPES experiments.

Initially, my goal is to study the odd-parity nematic phase in $\text{Cd}_2\text{Re}_2\text{O}_7$ as a function of pressure using first optical pump-probe and eventually RA-SHG close to 200 K. Other experimental probes

⁵For example, in the cuprate high- T_c superconductors, there is a competition between the antiferromagnetic and superconducting phases.

(mostly transport) have suggested a complete suppression of the nematic phase at ≈ 8 GPa where a quantum critical point is predicted to exist. An optical characterization of quantum criticality in $\text{Cd}_2\text{Re}_2\text{O}_7$ may shed some light on the microscopic mechanisms responsible for the nematic state. Furthermore, the superconducting T_c is enhanced from 1 K, at ambient pressure, up to roughly 3 K for hydrostatic pressures on the order of 10 GPa [99]. Therefore, if the cryostat, used for high pressure experiments (c.f. Sec. 9.4.3), can be configured to access the superconducting phase, *direct* evidence of topological superconductivity using SHG is possible.

9.4.2 Diamond anvil cell

9.4.2.1 Introduction

Experiments under high hydrostatic pressure, of the order of tens to hundred of GigaPascals (GPa), are performed in an apparatus known as the diamond anvil cell (DAC). A cross-section of the DAC close to the sample is shown in Fig. 9.4.1. The essential components are two equal-sized diamond anvils with their accompanying “seats,” a metal gasket, and a mechanical compression mechanism. Diamond is primarily chosen because of its hardness. The transparency to electromagnetic fields is a convenient feature.

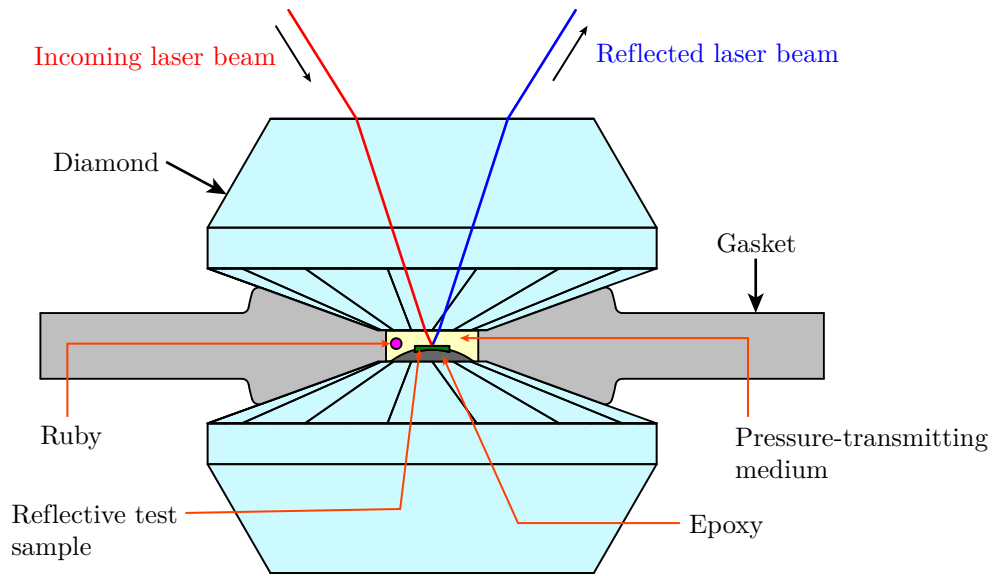


Figure 9.4.1: Cross-section of a diamond anvil cell. The metal gasket seals the pressure-transmitting medium.

9.4.2.2 Operating principle

The hydrostatic pressure, P , inside the DAC is given by

$$P = \frac{F}{A}, \quad (9.4.1)$$

where F is the force applied by the compression mechanism and $A (= \pi d^2/4)$ is the area of the face (typically the (100) crystallographic plane) of the diamond cutlet in contact with the pressure-transmitting medium. Typical values of maximum compression force and cutlet size (d) are on the order of a few kiloNewtons and $100 \mu\text{m}$ -1 mm respectively.

As can be seen in Fig. 9.4.1, the sample under measurement is hydrostatically pressurized directly by a low-strength pressure-transmitting medium. The medium is confined between a hole in the metal gasket and two opposing diamond anvils plugging that hole. It is the relative motion of the latter, *approximately* along the cylindrical axis of the gasket hole, which results in the pressure-transmitting medium varying the amount of pressure it applies on the sample. The DAC design presented in Sec. 9.4.2.3 uses a gas membrane whose expansion provides the compressive mechanism necessary for in situ pressure tuning.

The *ideal* pressure-transmitting medium is a zero-shear-strength fluid, capable of keeping stresses in the hydrostatic regime, at all spatial locations for all pressure ranges. Unfortunately, such an ideal fluid does not exist. The media which come closest to this ideal limit are inert gases such as Helium and Neon. These media are typically employed in the most demanding DAC applications. In the DAC to be used for experiments discussed in this thesis, however, the pressure-transmitting medium is a 4:1 methanol:ethanol mixture. For the following discussions, I will assume only this medium. The methanol/ethanol mixture starts to harden above 10 GPa at room temperature. So it is not possible to use it for experiments requiring more than ≈ 30 GPa.

The most commonly used pressure-calibration technique involves measurement of the shift in the fluorescence line of ruby. Ruby provides optical pressure-sensing feedback for pressures up to 200 GPa after which the fluorescence line broadens and weakens beyond practical utility. The pressure achieved at the record lowest temperature of 27 mK was 155 GPa in solid Xenon [100]. Since these specifications far exceed the experimental parameter range required for studying $\text{Cd}_2\text{Re}_2\text{O}_7$, ruby calibration suffices.

The metallic gasket is typically made of materials like work-hardened T301 stainless steel, Rhenium, Beryllium Copper, to name a few, as it requires both strength and just enough elasticity to maintain a good seal with the anvil cutlets. Moreover, proper sealing with the cutlet requires the hole in the gasket to be typically less than one third of the cutlet diameter.

9.4.2.3 Design

Fig. 9.4.2 shows the design of the specific diamond anvil cell (DAC) to be used in the high-pressure optical measurements on $\text{Cd}_2\text{Re}_2\text{O}_7$; it is referred to as Merrill-Bassett design [101]. The structural components of the compression mechanism (or pressure cell) are made of silicon aluminum bronze (C64200). The two cylindrical blocks, on which the diamond anvils are mounted, are pushed against one another using three brass screws. From here on out, I will refer to these blocks as “anvil mounts.” As shown in the CAD section view, the Belleville spring washers apply a restoring force to the screws. Moreover, three pins guide the motion of the two anvil mounts along the cylindrical axis.

The countersink through holes ($\approx 40^\circ$) at the center of each anvil mount provides the optical access for probe beams. A stainless Steel diaphragm membrane underneath the bottom anvil mount is used to tune the pressure between the anvils in situ. The membrane is driven by pressurized Helium gas (typically < 500 psi) transported to the pressure cell through a narrow inner diameter (< 0.010 ”) stainless Steel tube.

Fig. 9.4.3 shows a photograph of the gas-driven membrane inside the cap which mounts the pressure cell to the cryostat. The membrane is fabricated by electron beam welding two annular stainless Steel disks. The weld seam forms a vacuum seal between the high pressure gas (tens of psi) and the vacuum region ($\approx 10^{-7}$ torr) inside the cryostat. The membrane can be crudely thought of as one convolution of an edge-welded bellows (c.f. 6.3.6.1).

The inset of Fig. 9.4.3 shows a photograph of the gasket. The gasket is cut from ≈ 0.010 ” thick shim stock with approximate lateral dimensions $1/4$ ” \times $1/4$ ”. The gasket is indented to ≈ 0.010 ”

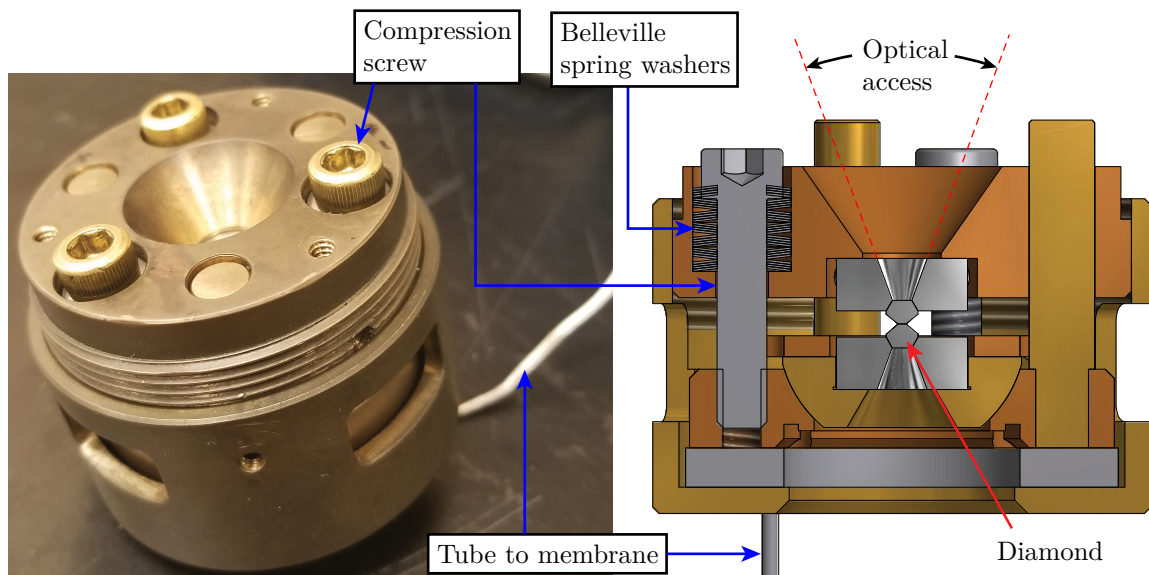


Figure 9.4.2: Left: photograph of the diamond anvil cell. Right: CAD section view of the diamond anvil cell illustrating the compression mechanism.

thickness. Depending on the size of the diamond cutlet, an appropriate size hole (typically $\approx 1/3$ of the cutlet) is generated using electrical discharge machining.

Fig. 9.4.3 also shows a photograph of a top anvil mount. The counterbore in the anvil mount houses the diamond cutlet seats. These seats are typically made of hard materials like Tungsten Carbide, Sapphire, and Silicon Nitride, to name a few. Tungsten Carbide is avoided in applications sensitive to magnetic fields. The seat is held in place by radial set screws in the anvil mount.

9.4.3 Microscopy cryostat customization

A new optical microscopy cryostat (RC102-CFM from CRYO Industries of America, Inc.) was purchased to accommodate the diamond anvil cell. Fig. 9.4.4 shows an overview of the design of said cryostat. Compared to the existing optical cryostats (ST-500 Janis Research Company, LLC), a new feature of this cryostat was the ability to perform optical measurements on (say) thin film samples in the transmission configuration, due to the existence of a threaded through hole at the center of the cold finger. The photograph in Fig. 9.4.4 shows a thin film sample, on a glass slide, from an ambient pressure optical transmission experiment. As evident from Fig. 9.4.2, transmission experiments are also possible in the diamond anvil cell.

In order to mount the pressure cell to the cold finger, an adapter between the latter and the cryostat-mounting cap (c.f. 9.4.3) was necessary. Therefore, I designed an adapter to be machined from a single piece of oxygen-free high conductivity (OFHC) Copper. The CAD model of the adapter is shown in an inset in Fig. 9.4.5. Once the cryostat-mounting cap is fastened to the adapter plate, using five #4-40 socket-head cap screws, the $1/2$ "-20 threaded shaft screws into the hole in the cold finger. Note that the adapter has $1/4$ " through hole in order to allow transmission measurements. The geometry of the adapter was optimized to provide maximum surface area between: (a) the cryostat-mounting cap and the adapter, (b) adapter and the cold finger. The U-shaped cut out in the adapter provides clearance for the tube connected to the gas membrane.

The height of the diamond anvil cell, once mounted onto the cold finger, did not allow using the o-ring-sealed vacuum lid. The latter also contained the optical window. Therefore, a new lid and

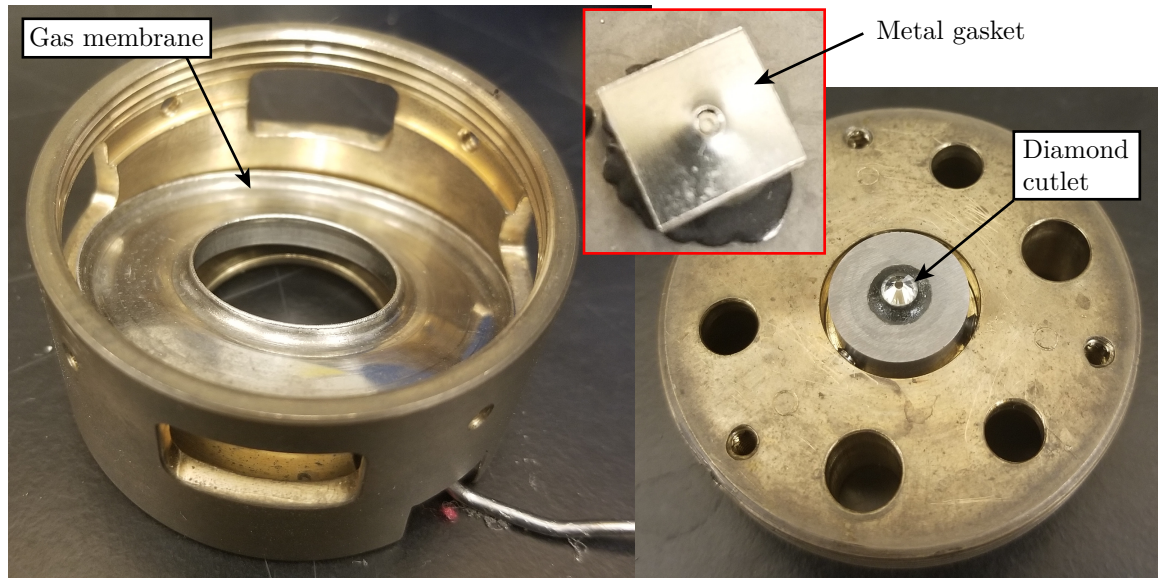


Figure 9.4.3: Left: stainless Steel gas membrane inside the cryostat-mounting cap. Right: Diamond outlet and its seat fastened to the top anvil mount.

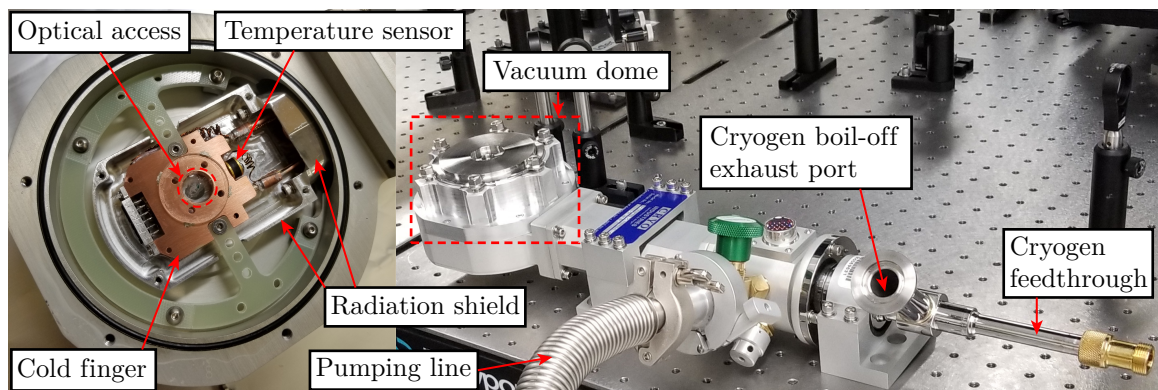


Figure 9.4.4: Left: photograph of the region of the cryostat where the diamond anvil cell is mounted. Right: custom Aluminum dome-shaped vacuum barrier to accommodate the diamond anvil cell.

window had to be designed. The original lid is similar to the one labeled “back side vacuum lid” in Fig. 9.4.5; i.e. the default front and back lids are identical. Therefore, I machined a dome-shaped lid from a single piece of 6061-T6 Aluminum; this custom lid is referred to as the “vacuum dome.” Fig. 9.4.4 shows a photograph of the vacuum dome installed on the cryostat during a leak test.

The final customization to the cryostat involved the design and installation of the gas delivery system to the membrane. This part of the customization procedure was the most complex since it involved an *almost* complete disassembly of the cryostat. The photograph in Fig. 9.4.5 gives a sense of the extent of the disassembly. Besides maintaining a high-pressure-to-vacuum seal, one of the design objectives was to minimize the heat load on the sample from the gas driving the membrane. The gas acts as a heat conduction medium from the 300 K Helium bottle to the diamond anvil cell. According to the manufacturer’s specifications, the latter could reach a base temperature of ≈ 4 K (≈ 1.5 K) with (without) pumping on the cryogen boil-off exhaust port (c.f. 9.4.4), with proper heat load management.

The stainless Steel tube carrying the gas has an inner (outer) diameter of 0.005" (1/16") and is 5 feet

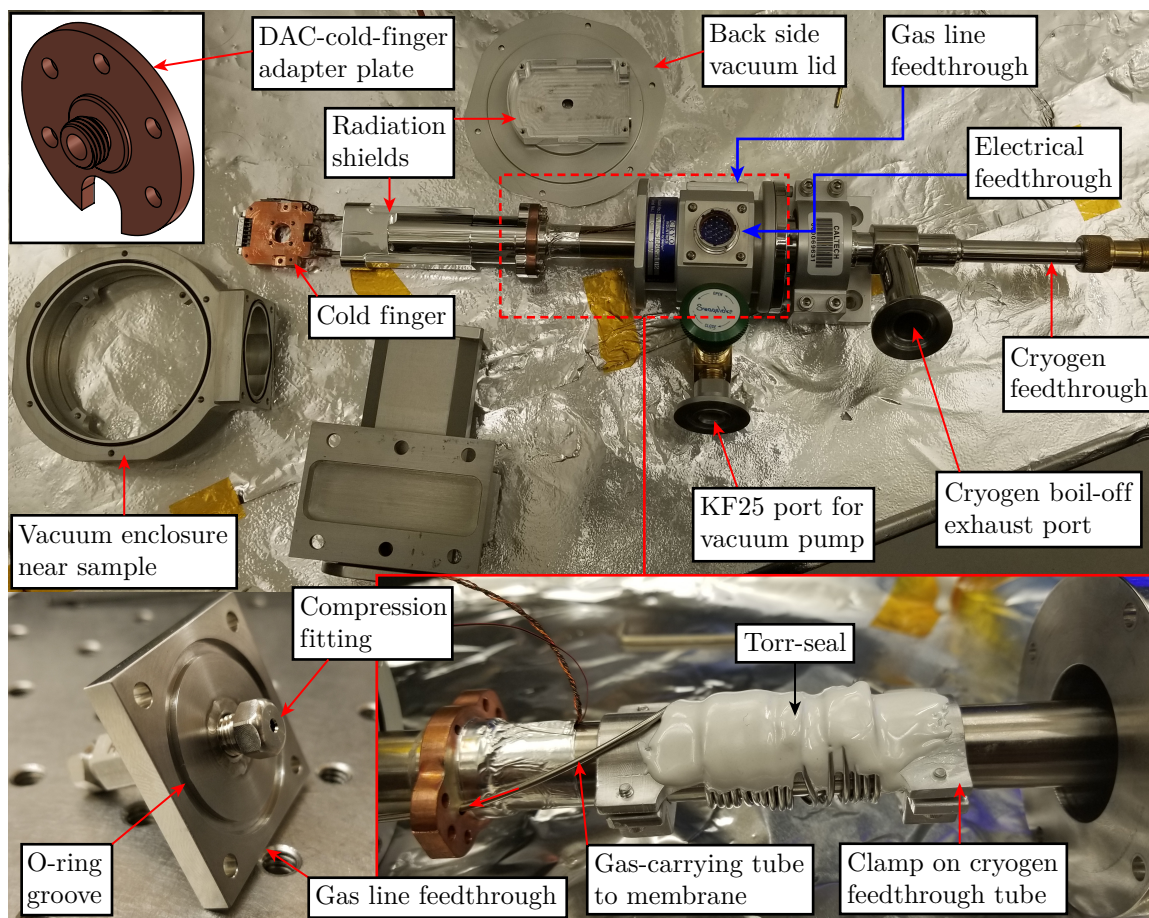


Figure 9.4.5: Photographs showing the customization to the components of the microscopy cryostat to accommodate the space constraints and in situ pressure tuning requirements of the diamond anvil cell design from Sec. 9.4.2.3.

long. As shown in Fig. 9.4.5, most of the tube length is heat sunk to a bobbin. The bobbin consists of an Aluminum piece clamped to the tube carrying the boiled-off cryogen gas to its exhaust. The stainless Steel tube is coiled around the clamp. Moreover, torr-seal is used in order to maximize the contact area between the tube and clamp.

The bottom-left photograph in Fig. 9.4.5 shows the custom feedthrough for the gas line. It is made of a $1.375'' \times 1.375'' \times 1/4''$ o-ring-sealed stainless Steel flange with a high pressure compression fitting in the center. A seam-welded vacuum seal is made between the flange and the fitting.

After the cryostat was re-assembled, the tube on the sample end was blanked off, and gas delivery system was stress tested to a pressure of 500 psi. The idea behind a stress test is to verify leak-free operation of the gas delivery system at a pressure much higher than its nominal value. The system passed the first leak test.

9.4.4 Work in progress

At the time of writing, some preliminary pump-probe experiments were performed, in collaboration with the Rosenbaum group, with the diamond anvil cell operated at a few GPa. One of the challenges

was finding the appropriate sample-mounting epoxy (c.f. Fig. 9.4.1). The epoxy needs to be both soft enough to not crack under pressure and rigid enough to not change sample alignment.

9.5 Order in systems with time-periodic drive

In Sec. 9.2.2, I briefly mentioned that, for most of this thesis, I have not considered the time, t , degree of freedom in the discussion of the order parameter, Ψ (c.f. Eq. (1.1.1)). Probes of topological superconductors (c.f. Chap. 2), using ARPES, and symmetry-breaking phases (c.f. Sec. 9.2.1.2 and 9.3.3), using RA-SHG, were designed for probing systems in equilibrium. It is, however, possible to design probes, using ARPES and optics, which can probe order in non-equilibrium systems. In this section, I will limit the discussion to a specific class non-equilibrium systems: Floquet.

After a brief overview of the theoretical and *recent* experimental background of Floquet systems, in Sec. 9.5.1 and 9.5.2, I will discuss a experimental proposal which, in my opinion, offers a promising route to achieving Floquet systems in condensed matter systems.

9.5.1 Introduction to time-periodic driven systems

In its simplest of definitions, when a time-periodic drive is added to a time-invariant system, the steady-state properties of the resultant system can be described by Floquet theory. In the context of condensed matter physics, a Floquet system of interest is (say) one where a time-periodic perturbation is applied to the Hamiltonian of a quantum degenerate electron system (e.g. band insulator). In this example, the minimal Bloch Hamiltonian for a two-band insulator is given by

$$\hat{\mathcal{H}}_0(\mathbf{k}) = \mathbf{d}(\mathbf{k}) \cdot \hat{\boldsymbol{\sigma}}, \quad (9.5.1)$$

where the Pauli matrix vector $\hat{\boldsymbol{\sigma}} = (\hat{\sigma}_x, \hat{\sigma}_y, \hat{\sigma}_z)$ is defined in the particle-hole basis and the vector $\mathbf{d}(\mathbf{k})$ encodes the properties of the specific insulator being investigated. Now, assume the following time-periodic perturbation is added to the Hamiltonian in (9.5.1)

$$\hat{\mathcal{V}}(\mathbf{k}, t) = \mathbf{V}(\mathbf{k}) \cdot \hat{\boldsymbol{\sigma}} \cos\left(\frac{2\pi t}{T}\right), \quad (9.5.2)$$

where $\mathbf{V}(\mathbf{k})$ characterizes the strength of the perturbation and T is the drive period. Then time evolution of a quantum state which was $\phi_{\mathbf{k}}$ at $t = 0$ can be written as

$$\phi_{\mathbf{k}}(t) = \hat{\mathcal{U}}_{\mathbf{k}}(t, 0)\phi_{\mathbf{k}}, \quad (9.5.3)$$

where the time evolution operator, $\hat{\mathcal{U}}_{\mathbf{k}}(t, 0)$, can be written in terms of (9.5.1) and (9.5.2) as

$$\hat{\mathcal{U}}_{\mathbf{k}}(t, 0) \equiv \mathcal{T}_t \exp\left(-i \int_0^t dt' \left[\hat{\mathcal{H}}_0(\mathbf{k}) + \hat{\mathcal{V}}(\mathbf{k}, t')\right]\right), \quad (9.5.4)$$

where \mathcal{T}_t is the time-ordering operator. Then the ‘‘Floquet Hamiltonian,’’ $\hat{\mathcal{H}}_{\mathbf{F}}(\mathbf{k})$, is stroboscopically defined as

$$\exp(-i\hat{\mathcal{H}}_{\mathbf{F}}(\mathbf{k})T) \equiv \hat{\mathcal{U}}_{\mathbf{k}}(T, 0). \quad (9.5.5)$$

Crudely, $\hat{\mathcal{H}}_{\mathbf{F}}(\mathbf{k})$ captures the net effect of the system evolution in one drive cycle. It can be noted that $\hat{\mathcal{H}}_{\mathbf{F}}(\mathbf{k})$ itself is time-independent. So it can, in principle, be written down in a form similar to (9.5.1) as

$$\hat{\mathcal{H}}_{\mathbf{F}}(\mathbf{k}) = \mathbf{n}(\mathbf{k}) \cdot \hat{\boldsymbol{\sigma}}, \quad (9.5.6)$$

where $\mathbf{n}(\mathbf{k})$ now depends on the original system details, described by $\mathbf{d}(\mathbf{k})$, as well as the properties of the drive $\mathbf{V}(\mathbf{k})$. This implies that, if $\mathbf{d}(\mathbf{k})$ possessed certain ‘‘undesirable’’ properties, they can be ‘‘rectified’’ with a $\mathbf{V}(\mathbf{k})$ of one’s choice. In other words, one can engineer materials on demand if equilibrium is sacrificed.

9.5.2 Photon Floquet systems

Floquet systems were revisited shortly after the discovery of topological insulators. The reason for this is that Floquet theory offers a unique route to engineering topological insulators in otherwise trivial insulators. The most versatile and well-engineered real-world example of a periodic drive is a single-mode continuous wave laser. Naturally, some of the first proposals, involving engineering 2D [102] and 3D [103] Floquet topological insulators (FTIs), involved the use of photons. While these theory proposals modeled continuous wave lasers for simplicity, the situation turned out much more difficult on the experimental front.

One of the major problems was managing the trade-off between the drive amplitude (i.e. laser power) and sample heating. Continuous wave lasers were simply not designed to operate at power levels required to create FTIs that were experimentally feasible to detect. In particular, the topological gap, in which the Floquet edge/surface states resided, was too small to be measured. Increasing the value of the gap would require increasing the laser power, which would eventually damage the sample. A compromise between the competing factors, of gap size vs. laser power, was eventually reached with a femtosecond laser. The peak electric fields in femtosecond pulses was high enough to achieve large enough Floquet gaps while the pulse duration and repetition rate were low enough to prevent sample damage.

Another problem, less serious than sample heating, that one has to worry about in photon Floquet experiments is photon-assisted photoemission. The interpretation of Floquet copies in an ARPES spectrum can be obfuscated by the fact that said copies could merely be a result of multi-photon absorption.

The first experiments which reported Floquet states in topological materials used femtosecond lasers to excite the surface states of Bi_2Se_3 [104]. The resulting electronic spectrum was probed using ARPES. As per the predictions of Floquet theory, multiple copies of the Dirac cone were observed translated along the energy axis.

9.5.3 Studying phonon-Floquet systems with ARPES

9.5.3.1 Comparison to photon Floquet

It turns out that electronic systems already sit in an oscillating environment: phonons! In ultrafast pump-probe reflectivity measurements, Bi_2Se_3 exhibits coherent phonon oscillations with a period of roughly 0.5 ps. These phonons could, in principle, create multiple Floquet copies which could be resolved in an appropriately designed ARPES experiment. Phonon Floquet systems have a few advantages over their photon counterparts. For one, phonon-assisted photoemission is not possible since there are no phonons in vacuum for the photoelectron to absorb! Secondly, it is possible to get large phonon drive amplitudes without damage to the sample.

9.5.3.2 Scientific goals

In this section, I will discuss an experiment I proposed to study a phonon Floquet system with the ARPES setup discussed in this thesis. This idea is based on a theoretical proposal by [105], which first provides an analytical mapping between photon and phonon Floquet systems, and follows it up with time-dependent density functional theory. A cartoon illustration of the proposed experiment is shown in Fig. 9.5.1.

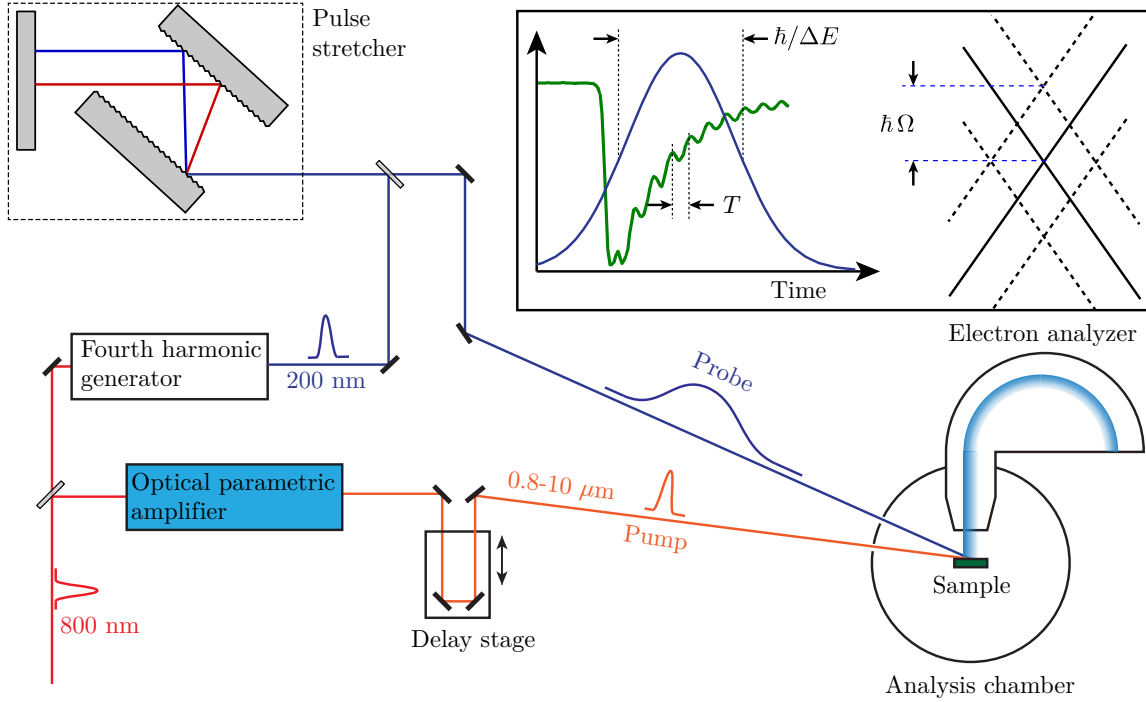


Figure 9.5.1: A cartoon illustration of the layout for a proposed phonon Floquet experiment. The inset conceptually illustrates temporal and spectral characteristics of the experiment.

In this case, after the generation of the fourth harmonic, the 200 nm beam is sent into a grating pair stretcher. This will expand the beam in time to the order of picoseconds. Assuming a Gaussian pulse of width, Δt , of (say) 2 ps, the energy uncertainty can be calculated as

$$\begin{aligned} \Delta E &\geq h \frac{\text{Gaussian time-bandwidth product}}{\Delta t}, \\ &\geq 4.14 \text{ meV} \cdot \text{ps} \frac{0.44}{2 \text{ ps}}, \\ &\geq 0.91 \text{ meV}. \end{aligned}$$

which hypothetically, in the absence of the space-charge effect, would be sufficient for high resolution ARPES. But for Floquet experiments, I think minor energy broadening from space-charge effects could be acceptable, since the proposed experiment probes a steady-state (as opposed to static) electronic systems. The phonon period $T \approx 0.5 \text{ ps}$ will create Floquet copies displaced by the phonon energy $\hbar\Omega$ ($= 4.14 \text{ meV} \cdot \text{ps}/0.5 \text{ ps} \approx 8 \text{ meV}$). This 8 meV gap can be easily resolved with $\Delta E \approx 1 \text{ meV}$.

In the time domain, this means that eight phonon oscillations can be fit into the probe pulse duration. This is roughly what is illustrated in the inset of Fig. 9.5.1. Even in the event that the space-charge effect does pose an issue, there exist material systems with phonon frequencies, Ω , high enough ($\hbar\Omega \approx 15 \text{ meV}$) that a sufficient amount of pulse stretching, combined with space-charge mitigation strategies, should allow resolution of the phonon Floquet copies.

9.5.3.3 Aliasing analogy

It's worth pointing out an information-theoretic telecommunications analogy: aliasing. This phonon Floquet experiment can be viewed from a completely different point of view as the aliasing prob-

lem associated with the Nyquist-Shannon sampling theorem. This theorem states that in order to faithfully discretize a time-varying signal, one needs to sample said signal at a frequency of at least twice the highest frequency (Nyquist frequency) component in the signal. For example, when (say) a sinusoidal signal, with frequency f , is sampled at a frequency of (say) $f/2$, which is less than the Nyquist frequency ($f_{\text{Nyquist}} = 2f$), then sine functions of an integer multiple of $f/2$ can be fit to the discrete data points.

In this case, by deliberately stretching out the probe pulse in the time domain to 4 ps, such that it is unable to resolve the individual 0.5 ps phonon oscillations, and having the analyzer try to “fit” the photoemission spectrum with a much better energy resolution, one can see Floquet copies (or aliases) in the ARPES spectrum.

Chapter 10

Conclusions and future directions

The through line of this thesis was the analysis of the order parameter, $\Psi(\mathbf{x}, t)$, introduced in Chapter 1. I presented examples of theoretical and experimental tools which have been developed to define and measure $\Psi(\mathbf{x}, t)$ respectively. My graduate research focused on the latter. In particular, as the thesis title suggests, the emphasis of research was on the *development* of tools which can measure a specific class of $\Psi(\mathbf{x}, t)$: topological. I sought to investigate topological phases in single crystals using experimental techniques involving angle-resolved photoelectron spectroscopy (ARPES) and non-linear optics under hydrostatic pressure.

As evident from Chapters 4-8, the construction and testing of a unique ARPES machine, with the potential of discovering topological superconductors, formed the largest portion my graduate work. The two main objectives of this ARPES machine were achieving: (a) sub-Kelvin temperatures, and (b) sub-meV energy resolution. Achieving these two specifications *simultaneously* was unprecedented at the beginning of the ARPES construction project. In Chapter 7, I demonstrated the ability of the ARPES machine in achieving sub-Kelvin temperatures. In Chapter 5, I demonstrated the ability of the electron detector to perform sub-meV measurements (c.f. Fig. 5.4.1). At the time of writing, I was involved in an ongoing ARPES optimization effort (c.f. Chapter 8) to push the energy resolution from 5 meV (c.f. Sec. 8.5.2.3) into the sub-meV regime.

In my opinion, a promising future direction to improve the current energy resolution (5 meV) would be the introduction of so-called “extended shields.” The shape of these extended shields would be similar to μ -metal layers inside the analysis chamber (c.f. Fig. 6.3.3). Through careful machined components, these shields can be thermally anchored to the 1 K plate and 4 K/77 K reservoirs. The idea behind this design is the maximization of the distance between the shields and the sample. Hopefully this would minimize the electromagnetic interference from the shields at the sample position. Moreover, the slots, through which the electrons have to inevitably pass through to get to the detector, can be widened without sacrificing the sub-Kelvin base temperature. In other words, the ratio of the slot area to the total shield surface area would be kept constant. In the last months of my involvement in the ARPES project, I completed the CAD design of the extended shields. These designs could aide in future ARPES optimization efforts.

In Chapter 9, I discussed my experience with performing non-linear optics experiments (c.f. Sec. 9.3.3). Moreover, I discussed my involvement in a project involving non-linear and ultrafast optical measurements on $\text{Cd}_2\text{Re}_2\text{O}_7$ under hydrostatic pressure (c.f. Sec. 9.4). In particular, I performed upgrades on an optical microscopy cryostat to accommodate the high-pressure cell (a.k.a. diamond anvil cell). At the time of writing, this cryostat is being used in an ultrafast high-pressure optics setup designed my colleagues in collaboration with Thomas Rosenbaum’s group.

As a result of my intimate involvement in the optics cryostat upgrade, I had an idea to use the 1 K pot pump, from the ARPES setup, to perform RA-SHG experiments (c.f. Sec. 9.3.2) on $\text{Nb}_x\text{Bi}_2\text{Se}_3$ to study point group symmetries of its superconducting order parameter. In the past, I performed these experiments using a pump with much lower mass conductance than the 1 K pot pump. Consequently, the superconducting state of $\text{Nb}_x\text{Bi}_2\text{Se}_3$ was not achieved. In my opinion, attempting to lower the base temperature of optics cryostats, using the 1 K pot pump, is a promising avenue to explore in the future.

In summary, as a result of my experience with experimental tools to study both topological (ARPES) and symmetry-breaking phases (RA-SHG), and communications with other condensed matter physicists about other state-of-the-art probes of $\Psi(\mathbf{x}, t)$, I am optimistic that mapping out the phase diagram in Fig. 1.5.1 might be a realistic goal in the next couple of decades.

Bibliography

- [1] Louis Michel. “Symmetry defects and broken symmetry. Configurations hidden symmetry.” *Reviews of Modern Physics* **52**, no. 3 (1980): 617.
- [2] Dieter Vollhardt and Peter Wolfe. (2013). “The superfluid phases of Helium 3.” *Courier Corporation*.
- [3] Klaus von Klitzing, Gerhard Dorda, and Michael Pepper. (1980). “New method for high-accuracy determination of the fine-structure constant based on quantized Hall resistance.” *Physical Review Letters* **45**, no. 6: 494.
- [4] David Mermin. (1979). “The topological theory of defects in ordered media.” *Reviews of Modern Physics* **51**, no. 3: 591.
- [5] John Kosterlitz and David J. Thouless. (1973). “Ordering, metastability and phase transitions in two-dimensional systems.” *Journal of Physics C: Solid State Physics* **6**, no. 7: 1181.
- [6] Markus König, Steffen Wiedmann, Christoph Brüne, Andreas Roth, Hartmut Buhmann, Laurens W. Molenkamp, Xiao-Liang Qi, and Shou-Cheng Zhang. (2007). “Quantum spin Hall insulator state in HgTe quantum wells.” *Science* **318**, no. 5851: 766-770.
- [7] David Hsieh, Dong Qian, Lewis Wray, Yiman Xia, Yew San Hor, Robert Joseph Cava, and M. Zahid Hasan. (2008). “A topological Dirac insulator in a quantum spin Hall phase.” *Nature* **452**, no. 7190: 970-974.
- [8] Cui-Zu Chang, Jinsong Zhang, Xiao Feng, Jie Shen, Zuocheng Zhang, Minghua Guo, Kang Li, Yunbo Ou, Pang Wei, Li-Li Wang, Zhong-Qing Ji, Yang Feng, Shuaihua Ji, Xi Chen, Jinfeng Jia, Xi Dai, Zhong Fang, Shou-Cheng Zhang, Ke He, Yayu Wang, Li Lu, Xu-Cun Ma, Qi-Kun Xue. (2013). “Experimental observation of the quantum anomalous Hall effect in a magnetic topological insulator.” *Science* **340**, no. 6129: 167-170.
- [9] Gregor Jotzu, Michael Messer, Rémi Desbuquois, Martin Lebrat, Thomas Uehlinger, Daniel Greif, and Tilman Esslinger. (2014). “Experimental realization of the topological Haldane model with ultracold fermions.” *Nature* **515**, no. 7526: 237-240.
- [10] Su-Yang Xu, Ilya Belopolski, Nasser Alidoust, Madhab Neupane, Guang Bian, Chenglong Zhang, Raman Sankar, Guoqing Chang, Zhujun Yuan, Chi-Cheng Lee, Shin-Ming Huang, Hao Zheng, Jie Ma, Daniel S. Sanchez, BaoKai Wang, Arun Bansil, Fangcheng Chou, Pavel P. Shibayev, Hsin Lin, Shuang Jia, M. Zahid Hasan. (2015). “Discovery of a Weyl fermion semimetal and topological Fermi arcs.” *Science* **349**, no. 6248: 613-617.
- [11] D. D. Osheroff, R. C. Richardson, and D. M. Lee. (1972). “Evidence for a new phase of solid He-3.” *Physical Review Letters* **28**, no. 14: 885.
- [12] Peng Zhang, Koichiro Yaji, Takahiro Hashimoto, Yuichi Ota, Takeshi Kondo, Kozo Okazaki, Zhijun Wang, Jinsheng Wen, Genda D. Gu, Hong Ding, Shik Shin. (2018). “Observation of topological superconductivity on the surface of an iron-based superconductor.” *Science* **360**, no. 6385: 182-186.

- [13] David J. Thouless, Mahito Kohmoto, M. Peter Nightingale, and Marcel den Nijs. (1982). “Quantized Hall conductance in a two-dimensional periodic potential.” *Physical Review Letters* **49**, no. 6: 405.
- [14] Robert Laughlin. (1981). “Quantized Hall conductivity in two dimensions.” *Physical Review B* **23**, 5632.
- [15] Michael Berry (1984). “Quantal phase factors accompanying adiabatic changes.” *Proceedings of the Royal Society A* **392**, 1802.
- [16] Jainendra Jain. (2007). “Composite fermions.” *Cambridge University Press*.
- [17] Sankar Das Sarma and Aron Pinczuk, eds. (1996). “Perspectives in quantum hall effects: Novel quantum liquids in low-dimensional semiconductor structures.” *John Wiley & Sons*.
- [18] L. D. Landau and E. M. Lifschitz. (1977). *Quantum Mechanics: Non-relativistic Theory. Course of Theoretical Physics. Vol. 3*. 3rd ed. London: Pergamon Press.
- [19] Charles Kane and Eugene Mele. (2005). “Quantum spin Hall effect in graphene.” *Physical Review Letters* **95**, no. 22: 226801.
- [20] Jun Hu, Jason Alicea, Ruqian Wu, and Marcel Franz. (2012). “Giant topological insulator gap in graphene with 5d adatoms.” *Physical Review Letters* **109**, no. 26: 266801.
- [21] B. Andrei Bernevig, Taylor L. Hughes, and Shou-Cheng Zhang. (2006). “Quantum spin Hall effect and topological phase transition in HgTe quantum wells.” *Science* **314**, no. 5806: 1757-1761.
- [22] Vivek Venkatachalam, Amir Yacoby, Loren Pfeiffer, and Ken West. (2011). “Local charge of the $\nu = 5/2$ fractional quantum Hall state.” *Nature* **469**, no. 7329: 185-188.
- [23] Tian-Heng Han, Joel S. Helton, Shaoyan Chu, Daniel G. Nocera, Jose A. Rodriguez-Rivera, Collin Broholm, and Young S. Lee. (2012). “Fractionalized excitations in the spin-liquid state of a kagome-lattice antiferromagnet.” *Nature* **492**, 406.
- [24] Michael R. Norman. (2016). “*Colloquium*: Herbertsmithite and the search for the quantum spin liquid.” *Reviews of Modern Physics* **88**, 041002.
- [25] Lucile Savary and Leon Balents. (2017). “Quantum spin liquids: a review.” *Reports on Progress in Physics* **80**, 016502.
- [26] Xie Chen, Zheng-Cheng Gu, Zheng-Xin Liu, and Xiao-Gang Wen. (2013). “Symmetry protected topological orders and the group cohomology of their symmetry group.” *Physical Review B* **87**, no. 15: 155114.
- [27] Xie Chen, Zheng-Cheng Gu, and Xiao-Gang Wen. (2010). “Local unitary transformation, long-range quantum entanglement, wave function renormalization, and topological order.” *Physical Review B* **82**, no. 15: 155138.
- [28] F. Duncan M. Haldane. (1983). “Nonlinear field theory of large-spin Heisenberg antiferromagnets: semiclassically quantized solitons of the one-dimensional easy-axis Néel state.” *Physical Review Letters* **50**, no. 15: 1153.
- [29] Ettore Majorana. (1937). “Teoria simmetrica dell’elettrone e del positrone (Symmetric theory of the electron and the positron).” *Il Nuovo Cimento (1924-1942)* **14**, no. 4: 171.
- [30] Chetan Nayak, Steven H. Simon, Ady Stern, Michael Freedman, and Sankar Das Sarma. (2008). “Non-Abelian anyons and topological quantum computation.” *Reviews of Modern Physics* **80**, no. 3: 1083.

- [31] Jason Alicea. (2012). “New directions in the pursuit of Majorana fermions in solid state systems.” *Reports on Progress in Physics* **75**, no. 7: 076501.
- [32] Michael Tinkham. (2004). “Introduction to superconductivity.” 2nd edition. *Courier Corporation*.
- [33] John Bardeen, Leon Cooper, and Robert Schrieffer. (1957). “Theory of superconductivity.” *Physical Review* **108**, no. 5: 1175.
- [34] Alexei Kitaev. (2001). “Unpaired Majorana fermions in quantum wires.” *Physics-Uspekhi* **44**, no. 10S: 131.
- [35] Nicholas Read and Dmitry Green. (2000). “Paired states of fermions in two dimensions with breaking of parity and time-reversal symmetries and the fractional quantum Hall effect.” *Physical Review B* **61**, no. 15: 10267.
- [36] Liang Fu and Charles L. Kane. (2008). “Superconducting proximity effect and Majorana fermions at the surface of a topological insulator.” *Physical Review Letters* **100**, no. 9: 096407.
- [37] Dongfei Wang, Lingyuan Kong, Peng Fan, Hui Chen, Shiyu Zhu, Wenyao Liu, Lu Cao, Yujie Sun, Shixuan Du, John Schneeloch, Ruidan Zhong, Genda Gu, Liang Fu, Hong Ding, Hong-Jun Gao. (2018). “Evidence for Majorana bound states in an iron-based superconductor.” *Science* **362**, no. 6412: 333-335.
- [38] Holger Bech Nielsen and Masao Ninomiya. (1981). “No-go theorem for regularizing chiral fermions.” *Physics Letters B* **105**, no. 2-3: 219-223.
- [39] Shingo Yonezawa. (2019). “Nematic superconductivity in doped Bi₂Se₃ topological superconductors.” *Condensed Matter* **4**, no. 1: 2.
- [40] Lattice structure of Bi₂Se₃ obtained from Materials Project website (date accessed: June 1, 2020). DOI: 10.17188/1266263
- [41] Liang Fu and Erez Berg. (2010). “Odd-parity topological superconductors: theory and application to Cu_xBi₂Se₃.” *Physical Review Letters* **105**, no. 9: 097001.
- [42] Satoshi Sasaki, M. Kriener, Kouji Segawa, Keiji Yada, Yukio Tanaka, Masatoshi Sato, and Yoichi Ando. (2011). “Topological superconductivity in Cu_xBi₂Se₃.” *Physical Review Letters* **107**, no. 21: 217001.
- [43] Jonathan A. Sobota, S-L. Yang, Dominik Leuenberger, Alexander F. Kemper, James G. Analytis, Ian R. Fisher, Patrick S. Kirchmann, Thomas P. Devereaux, and Z-X. Shen. (2014). “Distinguishing bulk and surface electron-phonon coupling in the topological insulator Bi₂Se₃ using time-resolved photoemission spectroscopy.” *Physical Review Letters* **113**, no. 15: 157401.
- [44] Yoichi Ando. (2013). “Topological insulator materials.” *Journal of the Physical Society of Japan* **82**, no. 10: 102001.
- [45] Haijun Zhang, Chao-Xing Liu, Xiao-Liang Qi, Xi Dai, Zhong Fang, and Shou-Cheng Zhang. (2009). “Topological insulators in Bi₂Se₃, Bi₂Te₃ and Sb₂Te₃ with a single Dirac cone on the surface.” *Nature Physics* **5**, no. 6: 438-442.
- [46] Suk Bum Chung and Shou-Cheng Zhang. (2009). “Detecting the Majorana Fermion Surface State of ³He-B through Spin Relaxation.” *Physical Review Letters* **103**, no. 23: 235301.
- [47] David Hsieh, Yuqi Xia, Dong Qian, L. Wray, J. H. Dil, Fedorov Meier, J. Osterwalder, L. Patthey, J. G. Checkelsky, N. P. Ong, Alexei V. Fedorov, H. Lin, Arun Bansil, D. Grauer, Y. S. Hor, R. J. Cava, and M. Z. Hasan. (2009). “A tunable topological insulator in the spin helical Dirac transport regime.” *Nature* **460**, no. 7259 : 1101-1105.

- [48] Ayo Kolapo, Tingxin Li, Pavan Hosur, and John H. Miller. (2019). “Possible transport evidence for three-dimensional topological superconductivity in doped β -PdBi₂.” *Scientific Reports* **9**, no. 1: 1-10.
- [49] Vincent Mourik, Kun Zuo, Sergey M. Frolov, S. R. Plissard, Erik PAM Bakkers, and Leo P. Kouwenhoven. (2012). “Signatures of Majorana fermions in hybrid superconductor-semiconductor nanowire devices.” *Science* **336**, no. 6084: 1003-1007.
- [50] Niv Levy, Tong Zhang, Jeonghoon Ha, Fred Sharifi, A. Alec Talin, Young Kuk, and Joseph A. Stroscio. (2013). “Experimental evidence for s -wave pairing symmetry in superconducting Cu_xBi₂Se₃ single crystals using a scanning tunneling microscope.” *Physical Review Letters* **110**, no. 11: 117001.
- [51] Takeshi Mizushima, Ai Yamakage, Masatoshi Sato, and Yukio Tanaka. (2014). “Dirac-fermion-induced parity mixing in superconducting topological insulators.” *Physical Review B* **90**, no. 18: 184516.
- [52] E. Lahoud, E. Maniv, M. Shaviv Petrushevsky, M. Naamneh, A. Ribak, S. Wiedmann, L. Petaccia, Z. Salman, K. B. Chashka, Y. Dagan, and A. Kanigel. (2013). “Evolution of the Fermi surface of a doped topological insulator with carrier concentration.” *Physical Review B* **88**, no. 19: 195107.
- [53] Kazuaki Matano, M. Kriener, K. Segawa, Y. Ando, and Guo-qing Zheng. (2016). “Spin-rotation symmetry breaking in the superconducting state of Cu_xBi₂Se₃.” *Nature Physics* **12**, no. 9: 852-854.
- [54] Heinrich Hertz. (1887). “Über einen Einfluss des ultravioletten Lichtes auf die elektrische Entladung (On the influence of ultraviolet light on the electric discharge).” *Annalen der Physik* **31**, 983.
- [55] Albert Einstein. (1905). “Über einen die Erzeugung und Verwandlung des Lichtes betreffenden heuristischen Gesichtspunkt (On a heuristic point of view concerning the generation and transformation of light).” *Annalen der Physik* **17**, 132.
- [56] Stefan Hüfner (2013). *Photoelectron spectroscopy: principles and applications*. 3rd edition. Springer Science & Business Media.
- [57] Felix Bloch. (1928). “Über die Quantenmechanik der Elektronen in Kristallgittern (About the quantum mechanics of electrons in crystal lattices).” *Zeitschrift für Physik* **52** (7-8): 555-600.
- [58] Lev Landau. (1956). “The Theory of a Fermi Liquid.” *Journal of Experimental and Theoretical Physics* (U.S.S.R.) **30**, 1058-1064.
- [59] R. Haight and D. R. Peale. (1994). “Tunable photoemission with harmonics of subpicosecond lasers.” *Review of Scientific Instruments* **65**, no. 6: 1853-1857.
- [60] J. D. Koralek, J. F. Douglas, N. C. Plumb, Z. Sun, A. V. Fedorov, M. M. Murnane, H. C. Kapteyn, S. T. Cundiff, Y. Aiura, K. Oka, H. Eisaki, and D. S. Dessau. (2006). “Laser based angle-resolved photoemission, the sudden approximation, and quasiparticle-like spectral peaks in Bi₂Sr₂CaCu₂O_{8+ δ} .” *Physical Review Letters* **96**, no. 1: 017005.
- [61] T. Kiss, T. Shimojima, F. Kanetaka, K. Kanai, T. Yokoya, S. Shin, Y. Onuki, T. Togashi, C. Q. Zhang, C. T. Chen, S. Watanabe. (2005). “Ultrahigh-resolution photoemission spectroscopy of superconductors using a VUV laser.” *Journal of Electron Spectroscopy and Related Phenomena* **144**, 953-956.
- [62] T. Kiss, T. Shimojima, K. Ishizaka, A. Chainani, T. Togashi, T. Kanai, X.-Y. Wang, C.-T. Chen, S. Watanabe, and S. Shin. (2008). “A versatile system for ultrahigh resolution, low temperature, and polarization dependent laser-angle-resolved photoemission spectroscopy.” *Review of Scientific Instruments* **79**, no. 2: 023106.

- [63] Shambhu Ghimire, Anthony D. DiChiara, Emily Sistrunk, Pierre Agostini, Louis F. DiMauro, and David A. Reis. (2011). “Observation of high-order harmonic generation in a bulk crystal.” *Nature Physics* **7**, no. 2: 138-141.
- [64] A. McPherson, G. Gibson, H. Jara, U. Johann, Ting S. Luk, I. A. McIntyre, Keith Boyer, and Charles K. Rhodes. (1987). “Studies of multiphoton production of vacuum-ultraviolet radiation in the rare gases.” *Journal of the Optical Society of America B* **4**, 595.
- [65] M. Ferray, Anne L’Huillier, X. F. Li, L. A. Lompre, G. Mainfray, and C. Manus. (1988). “Multiple-harmonic conversion of 1064 nm radiation in rare gases.” *Journal of Physics B: Atomic, Molecular and Optical Physics* **21**, no. 3: L31.
- [66] Anna Tamai, W. Meevasana, P. D. C. King, C. W. Nicholson, Alberto de la Torre, E. Rozbicki, and Félix Baumberger. (2013). “Spin-orbit splitting of the Shockley surface state on Cu (111).” *Physical Review B* **87**, no. 7: 075113.
- [67] Yu He, Inna M. Vishik, Ming Yi, Shuolong Yang, Zhongkai Liu, James J. Lee, Sudi Chen, Slavko N. Rebec, Dominik Leuenberger, Alfred Zong, C. Michael Jefferson, Robert G. Moore, Patrick S. Kirchmann, Andrew J. Merriam, and Zhi-Xun Shen. (2016). “High resolution angle resolved photoemission with tabletop 11 eV laser.” *Review of Scientific Instruments* **87**, no. 1: 011301.
- [68] S. Passlack, S. Mathias, O. Andreyev, D. Mittnacht, M. Aeschlimann, and M. Bauer. (2006). “Space charge effects in photoemission with a low repetition, high intensity femtosecond laser source.” *Journal of Applied Physics* **100**, no. 2: 024912.
- [69] S. Hellmann, K. Rossnagel, M. Marczynski-Bühlow, and L. Kipp. (2009). “Vacuum space-charge effects in solid-state photoemission.” *Physical Review B* **79**, no. 3: 035402.
- [70] Jeff Graf, Stefan Hellmann, Chris Jozwiak, C. L. Smallwood, Zahid Hussain, R. A. Kaindl, Lutz Kipp, Kai Rossnagel, and Alessandra Lanzara. (2010). “Vacuum space charge effect in laser-based solid-state photoemission spectroscopy.” *Journal of Applied Physics* **107**, no. 1: 014912.
- [71] Ulrich Eismann, Matthias Scholz, Tim Paasch-Colberg, and Jürgen Stuhler. (2016). “Novel Lasers: Short, shorter, shortest - Diode lasers in the deep ultraviolet.” *Laser Focus World* **52**, no. 6: 39-44.
- [72] Robert W. Boyd. (2019). “Nonlinear Optics.” 4th edition. *Elsevier*.
- [73] Eric D. Black. (2001). “An introduction to Pound-Drever-Hall laser frequency stabilization.” *American Journal of Physics* **69**, no. 1: 79-87.
- [74] K.S.E. Eikema, J. Walz, and T. W. Hänsch. (1999). “Continuous wave coherent Lyman- α radiation.” *Physical Review Letters* **83**, no. 19: 3828.
- [75] K.S.E. Eikema, J. Walz, and T. W. Hänsch. (2001). “Continuous coherent Lyman- α excitation of atomic hydrogen.” *Physical Review Letters* **86**, no. 25: 5679.
- [76] Wayne Huang, Tharon Morrison, Nathaniel McDonough, and Gerald Gabrielse. (2019). “Towards Continuous-wave Laser Cooling for Anti-hydrogen.” *Bulletin of the American Physical Society* **64**.
- [77] V. Yashchuk, S. Lee, and E. Paperno (2013). “Magnetic shielding.” Chapter in D. Budker & D. Jackson Kimball (Eds.), “Optical Magnetometry” (pp. 225-248). *Cambridge University Press*.
- [78] Richard Herzog. (1935). “Berechnung des Streufeldes eines Kondensators, dessen Feld durch eine Blende begrenzt ist (Calculation of the stray field of a capacitor whose field is limited by an aperture).” *Archiv für Elektrotechnik* **29**, no. 11, 790-802.

- [79] Mikhail Yavor. (2009). “Optics of Charged Particle Analyzers.” *Academic Press*. San Diego, CA.
- [80] Björn Wannberg. (2009). “Electron optics development for photo-electron spectrometers.” *Nuclear Instruments and Methods in Physics Research Section A* **601**, no. 1-2: 182-194.
- [81] Private communication with Dan Dessau (2019).
- [82] P. Baltzer, L. Karlsson, M. Lundqvist, and B. Wannberg. (1993). “Resolution and signal-to-background enhancement in gas-phase electron spectroscopy.” *Review of Scientific Instruments* **64**, no. 8: 2179-2189.
- [83] E. Frantzeskakis, S. V. Ramankutty, N. de Jong, Y. K. Huang, Y. Pan, A. Tytarenko, M. Radovic, N. C. Plumb, M. Shi, A. Varykhalov, A. de Visser, E. van Heumen, and M. S. Golden. (2017). “Trigger of the ubiquitous surface band bending in 3D topological insulators.” *Physical Review X* **7**, no. 4: 041041.
- [84] S. V. Borisenko. (2012). ““One-cubed” ARPES User Facility at BESSY II.” *Synchrotron Radiation News* **25**, no. 5: 6-11.
- [85] Frank Pobell. (2007). “Matter and methods at low temperatures.” Vol. 2. *Springer*. Berlin.
- [86] Syu-You Guan, Peng-Jen Chen, Ming-Wen Chu, Raman Sankar, Fangcheng Chou, Horng-Tay Jeng, Chia-Seng Chang, and Tien-Ming Chuang. (2016). “Superconducting topological surface states in the noncentrosymmetric bulk superconductor PbTaSe₂.” *Science Advances* **2**, no. 11: e1600894.
- [87] Michael F. Crommie, Christopher P. Lutz, and Donald M. Eigler. (1993). “Imaging standing waves in a two-dimensional electron gas.” *Nature* **363**, no. 6429: 524-527.
- [88] Alistair S. Cameron, Gerd Friemel, and Dmytro S. Inosov. (2016). “Multipolar phases and magnetically hidden order: review of the heavy-fermion compound Ce_{1-x}La_xB₆.” *Reports on Progress in Physics* **79**, no. 6: 066502.
- [89] John A. Mydosh and Peter M. Oppeneer. (2011). “Colloquium: Hidden order, superconductivity, and magnetism: The unsolved case of URu₂Si₂.” *Reviews of Modern Physics* **83**, no. 4: 1301.
- [90] Schlabitz *et al.* (1984) poster (unpublished). The first published report was by T. T. M. Palstra, A. A. Menovsky, J. Van den Berg, A. J. Dirkmaat, P. H. Kes, G. J. Nieuwenhuys, and J. A. Mydosh. (1985). “Superconducting and magnetic transitions in the heavy-fermion system URu₂Si₂.” *Physical Review Letters* **55**, no. 24: 2727.
- [91] Premala Chandra, Piers Coleman, and Rebecca Flint. (2013). “Hastatic order in the heavy-fermion compound URu₂Si₂.” *Nature* **493**, no. 7434: 621.
- [92] John Harter, Z. Y. Zhao, J-Q. Yan, D. G. Mandrus, and David Hsieh. (2017). “A parity-breaking electronic nematic phase transition in the spin-orbit coupled metal Cd₂Re₂O₇.” *Science* **356**, no. 6335: 295-299.
- [93] Hideo Aoki, Naoto Tsuji, Martin Eckstein, Marcus Kollar, Takashi Oka, and Philipp Werner. (2014). “Nonequilibrium dynamical mean-field theory and its applications.” *Reviews of Modern Physics* **86**, no. 2: 779.
- [94] Nuh Gedik, P. Blake, R. C. Spitzer, J. Orenstein, Ruixing Liang, D. A. Bonn, and W. N. Hardy. (2004). “Single-quasiparticle stability and quasiparticle-pair decay in YBa₂Cu₃O_{6.5}.” *Physical Review B* **70**, no. 1: 014504.

- [95] Daniele Fausti, R. I. Tobey, Nicky Dean, Stefan Kaiser, A. Dienst, Matthias C. Hoffmann, S. Pyon, T. Takayama, H. Takagi, and Andrea Cavalleri. (2011). “Light-induced superconductivity in a stripe-ordered cuprate.” *Science* **331**, no. 6014: 189-191.
- [96] Darius H. Torchinsky, Hao Chu, Tongfei Qi, Gang Cao, and David Hsieh. (2014). “A low temperature nonlinear optical rotational anisotropy spectrometer for the determination of crystallographic and electronic symmetries.” *Review of Scientific Instruments* **85**, no. 8: 083102.
- [97] John Harter, Lauren Niu, Anthony J. Woss, and David Hsieh. (2015). “High-speed measurement of rotational anisotropy nonlinear optical harmonic generation using position-sensitive detection.” *Optics letters* **40**, no. 20: 4671-4674.
- [98] Kyle Frohna, Tejas Deshpande, John Harter, Wei Peng, Bradford A. Barker, Jeffrey B. Neaton, Steven G. Louie, Osman M. Bakr, David Hsieh, and Marco Bernardi. (2018). “Inversion symmetry and bulk Rashba effect in methylammonium lead iodide perovskite single crystals.” *Nature Communications* **9**, no. 1: 1829.
- [99] Pallavi S. Malavi, S. Karmakar, and S. M. Sharma. (2016). “Cd₂Re₂O₇ under high pressure: Pyrochlore lattice distortion-driven metal-to-nonmetal transition.” *Physical Review B* **93**, no. 3: 035139.
- [100] Ho-Kwang Mao, Xiao-Jia Chen, Yang Ding, Bing Li, and Lin Wang. (2018). “Solids, liquids, and gases under high pressure.” *Reviews of Modern Physics* **90**, 015007.
- [101] Alexander Palmer, D. M. Silevitch, Yejun Feng, Yishu Wang, R. Jaramillo, Arnab Banerjee, Yang Ren, and Thomas F. Rosenbaum. (2015). “Sub-Kelvin magnetic and electrical measurements in a diamond anvil cell with in situ tunability.” *Review of Scientific Instruments* **86**, no. 9: 093901.
- [102] Netanel H. Lindner, Gil Refael, and Victor Galitski. (2011). “Floquet topological insulator in semiconductor quantum wells.” *Nature Physics* **7**, no. 6: 490.
- [103] Netanel H. Lindner, Doron L. Bergman, Gil Refael, and Victor Galitski. (2013). “Topological Floquet spectrum in three dimensions via a two-photon resonance.” *Physical Review B* **87**, no. 23: 235131.
- [104] Yihua H. Wang, Hadar Steinberg, Pablo Jarillo-Herrero, and Nuh Gedik. (2013). “Observation of Floquet-Bloch states on the surface of a topological insulator.” *Science* **342**, no. 6157: 453-457.
- [105] Hannes Hübener, Umberto De Giovannini, and Angel Rubio. (2018). “Phonon driven Floquet matter.” *Nano letters* **18**, no. 2: 1535-1542.
- [106] Leon N. Cooper. (1956). “Bound electron pairs in a degenerate Fermi gas.” *Physical Review* **104**, no. 4: 1189.
- [107] Peter Fulde and Richard A. Ferrell. (1964). “Superconductivity in a Strong Spin-Exchange Field.” *Physical Review* **135** (3A): A550-A563.
- [108] A. I. Larkin and Yu. N. Ovchinnikov. (1965). *Zhurnal Éksperimental’noi i Teoreticheskoi Fiziki* **47**, 1136.
- [109] Jacob Linder and Alexander V. Balatsky. (2019). “Odd-frequency superconductivity.” *Reviews of Modern Physics* **91**, no. 4: 045005.
- [110] H. Suderow, V. Crespo, I. Guillamon, S. Vieira, F. Servant, P. Lejay, J. P. Brison, and J. Flouquet. (2009). “A nodeless superconducting gap in Sr₂RuO₄ from tunneling spectroscopy.” *New Journal of Physics* **11**, no. 9: 093004.

- [111] H. Suderow, S. Vieira, J. D. Strand, S. Bud'ko, and P. C. Canfield. (2004). "Very-low-temperature tunneling spectroscopy in the heavy-fermion superconductor $\text{PrOs}_4\text{Sb}_{12}$." *Physical Review B* **69**, no. 6: 060504.
- [112] K. Matano, K. Arima, S. Maeda, Y. Nishikubo, K. Kudo, M. Nohara, and G. -Q. Zheng. (2014). "Spin-singlet superconductivity with a full gap in locally noncentrosymmetric SrPtAs ." *Physical Review B* **89**, no. 14: 140504.
- [113] K. Iwaya, Y. Kohsaka, K. Okawa, T. Machida, M. S. Bahramy, T. Hanaguri, and T. Sasagawa. (2017). "Full-gap superconductivity in spin-polarised surface states of topological semimetal $\beta\text{-PdBi}_2$." *Nature Communications* **8**, no. 1: 1-7.
- [114] Shun Chi, S. Grothe, Ruixing Liang, P. Dosanjh, W. N. Hardy, S. A. Burke, D. A. Bonn, and Y. Pennec. (2012). "Scanning tunneling spectroscopy of superconducting LiFeAs single crystals: evidence for two nodeless energy gaps and coupling to a bosonic mode." *Physical Review Letters* **109**, no. 8: 087002.
- [115] Krzysztof Gofryk, Minghu Pan, Claudia Cantoni, Bayrammurad Saparov, Jonathan E. Mitchell, and Athena S. Sefat. (2014). "Local inhomogeneity and filamentary superconductivity in Pr-doped CaFe_2As_2 ." *Physical Review Letters* **112**, no. 4: 047005.
- [116] Takeshi Kondo, A. F. Santander-Syro, O. Copie, Chang Liu, M. E. Tillman, E. D. Mun, J. Schmalian, S. L. Bud'ko, M. A. Tanatar, P. C. Canfield, and A. Kaminski. (2008). "Momentum dependence of the superconducting gap in $\text{NdFeAsO}_{0.9}\text{F}_{0.1}$ single crystals measured by angle resolved photoemission spectroscopy." *Physical Review Letters* **101**, no. 14: 147003.
- [117] Øystein Fischer, Martin Kugler, Ivan Maggio-Aprile, Christophe Berthod, and Christoph Renner. (2007). "Scanning tunneling spectroscopy of high-temperature superconductors." *Reviews of Modern Physics* **79**, no. 1: 353.
- [118] K. Kato. (1986). "Second-harmonic generation to 2048 Å in $\beta\text{-Ba}_2\text{O}_4$." *IEEE Journal of Quantum Electronics* **22**, no. 7: 1013-1014.

Appendix A

Superconductivity

A.1 BCS formalism

A.1.1 Solution to the interacting metal

In this section, I will provide some mathematical details I skipped in Sec. 2.2.2.1. For convenience, I am repeating (2.2.2) here

$$\hat{\mathcal{H}} = \sum_{i,j,\sigma} t_{ij} \hat{c}_{i,\sigma}^\dagger \hat{c}_{j,\sigma} + \sum_{i,j,k,l} \sum_{\alpha,\beta,\gamma,\delta} U_{ijkl,\alpha\beta\gamma\delta} \hat{c}_{i,\alpha}^\dagger \hat{c}_{j,\beta}^\dagger \hat{c}_{k,\gamma} \hat{c}_{l,\delta}, \quad (\text{A.1.1})$$

where t_{ij} is the hopping amplitude of the electron from site j to i ,¹ $\hat{c}_{i,\sigma}^\dagger$ ($\hat{c}_{i,\sigma}$) is the creation (annihilation) operator for an electron on lattice site i with pseudo-spin σ , and $U_{ijkl,\alpha\beta\gamma\delta}$ is a four-fermion scattering amplitude for two electrons at sites k and l , with spins γ and δ respectively, scattering into states at sites i and j , with spins α and β respectively.

In order to simplify the calculation, I will make some convenient assumptions about the quantities t_{ij} and $U_{ijkl,\alpha\beta\gamma\delta}$ defined in (A.1.1). At the end of the calculation, I will make a generalization which will effectively “reverse” the simplifying assumptions, without proving that these generalizations are possible. The interested reader can refer to more rigorous treatments in the literature (e.g. [2, 32]). My goal is to emphasize physical insight over mathematical rigor.

With that goal in mind, consider a simple case of

$$t_{ij} \equiv \begin{cases} -t & i \text{ and } j \text{ are nearest neighbors} \\ -\mu & i = j \\ 0 & \text{otherwise} \end{cases}, \quad (\text{A.1.2})$$

where μ is the chemical potential and $t \in \mathbb{R}^+$.² Then plugging (A.1.2) in (A.1.1) I get

$$\hat{\mathcal{H}} = \underbrace{-t \sum_{\langle ij \rangle, \sigma} \hat{c}_{i,\sigma}^\dagger \hat{c}_{j,\sigma}}_{(\text{A})} + \underbrace{\left\{ \sum_{i,j,k,l} \sum_{\alpha,\beta,\gamma,\delta} U_{ijkl,\alpha\beta\gamma\delta} \hat{c}_{i,\alpha}^\dagger \hat{c}_{j,\beta}^\dagger \hat{c}_{k,\gamma} \hat{c}_{l,\delta} \right\}}_{(\text{B})} - \underbrace{\mu \sum_{i,\sigma} \hat{c}_{i,\sigma}^\dagger \hat{c}_{i,\sigma}}_{(\text{C})}, \quad (\text{A.1.3})$$

¹In this discussion, I won't explicitly assume the number of spatial dimensions N . Therefore, the lattice indices i and j should be viewed as N dimensional indices (e.g. (i_1, i_2) in 2D).

²In general t can be complex. But then there would be an extra Hermitian conjugate term in the term (A). Since real t is valid for time-reversal symmetric systems, I'll assume that to be the case for algebraic simplicity.

where $\langle ij \rangle$ indicates that i and j are nearest neighbors and h.c. stands for Hermitian conjugate.³ It is straightforward to diagonalize terms (A) and (C)⁴ in (A.1.3) with a unitary Wannier-to-Bloch basis transformation. Therefore, I will replace the position space operators in (A.1.3) with the expression

$$\hat{c}_{i,\sigma}^\dagger \equiv \frac{1}{N} \sum_{\mathbf{k}} e^{i\mathbf{k}\cdot\mathbf{x}_i} \hat{c}_{\mathbf{k},\sigma}^\dagger, \quad (\text{A.1.4})$$

where \mathbf{x}_i is the position vector of lattice site i and N is some arbitrary normalization constant, such that it can be used in the definition of the Kronecker delta function, $\delta_{\mathbf{k},\mathbf{k}'}$, defined such that

$$\delta_{\mathbf{k},\mathbf{k}'} \equiv \frac{1}{|N|^2} \sum_i e^{i(\mathbf{k}-\mathbf{k}')\cdot\mathbf{x}_i}. \quad (\text{A.1.5})$$

Assuming that nearest neighbor sites i and j are related by a set of vectors $\{\mathbf{R}_j\}$, with $j = [1, M]$, where M is the number of nearest neighbors. Then I can simplify the Wannier-to-Bloch basis transformation by the substitution

$$\mathbf{x}_j = \mathbf{x}_i + \mathbf{R}_j, \quad (\text{A.1.6})$$

After some algebra, I can replace terms (A) and (C) in (A.1.3) with their momentum space representations to get

$$\hat{\mathcal{H}} = \sum_{\mathbf{k},\sigma} [\tilde{t}(\mathbf{k}) - \mu] \hat{c}_{\mathbf{k},\sigma}^\dagger \hat{c}_{\mathbf{k},\sigma} + \underbrace{\left\{ \sum_{i,j,k,l} \sum_{\alpha,\beta,\gamma,\delta} U_{ijkl,\alpha\beta\gamma\delta} \hat{c}_{i,\alpha}^\dagger \hat{c}_{j,\beta}^\dagger \hat{c}_{k,\gamma} \hat{c}_{l,\delta} \right\}}_{(\text{B})}, \quad (\text{A.1.7})$$

where

$$\tilde{t}(\mathbf{k}) \equiv -t \sum_{j=1}^M e^{-i\mathbf{k}\cdot\mathbf{R}_j}, \quad (\text{A.1.8})$$

As I stated earlier, I will generalize $\tilde{t}(\mathbf{k})$ without proof. It is conceivable that I could have obtained an expression similar to (A.1.8) even if (A.1.2) was a little more complicated by (say) having next-nearest neighbor hopping. In fact, $\tilde{t}(\mathbf{k})$ is a well-defined quantity even if it cannot be expressed as an analytic expression. It corresponds to the normal state dispersion or band structure. In conclusion, the first term in (A.1.7) is valid for an arbitrary metallic system on a lattice.

Term (B) contains the most important physics associated with superconductivity. Since this term is hard to diagonalize, I will use several approximations, the most important of which is the mean-field approximation.

First, I will bring term (B) into momentum space. The first approximation involves making an assumption about the momenta of the pairing electrons. Leon Cooper solved a problem involving two interacting electrons confined to region close to the Fermi surface where he showed that even an infinitesimal attractive interaction can result in a bound state [106]. In the solution to this problem, it is evident that the lowest energy solution is possible only when the total momentum of the two particles is zero.⁵

Then a Wannier-to-Bloch basis transformation for term (B) would look something like

$$(\text{B}) = \sum_{\mathbf{k},\mathbf{k}'} \sum_{\alpha,\beta,\gamma,\delta} \tilde{U}_{\alpha\beta\gamma\delta}(\mathbf{k},\mathbf{k}') \hat{c}_{\mathbf{k},\alpha}^\dagger \hat{c}_{-\mathbf{k},\beta}^\dagger \hat{c}_{\mathbf{k}',\gamma} \hat{c}_{-\mathbf{k}',\delta}, \quad (\text{A.1.9})$$

³The summation in term (A) will take care of its Hermiticity. Term (C) is already Hermitian.

⁴Actually term (C) is already diagonal. So the Wannier-to-Bloch basis transformation won't be a diagonalization step for this term.

⁵While there are examples, like the Fulde-Ferrell-Larkin-Ovchinnikov (FFLO) state [107, 108], where this assumption is violated, I will limit this discussion to the zero-momentum pairing case.

where I'll once again state without proof that $\tilde{U}_{\alpha\beta\gamma\delta}(\mathbf{k}, \mathbf{k}')$ can be obtained from $U_{ijkl,\alpha\beta\gamma\delta}$, analytic or otherwise, similar to how $\tilde{t}(\mathbf{k})$ was obtained from t_{ij} . The four-fermion scattering process can be schematically represented as shown in Fig. A.1.1.

There is another approximation I made implicitly: \mathbf{k} is close to \mathbf{k}_F in (A.1.17). Therefore the summation in (A.1.9) is limited to values of \mathbf{k} close to \mathbf{k}_F . The physical reason is that $\tilde{U}_{\alpha\beta\gamma\delta}(\mathbf{k}', \mathbf{k})$ is attractive in the four-fermion scattering process (c.f. Fig. A.1.1) only when the four operators have \mathbf{k} in a finite momentum region close to \mathbf{k}_F . Going forward, I'll apply the same restriction to the summation in the first term of (A.1.7). For Hamiltonians (A.1.21) and later, this \mathbf{k} space restriction will be automatically applied.

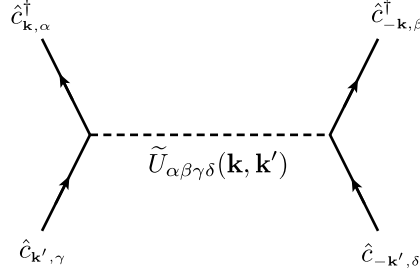


Figure A.1.1: Schematic representation of a four-fermion scattering process

Second, I will use the mean-field approximation to convert (A.1.9) into a term containing only bilinear operators. This simplification will make it easier to analytically diagonalize term (B). Once again, I will state without proof that operators $\hat{c}_{\mathbf{k},\alpha}^\dagger \hat{c}_{-\mathbf{k},\beta}^\dagger$ and $\hat{c}_{\mathbf{k}',\gamma} \hat{c}_{-\mathbf{k}',\delta}$ have finite expectation values in the superconducting ground state $|\psi_{\text{GS}}\rangle$. I will define these expectation values as

$$\tilde{\Delta}_{\mathbf{k},\alpha\beta} \equiv \sum_{\mathbf{k}'} \langle \psi_{\text{GS}} | \tilde{U}_{\alpha\beta\gamma\delta}(\mathbf{k}, \mathbf{k}') \hat{c}_{\mathbf{k}',\gamma} \hat{c}_{-\mathbf{k}',\delta} | \psi_{\text{GS}} \rangle, \quad (\text{A.1.10})$$

$$\tilde{\Delta}_{\mathbf{k},\gamma\delta}^* \equiv \sum_{\mathbf{k}'} \langle \psi_{\text{GS}} | \tilde{U}_{\alpha\beta\gamma\delta}(\mathbf{k}', \mathbf{k}) \hat{c}_{\mathbf{k}',\alpha}^\dagger \hat{c}_{-\mathbf{k}',\beta}^\dagger | \psi_{\text{GS}} \rangle, \quad (\text{A.1.11})$$

These operators can be trivially written as

$$\hat{c}_{\mathbf{k},\alpha}^\dagger \hat{c}_{-\mathbf{k},\beta}^\dagger = \tilde{\Delta}_{\mathbf{k},\alpha\beta}^* + \underbrace{\left\{ \hat{c}_{\mathbf{k},\alpha}^\dagger \hat{c}_{-\mathbf{k},\beta}^\dagger - \tilde{\Delta}_{\mathbf{k},\alpha\beta}^* \right\}}_{\hat{F}_{1,\alpha\beta}(\mathbf{k})}, \quad (\text{A.1.12})$$

$$\hat{c}_{\mathbf{k},\gamma} \hat{c}_{-\mathbf{k},\delta} = \tilde{\Delta}_{\mathbf{k},\gamma\delta} + \underbrace{\left\{ \hat{c}_{\mathbf{k},\gamma} \hat{c}_{-\mathbf{k},\delta} - \tilde{\Delta}_{\mathbf{k},\gamma\delta} \right\}}_{\hat{F}_{2,\gamma\delta}(\mathbf{k})}, \quad (\text{A.1.13})$$

where the newly defined operators $\hat{F}_{1,\alpha\beta}(\mathbf{k})$ and $\hat{F}_{2,\gamma\delta}(\mathbf{k})$ represent fluctuations from the ground state expectation or mean value. Plugging these into the four-fermion operator I get

$$\hat{c}_{\mathbf{k},\alpha}^\dagger \hat{c}_{-\mathbf{k},\beta}^\dagger \hat{c}_{\mathbf{k}',\gamma} \hat{c}_{-\mathbf{k}',\delta} = \left[\tilde{\Delta}_{\mathbf{k},\alpha\beta}^* + \hat{F}_{1,\alpha\beta}(\mathbf{k}) \right] \left[\tilde{\Delta}_{\mathbf{k}',\gamma\delta} + \hat{F}_{2,\gamma\delta}(\mathbf{k}') \right], \quad (\text{A.1.14})$$

$$= \tilde{\Delta}_{\mathbf{k},\alpha\beta}^* \tilde{\Delta}_{\mathbf{k}',\gamma\delta} + \tilde{\Delta}_{\mathbf{k},\alpha\beta}^* \hat{F}_{2,\gamma\delta}(\mathbf{k}') + \hat{F}_{1,\alpha\beta}(\mathbf{k}) \tilde{\Delta}_{\mathbf{k}',\gamma\delta} \quad (\text{A.1.15})$$

$$+ \underbrace{\hat{F}_{1,\alpha\beta}(\mathbf{k}) \hat{F}_{2,\gamma\delta}(\mathbf{k}')}_{\approx 0}, \quad (\text{A.1.16})$$

where the mean-field approximation has been used in (A.1.16). It is assumed that the fluctuations (i.e. the \hat{F} operators) from the mean (i.e. the $\tilde{\Delta}$ s) are small. So fluctuations are kept to first order

but ignored at second order. Then plugging (A.1.16) in (A.1.9) I get

$$(B) = E_0 + \frac{1}{2} \sum_{\mathbf{k}, \gamma, \delta} \Delta_{\mathbf{k}, \gamma \delta}^* \hat{c}_{\mathbf{k}, \gamma} \hat{c}_{-\mathbf{k}, \delta} + \frac{1}{2} \sum_{\mathbf{k}, \alpha, \beta} \Delta_{\mathbf{k}, \alpha \beta} \hat{c}_{\mathbf{k}, \alpha}^\dagger \hat{c}_{-\mathbf{k}, \beta}^\dagger, \quad (\text{A.1.17})$$

where⁶

$$E_0 \equiv \sum_{\mathbf{k}, \mathbf{k}'} \sum_{\alpha, \beta, \gamma, \delta} \tilde{U}_{\alpha \beta \gamma \delta}(\mathbf{k}, \mathbf{k}') \tilde{\Delta}_{\mathbf{k}, \alpha \beta}^* \Delta_{\mathbf{k}', \gamma \delta} - \sum_{\mathbf{k}, \mathbf{k}'} \sum_{\alpha, \beta, \gamma, \delta} \tilde{U}_{\alpha \beta \gamma \delta}(\mathbf{k}, \mathbf{k}') \tilde{\Delta}_{\mathbf{k}, \alpha \beta}^* \tilde{\Delta}_{\mathbf{k}', \gamma \delta} - \sum_{\mathbf{k}, \mathbf{k}'} \sum_{\alpha, \beta, \gamma, \delta} \tilde{U}_{\alpha \beta \gamma \delta}(\mathbf{k}, \mathbf{k}') \tilde{\Delta}_{\mathbf{k}, \alpha \beta} \tilde{\Delta}_{\mathbf{k}', \gamma \delta}, \quad (\text{A.1.18})$$

$$\Delta_{\mathbf{k}, \gamma \delta}^* \equiv 2 \sum_{\mathbf{k}', \alpha, \beta} \tilde{U}_{\alpha \beta \gamma \delta}(\mathbf{k}', \mathbf{k}) \tilde{\Delta}_{\mathbf{k}', \alpha \beta}^*, \quad (\text{A.1.19})$$

$$\Delta_{\mathbf{k}, \alpha \beta} \equiv 2 \sum_{\mathbf{k}', \gamma, \delta} \tilde{U}_{\alpha \beta \gamma \delta}(\mathbf{k}, \mathbf{k}') \tilde{\Delta}_{\mathbf{k}', \gamma \delta} \quad (\text{A.1.20})$$

Now, plugging (A.1.17) into (A.1.7) I get⁷

$$\begin{aligned} \hat{\mathcal{H}}'_{\text{MF}} &= \sum_{\mathbf{k}, \sigma} [\tilde{t}(\mathbf{k}) - \mu] \hat{c}_{\mathbf{k}, \sigma}^\dagger \hat{c}_{\mathbf{k}, \sigma} + \frac{1}{2} \sum_{\mathbf{k}, \gamma, \delta} \Delta_{\mathbf{k}, \gamma \delta}^* \hat{c}_{\mathbf{k}, \gamma} \hat{c}_{-\mathbf{k}, \delta} \\ &\quad + \frac{1}{2} \sum_{\mathbf{k}, \alpha, \beta} \Delta_{\mathbf{k}, \alpha \beta} \hat{c}_{\mathbf{k}, \alpha}^\dagger \hat{c}_{-\mathbf{k}, \beta}^\dagger + E_0, \end{aligned} \quad (\text{A.1.21})$$

I will make another simplification and assume spin singlet pairing. Moreover, I will absorb E_0 into $\hat{\mathcal{H}}'_{\text{MF}}$. Then I get

$$\hat{\mathcal{H}}''_{\text{MF}} = \underbrace{\sum_{\mathbf{k}, \sigma} [\tilde{t}(\mathbf{k}) - \mu] \hat{c}_{\mathbf{k}, \sigma}^\dagger \hat{c}_{\mathbf{k}, \sigma}}_{(D)} + \frac{1}{2} \sum_{\mathbf{k}} \left\{ \Delta_{\mathbf{k}}^* \hat{c}_{\mathbf{k}, \uparrow} \hat{c}_{-\mathbf{k}, \downarrow} + \Delta_{\mathbf{k}} \hat{c}_{\mathbf{k}, \uparrow}^\dagger \hat{c}_{-\mathbf{k}, \downarrow}^\dagger + \text{h.c.} \right\}, \quad (\text{A.1.22})$$

where h.c. stands for Hermitian conjugate. The right hand side of (A.1.22) is close to be diagonalizable. Term (D) needs to some formal manipulation. For convenience, after defining

$$\varepsilon_{\mathbf{k}} \equiv \tilde{t}(\mathbf{k}) - \mu, \quad (\text{A.1.23})$$

term (D) can be written as

$$\begin{aligned} (D) &= \frac{1}{2} \sum_{\mathbf{k}, \sigma} \varepsilon_{\mathbf{k}} \left[2 \hat{c}_{\mathbf{k}, \sigma}^\dagger \hat{c}_{\mathbf{k}, \sigma} \right], \\ &= \frac{1}{2} \sum_{\mathbf{k}, \sigma} \varepsilon_{\mathbf{k}} \left[\hat{c}_{\mathbf{k}, \sigma}^\dagger \hat{c}_{\mathbf{k}, \sigma} + 1 - \hat{c}_{\mathbf{k}, \sigma} \hat{c}_{\mathbf{k}, \sigma}^\dagger \right], \end{aligned} \quad (\text{A.1.24})$$

where in the second line I have used the fermionic anti-commutation relation

$$\{\hat{c}_{\mathbf{k}, \sigma}^\dagger, \hat{c}_{\mathbf{k}, \sigma}\} = 1, \quad (\text{A.1.25})$$

The formal manipulation (A.1.24) is commonly referred to as the Bogoliubov-de Gennes “trick.” This trick helps in reordering the operators in a way such that it is convenient to write the mean-field Hamiltonian in a matrix form (c.f. Eq. (A.1.31)).

⁶The factor of 2, in Eq. (A.1.19) and (A.1.20), has been introduced for the sake of convenience in dealing with later expressions.

⁷The sum of spin indices will take care of Hermiticity in (A.1.21).

Now, simplifying (A.1.24) further, and explicitly writing out the sum over spins, I get

$$(D) = E_1 + \frac{1}{2} \sum_{\mathbf{k}} \varepsilon_{\mathbf{k}} \left[\hat{c}_{\mathbf{k},\uparrow}^\dagger \hat{c}_{\mathbf{k},\uparrow} - \hat{c}_{\mathbf{k},\uparrow} \hat{c}_{\mathbf{k},\uparrow}^\dagger \right] + \underbrace{\frac{1}{2} \sum_{\mathbf{k}} \varepsilon_{\mathbf{k}} \left[\hat{c}_{\mathbf{k},\downarrow}^\dagger \hat{c}_{\mathbf{k},\downarrow} - \hat{c}_{\mathbf{k},\downarrow} \hat{c}_{\mathbf{k},\downarrow}^\dagger \right]}_{(E)}, \quad (\text{A.1.26})$$

where⁸

$$E_1 \equiv \frac{1}{2} \sum_{\mathbf{k},\sigma} \varepsilon_{\mathbf{k}}, \quad (\text{A.1.27})$$

In term (E) in (A.1.26) the change of variables $\mathbf{k} \rightarrow -\mathbf{k}$ simply changes the order of the summation while yielding the same result. Therefore, term (E) after this change would become

$$(E) = \frac{1}{2} \sum_{\mathbf{k}} \varepsilon_{-\mathbf{k}} \left[\hat{c}_{-\mathbf{k},\downarrow}^\dagger \hat{c}_{-\mathbf{k},\downarrow} - \hat{c}_{-\mathbf{k},\downarrow} \hat{c}_{-\mathbf{k},\downarrow}^\dagger \right], \quad (\text{A.1.28})$$

For a time-reversal symmetric system with centrosymmetry the following is true⁹

$$\varepsilon_{\mathbf{k}} = \varepsilon_{-\mathbf{k}}, \quad (\text{A.1.29})$$

Assuming (A.1.29), and plugging (A.1.28) and (A.1.26) in (A.1.22), I get

$$\begin{aligned} \hat{\mathcal{H}}_{\text{MF}} &= \sum_{\mathbf{k}} \varepsilon_{\mathbf{k}} \left[\hat{c}_{\mathbf{k},\uparrow}^\dagger \hat{c}_{\mathbf{k},\uparrow} - \hat{c}_{\mathbf{k},\uparrow} \hat{c}_{\mathbf{k},\uparrow}^\dagger + \hat{c}_{-\mathbf{k},\downarrow}^\dagger \hat{c}_{-\mathbf{k},\downarrow} - \hat{c}_{-\mathbf{k},\downarrow} \hat{c}_{-\mathbf{k},\downarrow}^\dagger \right] \\ &+ \sum_{\mathbf{k}} \left\{ \Delta_{\mathbf{k}}^* \hat{c}_{\mathbf{k},\uparrow} \hat{c}_{-\mathbf{k},\downarrow} + \Delta_{\mathbf{k}} \hat{c}_{\mathbf{k},\uparrow}^\dagger \hat{c}_{-\mathbf{k},\downarrow}^\dagger + \text{h.c.} \right\}, \end{aligned} \quad (\text{A.1.30})$$

where I have absorbed E_1 and the extra factor of 2 into $\hat{\mathcal{H}}_{\text{MF}}''$. The right hand side of (A.1.30) can be expressed in a convenient matrix form as

$$\hat{\mathcal{H}}_{\text{MF}} = \sum_{\mathbf{k}} \hat{C}_{\mathbf{k}}^\dagger h_{\text{MF}}(\mathbf{k}) \hat{C}_{\mathbf{k}}, \quad (\text{A.1.31})$$

where

$$h_{\text{MF}}(\mathbf{k}) \equiv \begin{bmatrix} \varepsilon_{\mathbf{k}} & \Delta_{\mathbf{k}} & 0 & 0 \\ \Delta_{\mathbf{k}}^* & -\varepsilon_{\mathbf{k}} & 0 & 0 \\ 0 & 0 & \varepsilon_{\mathbf{k}} & \Delta_{\mathbf{k}} \\ 0 & 0 & \Delta_{\mathbf{k}}^* & -\varepsilon_{\mathbf{k}} \end{bmatrix}, \quad (\text{A.1.32})$$

then

$$\hat{C}_{\mathbf{k}} = \begin{bmatrix} \hat{c}_{\mathbf{k},\uparrow} \\ \hat{c}_{-\mathbf{k},\downarrow}^\dagger \\ \hat{c}_{-\mathbf{k},\downarrow} \\ \hat{c}_{\mathbf{k},\uparrow}^\dagger \end{bmatrix}, \quad (\text{A.1.33})$$

A straightforward matrix diagonalization yields eigenvalues

$$\xi_{\mathbf{k}}^\pm = \pm \sqrt{\varepsilon_{\mathbf{k}}^2 + |\Delta_{\mathbf{k}}|^2}, \quad (\text{A.1.34})$$

The eigenvalue $\xi_{\mathbf{k}}^\pm$ represents the excitation energy relative to the Fermi level (μ). However, a word of caution is in order when interpreting Eq. (A.1.34).

⁸Note that, owing to the \mathbf{k} space restriction implicitly introduced in all summations in (A.1.21), (A.1.27) will just yield a finite constant which can be absorbed into the Hamiltonian.

⁹Non-centrosymmetric superconductors have spin-singlet and -triplet mixing.

Recall assumption number 4 from Sec. 2.2.2.1. When defining $\tilde{\Delta}_{\mathbf{k},\alpha\beta}$ and $\tilde{\Delta}_{\mathbf{k},\gamma\delta}^*$ in (A.1.10) and (A.1.11) respectively, I did not incorporate the energies of the particles in the four-fermion scattering process (c.f. Fig. A.1.1). As a result, the gap function ($\Delta_{\mathbf{k}}$) does not have an energy dependence.

As a result, with $\Delta_{\mathbf{k}}$ effectively being a constant in energy, diagonalization of $\hat{\mathcal{H}}_{\text{MF}}$ is equivalent to diagonalization of $h_{\text{MF}}(\mathbf{k})$ (c.f. A.1.31). In reality, however, the pairing strength (i.e. $\Delta_{\mathbf{k}}$) will vanish for energies far from the Fermi level (μ). Moreover, the weakening of $\Delta_{\mathbf{k}}$ away from μ will be continuous. Therefore, for precise measurements of $\xi_{\mathbf{k}}^{\pm}$, when the mean-field approximation is still valid, the energy dependence of $\Delta_{\mathbf{k}}$ needs to be considered. Furthermore, the energy dependence of the pairing amplitude is relevant in odd-frequency superconductors [109].

A.1.2 Bogoliubov quasiparticles

Finding the mapping from electron to Bogoliubov operators simply involves finding the eigenvalues of the matrix. Since the matrix is block-diagonal, I'll only consider one of the blocks. I start with the positive eigenvalue. The corresponding eigenvector can be found by solving

$$\begin{bmatrix} \varepsilon_{\mathbf{k}} & \Delta_{\mathbf{k}} \\ \Delta_{\mathbf{k}}^* & -\varepsilon_{\mathbf{k}} \end{bmatrix} \begin{bmatrix} x_1 \\ x_2 \end{bmatrix} = E_{\mathbf{k}}^+ \begin{bmatrix} x_1 \\ x_2 \end{bmatrix}, \quad (\text{A.1.35})$$

which gives

$$x_2 = \left(\frac{E_{\mathbf{k}}^+ - \varepsilon_{\mathbf{k}}}{\Delta_{\mathbf{k}}} \right) x_1, \quad (\text{A.1.36})$$

So defining $\Delta_{\mathbf{k}} \equiv |\Delta_{\mathbf{k}}|e^{i\theta_{\mathbf{k}}}$, I can express the eigenvector as

$$\begin{bmatrix} x_1 \\ x_2 \end{bmatrix} \propto \begin{bmatrix} |\Delta_{\mathbf{k}}|e^{i\theta_{\mathbf{k}}} \\ E_{\mathbf{k}}^+ - \varepsilon_{\mathbf{k}} \end{bmatrix}, \quad (\text{A.1.37})$$

The vector has to be represented in a normalized form to preserve the anti-commutation relations. So I add the normalization factor

$$\frac{1}{\sqrt{|x_1|^2 + |x_2|^2}} \begin{bmatrix} x_1 \\ x_2 \end{bmatrix} = \frac{1}{\sqrt{|\Delta_{\mathbf{k}}|^2 + |E_{\mathbf{k}}^+ - \varepsilon_{\mathbf{k}}|^2}} \begin{bmatrix} |\Delta_{\mathbf{k}}|e^{i\theta_{\mathbf{k}}} \\ E_{\mathbf{k}}^+ - \varepsilon_{\mathbf{k}} \end{bmatrix}, \quad (\text{A.1.38})$$

For further simplification, I'll express $|\Delta_{\mathbf{k}}|$ in terms of $E_{\mathbf{k}}^+$ and $\varepsilon_{\mathbf{k}}$. Plugging (A.1.34) in (A.1.38) I get

$$\begin{aligned} \frac{1}{\sqrt{|x_1|^2 + |x_2|^2}} \begin{bmatrix} x_1 \\ x_2 \end{bmatrix} &= \frac{1}{\sqrt{2E_{\mathbf{k}}^+(E_{\mathbf{k}}^+ - \varepsilon_{\mathbf{k}})}} \begin{bmatrix} \sqrt{(E_{\mathbf{k}}^+ - \varepsilon_{\mathbf{k}})(E_{\mathbf{k}}^+ + \varepsilon_{\mathbf{k}})}e^{i\theta_{\mathbf{k}}} \\ E_{\mathbf{k}}^+ - \varepsilon_{\mathbf{k}} \end{bmatrix}, \\ &= \begin{bmatrix} \sqrt{\frac{1}{2} \left(1 + \frac{\varepsilon_{\mathbf{k}}}{E_{\mathbf{k}}^+}\right)} e^{i\theta_{\mathbf{k}}/2} \\ \sqrt{\frac{1}{2} \left(1 - \frac{\varepsilon_{\mathbf{k}}}{E_{\mathbf{k}}^+}\right)} e^{-i\theta_{\mathbf{k}}/2} \end{bmatrix}, \\ &\equiv \begin{bmatrix} u_{\mathbf{k}} \\ v_{\mathbf{k}}^* \end{bmatrix}, \end{aligned} \quad (\text{A.1.39})$$

where, in the second line, I have symmetrized my definition of $u_{\mathbf{k}}$ and $v_{\mathbf{k}}$ by multiplying the vector with a factor, $e^{-i\theta_{\mathbf{k}}/2}$, which doesn't affect its norm.¹⁰ A straightforward repetition of the above

¹⁰The definition of $u_{\mathbf{k}}$ and $v_{\mathbf{k}}$ is not unique across the literature; only their norms are. Therefore, some texts use $\theta_{\mathbf{k}} = 0$ for convenience.

exercise for the $E_{\mathbf{k}}^-$ eigenvalue gives the matrix relationship

$$\begin{bmatrix} \hat{b}_{\mathbf{k},\uparrow} \\ \hat{b}_{-\mathbf{k},\downarrow}^\dagger \\ \hat{b}_{-\mathbf{k},\downarrow} \\ \hat{b}_{\mathbf{k},\uparrow}^\dagger \end{bmatrix} = \begin{bmatrix} u_{\mathbf{k}} & v_{\mathbf{k}}^* & 0 & 0 \\ v_{\mathbf{k}} & u_{\mathbf{k}}^* & 0 & 0 \\ 0 & 0 & v_{\mathbf{k}} & u_{\mathbf{k}}^* \\ 0 & 0 & u_{\mathbf{k}} & v_{\mathbf{k}}^* \end{bmatrix} \begin{bmatrix} \hat{c}_{\mathbf{k},\uparrow} \\ \hat{c}_{-\mathbf{k},\downarrow}^\dagger \\ \hat{c}_{-\mathbf{k},\downarrow} \\ \hat{c}_{\mathbf{k},\uparrow}^\dagger \end{bmatrix}, \quad (\text{A.1.40})$$

A.2 Data on superconducting gap and critical temperature

In Fig. 3.2.1, I presented the relationship between maximum superconducting gap, Δ_{\max} , and the superconducting critical temperature, T_c , for few examples of three classes of superconductors: (a) low- T_c , (c) high- T_c Iron-based, and (c) high- T_c Cuprates. In Table A.1, I have presented the same data in numeric format for the reader's convenience. Moreover, I have listed the literature references providing the (Δ_{\max} , T_c) information, and the experimental technique used to measure Δ_{\max} .

| Material | T_c | Experimental probe used to measure Δ_{\max} | Δ_{\max} | Reference |
|--|--------|--|-----------------|-----------|
| Sr_2RuO_4 | 1.5 K | STS | 0.28 meV | [110] |
| $\text{PrOs}_4\text{Sb}_{12}$ | 1.85 K | STS | 0.27 meV | [111] |
| SrPtAs | 2.4 K | NMR | 0.4 meV | [112] |
| $\text{Cu}_x\text{Bi}_2\text{Se}_3$ | 3.8 K | STS | 0.4 meV | [50] |
| $\beta\text{-PdBi}_2$ | 5.4 K | STS | 0.8 meV | [113] |
| $\text{FeTe}_{0.55}\text{Se}_{0.45}$ | 14.5 K | STS | 1.8 meV | [37] |
| LiFeAs | 17 K | STS | 5.3 meV | [114] |
| $\text{Ca}_{0.86}\text{Pr}_{0.14}\text{Fe}_2\text{As}_2$ | 45 K | STS | 12 meV | [115] |
| $\text{NdFeAsO}_{0.9}\text{F}_{0.1}$ | 53 K | ARPES | 18 meV | [116] |
| $\text{La}_{2-x}\text{Sr}_x\text{CuO}_4$ | 40 K | STS | 16 meV | [117] |
| $\text{YBa}_2\text{Cu}_3\text{O}_{7-\delta}$ | 92 K | STS | 30 meV | [117] |
| $\text{Bi}_2\text{Sr}_2\text{Ca}_2\text{Cu}_3\text{O}_{10+\delta}$ | 109 K | STS | 60 meV | [117] |
| $\text{HgBa}_2\text{Ca}_2\text{Cu}_3\text{O}_{8+\delta}$ | 135 K | STS | 75 meV | [117] |

Table A.1: Maximum superconducting gap, Δ_{\max} , and the superconducting critical temperature, T_c , for examples of unconventional superconductors.

Appendix B

Vacuum system

In this chapter, I will discuss certain technical aspects about the vacuum system that were not covered in Chap. 6. In particular, I will discuss details of the various commercial vacuum equipment in Sec. B.1-B.7. In Sec. B.8, I will discuss the customization of the bake-out setup.

B.1 Vacuum pumps

All of the pumps in the vacuum system described in Sec. 6.3 are dry pumps. In other words, oil is not required for lubrication of mechanical components. This choice is the result of wanting to avoid backstreaming of oil into the vacuum chambers. Furthermore, it is important to ensure magnetic fields emanating from the pumps do not affect the ARPES measurement. For the models of the turbo and ion pumps chosen, the rate of fall off of internal magnetic fields, as a function of distance, was found to meet the ARPES specifications.

B.1.1 Turbomolecular pumps

Through experience (e.g. pumps used in optics experiments) and feedback from vacuum professionals, all of the turbo pumps used in the ARPES vacuum system were purchased from Pfeiffer Vacuum.

B.1.1.1 HiPace®

The compression ratios ($\gtrsim 10^{11}$) of the HiPace 300 M and 700 M turbomolecular pumps make them ideal for generation of UHV in the prep (c.f. Fig. 6.3.10) and analysis chambers¹ respectively. It is the ultimate pressure achieved by the HiPaces, however, which is more important in the vacuum system described in Sec. 6.3.

The compression ratio is given by

$$R_{\text{compression}} = \frac{P_{\text{backing}}}{P_{\text{inlet}}}, \quad (\text{B.1.1})$$

¹Unlike the prep chamber, the HiPace 700 M is attached to the pump chamber (c.f. Fig. 6.3.5), instead of directly to the analysis chamber.

where P_{backing} and P_{inlet} are the pressure generated by the backing pump (HiCube) and pressure inside the chambers respectively. According to the manufacturer (Pfeiffer), backing provided by a roughing pump ($P_{\text{backing}} \lesssim 10^{-2}$ torr) is usually sufficient. In this system, however, the HiCube unit is used due to the convenience and low price of said unit, as well as its suitability for 24×7 operation with little to no servicing. In that case, with $P_{\text{backing}} \approx 10^{-7}$ torr, compression ratio ($\approx 10^3$) is less important than ultimate pressure of 10^{-10} torr.

Five-axis magnetic levitation of the rotors extends the pump lifetime compared to the ones with mechanical bearings. The pumping ports on the HiPace 300 M and 700 M have 6" and 8" ConFlat flanges respectively. The full speeds of the HiPace 300 M and 700 M are 60,000 rotations per minute (RPM) and 48,000 RPM respectively. At base pressure, the drive current is ≈ 0.5 Amperes. The pumps are equipped with (24 VDC) electronic vent valves which can be automatically activated when the rotor slows down to 10% of its full speed. The 10% vent threshold is programmable.

The exhausts of the HiPace 300 M and 700 M were isolated from the backing pump using pneumatic (24 VDC) solenoid-driven right-angle valves (c.f. Sec. B.2.2).

B.1.1.2 HiCube®

The HiCube unit is a relatively easily portable oil-free pumping station. The unit is a combination of an ≈ 70 liters/second turbomolecular pump backed by diaphragm pump (MVP 015). The synchronization of the main and backing pumps, by the built-in electronics, makes the HiCube unit an effectively turn-key system from atmosphere to the mid- to high- 10^{-8} torr. The full speed of the HiCube turbo is 90,000 RPM. At base pressure, the drive current is ≈ 0.5 Amperes.

The vacuum system described in Sec. 6.3 has a total of three HiCube units. Two of said units can be seen in Fig. 6.3.1 on the lower deck of the support frame (c.f. Fig. 8.1.2). The third HiCube unit, located on the top deck of said frame, pumps on the rotary seal of the θ manipulation stage (c.f. Fig. 7.5.4).

The first (of the two) lower deck HiCube is responsible for backing the two HiPace turbos (c.f. Fig. 6.3.6). The second lower deck HiCube is used for the pump down of the load-lock (c.f. Sec. 6.3.7.1). The vent port of the load-lock HiCube is fitted with a manual bellows-sealed Swagelok valve. This valve is used to purge the load-lock with Nitrogen gas. The vent ports of other two HiCubes have threaded blanks which can be slowly loosened to vent to air.

In the HiCube unit, the pumping port of the turbomolecular pump has a 4.5" ConFlat flange. For *most* HiCube units in the lab (ARPES and optics), a 4.5"-to-2.75" ConFlat-flanged reducer tee is used to attached a dedicated pressure gauge. The pressure gauge (PKR 251) is a unit composed of Pirani and cold cathode type gauges, with a 2.75" ConFlat flange, and a full range from atmosphere to $\approx 10^{-9}$ torr. For the HiCube unit pumping the load-lock, the tee is replaced by a formed bellows, and the gauge is directly attached to one of the ports of said load-lock (c.f. Fig. 6.3.10).

B.1.2 Ion pump

B.1.2.1 Pumping module

The pumping module of the ion pump is the TiTan 400L model from Gamma Vacuum Products. It has an 8" ConFlat pumping port and built-in (atmosphere) baking heaters which can be directly con-

nected to the electrical mains (120 VAC). The pumping element of the ion pump uses a conventional diode (CV). In other words, both anode and cathode are made of Titanium.²

With each element offering a pumping speed of ≈ 50 liters/second, the TiTan 400L has 8 such elements, two on each of the four sides. Each pumping elements (in UHV) are sandwiched between opposite poles of two permanent magnets. These are sintered class 8 ceramic ferrite magnets ($\text{BaO}\cdot 6\text{Fe}_2\text{O}_3$ or $\text{SrO}\cdot 6\text{Fe}_2\text{O}_3$) with magnetization strengths of ≈ 0.4 Tesla.

B.1.2.2 Controller

The pumping module of the ion pump is driven by the multi-pump controller (MPCe) from Gamma Vacuum. The controller has a single high voltage channel and has a maximum current and power output of 0.5 Amperes and 1000 Watts respectively. At typical analysis chamber base pressures (low- to mid- 10^{-10} torr), the voltage and current supplied to the pumping unit was 6800 V and few 100 μA respectively. The SAFECONNTM cable connection was made between the pumping module and the MPCe controller. The controller was also calibrated to provide *crude* measurements of the chamber pressure. Typically, these readings were found to be higher than the ion gauge (c.f. Sec. B.7.1.2).

B.1.3 Titanium sublimation pump

B.1.3.1 Sputtering shroud

As I discussed in Sec. 6.3.3.3, the Titanium sublimation pump (TSP) sputtering shroud (or simply TSP can) is made of Aluminum. Moreover, the shroud has fins to increase its surface area. The can has three stainless Steel ConFlat flanges: two 2.75" and one 8"; the latter is the pumping port. The transition between the flanges and the TSP can is achieved using bi-metal adapters. The TSP can was fabricated by Nor-Cal Vacuum Products. Due to its Aluminum body, the TSP can was easier to heat up during the bake-out.

As shown in Fig. 6.3.8, one of the 2.75" ConFlat flanges is used to connect the sublimation cartridge. The other 2.75" ConFlat flange is an auxiliary port which is typically blanked off. It is possible to (say) isolate the TSP can, using the gate valve in front of it (c.f. Fig. 6.3.5), and use the auxiliary port to vent and pump down the can. This could be useful for installing replacement cartridges. At the time of writing, only one of the three sublimation filaments on the first cartridge was used up. Hence the auxiliary port was not used.

B.1.3.2 Titanium cartridges and controller

A 2.75" ConFlat-flanged cartridge with three coiled 4.5 inch long sublimation filaments (85% Titanium and 15% Molybdenum; ≈ 3 grams each) was purchased from Gamma Vacuum. The four-pin electrical feedthrough is connected to the MPCe controller (same as the ion pump) using a high-current cable also sold by Gamma Vacuum.

Each filament was rated for a maximum of 50 Amperes current. The average lifetime of a filament is 20 hours. Typically, one "firing" of the TSP involved passing 40 Amperes of current through a

²By contrast, the noble diode (DI) element, the anode and cathode are made of Titanium and Tantalum respectively. The DI element has 80% of the pumping speed of its CV counterpart and is more expensive. But the former, as the name suggest, offers more stability to nobel gases like Argon.

single filament for a duration 90 seconds. The TSP is fired for a shorter duration (≈ 30 seconds) when degassing prior to turning off the bake-out. The TSP is typically only fired a couple of times after the bake-out; after that, it is rarely used. One example of its later usage was during a liquid Helium-4 cool down of the cryostat. Firing of the TSP helped bring the analysis chamber pressure from the low- 10^{-10} torr to the high- 10^{-11} torr.

The MPCe controller can be programmed to fire the TSP at period time intervals.

B.2 Vacuum valves

B.2.1 Gate valves

All of the six gate valves used in the vacuum system described in Sec. 6.3 belong to the 108 series from VAT Group AG. Analogous to the case of the turbo pumps (c.f. Sec. B.1.1), the VAT brand was chosen due to the overwhelmingly positive feedback from vacuum professionals.

Three 8" ConFlat-flanged gate valves (VAT model 10844-UE44) are placed in front of the three main pumps on the pump chamber (c.f. Fig. 6.3.5). A 6" ConFlat-flanged gate valve (VAT model 10840-UE44), is placed in front of the HiPace 300 M turbo on the prep chamber (c.f. Fig. 6.3.10). All four of the aforementioned valves are pneumatically actuated. This form of actuation was chosen in order to implement interlocks in the event of possible pump failures. These valves required 60-100 psi of compressed air to both open and close the gate using a 24 VDC solenoid. At the time of writing, no interlocks were implemented, and no pump failures were observed. The pneumatic gate valves were operated manually using electrical flip switches mounted on one of the legs of the analysis chamber table.

Two manual 4.5" ConFlat-flanged gate valves (VAT model 10836-UE08) separate: (a) analysis from prep chamber, and (b) prep chamber from the load-lock. These two valves can be seen in the photograph in Fig. 6.3.10. These two valves have a manual hand wheel operation because the gate could accidentally crash into the transfer arms passing through the former's bores due to (say) accidental flipping of the electrical switch of the pneumatic valve.

The 108 series gate valves have a viton o-ring-sealed seat and a metal-sealed bonnet. For the former, it uses the VATLOCK gate-sealing technology. Since viton is not an ideal atmosphere-to-UHV seal (c.f. Sec. 6.3.5.7), 108 series gate valves should only be used to separate two regions under vacuum. Isolation of UHV from atmosphere is only acceptable for short time intervals; not more than a couple of days.

For example, when the analysis chamber was vented, permeation of gas through the viton o-ring in the manual 4.5" ConFlat-flanged gate valve resulted in the pressure of prep chamber to go from 2×10^{-10} torr to $\approx 8 \times 10^{-10}$ torr after a couple of weeks.

All of the six gate valves have electronically-readable gate position indicators. At the time of writing, this feature was not utilized. Only the mechanical position indicator was monitored visually.

B.2.2 Pneumatic right-angle valve

The exhausts of the HiPace 300 M and 700 M are isolated from the HiCube using bellows-sealed KF16-flanged (SA0075PVQF) and KF25-flanged (SA0100PVQF) pneumatic right-angle valves purchased from Kurt J. Lesker Company. The bonnets and seats are both o-ring-sealed since these

valves are neither baked nor exposed directly to UHV. These valves are commonly referred to as “backing valves.”

Similar to the gate valves, the backing valves were chosen to be pneumatically actuated for interlocking purposes. Once again, the interlocks were not implemented at the time of writing.

The backing valves were operated manually using electrical flip switches mounted on the analysis chamber table. A built-in spring keeps these valves in the closed position by default. They are opened using 60-80 psi of compressed air with a 24 VDC solenoid.

The backing valves are useful in selectively venting the analysis or prep chambers. For example, when venting the analysis (prep) chamber, the valve backing the HiPace 700 M (300 M) is closed, leaving the other one open.

B.2.3 Compressed air supply

The compressed air used for pneumatic valve actuation is provided by the building. During construction on the ARPES project, brazed Copper tubing was installed on the support frame (c.f. Fig. 8.1.2). One branch of the Copper tubing was terminated on a support frame pillar near the analyzer and split into three subbranches. Gas flow in each subbranch was controlled by Swagelok ball valves (SS-4SKPS4-DE).

After the ball valves, flexible 1/4" outer diameter and 0.047" wall thickness Perfluoroalkoxy alkane (PFA) tubing was used to distribute compressed air. The tubes in each subbranch were between 3-6 feet long. In addition to high pressures, the PFA tubing was rigid enough to withstand vacuum without its walls collapsing. As a result, this tube was also used for some other tasks which simultaneously required vacuum and high pressure. Furthermore, the tubing could withstand bake-out temperatures (≥ 150 °C).

Two of the three aforementioned PFA tubing subbranches were directly connected to the compressed air inlet ports of pneumatic actuators on the gate valves isolating the TSP and ion pump (c.f. Fig. 6.3.5). For the HiPace 700 M turbo, a Swagelok tube fitting tee is used to split the compressed air between the pneumatic actuators on its gate and right-angle backing valves.

The second branch of the Copper tubing terminated at a single Swagelok ball valve on a support frame pillar near the prep chamber. After the ball valve, PFA tubing was used to distribute compressed air to the pneumatic actuators on the gate and right-angle backing valves of the HiPace 300 M turbo.

B.3 Mechanical feedthroughs

In this section, I will limit the discussion *primarily* to the mechanical feedthroughs installed on the vacuum system described in Sec. 6.3. In other words, I won't cover mechanical feedthroughs on the cryostat unless they were customized, like (say) coarse x - y manipulator upgrade (c.f. Sec. B.3.4). For technical information on the standard mechanical feedthroughs on the cryostat, the reader is referred to the cryostat's manual or SolidWorks model.

B.3.1 Transfer arms

The three 2.75" ConFlat-flanged transfer arms connected to the prep chamber (c.f. Fig. 6.3.10) are from the PowerProbe series sold by Kurt J. Lesker Company. The two short (PP35-609-H) and one long (PP35-1219-H) transfer arms have a linear travel range of 2 feet and 4 feet respectively.

This transfer arm design consists of an in-vacuum solid 5/8" diameter shaft placed inside and concentric to a 1.5" outer diameter tube; the latter serves as the atmosphere-to-UHV vacuum barrier. The linear and rotary motion of the solid shaft consists of translation along and rotation about the cylindrical axis of symmetry of the vacuum tube. Mechanical coupling between the in-vacuum solid shaft and an external sleeve (a.k.a thimble), at atmosphere, is achieved by a circular arrangement of pairs of 8-10 permanent magnets; half of the magnets are under vacuum. The solid shaft follows the linear and rotary motion of the thimble below certain threshold values of thrust (≈ 30 lbs) and torque (≈ 170 in · lbs).

The entire transfer arm can be baked out without removal of any components. Moreover, according to the manufacturer (UHV Design Limited) specifications, the leakage magnetic field from the thimble is less than the earth's magnetic field 2" away from said thimble. Being several feet away from the analysis chamber, the transfer arms will not realistically affect ARPES measurements.

With a prep chamber base pressure of low- to mid- 10^{-10} torr, a temporary spike in pressure, up to the mid- to high- 10^{-9} torr, has been observed during motion of a transfer arm. These spikes, which typically last a few seconds, are the result of outgassing resulting from friction between the solid shaft and in-vacuum linear and rotary bearings.

B.3.2 Port aligners

As evident from the photographs in Fig. 6.3.11 and 6.3.12, mechanical manipulation under UHV is sensitive to the position of the transfer arms. In practice, in addition to the errors from finite chamber tolerances (typically ± 0.030 "), transfer arms can be misaligned for various technical reasons. For example, there is a *practically* unavoidable deflection of the bellows between the analysis and prep chambers due to the vacuum force. A convenient misalignment mitigation strategy is the introduction of a port aligner.

A port aligner uses an assembly, involving edge-welded bellows, to tune the angle between two flanges. The motion of the mobile flange is guided by three studs arranged in a bolt circle configuration around the fixed flange. Once the desired angle is achieved, a *pair* of nuts, on each stud, are used to fixed the position of the mobile flange.

The vacuum system described in Sec. 6.3 has 2.75" ConFlat-flanged port aligners (PA35-H) purchased from Kurt J. Lesker Company. Each of the left and middle transfer arm uses one port aligner (c.f. Fig. 6.3.10). One port aligner suffices for the alignment between the left and right transfer arms. Therefore, the right transfer arm does not have a port aligner.

B.3.3 Wobble stick

The wobble stick used for cleaving samples under UHV (c.f. Fig. 6.3.12) was from the FWS series sold by Thermionics Laboratory, Inc. The 2.75" ConFlat-flanged wobble stick transmits mechanical power through a 3/8" outer diameter stainless Steel shaft. Motion of the shaft is made possible by edge-welded bellows with a 6" linear stroke. On the atmosphere side, the 3/8" shaft is attached to

a heim joint which gives it $\pm 7.5^\circ$ angular range. The end of the 3/8" shaft was customized, by the manufacturer, to include a hole with set screws.

During system assembly, a custom Aluminum rod was attached to the end of the 3/8" shaft using the custom hole and set screws. Moreover, after learning about the magnetic nature of the heim joint, said joint was replaced with an equivalent one made from Titanium and Bronze.

B.3.4 Coarse x - y stage upgrade

The 2.75" ConFlat-flanged linear and rotary feedthroughs shown in Fig. 7.8.4 were purchased from Thermionics Laboratory, Inc. The rotary feedthrough is from the FRM-25 series with a solid 1/4" diameter shaft. The manufacturer customized the 1/4" shaft such that the tip was tapered to a point. Moreover, $\approx 1/8$ " length near the taper had 1/4"-28 threads. These features aided in guiding the 1/4" shaft into the rigid shaft coupler.³ The manufacturer also installed a 5/8" outer diameter (1/4" thick) annular disk around the 1/4" shaft. The disk served as a hard stop for the 1/4" shaft when the in-vacuum x - y stage (c.f. Fig. 7.8.4) was simultaneously hitting its hard stop.

The linear feedthrough was from the Z-B275 series. The manually lead-screw-driven feedthrough had a 2" stroke. The 1.5" bore of the edge-welded bellows was more than enough to accommodate the shaft assembly (i.e. 5/8" outer diameter disk) of the FRM-25 series rotary feedthrough. The two 2.75" ConFlat flanges of the linear feedthrough were kept concentric by two guide rods on each side the the lead screw. The operator should be cautious, during UHV-clean handling, about the fact that the guide rods are lubricated by grease.

B.4 Optical windows

B.4.1 Viewing windows

For the vacuum system described in Sec. 6.3, the viewing windows with Kodial glass were purchased from Kurt J. Lesker Company primarily for their low price. The list of window flange sizes, and their applications, is as follows:

- **2.75" ConFlat (VPZL-275):**
 - the port above the wobble stick,
 - port at the back of the R8000 analyzer for viewing the sample, and
 - an auxiliary port on the prep chamber.
- **4.5" ConFlat (VPZL-450):** three viewports on the analysis chamber to aide sample loading.
- **6" ConFlat (VPZL-600):** two viewports on the prep chamber to aide manipulation of the sample garage and sample holders (c.f. Fig. 6.3.11).
- **8" ConFlat (VPZL-800):** bottom port of the pump chamber (c.f. Fig. 6.3.5) used for a floodlight illuminating components inside the analysis chamber.

³The rigid shaft couplers were machined by Michael Roy at the chemistry machine shop.

B.4.2 Laser windows

2.75" ConFlat-flanged DUV-grade⁴ fused silica windows were purchased from MPF Products. These windows were used as laser feedthroughs due to their superior optical properties.

B.5 Vacuum hardware

B.5.1 Sealants

Rubber o-rings for KF flanges were purchased primarily from Kurt J. Lesker Company. Standard Copper gaskets sizes (1.33", 2.75", 4.5", 6", 8", 10" ConFlat) were purchased from Duniway Stockroom Corporation.

B.5.2 Fasteners

The Silver-plated 12-point head bolts and studs used to fasten standard ConFlat flange sizes (2.75", 4.5", 6", 8", 10" ConFlat), and the corresponding plate nuts, were purchased from Duniway Stockroom Corporation. The silver plating provides dry lubrication. Moreover, the plate nuts are useful in tightening flanges with limited accessibility. Except for the 1/4"-28 bolts for the 2.75" ConFlat flanges, the remaining flanges use 5/16"-24 bolts.

The wingnut clamps used for KF flanges were lubricated using WD-40. The threads of the wingnut clamps from Kurt J. Lesker Company stripped over time. Therefore, subsequently wingnut clamps were only purchased from Nor-Cal Vacuum Products.

Fasteners for the non-standard flanges were typically non-Silver-plated stainless Steel hex head bolts. Such non-standard flanges include the 27.125" wire-seal and 16.5" ConFlat flanges on the cryostat. These fasteners were already lubricated with grease by Janis Research Company. The Silver-plated hex head M10×1.5 bolts for the bottom flange (18.5" ConFlat) of the analysis chamber were provided by VG Scienta.

B.5.3 Special gaskets

Around 5-10 spare Copper wire seals for the 27.125" flange on the cryostat were provided by Janis Research Company. Janis purchased the wire seals from MDC Vacuum Products, LLC. The 16.5" ConFlat flange on the cryostat's bottom shroud (c.f. Sec. 7.3.2.3) was the most frequently removed non-standard flange to change radiation shield tail configurations during ARPES optimization (c.f. Fig. 8). Gaskets for the 16.5" ConFlat flange were purchased from Kurt J. Lesker Company.

VG Scienta provided around 2-3 spare gaskets for the 18.5" ConFlat flange at the bottom of the analysis chamber (c.f. Fig. 6.3.3 or Fig. 6.3.4). At the time of writing, since the pump chamber was detached from the analysis chamber between 5-10 times, custom gaskets for the 18.5" ConFlat flange were ordered from Kurt J. Lesker Company, based on drawings provided by VG Scienta.

VG Scienta provided one spare "star-shaped" gasket for the flange on the hemispherical dome of the R8000 analyzer.

⁴DUV: deep ultraviolet.

B.6 Load-lock

The main body of the load-lock, used in the vacuum system described in Sec. 6.3, was a standard 4.5" ConFlat-flanged five-way cross from Kurt J. Lesker Company. An o-ring sealed quick-access door, also from Kurt J. Lesker (DS-LL0450VP), was attached to the top port of said cross. The quick-access door was used to load sample holders into the sample garage. Another convenient feature of the quick access door was the availability of a viewing window to ensure smooth transition of the sample garage to the prep chamber (c.f. Fig. 6.3.10).

B.7 Diagnostics

B.7.1 Pressure gauges

The vacuum system described in Sec. 6.3 has two pressure gauge controllers purchased from Stanford Research Systems (model IGC 100). Each controller is capable of reading two Pirani gauges simultaneously. While one IGC 100 unit has the option to simultaneously connect two ion gauges, it can only drive one at a time. As a result, one IGC 100 unit each was dedicated to the analysis and prep chamber volumes. The cables for the two Pirani and ion gauges were also purchased from Stanford Research Systems.

The IGC 100 has an RS-232 communication interface. This interface was used to monitor pressures during a bake-out (c.f. Sec. B.8.4)

B.7.1.1 Pirani gauge

Two Pirani gauges were purchased from MKS Instruments (model 275238). As I stated in Sec. 6.1.3.1, the Pirani gauges can provide reliable pressure readings from atmosphere to $\approx 10^{-4}$ torr. The IGC 100 can be programmed to switch from the Pirani to ion gauge automatically.

It is worth noting that, close to atmosphere, the Pirani gauge is calibrated assuming N_2 as the dominant gas. On one occasion, accidentally purging the analysis chamber with Helium-4 gas led to nonsensical readings from the Pirani gauge.

B.7.1.2 Ion gauge

One of the most popular ion gauges among vacuum professionals is the one from Granville-Phillips Company. During the time of purchase, 274 series Granville-Phillips-style ion gauges were sold by MKS Instruments. The vacuum system described in Sec. 6.3 used two nude Bayard-Alpert hot cathode gauges purchased from MKS Instruments (model 274042). The gauge filaments were coated with Thoria (ThO_2) to prevent damage from sudden overpressuring of the chambers. This feature proved to be very useful during sudden pressure spikes!

These ion gauges use up to 40 Watts of electron bombardment for degassing. Typically, ion gauge degassing during bake-outs was performed with a power of 25 Watts for 10 minutes. For pressures in the 10^{-10} torr range, a filament current of 10 mA was used. By lowering the filament currents, the pressure curve, as a function of time, gets noisier. It was empirically determined that setting

the filament current to 100 μA during the initial pump down and bake-out suffices. Operating the filament at a lower current extends its lifetime.

The ion gauges have two filaments. In that case, one can switch over to the second filament, without venting the system, if the first one reaches its end of life (or burns out). At the time of writing, only one of the filaments in the prep chamber burned out.

B.7.2 Residual gas analyzer

The vacuum system described in Sec. 6.3 uses a residual gas analyzer (RGA) purchased from Stanford Research Systems (model RGA 100). The upper limit of the mass spectrum in this model is 100 atomic mass units (amu). An optional electron multiplier was ordered for increased sensitivity. Windows operating system software is provided by Stanford Research Systems to control the RGA through an RS-232 communication interface.

Typically, the electronics unit of the RGA is removed during a bake-out. But it is not strictly necessary for the limited amount of heat to which said unit is exposed. Close to the end of the bake-out, the electronics unit needs to be attached for degassing the RGA using the software.

B.8 Bake-out

In this section, I will only discuss the bake-out of the analysis chamber region. The prep chamber was only baked out once or twice shortly after the ARPES system was assembled. For reasons discussed in Chap. 8, the bake-out tools and techniques presented here were developed specifically for the analysis chamber space. Although, in the future, these tools and techniques could be adapted and applied to the prep chamber, if necessary.

B.8.1 Bake-out preparation

Prior to starting the bake-out, heat-sensitive components of the vacuum systems need to be removed. Most of these components were on the R8000 electron analyzer. The list of items on the analyzer to be removed is as follows:

- Junction boxes labeled JL, JA, and JD
- The plastic turn counter attached to the shaft of the rotary feedthrough controlling the slit carousel
- CCD camera

The 1 foot \times 1 foot optical breadboard with three legs, which is bolted to the top of the analysis chamber table, is typically removed and placed on the ARPES optics table. This breadboard supports the lens and folding mirror encountered by the laser beam, originating from the Toptica laser, before said beam passes through the laser window on the analysis chamber. The floodlight under the 8" ConFlat-flanged window, at the bottom of the pump chamber, is also removed.

B.8.2 Heat generation and distribution

As I briefly discussed in Sec. 8.1.4.2, during a bake-out of the vacuum system described in Sec. 6.3, heat was generated using 12 feet long 3/16" diameter fiberglass-insulated heater cords from Omega Engineering (model HTC-120). Plugging these cords directly into the electrical mains (120 VAC) results in 1.8 W/in^2 of heat dissipation from Joule heating.

Depending on the surface area and texture of the stainless Steel surfaces, which served as vacuum barriers, different number of cords and routing paths were used for different vacuum components. Table B.1 lists the number of cords used in the different regions of the UHV system. Moreover, the nominal bake-out temperature achieved, at different locations, using said cords is also listed.

| Component | Location | Number of heater cords | Nominal temperature ($^{\circ}\text{C}$) |
|------------------|--------------------|------------------------|--|
| Cryostat | Top 27.125" flange | 1 | 70 |
| | Main shroud | 1 | 140 |
| | Bottom shroud | 1 | 160 |
| Analyzer | Front | 1 | 140 |
| | Back | 1 | 110 |
| Analysis chamber | | 2 | 140 |
| Pump chamber | | 2 | 120 |

Table B.1: Table showing the heater cord distribution across the external surfaces of the UHV system. The nominal temperatures achieved using each cord is also listed.

It is worth noting that the bake-out configuration described by Table B.1 only applies to the situation when the Indium seal inside the cryostat is periodically cooled with liquid Nitrogen (c.f. Sec. 6.4.3).

The heat output of the cords can be regulated using off-the-shelf light dimmers. For the configuration shown in Table B.1, the cords were operated at full power.

B.8.3 Insulation

When it became clear that bake-outs were essential to avoid charging during ARPES measurements (c.f. Sec. 8.4.2), the bake-out apparatus and procedure were significantly altered. The primary goal of said alteration was to reduce the duration of the bake-out by increasing bake-out temperature from below $90 \text{ }^{\circ}\text{C}$ to around $150 \text{ }^{\circ}\text{C}$. I briefly alluded to the switch to high-temperature bake-outs in Sec. 6.4.3.

The bake-out temperature can be increased by either or both: (a) increasing the power supplied to the heating element (i.e. heater cords), (b) thermally insulating the hot surfaces. I decided to pursue the latter.

In the first iteration, I used wool blankets. However, I soon learned that wool blankets disintegrated at high temperature and outgassed significantly. While the outgassing was in atmosphere, it was extreme enough to generate "fog" in the lab. The most obvious side effect of the fog was tarnishing of all silver-plated objects. That included the 12-point bolts, used for fastening ConFlat flanges, and the 77 K shield tail. Therefore, the wool blankets were discarded.

In the second iteration, I decided to go with ceramic fiber insulation. Being commonplace in furnaces, the ceramic fiber insulation's temperature rating ($\approx 1200 \text{ }^{\circ}\text{C}$) was significantly higher than the UHV bake-out requirement. So thermal disintegration was not a concern. A major drawback, however,

was that the ceramic fiber sheets produced dust. Firstly, this property of the ceramic fiber sheets is undesirable because the dust in an optics lab needs to be kept to minimum. Secondly, the dust caused irritation to the skin. Lastly, there was a risk of the dust entering the analysis chamber when the UHV system is vented.

Ultimately, it seemed like the benefits of the ceramic fiber insulation outweighed its drawbacks. For example, one way of minimizing dust in the lab was covering the *external* surface of the insulation with Aluminum foil.⁵

The ceramic fiber sheets were mechanically supported by a clamping force generated by an Aluminum wire tied around on cylindrical surfaces like those belonging to the cryostat and analysis chamber. For more complex shapes, like the analyzer, two or more ceramic fiber sheets were “stitched” together using the same Aluminum wire, in order to give the composite sheet the appropriate curvature.

The idea of creating ceramic fiber “blankets” was explored. The concept was similar to a commercial stuffed blanket. In this design, a high-temperature fabric would be stitched into a jacket, which would serve as a dust barrier for the ceramic fiber. Due to time constraints, not much progress was made on this design. This idea might be worth exploring in the future.

B.8.4 Temperature and pressure monitoring

The temperature of the bake-out was monitored using several 10 feet long Perfluoroalkoxy-alkane-insulated 24 AWG (American Wire Gauge) type K thermocouples from Omega Engineering (5SRTC-TT-K-24-120). The sensing end of the thermocouple was taped to the stainless Steel walls forming the vacuum barriers; a high-temperature fiberglass tape with a Silicone adhesive was used. The thermocouples were strain relieved as much as possible along their length prior to covering them up with Aluminum foil and thermal insulation.

On several occasions, nonsensical readings from the thermocouples were attributed to loss of thermal contact from the stainless Steel surface underneath the layers of foil and insulation. The loss of contact could have resulted from some mechanical or thermal stresses. Therefore, a redundant thermocouple was used for each temperature monitoring point.

Thermocouples were also placed on some sensitive unbaked equipment (e.g. HiPace 700 M turbo) to ensure they were not accidentally overheating.

Two 8-channel thermocouple readers from Omega Engineering (TC-08), with a USB (Universal Serial Bus) 2.0 interface, were used to log the temperature at various points of the vacuum system. The data logging was done by a custom software running on a desktop computer. Moreover, pressure inside the vacuum space being baked out was recorded, with another software, using an RS-232 interface with the ion gauge controller (c.f. Sec. B.7.1.2). Plots of pressure and bake-out temperatures were posted on a web page hosted by the same computer logging the data. With this setup, the bake-outs could, in principle, be monitored remotely for indefinite periods of time. As evident from Fig. 6.4.1, the duration of an average bake-out was of the order of weeks.

⁵Note that there is a layer on the inner surface of the insulation responsible for spreading heat from the heater cords. In effect, the insulation was sandwiched between two layers of Aluminum foil.

Appendix C

Cryogenics

The purpose of this chapter is to provide an intuitive explanation of some of the cryostat's technical features and operation procedures. In other words, pedagogy is prioritized over comprehensiveness. Therefore, this chapter should **not** be treated as a substitute for the cryostat manual. Moreover, the reader should note that some of the figures in this chapter have been modified from their counterparts in the manual (e.g. Fig. C.1.1) in order to fit the format of this document.

It is also worth noting that the contents of Sec. C.3 elaborate on the **custom** wiring procedure discussed in Sec. 7.8.4. Therefore, the design presented in Sec. C.3 differs from that presented in the cryostat manual.

C.1 Helium-3 plumbing circuit

C.1.1 Gas handling system

In Sec. 7.4.3.3, I discussed two configurations most commonly used in a Helium-3 cryostat: condensation (Fig. 7.4.7) and circulation (Fig. 7.4.8) of Helium-3. It is obvious from the block diagram representations for the corresponding plumbing circuits that switching between these two configurations is cumbersome. Moreover, there are several other plumbing configurations which the operator has to utilize for the smooth functioning of the system. Some examples are: leak testing different subsystems of the Helium-3 loop (c.f. Sec. C.2.2), impedance tests (c.f. Sec. C.2.3), Helium-3 cleaning, and cleaning the liquid Nitrogen cold trap.

An elegant solution to implementing all the aforementioned plumbing circuits, with minimal hardware and operator effort, is laying out a network of pressure valves and gauges into an assembly known as the *gas handling system*. For the Helium-3 cryostat I discussed in Chap. 7, a block diagram representation of the gas handling system is shown in Fig. C.1.1. The physical gas handling system consists of components such as valves, pressure gauges, Helium-3 dumps, and the flow meter. These components are connected together, inside the gas handling system unit, via Copper tubing and appropriate connectors (e.g. tees and crosses). The cold trap, pumps, and impedance are external to the physical gas handling system unit. This can be seen by the fact that the external components typically have at least one port (blue circle) and at least one valve to isolate them from the rest of the system.

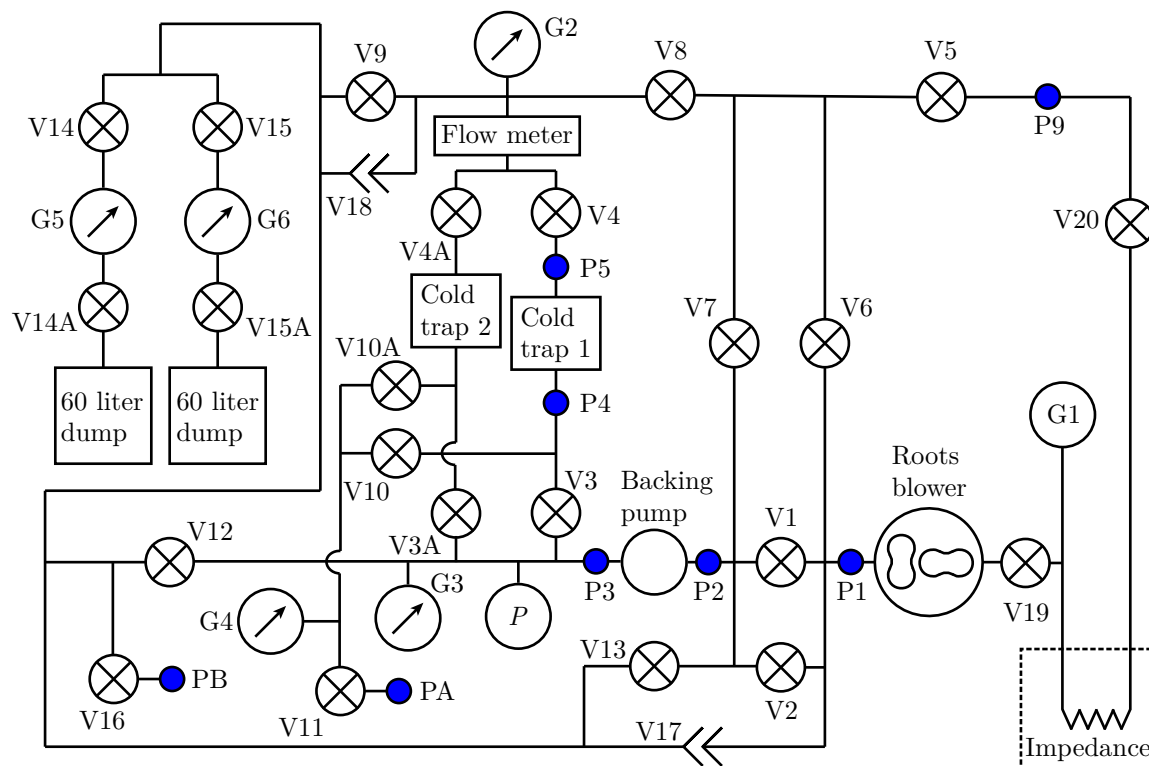


Figure C.1.1: Block diagram representation of the plumbing circuit in the gas handling system. The circles with an arrow inside them are compound (i.e. dial) pressure gauges. The circles with the cross inside them denote valves. The blue circles are KF flanged ports for outgoing/incoming gas lines. The double-arrow denotes a relief valve.

Except the V1, V2, and V19, all the valves are bellows-sealed Swagelok valves. V19 is a butterfly valve from Key High Vacuum Products, Inc. The pressure relief valves, V17 and V18, are connected to regions which are exposed to the largest pressures. It is important to keep the pressure in the entire Helium-3 plumbing circuit below an atmosphere. In that case, if an atmospheric leak occurs, ambient air will enter the plumbing circuit, as opposed to the loss of Helium-3 gas to atmosphere. While both cases are non-ideal, the latter is more damaging.

Except G1 and P , all the pressure gauges are compound (or dial) gauges. A compound gauges serve as crude pressure checks which typically only provide readings as low as a few torr ($-30''$ of Mercury). The Pirani gauge, G1, which has greater low-pressure sensitivity ($\approx 10^{-3}$ torr), is used for tasks which require quantitative measurement of pressure, like (say) impedance checks (c.f. Sec. C.2.3). G1 is attached on the KF16 port on the elbow, part of the Helium-3 pump path, on top of the cryostat (c.f. Fig. 7.4.1). P is a piezo pressure gauge with a range of 0.1-1000 mbar (MKS Instruments model 902). Both G1 and P are connected to the same vacuum gauge controller (MKS Instruments model 937B) which provides digital read outs.

The flow meter is a convenient feedback tool complementing the pressure gauges; it can measure flow rates up to 5 milli-mole/second (MKS Instruments 179A Mass-Flo®). Feedback from the flow meter can be useful for (say) identifying impedance blockage or ensuring the gas flow rate through the liquid Nitrogen cold trap does not get too high. Otherwise, for the latter, frost will form on the cold trap's ports.

C.1.2 Pumping station

As I stated in Sec. C.1.1, the two pumps part of the Helium-3 plumbing circuit are separate from the gas handling system. These pumps are part of a unit known as the Pfeiffer CombiLine™ pumping station. In order to keep the noise level in the lab to a minimum, the entire pumping station is placed inside a closet; a photograph of this setup is shown in Fig. C.1.2. The photograph also shows the KF- and ISO-flanged ports leading to the gas handling system and Helium-3 system respectively.

As I discussed in Sec. 7.1.3, the vapor pressure of Helium-3 needs to be lowered as much as possible to get to lower Helium-3 pot base temperatures (c.f. Fig. 7.1.1). Moreover, cooling power depends on the pumping speed (c.f. Eq. (7.1.4)). Therefore, the pumping station needs to strike a good balance between base pressure and pumping speed. The Pfeiffer Okta 500 can provide a pumping speed of over 50 liters/second at pressures of $\lesssim 10^{-3}$ torr. In this thesis, the Okta 500 is commonly referred to as the “roots blower.” Pumping action in a roots pump is generated by displacement of gas by two lobes rotated in the opposite direction. This feature is schematically represented in the gas handling system block diagram (c.f. Fig. C.1.1).

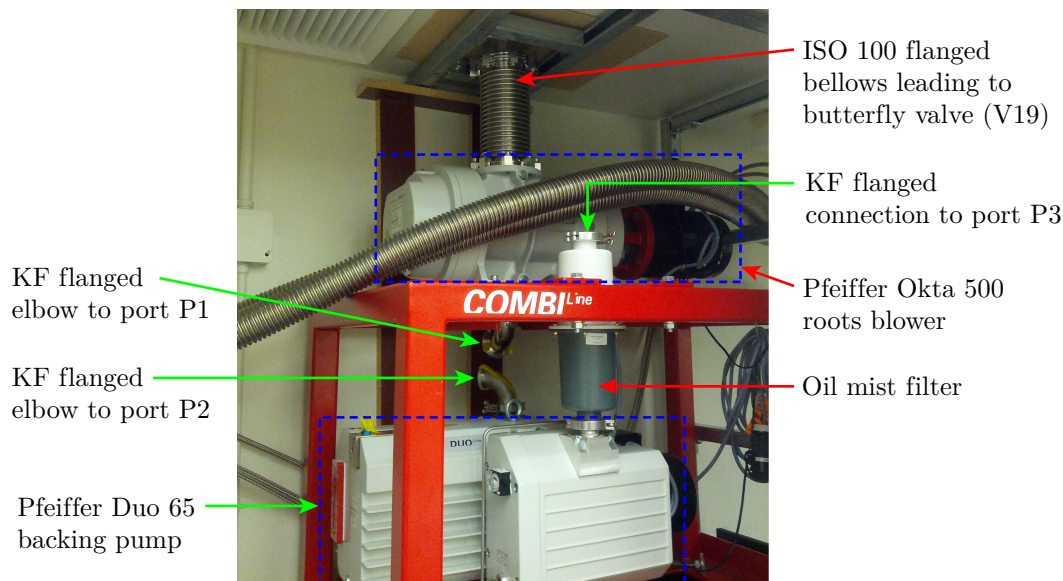


Figure C.1.2: Photograph of the Pfeiffer CombiLine™ pumping station.

Furthermore, an oil-sealed rotary vane pump (Pfeiffer Duo 65) is used to back the roots blower with a pumping speed of 20 liters/second at pressures of close to 1 torr. The backing pump is used for most Helium-3 circulation tasks except performing the cooling of the Helium-3 pot to base temperature (0.47 K). The backing pump’s speed drops by almost 3 orders of magnitude for pressures approaching 10^{-3} torr. Hence the roots blower is necessary to deliver the cooling power requirements of an ARPES system. Since rotary vane pumps are oil-sealed, the exhaust of the backing pump is equipped with an oil mist filter.

C.1.3 Liquid Nitrogen cold trap

Over time, contaminant gases accumulate in the Helium-3 circulation loop. Eventually the contaminants will reach a high enough partial pressure that they will condense inside the Helium-3 circulation loop. Such unwanted forms of condensation can (say) cause blockages in the impedance.

In less severe cases, such blockages can be fixed by heating the impedance. But such troubleshooting steps can be time-consuming and expensive.¹

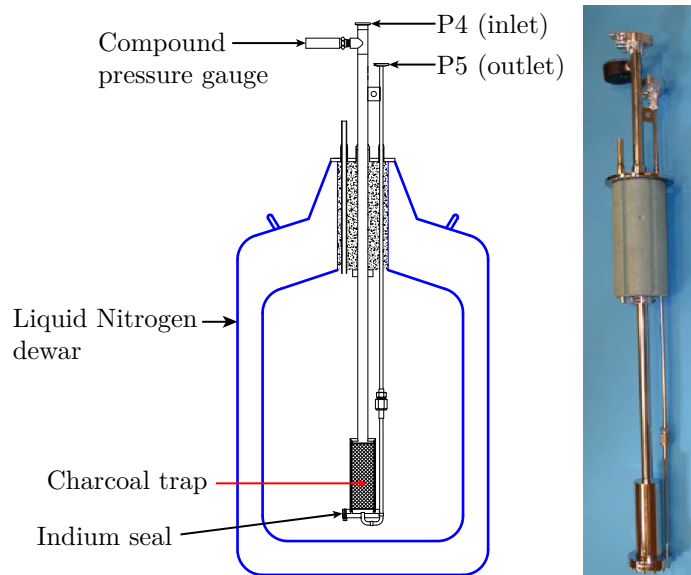


Figure C.1.3: Left: section view of the CAD model of the liquid-Nitrogen-cooled charcoal cold trap assembly. Right: photograph of the cold trap head without the liquid Nitrogen dewar.

The issue of contamination of the Helium-3 circulation loop can be mitigated by the use of a cleaning filter. The latter is typically implemented using a liquid-Nitrogen-cooled charcoal trap. A section view of the CAD model of the cold trap assembly and a photograph of the cold trap head is shown in Fig. C.1.3. The cold trap head consists of a vacuum-sealed stainless Steel enclosure with KF-flanged inlet (P4) and outlet ports (P5). The lid connected to P5 at the bottom forms an Indium seal with the can enclosing the charcoal. As shown in Fig. C.1.3, the cold trap head is immersed in liquid Nitrogen in order to enhance its impurity “pumping.”

C.2 Helium-3 cryostat cool down

C.2.1 Cryogen stock

Conservatively, at least two 160 liter dewars of liquid Nitrogen should be available during the cool down. The liquid Helium-4 cool down from $\approx 77\text{ K}$ to a sample temperature of $\approx 2\text{ K}$ typically consumes an entire 100 liter dewar of liquid Helium-4. For ARPES measurements discussed in this thesis, liquid Helium-4 cool downs were performed without Helium-3 circulation. In that case, each cool down required a total of two 100 liter dewars of liquid Helium-4. In principle, the cryostat can be kept at base temperature indefinitely by repeated liquid Helium-4 refills.

For the liquid Helium-4 dewars, a custom cross with NPT (National Pipe Thread) fittings is used. The four ends of the cross are connected to:

1. the gas vent port of the dewar,

¹Liquid Helium-4 boil off during troubleshooting is the primary cost driver.

2. a compound (or dial) pressure gauge with a maximum pressure reading of 3 psi,
3. a ball valve for venting, and
4. an adapter to a high pressure Helium-4 gas line and a valve to control the gas flow.

C.2.2 Leak tests

In Sec. 7.7.1.1, I discussed the importance of leak tests on the cryostat's subsystems. The cryostat components have up to a total of the following vacuum interfaces:

1. Atmosphere-to-UHV
2. Rough-vacuum-to-UHV
3. Rough-vacuum-to-atmosphere

Different types of leak test configurations and tools are required depending on which subset of the above interfaces a given component possesses. In this section, I will discuss the details of leak tests on some the components.

C.2.2.1 Helium-3 insert

Due to the high price and limited availability of Helium-3, leak testing its closed-loop circulation path is the most critical pre-cooling diagnostic step.² In this section, I will focus on leak testing only one component of said circulation path: the Helium-3 insert. The reader is referred to the cryostat manual for a thorough leak testing protocol for the *entire* Helium-3 circulation path.

The Helium-3 insert consists two (out of three) vacuum interfaces: (a) rough-vacuum-to-atmosphere and (b) rough-vacuum-to-UHV. For the latter, one way of leak testing is using the RGA (c.f. Sec. 6.5.1) connected to the UHV system. With the RGA set to monitor partial pressure of Helium-4, the insert can be evacuated using a roughing pump, and subsequently filled with Helium-4 gas. If a spike in the Helium-4 pressure is observed, the UHV system would have to be vented, and the insert removed. Then the location of the leak can be determined by performing a leak test on the isolated insert using a standard leak detector.

For the rough-vacuum-to-atmosphere leak test, a standard leak detector has to be used. One such leak test configuration that requires least hardware changes is shown in Fig. C.2.1. First, ensure that the gas handling system is leak tight. Then, the leak detector, set to detect Helium-4, is connected to port "PB" of the gas handling system. In order to avoid virtual leaks from interfering with the test, the Helium-3 insert is pumped from both sides of the impedance. The leak test is then performed by spraying Helium-4 gas around: (a) the Indium and KF flanges of the Helium-3 pumping path elbow (c.f. Fig. 7.4.1), (b) the butterfly valve (V19), (c) return line valve V20 and corresponding tubes on top of the Helium-3 insert, and (d) the flexible lines connecting the Helium-3 pumping and return paths to the roots blower and gas handling system respectively.

²Note that the necessity of Helium-3 in a cool down depends on the target base temperature. This step can be skipped if the experiment does not demand sub-Kelvin operation.

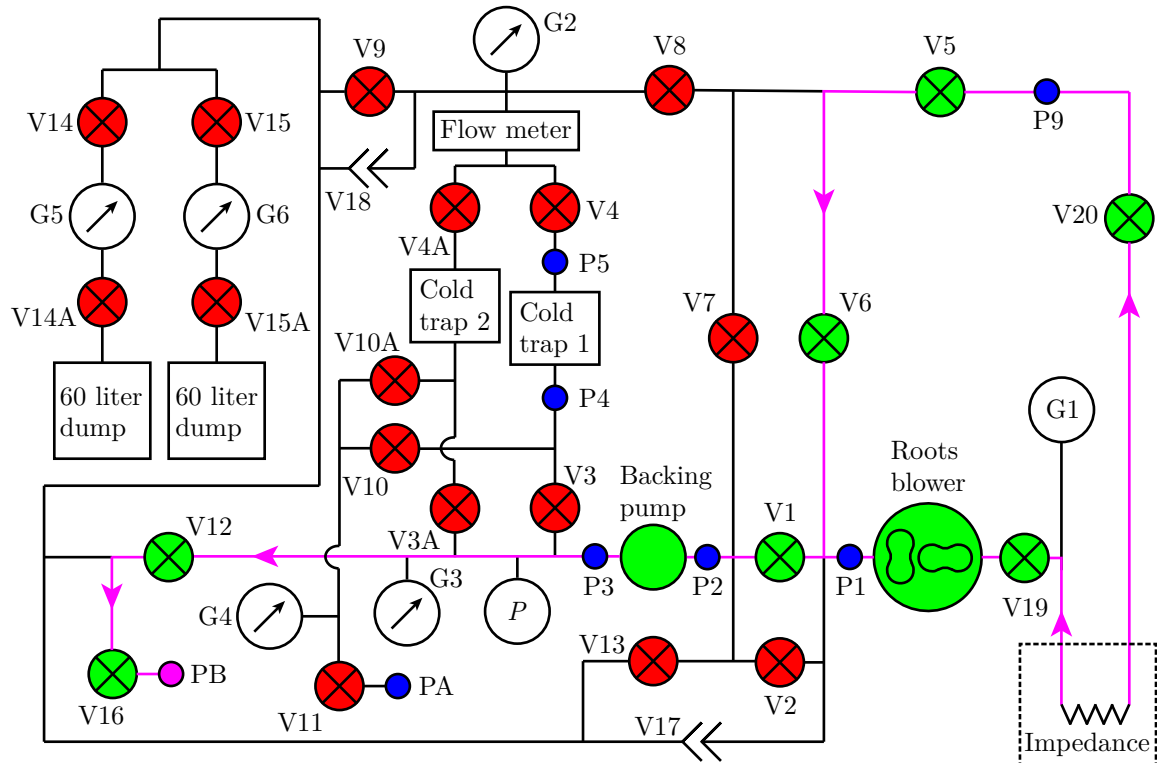


Figure C.2.1: Configuration of the gas handling system when leak testing the Helium-3 insert. The open (closed) valves and on (off) pumps are color-coded red (green). Pink lines with arrows represent the pumping path.

C.2.2.2 1 K pot circuit

The 1 K pot circuit (c.f. Sec. 7.4.2.2) consists of all three of the aforementioned vacuum interfaces. Leak tests associated with each interface are as follows:

- **Atmosphere-to-UHV:** these types of seals (welding and soldering) are used in the fabrication of the 1 K pot and the capillary connecting said pot to the 4 K reservoir. Leaks in these seals can be diagnosed by: (a) setting the RGA to detect Helium-4, (b) closing the needle valve,³ (c) evacuation of the 1 K pot with a roughing pump, and (d) purging the 1 K pot with Helium-4 gas.
- **Rough-vacuum-to-UHV:** in this particular subsystem, the atmosphere-to-UHV seals simultaneously serve as the rough-vacuum-to-UHV seals. Therefore, the same RGA leak detection technique can be used for both seals.
- **Rough-vacuum-to-atmosphere:** these types of seals exist in the pumping path from the 1 K pot to its pump. This includes: (a) the o-ring and weld seams on the 1 K pot pumping elbow (c.f. Fig. 7.4.1), (b) epoxy on NPT (National Pipe Thread) connector of the pressure relief valve on the side of the elbow, (c) the viton (or buna) seal on the spring-loaded vent of the pressure relief valve, (d) the diaphragm valve at the output of the elbow, (e) the seam-welded formed bellows connecting the elbow to the 1 K pot pump, and (f) seals on the components of the 1 K pot pump assembly.

³For a more thorough leak test, the 1 K pot can be leak tested simultaneously with the 4 K reservoir (c.f. Sec. C.2.2.3).

C.2.2.3 Cryogen reservoirs

The vacuum seals on the 4 K and 77 K reservoirs form the atmosphere-to-UHV interface. During a leak test, two of the three fill ports will be blanked off. Setting the RGA to detect Helium-4, the third fill port is used to evacuate and subsequently purge these reservoirs with Helium-4 gas. This method was used to identify the leak in the 4 K reservoir (c.f. Sec. 7.8.1.1).

C.2.3 Pre-cool Helium-3 circulation and impedance tests

If the user plans on using Helium-3 for the cool down, it is important to ensure that the condensing impedance capillary does not clog during its pre-cooling from 300 K to 1.5 K. This could happen, for example, if impurities that are not efficiently pumped out, during the initial evacuation of the Helium-3 line, condense inside the impedance capillary at any point during the pre-cool-down. One way to mitigate such problems is introducing a fraction of the available Helium-3 gas into its normal circulation loop. Another mitigation strategy is to pump both sides of the impedance capillary with the backing pump (Pfeiffer Duo 65).

Fig. C.2.2 shows the configuration of the gas handling system for the case where Helium-3 gas is circulated during the cool down from 300 K to 1.5 K. Note that most of the Helium-3 gas is stored in the dumps in the pre-cool-down circulation configuration. Valves V1 and V2 provide parallel conductance to the backing pump. The former has a higher conductance.

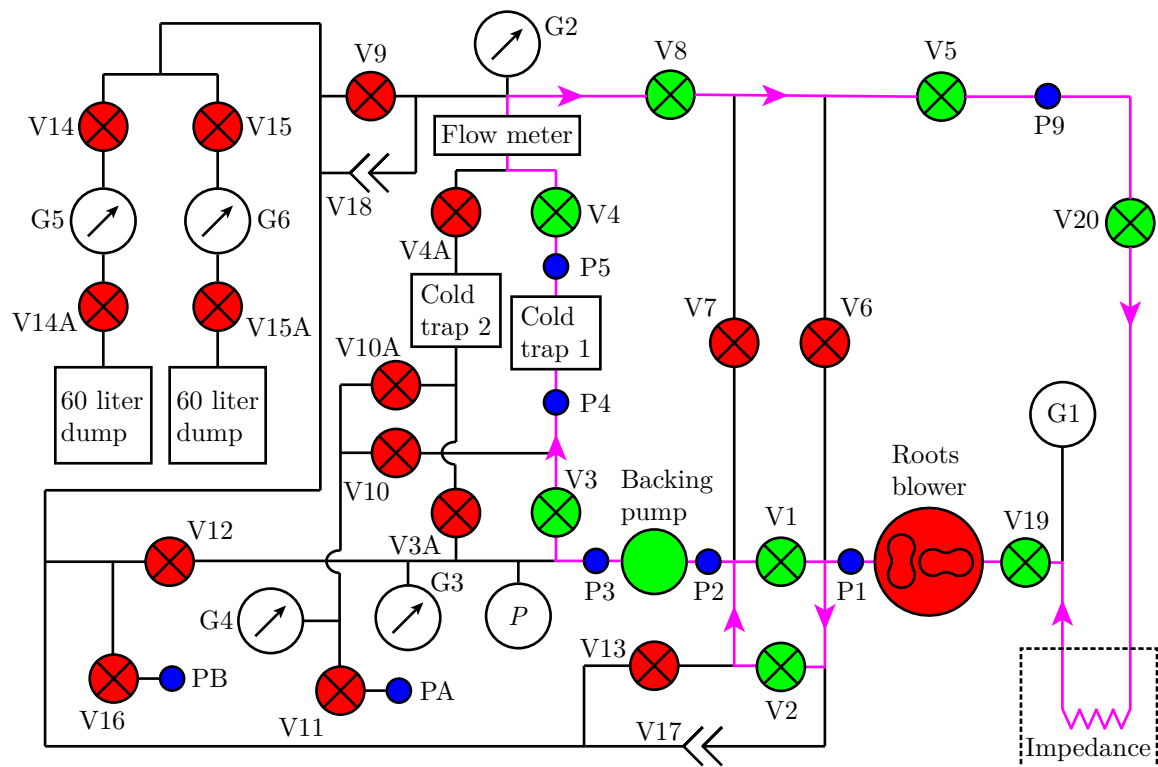


Figure C.2.2: Configuration of the gas handling system when circulating Helium-3 during the cool down. The open (closed) valves and on (off) pumps are color-coded red (green). Pink lines with arrows represent flow path of the Helium-3 gas.

It is good practice to get feedback on the state of the impedance capillary during one or more points during the pre-cool-down. To that end, one needs to perform so-called impedance tests at different

temperatures, and compare them to their room temperature counterpart. The operating principle of the impedance test is as follows. If at a certain time ($t = 0$), one side of the impedance capillary is at a pressure, P_{head} , of a few hundred millibar (but less than 1 bar), while the pressure at the other end, $P_{\text{tail}}(t)$, is initially negligible ($P_{\text{tail}}(0) \ll P_{\text{head}}$), then the rate $dP(t)/dt$ measured for $t > 0$ (typically few minutes) is inversely proportional the capillary's flow impedance.

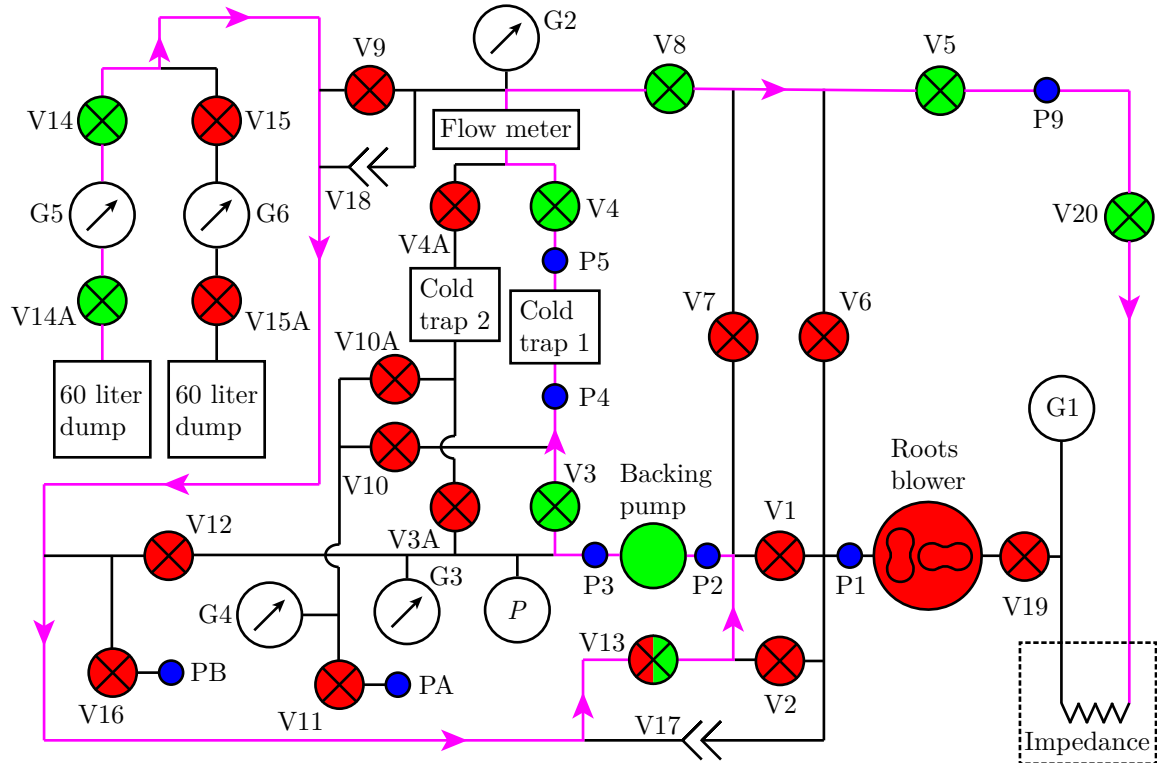


Figure C.2.3: Configuration of the gas handling system when performing an impedance test. The open (closed) valves and on (off) pumps are color-coded red (green). Pink lines with arrows represent the flow of Helium-3 gas. The partially red and green valve indicates the valve used to regulate the amount of Helium-3 in the system.

In order to perform an impedance test, the configuration of the gas handling system needs to be switched from the one shown in Fig. C.2.2 to that in Fig. C.2.3. The first step is extracting additional Helium-3 gas from the dump, and introducing it into the circulation loop, in order to build sufficient pressure at the head of the impedance capillary, P_{head} . One way of doing this is as follows:

1. Open V14A and V14.
2. Close V19, V1, V2, and V5.
3. Open V13 slowly while keeping an eye on the pressure gauge P .
4. Close V13 when P reads a few hundred mbar.

Note down the pressure reading from P . While P will not be exactly equal to P_{head} once V5 is opened, it serves as a crude form of feedback in controlling the amount of Helium-3 to pull out of the dump. Moreover, gauge G1 will serve as a crude form of feedback on the evolution of the pressure at the tail of the impedance capillary, $P_{\text{tail}}(t)$, as a function of time.

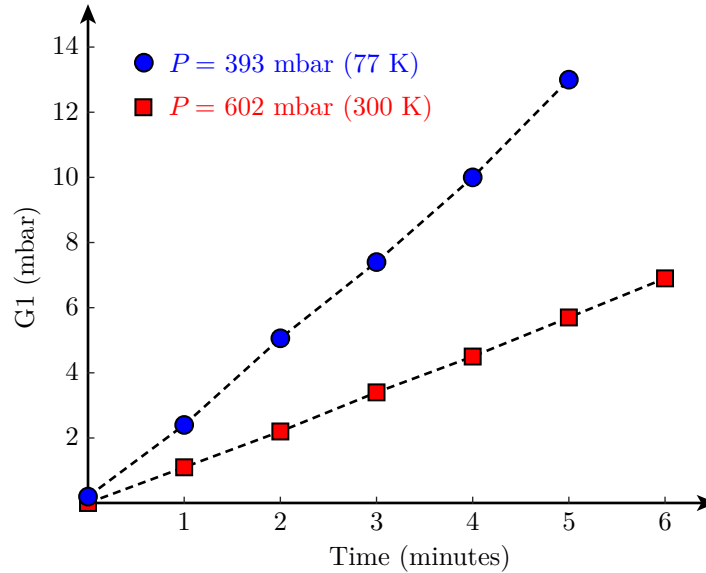


Figure C.2.4: Rise in the tail pressure of the impedance capillary, as measured by G1, at 77 K and room temperature. The initial head pressures, as measured by P , are approximately 400 and 600 mbar respectively.

Now, open V5 at $t = 0$, and monitor G1 as a function of time, for around 5-10 minutes. An example of the dependence of G1 on time (t) is plotted in Fig. C.2.4 at room temperature and 77 K. By the slopes of the two curves, it can be seen that the flow impedance of the capillary at 77 K is approximately half of its room temperature value. The system passes the impedance test if this behavior can approximately be reproduced.

After the impedance test, and after pushing the excess Helium-3 gas back into the dump, revert back to the configuration in Fig. C.2.2 and continue the cool down.

C.2.4 Liquid Nitrogen cool down

The support frame is equipped with a plumbing circuit, which allows transportation of liquid Nitrogen from a dewar, placed on the lab floor, to the top deck of the support frame (c.f. Fig. 8.1.4). The primary path of the plumbing circuit consists of (thermally insulated) rigid Copper tubing mechanically fastened to the support frame. Flexible braided stainless steel tubes are attached on either end of the Copper tubing to mate with the cryostat and dewar.

On the dewar end, the flexible tube is attached to a foot-long stainless Steel tube of 3/8" outer diameter. The rigid tube merely serves as an adapter to a *custom* brass fitting⁴ that directly attaches to the dewar. On the cryostat end, exists another flexible tube, which attaches to a rigid L-shaped stainless Steel tube of 3/8" outer diameter. This L-shaped tube is directly inserted into the fill ports of the 4 K and 77 K reservoirs.

As discussed in Sec. 7.3.1, both reservoirs have three fill ports. For the 77 K reservoir, I will refer to these ports as $A_{77\text{K}}$, $B_{77\text{K}}$, and $C_{77\text{K}}$ (counterclockwise from the top) in the following discussion. Port $A_{77\text{K}}$ is closest to the liquid Nitrogen transfer plumbing circuit. Hence that port is always using for transferring liquid Nitrogen. Port $B_{77\text{K}}$ will be used for venting the boiled off liquid Nitrogen

⁴This fitting was provided by Caltech facilities. It was in limited supply at the time of writing.

gas. A level monitor probe is inserted in port $C_{77\text{K}}$. Similar to the 77 K reservoir, I will label the ports of the 4 K reservoir as $A_{4\text{K}}$, $B_{4\text{K}}$, and $C_{4\text{K}}$. One difference is that the level probe is inserted in port $B_{4\text{K}}$. Moreover, a tee on port $B_{4\text{K}}$ is used to attach a Swagelok valve for controlling the gas pressure inside 4 K reservoir.

In the next couple of sections (Sec. C.2.4.1-C.2.4.3), I will describe the procedure to bring every component of the cryostat to a temperature below 100 K using liquid Nitrogen.

C.2.4.1 Filling the 77 K reservoir with liquid Nitrogen

Step 1: Connect the custom brass fitting, part of the aforementioned liquid Nitrogen transfer plumbing circuit, to a dewar containing at least (estimated) 60-100 liters of liquid Nitrogen.

Step 2: Insert the aforementioned L-shaped tube into port $A_{77\text{K}}$ of the 77 K reservoir. Tie down the L-shaped tube to something rigid using (say) zip ties. At the beginning of the liquid Nitrogen transfer, high pressure Nitrogen gas from the dewar, hitting the bottom of the cryostat's reservoir, can provide a large enough thrust to eject the L-shaped tube.⁵

Step 3: Put a PVC tube, of approximately 1" inner diameter, over port $B_{77\text{K}}$ to direct the vented Nitrogen gas away from the cryostat. Otherwise the frost the gas generates on the cryostat components might pose as anywhere between a minor inconvenience to a major operation hazard.

Step 4: Make sure the BNC cable from the level monitor (Cryomagnetics LM-500) is attached to the end of the level probe in port $C_{77\text{K}}$. Turn on the level monitor.

Step 5: Initiate the liquid Nitrogen transfer by opening the valve on the dewar, which controls the flow of liquid Nitrogen, all the way.

Step 6: Monitor the amount of liquid Nitrogen accumulated in its reservoir using the level monitor. When the level reads 22 inches, stop the transfer of liquid Nitrogen; at this point, the 77 K reservoir will be close to its full capacity (≈ 50 liters). If one hears a whistling sound, before the level monitor reads 22 inches, then the dewar is close to empty. In that case, replace that dewar after disconnecting the custom fitting. The rest of the liquid Nitrogen transfer plumbing circuit does not need to be warmed up. Once the new dewar is attached to said circuit, continue the liquid Nitrogen transfer.

C.2.4.2 Filling the 4 K reservoir with liquid Nitrogen

Step 1: Attach a pressure relief valve ($\lesssim 4$ psi bleed pressure) to port $C_{4\text{K}}$ of the 4 K reservoir using quick disconnect fittings. These valves both seal the 4 K reservoir from ambient air and, as the name suggests, prevent over-pressuring said reservoir.

Step 2: Make sure the Swagelok valve on port $B_{4\text{K}}$ is closed. Note that the level probe on port $B_{4\text{K}}$ can only detect the level of liquid Helium-4. Hence this probe will be unused in the liquid Nitrogen pre-cooling step.

Step 3: Prepare the vent port for the 4 K reservoir. This port has a KF 25 flange connection and is located on top of the Helium-3 insert. For the liquid Nitrogen pre-cooling step, it is not necessary to

⁵In practice, the flexible Stainless steel tube has enough rigidity to avoid the tube ejection problem. This was only an issue in an older design involving flexible rubber hoses. Nevertheless, tying down the L-shaped tube remaining a safety practice.

use the diversion system described in Sec. 7.7.1.3. The user has the option to use a simpler diversion system like the one involving the PVC tube in the case of the 77 K reservoir.

Step 4: Remove the L-shaped tube from port $A_{77\text{K}}$ of the 77 K reservoir and insert it into port $A_{4\text{K}}$ of the 4 K reservoir. Tie down the L-shaped tube to something rigid.

Step 5: Make sure the needle valve is closed. Evacuate the 1 K pot with its pump (Pfeiffer Hena 60). Fill up the 1 K pot, as well as the entire pumping line, with 1.2 bar of Helium-4 gas. Keeping this region above atmosphere prevents ambient air from leaking in and contaminating the 1 K pot with ice. Use a pressure relief valve ($\lesssim 4$ psi bleed pressure) to avoid over-pressurization of the 1 K pot.

Step 6: If the same dewar, from Sec. C.2.4.1, is not still attached to the liquid Nitrogen transfer plumbing circuit, attach a new dewar and start the liquid Nitrogen transfer using the procedure discussed in Sec. C.2.4.1.

Step 7: Stop the transfer of liquid Nitrogen when the temperature sensor, at the bottom of the 4 K reservoir, falls to $\approx 100\text{K}$. This is a heuristically determined threshold for the appropriate amount of liquid Nitrogen transfer to the 4 K reservoir. The goal is to fill just enough liquid Nitrogen to last until the liquid Helium-4 transfer. Any excess, liquid Nitrogen will have to be forced out prior to the liquid Helium-4 transfer. However, if a liquid Helium-4 cool down is not necessary for the desired experiments, more liquid Nitrogen can be transferred to the 4 K reservoir at the user's discretion.

Step 8: After stopping the transfer of liquid Nitrogen, ensure all ports on the 4 K reservoir are sealed, in order to minimize the formation of ice inside said reservoir.

C.2.4.3 Cooling the Helium-3 insert and sample probe assembly

Step 1: Make sure the heat switch is fully engaged. Throughout the cool down process, perform periodic checks to ensure the mechanical switch is still engaged. Thermal contraction of the heat switch rod can cause the heat switch to disengage on its own.

Step 2: Open the needle valve 1-2 turns to transfer liquid Nitrogen from the 4 K reservoir to the 1 K pot. Close and re-open the needle valve periodically until the temperature of the 1 K pot falls below $\approx 100\text{K}$. The friction from the needle valve motion prevents ice from blocking said valve.

Step 3: The rate of temperature drop of the 1 K pot varies considerably depending on the circumstances. In my experience, a 0.5-1 K/min rate is reasonable. If, however, the rate is much slower than 1 K/min, there are a couple of methods/factors which can help speed up the cool down. Firstly, the 1 K pot pump can be used to suck liquid Nitrogen from the 4 K reservoir to the 1 K pot. Secondly, the pressure built up inside the *sealed* 4 K reservoir, from the liquid Nitrogen boil off, helps push the liquid Nitrogen from the 4 K reservoir into the 1 K pot. Either one or both of these factors can be exploited by the user depending on the circumstances. For example, I once used the 1 K pot pump to set up a sufficiently high flow rate of liquid Nitrogen from the 4 K reservoir to the 1 K pot. After turning off the pump, the pressure built up inside the 4 K reservoir was enough to sustain the flow. When the 1 K pot pump was off, I did not have to fill up the 1 K pot with Helium-4 gas, because the 1 K pot line was always over atmosphere, due to the liquid Nitrogen boil off from the cooling action on the 1 K pot.

C.2.4.4 77 K impedance test

This step is not relevant if the user does not plan on using Helium-3 for the cool down. Otherwise, the impedance test needs to be performed, using the procedure described in Sec. C.2.3, after the system has reached the end of the liquid Nitrogen cool down. Recall that the impedance measured at this stage is close to half its value at room temperature.

C.2.5 Liquid Helium-4 cool down

During the pre-cool-down, liquid Nitrogen was used bring the 4 K reservoir and the Helium-3 insert close to 100 K (c.f. Fig. C.2.4.2). As the name suggests, the 4 K reservoir has to be eventually brought close to 4 K using liquid Helium-4. Moreover, pumped liquid Helium-4 is required to bring the temperature of the 1 K and Helium-3 pots close to 1.5 K. In this section, I will describe the steps required to achieve these two goals.

C.2.5.1 Removing residual liquid Nitrogen from the 4 K reservoir and 1 K pot

In practice, there is always some residual liquid Nitrogen, in the 4 K reservoir and 1 K pot, leftover from the liquid Nitrogen pre-cool-down. It is very important to ensure liquid Helium-4 does not come in contact with that residual liquid Nitrogen. Otherwise the liquid Nitrogen will solidify and block the needle valve. The liquid Nitrogen removal step requires a hitherto unused port leading to the 4 K reservoir.

There is a fourth liquid Helium-4 fill port, in addition to the ones I defined in Sec. C.2.4; I will denote it D_{4K} . The difference between D_{4K} and rest of three ports (A_{4K} , B_{4K} , C_{4K}) is that the former is located on top of the Helium-3 insert. Note that there exists a step on the floor of the 4 K reservoir (c.f. Fig. 7.4.1) where the flange on top of the Helium-3 insert mates with the flange at the bottom of the 4 K reservoir. Only D_{4K} has direct line of sight to this lower section of the reservoir floor.

The steps for one method of liquid Nitrogen removal are as follows.

Step 1: Slowly remove the o-ring-sealed blank covering D_{4K} . Make sure to wear protective gloves and stay away from the path of the gas vented from D_{4K} .

Step 2: Insert an L-shaped tube through D_{4K} , long enough to reach the bottom of the 4 K reservoir, and make an approximate⁶ air-tight seal using quick disconnect fittings.

Step 3: Connect one end of a flexible (e.g. rubber) tube to the available end of the L-shaped tube. Insert the other end of the flexible tube into the closest 77 K reservoir fill port (e.g. A_{77K}).

Step 4: Connect a high pressure Helium-4 gas line to the Swagelok valve on port B_{4K} . Use the Swagelok valve to regulate the pressure inside the 4 K reservoir. Once the flow of liquid Nitrogen begins, leaving the Swagelok valve closed usually suffices. If the flow slows down or stops, open the Swagelok valve, as needed, to resume the liquid Nitrogen flow. The end of this liquid Nitrogen transfer is reached when opening the Swagelok valve only increases amount of gas vented from the flexible hose.

Step 5: Detach the flexible hose from the end of the L-shaped tube. Remove one of the blanks or relief valves from ports A_{4K} or C_{4K} . Detach the high pressure Helium-4 gas line from the Swagelok

⁶The sealing won't be perfect due to loss of elasticity in the quick disconnect o-rings.

valve and attach it to the end of the L-shaped tube. Make sure the Swagelok valve is closed. In this step, the goal is to use hot Helium-4 gas to evaporate any residual liquid Nitrogen at the lower section of the 4 K reservoir floor.

Step 6: Use the Lakeshore temperature controllers to set the temperatures of the two heater blocks (c.f. Fig. 7.6.3) at the bottom of the 4 K reservoir to (say) 80 K. Monitor the percentage of heater output. Over time, as the liquid Nitrogen boils off, the heater output will drop.

Step 7: Detach the high pressure Helium-4 gas line from the end of the L-shaped tube when the heater output on the Lakeshore controller reads zero. Moreover, if the temperature of the two heater blocks is close to 80 K, and rises slowly with the heaters off, then there is no more liquid Nitrogen left in the 4 K reservoir.

Step 8: Seal the 4 K reservoir from atmosphere by reattaching the appropriate blanks or relief valves to ports A_{4K} , C_{4K} , and D_{4K} and ensuring the Swagelok valve on port B_{4K} is closed.

Step 9: Repeat the *equivalents* of steps 5-7 for the 1 K pot. The main differences will be: (a) hot Helium-4 gas will be fed to the 1 K pot using its elbowed pumping path, instead of the L-shaped tube, and (b) the heater blocks on the 1 K plate will be used.

Step 10: Close the needle valve and start pumping on the 1 K pot with its pump (Pfeiffer Hena 60).

Note that, throughout *most* of the liquid Nitrogen removal process, the 4 K reservoir and 1 K pot are over-pressurized. The remainder of the steps, involving minor hardware reconfiguration, should be performed as quickly as possible. In that way, the degree of ice contamination in the the 4 K reservoir and 1 K pot are kept to a minimum.

C.2.5.2 Liquid Helium-4 transfer

Step 1: Fill the 77 K reservoir, to its full capacity, with liquid Nitrogen (c.f. Sec. C.2.4.1). This will minimize liquid Helium-4 boil off due to radiative heating from the 77 K reservoir.

Step 2: Remove the blank on port D_{4K} and attach the rigid liquid Helium-4 bayonet transfer line to said port with an extension tip that reaches the lower section of the 4 K reservoir floor. Port D_{4K} is used as the fill port in the initial liquid Helium-4 transfer to minimize boil off losses. If say, port A_{4K} was used,⁷ accumulation would take longer due to unfocused “spraying” of liquid Helium-4 on the walls of the 4 K reservoir. Port A_{4K} can, however, be used for liquid Helium-4 refills.

Step 3: Connect the Helium-4 diversion system (c.f. Sec. 7.7.1.3) to the KF 25 vent port on top of the Helium-3 insert.

Step 4: Make sure the cable from the level monitor (Cryomagnetics LM-500) is attached to the end of the level probe in port B_{4K} . Turn on the level monitor.

Step 5: Position the flexible liquid Helium-4 transfer line such that downstream end is within a few feet of the bayonet transfer line. Use (say) zip ties to support and strain relieve the flexible transfer line on the closest guard rail of the support frame (c.f. Fig. 8.1.2).

Step 6: Lower the upstream end of the flexible transfer line into a 100 liter dewar of liquid Helium-4. Lower the transfer line into the dewar slowly ($\approx 5"/\text{min}$) to pre-cool the former and minimize liquid

⁷Note that the extension tip won't be used in this case.

Helium-4 boil off. Keep an eye on the downstream end of the flexible transfer line for visible emission. Depending on the circumstances, this emission could appear as a blue “plume” or a colorless fog.

Step 7: Once any form of emission from the downstream end of the flexible transfer line appears, halt lowering upstream end of said transfer line into the dewar.⁸ Quickly insert the downstream end of the flexible transfer line into the bayonet transfer line and make an o-ring seal between both transfer lines with the quick disconnect fittings on them.

Step 8: Continue lowering the upstream end of the flexible transfer line into the dewar until the former hits the bottom of the latter. Raise the transfer line ≈ 1 " higher and tighten its quick disconnect fitting onto the dewar. This is done to avoid ice at the bottom of the dewar from clogging the transfer line.

Step 9: Using the valve, in front of the high pressure Helium-4 gas line, on the custom cross with NPT (National Pipe Thread) fittings (c.f. Sec. C.2.1), maintain the reading on the compound gauge at 1/2 psi until accumulation of liquid Helium-4 starts in the 4 K reservoir. Initially, liquid Helium-4 emitted by the bottom of the bayonet transfer line will evaporate immediately after it hits the bottom of the 4 K reservoir. Accumulation of liquid Helium-4 will only start once the temperature of the bottom of the 4 K reservoir gets low enough to sustain the former.

Step 10: When accumulation of liquid Helium-4 starts, set the pressure on the compound gauge to 1 psi. Note that the liquid Helium level probe in port B_{4K} is ≈ 2 " higher than the lower section of the 4 K reservoir floor. Therefore, the level monitor will not provide any reliable reading until the actual liquid Helium level is above 2".

Step 11: Similar to the liquid Nitrogen pre-cooling step (c.f. Sec. C.2.4.3), open and close the needle valve periodically to prevent said valve from freezing. Moreover, periodically tighten the mechanical heat switch to compensate for its contraction during the cool down.

Step 12: Be prepared to stop the liquid Helium-4 transfer as the level monitor reading approaches 16". In practice, however, for previous cool downs the 100 liter dewar was empty before the 4 K reservoir reached its full capacity. The liquid Helium-4 dewar makes the same whistling sound as the liquid Nitrogen one when it is close to empty. Nevertheless, if the liquid Helium-4 transfer does need to be stopped for any reason, then the following steps must be followed:

- Bleed the pressure in the dewar using the ball valve on the custom cross with NPT (National Pipe Thread) fittings.
- Remove the upstream end of the flexible liquid Helium-4 transfer line from the dewar.
- Disconnect the downstream end of the flexible transfer line from the bayonet transfer line.
- Remove the the bayonet transfer line from port D_{4K} and blank off the latter.
- Disconnect the Helium-4 diversion system and blank off the KF 25 vent port on top of the Helium-3 insert.

In case of a liquid Helium-4 refill, insert the bayonet transfer line into port A_{4K} , without the extension tip, and resume the transfer using the steps discussed above.

Step 13: Open the needle valve approximately a 1/4 turn and leave the 1 K pot pump on. After completion of the liquid Helium-4 transfer, it usually takes 10-12 hours for the 1 K pot to reach its base temperature (≈ 1.5 K).

⁸Fix the position of the upstream end of flexible transfer line using (say) a small clamp.

C.3.1 Sleeveless wiring

As I mentioned in Sec. 7.8.4.1, since the dust from the fiberglass sleeves (c.f. Fig. 7.6.5) posed a serious risk to the analyzer, the former was eliminated from the new wiring design. Based on feedback from the Janis technician of another ARPES Helium-3 system, I decided to pursue a sleeveless design. In this design, the protection aspect of the sleeves was *effectively* provided by the Kapton-insulated Copper wires. Since the Manganin wire is too frail to be installed on its own, it is bundled with Copper wires. Two pairs of Manganin and one pair of Copper wires were grouped according to the sensor-heater pairs to which they belonged. The wire bundle was tied together using a 0.0075" diameter PEEK string. In fact, as shown in Fig. C.3.1, the PEEK string was also used to fix the wires to mechanical anchor points in the cryostat.

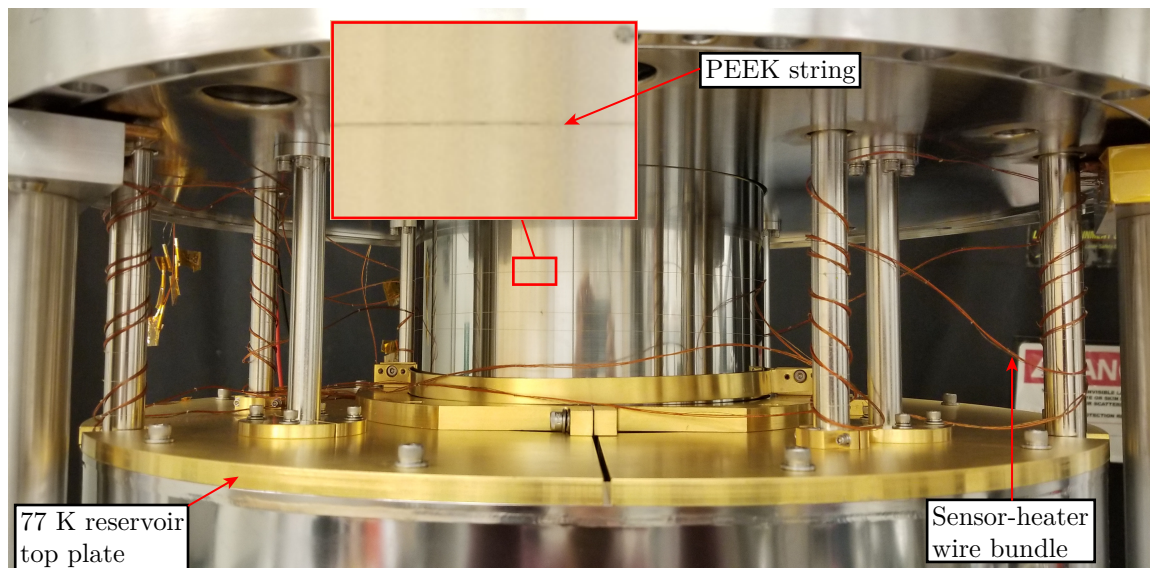


Figure C.3.1: Photograph of the sleeveless wiring network near the radiation shielding plate at the top of the 77 K reservoir

For reasons discussed in Sec. 7.6.3.2, each wire bundle was made of roughly 15 feet long wires. For the sake of organization, it was convenient to start over with a new batch of wiring, and discarding the old ones. Most of the sensors,¹⁰ heaters, and heater blocks (c.f. Sec. 7.6.2) were salvaged from the old design.¹¹ Moreover, all the sensors and heaters were fitted with detachable connectors.

One of the major drawbacks of the sleeveless design, however, was the susceptibility of the Manganin wires to damage from handling. It is easy to see from Fig. C.3.1, that as the density of the wire bundles grew, so did the likelihood of wire damage. This made the wire installation (or wire routing) very difficult. But it was decided to trade ease of installation for the security of a fiberglass-free wiring system. Upon completion of the wiring process, some non-essential sensor and heater wires were found to be broken. At the time, these damages were considered acceptable, and a cool down test was performed on the cryostat. Unfortunately, the thermal contraction from the cool down led to further sensor damages; most notably the 1 K pot and plate sensors. After some damage analysis, a new wiring plan was devised.

¹⁰In this context, sensors refers to the entire “chip + bobbin unit” shown in the photograph in the inset of Fig. 7.6.2.

¹¹All of the heaters and heater blocks were salvaged. 15 out of 16 sensors could be salvaged. 1 new silicon diode sensor was purchased and repackaged into a new bobbin.

C.3.2 Modular network with PEEK sleeves

Before describing the new design, I will discuss some of the lessons that were learned from the sleeveless design. Aside from the lack of sleeves, the biggest factor which contributed to wire damage was lack of modularity. It impractical to guarantee a 15 feet long Manganin wire, of 0.005" diameter, to remain intact after being routed through an already congested cryostat (c.f. Fig. C.3.1). Moreover, replacement of a damaged wire infeasible because the dense network of wires inevitably became entangled.

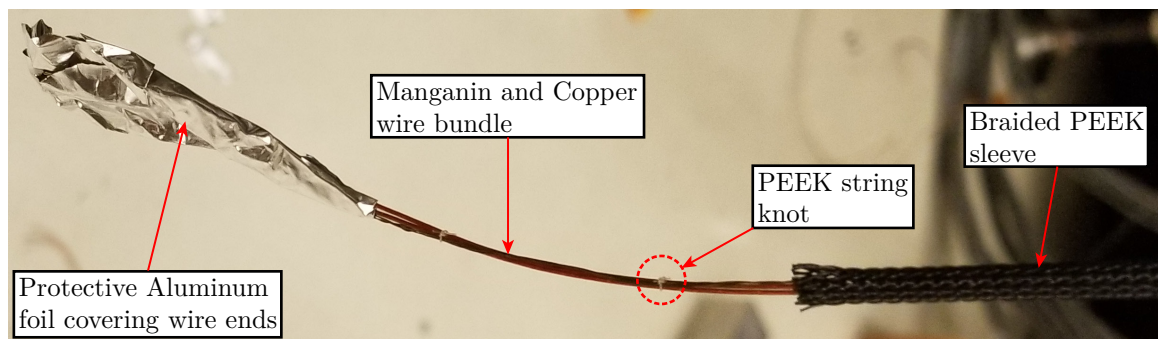
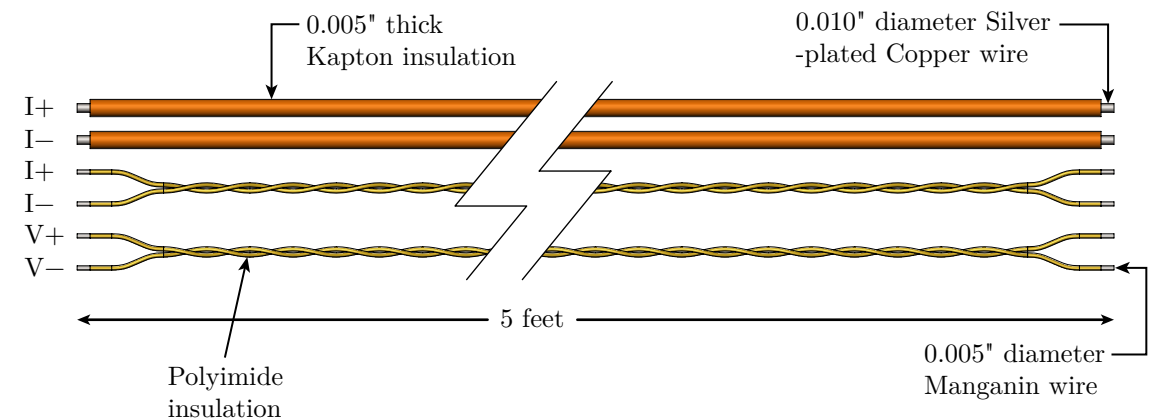


Figure C.3.2: CAD model of photograph of a bundle of two and one pair of insulated Manganin and Copper wires respectively. The photograph shows the protective braided PEEK sleeve. This entity is defined as a *wire module*.

In the new design, the 15 feet long continuous wire bundle (1 bundle = 4 Manganin + 2 Copper wires) was divided into three 5 feet long segments; I will refer to this segment as a *wire module*. Around the same time the modular wiring design was being formulated, I discovered the availability of commercial braided PEEK sleeves, which did not suffer from the dust problem of their fiberglass counterparts. Fig. C.3.2 shows a photograph of the end of one of the wire modules with the PEEK sleeve installed. A sketch of the wire module is also shown for ease of visualization.

In Fig. C.3.2, note that the two pairs of Manganin and one pair of Copper wires are bound using PEEK string knots in the regions they are not covered by the PEEK sleeve. In the sleeveless design, a 15 feet long wire bundle required close to 150 such knots! Therefore, the use of PEEK sleeves made preparation of the wire bundle significantly easier.¹²

¹²In fact, I would argue that the time saved from not having to tie these knots was greater than the extra time it took to solder pin connectors (c.f. Fig. C.3.3) onto the wires.

C.3.3 Wire heat sinking

One highly beneficial use of modularity in the new design was in the design of heat sinks. Two wire modules (c.f. Fig. C.3.2) are connected to heat sinks using the gendered pin connectors shown in Fig. C.3.3. This design has the following advantages over the original one (c.f. Fig. 7.6.6):

- the increase in effective contact area by the epoxy improves thermal conductance between the wires and the bobbin,
- elimination of the wire clamp avoids the risk of cutting wires, after thermal contraction, by the sharp edges of the former and the bobbin,
- stripping of the sleeves at the heat sink locations is not required,¹³ and most importantly,
- since the new heat sink serves as an independent module, it can be replaced by simply changing the pin connections.

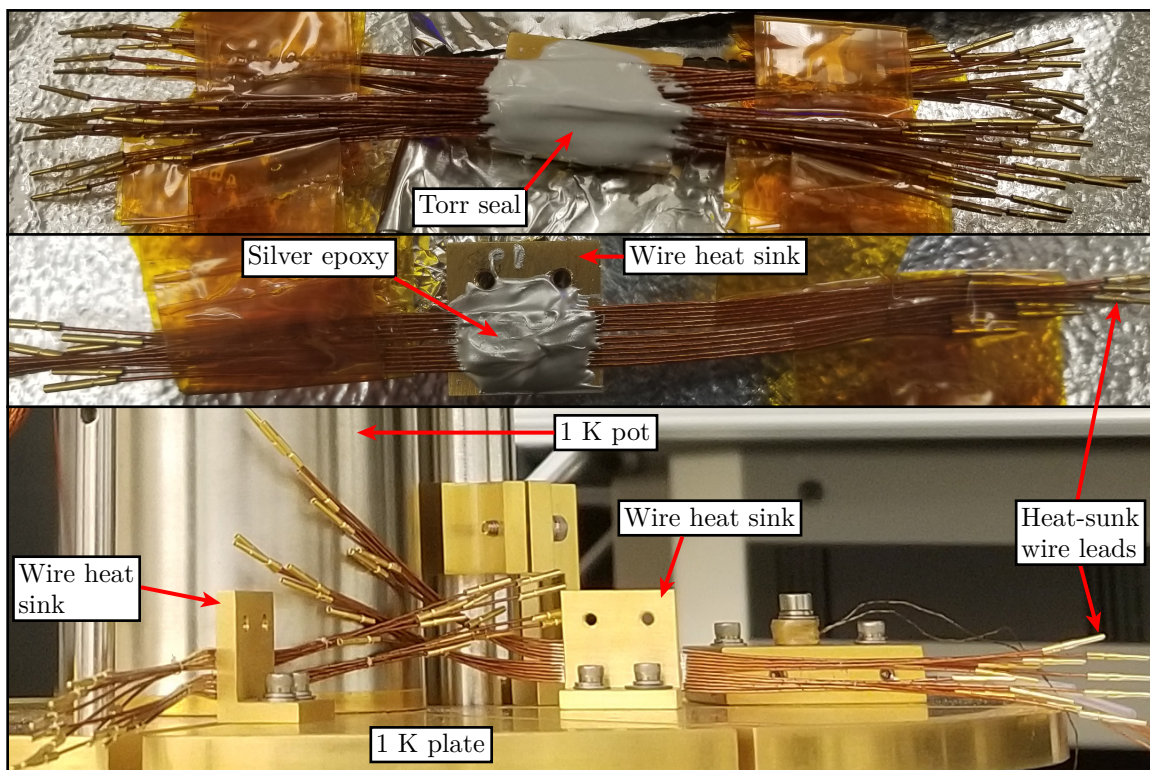


Figure C.3.3: The upper two photographs show Kapton-insulated Copper wires epoxied to the heat sinks to be connected to the 1 K plate (Silver epoxy) and the top of the 77 K reservoir (Torr seal). The lower photograph shows the heat sinks thermally anchored to the 1 K plate.

Fig. C.3.3 shows Kapton-insulated Copper wires epoxied to the heat sinks using Silver epoxy (EPO-TEK® H20E) and Torr Seal®. Due to the high cost per unit volume of Silver epoxy, it was only used for lower temperature heat sinks like the ones anchored to the 4 K reservoir bottom and 1 K plate. Moreover, Silver epoxy is significantly more thermally conductive than Torr seal at lower temperatures. The heat sink with Torr seal was anchored to the top of the 77 K reservoir (c.f.

¹³In the original design (c.f. Sec. 7.6.3.3), stripping of the sleeves was a source of fiberglass dust.

Fig. C.3.1).¹⁴ Note that only Copper wires are used for heat sinking both sensor and heater wires. This is done for two reasons: (a) the Copper wires are more robust to damage compared to their Manganin counterparts, and (b) large thermal conductivity to a heat sink is desired.

C.3.4 Fabrication

I discussed the fabrication of the wire modules in Sec. C.3.2. In this section I'll focus on the connectors. The two main gendered connectors used in this wiring design were: (a) 4-pin PEEK connectors, and (b) 1-pin connectors. Due to the small size of the connectors,¹⁵ and fragility of the Manganin wires, an elaborate soldering setup (c.f. Fig. C.3.4) was required for efficient wire fabrication.

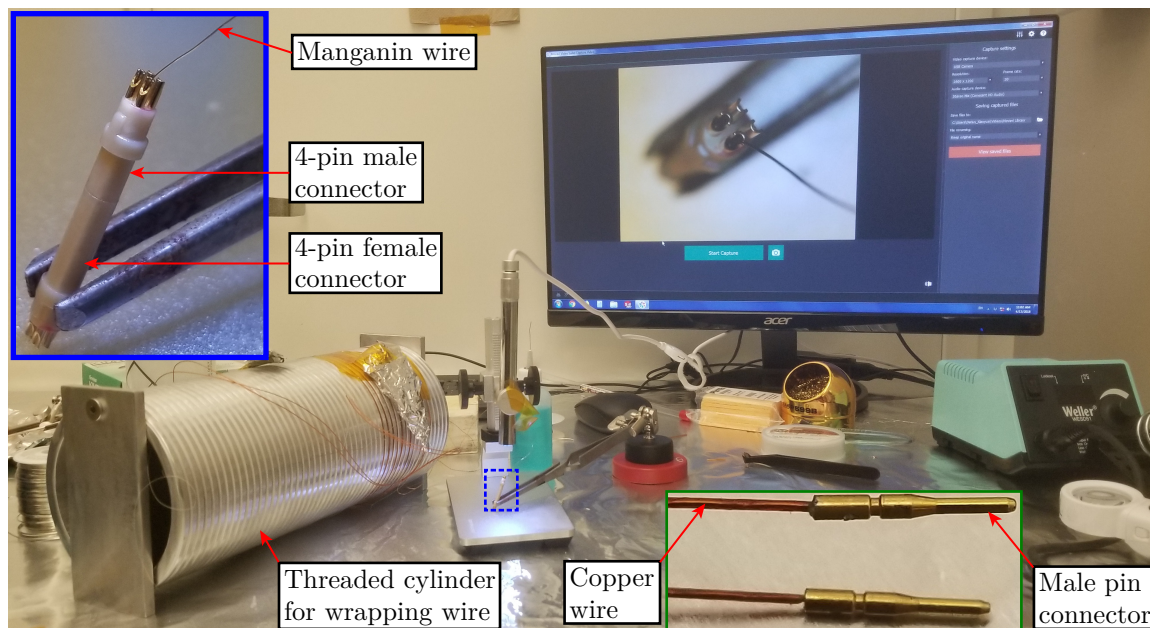


Figure C.3.4: An example of an apparatus for soldering Manganin wires on 4-pin connector.

The 4-pin connectors were only connected to Manganin wires due to the former's small size. Whereas the 1-pin connectors were used for both Copper and Manganin wires. A female 4-pin connector was connected to the 4 Manganin wires ($V+$, $V-$, $I+$, and $I-$) emerging from the epoxy on the sensor bobbin (c.f. Fig. 7.6.2). Both ends of the wire module (c.f. Fig. C.3.2) were fitted with 1-pin connectors except the last module which directly connected to a sensor. The 4 Manganin wires on one end of the last wire module were fitted with a male 4-pin connector. Female 1-pin connectors were attached to the two terminals of the firerod heaters (c.f. Fig. 7.6.3) and wire-wound heaters. In order to connect two firerod heaters in parallel, a Y-shaped adapter was fabricated using Copper wires and 1-pin connectors.

Furthermore, the UHV-incompatible feedthrough pins (c.f. Fig. 7.6.4), from the original wiring system, were replaced by mechanically similar ones made of gold-plated Beryllium Copper.

Lead- and Cadmium-free Stay Brite® (96% Tin and 4% Silver) solder, with a melting point of 430 °F, was used to attach the connectors onto the wires. An organic soldering flux called Superior No. 30 SuperSafe™ was used.

¹⁴Since the bobbin on top of 77 K reservoir is first stage heat sinking stage, it has to accommodate 88 (out of 100) wires, and therefore significantly more epoxy was required.

¹⁵Each pin in either type of connector (1- or 4-pin) was about 1 mm in diameter or less.

After soldering the Manganin wires on the 4-pin connector, protective Kapton sleeves were used to cover the soldered region. This was done to avoid accidental shorting out of the pins due to their potential deflection under mechanical or thermal stresses.¹⁶ Moreover, since the 1-pin connectors did not have an insulation layer like their 4-pin counterparts (i.e. PEEK), a Teflon™ sleeve was used to cover the former. In some cases, tension in the wire modules would decouple the 1-pin connectors. Therefore, some of the Teflon™ sleeves were replaced with UHV-compatible heat shrink tubes made of Polyvinylidene fluoride (PVDF). Furthermore, at the heat sink locations, tension in the wire modules would cause the Manganin wires to break. Therefore, additional mechanical support was provided to the Manganin wires using Kapton tape (c.f. Fig. C.3.5). The Kapton tape is backed with a Silicone-based (UHV-compatible) adhesive.

The final, and most important step, of fabrication was cleaning. This step removed non-UHV-compatible remnants like the dirt from the soldering iron and residue to the organic soldering flux. All wiring components were sonicated in acetone bath followed by a methanol rinse.

C.3.5 Wiring labels

In Sec. 7.6.3.1, I briefly mentioned the importance of labeling the wires. In the original (non-modular) wiring system, the wires were only labeled close to the 20-pin feedthrough using UHV-incompatible plastic rings (c.f. Fig. 7.6.4). One of the design goals of the new design was to eliminate the latter. Moreover, the new design, due to its modular nature, required labels at multiple locations.

Fig. C.3.5 shows the new labels generated by stamping aluminum blanks. Two types of blanks were used:

- smaller elliptical labels for the feedthrough pins, and
- larger rectangular labels for the wire modules.

The latter was installed on both ends of the wire module.

¹⁶For some 4-pin connectors, the solder “blobs,” on nearby pins, left a very small gap between each other.

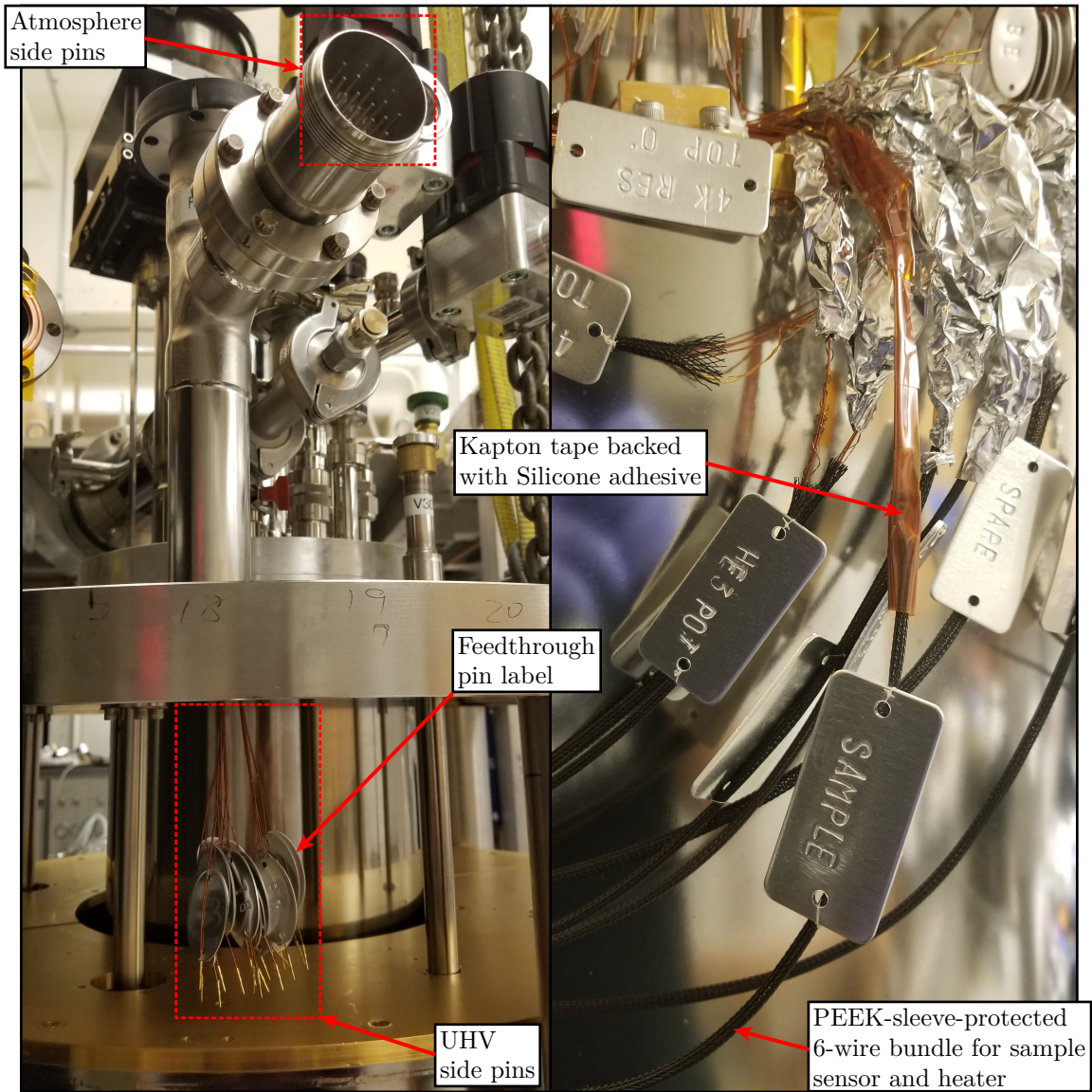


Figure C.3.5: Examples of metal-stamped labels for the feedthrough pins and wire bundles.

Appendix D

Optics

D.1 Non-zero $\chi^{(2)}$ tensor elements

Using the form of $\chi^{(2)}$ defined in Eq. (9.3.2), some examples of the non-zero tensor elements are schematically given by Fig. D.1.1. The small (large) dot corresponds to a zero (non-zero) element. The matrix components connected by a line represent elements with equal magnitude. Open and closed symbols connected by a line have opposite sign. The square represents an element that is zero when Kleinman's symmetry is present. Dashed lines are only valid in the presence of Kleinman's symmetry.

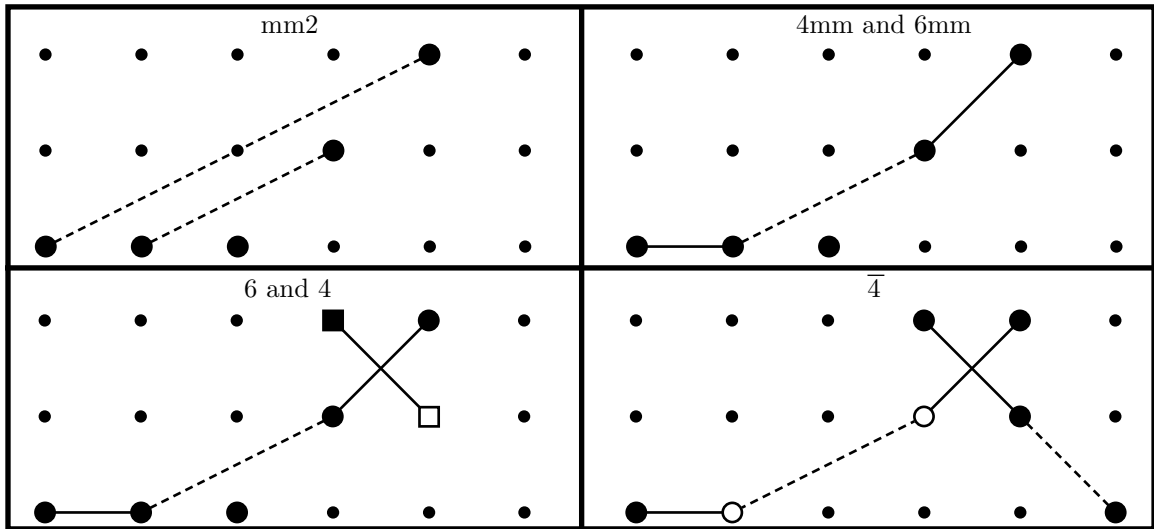


Figure D.1.1: The non-zero elements of the $\chi^{(2)}$ tensor for classes mm2, 4mm, 6mm, 6, 4, and $\bar{4}$.

D.2 RA-SHG analysis for of $\text{CH}_3\text{NH}_3\text{PbI}_3$

The theoretical SHG patterns for *surface* point group mm2 for different polarizations are:

$$I_{P_{\text{in}}-P_{\text{out}}}^{\text{mm}2}(\phi) = \sin^2(\theta) [\chi_{zzz} \sin^2(\theta) + \{\cos^2(\theta) \{ (2\chi_{xxz} + \chi_{zxx}) \cos^2(\phi) \} + (2\chi_{yyz} + \chi_{zyy}) \sin^2(\phi) \}]^2, \quad (\text{D.2.1})$$

$$I_{S_{\text{in}}-P_{\text{out}}}^{\text{mm}2}(\phi) = \sin^2(\theta) [\chi_{zyy} \cos^2(\phi) + \chi_{zxx} \sin^2(\phi)]^2, \quad (\text{D.2.2})$$

$$I_{P_{\text{in}}-S_{\text{out}}}^{\text{mm}2}(\phi) = \frac{1}{4} \sin^2(2\theta) [\chi_{xxz} - \chi_{yyz}]^2 \sin^2(2\phi), \quad (\text{D.2.3})$$

$$I_{S_{\text{in}}-S_{\text{out}}}^{\text{mm}2}(\phi) = 0. \quad (\text{D.2.4})$$

where ϕ and θ are the scattering plane angle and angle of laser incidence respectively. With $\theta \approx 10^\circ$, I can fit (D.2.1)-(D.2.3) to the data I get

$$\chi_{xxz} = 2.66041, \quad (\text{D.2.5})$$

$$\chi_{yyz} = -1.44669, \quad (\text{D.2.6})$$

$$\chi_{zyy} = -0.0333659, \quad (\text{D.2.7})$$

$$\chi_{zxx} = -4.75148, \quad (\text{D.2.8})$$

$$\chi_{zzz} = 161.593. \quad (\text{D.2.9})$$

The theoretical SHG patterns for *bulk* point group 4mm for different polarizations in the 100 direction are:

$$I_{P_{\text{in}}-P_{\text{out}}}^{4\text{mm}}(\phi) = \cos^2(\theta) \cos^2(\phi) \left[(2\chi_{xxz} + \chi_{zxx}) \sin^2(\theta), \right. \\ \left. + \cos^2(\theta) \{ \chi_{zzz} \cos^2(\phi) + (2\chi_{xxz} + \chi_{zxx}) \sin^2(\phi) \} \right]^2, \quad (\text{D.2.10})$$

$$I_{S_{\text{in}}-P_{\text{out}}}^{4\text{mm}}(\phi) = \cos^2(\theta) \cos^2(\phi) [\chi_{zxx} \cos^2(\phi) + (-2\chi_{xxz} + \chi_{zzz}) \sin^2(\phi)]^2, \quad (\text{D.2.11})$$

$$I_{P_{\text{in}}-S_{\text{out}}}^{4\text{mm}}(\phi) = \sin^2(\phi) [\chi_{zxx} \sin^2(\theta) + \cos^2(\theta) \{ (-2\chi_{xxz} + \chi_{zzz}) \cos^2(\phi) \\ + \chi_{zxx} \sin^2(\phi) \}]^2, \quad (\text{D.2.12})$$

$$I_{S_{\text{in}}-S_{\text{out}}}^{4\text{mm}}(\phi) = \sin^2(\phi) [(2\chi_{xxz} + \chi_{zxx}) \cos^2(\phi) + \chi_{zzz} \sin^2(\phi)]^2. \quad (\text{D.2.13})$$

D.3 Phase matching

Fig. D.3.1 illustrates the propagation of extraordinary and ordinary rays in a (uniaxial) birefringent crystal. In this configuration, the refractive index, $\tilde{n}_e(\theta)$, experienced by the extraordinary ray is

$$\frac{1}{\tilde{n}_e^2(\theta)} = \frac{\cos^2(\theta)}{n_o^2} + \frac{\sin^2(\theta)}{n_e^2}, \quad (\text{D.3.1})$$

where n_e and n_o are the refractive indices experienced by a wave with polarization parallel and perpendicular to the optical axis respectively.

The Sellmeier equations for BBO are [118]

$$n_o^2(\lambda) = 2.7359 + \frac{0.01878}{\lambda^2 - 0.01822} - 0.01354\lambda^2, \quad (\text{D.3.2})$$

$$n_e^2(\lambda) = 2.3753 + \frac{0.01224}{\lambda^2 - 0.01667} - 0.01516\lambda^2, \quad (\text{D.3.3})$$

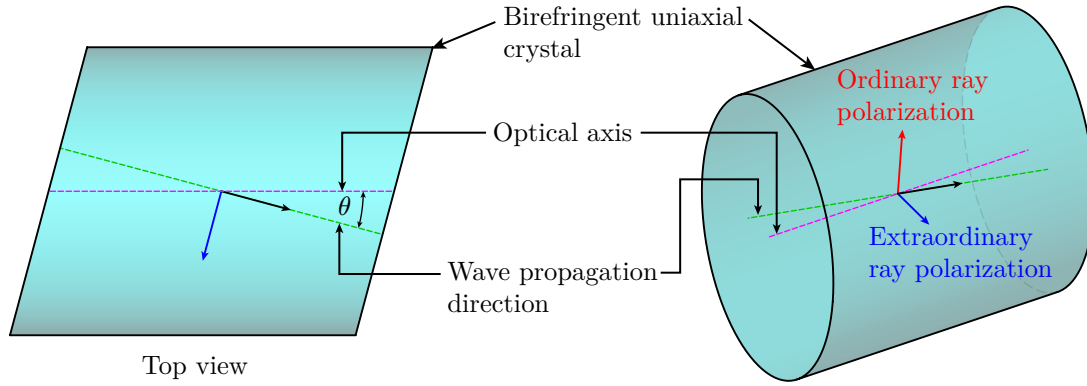


Figure D.3.1: Propagation of an electromagnetic wave through a birefringent material.

where λ is measured in microns. For type 1 phase matching, I am interested in determining the angle of propagation, θ , at which two ordinary rays photons at the fundamental wavelength, λ_f , combine to produce one extraordinary ray photon with wavelength $\lambda_{\text{SHG}} = \lambda_f/2$. In other words, I need to solve the equation

$$\tilde{n}_e(\theta, \lambda_{\text{SHG}}) = n_o(\lambda_f), \quad (\text{D.3.4})$$

to find θ . Therefore, plugging (D.3.1) in (D.3.4) I get

$$\frac{1}{n_o^2(\lambda_f)} = \frac{\cos^2(\theta)}{n_o^2(\lambda_f/2)} + \frac{\sin^2(\theta)}{n_e^2(\lambda_f/2)}, \quad (\text{D.3.5})$$

$$\theta = \sin^{-1} \left[\frac{n_e(\lambda_f/2)}{n_o(\lambda_f)} \left(\frac{n_o^2(\lambda_f/2) - n_o^2(\lambda_f)}{n_o^2(\lambda_f/2) - n_e^2(\lambda_f/2)} \right)^{1/2} \right]. \quad (\text{D.3.6})$$

If I denote θ_{SHG} and θ_{FHG} as the propagation directions for the SHG process corresponding to $822 \text{ nm} \rightarrow 411 \text{ nm}$ and $411 \text{ nm} \rightarrow 205.5 \text{ nm}$ respectively, then using (D.3.2) and (D.3.3) in (D.3.6) I get

$$\theta_{\text{SHG}} = 28.40^\circ, \quad (\text{D.3.7})$$

$$\theta_{\text{FHG}} = 84.64^\circ, \quad (\text{D.3.8})$$